Multifunctional implants Prevention is better than cure

van Hengel, I.A.J.

DOI
10.4233/uuid:4a63988e-dcd7-4305-b86a-5e8fe82b8519

Publication date
2022

Document Version
Final published version

Citation (APA)
van Hengel, I. A. J. (2022). *Multifunctional implants Prevention is better than cure*. [Dissertation (TU Delft), Delft University of Technology]. https://doi.org/10.4233/uuid:4a63988e-dcd7-4305-b86a-5e8fe82b8519

Important note
To cite this publication, please use the final published version (if applicable).
Please check the document version above.

Multifunctional implants
Prevention is better than cure

Ingmar van Hengel

Multifunctional implants
Prevention is better than cure

PROEFSCHRIFT

Ter verkrijging van de graad van doctor
aan de Technische Universiteit Delft,
op gezag van de Rector Magnificus Prof.dr.ir. T.H.J.J. van der Hagen,
voorzitter van het College voor Promoties,
in het openbaar te verdedigen op
vrijdag 23 september 2022 om 12:30 uur

door

Ingmar Aeneas Jan VAN HENGEL

Biomedisch Ingenieur, Technische Universiteit Delft, Nederland
en
Biomedisch Wetenschapper, Universiteit Leiden, Nederland

Geboren te Driebergen-Rijsenburg, Nederland

Dit proefschrift is goedgekeurd door de promotor.

Samenstelling promotiecommissie bestaat uit:

Rector Magnificus	Voorzitter
Prof.dr. A.A. Zadpoor	Technische Universiteit Delft, Nederland, *Promotor*
Dr.ir. I. Apachitei	Technische Universiteit Delft, Nederland, *Copromotor*
Onafhankelijke leden:	
Prof.dr.ir. J.M.C. Mol	Technische Universiteit Delft, Nederland
Prof.dr. H.E.J. Veeger	Technische Universiteit Delft, Nederland
Prof.dr. H.C. van der Mei	Rijksuniversiteit Groningen, Nederland
Prof.dr. D.W. Grainger	The University of Utah, Verenigde Staten
Dr.ir. M.J.M. Hermans	Technische Universiteit Delft, Nederland

Keywords:	implant associated infection, surface biofunctionalization, biomaterials, additive manufacturing, bone tissue engineering, multifunctional implants
Cover design:	the author and Scixel Reproduced from *Van Hengel et al.*, with permission from the Royal Society of Chemistry.
Layout:	Publiss | www.publiss.nl
Printed by:	Ridderprint | www.ridderprint.nl

Distribution of this thesis was supported by:
Anna Fonds | NOREF

The research leading to these results has received funding from Interreg VA Flanders – The Netherlands program, CCI grant no. 2014TC16RFCB046.

ISBN 978-94-6384-359-1

An electronic version of this dissertation is available at https://repository.tudelft.nl/.

FOREWORD

"Everyone knows someone with a hip or knee implant". Over the course of four years I started numerous presentations with this statement and it turned out to be nearly always correct. That this topic is very tangible is one of the reasons why I decided to perform my PhD in this area. Many people inquired, albeit often jokingly, when they could receive one of the implants we were developing and there is already a substantial 'waiting list'. I was even contacted by a patient from abroad who wondered whether our implants would soon be ready for clinical use. It surprised me how frequently complications occur after orthopedic surgeries. All these stories left a great impression and motivated me to conduct this research, and I am grateful to everyone who shared their story.

In this thesis you will find only the scientific output of my research that resulted in journal publications. The work behind the scenes, *i.e.* the 'blood, sweat and tears', cannot be captured on paper. However, in my opinion these experiences are truly what a PhD is about. Not the success stories we tell at conferences capture the essence of scientific research, but rather what we do at the end of the day when we encounter yet another unexpected result. All publications in this thesis did not go according to the initial plan. And it is probably for the better that they did not.

Ingmar van Hengel

SUMMARY

Millions of people around the globe receive orthopedic implants every year. These implants help people to regain their mobility and contribute tremendously to improve the quality of life. However, a significant number of patients suffer from complications, such as implant associated infections (IAI) and aseptic loosening. The number of orthopedic implants is expected to increase due to an aging and increasingly obese population. As a result, the number of complications will rise too. In addition, the treatment of IAI is complicated by the development of antibiotic resistant bacteria. The focus of researchers has, therefore, shifted more and more towards the prevention of complications. In the words of Desiderius Erasmus: "Prevention is better than cure."

To tackle both IAI and aseptic loosening, it is important to develop multifunctional implants with optimal mechanical, chemical, and biological characteristics. The (surface) properties of these implants should be such that bacteria cannot attach onto the implant surface while bone regeneration is promoted. These properties will contribute to infection prevention and proper implant fixation. Implants with mechanical properties that are adjusted to meet the patient's needs may be nowadays produced by additive manufacturing (AM), which enables the fabrication of previously impossible volume-porous implant designs. These implants can be designed to prevent stress shielding, thereby stimulating bone ingrowth while also enhancing their fatigue life and, thus, the longevity. To optimize the chemical and biological properties of the implant, the implant surface needs to be biofunctionalized through surface treatment.

The goal of this thesis was to manufacture multifunctional implants and assess their antibacterial and osteogenic properties. Highly porous implants were rationally designed and subsequently produced using AM. Consequently, the surface of these implants was biofunctionalized by plasma electrolytic oxidation (PEO), which is an electrochemical surface modification technique. Through the incorporation of antibacterial elements, such as silver, copper, and zinc nanoparticles (NPs), on the one hand and osteogenic elements, such as calcium, phosphate, and strontium, on the other, the implants were biofunctionalized to both prevent IAI and improve osseointegration. Different combinations of silver NPs with copper, zinc, and strontium were investigated to determine and exploit their synergistic antibacterial activity and block the development of bacterial resistance.

The biomaterial characteristics, such as the surface morphology, chemical and phase composition, and ion release kinetics were assessed, followed by investigations of the antibacterial properties as well as the effects on biocompatibility and osteogenic differentiation. The antibacterial tests were performed against methicillin-resistant *Staphylococcus aureus*

(MRSA), a resistant strain which is frequently involved in IAI and difficult to treat with antibiotics. These tests were initially conducted *in vitro*, yet the antibacterial properties were also tested *ex vivo* and *in vivo* in a bone infection model.

First, we thoroughly reviewed the progress made in the biofunctionalization of titanium biomaterials using PEO and supplemented with silver, copper, and/or zinc to produce antibacterial implants (Chapter 2). We analyzed the PEO processing parameters, methodologies of antibacterial testing, and the investigations of biocompatibility. In addition, we reported and compared the results of the studies. We observed that silver had the strongest antibacterial activity, but also induced the most cytotoxicity, while combining two elements of silver, copper, and/or zinc resulted in potent antibacterial activity without inducing cytotoxicity. Most studies tested antibacterial behavior against *S. aureus*, usually with a single antibacterial assay, which limits the validity of the results of most studies. We identified the combination of silver, copper, and zinc as a promising strategy for future research. Furthermore, testing future implants should be done in models designed to analyze the prevention (and not the treatment) of IAI. Moreover, to date, no *in vivo* studies have been performed using bone infection models to evaluate the performance of PEO-biofunctionalized implants.

Subsequently, we tested whether porous AM implants could be biofunctionalized successfully using PEO and silver NPs (Chapter 3). In addition, we assessed those implants in a novel *ex vivo* bone infection model. Therefore, porous implants were designed and fabricated which had a 3.75 times larger surface area as compared to their solid counterparts. This resulted in the successful incorporation of silver NPs onto the porous implant surfaces with a four-fold increase in the ion release as compared to solid (*i.e.,* fully dense) implants. Furthermore, hydroxyapatite, was formed on porous implants but was not observed on solid implants. Porous implants showed enhanced antibacterial activity *in vitro* and *ex vivo*. Meanwhile, PEO biofunctionalization with silver implants did not induce cytotoxicity and even enhanced the metabolic activity of human mesenchymal stem cells. Porous implants biofunctionalized with silver NPs demonstrated potent antibacterial activity, which was enhanced as compared to solid implants.

Next, we investigated the performance of AM porous titanium implants biofunctionalized with a combination of silver NPs and either copper NPs (Chapter 4) or zinc NPs (Chapter 5), elements which are known to have both antibacterial and osteogenic properties. Therefore, silver and copper or zinc NPs were mixed in PEO electrolytes with different ratios ranging from 0 to 100%. Biofunctionalization with both silver and copper or zinc NPs resulted in reduced silver ion release in the first 24 hours as well as a continuous ion release of all elements for at least 28 days. Furthermore, the antibacterial activity was synergistically enhanced and the dose of silver ions was reduced by one or two orders of magnitude when combined with

copper or zinc, respectively. There were also no signs of cytotoxicity against preosteoblasts. Combining silver NPs with copper and/or zinc NPs is, thus, a promising strategy to enhance antibacterial properties and biocompatibility while simultaneously reducing the likelihood of bacterial resistance.

We analyzed the biofunctionalization of titanium implants with silver NPs and strontium (Chapter 6), an osteogenic element used to treat patients with osteoporosis. We observed a synergistic antibacterial behavior between strontium and silver ions, which enabled a 4-32 folds reduction in the release of silver ions. We also did not observe any signs of cytotoxicity against preosteoblasts while the addition of strontium enhanced the metabolic activity and osteogenic differentiation. Combining silver NPs with strontium resulted in functionality-packed implants that are highly antibacterial and enhance the osteogenic properties of the implants.

Thereafter, we assessed the effects of the PEO processing parameters on the surface morphology, surface chemistry, and the accompanying osteogenic properties of AM volume-porous implants (Chapter 7). Different oxidation times and current densities were investigated using PEO electrolytes that did or did not include strontium. We observed that increasing the oxidation times and current densities resulted in an enhanced titanium oxide layer thickness as well as increased release of ions and different phase compositions. The addition of strontium to the PEO electrolyte resulted in reduced calcium incorporation into the titanium oxide layer, thinner oxide layers, and enhanced porosity as compared to solely calcium- and phosphate- containing PEO electrolytes. These changes resulted in an enhanced osteogenic differentiation of preosteoblasts. Varying the PEO parameters is, thus, a powerful approach for optimizing the surface chemistry and morphology of implant surfaces to achieve optimal biofunctionalities.

To evaluate whether inorganic elements could be also used to enhance the formation of blood vessels (*i.e.*, angiogenesis), the literature was reviewed for five different elements (Chapter 8). The important role of angiogenesis in bone regeneration was highlighted followed by the methodology used to evaluate the effects of inorganic elements on endothelial cells. The methodology and results on the ion release profiles, cell specificity, direct versus indirect assays, and incubation time were summarized and compared. Based on this review, we concluded that strontium and silicon are the most promising candidates to incorporate into titanium implants to enhance angiogenesis.

Finally, the synthesized multifunctional implants were assessed in an *in vivo* bone infection model (Chapter 9). Therefore, larger implants were manufactured to be implanted into the intramedullary tibial canal of a rat and were biofunctionalized with silver NPs using PEO. A bioluminescent MRSA strain was employed to follow the infection over time and the

bacterial load was assessed after 1 week. We demonstrated that the implants biofunctionalized with silver NPs significantly reduced the bacterial load associated with the implants and in the bone. However, this was dependent on the way of initiating infection, which shows that the *in vitro* inoculation of the implants prior to implantation may be a better way to assess the prevention of infection, as compared to the *in vivo* infection of the intramedullary canal. This study demonstrates the potential of PEO-biofunctionalized implants in pre-clinical studies.

Ultimately, in the final chapter (Chapter 10) of this thesis, we reflect on the obtained results, provide a general discussion on multifunctional implants, and present a future outlook. Altogether, this thesis demonstrates that the AM porous implants biofunctionalized with PEO exhibit various types of favorable properties. We also demonstrated the potential of using combinations of silver with copper, zinc, and strontium. Furthermore, implants biofunctionalized with silver NPs reduce the infection burden *in vivo*. Therefore, the multifunctional implants developed in this thesis are promising candidates for further preclinical development and form a basis for the development of the future generations of implants that will prevent complications and serve a lifetime.

SAMENVATTING

Ieder jaar krijgen miljoenen mensen een orthopedisch implantaat. Deze implantaten zorgen ervoor dat mensen hun mobiliteit terugkrijgen en dragen derhalve sterk bij aan verhoogde kwaliteit van leven. Echter, een significant aantal patiënten krijgt te maken met complicaties zoals implantaatinfecties en loslating van implantaatcomponenten. De verwachting is dat het aantal orthopedische implantaten de komende jaren zal stijgen vanwege een steeds oudere populatie en een groeiend aantal mensen met overgewicht en obesitas. Als gevolg hiervan zal het aantal complicaties ook toenemen. Daarnaast wordt de behandeling van implantaatinfecties gecompliceerd door de ontwikkeling van antibioticaresistente bacteriën. Om derhalve implantaten te ontwikkelen die een leven lang meegaan is de focus verschoven naar het voorkomen van complicaties. Zoals Desiderius Erasmus zei: "Voorkomen is beter dan genezen."

Om zowel implantaatinfecties als loslating van het implantaat te voorkomen is het van belang om multifunctionele implantaten te ontwikkelen met optimale mechanische, chemische en biologische eigenschappen. De (oppervlakte) eigenschappen van dergelijke implantaten moeten zodanig zijn dat bacteriën zich niet kunnen hechten aan het implantaatoppervlak terwijl botregeneratie wordt gestimuleerd. Deze eigenschappen dragen eraan bij dat infectie wordt voorkomen en sterke fixatie tussen implantaat en botweefsel geïnduceerd. Implantaten met mechanische eigenschappen die zijn afgestemd op de behoefte van de patiënt kunnen tegenwoordig gefabriceerd worden door middel van 3D printen. Hierdoor wordt het mogelijk om voorheen onmogelijke ontwerpen te fabriceren die hoog poreus zijn. Deze implantaten worden dusdanig ontworpen om spanning-afscherming te voorkomen en daarmee bot ingroei te stimuleren terwijl tegelijkertijd de vermoeiing en levensduur van het implantaat verbeterd worden. Daarnaast dient het implantaatoppervlak behandelt te worden om optimale chemische en biologische eigenschappen te genereren.

Het doel van dit proefschrift was om multifunctionele implantaten te ontwikkelen en de antibacteriële en bot-stimulerende eigenschappen te onderzoeken. Implantaten met een zeer hoge porositeit werden rationeel ontworpen en vervolgens geproduceerd met een 3D printer. Vervolgens werd het oppervlak van deze implantaten behandeld met plasma elektrolytische oxidatie (PEO), een elektrochemische oppervlaktebehandelingsmethode. Door incorporatie van antibacteriële elementen zoals zilver, koper en zink nanodeeltjes samen met bot-stimulerende componenten zoals calcium, fosfaat en strontium werden implantaten gegenereerd die enerzijds implantaatinfecties voorkomen terwijl anderzijds botregeneratie werd versterkt. Verschillende combinaties van zilver nanodeeltjes met koper, zink en strontium werden gebruikt om synergistische antibacteriële activiteit te verkrijgen en de ontwikkeling van bacteriële resistentie te dwarsbomen.

De biomateriaaleigenschappen zoals de oppervlaktemorfologie, chemische- en fasecompositie, en afgifte van ionen werden bestudeerd, gevolgd door het onderzoeken van de antibacteriële eigenschappen alsmede de effecten op de biocompatibiliteit en osteogene differentiatie. De antibacteriële testen werden uitgevoerd met methicilline-resistente *Staphylococcus aureus* (MRSA), een resistente bacteriestam die frequent implantaatinfecties veroorzaakt en moeilijk te behandelen is met antibiotica. De antibacteriële testen werden voornamelijk *in vitro* uitgevoerd, maar de antibacteriële eigenschappen zijn ook getest in *ex vivo* en *in vivo* botinfectiemodellen.

Allereerst hebben we een grondig literatuuronderzoek uitgevoerd op het gebied van titanium biomaterialen waarvan het oppervlak behandeld werd door PEO met zilver, koper en/of zink, om antibacteriële implantaten te genereren (Hoofdstuk 2). We analyseerden de PEO procesparameters en methoden voor bepaling van antibacteriële activiteit en biocompatibiliteit. Daarnaast rapporteerden en vergeleken we de resultaten van de geïncludeerde studies. We concludeerden dat zilver de grootste antibacteriële activiteit bezat, maar tegelijkertijd ook het meeste cytotoxiciteit induceerde, terwijl een combinatie van zilver, koper en/of zink resulteerde in verhoogde antibacteriële activiteit zonder cytotoxiciteit. De meeste studies gebruikten *S. aureus* om de antibacteriële activiteit te bepalen en slechts een testmethode, wat de validiteit van deze studies verlaagde. We identificeerden het gebruik van de combinatie van zilver, koper en/of zink als een veelbelovende strategie voor toekomstig onderzoek. Bovendien zouden implantaten getest moeten worden in modellen die ontworpen zijn om de preventie van implantaatinfecties te onderzoeken, in plaats van behandeling van infectie zoals in de meeste modellen gebruikelijk is. Tot dusver zijn er geen onderzoeken uitgevoerd met *in vivo* botinfectiemodellen waarbij gebruik is gemaakt van PEO-gemodificeerde implantaten.

In Hoofdstuk 3 hebben we onderzocht of het oppervlak van poreuze 3D geprinte implantaten gemodificeerd kon worden door PEO met zilver nanodeeltjes. Daarnaast hebben we deze implantaten getest in een nieuw *ex vivo* botinfectiemodel. Poreuze implantaten werden ontworpen en gefabriceerd met een 3,75 keer vergroot oppervlakte vergeleken met massieve implantaten. Dit resulteerde in succesvolle incorporatie van zilver nanodeeltjes in het oppervlak van de poreuze implantaten met 4 keer verhoogde ion afgifte vergeleken met massieve implantaten. Dit resulteerde in verhoogde antibacteriële activiteit van poreuze implantaten *in vitro* en *ex vivo*. Terwijl PEO-behandeling op poreuze implantaten leidde tot vorming van hydroxyapatiet werd dit niet geobserveerd op massieve implantaten. De gefabriceerde implantaten met zilver nanodeeltjes induceerden geen cytotoxiciteit en verhoogden de metabole activiteit van humane mesenchymale stamcellen. Kortom, poreuze implantaten gemodificeerd met zilveren nanodeeltjes vertoonden verhoogde antibacteriële activiteit vergeleken met massieve implantaten.

Vervolgens hebben we modificatie van poreuze 3D geprinte implantaten met een combinatie van zilver nanodeeltjes met koper nanodeeltjes (Hoofdstuk 4) of zink nanodeeltjes (Hoofdstuk 5) onderzocht. Koper en zink zijn beiden elementen met zowel antibacteriële als bot-stimulerende eigenschappen. Om de nanodeeltjes in het oppervlakte van de implantaten te incorporeren werden zilver nanodeeltjes gemixt met koper of zink nanodeeltjes in PEO elektrolyten in ratio's variërend van 0 tot 100%. We observeerden dat oppervlaktebehandeling met zilver en koper of zink nanodeeltjes resulteerde in verlaagde zilver ion afgifte in de eerste 24 uur en continue ion afgifte voor tenminste 28 dagen. De antibacteriële activiteit was synergistisch verhoogd en de dosis zilver ionen kon verlaagd worden met een factor 10 voor koper en een factor 100 voor zink wanneer beide elementen gecombineerd werden. Tegelijkertijd waren er geen tekenen van cytotoxiciteit voor preosteoblasten. Het combineren van zilver met koper en zink is een veelbelovende strategie voor het verhogen van de antibacteriële eigenschappen en biocompatibiliteit alsmede het verlagen van de kans op bacteriële resistentie.

In het volgende hoofdstuk hebben we de oppervlaktebehandeling van titanium implantaten met zilver nanodeeltjes en strontium onderzocht (Hoofdstuk 6). Strontium is een bot-stimulerend element dat gebruikt wordt om patiënten met osteoporose te behandelen. We vonden dat een combinatie van zilver en strontium ionen resulteerde in synergistische verhoogde antibacteriële activiteit en maakte het mogelijk om de hoeveelheid zilver ionen met 4-32 keer te verlagen. Er werd geen cytotoxiciteit gevonden en strontium verhoogde de metabole activiteit en de osteogene differentiatie van preosteoblasten. Het combineren van zilveren nanodeeltjes met strontium resulteert in multifunctionele implantaten met sterke antibacteriële activiteit en verhoogde botvormende eigenschappen.

Daarna hebben we de effecten van PEO procesparameters op de oppervlaktemorfologie, chemische samenstelling en bijbehorende botvormende eigenschappen van poreuze implantaten onderzocht (Hoofdstuk 7). De oxidatietijd en stroomsterkte werden gevarieerd tijdens het PEO proces waarbij elektrolyten met en zonder strontium werden gebruikt. Langere oxidatietijden en grotere stroomsterktes resulteerden in een dikkere titaniumoxide laag, verhoogde afgifte van ionen en gevarieerde fasecomposities. Oppervlaktebehandeling met PEO elektrolyten die strontium bevatten leidde tot verlaagde hoeveelheden calcium in het implantaatoppervlak, dunnere titaniumoxide lagen en vergrote porositeit vergeleken met elektrolyten die alleen calcium en fosfaat bevatten. Deze veranderingen resulteerden in verhoogde osteogene differentiatie van preosteoblasten. Variatie van PEO procesparameters is een hulpmiddel voor het optimaliseren van de morfologie en chemische samenstelling van implantaatoppervlakken en het stimuleren van botvorming.

Voor botvorming is het essentieel dat er bloedvaten gevormd worden, dit proces wordt angiogenese genoemd. Derhalve hebben we een literatuuronderzoek uitgevoerd waarbij

we de potentie hebben onderzocht van vijf anorganische elementen voor het stimuleren van angiogenese in titanium implantaten (Hoofdstuk 8). De rol van angiogenese in botvorming werd uitgelicht gevolgd door een studie van de methoden die gebruikt werden voor het analyseren van de effecten van de anorganische elementen op endotheelcellen. De methodologie en resultaten betreffende ion afgifte, celspecificiteit, directe versus indirecte assays en incubatietijd werden samengevat en vergeleken. Uit deze analyse werd de conclusie getrokken dat strontium en silicium het grootste potentieel hebben om angiogenese in titanium implantaten te stimuleren.

Tot slot werden de gefabriceerde multifunctionele implantaten onderzocht in een *in vivo* botinfectiemodel (Hoofdstuk 9). Daarvoor werden grotere implantaten gefabriceerd die geïmplanteerd werden in het intramedulaire kanaal in de tibia van een rat. Deze implantaten werden behandeld door PEO met zilver nanodeeltjes. Door gebruik te maken van bioluminescente MRSA bacteriën was het mogelijk om de infectie gedurende de tijd te volgen. Na een week werd de bacteriële hoeveelheid in de tibia gekwantificeerd. We observeerden dat implantaten met zilver nanodeeltjes de hoeveelheid bacteriën verlaagden op het implantaat en in het bot. Dit was echter afhankelijk van de methode waarop infectie geïnitieerd werd: *in vitro* inoculatie van het implantaat voor implantatie is mogelijk een betere methode om infectiepreventie te bestuderen dan wanneer de bacteriën *in vivo* ingespoten worden in het intramedulaire kanaal. Deze studie toont het potentieel van PEO-behandelde implantaten aan in een preklinische studie.

In het laatste hoofdstuk van dit proefschrift wordt een reflectie op de behaalde resultaten gegeven samen met een algemene discussie over multifunctionele implantaten en suggesties voor toekomstig onderzoek (Hoofdstuk 10). Samenvattend beschrijft dit proefschrift dat de fabricatie van 3D geprinte multifunctionele implantaten door middel van PEO oppervlaktebehandeling resulteert in implantaten met een verscheidenheid aan eigenschappen. We tonen het potentieel aan van het gebruik van combinaties van zilver met koper, zink of strontium. Daarnaast verminderden implantaten met zilver nanodeeltjes infectie *in vivo*. Derhalve zijn de gefabriceerde implantaten potentiële kandidaten voor verder preklinisch onderzoek en vormen ze een prototype van toekomstige implantaten die complicaties bij patiënten voorkomen en een leven lang meegaan.

An ounce of prevention is worth a pound of cure

- Benjamin Franklin

CONTENTS

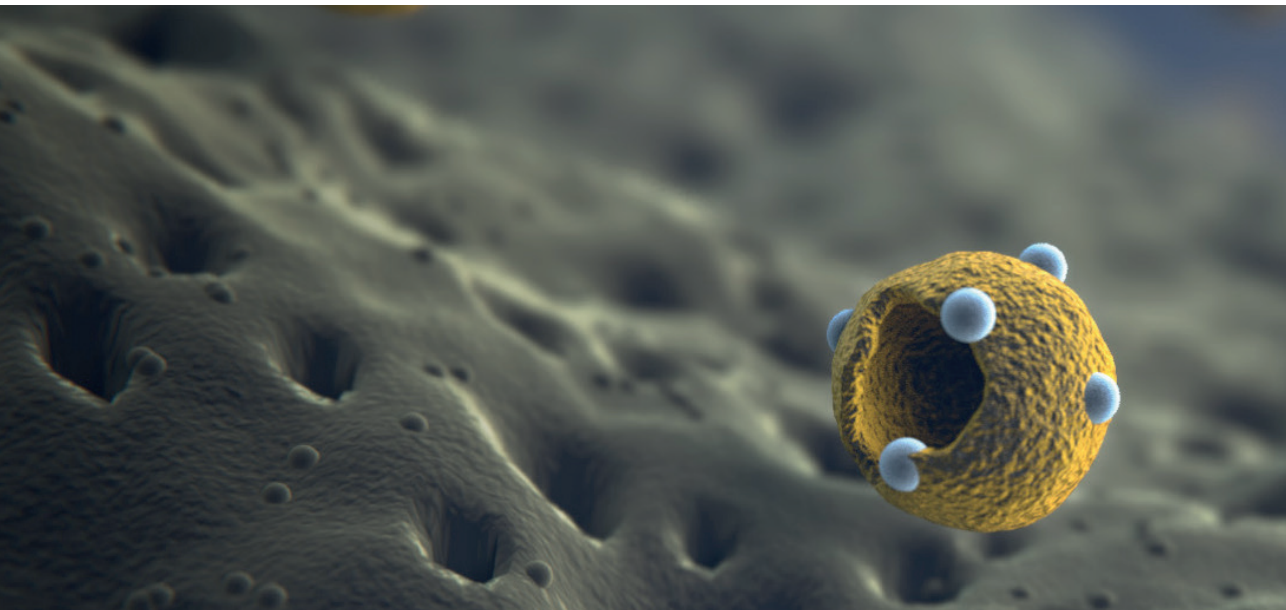

CHAPTER 01

Introduction

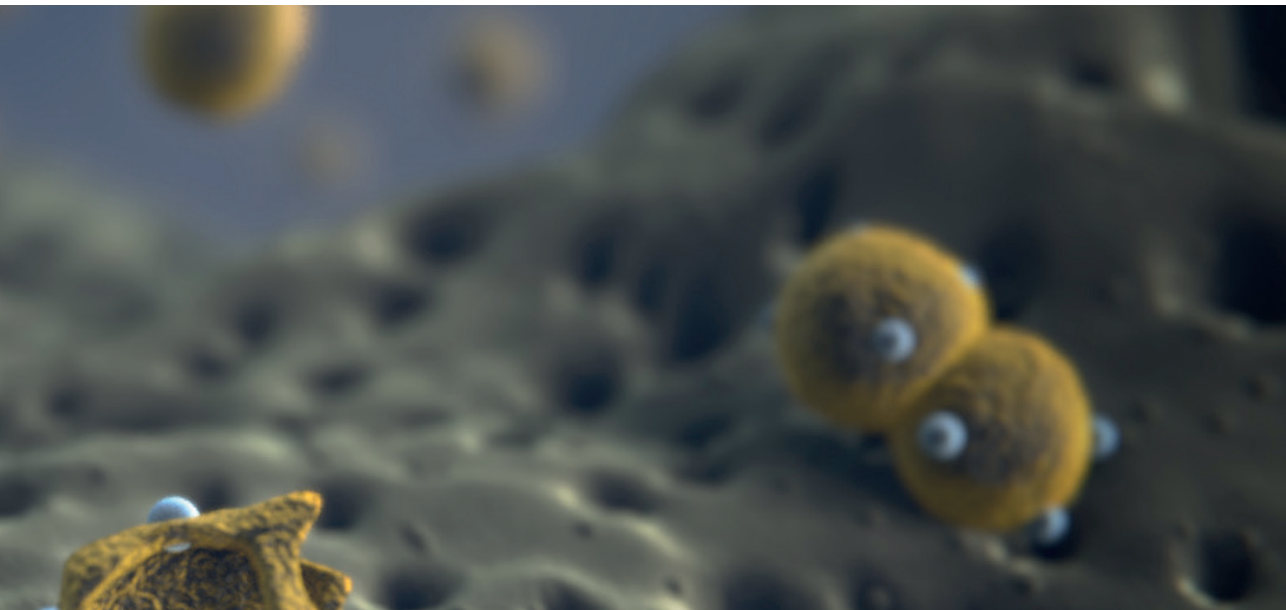

1.1 Need for life-long orthopedic implants

The use of orthopedic implants has been among the biggest success stories in the history of medicine. Every year, millions of people around the globe regain their mobility thanks to orthopedic implants that replace malfunctioning joints or bones. The majority of patients requiring an orthopedic implant suffer from osteoarthritis [1], but also patients with other diseases affecting joint functioning, such as rheumatoid arthritis [2] as well as patients requiring a bone-replacing implant, such as after a tumor resection [3] all benefit from metallic implants that replace the site of injury and fulfill the function of the resected tissue.

The need for orthopedic implants is expected to increase in the near future due to an increased life-expectancy [4] as well as an enhanced prevalence of medical conditions such as obesity [5]. The aging population will enhance the need for implants since old age is a major risk factor for the development of osteoarthritis [6]. Given that 18-42% of implants do not last longer than 25 years [7, 8], patients may outlive their implants. The patients will then require a revision surgery to install a new implant, which enhances the risk of complications. The extra body mass in obese patients increases the load on the joints, thereby damaging the cartilage [9]. Increased fat in obese patients also leads to inflammatory responses that are detrimental to cartilage health [10, 11]. Since such obese patients are more likely to receive their implants at a younger age, the likelihood of a revision surgery is increased. Therefore, orthopedic implants with longer service lives are urgently needed.

1.2 Implant associated infections and aseptic loosening

As the number of implants increases, so does the number of complications. The current data suggest that 4-12% of patients will have to deal with such complications of which 4-5% requires medical intervention [12-14]. Eventually, complications may lead to implant failure. The two major complications resulting in implant failure are implant-associated infections (IAI) and aseptic loosening.

IAI may be, for example, caused by the bacteria that invade the wound cavity during the surgery and subsequently adhere to the surface of the implant. The presence of a foreign body (*i.e.*, the implant) hampers the function of the immune system and the clearance of the bacteria, making infections more likely [15]. IAI can be classified into three major categories: 1. early post-operative infections within 3 months of surgery, 2. delayed infections within 2 years, and 3. late infections after 2 years. Early and delayed IAI are most likely established during the surgery as bacteria may stem from the tissues that are cut during the surgery (*e.g.*, skin), the hands of the surgeon, or improperly sterilized surgical instruments [16]. Meanwhile, late infections predominantly have a hematogenous origin and may be the result of bacterial

contamination due to surgery or trauma [17]. Following orthopedic surgery, between 0.5-9% of implants will become infected [18], of which 45% are early, 23% are delayed and 32% are late infections [19]. Higher infection rates of over 30% are seen for fracture-related procedures and trauma surgeries [20, 21].

In addition to IAI, implant failure is frequently caused by aseptic loosening, which refers to the large variety of cases not involving infections but is often associated with improper fixation of the implant as well as a lack of osseointegration or osteolysis induced by wear particles [22, 23]. After the primary mechanical fixation of uncemented implants (*e.g.*, through press-fitting), secondary fixation is ideally achieved by sufficient ingrowth of the bone into the porous structure of the implant. This process can be disturbed by wear particles that may induce an inflammatory response, leading to the formation of a fibrous tissue layer between the implant and its surrounding bony tissue, ultimately resulting in implant loosening [24].

When implants fail, a revision surgery is often required. Revision surgeries have a higher risk of infection than primary surgeries [25]. In addition, candidates for revision often suffer from co-morbidities that adversely affect the clinical outcome [26-28]. Implants should, therefore, be designed such that they outlive the patients.

1.3 Multifunctional implants

To ensure that implants are life-lasting, they need to demonstrate multiple functionalities at the same time, including bone-mimicking mechanical properties [29], antibacterial activity to ward off IAI [30] and osteogenic surface to promote bone ingrowth [31]. Furthermore, in order to fulfill its loadbearing function, the implants need to be rationally designed and properly adjusted to fill the defect [32]. To synthesize these implants, additive manufacturing is used since this layer-by-layer fabrication method allows for the free-form fabrication of increasingly complex designs. In addition, the implant surface needs to be tailored such that it actively repels bacteria and attracts bone stem cells [33]. Therefore, these implant surfaces need to have such properties to fulfill these criteria. In order to generate implants with the desired bioactive functions, one of the most effective options is to biofunctionalize the surface of the implants.

1.4 Additive manufacturing

Thanks to rapid progress in the field of additive manufacturing (AM), implants can nowadays be designed to possess optimal mechanical properties. Such implants often have a highly porous structure that can be only produced by AM, as it allows for nearly complete free-form fabrication. AM also allows for the adjustment of the bone-mimicking properties as well as

for the fabrication of implants with different sizes and shapes to fill up the bony defect. The properties of these biomaterials are directly derived from their microarchitecture. AM, therefore, enables the fabrication of materials with unique properties [34]. The high level of interconnected porosity of these AM implants translates to favorable mass transport properties, which will in turn facilitate the supply of nutrients and oxygen and the outbound transfer of metabolism byproducts [35]. Furthermore, these implants possess a vast internal surfaces area, often surpassing that of their solid counterparts by multiple orders of magnitude. While this may be beneficial for bony ingrowth, it may also enhance the risk of infection as there is a larger surface area for bacteria to attach to. Furthermore, once such an implant is fully integrated into the surrounding bone tissue, it will be difficult to remove it during a revision surgery. This complicates the treatment of IAI [36].

Most orthopedic implants are made of titanium or titanium alloys such as Ti6Al4V and Ti6Al7Nb due to their excellent mechanical, fatigue, and corrosion properties [37, 38]. Biodegradable implants made from biodegradable metals, such as magnesium [39], iron [40] and zinc [41] have shown potential. However, controlling the biodegradation behavior and the potential inflammatory response caused by the degradation products remains challenging [42, 43]. Moreover, not all patients and procedures may benefit from biodegradable implants as elderly patients have only limited bone regeneration capacity to replace the lost or damaged tissue [44].

1.5 Inorganic nanoparticles as antibacterial agents

Nowadays, the systemic intake of antibiotics is the main measure taken to prevent IAI [45]. Over the years, however, bacteria have developed ever-increasing levels of resistance against antibiotics [46, 47]. Furthermore, the efficacy of antibiotics against bacterial biofilms is low [48]. Antibiotic resistance is of major concern for the future treatments of IAI since over 50% of all IAIs is inflicted by *Staphylococci* and the evolution of resistant strains, such as methicillin-resistant *Staphylococcus aureus* (MRSA), has given rise to an increased number of untreatable infections [49]. As a result, the clinical outcome of patients with an IAI caused by resistant strains is worse compared to antibiotic-susceptible strains [50].

The use of inorganic nanoparticles (NPs) composed from elements, such as silver, copper, and zinc, has been intensively studied during the recent years. These elements have shown to target a wide bacterial spectrum, including multi-drug resistant bacteria [51]. Furthermore, the small size and high surface area to volume

ration of NPs makes them highly effective against bacteria. As a result, inorganic metallic NPs are effective at a low dose, which reduces the likelihood of side effects [52]. To date, bacteria have developed little resistance against such types of elements [53]. Combining these NPs may even further enhance the multifunctional properties of implants embedded with these NPs [54], to prevent the development of bacterial resistance, reduce side effects, and enhance bony ingrowth and the fixation of the implant.

1.6 Surface biofunctionalization by plasma electrolytic oxidation

In order to endow the implant surface with the required antibacterial and osteogenic properties, the surface needs to be biofunctionalized. However, the biofunctionalization of AM volume-porous implants is challenging due to the highly porous nature of these structures. Therefore, not all surface biofunctionalization techniques can be used. Electrochemical surface modification techniques are capable of transforming the surfaces of volume-porous implants [55]. Among these techniques, plasma electrolytic oxidation (PEO) has shown great potential to generate both antibacterial and osteogenic surfaces on titanium implants [56, 57].

A PEO setup consists of two electrodes, the anode and the cathode, which are placed in an electrolyte. Through the application of either a constant current or voltage, the formation of an oxide layer is initiated on the anode, which is formed by the implant. Following the dielectric breakdown, the oxide layer is thickened and sparks discharge, resulting in pore formation on the implant surface. PEO biofunctionalization, therefore, significantly modifies the surface morphology into a highly micro/nano-porous surface with a vast internal surface area. During PEO processing, the chemical elements present in the PEO electrolyte become part of the implant surface. Therefore, PEO electrolytes are frequently composed of calcium and phosphate elements because these elements make up the mineral part of the bone tissue and are known to promote bony ingrowth. The osteogenic capacity can be further improved through the addition of elements such as strontium [58]. In addition, PEO enables the incorporation of inorganic NPs onto the implant surface. As a result, antibacterial elements, such as inorganic NPs, can be added to the PEO electrolyte in order to generate implant surfaces with antibacterial properties [59].

The tight embedding of the incorporated chemical elements into the implant surface prevents nanotoxicity while also enabling the adjustment of the rate of metallic ion release over time [60]. Furthermore, the biofunctionalized surface layer has a high degree of bonding strength with the substrate as it is a converted surface layer rather than a deposited coating [61]. As the implant is fully immerged into the PEO electrolyte, PEO can biofunctionalize the entire surface of highly complex and porous geometries, such as AM implants. In addition,

the PEO parameters, such as the oxidation time and current or voltage, can be regulated to tailor the chemistry and surface morphology of the formed oxide layer such that it meets the desired performance criteria [62]. PEO occurs within a low (*i.e.*, room) temperature environment, even though the plasma discharges take place at > 2000 °C. Furthermore, PEO is easily scalable to clinically-relevant sized implants [63]. Finally, PEO does not alter the bulk material of the implant, thereby leaving the beneficial mechanical properties of AM implants intact [64].

1.7 Thesis aim and objective

The increased number of implants and the projected number of complications underline the need for multifunctional implants that can prevent complications as much as possible and approach the ultimate aim of creating lifelong implants. The aim of this thesis, therefore, is to develop AM volume-porous implants biofunctionalized using PEO with the help of inorganic agents, and to evaluate their material, antibacterial, and osteogenic characteristics. To achieve this goal multiple research objectives were set:

- reviewing the state-of-the-art in this research area.
- design, synthesis, and biofunctionalization of volume-porous implants with multifunctional properties.
- comparing the functionalities of volume-porous implants with their solid counterparts.
- incorporating multiple antibacterial and/or osteogenic elements onto the surface of AM implants to harvest their potential additive and synergetic effects.
- study the role of PEO processing parameters on the surface morphology and osteogenic properties of the resulting implants.
- investigate the angiogenic potential of inorganic elements.
- test the developed multifunctional implants in a preclinical bone infection model.

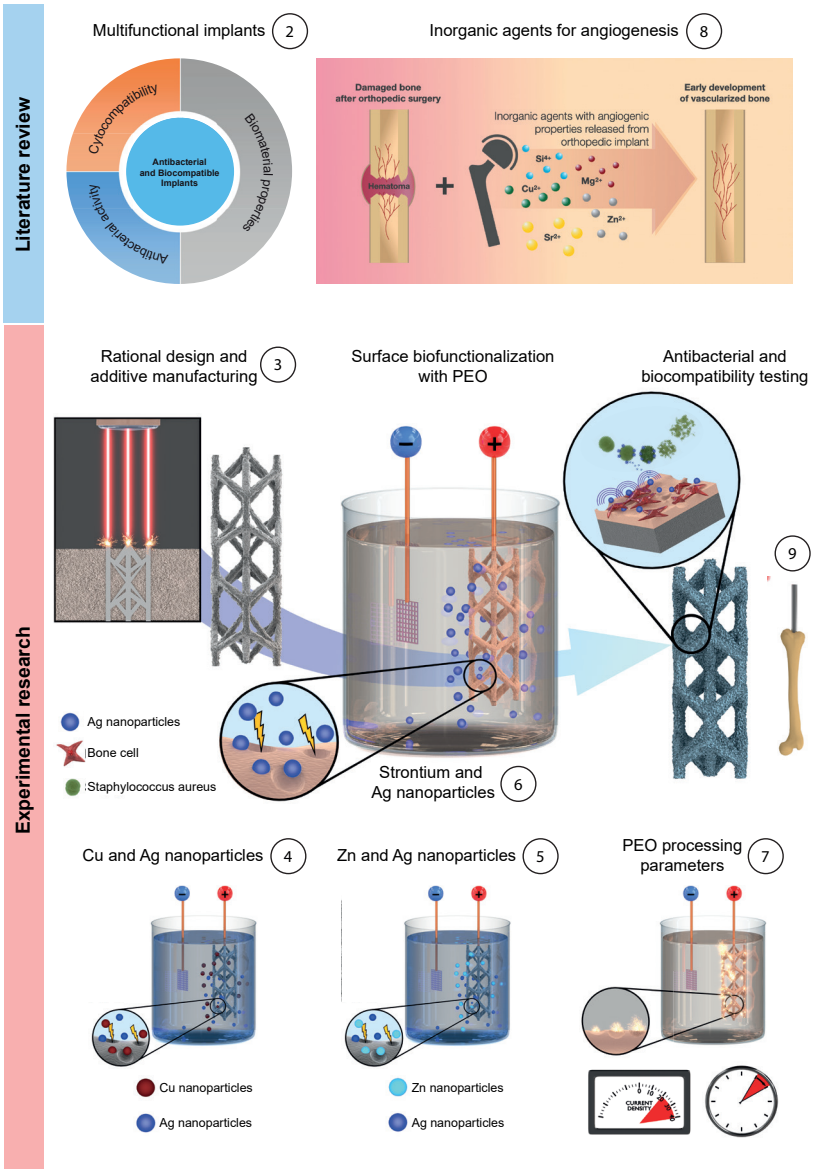

Figure 1. A graphical overview of this thesis. The experiments generally start with the rational design and AM of titanium implants followed by surface biofunctionalization by PEO and subsequent testing of the antibacterial behavior and cytocompatibility of the biofunctionalized implants. The numbers indicate the focus of the different chapters: (2) literature review on antibacterial and biocompatible implants; (3) rational design and surface biofunctionalization of porous implants; enhancing their multifunctional properties by combining silver nanoparticles with (4) copper nanoparticles, (5) zinc nanoparticles, or (6) strontium; (7) investigating the effects of PEO processing parameters on the surface morphology of the implant and their osteogenic properties; (8) a literature review on the inorganic agents that may be beneficial for angiogenesis; (9) the preclinical testing of the synthesized implants in an *in vivo* bone infection model.

1.8 Thesis outline

This thesis consists of nine different chapters that reflect the research objectives stated above (**Figure 1 & Table 1**). Chapter 2 presents an overview of the state-of-the-art of PEO-based biofunctionalization of titanium implants using silver, copper, or zinc. A thorough overview is presented on the processing parameters of PEO, the antibacterial properties of the resulting implants, and the relevant biocompatibility aspects.

In Chapter 3, the design and AM of volume-porous implants followed by PEO biofunctionalization with silver NPs is presented. These implants are compared to solid implants with similar dimensions. The biomaterial characteristics, antibacterial properties, and biocompatibility are investigated. In addition, the use of an *ex vivo* bone infection model is explored to investigate the antibacterial properties of the implants in a bony environment.

In Chapters 4-6, the combinations of silver NPs with copper NPs (Chapter 4), zinc NPs (Chapter 5), and strontium (Chapter 6) embedded through PEO on AM volume-porous implants are investigated. We study the effects of combining multiple agents on the surface properties and evaluated the synergistic antibacterial behavior. In addition, the effects of these combinations on the viability and osteogenic differentiation of bone cells are explored.

In Chapter 7, the contribution of different PEO processing parameters to the surface morphology, chemical composition, and phase composition of the implants biofunctionalized with strontium-containing PEO electrolytes are described. Furthermore, we analyze whether the observed changes in the implant surface morphology alter the osteogenic behavior.

In Chapter 8, we review the angiogenic potential of inorganic elements incorporated onto the surface of titanium implants. The role of angiogenesis in fracture healing and bone formation is discussed. Subsequently, an overview of the methodologies used for the *in vitro* assessment of the angiogenic properties is presented.

In Chapter 9, we analyze the preclinical potential of the generated multifunctional implants by testing the implants using an *in vivo* bone infection model. The implants are implanted intramedullary in the tibia of rats and the infection is continuously monitored using bioluminescent MRSA bacteria. The bacterial load, bone morphological changes, and immune response are analyzed.

The final chapter concludes this thesis with a general discussion of the obtained results. Furthermore, the future of this line of research is discussed with special attention to the research required for the development of clinically-relevant implants.

Table 1. The structure of this thesis.

Multifunctional implants: Prevention is better than cure	
Chapter 1	Introduction
Chapter 2	What is the state of the art of antibacterial titanium implants biofunctionalized by PEO with silver, zinc or copper?
Chapter 3	Can porous implants be biofunctionalized by PEO and how do these implants compare to solid implants?
Chapter 4,5 & 6	Can we enhance the multifunctional properties of the implants by combining silver nanoparticles with copper, zinc or strontium?
Chapter 7	How do PEO processing parameters affect implant surface morphology and osteogenic properties?
Chapter 8	Which inorganic elements can be used to enhance angiogenesis of orthopedic implants?
Chapter 9	How do multifunctional implants perform in preclinical infection models?
Chapter 10	Discussion, reflection and future outlook

REFERENCES

[1] Y. Zhang, J.M. Jordan, Epidemiology of osteoarthritis, Clin Geriatr Med 26(3) (2010) 355-69.

[2] K. Almutairi, J. Nossent, D. Preen, H. Keen, C. Inderjeeth, The global prevalence of rheumatoid arthritis: a meta-analysis based on a systematic review, Rheumatol Int 41(5) (2021) 863-877.

[3] M. Fujiki, T. Kimura, A. Takushima, Limb-salvage surgery with vascular reconstruction after lower extremity sarcoma resection: A systematic review and meta-analysis, Microsurgery 40(3) (2020) 404-413.

[4] V. Kontis, J.E. Bennett, C.D. Mathers, G. Li, K. Foreman, M. Ezzati, Future life expectancy in 35 industrialised countries: projections with a Bayesian model ensemble, The Lancet 389(10076) (2017) 1323-1335.

[5] F. Janssen, A. Bardoutsos, N. Vidra, Obesity Prevalence in the Long-Term Future in 18 European Countries and in the USA, Obes Facts 13(5) (2020) 514-527.

[6] A. Shane Anderson, R.F. Loeser, Why is osteoarthritis an age-related disease?, Best Pract Res Clin Rheumatol 24(1) (2010) 15-26.

[7] J.T. Evans, J.P. Evans, R.W. Walker, A.W. Blom, M.R. Whitehouse, A. Sayers, How long does a hip replacement last? A systematic review and meta-analysis of case series and national registry reports with more than 15 years of follow-up, The Lancet 393(10172) (2019) 647-654.

[8] J.T. Evans, R.W. Walker, J.P. Evans, A.W. Blom, A. Sayers, M.R. Whitehouse, How long does a knee replacement last? A systematic review and meta-analysis of case series and national registry reports with more than 15 years of follow-up, The Lancet 393(10172) (2019) 655-663.

[9] B. Raud, C. Gay, C. Guiguet-Auclair, A. Bonnin, L. Gerbaud, B. Pereira, M. Duclos, Y. Boirie, E. Coudeyre, Level of obesity is directly associated with the clinical and functional consequences of knee osteoarthritis, Sci Rep 10(1) (2020) 3601.

[10] H. Urban, C.B. Little, The role of fat and inflammation in the pathogenesis and management of osteoarthritis, Rheumatology (Oxford) 57 (2018) iv10-iv21.

[11] T. Kanthawang, J. Bodden, G.B. Joseph, N.E. Lane, M. Nevitt, C.E. McCulloch, T.M. Link, Obese and overweight individuals have greater knee synovial inflammation and associated structural and cartilage compositional degeneration: data from the osteoarthritis initiative, Skeletal Radiol 50 (2021) 217-229.

[12] S.M. Heo, I. Harris, J. Naylor, A.M. Lewin, Complications to 6 months following total hip or knee arthroplasty: observations from an Australian clinical outcomes registry, BMC Musculoskelet Disord 21(1) (2020) 602.

[13] P.J. Belmont, Jr., G.P. Goodman, B.R. Waterman, J.O. Bader, A.J. Schoenfeld, Thirty-day postoperative complications and mortality following total knee arthroplasty: incidence and risk factors among a national sample of 15,321 patients, J Bone Joint Surg Am 96(1) (2014) 20-6.

[14] N.T. O'Malley, F.J. Fleming, D.D. Gunzler, S.P. Messing, S.L. Kates, Factors independently associated with complications and length of stay after hip arthroplasty: analysis of the National Surgical Quality Improvement Program, J Arthroplasty 27(10) (2012) 1832-7.

[15] K. Merritt, J.W. Shafer, S.A. Brown, Implant site infection rates with porous and dense materials, Journal of Biomedical Materials Research 13 (1979).

[16] M. Ribeiro, F.J. Monteiro, M.P. Ferraz, Infection of orthopedic implants with emphasis on bacterial adhesion process and techniques used in studying bacterial-material interactions, Biomatter 2(4) (2012) 176-94.

[17] R.A. Brady, J.G. Leid, J.W. Costerton, M.E. Shirtliff, Osteomyelitis: Clinical overview and mechanisms of infection persistence, Clinical Microbiology Newsletter 28(9) (2006) 65-72.

[18] W. Zimmerli, Clinical presentation and treatment of orthopaedic implant-associated infection, J Intern Med 276(2) (2014) 111-9.

[19] R.R. Laffer, P. Graber, P.E. Ochsner, W. Zimmerli, Outcome of prosthetic knee-associated infection: evaluation of 40 consecutive episodes at a single centre, Clin Microbiol Infect 12 (2006) 433-9.

[20] C. Papakostidis, N.K. Kanakaris, J. Pretel, O. Faour, D.J. Morell, P.V. Giannoudis, Prevalence of complications of open tibial shaft fractures stratified as per the Gustilo-Anderson classification, Injury 42(12) (2011) 1408-15.

[21] A. Trampuz, W. Zimmerli, Diagnosis and treatment of infections associated with fracture-fixation devices, Injury 37 Suppl 2 (2006) S59-66.

[22] Y. Abu-Amer, I. Darwech, J.C. Clohisy, Aseptic loosening of total joint replacements: mechanisms underlying osteolysis and potential therapies, Arthritis Res Ther 9 Suppl 1 (2007) S6.

[23] M. Sundfeldt, L.V. Carlsson, C.B. Johansson, P. Thomsen, C. Gretzer, Aseptic loosening, not only a question of wear: a review of different theories, Acta Orthop 77(2) (2006) 177-97.

[24] Q. Gu, Q. Shi, H. Yang, The role of TLR and chemokine in wear particle-induced aseptic loosening, J Biomed Biotechnol 2012 (2012) 596870.

[25] L. Montanaro, P. Speziale, D. Campoccia, S. Ravaioli, I. Cangini, G. Pietrocola, S. Giannini, C.R. Arciola, Scenery of Staphylococcus implant infections in orthopedics, Review Future Microbiology 6 (2011) 1329–1349.

[26] M. Lespasio, M. Mont, A. Guarino, Identifying Risk Factors Associated With Postoperative Infection Following Elective Lower-Extremity Total Joint Arthroplasty, Perm J 24 (2020) 1-3.

[27] M.C. Castano-Betancourt, R. Fruschein Annichino, E.S.M.M. de Azevedo, E. Gomes Machado, M.V. Lipay, E. Marchi, Identification of high-risk groups for complication after arthroplasty: predictive value of patient's related risk factors, J Orthop Surg Res 13(1) (2018) 328.

[28] D.K. Wukich, Diabetes and its negative impact on outcomes in orthopaedic surgery, World J Orthop 6(3) (2015) 331-9.

[29] R. Huiskes, H. Weinans, B. van Rietbergen, The relationship between stress shielding and bone resorption around total hip stems and the effects of flexible materials, Clinical Orthopaedics and Related Research 274 (1992) 124-134.

[30] F. Jahanmard, F.M. Dijkmans, A. Majed, H.C. Vogely, B.C.H. van der Wal, D.A.C. Stapels, S.M. Ahmadi, T. Vermonden, S. Amin Yavari, Toward Antibacterial Coatings for Personalized Implants, ACS Biomater Sci Eng 6(10) (2020) 5486-5492.

[31] C. Stewart, B. Akhavan, S.G. Wise, M.M.M. Bilek, A review of biomimetic surface functionalization for bone-integrating orthopedic implants: Mechanisms, current approaches, and future directions, Progress in Materials Science 106 (2019).

[32] H.M.A. Kolken, S. Janbaz, S.M.A. Leeflang, K. Lietaert, H.H. Weinans, A.A. Zadpoor, Rationally designed meta-implants: a combination of auxetic and conventional meta-biomaterials, Materials Horizons 5(1) (2018) 28-35.

[33] J. Raphel, M. Holodniy, S.B. Goodman, S.C. Heilshorn, Multifunctional coatings to simultaneously promote osseointegration and prevent infection of orthopaedic implants, Biomaterials 84 (2016) 301-314.

[34] A.A. Zadpoor, Mechanical meta-materials, Materials Horizons 3(5) (2016) 371-381.

[35] F.S.L. Bobbert, K. Lietaert, A.A. Eftekhari, B. Pouran, S.M. Ahmadi, H. Weinans, A.A. Zadpoor, Additively manufactured metallic porous biomaterials based on minimal surfaces: A unique combination of topological, mechanical, and mass transport properties, Acta Biomater 53 (2017) 572-584.

[36] G. Reith, V. Schmitz-Greven, K.O. Hensel, M.M. Schneider, T. Tinschmann, B. Bouillon, C. Probst, Metal implant removal: benefits and drawbacks--a patient survey, BMC Surg 15 (2015) 96.

[37] C.N. Elias, D.J. Fernandes, F.M.d. Souza, E.d.S. Monteiro, R.S.d. Biasi, Mechanical and clinical properties of titanium and titanium-based alloys (Ti G2, Ti G4 cold worked nanostructured and Ti G5) for biomedical applications, Journal of Materials Research and Technology 8(1) (2019) 1060-1069.

[38] J.B. Wang, Z.Y. Shang, Z.S. Yuan, J. Zhou, Z.W. Feng, W.D. Miao, M. Zhu, Study on the Mechanical Property and Microstructure of Surgical Implanted Ti-6Al-7Nb Titanium Alloy, Advanced Materials Research 535-537 (2012) 945-949.

[39] Y. Li, J. Zhou, P. Pavanram, M.A. Leeflang, L.I. Fockaert, B. Pouran, N. Tumer, K.U. Schroder, J.M.C. Mol, H. Weinans, H. Jahr, A.A. Zadpoor, Additively manufactured biodegradable porous magnesium, Acta Biomater 67 (2018) 378-392.

[40] Y. Li, H. Jahr, K. Lietaert, P. Pavanram, A. Yilmaz, L.I. Fockaert, M.A. Leeflang, B. Pouran, Y. Gonzalez-Garcia, H. Weinans, J.M.C. Mol, J. Zhou, A.A. Zadpoor, Additively manufactured biodegradable porous iron, Acta Biomater 77 (2018) 380-393.

[41] H. Yang, B. Jia, Z. Zhang, X. Qu, G. Li, W. Lin, D. Zhu, K. Dai, Y. Zheng, Alloying design of biodegradable zinc as promising bone implants for load-bearing applications, Nat Commun 11(1) (2020) 401.

[42] M. Sikora-Jasinska, P. Chevallier, S. Turgeon, C. Paternoster, E. Mostaed, M. Vedani, D. Mantovani, Long-term in vitro degradation behaviour of Fe and Fe/Mg2Si composites for biodegradable implant applications, RSC Advances 8(18) (2018) 9627-9639.

[43] K. Pichler, S. Fischerauer, P. Ferlic, E. Martinelli, H.-P. Brezinsek, P.J. Uggowitzer, J.F. Löffler, A.-M. Weinberg, Immunological Response to Biodegradable Magnesium Implants, Jom 66(4) (2014) 573-579.

[44] D. Clark, M. Nakamura, T. Miclau, R. Marcucio, Effects of Aging on Fracture Healing, Curr Osteoporos Rep 15(6) (2017) 601-608.

[45] J. Gaudias, Antibiotic prophylaxis in orthopedics-traumatology, Orthop Traumatol Surg Res 107(1S) (2021) 102751.

[46] L.B. Rice, The clinical consequences of antimicrobial resistance, Curr Opin Microbiol 12(5) (2009) 476-81.

[47] R. Laxminarayan, T. Van Boeckel, I. Frost, S. Kariuki, E.A. Khan, D. Limmathurotsakul, D.G.J. Larsson, G. Levy-Hara, M. Mendelson, K. Outterson, S.J. Peacock, Y.-G. Zhu, The Lancet Infectious Diseases Commission on antimicrobial resistance: 6 years later, The Lancet Infectious Diseases 20(4) (2020) e51-e60.

[48] A.W. Smith, Biofilms and antibiotic therapy: is there a role for combating bacterial resistance by the use of novel drug delivery systems?, Adv Drug Deliv Rev 57(10) (2005) 1539-50.

[49] D. Campoccia, L. Montanaro, C.R. Arciola, The significance of infection related to orthopedic devices and issues of antibiotic resistance, Biomaterials 27(11) (2006) 2331-9.

[50] D. Teterycz, T. Ferry, D. Lew, R. Stern, M. Assal, P. Hoffmeyer, L. Bernard, I. Uckay, Outcome of orthopedic implant infections due to different staphylococci, Int J Infect Dis 14(10) (2010) e913-8.

[51] N.Y. Lee, W.C. Ko, P.R. Hsueh, Nanoparticles in the Treatment of Infections Caused by Multidrug-Resistant Organisms, Front Pharmacol 10 (2019) 1153.

[52] L. Wang, C. Hu, L. Shao, The antimicrobial activity of nanoparticles: present situation and prospects for the future, Int J Nanomedicine 12 (2017) 1227-1249.

[53] A. Panacek, L. Kvitek, M. Smekalova, R. Vecerova, M. Kolar, M. Roderova, F. Dycka, M. Sebela, R. Prucek, O. Tomanec, R. Zboril, Bacterial resistance to silver nanoparticles and how to overcome it, Nat Nanotechnol 13(1) (2018) 65-71.

[54] C. Bankier, R.K. Matharu, Y.K. Cheong, G.G. Ren, E. Cloutman-Green, L. Ciric, Synergistic Antibacterial Effects of Metallic Nanoparticle Combinations, Sci Rep 9(1) (2019) 16074.

[55] S. Bakhshandeh, Z. Gorgin Karaji, K. Lietaert, A.C. Fluit, C.H.E. Boel, H.C. Vogely, T. Vermonden, W.E. Hennink, H. Weinans, A.A. Zadpoor, S. Amin Yavari, Simultaneous Delivery of Multiple Antibacterial Agents from Additively Manufactured Porous Biomaterials to Fully Eradicate Planktonic and Adherent Staphylococcus aureus, ACS Appl Mater Interfaces 9(31) (2017) 25691-25699.

[56] B.S. Necula, L.E. Fratila-Apachitei, S.A. Zaat, I. Apachitei, J. Duszczyk, In vitro antibacterial activity of porous TiO2-Ag composite layers against methicillin-resistant Staphylococcus aureus, Acta Biomater 5(9) (2009) 3573-80.

[57] A. Santos-Coquillat, R. Gonzalez Tenorio, M. Mohedano, E. Martinez-Campos, R. Arrabal, E. Matykina, Tailoring of antibacterial and osteogenic properties of Ti6Al4V by plasma electrolytic oxidation, Applied Surface Science 454 (2018) 157-172.

[58] B. Wan, R. Wang, Y. Sun, J. Cao, H. Wang, J. Guo, D. Chen, Building Osteogenic Microenvironments With Strontium-Substituted Calcium Phosphate Ceramics, Front Bioeng Biotechnol 8 (2020) 591467.

[59] S. Ferraris, S. Spriano, Antibacterial titanium surfaces for medical implants, Mater Sci Eng C Mater Biol Appl 61 (2016) 965-78.

[60] M. Mohedano, B.J.C. Luthringer, B. Mingo, F. Feyerabend, R. Arrabal, P.J. Sanchez-Egido, C. Blawert, R. Willumeit-Römer, M.L. Zheludkevich, E. Matykina, Bioactive plasma electrolytic oxidation coatings on Mg-Ca alloy to control degradation behaviour, Surface and Coatings Technology 315 (2017) 454-467.

[61] H. Sharifi, M. Aliofkhazraei, G.B. Darband, S. Shrestha, A Review on Adhesion Strength of Peo Coatings by Scratch Test Method, Surface Review and Letters 25(03) (2018).

[62] Q. Li, W. Yang, C. Liu, D. Wang, J. Liang, Correlations between the growth mechanism and properties of micro-arc oxidation coatings on titanium alloy: Effects of electrolytes, Surface and Coatings Technology 316 (2017) 162-170.

[63] B.S. Necula, I. Apachitei, L.E. Fratila-Apachitei, E.J. van Langelaan, J. Duszczyk, Titanium bone implants with superimposed micro/nano-scale porosity and antibacterial capability, Applied Surface Science 273 (2013) 310-314.

[64] Z. Gorgin Karaji, R. Hedayati, B. Pouran, I. Apachitei, A.A. Zadpoor, Effects of plasma electrolytic oxidation process on the mechanical properties of additively manufactured porous biomaterials, Mater Sci Eng C Mater Biol Appl 76 (2017) 406-416.

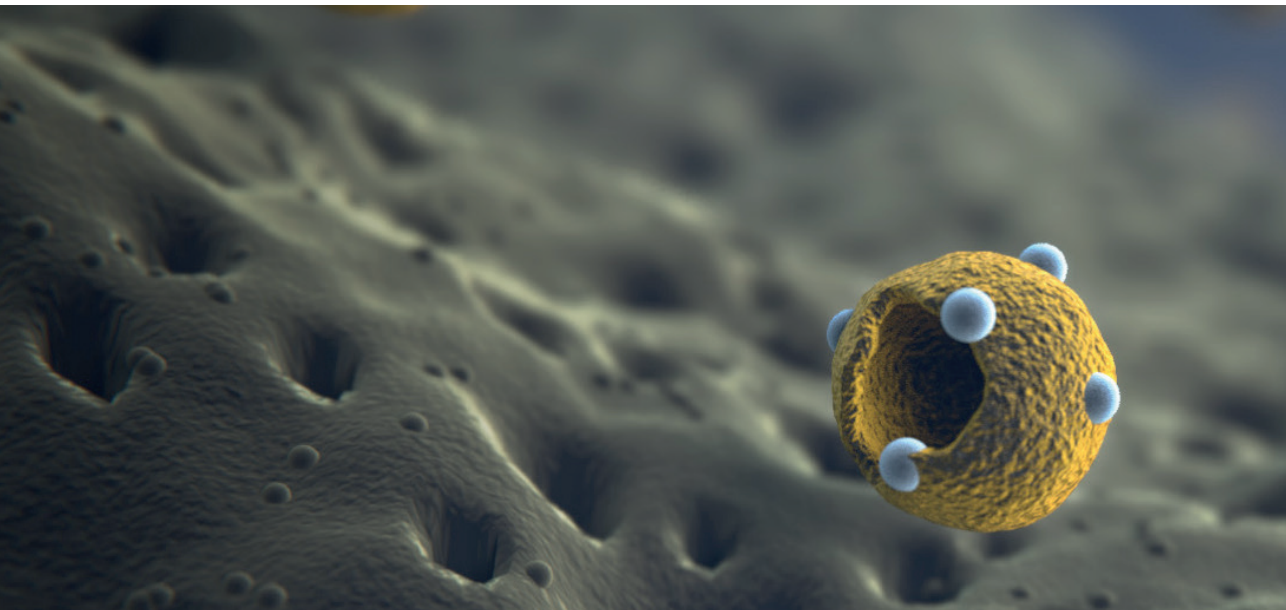

CHAPTER 02

Antibacterial titanium implants biofunctionalized by plasma electrolytic oxidation with silver, zinc and copper

I.A.J. van Hengel, M.W.A.M. Tierolf, L.E. Fratila-Apachitei, I. Apachitei, A.A. Zadpoor, Antibacterial Titanium Implants Biofunctionalized by Plasma Electrolytic Oxidation with Silver, Zinc, and Copper: A Systematic Review, International Journal of Molecular Sciences 22 (2021).

Patients receiving orthopedic implants are at risk for implant-associated infections (IAI). A growing number of antibiotic resistant bacteria threatens to hamper the treatment of IAI. The focus has, therefore, shifted towards the development of implants with intrinsic antibacterial activity to prevent the occurrence of infection. The use of Ag, Cu, and Zn has gained momentum as these elements display strong antibacterial behavior and target a wide spectrum of bacteria. In order to incorporate these elements into the surface of titanium-based bone implants, plasma electrolytic oxidation (PEO) has been widely investigated as a single-step process that can biofunctionalize these (highly porous) implant surfaces. Here, we present a systematic review of the studies published from 2009 until 2020 on the biomaterial properties, antibacterial behavior, and biocompatibility of titanium implants biofunctionalized by PEO using Ag, Cu, and Zn. We observed that 100% of surfaces bearing Ag (Ag-surfaces), 93% of surfaces bearing Cu (Cu-surfaces), 73% of surfaces bearing Zn (Zn-surfaces), and 100% of surfaces combining Ag, Cu, and Zn resulted in a significant (*i.e.*, > 50%) reduction of bacterial load, while 13% of Ag-surfaces, 10% of Cu-surfaces, and none of Zn or combined Ag, Cu, and Zn surfaces reported cytotoxicity against osteoblasts, stem cells and immune cells. A majority of the studies investigated the antibacterial activity against *S. aureus*. Important areas for future research include the biofunctionalization of additively manufactured porous implants and surfaces combining Ag, Cu, and Zn. Furthermore, the antibacterial activity of such implants should be determined in assays focused on prevention, rather than the treatment of IAIs. These implants should be tested using appropriate *in vivo* bone infection models capable of assessing whether titanium implants biofunctionalized by PEO with Ag, Cu, and Zn can contribute to protect patients against IAI.

2.1 INTRODUCTION

Implant-associated infections (IAI) are a devastating complication for patients receiving bone implants in total joint arthroplasty, trauma surgeries, and malignant bone tumor resections [1-3]. These infections form a tremendous burden for both patients and society. As the number of implantations continues to grow annually [4-6], the need for a cure increases. Given that the treatment of such infections is highly costly from both financial and societal points of view, the focus has shifted towards the prevention of IAI through the development of implants with intrinsic antibacterial activity.

Antibiotics form the primary source of antibacterial agents used to treat bacterial infections. However, a vast number of IAI is caused by *Staphylococci* and multiple strains have developed high levels of antibiotic resistance [7, 8], raising concerns for the future treatments of IAI. Infection by methicillin-resistant *Staphylococcus aureus* (MRSA) highly complicates the treatment of IAI and adversely affects the treatment outcomes [9, 10]. Other antibacterial agents are, therefore, being investigated. Metallic elements, such as Ag, Cu, and Zn have shown strong antibacterial behavior against a wide microbial spectrum, including resistant bacterial strains [11-14].

Ag has excellent antibacterial properties, but may also induce cytotoxicity [15, 16]. Cu and Zn, on the other hand, exhibit lower levels of antibacterial behavior but are essential trace elements. Furthermore, they have been found to enhance the cytocompatibility of implant surfaces [17, 18]. Therefore, combining these elements may result in the right balance between antibacterial behavior, chemical biocompatibility, and osteogenic response [19, 20].

The local administration of antibacterial agents at the implant site has been shown to greatly complement the systemic administration of antibiotics [21, 22]. The side effects of such agents can also be prevented as the required antibacterial dose is generally lower [23]. To deliver antibacterial agents locally, the surface of the implants can be biofunctionalized through surface treatment techniques. Antibacterial agents can be attached to implants either as a coating layer, embedded directly onto the implant surface, or incorporated as part of a converted surface layer [24].

Antibacterial agents can be deposited onto the implant surface by means of polymeric, ceramic or metallic coatings. To produce these coatings usually low temperatures are used and therefore little interaction occurs with the implant substrate. Coatings have a tendency to be thin and fragile, thereby limiting the availability of the antibacterial agent and hampering their use during surgical implantation. To enhance the diffusion, the antibacterial agent can be incorporated in a biodegradable polymer coating. In this way implants have been manufactured that contain Ag [25, 26], Cu [27] and Zn [28]. Polymeric coatings can be

attached onto an implant by dipping and drying, sol-gel technology, spray drying, layer-by-layer manufacturing, and self-assembly monolayers. Downsides are the limited mechanical and chemical stability, local inflammatory response due to degradation products and uncontrolled release kinetics.

Another strategy is direct embedding of the antibacterial agent into the implant surface. In this way no new material is added on top of the substrate but the composition of the outermost layer of the implant substrate is altered. Examples of such methods are ion implantation, plasma immersion ion implantation [29] and in situ reduction [30]. Advantages are that the implant surface morphology remains intact, and the corrosive and biocompatible properties of the substrate material retained. However, this strategy is difficult to perform on complex geometries and does not allow for optimization of the surface morphology.

A third approach to incorporate Ag, Cu and Zn in the implant surface is through generation of a converted surface layer. One of such techniques is plasma electrolytic oxidation (PEO) which has been investigated to biofunctionalize the surface of highly porous implants made of specific metallic biomaterials [31]. During PEO, the native titanium oxide layer is transformed into a crystalline and microporous surface in a swift and single-step process.

Through the addition of antibacterial elements into the PEO electrolyte, these elements become part of the converted surface layer and result in a surface exhibiting antibacterial behavior [32, 33].Due to the tight embedding of the antibacterial agents into the surface, the release of these ions can be controlled and the undesired circulation of agents can be prevented, thereby avoiding nanotoxic effects [34]. PEO has been applied to generate titanium implants with antibacterial properties using Ag, Cu, and Zn [35-37]. In addition to the antibacterial behavior, PEO biofunctionalized surfaces have been shown to enhance osseointegration and stimulate bony ingrowth *in vivo* [38, 39].

Bone implants are increasingly produced through additive manufacturing (AM), as this allows free-form fabrication and customized treatment for patients. AM allows for the fabrication of highly porous implants with vast internal surface areas, which may make the implants more prone to infection while at the same time providing a challenging surface to modify through surface biofunctionalization techniques. PEO is capable of biofunctionalizing the surface of complex geometries. In addition, the parameters of the PEO process can be controlled which allows to tailor the chemistry of the surface layer [40, 41]. Furthermore, the synthesized surface layer adheres strongly to the implant substrate. Moreover, the method is easily scalable towards clinically sized implants. Limitations of PEO are that the surface morphology and chemistry of the surface are modified simultaneously and this makes the individual tuning of these properties difficult. Furthermore, the exact mechanism of plasma discharging is still

unknown, and thereby the fine-tuning of the PEO processing parameters difficult to predict [42].In order to develop clinically relevant antibacterial implants, it is important to assess the progress made in this area and compare the outcomes of different studies. As most implants available for current clinical use are made of titanium, we performed a systematic review on titanium implants biofunctionalized by PEO using Ag, Cu, and Zn. In order to illustrate the progress made in this area, we screened the studies published between 2009 and December 2020. This area of research involves several scientific disciplines, including engineering, material sciences, microbiology, and orthopedics. We, therefore, analyzed a broad spectrum of aspects including the implant substrate, PEO parameters, surface characteristics, antibacterial assays, and cytocompatibility testing.

2.2 METHODS

2.2.1 Literature search

A comprehensive electronic search was performed using Scopus and Google Scholar search engines up until December 2020. In addition, a global screening was performed using PubMed. The article search was conducted using different combinations of the following keywords: plasma electrolytic oxidation, micro-arc oxidation, antibacterial activity, Ag, Cu, and Zn. To ensure that relevant publications were not excluded, combinations of subject headings, text-word terms, and the Boolean operators AND and OR were used. The searches were limited to those studies published in English between 2009 and 2020. The reference lists of the included eligible studies were scanned to ensure no eligible studies were omitted. The last search date was 24 December 2020. This systematic review was written according to the PRISMA (Preferred Reporting Items for Systematic Review and Meta-Analyses) statement [43].

2.2.2 Inclusion and exclusion criteria

The inclusion criteria were – (1) the surface modification technique: plasma electrolytic oxidation (PEO), micro-arc oxidation (MAO), or anodic spark deposition (ASD); (2) implant substrate: titanium and its alloys; (3) antibacterial agents: Ag, Cu and Zn; (4) metallic-based antibacterial agents should have been incorporated in PEO-modified Ti-based surfaces and (5) assessment of the antibacterial behavior should have been performed. A study was excluded if it did not report any outcome variable. Furthermore, studies were not eligible for inclusion when – (1) articles were not published in English; (2) no surface modification technique was utilized; (3) PEO was performed in combination with other surface modification techniques or treatments; (4) no antibacterial testing was performed and (5) study was of one of the following document types: reviews, patents, conference abstracts/papers and case reports.

2.2.3 Study selection

The titles and abstracts were screened to assess the suitability of the search results. Subsequently, the full text of the studies selected in the first stage of screening were analyzed to assess whether or not they satisfied the inclusion criteria.

2.2.4 Risk of bias

The methodological details of the included studies were analyzed to minimize the risks of biases in the individual studies. Furthermore, excluding grey literature in Google Scholar decreased the risk of biases in the evaluation.

2.2.5 Data extraction

Extracted information included the type of the titanium substrate, electrolyte composition, PEO processing parameters, surface topography, XRD phase composition, surface content of the incorporated elements, the release profile of the metallic (*i.e.*, Ag, Cu, and Zn) ions, antibacterial assays, tested pathogens, eukaryotic cell types, and the outcomes (*i.e.*, antibacterial behavior and cytocompatibility). The results were considered significant when $p < 0.05$.

2.2.6 Search results

A total of 1261 studies were identified in the two search engines: 1190 from Google Scholar and 71 from Scopus. After screening the titles and abstracts, 1158 studies were excluded. The primary reasons for exclusion were no antibacterial or biocompatibility tests, PEO performed in combination with other surface modification techniques, and document types: reviews, patents, conference abstracts/papers, citations and case reports. As a result, 103 studies were selected for full-text analysis. The analysis led to the exclusion of 59 studies, as they failed to meet the inclusion criteria. Finally, 49 studies were included in this systematic review and were used for a qualitative analysis of their data and for comparison with each other. A flow diagram was created to represent the entire systematic search of the relevant studies (**Suppl. fig. 1**). The outline of the review is presented in **Figure 1**.

Figure 1. A graphical presentation of the outline of this systematic review.

2.3 SUMMARY OF STUDY CHARACTERISTICS

A summary of the study characteristics is presented in **Figure 2**. Of the analyzed studies, 43% used Ag, 26% used Cu, and 21% worked with Zn, while 9% investigated a combination of Ag, Cu, and Zn (*i.e.*, using two or more metallic agents. Various types of parameters have been reported in the studies (**Figure 2A**), including the PEO processing parameters (98%), phase composition (87%), surface content of the incorporated elements (80%), and ion release kinetics (48%). Furthermore, 92% of the studies have quantified the antibacterial activity, which was reported to be > 50% for 100% of the studies using Ag, 93% of the studies using Cu, and 73% of those employing Zn as well as 100% of the studies combining multiple metallic agents (**Figure 2B**). Of those studies, 57% tested the efficacy of the surfaces against *S. aureus*,

31% of the studies tested their specimens against *E. coli* while 12% of the studies chose other bacterial species. Furthermore, the antibacterial activity was determined against adherent bacteria in 42% of the studies, while 35% of the studies assessed the antibacterial activity of their specimens against planktonic bacteria, and 23% assessed both.

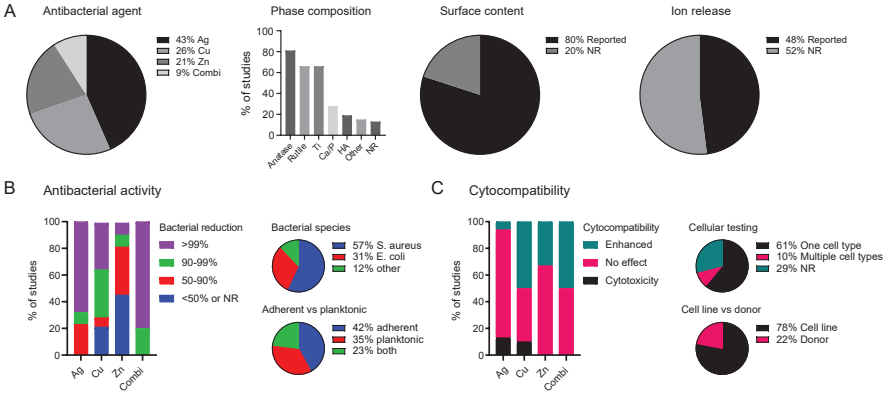

Figure 2. An overview of the (A) biomaterial, (B) antibacterial and (C) cytocompatibility specifications of the studies included in this systematic review of the literature. Combi: combination of Ag, Cu and/or Zn, HA: hydroxyapatite, NR: not reported.

Cytocompatibility was tested in 71% of all studies, of which 10% tested against multiple cell types (**Figure 2C**). Of the studies assessing the cytocompatibility of their specimens, 78% used a cell line while 22% used cells obtained from a donor. The addition of the metallic antibacterial agent resulted in cytotoxicity for 13% of the Ag studies, 10% of the Cu studies, 0% of the Zn studies and 0% of the studies combining two or more metals. Meanwhile, improved cell response (*i.e.*, enhanced cell viability and/or osteogenic differentiation) was observed for 7% of the Ag surfaces, 50% of the Cu surfaces, and 33% of the Zn surfaces, as well as for 50% of the surfaces combining Ag, Cu, and Zn.

2.4 SYNTHESIS AND CHARACTERIZATION OF PEO BIOFUNCTIONALIZED SURFACES

PEO is an electrochemical process that converts the outer oxide layer of valve metals into a ceramic surface layer and is applied to enhance corrosion resistance [44], dielectric properties [45], and biocompatibility [46] of the substrates. A PEO setup has two electrodes: the cathode and anode (**Figure 3A**). Usually, either a constant current or voltage is applied, leading to the formation of an oxide layer on the anode (*i.e.*, the specimen to be treated). After dielectric

breakdown, the oxide layer is thickened by spark discharges that lead to pore formation [47] (**Figure 3B**). As the process continues, the sparks become more intense, resulting in the formation of larger pores.

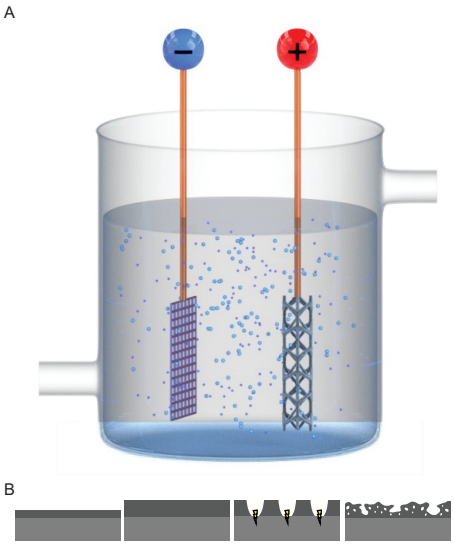

Figure 3. (A) A schematic drawing of the PEO setup with a cathode and an anode (implant). (B) During PEO processing, initially the titanium oxide layer grows outwards. After dielectric breakdown, plasma discharges occur at the surface, resulting in a highly porous structure.

PEO biofunctionalization results in an altered surface morphology and chemical composition. In order to relate the antibacterial activity to certain surface characteristics, the surface of the biofunctionalized specimens is usually characterized (**Table 1-4**). The important surface parameters in this regard are the surface topography, chemical composition, phase composition, and ion release profile. In the following sections, we will discuss the results regarding each of these parameters in more detail.

Table 1. The methodological details of the included studies in which Ag has been used as the antibacterial agent.

		PEO processing parameters								
Substrate	**# of exp groups with Ag**	**Electrolyte**	**Voltage (V)**	**Current density (A/dm^2)**	**Time (min)**	**Surface topography**	**Phase composition**	**Surface content of Ag**	**Cumulative Ag ion release (ppb)**	**Ref**
Ti6Al7Nb	2	0.02 M CA, 0.15 M Ca-GP, and (0.3 and 3.0) g/L Ag NPs	-	20	5	Porous structures (<5 μm)	-	-	12 – day 7 89 – day 7	[15]
Ti6Al4V	2	0.15 M CA, 0.02 M Ca-GP and 3.0 g/L Ag NPs	-	20	5	Micro- and nano-porous structures with Ag NPs of 7-25 nm	Ti, anatase, rutile, HA, $CaTiO_3$ and $Ca_3(PO_4)_2$	-	138 – day 28 600 – day 28	[31]
Ti6Al7Nb	1	0.15 M CA, 0.02 M Ca-GP and 3.0 g/L Ag NPs	-	20	5	Porous structures (<3 μm) with Ag NPs of 37 nm	Ti, anatase and rutile	0.03wt%	-	[32]
CP-Ti	3	0.4 M CA, 0.04 M β-GP and (0.00003, 0.00006 and 0.004 M) AgNO3	380-420	-	180	Irregular and rough morphology with spherical particles and flakes	Rutile, α-TCP, β-Ca2P2O7 and HA	<0.1wt% <0.1wt% 0.21-0.45wt%	-	[35]
CP-Ti	1	0.15 M CA, 0.05 M NaH_2PO_4, 0.25 mM $AgNO_3$	280-320	-	6	Porous surface with 1.5 μm pore size and 8.5% pore density	Anatase, rutile	0.13at%	48 – day 18	[48]
CP-Ti	3	0.4 g/L NaOH, 4.0 g/L NaH_2PO_4 and 0.1-1.0 g/L Ag NPs	400	-	5	Homogenous porous surface layer	Ti, anatase, rutile	1.5at% 3.5at% 5.8at%	40 – day 7 200 – day 7 240 – day 7	[49]

PEO processing parameters										
Substrate	**# of exp groups with Ag**	**Electrolyte**	**Voltage (V)**	**Current density (A/dm^2)**	**Time (min)**	**Surface topography**	**Phase composition**	**Surface content of Ag**	**Cumulative Ag ion release (ppb)**	**Ref**
Ti6Al4V	2	0.15 M CA, 0.02 M Ca-GP, 0.3 M SrA and 3.0 g/L Ag NPs	-	20	5	Uniform coverage with a micro-/nanopores. Addition of SrA resulted in smaller pore size.	Ti, anatase, rutile, HA, $SrTiO_3$, $Sr_2Ca(PO_4)_2$	-	1500 – day 28 1800 – day 28	[50]
CP-Ti	3	100 mM Ca-GP, 150 mM CA, 0,5 and 10 mM $AgNO_3$	-	2.51	10	Porous oxide layer for 0 and 5 mM Ag, non-porous surface for 10mM Ag	Anatase, α-Ti	0.5at% 1.5at% 3.0at%	300 – day 28 3000 – day 28 10^4 – day 28	[51]
CP-Ti, Ti-40Nb	2	Na_2HPO_4, NaOH, β-$Ca_3(PO_4)_2$ and 0.3 – 1 g/L $AgNO_3$	200-450	-	5-10	Uniformly distributed β-TCP particles over a porous surface with 0-8 μm pore sizes	Anatase, α-TCP, β-TCP	0.2at% 0.8at%	-	[52]
CP-Ti	4	Na_2HPO_4, NaOH, β-$Ca_3(PO_4)_2$ and 1 g/L $AgNO_3$	200-450	-	5-10	Uniformly distributed β-TCP particles over a porous surface with 0-8 μm pore sizes	Anatase, α-TCP, β-TCP	0.3at% 0.5at% 0.8at%	-	[53]
CP-Ti	3	0.1 M CA, 0.06 M NaH_2P and 0.01 – 0.05 M Ag_2O NPs	-	10	10	Porous structure with typical micro-sized pores	Anatase, rutile	1.6wt% 3.1wt% 5.8wt%	2000 – day 28 4000 – day 28 10^4 – day 28	[54]

	PEO processing parameters									
Substrate	**# of exp groups with Ag**	**Electrolyte**	**Voltage (V)**	**Current density (A/dm^2)**	**Time (min)**	**Surface topography**	**Phase composition**	**Surface content of Ag**	**Cumulative Ag ion release (ppb)**	**Ref**
CP-Ti	1	CA, Na_2HPO_4 and 0.0025 M Ag-A	380	-	5	Flake-like morphology with regional Ag particles of <200 nm	Ti, anatase, rutile, HA and $CaTiO_3$	4.6wt%	-	[55]
CP-Ti	3	20.5 g/L CA, 7.2 G/L Na_2HPO_4, and (0.0005, 0.001 and 0.002) M Ag-A	400	-	5	Micro-porous structures with Ag NPs surrounding micro-pores	Ti, anatase, rutile, HA and $CaTiO_3$	1.14wt%	-	[56]
Ti6Al4V	1	20.5 g/L CA, 7.2 g/L Na_2HPO_4 and 0.001 M Ag-A	400	-	5	Micro-porous structures with Ag NPs of <100 nm surrounding micro-pores	Ti, anatase, rutile, HA and $CaTiO_3$	0.7wt%	1500 – day 14	[57]
Ti6Al4V	2	CA, β-GP and (0.1 and 0.4) g/L $AgNO_3$	400	-	5	Granular and needle-like morphology with Ag NPs of 20-30 nm	Ti, anatase, rutile, HA and $CaTiO_3$	0.6wt% 2.1wt%	2500 – day 14 8000 – day 14	[58]
Ti-29Nb-13Ta-4.6Zr	2	0.15 M CA, 0.1 M Ca-GP, and (0.0005 and 0.0025) M $AgNO_3$	-	2.51	10	Porous structures (<10μm)	-	0.01wt% 0.01wt%	-	[59]
CP-Ti	3	0.1 M KOH, 0.015 M $K_4P_2O_7$ and (0.1, 0.3 and 0.5) g/L Ag NPs	-	10	5	Micro-porous structures with Ag NPs of <20 nm (3-7.5 μm)	-	0.53at% 0.69at% 0.80at%	12.2 – day 1 22.7 – day 1 28.8 – day 1	[60]

		PEO processing parameters								
Substrate	**# of exp groups with Ag**	**Electrolyte**	**Voltage (V)**	**Current density (A/dm^2)**	**Time (min)**	**Surface topography**	**Phase composition**	**Surface content of Ag**	**Cumulative Ag ion release (ppb)**	**Ref**
CP-Ti	1	0.3 M CA, 0.02 M GP and 0.62 g/L Ag NPs	290	-	10	Porous structures with volcano top-like micro-pores	Ti, anatase and rutile	1.07at%	-	[61]
CP-Ti	1	0.3 M CA, 0.02 M GP and 0.62 g/L Ag NPs	290	-	10	Porous structures with Ag NPs of <100 nm	Ti, anatase and rutile	-	-	[62]
Ti6Al4V	1	Pure water and AgPURE^{TM} W10 nanosilver suspension	-	20	0.5	Flake-like morphology with Ag particles of <200 nm	-	3.6at%	-	[63]
Ti6Al4V	2	0.2 M CA, 0.02 M β-GP and (0.005 and 0.05) g/L Ag NPs	387±3 385±2	8	3	Porous structures with volcano top-like micro-pores (<3 μm)	Ti, rutile and HA	<0.1wt% <0.1wt%	-	[64]
CP-Ti	3	2.0 g/L $NaH_2PO_4{\cdot}2H_2O$, 5.0 g/L CA and 0.1, 0.5 and 0.8 g/L Ag-A	500	-	5	Porous structures uniformly covering surface	Ti, anatase, rutile, HA, $CaTiO_3$	0.8at% 1.5at% 2.2at%	264 – day 7 813 – day 7 1110 – day 7	[65]
CP-Ti	2	NTA, $Ca(OH)_2$, and 180 mg/L Ag NPs	250-300	-	5	Rough, thick oxide layer with a highly porous structure	-	0.3wt% 0.7wt%	-	[66]

Ag-A: silver acetate, CA: calcium acetate, Ca-GP : calcium glycerophosphate, GP: glycerophosphate, HA: hydroxyapatite, KOH: potassium hydroxide, NPs: nanoparticles, NTA: nitrilotriacetic acid, SrA: strontium acetate, TCP: tricalcium phosphate.

Table 2. The methodological details of the included studies in which Cu has been used as the antibacterial agent.

		PEO processing parameters								
Substrate	**# of exp groups with Cu**	**Electrolyte**	**Voltage (V)**	**Current density (A/dm^2)**	**Time (min)**	**Surface topography**	**Phase composition**	**Surface content of Cu**	**Cumulative Cu ion release (ppb)**	**Ref**
CP-Ti	1	0.1 M CA, 0.05 M GP and 0.05 M $Cu(OAc)_2$	-	16.5	4	Micro-porous or crater structures (3-5 μm) with nano-grains of 30-50 nm	Ti and anatase	1.4±0.08wt%	-	[36]
CP-Ti, Ti-40Nb	2	H_3PO_4, 50-75 g/L $CaCO_3$, 40-60 g/L Cu-substituted HA	200-450	-	5-10	Uniformly distributed β-TCP particles over a porous coating surface with 0-8 μm pore sizes.	Anatase, β-TCP, α-TCP, $Ca_2P_2O_7$	0.1at% 0.2at%	-	[52]
CP-Ti	1	0.02 M $C_{12}H_{22}CaO_{14}$, 0.01 M $(NaPO_3)_6$, 0.02 M $C_{12}H_{22}CuO_{14}$	NR	NR	6	Porous surface with irregularly shaped and sized pores	-	-	-	[67]
CP-Ti	2	0.1 M CA, 0.06 M NaH_2P, 5-10 g/L Na_2Cu-EDTA	-	10	10	Highly porous area with micro-sized pores and a rough less porous area	-	2.3wt% 4.2wt%	$3.3/cm^2$ – day 8 $8.1/cm^2$ – day 8	[68]
CP-Ti	3	H_3PO_4, 300-600 g/L $Cu(NO_3)_2{\cdot}H_2O$	450	-	5	With increasing Cu-salt levels sharpening of pores	Ti, anatase	0.54at% 0.55at% 0.72at%	-	[69]

		PEO processing parameters								
Substrate	**# of exp groups with Cu**	**Electrolyte**	**Voltage (V)**	**Current density (A/dm^2)**	**Time (min)**	**Surface topography**	**Phase composition**	**Surface content of Cu**	**Cumulative Cu ion release (ppb)**	**Ref**
Ti6Al4V	2	11 g/L KOH, 10 g/L EDTA-$CuNa_2$, 5 or 15 g/L phytic acid	-	10	3	Uniformly distributed three-dimensional porous structure	Anatase, rutile and TiP_2O_7	1.01wt% 1.92wt%	192 – day 8 197 – day 8	[70]
CP-Ti	1	0.2 M CA monohydrate, 0.02 M NaH_2PO_4, 0.01 M CuA monohydrate	-	3.25	5	Volcanic uniform porous morphology with 1-5 μm pores	Ti, rutile, anatase, $Ca_3(PO_4)_2$	5.05at%	32.8 – day 14	[71]
CP-Ti	4	0.2 M CA, 0.02 M β-GP and (0.00125, 0.0025, 0.00375 and 0.005) M $Cu(OAc)_2$	450	-	1.5	Micro-porous structures (1-4 μm)	Ti, anatase and rutile	0.67wt% 1.17wt% 1.51wt% 1.93wt%	6.75 – day 21 - - 60.2 – day 21	[72]
CP-Ti	2	0.1 M Na_2, 0.25 M NaOH, 0.1 M CA, 0.02 M Na_2SiO_3 and (0.0002 and 0.002) M $CuSO_4$	250	-	5	Macro-pores or crater structures (>100 μm) with nano-grains	-	-	411.3 – day 2 27.0 – day 2	[73]
CP-Ti	1	15 g/L NaH_2PO_4, 2 g/L NaOH and 3.0 g/L Cu NPs	-	20	5	Porous structures (<5 μm) with Cu NPs of <60 nm	Ti, anatase and rutile	-	-	[74]

PEO processing parameters										
Substrate	**# of exp groups with Cu**	**Electrolyte**	**Voltage (V)**	**Current density (A/dm^2)**	**Time (min)**	**Surface topography**	**Phase composition**	**Surface content of Cu**	**Cumulative Cu ion release (ppb)**	**Ref**
CP-Ti	2	15 g·L-1 NaH_2PO_4, 2 g/L NaOH and (0.3 and 3.0) g/L Cu NPs	470±3 465±3	20	5	Micro-porous structures (1-5 µm)	Ti, anatase	1.30at% 2.76at%	0.117 – day 1 0.135 – day 1	[75]
Ti6Al4V	3	Phosphate electrolyte with (2,6 and 10) g/L Cu_2O NPs	450	-	15	Micro-porous structures (<30 µm) with Cu_2O NPs of 20-30 nm	Ti, anatase, rutile, Cu, Cu_2O and CuO	16.0wt% 23.2wt% 24.5wt%	-	[76]
CP-Ti	1	0.002 M CA, 0.02 M β-GP, and 0.0013 M $Cu(OAc)_2$	480	-	2	Micro-porous structures (1-4 µm)	Ti, anatase and rutile	0.77wt%	4.5 – day 7	[77]
Ti6Al4V	1	50 g/L Na_2SiO_3 and 4 g/L Cu_2O NPs	350	-	15	Porous structures (<3 µm) with Cu_2O NPs of 20-50 nm	Ti, anatase, rutile, Cu, Cu_2O and CuO	27.27wt%	-	[78]

CA: calcium acetate, Ca-GP: calcium glycerophosphate, CuA: copper acetate, GP: glycerophosphate, HA: hydroxyapatite, KOH: potassium hydroxide, NPs: nanoparticles, NR: not reported, TCP: tricalcium phosphate.

Table 3. The methodological details of the included studies in which Zn has been used as the antibacterial agent.

			PEO processing parameters						
Substrate	**# of exp groups with Zn**	**Electrolyte**	**Voltage (V)**	**Current density (A/dm^2)**	**Time (min)**	**Surface topography**	**Phase composition**	**Surface content of Zn**	**Cumulative Zn ion release (ppb)**	**Ref**
CP-Ti	3	20 g/L Na_3PO_4, 4 g/L NaOH and (5, 10 and 15) g/L NPs	301 304 310	1000	7	Porous structures with ZnO NPs of 25 nm (<1.51-0.98 μm)	Ti, anatase and rutile	20wt% 25wt% 35wt%	-	[37]
CP-Ti, Ti-40Nb	2	H_3PO_4, 50-75 g/L $CaCO_3$, 40–60 g/L Zn-substituted HA	200-450	-	5-10	Uniformly distributed β-TCP particles over a porous coating surface with 0-8 μm pore sizes	Anatase, β-TCP, α-TCP, $Ca_2P_2O_7$	0.28at% 0.4at%	-	[52]
Ti6Al4V	1	50 g/L Na_2SiO_3 and 4 g/L ZnO NPs	350	-	15	Porous structures (<3 μm) with ZnO NPs of 20-50 nm	Ti, anatase, rutile and ZnO	35.54wt%	-	[78]
CP-Ti	2	0.1 M CA, 0.06 M NaH_2P, 0.02 M Na_2Zn-EDTA or 0.02 M ZnO NPs	-	10	10	Porous surface at micrometre scale	Anatase, rutile, ZnO	-	-	[79]
CP-Ti	3	0.15 M CA, 0.1 M Ca-GP, 0.5-2.5 mM $ZnCl_2$	-	2.51	10	Continuous porous surface with circular pores of 5.3 μm in size	α-Ti, anatase	3.3at%	250 – day 7	[80]

		PEO processing parameters								
Substrate	**# of exp groups with Zn**	**Electrolyte**	**Voltage (V)**	**Current density (A/dm²)**	**Time (min)**	**Surface topography**	**Phase composition**	**Surface content of Zn**	**Cumulative Zn ion release (ppb)**	**Ref**
CP-Ti	1	15 g EDTA-$_2$Na, 8.8 g $Ca(CH_3COO)_2 \cdot H_2O$, 6.3 g $Ca(H_2PO_4) \cdot H_2O$, 7.1 g $Na_2SiO_3 \cdot 9H_2O$, 5 g NaOH, 6 ml H_2O_2, 8.5 g $Zn(CH_3COO)_2$ in 1 L	350-500	-	7	Porous and rough surface with 1-3 μm pore sizes increasing voltages resulting in decreasing pore density and increased pore sizes	Ti, anatase, rutile	2at%	250 – day 15	[81]
CP-Ti	1	0.15 M CA, 0.15 M Ca-GP and 0.02 M ZnA	350	-	1	Porous structures with volcano shaped structures	Ti, anatase and rutile	9.7at%	300 – day 1 <1000 – day 28	[82]
CP-Ti	3	0.1 M CA, 0.05 GP and (0.02, 0.04 and 0.06) M ZnA	-	16.5	4	Porous (<5 μm) with nano-grains of 20-100 nm	Ti, anatase and rutile	4.6±0.7wt% 7.1±0.6wt% 9.3±0.8wt%	1180 – day 14 2235 – day 14 3620 – day 14	[83]
CP-Ti	1	0.02 M CA, 0.15 M Ca-GP and 0.06 M ZnA	-	30	5	Porous structures (<5 μm)	Ti, anatase and rutile	8.7at%	-	[84]
CP-Ti	3	0.1 M CA, 0.025 M $Na_5P_3O_{10}$ and (0.01, 0.03 and 0.05) M ZnA	380	-	20	Micro-porous structures	-	0.199at% 0.574at% 1.995at%	-	[85]
Ti-15Mo	3	0.1M $Ca(H_2PO_2)_2$, 10 g/L ZnO or 25 g/L $Zn_3(PO_4)_2$ or 10 g/L $Ca_3(PO_4)_2$ and 10 g/L $Zn_3(PO_4)_2$ particles	300	15	5	Porous oxide layer with micropores	-	1.5at% 1.1at% 0.2at%	115 – week 16 64 – week 16 60 – week 16	[86]

CA: calcium acetate, Ca-GP: calcium glycerophosphate, GP: glycerophosphate, HA: hydroxyapatite, KOH: potassium hydroxide, NPs: nanoparticles, NR: not reported, TCP: tricalcium phosphate, ZnA: zinc acetate.

Table 4. The methodological details of the included studies in which multiple antibacterial agents have been used.

			PEO processing parameters							
Substrate	**# of exp groups**	**Electrolyte**	**Voltage (V)**	**Current density (A/dm^2)**	**Time (min)**	**Surface topography**	**Phase composition**	**Surface content of Zn**	**Cumulative ion release (ppb)**	**Ref**
Ag and Cu										
Ti6Al4V	6	0.15 M CA, 0.02 M Ca-GP, 0.75-3.0 g/L Ag and/or Cu NPs in ratios 0-100 %	-	20	5	Homogeneous porous surface with circular pores. Ag and/or Cu NPs scattered on surface.	-	-	Day 28: 1491 (Ag) / - 1906 (Ag) / - 1573 (Ag) / 1527 (Cu) 1425 (Ag) / 1392 (Cu) 1291 (Ag) / 1225 (Cu) - / 1981 (Cu)	[19]
Ag and Zn										
Ti6Al4V	6	0.15 M CA, 0.02 M Ca-GP, 0.75-3.0 g/L Ag and/or Zn NPs in ratios 0-100 %	-	20	5	Homogeneous porous surface with circular pores. Ag and/or Zn NPs scattered on surface.	-	-	Day 28: 1491 (Ag) / - 1906 (Ag) / - 1573 (Ag) / 1467 (Zn) 1682 (Ag) / 1697 (Zn) 1749 (Ag) / 1678 (Zn) - / 2281 (Zn)	[20]
CP-Ti	3	0.1 M CA, 0.02 M β-GP, 0.25 g·L-1 SDBS, 0.1 M ZnA and 6 g/L Ag NPs	390	-	0.5 1.5 2	Micro-porous structures with nano-grains of 5-40 nm and Ag NPs of <20 nm (1-4 μm)	Ti, anatase, rutile and ZnO	1.06 (Ag) / 22.19 (Zn) 1.42 (Ag) / 26.93 (Zn) 1.56 (Ag) / 29.38 (Zn)	Week 36 - - 684 (Ag) / 6880 (Zn)	[87]

		PEO processing parameters								
Substrate	**# of exp groups**	**Electrolyte**	**Voltage (V)**	**Current density (A/dm^2)**	**Time (min)**	**Surface topography**	**Phase composition**	**Surface content of Zn**	**Cumulative ion release (ppb)**	**Ref**
Cu and Zn										
CP-Ti	5	0.002 M CA, 0.02 M β-GP, (0, 0.005, 0.01, 0.02 and 0.04 M ZnA and 0.0013 M $Cu(OAc)_2$	480	-	2	Micro-porous structures (1-4 μm)	Ti, anatase and rutile	0.77 (Cu) 0.62 (Cu) / 1.79 (Zn) 0.55 (Cu) / 2.53 (Zn) 0.39 (Cu) / 6.47 (Zn) 0.33 (Cu) / 8.92 (Zn)	Day 20: 4.5 (Cu) 3.2 (Cu) / 7.8 (Zn) 2.7 (Cu) / 23.2 (Zn) 2.3 (Cu) / 64.5 (Zn) 1.9 (Cu) / 94.9 (Zn)	[77]
Ti6Al4V	9	3-9 g/L KOH, 5-11 g/L phytic acid, 2-10 g/L EDTA-$CuNa_2$, 2-10 g/L EDTA-$ZnNa_2$	-	11	3	Porous surface with increasing pore sizes for increased levels of Cu and/or Zn in surface	Ti, anatase	- / 3.47 (Zn) - / 9.84 (Zn) - / 7.90 (Zn) 0.61 (Cu) / 11.41 (Zn) 0.98 (Cu) / 4.42 (Zn) 2.15 (Cu) / 5.42 (Zn) - / 5.64 (Zn) 1.25 (Cu) / 6.71 (Zn) 4.18 (Cu) / 2.89 (Zn)	-	[88]

CA: calcium acetate, Ca-GP: calcium glycerophosphate, GP: glycerophosphate, HA: hydroxyapatite, KOH: potassium hydroxide, NPs: nanoparticles, NR: not reported, SDBS: sodium dodecyl benzene sulfonate, TCP: tricalcium phosphate, ZnA: zinc acetate.

2.4.1 Titanium substrate

Of the reviewed studies, most used commercially pure (CP) titanium (62%) followed by Ti6Al4V (23%), Ti6Al7Nb (4%) [15, 32], Ti40Nb [52], Ti29Nb13Ta4.6Zr [59], and Ti15Mo [86]. Titanium is used for bone implants because of its mechanical properties, corrosion resistance and chemical biocompatibility [46, 89]. Ti6Al4V has a higher strength to weight ratio than CP titanium and is, therefore, the natural choice for load-bearing applications, such as joint replacing implants, while CP titanium is more frequently applied for non-load bearing applications, such as maxillofacial implants [90]. Clinical studies comparing the longterm outcomes of patients treated with either CP-Ti or Ti-alloys are lacking [91, 92].

Ti6Al4V implants may release vanadium and aluminum ions that can induce cytotoxicity [93]. Other alloys employing niobium have, therefore, been developed, including Ti6Al7Nb and Ti40Nb that have similar mechanical properties but do not induce cytotoxicity [94]. In addition, the cytotoxic effects of Al and/or V can be mitigated by PEO since it reduces the ion release of those species [89]. PEO is easily scalable and can be applied to human-sized implants [95]. In order to translate the results from *in vitro* studies, it is, therefore, interesting to investigate the antibacterial behavior of substrates that are designed and produced like an implant, for instance, through additive manufacturing. This also highlights one of the advantages of PEO, namely that it can be applied on highly porous surfaces [31].

2.4.2 PEO electrolyte

The bioactivity of PEO-biofunctionalized implant surfaces is determined for a large part by the composition of the PEO electrolyte, as the elements in the electrolyte eventually make up the chemical composition of the implant surface. More than 50% of the studies included in this systematic review used electrolytes with Ca and P elements. The presence of Ca and P in the electrolyte can result in the formation of hydroxyapatite, which forms more than 60% of bone tissue and is associated with a Ca/P ratio of 1.67 [96, 97]. Calcium acetate and calcium glycerophosphate were the primary source of Ca while $CaCO_3$ [52] and $C_{12}H_{22}CaO_{14}$ [67] were also used in some studies. P is usually added in the form of calcium glycerophosphate, β-glycerophosphate, H_3PO_4 [52, 69], $K_4P_2O_7$ [60], NaH_2PO_4 [48, 49, 65, 71, 74, 75], $NaPO_3$ [67], or $Na_5P_3O_{10}$ [85]. Another element used in about 30% of the included studies is Na in the form of NaOH, NaH_2PO_4 [48, 49, 65, 71, 74, 75], $NaPO_3$ [67], $Na_5P_3O_{10}$ [85], or Na_2SiO_3 [73, 76, 78, 98]. The addition of Na roughens the surface and enhances the Ca/P ratio [99], which has been shown to enhance the osteogenic cell response [100, 101]. In addition, the implantation of Na through plasma immersion has been found to stimulate the osteogenic differentiation of cells [102]. Moreover, KOH [60, 70, 88] is used as an alternative base for NaOH given its similar effects on osteogenic differentiation [103].

2.4.3 PEO processing parameters

The electrical parameters of the PEO process affect the surface morphology [42] including the porosity [104], pore size [105], pore shape [106], and pore density [107] as well as the surface chemistry [83, 84]. Of the included studies, 54% controlled the voltage, 31% controlled the current density, and 13% controlled both while 1 study did not report the PEO processing parameters. The oxidation times ranged between 0 and 180 min, with 21% between 0 – 4 min, 50% between 5 – 9 min, 19% between 10 – 14 min, 6% between 15 – 19 min, and 4% ≥ 20 min. As the current density, voltage, or oxidation time increases, the spark discharge energy amplifies, affecting the mass of the oxide layer formed by a single pulse and resulting in enhanced growth of the oxide layer [40, 108]. Furthermore, as temperature of the local discharge area increases, the plasma effect is enhanced, resulting in larger pore sizes and the transformation of amorphous TiO_2 to anatase and rutile phases. Meanwhile, the intensity of the spark discharge enhances with time, meaning that prolonged oxidation times results in the formation of hydroxyapatite on the implant surface [109, 110]. As such, PEO processing parameters largely affect the chemical and phase composition as well as the surface topography of the implant surface.

2.4.4 Surface morphology

As PEO greatly affects the surface topography of titanium surfaces, all studies investigated the surface topography by scanning electron microscopy (SEM) and most studies reported a porous surface topography with rounded pores (**Figure 4A**). PEO transforms the native titanium oxide layer into a highly porous surface with interconnected porous networks, which is frequently described as a volcanic landscape with micropores that are < 10 μm in diameter. In addition, flake-like morphologies [35, 55, 63] and needle-like structures [58] are often observed. Furthermore, the thickness and porosity of the oxide layer have been shown to depend on the composition of the PEO electrolyte and PEO processing parameters [54, 111]. The specifications of the surface morphology in turn have been shown to greatly influence the antibacterial behavior [112] and osteogenic properties [113, 114] of the implant surfaces.

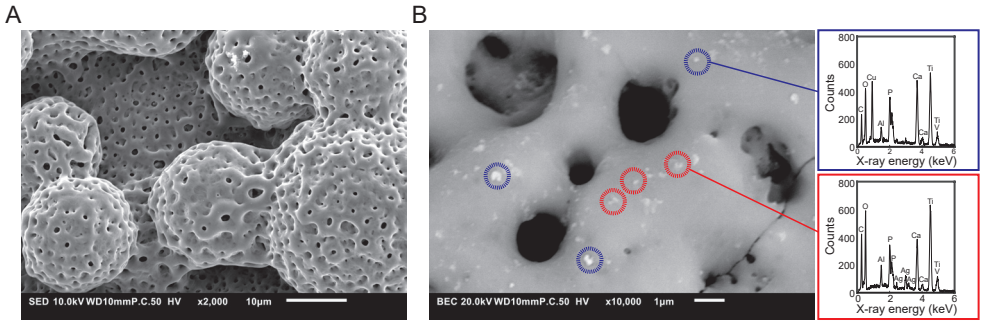

Figure 4. (A) SEM images of the typical surface morphology of titanium implants after PEO processing. (B) EDS analysis of the implant surface to characterize its chemical composition with spectrum of Cu (blue) and Ag (red) nanoparticles.

2.4.5 Phase composition by XRD

One component of the surface that plays a major role in the biological behavior is the phase composition of the implants [115]. These phases can be analyzed with X-ray diffraction (XRD). Among the included studies, 87% analyzed the phase composition. Of those, all studies analyzed Ti phases and observed bare Ti (66%), anatase (81%), and/or rutile (66%). Some studies observed both Ti and anatase, but no studies reported solely Ti and rutile. This is in line with the observation that during PEO processing first the metastable anatase is formed, which then turns into the stable rutile [116]. While all studies that performed XRD analysis identified the TiO_2 phases, not all studies analyzed the other phases formed by the elements incorporated from the electrolyte. Since many PEO electrolytes contain both Ca and P, 19% of the studies observed hydroxyapatite [31, 35, 50, 55-58, 64, 65] and 28% other Ca/P phases including α-TCP [35, 52, 53], β-TCP [52, 53], TiP_2O_7 [70], $CaTiO_3$ [31, 55-58, 65], $Ca_2P_2O_7$ [35, 52] and $Ca_3(PO_4)_2$ [31, 71]. In addition, phases with Cu, Cu_2O, and CuO [76, 78] as well as ZnO [78, 79, 87] were observed.

These phases have been shown to affect the biological response. For instance, TiO_2 is transformed from an amorphous phase into crystalline anatase and rutile phases that have been shown to produce reactive oxygen species (ROS) [117], which in turn contribute to the desired antibacterial behavior [118].

2.4.6 Content of the antibacterial elements incorporated in the PEO layers

The antibacterial activity of Ag, Cu and, Zn that may be present on the implant surface is dose-dependent [119-121]. Therefore, it is important to quantify the content of these elements on

the implant surface after PEO biofunctionalization. This analysis is usually done either by energy dispersive X-ray spectroscopy (EDS; **Figure 4B**) or X-ray photoelectron spectroscopy (XPS). Among the included studies, 80% reported the elemental composition of the surface while 20% did not. The studies have generally reported the elemental composition either in terms of atomic % or weight % and have found them to correlate with the amount of Ag, Cu, and Zn dispersed in the PEO electrolyte. The amount of Ag incorporated in the implant surfaces tended to be lower (1.35 ± 1.82 wt%) than Cu (7.70 ± 10.17 wt%) and Zn (18.79 ± 12.06 wt%), reflecting the lower minimal inhibitory concentration (MIC) of Ag (0.03-8 μg/ml) as compared to Cu (256-448 μg/ml) and Zn (765 μg/ml) [122]. However, EDS does not exclusively measure the elemental composition of the surface but may penetrate deeper into the oxide layer. This is an important point, because it is not clear to what extent the species present deeper inside the oxide layer, which can be up to 10 μm in thickness, contribute to the antibacterial properties of biofunctionalized implants [15]. The amount of active agents present on the implant surface may not be directly related to the antibacterial activity, since the form in which the element is present on the surface (*i.e.*, ionic species, nanocrystals or nanoparticles) affects the antibacterial properties as well [123, 124].

2.4.7 Ion release

An important antibacterial mechanism is through the release of metallic ions from the implant surface. These released ions do not only play a role in contact-killing but also target planktonic bacteria in the implant surrounding, as this area could form a niche for bacteria [125]. Ion release was studied in 48% of the included studies and was measured from 12 h up to 56 days. Overall, the release of Ag, Cu, and Zn ions was found to be higher for the implant surfaces with a higher elemental content and a higher concentration of the active agents in the PEO electrolyte. The combination of Ag with Cu or Zn NPs on the implant surface resulted in enhanced Cu or Zn release while the Ag release was reduced in the first 24 h [19, 20]. Similarly, higher concentrations of zinc acetate added to copper acetate resulted in enhanced Zn ion release while Cu ion release was reduced with higher concentrations of zinc acetate [77]. This may stem from galvanic coupling favoring the oxidation and release of one element over the other [126, 127]. When studied in detail, this may allow for controlled release profiles and accompanying antibacterial effects.

Ion release results depend on the liquid in which these measurements are performed. Frequently used liquids are phosphate-buffered saline (PBS) and simulated body fluid (SBF) [128]. Ion release does not only depend on the surface content, but also on the form in which the antibacterial agent is present on the surface (*i.e.*, as ionic species, nanoparticles, or other

forms) [124]. Ideally, one could control the release of ions to not only prevent infection immediately after surgery but also ward off late implant-associated infections [129]. However, comparing the reported ions release kinetics is difficult due to the different units, specimen designs, and measurement setups being used. In addition to the previously mentioned parameters, the surface area plays an important role in determining the concentration of the released ions, as a larger area allows for more agents to be incorporated on the surface, in turn leading to a higher release rate [31]. The reported concentrations of release ions should, therefore, be normalized with respect to the surface area of the specimens to enable direct comparison between different studies. The information regarding the surface area is generally not reported in the studies, rendering a direct comparison impossible.

2.5 ANTIBACTERIAL PROPERTIES

Surface biofunctionalization by PEO with Ag, Cu, and Zn results in antibacterial surfaces. In the following section, we will first compare the antibacterial activity of PEO biofunctionalized titanium implants bearing Ag, Cu, and Zn found by *in vitro* and *ex vivo* studies (**Table 5**). Then, we will discuss the factors that determine the antibacterial activity. First of all, the types of the bacterial species and strains have been shown to affect the susceptibility and resistance of bacteria to antibacterial agents [130], their ability to infect host cells [131], and their pathogenicity [132]. Moreover, the type of assay, the inoculation dose and the culture time used in the studies may affect the observed antibacterial activity. Finally, the activity against adherent and/or planktonic bacteria is discussed, as the adherence of bacteria may initiate biofilm formation while planktonic bacteria form a source for reinfection and host cell invasion [133].

Table 5. Antibacterial tests and results on PEO-modified Ti-surfaces bearing single or multiple elements.

Bacterial Species	Bacterial Strain	Source	Analysis method	Duration (h)	Test inoculum	Planktonic / adherent	Main outcomes	Ref
Ag								
MRSA	AMC201	Ag NPs	Modified version of JIS Z 2801:2000	24	10^7 CFU/ml	Adherent	After 24 h: 98 and 99.75% reduction by incorporation of 0.3 and 3 g/L Ag NPs	[15]
MRSA	AMC201	Ag NPs	Petrifilm™ assay Zone of inhibition CFU count SEM *Ex vivo*	48	10^3-10^8 CFU/ml	Adherent	Significantly reduced numbers of viable bacterial colonies by incorporation of Ag NPs in the surface after 15 min Four-logs reduction in the numbers of viable bacterial colonies in the *ex vivo* infection model by incorporation of Ag, compared with a 2-logs reduction in absence of Ag after 24 h Prevention biofilm formation for at least 48 h	[31]
MRSA	AMC201	Ag NPs	Modified version of JIS Z 2801:2000	24	10^7 CFU/ml	Adherent	100% killed by incorporation of 0.03wt% Ag at 24 h	[32]
S. aureus *E. coli*	ATCC6538 ATCC25922	$AgNO_3$	Spread plate analysis	24	$1.6 \cdot 10^5$ CFU/ml	Planktonic	After 24 h: >99.8 reduction by incorporation of >0.1wt% Ag, compared with a reduction of 20% in absence of Ag	[35]
E. coli	ATCC25933	$AgNO_3$	Spread plate analysis	12	10^6 CFU/ml	Adherent	After 12 h: >99.9% eradication of *E. coli*	[48]
S. aureus *E. coli*	ATCC6538 ATCC25922	Ag NPs	CFU count Fluorescence measurement	24	0.0001 OD_{590}	Adherent	After 24 h: complete eradication for *E.coli* and 6-log reduction for *S.aureus* with 5.8at% Ag Stronger antibacterial effect on *E.coli* compared to *S. aureus*	[49]

Bacterial Species	Bacterial Strain	Source	Analysis method	Duration (h)	Test inoculum	Planktonic / adherent	Main outcomes	Ref
MRSA	USA300	Ag NPs	Zone of inhibition CFU count SEM *Ex vivo*	48	10^4-10^7 CFU/ml	Adherent Planktonic	After 24 h: enhanced zone of inhibition for PT-AgSr samples compared to PT-Ag samples. Complete eradiation of adherent and planktonic bacteria *in vitro* and *ex vivo*. After 48 h: prevention of biofilm formation in Ag-containing surfaces.	[50]
S.aureus *E.coli*	NBRC122135 NBRC3972	$AgNO_3$	ISO 22196:2007	24	0.4-3.0 · 10^6 CFU/ml	Adherent	After 24 h: > 0.05 mM Ag in PEO electrolyte reduced bacteria >90% Inhibitory effect was stronger for *E. coli* compared to *S. aureus*	[51]
S. aureus	209P	$AgNO_3$	Spread plate analysis	2	500 CFU/ml	Planktonic	After 2 h: 53% reduction in CFU after incubation in supernatant	[52]
S. aureus	ATCC6538-P	$AgNO_3$	Spread plate analysis	2	250 CFU/ml	Planktonic	After 2 h: 70% reduction in CFU and 45% antibacterial rate for >0.3%at Ag	[53]
S. aureus	NR	Ag_2O	Spread plate analysis	24	10^5 CFU/ml	Adherent	After 24 h: antibacterial rate >1 with 5.8wt% Ag	[54]
S. aureus *E. coli*	ATCC6538 ATCC25822	Ag-A	Spread plate analysis	24	2.5 · 10^5 CFU/ml	Planktonic	At 24 h: 99.9 and 58.3% reduction of E. coli for 4.6wt% Ag and Ag-free At 24 h: 99.8 and 47.8% reduction of S. aureus for 4.6wt% Ag and Ag-free	[55]
S. aureus	ATCC6538	Ag-A	Modified version of JIS Z 2801:2000	24	2.5 · 10^5 CFU/ml	Planktonic	After 24 h: 99.98% reduction by incorporation of 1.14wt% Ag	[56]
S. mutans	ATCC25175	Ag-A	Spread plate analysis SEM	16.5	1.5 · 10^8 CFU/ml	Adherent	After 16.5 h: 67% reduction by incorporation of 0.7wt% Ag	[57]
E. coli	ATCC25822	$AgNO_3$	Spread plate analysis	24	10^9 CFU/ml	Planktonic	After 24 h: 97.4 and 99.2% reduction by incorporation of 0.6 and 2.1wt% Ag, compared with a reduction of 22.7% in absence of Ag: Ag-free PEO-modified surface	[58]

Bacterial Species	Bacterial Strain	Source	Analysis method	Duration (h)	Test inoculum	Planktonic / adherent	Main outcomes	Ref
E. coli	NBRC3972	$AgNO_3$	ISO 22196:2011	24	$5 \cdot 10^6$ CFU/ml	Planktonic	100% killed in presence of 0.01wt% Ag at 24 h	[59]
E. coli	ATCC25922	Ag NPs	Spread plate analysis	24	10^6 CFU/ml	Planktonic	100% killed by incorporation of 0.53wt% Ag within 12 h	[60]
S. sanguinis	IAL1832	Ag NPs	Spread plate analysis	24	10^7 CFU/ml	Planktonic	At 24 h: 62 and 53% reduction by incorporation of 1.9wt% Ag, compared to pure Ti and the Ag-free PEO-modified surface, respectively	[61]
S. epidermidis	ATCC35984	Ag NPs	Spread plate analysis SEM	18	10^6 CFU/ml	Adherent Planktonic	100% killed by incorporation of 3.6at% Ag within 12 h	[63]
P. gingivalis	NR	Ag NPs	Microbial Viability Assay SEM	24	10^7 CFU/ml	Adherent	Reduction of the bacterial viability to 21-31% by incorporation of <0.1wt% Ag at 8 h, compared with a mean viability of 96.6% in absence of Ag in the PEO-modified surface	[64]
E. coli *S. aureus* MRSA	ATCC25922 ATCC6538 Mu50	Ag-A	CFU count SEM	24	0.0005 OD_{590}	Adherent	4-6 log inhibition of *E. coli*, 3-5 log inhibition of *S. aureus* and 2-5 log inhibition of MRSA after 24 h for 0.1 and 0.5 and 0.8 g/L Ag respectively	[65]
S. aureus	B 918	Ag NPs	Spread plate analysis	24	10^6 CFU/ml	Adherent	Lower amounts of adherent bacteria after 2 h. No inhibition at later time points	[66]
Cu								
S. aureus	NR	$Cu(OAc)_2$	Spread plate analysis	4	10^6 CFU/ml	Planktonic	Significantly reduced numbers of bacterial colonies by incorporation of 1.4wt% Cu in the surface after 4 h	[36]
S. aureus	209P	Cu-substituted HA	Spread plate analysis	2	500 CFU/ml	Planktonic	After 2 h: 27% reduction in optical density after incubation in supernatant	[52]

Bacterial Species	Bacterial Strain	Source	Analysis method	Duration (h)	Test inoculum	Planktonic / adherent	Main outcomes	Ref
S. aureus	NR	$C_{12}H_{22}$-CuO_{14}	Spread plate analysis SEM	24	10^4 CFU/ml	Adherent	After 24 h: 100% antibacterial rate on Cu surfaces Morphological changes and disrupted membrane of bacterial cells.	[67]
S. aureus	ATCC6538	EDTA-$CuNa_2$	Live/dead staining SEM	24	10^5 CFU/ml	Adherent	After 24 h: more dead bacteria on Cu surface compared to Ti control Shape changes and membrane disruption of bacteria under SEM	[68]
E. coli	ATCC25922	$Cu(NO_3)_2 \cdot H_2O$	Zone of inhibition Adhesion test	24	10^8 CFU/ml	Adherent Planktonic	After 24 h: zone of inhibition around 0.54-0.72wt% Cu No bacterial cells adhering after 24 h	[69]
S. aureus *E. Coli*	ATCC43300 ATCC25922	EDTA-$CuNA_2$	Spread plate analysis	24	$5 \cdot 10^5$ CFU/ml	Adherent	After 24 h: complete eradication of *S. aureus* and *E. coli* for 1.92wt% Cu After 14 days no antibacterial activity.	[70]
S. aureus	ATCC6538	CuA monohydrate	Spread plate analysis	24	10^5 CFU/ml	Adherent	After 24 h: >99% growth reduction with 5.05at% Cu in the surface.	[71]
S. aureus	ATCC25923	$Cu(OAc)_2$	Spread plate analysis Live/dead staining SEM	96	10^5 CFU/ml	Adherent Planktonic	At 6 h: 0.6 x 10^5 CFU/cm^2 on 1.93wt% Cu-PEO and 1.5 x 10^5 CFU/cm^2 on Cu-free At 24 h: 0.6 x 10^5 CFU/cm^2 on 1.93wt% Cu-PEO and 9.7 x 10^5 CFU/cm^2 on Cu-free At 6 h: 1.0 x 10^5 CFU/ml for 1.93wt% Cu- PEO and 3.8 x 10^5 CFU/ml on Cu-free At 24 h: 5.2 x 10^5 CFU/ml for 1.93wt% Cu-PEO and 200 x 10^5 CFU/ml on Cu-free	[72]
S. aureus	NR	$CuSO_4$	Macrophage bactericidal assay SEM	2	10^7 CFU/ml	Planktonic	Significantly enhanced macrophage-bactericidal capacity on 2mM Cu-incorporated PEO-modified surface	[73]

Bacterial Species	Bacterial Strain	Source	Analysis method	Duration (h)	Test inoculum	Planktonic / adherent	Main outcomes	Ref
S. aureus *E. coli*	NR	Cu NPs	Live/dead staining	24	10^5 CFU/ml	Adherent	Majority of bacteria killed after 24 h	[74]
S. aureus	NR	Cu NPs	Spread plate analysis Live/dead staining SEM	24	10^7 CFU/ml	Adherent Planktonic	100% killed by incorporation of 2.8at% Cu at 24 h	[75]
E. coli	CMCC44102	Cu_2O NPs	ASTM G21-13	24	NR	Adherent	At 24 h: 99.74% killed by incorporation of 10 g·L-1 Cu_2O NPs, compared to 95.25% killed in absence of Cu in the PEO-modified surface	[76]
Zn								
S. aureus *E. coli*	ATCC25923 ATCC25922	ZnO NPs	ASTM G21-1996	24	10^6 CFU/ml	Planktonic	After 24 h: reduced numbers of viable colonies by incorporation of Zn compared with Zn-free surfaces	[37]
S. aureus	209P	Zn-substituted HA	Spread plate analysis	2	500 CFU/ml	Planktonic	After 2h: 40% reduction in optical density after incubation in supernatant	[52]
E. coli	NR	ZnO NPs Zn-EDTA	Measurement of OD_{600}	24	NR	Planktonic	After 24 h: 50% reduction in OD_{600} values of culture medium	[79]
E. coli	NBRC3972	$ZnCl_2$	Spread plate analysis	24	$4.9 \cdot 10^6$ CFU/ml	Adherent	After 24 less than 1 log reduction	[80]
S. aureus *E. coli*	ATCC25923 ATCC25922	ZnA	Spread plate analysis SEM	24	10^7 CFU/ml	Planktonic	After 24 h: 40% enhanced antibacterial rate on *E.coli* No effect on *S. aureus*	[81]
S. aureus *P. aeruginosa*	NR	ZnA	Live/dead staining SEM	24	$OD_{600} \sim 0.35$	Adherent	Significantly reduced numbers of viable colonies by incorporation of 9.7at% Zn at 6 and 24 h	[82]
S. aureus *E. coli*	ATCC25923 ATCC25922	ZnA	Spread plate analysis SEM	24	10^7 CFU/ml	Adherent	At 24 h: 40.2, 99.2 and 100% reduction of *E. coli* for 4.6, 7.1 and 9.3wt% Zn At 24 h: 96.3, 99.5 and 99.8% reduction of *S. aureus* for 4.6, 7.1 and 9.3wt% Zn	[83]

Bacterial Species	Bacterial Strain	Source	Analysis method	Duration (h)	Test inoculum	Planktonic / adherent	Main outcomes	Ref
S. aureus *E. coli*	NR	ZnA	Spread plate analysis Live/dead staining SEM	24	10^5 CFU/ml	Adherent Planktonic	>90% killed at 24 h	[84]
S. mutans	ATCC 25175	ZnA	Spread plate analysis SEM	48	10^9 CFU/ml	Adherent	At 24 h: 62.54, 69.84 and 79.19% reduction for 0.199, 0.574 and 1.995at% Zn	[85]
S. aureus MRSA *S. epidermidis*	ATCC25923 MRSA1030 ATCC700296 *S. epidermidis* 15560	ZnO and $Zn_3(PO_4)_2$ particles	Spread plate analysis	4	10^6 CFU/ml	Adherent	After 4 h no growth inhibition for *S. aureus* and MRSA, and 90% eradication of *S. epidermidis* on Zn-bearing surfaces.	[86]
Ag and Cu								
MRSA	USA300	Ag and Cu NPs	Zone of inhibition CFU count SEM *Ex vivo*	24	10^4-10^7 CFU/ml	Adherent Planktonic	After 24 h: zone of inhibition and eradication of adhering and planktonic bacteria *in vitro* and *ex vivo* for surface containing >50% Ag and Cu NPs No antibacterial properties for solely Cu NP bearing surfaces and controls.	[19]
Ag and Zn								
MRSA	USA300	Ag and Zn NPs	Zone of inhibition CFU count SEM *Ex vivo*	24	10^4-10^7 CFU/ml	Adherent Planktonic	After 24 h: zone of inhibition and eradication of adhering and planktonic bacteria *in vitro* and *ex vivo* for surface containing >50% Ag and Zn NPs No antibacterial properties for solely Zn NP bearing surfaces and controls.	[20]

Bacterial Species	Bacterial Strain	Source	Analysis method	Duration (h)	Test inoculum	Planktonic / adherent	Main outcomes	Ref
S. aureus	ATCC25923	Ag NPs and ZnA	Spread plate analysis SEM	24	10^5 CFU/ml	Adherent Planktonic	At 24 h: 4.1, 2.5 and 2.4 · 10^3 CFU/cm^2 on Ag and Zn co-doped surfaces compared with 2.3 · 10^6 CFU/cm^2 on polished Ti, respectively. Significantly reduced numbers of viable colonies by incorporation of Ag NPs and Zn compared to polished Ti.	[87]
Cu and Zn								
S. aureus	ATCC25923	$Cu(OAc)_2$ ZnA	Spread plate analysis Live/dead staining SEM	24	10^5 CFU/ml	Adherent Planktonic	At 6 h: 2.63, 1.47 and 0.84 · 10^5 CFU/cm^2 on Cu and Zn co-doped surfaces compared with 1.8, and 8.5 · 10^5 CFU/cm-2 on Cu-single doped and Cu-free surfaces, respectively. At 24 h: 3.72, 2.89 and 1.32 · 10^5 CFU/cm^2 on Cu and Zn co-doped surfaces compared to 2.89 and 16 · 10^5 CFU/cm^2 on Cu-single doped and Cu-free surfaces, respectively. Significantly reduced number of viable colonies by incorporation of >2.53wt% Zn and <0.55wt% Cu, compared to 0.77wt% Cu	[77]
E. coli	CMCC44102	Cu_2O and ZnO NPs	ASTM G21-13	24	10^6 CFU/ml	Planktonic	PEO-modified surfaces bearing Cu_2O NPs demonstrated a superior antibacterial activity ~ 100% killed, compared with PEO-modified surfaces bearing ZnO NPs	[78]
MRSA *S. aureus* *E. coli*	ATCC43300 CGMCC12465 CGMCC13373	EDTA-$CuNa_2$ EDTA-$ZnNa_2$	Spread plate analysis	24	10^6 CFU/ml	Adherent	After 24 h: complete prevention of growth with > 6 g/L Cu or Zn in PEO electrolyte against MRSA, *S. aureus* and *E. coli*.	[88]

Ag-A: silver acetate, ASTM: American Society for Testing and Materials, CFU: colony forming unit, CuA: copper acetate HA; hydroxyapatite, JIS: Japanese Industrial Standards, NPs: nanoparticles, NR: not reported, SEM: scanning electron microscopy, ZnA: zinc acetate.

2.5.1 Comparing antibacterial activities of Ag, Cu, and Zn

All the included studies reported antibacterial activity. Guidelines designate a material as antibacterial when it induces a > 99.9% (*i.e.*, 3-log) reduction in the number of viable bacteria [134]. However, this is a guideline for treatment, while the required reduction in the bacterial load for the prevention of IAI is not known. In fact, 48% of the studies using Ag, 14% of the studies with Cu, 10% of the studies with Zn, and 80% of the studies that combined these metallic agents reduced the bacterial load by > 99.9%. This indicates that surfaces biofunctionalized with Ag demonstrate the highest degree of antibacterial activity while Cu and Zn are less effective, which is not surprising given the much lower MIC for Ag as compared to Cu and Zn [122]. Interestingly, combining Ag, Cu, and Zn resulted in much higher levels of antibacterial activity while the doses of single elements can be reduced [19, 20, 87, 88].

Studies that focused on the antibacterial mechanisms of Ag, Cu and Zn NPs suggest that two antibacterial mechanisms play a role: ion release killing [135] and the generation of reactive oxygen species (ROS) [136]. Ions released from the implant diffuse across the bacterial cell wall and penetrate into bacteria where vital bacterial structures are targeted. Meanwhile, ROS are highly reactive and cause lysis of the bacterial cell wall. It was found that Cu shows best antibacterial activity as a result of contact killing [137], while Ag exhibits most of its antibacterial activity through both ion release and contact killing [138]. Furthermore, the synergistic antibacterial properties of AgNPs and Zn ions were observed to stem from long range Zn ion release and contact-killing effects from Ag through microgalvanic coupling [29, 139].

We have plotted a 3D graph showing the correlation between antibacterial activity, cytocompatibility and surface content of the antibacterial agent for the titanium substrates biofunctionalized by PEO with Ag, Cu or Zn (**Figure 5**). Very few studies reported all of these 3 parameters. This analysis shows that Ag indeed results in the highest levels of antibacterial activity at lower doses compared to Cu and Zn, yet also induces cytotoxicity more frequently. However, a direct comparison between the included studies, and thereby of Ag, Cu, and Zn bearing surfaces, is hampered by a large number of variables that differ in the various studies and are addressed in the next paragraphs of this section.

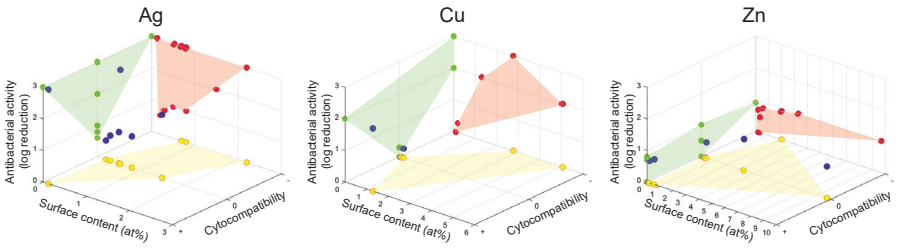

Figure 5. The relation between the antibacterial activity, cytocompatibility and surface content for titanium surfaces biofunctionalized by PEO with Ag, Cu or Zn. The reported antibacterial activity as a function of surface content and cytocompatibility is depicted by the blue dots. The green, red and yellow projections enable a comparison between the parameters. Cytocompatibility is depicted as cytotoxicity (-), no effect (0) or enhanced cytocompatibility (+).

2.5.2 Bacterial species and strains

Antibacterial results are affected by the tested bacterial species. Of the reviewed studies, 57% used *S. aureus*, 31% *E. coli*, and 12% other bacterial species, including *S. epidermidis* [63, 86], *S. sanguinis* [61], *S. mutans* [57, 85], *P. aeruginosa* [82], and *P. gingivalis* [64]. Given that Ag, Cu, and Zn form an alternative to antibiotics, it is important to analyze the results on antibiotic resistant bacteria, such as MRSA, which are involved in up to 32% of fracture-related infections [140, 141]. MRSA was investigated in 9 studies and found to be strongly inhibited by Ag [15, 31, 32, 50, 65], Ag and Cu [19], Ag and Zn [20], Cu and Zn [88] bearing surfaces, while one study that included Zn surfaces did not observe any inhibition [86]. Thukkaram et al. observed that the antibacterial effect of Ag containing surfaces against MRSA was lower compared to *S. aureus* and *E. coli*, although with increasing doses of Ag all bacterial species were targeted equally [65]. Furthermore, testing on multiple species was performed in 19% of the included studies. No studies tested multiple species in a single experiment (*i.e.*, co-culture of multiple species), which would be of interest given that 10-20% of IAI are induced by polymicrobial infections [142, 143].

We can, thus, conclude that most studies investigated antibacterial behavior against *S. aureus*. This bacterial species causes 20-46% of IAI [144-146]. Other gram-positive species, such as *Streptococci* caused up to 10% and *Enterococci* 3-7% of cases [147]. *Enterococci* have not been tested in studies with PEO-treated surfaces bearing Ag, Cu, or Zn. Gram-negative bacteria, such as *P. aeruginosa* and *Enterobacteriaceae* induce 6-17% of IAI [143, 148]. Given the relatively low rate of IAI induced by *Enterobacteriaceae*, it is surprising that 31% of the studies investigated the effects of the implant surfaces on *E. coli*. While some studies that analyzed both *S. aureus* and *E. coli* reported a stronger antibacterial effect against *E. coli* as compared to *S. aureus* [49, 51, 55, 65, 83, 98] others have reported a similar antibacterial effect

for both species [35, 37, 70, 74, 84, 88]. Interestingly, up to 42% of IAI in patients have been caused by culture-negative (*i.e.*, undefined) bacteria [149, 150] and therefore warrant for an antibacterial agent effective against a wide antimicrobial spectrum.

Among bacterial species, different levels of sensitivity to antibacterial agents have been reported [151], including against Ag and Cu [152]. To what extent the differences between strains does play a role depends on the bacterial species. The differences between strains in terms of their MIC/MBC values have been found to be negligible for *S. aureus* but are quite large in the case of *E. coli* strains [153]. It is, therefore, important that the bacterial strain is properly reported, which was done only in 79% of the included studies. Only one study, conducted by Leśniak-Ziółkowska et al., compared different strains within a bacterial species, namely *S. aureus* (ATCC 25923 and clinical MRSA 1030) and *S. epidermidis* (ATCC 700296 and clinical 15560) [86]. No strain-dependent differences were observed after 4 h using a bacterial adhesion test.

2.5.3 Source of antibacterial agent

The antibacterial behavior depends not exclusively on the antibacterial agent but also on the form in which Ag, Cu, and Zn are added to the PEO electrolyte and are subsequently incorporated onto the titanium implant surface [124]. Ag, Cu, and Zn elements are either completely dissolved in the electrolyte or are added in the form of NPs that form a suspension. The former will end up in the form of chemical compounds present all over the surface, while the latter (NPs) are spread over the surface. NPs may form a reservoir from which ions are released, thereby ensuring prolonged antibacterial activity [154]. In addition, the shape of the NPs determines the antibacterial activity as the surface-to-volume ratio affects the ion release and, thus, the efficacy of the surface biofunctionalization process [155]. Ionic forms only induce antibacterial activity through the action of ions, while NPs also produce reactive oxygen species and induce contact-killing [156]. Among the included studies, 33% used NPs, 64% employed ionic species, and only a study by Zhang et al., combined ions and NPs [87]. This study combined Ag NPs with Zn acetate which resulted in much higher release of Zn ions compared to Ag ions. Furthermore, the antibacterial activity was assessed against both adherent and planktonic *S. aureus* after 24 h. The develop surface demonstrated significant antibacterial behavior with increasing concentrations of Ag and Zn leading to further reduction of viable bacteria. The authors reason that the antibacterial activity stems from ROS generation by both Ag and Zn as well as Ag+ release. Moreover, both Ag and Zn ion concentrations remain below cytotoxicity levels and thus stress the utility of combining these elements. Studies that investigate the differences in the antibacterial properties induced by NP and ionic forms are lacking.

2.5.4 Analysis method

The antibacterial properties can be investigated by different assays. Properties often investigated are the antibacterial leaching activity, the killing of adherent bacteria, and the prevention of biofilm formation. Although most of the included studies have used only one antibacterial assay (53%), the use of several assays is required for the assessment of the various types of antibacterial properties [157]. Therefore, 32%, 8%, and 8% of the included studies have used 2, 3, and 4 assays, respectively. To determine the leaching effects of the antibacterial ions released from the PEO surfaces, a zone of inhibition assay or a Kirby-Bauer assay is often used. The number of bacteria can be quantified either through a direct CFU count, by spread plate analysis, or by staining the live cells using a fluorescent dye. A few studies refer to ISO [51, 59] and ASTM [37, 76, 78] standards. With SEM, adherent bacteria and/or biofilm formation can be visualized in a non-quantitative manner. A wide variety in the type of assays used in the studies was found, with spread plate analysis (33%), SEM (24%), and viability fluorescence imaging (12%) being the most frequently applied assays.

In addition to *in vitro* assays, *ex vivo* models have been explored in which infected implants biofunctionalized with Ag and Cu, Zn, or Sr are inserted into a murine femur [19, 20, 31, 50]. Subsequently, the number of CFU present are quantified (*e.g.*, after 24 h). Although this *ex vivo* model does not allow to assess the effects of the implants on the immune system or bony ingrowth, some of the other *in vivo* effects such as those of the extracellular matrix and bone tissue [158] can be captured to some extent. Indeed, the gene expression profile of osteocytes has been found to be similar between an *ex vivo* bone infection model and tissue samples from IAI patients [159]. Thus far, no study has tested the antibacterial activity of titanium implants biofunctionalized by PEO with Ag, Cu, and Zn *in vivo*.

2.5.5 Duration and inoculum of antibacterial assay

Over two third of IAIs are initiated during surgery [160]. A rapid antibacterial response to prevent the adherence of the bacteria that enter the human body peri-operatively is, therefore, desired. Almost all of the included studies (94%) have tested the antibacterial properties within 24 h and 10% even within 2 h. However, IAI can also be initiated long after surgery, stemming from hematogenous origins. Prolonged antibacterial activity is, thus, desirable too [72, 85, 161]. Zhang et al., reported on the antibacterial activity of Cu-containing surfaces for longer periods of time [72]. It was observed that the number of viable adherent bacteria was significantly reduced on surfaces containing 0.67 – 1.98 wt% Cu up to 96 h. However, this is one of the few studies aiming to assess longterm antibacterial behavior, since prolonged *in vitro* culture of bacteria is challenging. Research into late IAI is, therefore, primarily performed *in vivo* [162, 163].

The inoculum used in the antibacterial assays is another factor determining the antibacterial behavior of PEO-biofunctionalized implants. The exact number of bacteria required for IAI is unknown, but it has been shown that the presence of a foreign body can reduce the infection dose by 6 orders of magnitude [164] due to a hampered immune response [165]. The inoculum used in the included studies varied widely between 250 [53] and 109 CFU/ml [58, 85], and was not reported in two studies. Currently, most inocula are presented per volume or as a measure of optical density. However, also the surface area of the implant is of importance, as more area with more incorporated antibacterial agent is likely to have a greater antibacterial effect. Therefore, presenting the inoculum per volume per surface area would support comparative analyses of different studies.

2.5.6 Planktonic vs. adherent bacteria

As both planktonic and adherent bacteria play an important role in IAIs, antibacterial implants should target both types of bacteria. Planktonic bacteria are present in the fluid and tissue surrounding the implant and have shown to be a reservoir for late-stage reinfections [125]. Once the bacteria adhere to the implant, bacteria should be targeted in order to prevent biofilm formation as this would induce bacterial resistance to antibiotic treatment [166]. In this respect, 42% of the included studies investigated antibacterial activity against adherent, 35% against planktonic, and 23% against both planktonic and adherent bacteria. Targeting both planktonic and adherent bacteria should, therefore, be emphasized more in future studies.

2.6 BIOCOMPATIBILITY

In addition to antibacterial properties, PEO-biofunctionalized implant surfaces should not induce cytotoxicity, and ideally even enhance cell response and bony ingrowth. The compatibility of the implants with mammalian cells is, therefore, an important topic that needs to be thoroughly investigated for any such implant. Several of the included studies report the results of such *in vitro* cytocompatibility experiments, which are affected by the type of the assay, cell type, and cell source (**Supplementary Table 1**).

2.6.1 Cytocompatibility of Ag, Cu and Zn surfaces

Cytocompatibility was investigated in 71% of studies. In those studies, Ag induced cytotoxicity in 13% of the studies while 10% of the studies investigating Cu and 0% of those employing Zn have reported cytotoxic effects. None of the studies combining Ag, Cu, and Zn reported cytotoxicity. Cell response of the implants was improved in 7% of the studies using Ag,

50% of the studies focused on Cu, and 33% of the studies with Zn, as well as for 50% of the studies in which two or more antibacterial agents were combined. The control group often consists of PEO biofunctionalized surfaces without antibacterial elements. Cytotoxicity is, therefore, not considered a major concern by the vast majority of the included studies. Indeed, Cu and to somewhat lesser extent Zn have been shown to improve the cytocompatibility of PEO-treated implants.

2.6.2 Type of assay

Several processes that occur in bone regeneration are investigated *in vitro*. Cells need to attach to the implant surface [167], spread [168], stay viable [169], proliferate, differentiate towards the osteogenic lineage [170], and eventually form an extracellular matrix [171]. Indicators for the bone regeneration process include cell morphology [172], expression of osteogenic markers [173], metabolic activity [174], and the production of specific proteins [175]. The parameters studied the most in the included studies were viability and proliferation (analyzed in 56% of the included studies), followed by adhesion and attachment (36%), differentiation (25%), cell spreading (22%), matrix calcification and mineralization (11%), metabolic activity (8%), gene expression (8%), morphology (3%), cell seeding (3%), and other assays (6%) including protein production, mitochondrial functioning, and cytokine production.

2.6.3 Cell type

The cellular response has shown to differ in *in vitro* experiments between different cell types [176, 177]. In the reviewed studies, pre-osteoblasts (32%), osteosarcoma cells (22%), fibroblasts (20%), MSCs (17%) and SV-HFO, macrophages, adipose stem cells, and endothelial cells (each in 1 study) have been used. Pre-osteoblasts and MSCs are the main cells responsible for bone formation [178, 179]. Osteosarcoma and SV-HFO cells [180] are immortalized cells stemming from the osteogenic lineage. However, osteosarcoma has been shown to stem from defective differentiation [181]. Since these titanium implants will be used in bone tissue, it is surprising that 29% of the studies did not analyze the effects of the implants on bone-forming cells. Other cell types may support bone formation through indirect pathways. Endothelial cells play a role in angiogenesis, which plays a major role in bone regeneration as blood vessels carry nutrients and oxygen and facilitate the transport of immune cells to the regenerating bone tissue [182]. Meanwhile, macrophages form an important part of the immune response against IAI. Any potential toxicity of the synthesized implants against this cell type is of concern, as it may hamper the clearance of infections [16, 183]. Finally, fibroblasts have been shown to regulate osteoblast activity through tight junction interactions [184].

2.6.4 Cell source

About 22% of the included studies have used primary cells, whereas 78% have utilized cell lines. Primary cells are more representative of the clinical situation, as they have been isolated from donors. However, their variability is high. Cells from multiple donors, therefore, need to be tested [185]. Cell lines, on the other hand, are homogenous and stable, while exhibiting little variability. However, their immortalized nature makes them differ from the clinical situation [186]. Furthermore, the source of animal species from which the cells were derived differed greatly between the included studies with 56% using murine cells, 34% human cells, and 10% rat cells. The osteogenic differentiation capacity of stem cells is known to differ between human, mice, and rat MSCs [187, 188]. These differences in animal species make it difficult (if not impossible) to directly compare the cytocompatibility results reported in the different studies.

2.7 DISCUSSION

In order to prevent IAI, the biofunctionalization of titanium implants by PEO using Ag, Cu, and Zn as the active agents has gained significant momentum in the last decade. Therefore, we systematically reviewed the progress made on those implants and summarized the various types of properties measured for such types of PEO-biofunctionalized implants.

2.7.1 Antibacterial results

From the results of this study, it can be concluded that Ag is the most potent antibacterial agent followed by Cu and Zn. It is important to stress that different studies utilize different experimental protocols to determine the antibacterial properties of PEO-biofunctionalized implants. It has been shown that titanium surfaces bearing Ag, Cu, and Zn can kill bacteria through antibacterial leaching activity, contact killing, and the formation of ROS [156, 189]. These properties cannot be assessed in a single assay. The use of multiple assays is, therefore, warranted to support the claim of antibacterial activity [157]. Finally, it is important to make sure that the assays assess infection prevention rather than infection treatment.

Furthermore, the bacterial species and strains used are found to affect the level of antibacterial activity. For instance, surfaces demonstrating antibacterial activity against *E. coli* may not do the same against *S. aureus* [51, 55, 98]. Most studies have investigated the antibacterial activity of the implants against *S. aureus* or *E. coli*. While a large proportion of IAI is induced by *S. aureus*, only a small proportion of infections is caused by *E. coli* [144, 147]. The rationale for choosing *E. coli* is, thus, primarily methodological convenience rather than clinical prevalence. Meanwhile, *S. epidermidis* or polymicrobial infections are rarely studied, even though they cause a significant

proportion of IAI [142-144]. Moreover, the antibacterial behavior of PEO-biofunctionalized implants should be assessed in environments co-habited by multiple bacterial species, as this has been shown to influence the resistance profiles of bacteria [130].

The antibacterial experiments aim to mimic the clinical situation as closely as possible. In this respect, both adherent and planktonic bacteria should be warded off as adherent bacteria can form biofilms [133], while planktonic bacteria may infect the peri-implant tissue and form a reservoir for late-stage reinfection [125]. Furthermore, an antibacterial implant should prevent infections that occur immediately after surgery, as that is the point where most IAI occur [160] as well as late-stage infections from hematogenous origins [161]. At the moment, the focus primarily lies on preventing early-stage infections. Ultimately, Ag, Cu, and Zn may form an alternative to antibiotics, as bacteria are developing ever growing degrees of antibiotics resistance [144, 190]. As such, the development of resistance against Ag, Cu, and Zn and combination thereof is worthwhile to investigate given that resistance against Ag, Cu, and Zn has been reported *in vitro* [191-193] and in patients [194].

The observed antibacterial activity depends on a wide variety of factors described in this review, including the titanium substrate, composition of the PEO electrolyte, and PEO processing parameters that in turn affect the surface morphology, phase composition, surface content of the incorporated antibacterial agent, and ion release profile. These parameters determine the antibacterial properties and biocompatiblity of the implants. The measured antibacterial properties are highly dependent on the bacterial species and strains used, experimental techniques, the duration of the assays, bacterial inoculum, and the type of bacteria against which the implant performance is measured (*i.e.*, planktonic and/or adherent). As for biocompatibility, the type of the assays, cell type, and cell source could all influence the final read-outs. These factors vary between the studies included in this review and make a one-to-one comparison between the different studies challenging.

The antibacterial activity is dependent on the dose of Ag, Cu, an Zn present on the surface of the titanium implants [119-121]. It is, therefore, essential to determine the amount of these elements present on the surface. In addition, the Ag, Cu, and Zn ions released from the implant surface are responsible for a significant part of the antibacterial activity, which is why it is important to measure the concentration of the ions released from the implant surface. From the results, it is clear that the surfaces bearing Ag have much lower elemental content and ion release as compared to those bearing Cu and Zn, which is expected due to the lower MIC of Ag as compared to Cu and Zn [122]. Both the surface content and ion release are also dependent on the surface area, as a larger surface area allows for the incorporation of a greater amount of elements and, thus, increased ion release [31]. Therefore, describing these properties relative to the surface area may aid in a comparison between the results of different studies.

2.7.2 Biocompatibility

Most of the included studied have found cytotoxicity to be a minor concern, with Ag inducing cytotoxicity in 13% of the studies. It is striking that 29% of the included studies have not investigated the effects of the implants on bone-forming cells, even though the implants are intended for bone tissue. In addition, cytotoxicity against other cell types, such as endothelial cells and immune cells is of interest, as these cells contribute to bone regeneration as well [195, 196]. Furthermore, the use of cell lines vs. donor cells and different mammalian species complicates the comparisons between different studies [197]. Moreover, biocompatibility needs to be investigated both *in vitro* and *in vivo*, as the results of *in vitro* and *in vivo* experiments are known to differ, for instance, in the case of Ag-bearing surfaces [16].

Another way to enhance the cytocompatibility of PEO-biofunctionalized implants is by combining two or more antibacterial metals (*i.e.*, Ag, Cu, and Zn), as synergic effects between various such agents are reported to exist [19, 20] and could be used to reduce the concentration of Ag [126, 198]. In addition, combining these elements with other osteogenic elements, such as Sr [50] may enhance their antibacterial and biocompatible properties. Finally, the combination of multiple antibacterial elements significantly reduces the risk of the development of bacterial resistance, thereby ensuring that the prolonged use of these elements will remain possible [199].

PEO is frequently applied in combination with other surface treatments, such as hydrothermal treatment [200] and physical vapor deposition [201] to alter the chemical and phase composition of the surface. This may result in improved antibacterial behavior [98]. Furthermore, hydrothermal treatment has resulted in the enhanced formation of hydroxyapatite crystals, yet may reduce corrosion resistance too [202]. A major disadvantage of these additional surface treatments is that they make the entire process lengthier and more complex, thus making it more difficult to upscale the production of clinically sized implants.

2.7.3 Towards clinically relevant implants

A decade of PEO biofunctionalization of titanium implants with Ag, Cu, and Zn has confirmed the great potential of this method as an effective, fast, and scalable process. At the moment, however, the research on antibacterial PEO-biofunctionalized titanium implants is still far away from clinical application, as the research has been primarily conducted *in vitro* with few studies also exploring *ex vivo* models [20, 50]. Furthermore, PEO has been shown to enhance the osteogenic capacity of titanium implants *in vivo* [38, 39, 203] including surfaces bearing Zn [204]. However, these studies did not analyze the antibacterial properties of such implants, which should be evaluated using bone infection models [205]. In this

respect, a major limitation of the state-of-the-art techniques is their limited relevance for the assessment of the preventive potential of antibacterial implants (as opposed to their treatment potential). However, studying prevention requires a much larger sample size, as it is associated with lower bacterial loads, meaning that infections are less likely to occur. This lower risk of infection has major ethical and financial implications. In addition, future implants will most likely be fabricated by AM and as such be highly porous. Not only is the risk of infection of such volume-porous implants higher, their IAI treatment is also highly challenging due to their usually high degree of bony ingrowth that may cause significant bone loss during their removal. The development of antibacterial surface treatments for such types of implants is, thus, highly relevant. In fact, the additional surface area of such implants may be exploited to enhance the bioactivity of PEO- biofunctionalized implants [31].

2.8 CONCLUSIONS

In order to combat IAI, the biofunctionalization of titanium implants by Ag, Cu, and Zn has gained significant momentum in recent years and has resulted in the synthesis of potent antibacterial and biocompatible surfaces. Implant biofunctionalized with Ag, Cu, and Zn have demonstrated significant antibacterial behavior against a wide bacterial spectrum, including antibiotic-resistant bacterial strains. However, the antibacterial properties of these implants have been primarily investigated *in vitro* and occasionally *ex vivo*. Furthermore, many studies do not reach sufficiently high antibacterial levels, as indicated by international guidelines. Moreover, the biofunctionalization of volume-porous AM implants has not been investigated extensively. Finally, combining Ag, Cu, and Zn on the surface of titanium implants has been shown to result in potent antibacterial surfaces with reduced cytotoxicity. In order to take the PEO biofunctionalization of titanium implants by Ag, Cu, and Zn to clinical settings, *in vivo* studies should be conducted using relevant infection models for both solid and volume-porous bone implants.

Acknowledgements

The research for this paper was financially supported by the Prosperos project, funded by the Interreg VA Flanders – The Netherlands program, CCI grant no. 2014TC16RFCB046.

REFERENCES

[1] W. Zimmerli, Clinical presentation and treatment of orthopaedic implant-associated infection, J Intern Med 276(2) (2014) 111-9.

[2] G.A.M. Govaert, R. Kuehl, B.L. Atkins, A. Trampuz, M. Morgenstern, W.T. Obremskey, M.H.J. Verhofstad, M.A. McNally, W.J. Metsemakers, G. Fracture-Related Infection Consensus, Diagnosing Fracture-Related Infection: Current Concepts and Recommendations, J Orthop Trauma 34(1) (2020) 8-17.

[3] S.K. Kapoor, R. Thiyam, Management of infection following reconstruction in bone tumors, J Clin Orthop Trauma 6(4) (2015) 244-51.

[4] J.A. Singh, Epidemiology of Knee and Hip Arthroplasty: A Systematic Review, The Open Orthopaedics Journal 5 (2011) 80-85.

[5] H. Maradit Kremers, D.R. Larson, C.S. Crowson, W.K. Kremers, R.E. Washington, C.A. Steiner, W.A. Jiranek, D.J. Berry, Prevalence of Total Hip and Knee Replacement in the United States, J Bone Joint Surg Am 97(17) (2015) 1386-97.

[6] J.A. Singh, S. Yu, L. Chen, J.D. Cleveland, Rates of Total Joint Replacement in the United States: Future Projections to 2020-2040 Using the National Inpatient Sample, J Rheumatol 46(9) (2019) 1134-1140.

[7] H.F. Chambers, F.R. Deleo, Waves of resistance: Staphylococcus aureus in the antibiotic era, Nat Rev Microbiol 7(9) (2009) 629-41.

[8] Y. Guo, G. Song, M. Sun, J. Wang, Y. Wang, Prevalence and Therapies of Antibiotic-Resistance in Staphylococcus aureus, Front Cell Infect Microbiol 10 (2020) 107.

[9] D. Teterycz, T. Ferry, D. Lew, R. Stern, M. Assal, P. Hoffmeyer, L. Bernard, I. Uckay, Outcome of orthopedic implant infections due to different staphylococci, Int J Infect Dis 14(10) (2010) e913-8.

[10] O.H. Cho, I.G. Bae, S.M. Moon, S.Y. Park, Y.G. Kwak, B.N. Kim, S.N. Yu, M.H. Jeon, T. Kim, E.J. Choo, E.J. Lee, T.H. Kim, S.H. Choi, J.W. Chung, K.C. Kang, J.H. Lee, Y.M. Lee, M.S. Lee, K.H. Park, Therapeutic outcome of spinal implant infections caused by Staphylococcus aureus: A retrospective observational study, Medicine (Baltimore) 97(40) (2018) e12629.

[11] T.M. Gross, J. Lahiri, A. Golas, J. Luo, F. Verrier, J.L. Kurzejewski, D.E. Baker, J. Wang, P.F. Novak, M.J. Snyder, Copper-containing glass ceramic with high antimicrobial efficacy, Nat Commun 10(1) (2019) 1979.

[12] H.H. Lara, N.V. Ayala-Núñez, L.d.C. Ixtepan Turrent, C. Rodríguez Padilla, Bactericidal effect of silver nanoparticles against multidrug-resistant bacteria, World Journal of Microbiology and Biotechnology 26(4) (2009) 615-621.

[13] A. Nanda, M. Saravanan, Biosynthesis of silver nanoparticles from Staphylococcus aureus and its antimicrobial activity against MRSA and MRSE, Nanomedicine 5(4) (2009) 452-6.

[14] K.S. Siddiqi, A. Ur Rahman, Tajuddin, A. Husen, Properties of Zinc Oxide Nanoparticles and Their Activity Against Microbes, Nanoscale Res Lett 13(1) (2018) 141.

[15] B.S. Necula, J.P. van Leeuwen, L.E. Fratila-Apachitei, S.A. Zaat, I. Apachitei, J. Duszczyk, In vitro cytotoxicity evaluation of porous TiO(2)-Ag antibacterial coatings for human fetal osteoblasts, Acta Biomater 8(11) (2012) 4191-7.

[16] M. Croes, S. Bakhshandeh, I.A.J. van Hengel, K. Lietaert, K.P.M. van Kessel, B. Pouran, B.C.H. van der Wal, H.C. Vogely, W. Van Hecke, A.C. Fluit, C.H.E. Boel, J. Alblas, A.A. Zadpoor, H. Weinans, S. Amin Yavari, Antibacterial and immunogenic behavior of silver coatings on additively manufactured porous titanium, Acta Biomater 81 (2018) 315-327.

[17] C. Bergemann, S. Zaatreh, K. Wegner, K. Arndt, A. Podbielski, R. Bader, C. Prinz, U. Lembke, J.B. Nebe, Copper as an alternative antimicrobial coating for implants - An in vitro study, World J Transplant 7(3) (2017) 193-202.

[18] Q. Ding, X. Zhang, Y. Huang, Y. Yan, X. Pang, In vitro cytocompatibility and corrosion resistance of zinc-doped hydroxyapatite coatings on a titanium substrate, Journal of Materials Science 50(1) (2014) 189-202.

[19] I.A.J. van Hengel, M. Tierolf, V.P.M. Valerio, M. Minneboo, A.C. Fluit, L.E. Fratila-Apachitei, I. Apachitei, A.A. Zadpoor, Self-defending additively manufactured bone implants bearing silver and copper nanoparticles, J Mater Chem B 8 (2020) 1589-1602.

[20] I.A.J. van Hengel, N.E. Putra, M. Tierolf, M. Minneboo, A.C. Fluit, L.E. Fratila-Apachitei, I. Apachitei, A.A. Zadpoor, Biofunctionalization of selective laser melted porous titanium using silver and zinc nanoparticles to prevent infections by antibiotic-resistant bacteria, Acta Biomater 107 (2020) 325-337.

[21] J. Yoshitani, T. Kabata, H. Arakawa, Y. Kato, T. Nojima, K. Hayashi, M. Tokoro, N. Sugimoto, Y. Kajino, D. Inoue, K. Ueoka, Y. Yamamuro, H. Tsuchiya, Combinational therapy with antibiotics and antibiotic-loaded adipose-derived stem cells reduce abscess formation in implant-related infection in rats, Sci Rep 10(1) (2020) 11182.

[22] D.L. Cavanaugh, J. Berry, S.R. Yarboro, L.E. Dahners, Better prophylaxis against surgical site infection with local as well as systemic antibiotics. An in vivo study, J Bone Joint Surg Am 91(8) (2009) 1907-12.

[23] W.J. Metsemakers, A.T. Fragomen, T.F. Moriarty, M. Morgenstern, K.A. Egol, C. Zalavras, W.T. Obremskey, M. Raschke, M.A. McNally, g. Fracture-Related Infection consensus, Evidence-Based Recommendations for Local Antimicrobial Strategies and Dead Space Management in Fracture-Related Infection, J Orthop Trauma 34(1) (2020) 18-29.

[24] J.P. Celis, D. Drees, M.Z. Huq, P.Q. Wu, M. De Bonte, Hybrid processes — a versatile technique to match process requirements and coating needs, Surface and Coatings Technology 113 (1999) 165–181.

[25] R. Kumar, H. M.unstedt, Silver ion release from antimicrobial polyamide/silver composites, Biomaterials 26 (2004) 2081-2088.

[26] V. Zaporojtchenko, R. Podschun, U. Schurmann, A. Kulkarni, F. Faupel, Physico-chemical and antimicrobial properties of co-sputtered Ag–Au/PTFE nanocomposite coatings, Nanotechnology 17 (2006) 4904-4908.

[27] H. Gollwitzer, M. Haenle, W. Mittelmeier, F. Heidenau, N. Harasser, A biocompatible sol–gel derived titania coating for medical implants with antibacterial modification by copper integration, AMB express 8 (2018) 1-9.

[28] Y. Su, K. Wang, J. Gao, Y. Yang, Y. Qin, Y. Zheng, D. Zhu, Enhanced cytocompatibility and antibacterial property of zinc phosphate coating on biodegradable zinc materials, Acta Biomaterialia 98 (2019) 174-185.

[29] H. Cao, X. Liu, F. Meng, P.K. Chu, Biological actions of silver nanoparticles embedded in titanium controlled by micro-galvanic effects, Biomaterials 32 (2011) 693-705.

[30] I. Piwonski, K. Kadzioła, A. Kisielewska, K. Soliwoda, M. Wolszczak, K. Lisowska, N. Wronska, A. Felczak, The effect of the deposition parameters on size, distribution and antimicrobial properties of photoinduced silver nanoparticles on titania coatings, Applied Surface Science 257 (2011) 7076-7082.

[31] I.A.J. van Hengel, M. Riool, L.E. Fratila-Apachitei, J. Witte-Bouma, E. Farrell, A.A. Zadpoor, S.A.J. Zaat, I. Apachitei, Selective laser melting porous metallic implants with immobilized silver nanoparticles kill and prevent biofilm formation by methicillin-resistant Staphylococcus aureus, Biomaterials 140 (2017) 1-15.

[32] B.S. Necula, L.E. Fratila-Apachitei, S.A. Zaat, I. Apachitei, J. Duszczyk, In vitro antibacterial activity of porous TiO2-Ag composite layers against methicillin-resistant Staphylococcus aureus, Acta Biomater 5(9) (2009) 3573-80.

[33] M. Rizwan, R. Alias, U.Z. Zaidi, R. Mahmoodian, M. Hamdi, Surface modification of valve metals using plasma electrolytic oxidation for antibacterial applications: A review, J Biomed Mater Res A 106(2) (2018) 590-605.

[34] P.V. Asharani, G. Low Kah Mun, M. Prakash Hande, S. Valiyaveettil, Cytotoxicity and genotoxicity of silver nanoparticles in human cells, ACS Nano 3 (2009) 279–290.

[35] W.H. Song, H.S. Ryu, S.H. Hong, Antibacterial properties of Ag (or Pt)-containing calcium phosphate coatings formed by micro-arc oxidation, J Biomed Mater Res A 88(1) (2009) 246-54.

[36] W. Zhu, Z. Zhang, B. Gu, J. Sun, L. Zhu, Biological Activity and Antibacterial Property of Nano-structured TiO2 Coating Incorporated with Cu Prepared by Micro-arc Oxidation, Journal of Materials Science & Technology 29(3) (2013) 237-244.

[37] M. Roknian, A. Fattah-alhosseini, S.O. Gashti, M.K. Keshavarz, Study of the effect of ZnO nanoparticles addition to PEO coatings on pure titanium substrate: Microstructural analysis, antibacterial effect and corrosion behavior of coatings in Ringer's physiological solution, Journal of Alloys and Compounds 740 (2018) 330-345.

[38] A. Santos-Coquillat, E. Martínez-Campos, M. Mohedano, R. Martínez-Corriá, V. Ramos, R. Arrabal, E. Matykina, In vitro and in vivo evaluation of PEO-modified titanium for bone implant applications, Surface and Coatings Technology 347 (2018) 358-368.

[39] C.J. Chung, R.T. Su, H.J. Chu, H.T. Chen, H.K. Tsou, J.L. He, Plasma electrolytic oxidation of titanium and improvement in osseointegration, J Biomed Mater Res B Appl Biomater 101(6) (2013) 1023-30.

[40] J. Martin, A. Melhem, I. Shchedrina, T. Duchanoy, A. Nominé, G. Henrion, T. Czerwiec, T. Belmonte, Effects of electrical parameters on plasma electrolytic oxidation of aluminium, Surface and Coatings Technology 221 (2013) 70-76.

[41] I.A.J. Van Hengel, M. Laçin, M. Minneboo, L.E. Fratila-Apachitei, I. Apachitei, A.A. Zadpoor, The effects of plasma electrolytically oxidized layers containing Sr and Ca on the osteogenic behavior of selective laser melted Ti6Al4V porous implants, Journal of Materials Science and Engineering C (2021).

[42] T.W. Clyne, S.C. Troughton, A review of recent work on discharge characteristics during plasma electrolytic oxidation of various metals, International Materials Reviews 64(3) (2018) 127-162.

[43] D. Moher, A. Liberati, J. Tetzlaff, D.G. Altman, Preferred reporting items for systematic reviews and meta-analyses: the PRISMA statement, PLoS Med 6 (2009) e1000097.

[44] A.L. Yerokhin, X. Nie, A. Leyland, A. Matthews, S.J. Dowey, Plasma electrolysis for surface engineering, Surface and Coatings Technology 122 (1999) 73-93.

[45] J.A. Curran, T.W. Clyne, Thermo-physical properties of plasma electrolytic oxide coatings on aluminium, Surface and Coatings Technology 199(2-3) (2005) 168-176.

[46] Y. Wang, H. Yu, C. Chen, Z. Zhao, Review of the biocompatibility of micro-arc oxidation coated titanium alloys, Materials & Design 85 (2015) 640-652.

[47] E. Matykina, P. Skeldon, G.E. Thompson, Fundamental and practical evaluations of PEO coatings of titanium, International Heat Treatment and Surface Engineering 3(1-2) (2013) 45-51.

[48] L. Zhang, B. Li, X. Zhang, D. Wang, L. Zhou, H. Li, C. Liang, S. Liu, H. Wang, Biological and antibacterial properties of TiO2 coatings containing Ca/P/Ag by one-step and two-step methods, Biomed Microdevices 22(2) (2020) 24.

[49] M. Thukkaram, P. Cools, A. Nikiforov, P. Rigole, T. Coenye, P. Van Der Voort, G. Du Laing, C. Vercruysse, H. Declercq, R. Morent, L. De Wilde, P. De Baets, K. Verbeken, N. De Geyter, Antibacterial activity of a porous silver doped TiO2 coating on titanium substrates synthesized by plasma electrolytic oxidation, Applied Surface Science 500 (2020).

[50] I.A.J. van Hengel, F.S.A. Gelderman, S. Athanasiadis, M. Minneboo, H. Weinans, A.C. Fluit, B.C.J. van der Eerden, L.E. Fratila-Apachitei, I. Apachitei, A.A. Zadpoor, Functionality-packed additively manufactured porous titanium implants, Materials Today Bio 7 (2020).

[51] M. Shimabukuro, Y. Tsutsumi, R. Yamada, M. Ashida, P. Chen, H. Doi, K. Nozaki, A. Nagai, T. Hanawa, Investigation of Realizing Both Antibacterial Property and Osteogenic Cell Compatibility on Titanium Surface by Simple Electrochemical Treatment, ACS Biomaterials Science & Engineering 5(11) (2019) 5623-5630.

[52] M.B. Sedelnikova, E.G. Komarova, Y.P. Sharkeev, A.V. Ugodchikova, L.S. Mushtovatova, M.R. Karpova, V.V. Sheikin, L.S. Litvinova, I.A. Khlusov, Zn-, Cu- or Ag-incorporated micro-arc coatings on titanium alloys: Properties and behavior in synthetic biological media, Surface and Coatings Technology 369 (2019) 52-68.

[53] M.B. Sedelnikova, E.G. Komarova, Y.P. Sharkeev, A.V. Ugodchikova, T.V. Tolkacheva, J.V. Rau, E.E. Buyko, V.V. Ivanov, V.V. Sheikin, Modification of titanium surface via Ag-, Sr- and Si-containing micro-arc calcium phosphate coating, Bioact Mater 4 (2019) 224-235.

[54] Y. Lv, Y. Wu, X. Lu, Y. Yu, S. Fu, L. Yang, Z. Dong, X. Zhang, Microstructure, bio-corrosion and biological property of Ag-incorporated TiO2 coatings: Influence of Ag2O contents, Ceramics International 45(17) (2019) 22357-22367.

[55] D. Teker, F. Muhaffel, M. Menekse, N.G. Karaguler, M. Baydogan, H. Cimenoglu, Characteristics of multi-layer coating formed on commercially pure titanium for biomedical applications, Mater Sci Eng C Mater Biol Appl 48 (2015) 579-85.

[56] D. Teker Aydogan, F. Muhaffel, M. Menekse Kilic, O. Karabiyik Acar, G. Cempura, M. Baydogan, N.G. Karaguler, G. Torun Kose, A. Czyrska-Filemonowicz, H. Cimenoglu, Optimisation of micro-arc oxidation electrolyte for fabrication of antibacterial coating on titanium, Materials Technology 33(2) (2017) 119-126.

[57] T. Dilek Aydogan, F. Muhaffel, O.K. Acar, E.N. Topcuoglu, H.G. Kulekci, G.T. Kose, M. Baydogan, H. Cimenoglu, Surface modification of Ti6Al4V by micro-arc oxidation in AgC2H3O2-containing electrolyte, Surface Innovations 6(4–5) (2018) 277-285.

[58] F. Muhaffel, G. Cempura, M. Menekse, A. Czyrska-Filemonowicz, N. Karaguler, H. Cimenoglu, Characteristics of multi-layer coatings synthesized on Ti6Al4V alloy by micro-arc oxidation in silver nitrate added electrolytes, Surface and Coatings Technology 307 (2016) 308-315.

[59] Y. Tsutsumi, M. Niinomi, M. Nakai, M. Shimabukuro, M. Ashida, P. Chen, H. Doi, T. Hanawa, Electrochemical Surface Treatment of a β-titanium Alloy to Realize an Antibacterial Property and Bioactivity, Metals 6(4) (2016).

[60] K.R. Shin, Y.S. Kim, G.W. Kim, H.W. Yang, Y.G. Ko, D.H. Shin, Effects of concentration of Ag nanoparticles on surface structure and in vitro biological responses of oxide layer on pure titanium via plasma electrolytic oxidation, Applied Surface Science 347 (2015) 574-582.

[61] I.D. Marques, V.A. Barao, N.C. da Cruz, J.C. Yuan, M.F. Mesquita, A.P. Ricomini-Filho, C. Sukotjo, M.T. Mathew, Electrochemical behavior of bioactive coatings on cp-Ti surface for dental application, Corros Sci 100 (2015) 133-146.

[62] S. Marques Ida, M.F. Alfaro, M.T. Saito, N.C. da Cruz, C. Takoudis, R. Landers, M.F. Mesquita, F.H. Nociti Junior, M.T. Mathew, C. Sukotjo, V.A. Barao, Biomimetic coatings enhance tribocorrosion behavior and cell responses of commercially pure titanium surfaces, Biointerphases 11(3) (2016) 031008.

[63] C. Gasquères, G. Schneider, R. Nusko, G. Maier, E. Dingeldein, A. Eliezer, Innovative antibacterial coating by anodic spark deposition, Surface and Coatings Technology 206(15) (2012) 3410-3414.

[64] L. Zhou, G.-H. Lü, F.-F. Mao, S.-Z. Yang, Preparation of biomedical Ag incorporated hydroxyapatite/titania coatings on Ti6Al4V alloy by plasma electrolytic oxidation, Chinese Physics B 23(3) (2014).

[65] M. Thukkaram, R. Coryn, M. Asadian, P.S. Esbah Tabaei, P. Rigole, N. Rajendhran, A. Nikiforov, J. Sukumaran, T. Coenye, P. Van Der Voort, G. Du Laing, R. Morent, A. Van Tongel, L. De Wilde, P. De Baets, K. Verbeken, N. De Geyter, Fabrication of microporous coatings on titanium implants with improved mechanical, antibacterial, and cell-interactive properties, ACS Appl Mater Interfaces 12 (2020) 30155-30169.

[66] O. Oleshko, I. Liubchak, Y. Husak, V. Korniienko, A. Yusupova, T. Oleshko, R. Banasiuk, M. Szkodo, I. Matros-Taranets, A. Kazek-Kesik, W. Simka, M. Pogorielov, In vitro biological characterization of silver-doped anodic oxide coating on titanium, Materials 13 (2020) 4359.

[67] Q. Zhao, L. Yi, A. Hu, L. Jiang, L. Hong, J. Dong, Antibacterial and osteogenic activity of a multifunctional microporous coating codoped with Mg, Cu and F on titanium, Journal of Materials Chemistry B 7(14) (2019) 2284-2299.

[68] X. Zhang, Z. Peng, X. Lu, Y. Lv, G. Cai, L. Yang, Z. Dong, Microstructural evolution and biological performance of Cu-incorporated TiO2 coating fabricated through one-step micro-arc oxidation, Applied Surface Science 508 (2020).

[69] K. Rokosz, T. Hryniewicz, W. Kacalak, K. Tandecka, S. Raaen, S. Gaiaschi, P. Chapon, W. Malorny, D. Matysek, K. Pietrzak, E. Czerwinska, A. Iwanek, L. Dudek, Porous Coatings Containing Copper and Phosphorus Obtained by Plasma Electrolytic Oxidation of Titanium, Materials (Basel) 13(4) (2020).

[70] T. Liang, Y. Wang, L. Zeng, Y. Liu, L. Qiao, S. Zhang, R. Zhao, G. Li, R. Zhang, J. Xiang, F. Xiong, A. Shanaghi, H. Pan, Y. Zhao, Copper-doped 3D porous coating developed on Ti-6Al-4V alloys and its in vitro long-term antibacterial ability, Applied Surface Science 509 (2020).

[71] X. He, G. Zhang, H. Zhang, R. Hang, X. Huang, X. Yao, X. Zhang, Cu and Si co-doped microporous TiO2 coating for osseointegration by the coordinated stimulus action, Applied Surface Science 503 (2020).

[72] L. Zhang, J. Guo, X. Huang, Y. Zhang, Y. Han, The dual function of Cu-doped TiO2 coatings on titanium for application in percutaneous implants, Journal of Materials Chemistry B 4(21) (2016) 3788-3800.

[73] Q. Huang, X. Li, T.A. Elkhooly, X. Liu, R. Zhang, H. Wu, Q. Feng, Y. Liu, The Cu-containing TiO2 coatings with modulatory effects on macrophage polarization and bactericidal capacity prepared by micro-arc oxidation on titanium substrates, Colloids Surf B Biointerfaces 170 (2018) 242-250.

[74] X. Yao, X. Zhang, H. Wu, L. Tian, Y. Ma, B. Tang, Microstructure and antibacterial properties of Cu-doped TiO2 coating on titanium by micro-arc oxidation, Applied Surface Science 292 (2014) 944-947.

[75] X. Zhang, J. Li, X. Wang, Y. Wang, R. Hang, X. Huang, B. Tang, P.K. Chu, Effects of copper nanoparticles in porous TiO2 coatings on bacterial resistance and cytocompatibility of osteoblasts and endothelial cells, Mater Sci Eng C Mater Biol Appl 82 (2018) 110-120.

[76] D. Zhao, Y. Lu, X. Zeng, Z. Wang, S. Liu, T. Wang, Antifouling property of micro-arc oxidation coating incorporating Cu2O nanoparticles on Ti6Al4V, Surface Engineering 33(10) (2017) 796-802.

[77] L. Zhang, J. Guo, T. Yan, Y. Han, Fibroblast responses and antibacterial activity of Cu and Zn co-doped TiO2 for percutaneous implants, Applied Surface Science 434 (2018) 633-642.

[78] D. Zhao, Y. Lu, Z. Wang, X. Zeng, S. Liu, T. Wang, Antifouling properties of micro arc oxidation coatings containing Cu2O/ZnO nanoparticles on Ti6Al4V, International Journal of Refractory Metals and Hard Materials 54 (2016) 417-421.

[79] X. Zhang, C. Li, Y. Yu, X. Lu, Y. Lv, D. Jiang, Z. Peng, J. Zhou, X. Zhang, S. Sun, Z. Dong, Characterization and property of bifunctional Zn-incorporated TiO2 micro-arc oxidation coatings: The influence of different Zn sources, Ceramics International 45(16) (2019) 19747-19756.

[80] M. Shimabukuro, Y. Tsutsumi, K. Nozaki, P. Chen, R. Yamada, M. Ashida, H. Doi, A. Nagai, T. Hanawa, Chemical and Biological Roles of Zinc in a Porous Titanium Dioxide Layer Formed by Micro-Arc Oxidation, Coatings 9(11) (2019).

[81] Q. Du, D. Wei, Y. Wang, S. Cheng, S. Liu, Y. Zhou, D. Jia, The effect of applied voltages on the structure, apatite-inducing ability and antibacterial ability of micro arc oxidation coating formed on titanium surface, Bioact Mater 3(4) (2018) 426-433.

[82] L. Sopchenski, K. Popat, P. Soares, Bactericidal activity and cytotoxicity of a zinc doped PEO titanium coating, Thin Solid Films 660 (2018) 477-483.

[83] H. Hu, W. Zhang, Y. Qiao, X. Jiang, X. Liu, C. Ding, Antibacterial activity and increased bone marrow stem cell functions of Zn-incorporated TiO2 coatings on titanium, Acta Biomater 8(2) (2012) 904-15.

[84] X. Zhang, H. Wang, J. Li, X. He, R. Hang, X. Huang, L. Tian, B. Tang, Corrosion behavior of Zn-incorporated antibacterial TiO2 porous coating on titanium, Ceramics International 42(15) (2016) 17095-17100.

[85] B.H. Zhao, W. Zhang, D.N. Wang, W. Feng, Y. Liu, Z. Lin, K.Q. Du, C.F. Deng, Effect of Zn content on cytoactivity and bacteriostasis of micro-arc oxidation coatings on pure titanium, Surface and Coatings Technology 228 (2013) S428-S432.

[86] K. Leśniak-Ziółkowska, A. Kazek-Kęsik, K. Rokosz, S. Raaen, A. Stolarczyk, M. Krok-Borkowicz, E. Pamuła, M. Gołda-Cępa, M. Brzychczy-Włoch, W. Simka, Electrochemical modification of the Ti-15Mo alloy surface in solutions containing ZnO and Zn3(PO4)2 particles, Materials Science and Engineering: C 115 (2020).

[87] L. Zhang, Q. Gao, Y. Han, Zn and Ag Co-doped Anti-microbial TiO2 Coatings on Ti by Micro-arc Oxidation, Journal of Materials Science & Technology 32 (2016) 919-924.

[88] Y. Wang, S. Zhao, G. Li, S. Zhang, R. Zhao, A. Dong, R. Zhang, Preparation and in vitro antibacterial properties of anodic coatings co-doped with Cu, Zn, and P on a Ti–6Al–4V alloy, Materials Chemistry and Physics 241 (2020).

[89] E. Matykina, R. Arrabal, B. Mingo, M. Mohedano, A. Pardo, M.C. Merino, In vitro corrosion performance of PEO coated Ti and Ti6Al4V used for dental and orthopaedic implants, Surface and Coatings Technology 307 (2016) 1255-1264.

[90] R. Wauthle, S.M. Ahmadi, S. Amin Yavari, M. Mulier, A.A. Zadpoor, H. Weinans, J. Van Humbeeck, J.P. Kruth, J. Schrooten, Revival of pure titanium for dynamically loaded porous implants using additive manufacturing, Mater Sci Eng C Mater Biol Appl 54 (2015) 94-100.

[91] F.A. Shah, P. Thomsen, A. Palmquist, Osseointegration and current interpretations of the bone-implant interface, Acta Biomater 84 (2019) 1-15.

[92] F.A. Shah, M. Trobos, P. Thomsen, A. Palmquist, Commercially pure titanium (cp-Ti) versus titanium alloy (Ti6Al4V) materials as bone anchored implants - Is one truly better than the other?, Mater Sci Eng C Mater Biol Appl 62 (2016) 960-6.

[93] C.N. Elias, D.J. Fernandes, F.M.d. Souza, E.d.S. Monteiro, R.S.d. Biasi, Mechanical and clinical properties of titanium and titanium-based alloys (Ti G2, Ti G4 cold worked nanostructured and Ti G5) for biomedical applications, Journal of Materials Research and Technology 8(1) (2019) 1060-1069.

[94] V.S. Challa, S. Mali, R.D. Misra, Reduced toxicity and superior cellular response of preosteoblasts to Ti-6Al-7Nb alloy and comparison with Ti-6Al-4V, J Biomed Mater Res A 101(7) (2013) 2083-9.

[95] A. Krząkała, A. Kazek-Kęsik, W. Simka, Application of plasma electrolytic oxidation to bioactive surface formation on titanium and its alloys, RSC Advances 3(43) (2013).

[96] A.R. Rafieerad, M.R. Ashra, R. Mahmoodian, A.R. Bushroa, Surface characterization and corrosion behavior of calcium phosphate-base composite layer on titanium and its alloys via plasma electrolytic oxidation: A review paper, Mater Sci Eng C Mater Biol Appl 57 (2015) 397-413.

[97] A. Lugovskoy, S. Lugovskoy, Production of hydroxyapatite layers on the plasma electrolytically oxidized surface of titanium alloys, Mater Sci Eng C Mater Biol Appl 43 (2014) 527-32.

[98] Q. Du, D. Wei, S. Liu, S. Cheng, N. Hu, Y. Wang, B. Li, D. Jia, Y. Zhou, The hydrothermal treated Zn-incorporated titania based microarc oxidation coating: Surface characteristics, apatite-inducing ability and antibacterial ability, Surface and Coatings Technology 352 (2018) 489-500.

[99] D.K. Lee, D.R. Hwang, Y.-S. Sohn, Surface properties of plasma electrolytic oxidation coatings on Ti-alloy in phosphate–based electrolytes with the addition of sodium metasilicate, Molecular Crystals and Liquid Crystals 687(1) (2019) 7-13.

[100] M. Mohedano, R. Guzman, R. Arrabal, J.L. Lopez Lacomba, E. Matykina, Bioactive plasma electrolytic oxidation coatings--the role of the composition, microstructure, and electrochemical stability, J Biomed Mater Res B Appl Biomater 101(8) (2013) 1524-37.

[101] X. Lu, M. Mohedano, C. Blawert, E. Matykina, R. Arrabal, K.U. Kainer, M.L. Zheludkevich, Plasma electrolytic oxidation coatings with particle additions – A review, Surface and Coatings Technology 307 (2016) 1165-1182.

[102] M.F. Maitz, R.W. Poon, X.Y. Liu, M.T. Pham, P.K. Chu, Bioactivity of titanium following sodium plasma immersion ion implantation and deposition, Biomaterials 26(27) (2005) 5465-73.

[103] K. Cai, M. Lai, W. Yang, R. Hu, R. Xin, Q. Liu, K.L. Sung, Surface engineering of titanium with potassium hydroxide and its effects on the growth behavior of mesenchymal stem cells, Acta Biomater 6(6) (2010) 2314-21.

[104] X. Zhang, Z. Yao, Z. Jiang, Y. Zhang, X. Liu, Investigation of the plasma electrolytic oxidation of Ti6Al4V under single-pulse power supply, Corrosion Science 53(6) (2011) 2253-2262.

[105] M. Shokouhfar, C. Dehghanian, M. Montazeri, A. Baradaran, Preparation of ceramic coating on Ti substrate by plasma electrolytic oxidation in different electrolytes and evaluation of its corrosion resistance: Part II, Applied Surface Science 258(7) (2012) 2416-2423.

[106] O.A. Galvis, D. Quintero, J.G. Castaño, H. Liu, G.E. Thompson, P. Skeldon, F. Echeverría, Formation of grooved and porous coatings on titanium by plasma electrolytic oxidation in H2SO4/H3PO4 electrolytes and effects of coating morphology on adhesive bonding, Surface and Coatings Technology 269 (2015) 238-249.

[107] S. Durdu, S. Bayramoğlu, A. Demirtaş, M. Usta, A.H. Üçışık, Characterization of AZ31 Mg Alloy coated by plasma electrolytic oxidation, Vacuum 88 (2013) 130-133.

[108] Z. Li, Y. Yuan, X. Jing, Effect of current density on the structure, composition and corrosion resistance of plasma electrolytic oxidation coatings on Mg–Li alloy, Journal of Alloys and Compounds 541 (2012) 380-391.

[109] M. Montazeri, C. Dehghanian, M. Shokouhfar, A. Baradaran, Investigation of the voltage and time effects on the formation of hydroxyapatite-containing titania prepared by plasma electrolytic oxidation on Ti–6Al–4V alloy and its corrosion behavior, Applied Surface Science 257(16) (2011) 7268-7275.

[110] A. Kossenko, S. Lugovskoy, N. Astashina, A. Lugovskoy, M. Zinigrad, Effect of time on the formation of hydroxyapatite in PEO process with hydrothermal treatment of the Ti-6Al-4V alloy, Glass Physics and Chemistry 39(6) (2013) 639-642.

[111] B.S. Necula, I. Apachitei, F.D. Tichelaar, L.E. Fratila-Apachitei, J. Duszczyk, An electron microscopical study on the growth of TiO2-Ag antibacterial coatings on Ti6Al7Nb biomedical alloy, Acta Biomater 7(6) (2011) 2751-7.

[112] J. Hasan, S. Jain, R. Padmarajan, S. Purighalla, V.K. Sambandamurthy, K. Chatterjee, Multi-scale surface topography to minimize adherence and viability of nosocomial drug-resistant bacteria, Mater Des 140 (2018) 332-344.

[113] Y. Zhang, S.E. Chen, J. Shao, J. van den Beucken, Combinatorial Surface Roughness Effects on Osteoclastogenesis and Osteogenesis, ACS Appl Mater Interfaces 10(43) (2018) 36652-36663.

[114] L. Sun, D. Pereira, Q. Wang, D.B. Barata, R. Truckenmuller, Z. Li, X. Xu, P. Habibovic, Controlling Growth and Osteogenic Differentiation of Osteoblasts on Microgrooved Polystyrene Surfaces, PLoS One 11(8) (2016) e0161466.

[115] M. Yamada, T. Ueno, N. Tsukimura, T. Ikeda, K. Nakagawa, N. Hori, T. Suzuki, T. Ogawa, Bone integration capability of nanopolymorphic crystalline hydroxyapatite coated on titanium implants, Int J Nanomedicine 7 (2012) 859-73.

[116] G.-W. Lin, J.-S. Chen, W. Tseng, F.-H. Lu, Formation of anatase TiO2 coatings by plasma electrolytic oxidation for photocatalytic applications, Surface and Coatings Technology 357 (2019) 28-35.

[117] Y. Nosaka, A.Y. Nosaka, Generation and Detection of Reactive Oxygen Species in Photocatalysis, Chem Rev 117(17) (2017) 11302-11336.

[118] M.Y. Memar, R. Ghotaslou, M. Samiei, K. Adibkia, Antimicrobial use of reactive oxygen therapy: current insights, Infect Drug Resist 11 (2018) 567-576.

[119] K. Li, C. Xia, Y. Qiao, X. Liu, Dose-response relationships between copper and its biocompatibility/antibacterial activities, J Trace Elem Med Biol 55 (2019) 127-135.

[120] E. Pazos-Ortiz, J.H. Roque-Ruiz, E.A. Hinojos-Márquez, J. López-Esparza, A. Donohué-Cornejo, J.C. Cuevas-González, L.F. Espinosa-Cristóbal, S.Y. Reyes-López, Dose-Dependent Antimicrobial Activity of Silver Nanoparticles on Polycaprolactone Fibers against Gram-Positive and Gram-Negative Bacteria, Journal of Nanomaterials 2017 (2017) 1-9.

[121] P. Horky, S. Skalickova, L. Urbankova, D. Baholet, S. Kociova, Z. Bytesnikova, E. Kabourkova, Z. Lackova, N. Cernei, M. Gagic, V. Milosavljevic, V. Smolikova, E. Vaclavkova, P. Nevrkla, P. Knot, O. Krystofova, D. Hynek, P. Kopel, J. Skladanka, V. Adam, K. Smerkova, Zinc phosphate-based nanoparticles as a novel antibacterial agent: in vivo study on rats after dietary exposure, J Anim Sci Biotechnol 10 (2019) 17.

[122] S. Ferraris, S. Spriano, Antibacterial titanium surfaces for medical implants, Mater Sci Eng C Mater Biol Appl 61 (2016) 965-78.

[123] A. Kedziora, M. Speruda, E. Krzyzewska, J. Rybka, A. Lukowiak, G. Bugla-Ploskonska, Similarities and Differences between Silver Ions and Silver in Nanoforms as Antibacterial Agents, Int J Mol Sci 19(2) (2018).

[124] L.M. Stabryla, K.A. Johnston, J.E. Millstone, L.M. Gilbertson, Emerging investigator series: it's not all about the ion: support for particle-specific contributions to silver nanoparticle antimicrobial activity, Environmental Science: Nano 5(9) (2018) 2047-2068.

[125] M. Riool, L. de Boer, V. Jaspers, C.M. van der Loos, W.J.B. van Wamel, G. Wu, P.H.S. Kwakman, S.A.J. Zaat, Staphylococcus epidermidis originating from titanium implants infects surrounding tissue and immune cells, Acta Biomater 10(12) (2014) 5202-5212.

[126] G. Jin, H. Qin, H. Cao, S. Qian, Y. Zhao, X. Peng, X. Zhang, X. Liu, P.K. Chu, Synergistic effects of dual Zn/Ag ion implantation in osteogenic activity and antibacterial ability of titanium, Biomaterials 35(27) (2014) 7699-713.

[127] G. Jin, H. Qin, H. Cao, Y. Qiao, Y. Zhao, X. Peng, X. Zhang, X. Liu, P.K. Chu, Zn/Ag micro-galvanic couples formed on titanium and osseointegration effects in the presence of S. aureus, Biomaterials 65 (2015) 22-31.

[128] T. Kokubo, H. Takadama, How useful is SBF in predicting in vivo bone bioactivity?, Biomaterials 27(15) (2006) 2907-15.

[129] S.H. Uhm, J.S. Kwon, D.H. Song, E.J. Lee, W.S. Jeong, S. Oh, K.N. Kim, E.H. Choi, K.M. Kim, Long-Term Antibacterial Performance and Bioactivity of Plasma-Engineered Ag-NPs/TiO(2), J Biomed Nanotechnol 12(10) (2016) 1890-1906.

[130] B. Otarigho, M.O. Falade, Analysis of antibiotics resistant genes in different strains of Staphylococcus aureus, Bioinformation 14(3) (2018) 113-122.

[131] L. Cremet, A. Broquet, B. Brulin, C. Jacqueline, S. Dauvergne, R. Brion, K. Asehnoune, S. Corvec, D. Heymann, N. Caroff, Pathogenic potential of Escherichia coli clinical strains from orthopedic implant infections towards human osteoblastic cells, Pathog Dis 73(8) (2015) ftv065.

[132] W. Zimmerli, C. Moser, Pathogenesis and treatment concepts of orthopaedic biofilm infections, FEMS Immunol Med Microbiol 65(2) (2012) 158-68.

[133] S.J. McConoughey, R. Howlin, J.F. Granger, M.M. Manring, J.H. Calhoun, M. Shirtliff, S. Kathju, P. Stoodley, Biofilms in periprosthetic orthopedic infections, Future Microbiol 9(8) (2014) 987-1007.

[134] P.A. Wayne, Methods for determining bactericidal activity of antimicrobial agents; approved guideline, in: CLSI (Ed.) 1999.

[135] Z. Jia, P. Xiu, M. Li, X. Xu, Y. Shi, Y. Cheng, S. Wei, Y. Zheng, T. Xi, H. Cai, Z. Liu, Bioinspired anchoring AgNPs onto micro-nanoporous TiO2 orthopedic coatings: trap-killing of bacteria, surface-regulated osteoblast functions and host responses, Biomaterials 75 (2016) 203-222.

[136] G. Applerot, J. Lellouche, A. Lipovsky, Y. Nitzan, R. Lubart, A. Gedanken, E. Banin, Understanding the antibacterial mechanism of CuO nanoparticles: revealing the route of induced oxidative stress, Small 8 (2012) 3326-3337.

[137] M. Hans, A. Erbe, S. Mathews, Y. Chen, M. Solioz, F. Mücklich, Role of copper oxides in contact killing of bacteria, Langmuir 29 (2013) 16160-16166.

[138] M.A.F. Afzal, S. Kalmodia, P. Kesarwani, B. Basu, K. Balani, Bactericidal effect of silver-reinforced carbon nanotube and hydroxyapatite composites, Journal of Biomaterials Applications 27 (2012) 967-978.

[139] H. Cao, Y. Qiao, X. Liu, T. Lu, T. Cui, F. Meng, C.K. Paul, Electron storage mediated dark antibacterial action of bound silver nanoparticles: smaller is not always better, Acta Biomaterialia 9 (2013) 5100-5110.

[140] J.T. Torbert, M. Joshi, A. Moraff, P.E. Matuszewski, A. Holmes, A.N. Pollak, R.V. O'Toole, Current bacterial speciation and antibiotic resistance in deep infections after operative fixation of fractures, J Orthop Trauma 29 (2015) 7-17.

[141] A.F. Chen, V.M. Schreiber, W. Washington, N. Rao, A.R. Evans, What is the rate of methicillin-resistant Staphylococcus aureus and Gram-negative infections in open fractures?, Clin Orthop Relat Res 471 (2013) 3135-40.

[142] A.J. Tande, R. Patel, Prosthetic joint infection, Clin Microbiol Rev 27 (2014) 302-45.

[143] S. Corvec, M.E. Portillo, B.M. Pasticci, O. Borens, A. Trampuz, Epidemiology and new developments in the diagnosis of prosthetic joint infection, Int J Artif Organs 35(10) (2012) 923-34.

[144] D. Campoccia, L. Montanaro, C.R. Arciola, The significance of infection related to orthopedic devices and issues of antibiotic resistance, Biomaterials 27(11) (2006) 2331-9.

[145] L. Montanaro, P. Speziale, D. Campoccia, S. Ravaioli, I. Cangini, G. Pietrocola, S. Giannini, C.R. Arciola, Scenery of Staphylococcus implant infections in orthopedics, Future Microbiol. 6 (2011) 1329–1349.

[146] C.R. Arciola, D. Campoccia, Y.H. An, L. Baldassarri, V. Pirini, M.E. Donati, F. Pegreffi, L. Montanaro, Prevalence and antibiotic resistance of 15 minor staphylococcal species colonizing orthopedic implants, The International Journal of Artificial Organs 29 (2006) 395-401.

[147] T.F. Moriarty, R. Kuehl, T. Coenye, W.J. Metsemakers, M. Morgenstern, E.M. Schwarz, M. Riool, S.A.J. Zaat, N. Khana, S.L. Kates, R.G. Richards, Orthopaedic device-related infection: current and future interventions for improved prevention and treatment, EFORT Open Rev 1(4) (2016) 89-99.

[148] J.L. Del Pozo, R. Patel, Infection associated with prosthetic joints, N Engl J Med 361 (2009) 787-94.

[149] T.L. Tan, M.M. Kheir, N. Shohat, D.D. Tan, M. Kheir, C. Chen, J. Parvizi, Culture-Negative Periprosthetic Joint Infection: An Update on What to Expect, JB JS Open Access 3(3) (2018) e0060.

[150] H.K. Yoon, S.H. Cho, D.Y. Lee, B.H. Kang, S.H. Lee, D.G. Moon, D.H. Kim, D.C. Nam, S.C. Hwang, A Review of the Literature on Culture-Negative Periprosthetic Joint Infection: Epidemiology, Diagnosis and Treatment, Knee Surg Relat Res 29(3) (2017) 155-164.

[151] T. van Opijnen, S. Dedrick, J. Bento, Strain Dependent Genetic Networks for Antibiotic-Sensitivity in a Bacterial Pathogen with a Large Pan-Genome, PLoS Pathog 12(9) (2016) e1005869.

[152] C. Losasso, S. Belluco, V. Cibin, P. Zavagnin, I. Micetic, F. Gallocchio, M. Zanella, L. Bregoli, G. Biancotto, A. Ricci, Antibacterial activity of silver nanoparticles: sensitivity of different Salmonella serovars, Front Microbiol 5 (2014) 227.

[153] J.P. Ruparelia, A.K. Chatterjee, S.P. Duttagupta, S. Mukherji, Strain specificity in antimicrobial activity of silver and copper nanoparticles, Acta Biomater 4(3) (2008) 707-16.

[154] A. Shivaram, S. Bose, A. Bandyopadhyay, Understanding long-term silver release from surface modified porous titanium implants, Acta Biomater 58 (2017) 550-560.

[155] Y. Zhai, E.R. Hunting, M. Wouters, W.J. Peijnenburg, M.G. Vijver, Silver Nanoparticles, Ions, and Shape Governing Soil Microbial Functional Diversity: Nano Shapes Micro, Front Microbiol 7 (2016) 1123.

[156] B. Reidy, A. Haase, A. Luch, K.A. Dawson, I. Lynch, Mechanisms of Silver Nanoparticle Release, Transformation and Toxicity: A Critical Review of Current Knowledge and Recommendations for Future Studies and Applications, Materials (Basel) 6(6) (2013) 2295-2350.

[157] M. Balouiri, M. Sadiki, S.K. Ibnsouda, Methods for in vitro evaluating antimicrobial activity: A review, J Pharm Anal 6(2) (2016) 71-79.

[158] M.C. Hudson, W.K. Ramp, K.P. Frankenburg, Staphylococcus aureus adhesion to bone matrix and bone-associated biomaterials, FEMS Microbiology Letters 173 (1999) 279-284.

[159] D. Yang, A.R. Wijenayaka, L.B. Solomon, S.M. Pederson, D.M. Findlay, S.P. Kidd, G.J. Atkins, Novel Insights into Staphylococcus aureus Deep Bone Infections: the Involvement of Osteocytes, mBio 9(2) (2018).

[160] W. Zimmerli, A. Trampuz, P.E. Ochsner, Prosthetic-Joint Infections, N Engl J Med 351 (2004) 1645-54.

[161] L. Barrett, B. Atkins, The clinical presentation of prosthetic joint infection, J Antimicrob Chemother 69 (2014) i25-7.

[162] N.P. Jorgensen, R.L. Meyer, F. Dagnaes-Hansen, K. Fuursted, E. Petersen, A modified chronic infection model for testing treatment of Staphylococcus aureus biofilms on implants, PLoS One 9(10) (2014) e103688.

[163] D. Lebeaux, A. Chauhan, O. Rendueles, C. Beloin, From in vitro to in vivo Models of Bacterial Biofilm-Related Infections, Pathogens 2(2) (2013) 288-356.

[164] W. Zimmerli, F.A. Waldvogel, P. Vaudaux, U.E. Nydegger, Pathogenesis of foreign body infection: description and characteristics of an animal model, The Journal of Infectious Diseases 146 (1982) 487-497.

[165] S.N. Christo, K.R. Diener, A. Bachhuka, K. Vasilev, J.D. Hayball, Innate Immunity and Biomaterials at the Nexus: Friends or Foes, Biomed Res Int 2015 (2015) 342304.

[166] A.W. Smith, Biofilms and antibiotic therapy: is there a role for combating bacterial resistance by the use of novel drug delivery systems?, Adv Drug Deliv Rev 57 (2005) 1539-50.

[167] K.H. Chan, S. Zhuo, M. Ni, Priming the Surface of Orthopedic Implants for Osteoblast Attachment in Bone Tissue Engineering, Int J Med Sci 12(9) (2015) 701-7.

[168] M. Jayaraman, U. Meyer, M. Bühner, U. Joos, H.-P. Wiesmann, Influence of titanium surfaces on attachment of osteoblast-like cells in vitro, Biomaterials 25(4) (2004) 625-631.

[169] J.J. Yao, E.A. Lewallen, W.H. Trousdale, W. Xu, R. Thaler, C.G. Salib, N. Reina, M.P. Abdel, D.G. Lewallen, A.J. van Wijnen, Local Cellular Responses to Titanium Dioxide from Orthopedic Implants, Biores Open Access 6(1) (2017) 94-103.

[170] C. Stewart, B. Akhavan, S.G. Wise, M.M.M. Bilek, A review of biomimetic surface functionalization for bone-integrating orthopedic implants: Mechanisms, current approaches, and future directions, Progress in Materials Science 106 (2019).

[171] A. Shekaran, A.J. Garcia, Extracellular matrix-mimetic adhesive biomaterials for bone repair, J Biomed Mater Res A 96(1) (2011) 261-72.

[172] E.G. Long, M. Buluk, M.B. Gallagher, J.M. Schneider, J.L. Brown, Human mesenchymal stem cell morphology, migration, and differentiation on micro and nano-textured titanium, Bioact Mater 4 (2019) 249-255.

[173] H. Jiang, T. Hong, T. Wang, X. Wang, L. Cao, X. Xu, M. Zheng, Gene expression profiling of human bone marrow mesenchymal stem cells during osteogenic differentiation, J Cell Physiol 234(5) (2019) 7070-7077.

[174] M.E. Klontzas, S.I. Vernardis, M. Heliotis, E. Tsiridis, A. Mantalaris, Metabolomics Analysis of the Osteogenic Differentiation of Umbilical Cord Blood Mesenchymal Stem Cells Reveals Differential Sensitivity to Osteogenic Agents, Stem Cells Dev 26(10) (2017) 723-733.

[175] K.P. Bennett, C. Bergeron, E. Acar, R.F. Klees, S.L. Vandenberg, B. Yener, G.E. Plopper, Proteomics reveals multiple routes to the osteogenic phenotype in mesenchymal stem cells, BMC Genomics 8 (2007) 380.

[176] F.S. Hosseini, F. Soleimanifar, A. Ardeshirylajimi, S. Vakilian, M. Mossahebi-Mohammadi, S.E. Enderami, A. Khojasteh, S. Zare Karizi, In vitro osteogenic differentiation of stem cells with different sources on composite scaffold containing natural bioceramic and polycaprolactone, Artif Cells Nanomed Biotechnol 47(1) (2019) 300-307.

[177] M. Pineiro-Ramil, C. Sanjurjo-Rodriguez, R. Castro-Vinuelas, S. Rodriguez-Fernandez, I.M. Fuentes-Boquete, F.J. Blanco, S.M. Diaz-Prado, Usefulness of Mesenchymal Cell Lines for Bone and Cartilage Regeneration Research, Int J Mol Sci 20(24) (2019).

[178] R. Florencio-Silva, G.R. Sasso, E. Sasso-Cerri, M.J. Simoes, P.S. Cerri, Biology of Bone Tissue: Structure, Function, and Factors That Influence Bone Cells, Biomed Res Int 2015 (2015) 421746.

[179] Y. Qin, J. Guan, C. Zhang, Mesenchymal stem cells: mechanisms and role in bone regeneration, Postgrad Med J 90(1069) (2014) 643-7.

[180] H. Chiba, N. Sawada, T. Ono, S. Ishii, M. Mori, Establishment and characterization of Simian virus-40 immortalized osteoblastic cell line from normal human bone, Jpn. J. Cancer Res. 84 (1993) 290-297.

[181] E.R. Wagner, G. Luther, G. Zhu, Q. Luo, Q. Shi, S.H. Kim, J.L. Gao, E. Huang, Y. Gao, K. Yang, L. Wang, C. Teven, X. Luo, X. Liu, M. Li, N. Hu, Y. Su, Y. Bi, B.C. He, N. Tang, J. Luo, L. Chen, G. Zuo, R. Rames, R.C. Haydon, H.H. Luu, T.C. He, Defective osteogenic differentiation in the development of osteosarcoma, Sarcoma 2011 (2011) 325238.

[182] K.D. Hankenson, M. Dishowitz, C. Gray, M. Schenker, Angiogenesis in bone regeneration, Injury 42(6) (2011) 556-61.

[183] F. Razzi, L.E. Fratila-Apachitei, N. Fahy, Y.M. Bastiaansen-Jenniskens, I. Apachitei, E. Farrell, A.A. Zadpoor, Immunomodulation of surface biofunctionalized 3D printed porous titanium implants, Biomed Mater 15(3) (2020) 035017.

[184] R.P. Pirraco, M.T. Cerqueira, R.L. Reis, A.P. Marques, Fibroblasts regulate osteoblasts through gap junctional communication, Cytotherapy 14(10) (2012) 1276-87.

[185] I. Pennings, L.A. van Dijk, J. van Huuksloot, J.O. Fledderus, K. Schepers, A.K. Braat, E.C. Hsiao, E. Barruet, B.M. Morales, M.C. Verhaar, A. Rosenberg, D. Gawlitta, Effect of donor variation on osteogenesis and vasculogenesis in hydrogel cocultures, J Tissue Eng Regen Med 13(3) (2019) 433-445.

[186] L. Zhao, G. Li, K.M. Chan, Y. Wang, P.F. Tang, Comparison of multipotent differentiation potentials of murine primary bone marrow stromal cells and mesenchymal stem cell line C3H10T1/2, Calcif Tissue Int 84(1) (2009) 56-64.

[187] A. Scuteri, E. Donzelli, D. Foudah, C. Caldara, J. Redondo, G. D'Amico, G. Tredici, M. Miloso, Mesengenic differentiation: comparison of human and rat bone marrow mesenchymal stem cells, Int J Stem Cells 7(2) (2014) 127-34.

[188] B. Levi, E.R. Nelson, K. Brown, A.W. James, D. Xu, R. Dunlevie, J.C. Wu, M. Lee, B. Wu, G.W. Commons, D. Vistnes, M.T. Longaker, Differences in osteogenic differentiation of adipose-derived stromal cells from murine, canine, and human sources in vitro and in vivo, Plast Reconstr Surg 128(2) (2011) 373-86.

[189] L. Zhao, H. Wang, K. Huo, L. Cui, W. Zhang, H. Ni, Y. Zhang, Z. Wu, P.K. Chu, Antibacterial nano-structured titania coating incorporated with silver nanoparticles, Biomaterials 32 (2011) 5706-16.

[190] L. Drago, E. De Vecchi, M. Bortolin, L. Zagra, C.L. Romano, L. Cappelletti, Epidemiology and Antibiotic Resistance of Late Prosthetic Knee and Hip Infections, J Arthroplasty 32 (2017) 2496-2500.

[191] A. Panacek, L. Kvitek, M. Smekalova, R. Vecerova, M. Kolar, M. Roderova, F. Dycka, M. Sebela, R. Prucek, O. Tomanec, R. Zboril, Bacterial resistance to silver nanoparticles and how to overcome it, Nat Nanotechnol 13(1) (2018) 65-71.

[192] D. Richard, V. Ravigne, A. Rieux, B. Facon, C. Boyer, K. Boyer, P. Grygiel, S. Javegny, M. Terville, B.I. Canteros, I. Robene, C. Verniere, A. Chabirand, O. Pruvost, P. Lefeuvre, Adaptation of genetically monomorphic bacteria: evolution of copper resistance through multiple horizontal gene transfers of complex and versatile mobile genetic elements, Mol Ecol 26(7) (2017) 2131-2149.

[193] L.M. Cavaco, H. Hasman, F.M. Aarestrup, Zinc resistance of Staphylococcus aureus of animal origin is strongly associated with methicillin resistance, Vet Microbiol 150(3-4) (2011) 344-8.

[194] S.L. Percival, P.G. Bowler, D. Russell, Bacterial resistance to silver in wound care, J Hosp Infect 60(1) (2005) 1-7.

[195] U. Saran, S. Gemini Piperni, S. Chatterjee, Role of angiogenesis in bone repair, Arch Biochem Biophys 561 (2014) 109-17.

[196] J. Lee, H. Byun, S.K. Madhurakkat Perikamana, S. Lee, H. Shin, Current Advances in Immunomodulatory Biomaterials for Bone Regeneration, Adv Healthc Mater 8(4) (2019) e1801106.

[197] R.J. Geraghty, A. Capes-Davis, J.M. Davis, J. Downward, R.I. Freshney, I. Knezevic, R. Lovell-Badge, J.R. Masters, J. Meredith, G.N. Stacey, P. Thraves, M. Vias, U.K. Cancer Research, Guidelines for the use of cell lines in biomedical research, Br J Cancer 111 (2014) 1021-46.

[198] C. Bankier, R.K. Matharu, Y.K. Cheong, G.G. Ren, E. Cloutman-Green, L. Ciric, Synergistic Antibacterial Effects of Metallic Nanoparticle Combinations, Sci Rep 9 (2019) 16074.

[199] R.J. Worthington, C. Melander, Combination approaches to combat multidrug-resistant bacteria, Trends Biotechnol 31(3) (2013) 177-84.

[200] A. Sobolev, A. Valkov, A. Kossenko, I. Wolicki, M. Zinigrad, K. Borodianskiy, Bioactive Coating on Ti Alloy with High Osseointegration and Antibacterial Ag Nanoparticles, ACS Appl Mater Interfaces 11(43) (2019) 39534-39544.

[201] S. Durdu, Characterization, Bioactivity and Antibacterial Properties of Copper-Based TiO2 Bioceramic Coatings Fabricated on Titanium, Coatings 9(1) (2018).

[202] M. Fazel, H.R. Salimijazi, M. Shamanian, I. Apachitei, A.A. Zadpoor, Influence of hydrothermal treatment on the surface characteristics and electrochemical behavior of Ti-6Al-4V bio-functionalized through plasma electrolytic oxidation, Surface and Coatings Technology 374 (2019) 222-231.

[203] T.-E. Park, H.-C. Choe, W.A. Brantley, Bioactivity evaluation of porous TiO2 surface formed on titanium in mixed electrolyte by spark anodization, Surface and Coatings Technology 235 (2013) 706-713.

[204] J. He, W. Feng, B.H. Zhao, W. Zhang, Z. Lin, In Vivo Effect of Titanium Implants with Porous Zinc-Containing Coatings Prepared by Plasma Electrolytic Oxidation Method on Osseointegration in Rabbits, Int J Oral Maxillofac Implants 33(2) (2018) 298-310.

[205] M. Croes, H. de Visser, B.P. Meij, K. Lietart, B.C.H. van der Wal, H.C. Vogely, A.C. Fluit, C.H.E. Boel, J. Alblas, H. Weinans, S. Amin Yavari, Data on a rat infection model to assess porous titanium implant coatings, Data Brief 21 (2018) 1642-1648.

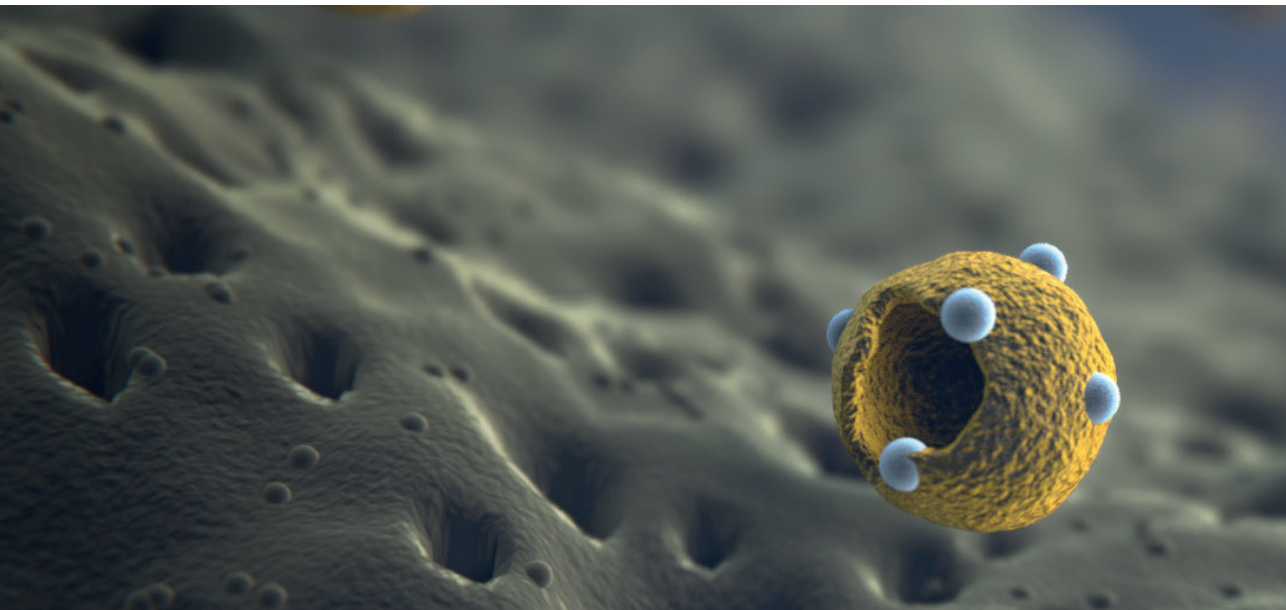

CHAPTER 03

Biofunctionalization of porous versus solid titanium implants

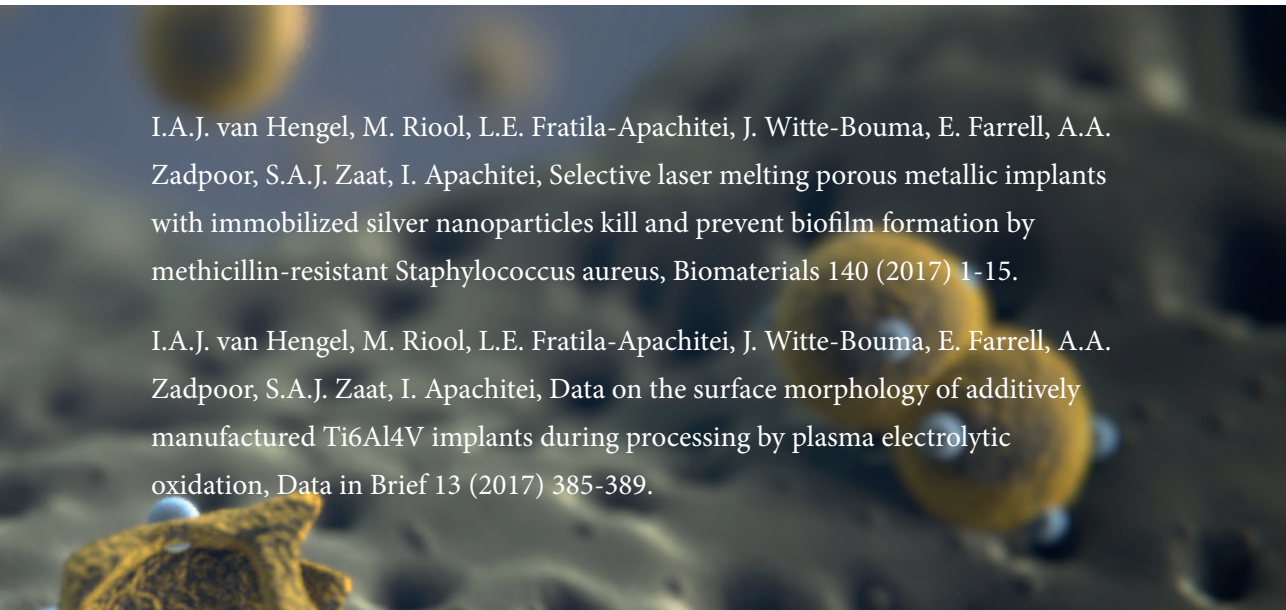

I.A.J. van Hengel, M. Riool, L.E. Fratila-Apachitei, J. Witte-Bouma, E. Farrell, A.A. Zadpoor, S.A.J. Zaat, I. Apachitei, Selective laser melting porous metallic implants with immobilized silver nanoparticles kill and prevent biofilm formation by methicillin-resistant Staphylococcus aureus, Biomaterials 140 (2017) 1-15.

I.A.J. van Hengel, M. Riool, L.E. Fratila-Apachitei, J. Witte-Bouma, E. Farrell, A.A. Zadpoor, S.A.J. Zaat, I. Apachitei, Data on the surface morphology of additively manufactured Ti6Al4V implants during processing by plasma electrolytic oxidation, Data in Brief 13 (2017) 385-389.

Implant-associated infection (IAI) and limited longevity are two major challenges that orthopedic devices need to simultaneously address. Additively manufactured porous implants have recently shown tremendous promise in improving bone regeneration and osseointegration, but, as any conventional implant, are threatened by infection. In this study, we therefore used rational design and additive manufacturing in the form of selective laser melting (SLM) to fabricate porous titanium implants with interconnected pores, resulting in a 3.75 times larger surface area than corresponding solid implants. The SLM implants were biofunctionalized by embedding silver nanoparticles in an oxide surface layer grown using plasma electrolytic oxidation (PEO) in Ca/P-based electrolytes. The PEO layer of the SLM implants released silver ions for at least 28 days. X-ray diffraction analysis detected hydroxyapatite on the SLM PEO implants but not on the corresponding solid implants. *In vitro* and *ex vivo* assays showed strong antimicrobial activity of these novel SLM PEO silver-releasing implants, without any signs of cytotoxicity. The rationally designed SLM porous implants outperformed solid implants with similar dimensions undergoing the same biofunctionalization treatment. This included four times larger amount of released silver ions, two times larger zone of inhibition, and one additional order of magnitude of reduction in numbers of bacteria in an *ex vivo* mouse infection model.

3.1 INTRODUCTION

Multifunctional orthopedic biomaterials [1] that improve bone regeneration and fixation [2-4] and at the same time offer protection against infections [5-11] are intensively researched. Unmet clinical needs, particularly in the case of large bony defects [12-14], complex bone reconstructions [15,16], and patients with compromised bone metabolism and immune systems such as those with malignant bone tumors that might receive large limb salvaging prostheses [17-20] motivate most of that research. Recent advances in additive manufacturing techniques have given rise to a new paradigm in which the novel functionalities of biomaterials do not necessarily depend on discovery of new materials with unique properties, but are rather driven by *rational design* of biomaterials.

The properties and, thus, functionalities of rationally designed biomaterials are direct functions of their topologies otherwise known as their micro-architectures. The seemingly limitless form-freedom offered by additive manufacturing techniques in fabricating arbitrarily complex topologies has been exploited in the last few years to design and manufacture porous biomaterials with unique properties. It has been, for example, shown that the type and dimensions of the repeating unit cell can be adjusted to achieve mechanical properties close to those of native bone [21], thereby preventing stress-shielding and improving implant longevity. The other geometrical parameters of the porous biomaterials such as pore size [22], pore shape [23], porosity [22], and curvature [24,25] that have been shown to influence bone tissue regeneration [26] can be also rationally designed to achieve improved tissue regeneration performance and implant fixation. Finally, rationally designed and additively manufactured fully porous biomaterials can achieve surface areas that are up to several orders of magnitude larger than those of the corresponding solid biomaterials. Such a huge surface area, as we have shown before [27], can then be used for biofunctionalization purposes to markedly improve bone tissue regeneration performance. A potential risk of increasing the surface area is that bacteria contaminating the surgical site at implantation may have a higher chance of adhering to the surface and initiate biofilm formation. It is therefore vital to protect this increased surface area against infecting bacteria.

In this study, we aimed to develop rationally designed and additively manufactured porous metallic implants equipped with antimicrobial functionality to prevent implant-associated infection (IAI), including infections by worst case pathogens such as methicillin-resistant *Staphylococcus aureus* (MRSA). The use of porous metallic biomaterials provides the benefit of a superior mechanical support relative to the biodegradable candidate materials. Furthermore, for applications such as spinal cages or parts for reconstruction surgery in orthopedics and dentistry, permanent metallic porous implants are needed. However, the presence of such implants in the body for the rest of the patients' lifetime poses challenges with regard to cytotoxicity and IAI.

Long (*i.e.* high aspect-ratio) implants were rationally designed and additively manufactured using selective laser melting (SLM) from Ti6Al4V to increase the surface area. The surface of the implants was then biofunctionalized using plasma electrolytic oxidation (PEO), chosen because of its great potential for inducing multiple functionalities in a fast single-step process. When performed in presence of silver nanoparticles (AgNPs), PEO not only results in a bioactive surface with interconnected micro-/nano-porosity that can improve implant osseointegration [28-31] but also dopes the surface of the implants with fully dispersed and firmly attached AgNPs all within the span of a few minutes. AgNPs were chosen because, when oxidized, they release Ag ions that are known to be potent antimicrobial agents and have shown strong bactericidal behavior against a wide spectrum of bacteria including MRSA [32-37] through multiple mechanisms such as damage to bacterial membranes and production of reactive oxygen species [38].

The most important feature of PEO-treated surfaces that sets them apart from other antimicrobial surfaces based on AgNPs is the fact that in PEO the AgNPs are entrapped in an *in-depth growing* oxide layer which fully immobilizes them and prevents them from freely circulating through the blood stream, thereby preventing any potential nanotoxic effects [39,40]. At the same time, AgNPs are fully dispersed within the huge and hierarchical surface area of additively manufactured porous implants which greatly facilitates oxidation of the AgNPs and, thus, the release of Ag ions. Following biomaterials synthesis and characterization, their antimicrobial activity and cytotoxicity were assessed.

3.2 MATERIALS AND METHODS

3.2.1 Rational design and additive manufacturing

We designed implants suitable for implantation in a mouse femur model, which therefore needed to simultaneously meet multiple design criteria. First, the entire volume of the implant was designed to be porous with the aim of substantially increasing the surface area while providing ample space for bone ingrowth and implant fixation. Second, the pore size was required to be larger than 300 μm to maximize the bone regeneration performance of the porous biomaterials [22]. Third, the diameter of the implant was defined not to exceed 0.5 mm to make sure the implants can be fit in murine femurs used to assess *ex vivo* antimicrobial activity. Fourth, the porous structure had to be designed for selective laser melting (SLM) additive manufacturing. Since the laser spot in metal additive manufacturing techniques is between 100-150 μm, not every porous structure with the desired diameter of 500 μm (only 3-4 times the laser spot size) can be additively manufactured. Various designs of unit cells were evaluated against the above-mentioned criteria using design and computational software. Two-dimensional cross-section drawings were first produced in SolidWorks

(Dassault Systèmes, Vélizy-Villacoublay, France) to evaluate the porosity and pore size of the porous structure. The two-dimensional drawings were then used to create the required three-dimensional geometries based on a vector space generated using a MATLAB (MathWorks, Natick, Massachusetts, United States) script. Moreover, design constraints were imposed on the coordinates of the top and bottom planes of the unit cell to ascertain the designed unit cells were space-filling, *i.e.* they could be repeated along the required directions to give rise to the desired porous structure. The unit cell fulfilling all the above-mentioned criteria, *i.e.* hexagonal unit cell was selected for SLM manufacturing of the implants.

Implants of 4 cm in length were produced at the Additive Manufacturing Lab (TU Delft, Delft, The Netherlands) using an SLM machine (SLM-125, Realizer, Borchem, Germany) with YLM-400-AC Ytterbium fibre laser (IPG Photonics Corporation, Oxford, USA), under inert atmosphere (*i.e.* Argon) with an oxygen content below 0.2%. Medical-grade (grade 23, ELI) Ti6Al4V powder (AP&C, Boisbriand, Quebec, Canada) with particle sizes between 10 and 45 μm and spherical particle morphology was used. The laser spot size and layer thickness were 145 μm and 50 μm, respectively. A parametric study was performed to determine the optimum laser processing parameters, which resulted in an exposure time of 300 μs, a wavelength of 1070 ± 10 nm and laser power of 96 W. After the SLM procedure, the loose powder was removed by vacuum cleaning followed by ultrasonication in acetone, 96% ethanol, and demineralized water for 5 minutes each. For comparison with SLM implants, solid annealed Ti6Al4V implants (Goodfellow, Cambridge, England) with a diameter of 500 μm were used.

3.2.2 Surface biofunctionalization

The surface of the implants was biofunctionalized using an electrochemical process, namely PEO. The PEO electrolyte consisted of 0.02 M calcium glycerophosphate and 0.15 M calcium acetate as well as AgNPs. The AgNPs (Sigma-Aldrich, St. Louis, Missouri, United States) ranging in size between 7 and 25 nm and with a spherical shape were dispersed in the PEO electrolyte at a concentration of 3.0 g/l. To obtain a homogeneous dispersion of AgNPs, the electrolyte was ultrasonicated 2 times 3 min. In between the sonication steps, the electrolyte was stirred at 500 rpm for 5 min using a magnetic stirrer (IKA-Werke GmbH & Co. KG, Staufen, Germany) with a stir bar of 40×8 mm (Radnor, Pennsylvania, United States).

A custom-made PEO setup [41-43] consisting of an AC power source (50Hz, type ACS 1500; ET Power Systems Ltd, Eyam, England), a computer interface connected to the power supply through a data acquisition board (SCXI, National Instruments, Austin, Texas, United States) and a double-walled glass electrolytic cell with two electrodes containing 800 ml electrolyte was used. The implant (4 cm in length and 0.5 mm in diameter) functioned as the anode during the

PEO process performed under galvanostatic conditions. A cylindrical-shaped stainless steel cathode was placed against the inner wall of the electrolytic cell. A current density of 20 A/dm^2 has been applied via the power source. The temperature of the electrolyte was kept constant at 5 ± 2 °C with a thermostatic bath (Thermo Haake, Karisruhe, Germany) that delivered cooling liquid to the electrolytic cell through a pump system. To ensure a homogeneous particle distribution the electrolyte was continuously stirred at 500 rpm. The voltage-time (V-t) curves were recorded during the PEO process at a sampling rate of 1 Hz. After PEO treatment, implants were rinsed for 1 min in running tap water to remove residual electrolyte. Subsequently, the implants were sterilized by ultrasonication for 30 s in 70% ethanol, 5 min submersion in demineralized water, 30 s ultrasonication in demineralized water and heat treatment for 1 hour at 110 °C in an oven (Nabertherm TR60, New Castle, United States).

A series of SLM implants were biofunctionalized using PEO but without inclusion of AgNPs in the electrolyte. The resulting implants (SLM PEO) served as controls to enable separating the effects of PEO treatment from those of AgNPs. SLM implants without any biofunctionalizing treatment (SLM NT) served as additional controls. Solid and SLM implants biofunctionalized using PEO including AgNPs were labeled as solid PEO+Ag and SLM PEO+Ag, respectively. The solid implants undergoing only the PEO treatment were labeled as solid PEO. An overview of all experimental groups is depicted in **Table 1**.

Table 1. Overview of the experimental groups

Abbreviation	Content
SLM NT	Selective laser melting Ti6Al4V implants non-treated
SLM PEO	Selective laser melting Ti6Al4V implants oxidized by plasma electrolytic oxidation
SLM PEO+Ag	Selective laser melting Ti6Al4V implants oxidized by plasma electrolytic oxidation + silver nanoparticles
Solid PEO	Solid Ti6Al4V implants oxidized by plasma electrolytic oxidation
Solid PEO+Ag	Solid Ti6Al4V implants oxidized by plasma electrolytic oxidation + silver nanoparticles

3.2.3 Biomaterial characterization

Scanning electron microscopy (SEM)

The surface morphology of the implants before and after biofunctionalization and throughout the *in vitro* and *ex vivo* assays was assessed using two scanning electron microscopes, namely JSM-6500F (JEOL, Tokyo, Japan) and JSM-IT100LA (JEOL). Beam energies ranging between 5 and 20 kV and a working distance of 10 mm were used. Prior to imaging, the implants (n = 3/group) were cleaned in acetone and 2-propanol (Sigma-Aldrich) for 30 s each and coated

with a carbon or gold layer of 5 ± 2 nm to improve electrical conductivity. Energy-dispersive X-ray spectroscopy (EDS) was performed to investigate the presence of AgNPs through spot analyses that revealed the chemical composition at specific areas on the surface.

X-ray diffraction (XRD)

The phase composition of SLM NT, SLM PEO and solid PEO specimens (n = 2/group) was studied using a Bruker D8 (Bruker, Billerica, Massachusetts, United States) advanced X-ray diffractometer with Bragg-Brentano geometry and Lynxeye position sensitive detector. The following settings were used: Cu Kα radiation detector: LL 0.11 W 0.14, divergence slit: V6, scatter screen height: 5 mm, voltage: 45 kV, and current: 40 mA. The samples were analyzed without spinning. Measurements were performed with coupled θ-2θ scan from 20-120° using a step size of 0.034° 2θ and counting speed of 10s/step. Data was evaluated with the Bruker DiffracSuite.Eva 4.1 software (Bruker).

Inductively coupled plasma (ICP)

The release kinetics of Ag ions was studied by inductively coupled plasma optical emission spectrometry (ICP-OES) with a ThermoFisher iCAP6300 Duo instrument (Thermo Fisher Scientific, Waltham, Massachusetts, USA). SLM PEO+Ag and solid PEO+Ag implants (n = 3/group) were immersed in 1 ml phosphate buffered saline (PBS) in a brown glass vial, and incubated at 37 °C in a water bath. The PBS was collected and refreshed after 0.5, 1, 2, 4, 7, 14, and 28 days and the concentration of Ag ions measured.

3.2.4 Antimicrobial assays

Preparation of bacterial inoculum

A bacterial inoculum was prepared by adding a single colony of methicillin-resistant *Staphylococcus aureus* (MRSA) strain AMC201 [44,45] from a blood agar plate to 5 ml tryptic soy broth (TSB; Sigma-Aldrich) and incubating the suspension overnight at 37 °C, shaking. The overnight culture was diluted 50-fold in TSB and incubated for 4-5 hours at 37 °C at 200 rpm. Thereafter, 1 ml of this culture was centrifuged for 30 s at 14,000 rpm and the pellet was resuspended and washed twice in 1 ml of 10 mM phosphate buffer containing 1% TSB (PT). After final resuspending in 1 ml PT the optical density at 620 nm (OD_{620}) was measured. Based on this OD_{620}, the culture was diluted to the required bacterial concentration using PT. This inoculum was quantitatively cultured by plating quadruplicate 10 µl aliquots of 10-fold serial dilutions on blood agar plates (Biomerieux, Marcy-l'Étoile, France), incubating overnight at 37 °C and counting colony forming units (CFU) the following day. All implants used in antimicrobial assays had a length of 1 cm and a diameter of 0.5 mm.

In vitro leachable antimicrobial activity assays

To study the *in vitro* leachable antimicrobial activity of the implants, a modified version of the Petrifilm assay was performed. The Petrifilm Aerobic Count Plates (3M Health Care) consists of a bottom film containing a gelling agent, nutrients, and indicators for bacterial growth. To inoculate, 1 ml of bacterial suspension containing 10^7 CFU/ml was pipetted in the center of the bottom film and the transparent top cover film was closed on top of it and uniform distribution was obtained by gentling applying pressure. After 2 min of gelation, the top cover was lifted, an implant was placed on the bottom gel using forceps, and the cover was closed. The Petrifilm plate was incubated for 24 hr in a humid atmosphere at 37 °C. The diameter of the zone of growth inhibition was measured using image processing software (analySIS auto5, Olympus, Tokyo, Japan) to quantify antimicrobial activity (n = 3/group).

Agar assay for implant bactericidal activity

To determine the bactericidal capacity of implants, an agar assay was performed. To produce the agar, 0.1 gram of low electro-endosmosis agarose powder (Sigma-Aldrich) was dissolved in 10 ml modified RPMI 1640 medium (R7388, Gibco, Gaithersburg, Maryland, United States) and heated to boiling in a microwave oven under continuous shaking. Subsequently, aliquots of 1.5 ml were prepared and placed in a 45 °C thermostatic bath to prevent solidification of the agar. To these aliquots 15 µl of inoculum suspension containing 3×10^7 CFU of MRSA strain AMC201 was added and 400 µl was pipetted onto preheated microscopic slides and covered with a cover glass. Samples were kept at 37 °C for 3 min and cooled down for another 3 min to allow solidification. Next, the cover glass was removed with a disposable scalpel and implants were placed in the center of the agar layer. These agar slides were incubated for 24 hr at 37 °C in a humid environment. In order to assess whether the bacteria within the zone of growth inhibition had been killed, samples of the agar were taken with a pipet tip from three different locations: (i) under the implant, (ii) in the zone of inhibition, and (iii) outside the zone of inhibition. In case of no zone of inhibition, the sample was taken under the implant. The agar samples were sonicated in 100 µl PT and numbers of CFU were assessed by quantitative culture. Two specimens were used for every type of implant and for each location per implant.

Surface bactericidal activity assay

The capacity of the antimicrobial implants to kill surface-adherent bacteria was assessed using a simplified surface bactericidal activity assay. Implants were inoculated with 2 µl of 10^2 CFU/µl of MRSA AMC201 in demineralized water. To assess rapid bactericidal activity, the implants (n = 3/group) were incubated for 3 and 15 min in a laminar flow cabinet, which

resulted in drying of the applied inoculum. Subsequently, the implants were sonicated in 100 µl PT, and the sonicates were quantitatively cultured.

Biofilm formation and characterization

Biofilm formation was assessed by static incubation of the implants at 37 °C in 1 ml TSB medium containing 1% glucose (D(+)-glucose, Merck, Darmstadt, Germany) and inoculated with 10^8 CFU/ml of MRSA AMC201 [46]. After 24 and 48 hr, the implants were fixed using the McDowels fixative (4% paraformaldehyde and 1% glutaraldehyde in phosphate buffer at pH 7.4) and stored at 4 °C. For SEM imaging, they were rinsed in demineralized water for 10 min, dehydrated in ethanol (15 min in 50%, 20 min in 70%, and 20 min in 96%) and hexamethyldisilazane (HDMS) for 30 min, dried in air for 2 hr and coated with a gold layer of 5 ± 2 nm. Two specimens (n = 2/group) were used for each experimental group per time point.

Ex vivo experiments

The antimicrobial activity of the implants was evaluated in an *ex vivo* model utilizing explanted femurs from mouse cadavers, provided by the Animal Research Institute AMC (ARIA) of the AMC (Amsterdam, The Netherlands). After removal of adherent soft tissue the femurs were sterilized in 70% ethanol for 10 min followed by 10 min submersion in demineralized water to remove residual traces of ethanol. Thereafter, the femurs were prepared to receive the implant. Using a 0.5 mm drill, a hole was drilled through the epicondyle into the intramedullary canal. Subsequently, bone marrow was removed with a syringe. To mimic the *in vivo* wet environment, 2 µl of PT was injected into the bone cavity. Before implantation the implants were inoculated with 2 µl PT containing 200 CFU of MRSA AMC201 and left to dry in a laminar flow cabinet for 15 min. Subsequently, the implants (n = 3/group) were implanted under slight pressure.

To confirm effective sterilization of the femurs prior to implantation, one femur did not receive an implant and was not challenged with bacteria but was subjected to the homogenization and culturing procedure after the drilling step (sterilization control). To determine the validity of the model, 2 µl of doxycycline (50 mg/ml; Sigma-Aldrich) was injected into the bone cavity prior to implantation of an inoculated SLM NT implant (positive control). After implantation, the femurs were incubated in 0.5 ml tubes for 24 hr at 37 °C on a rotating platform to allow intraosseous flow of fluid.

Following incubation, the femurs including the implant were submersed in 800 µl PT with 15 zirconia beads (Ø 2 mm, BioSpec, Bartlesville, Oklahoma, United States) and the bone was homogenized using a MagNA Lyser (Roche Diagnostics, Risch-Rotkreuz, Switzerland) at 7000 rpm for 2 cycles of 30 s each, with cooling on ice for 30 s in between. The resulting homogenates were quantitatively cultured.

3.2.5 Cytotoxicity

The cytotoxicity of the SLM implants for human mesenchymal stem cells (hMSCs) was evaluated by live/dead staining and MTT ([3-(4,5-dimethylthiazol-2-yl)-2,5-diphenyl tetrazolium bromide]) metabolic activity assay.

Live/dead staining

SLM NT, SLM PEO and SLM PEO+Ag implants (n = 3/group) with a length of 1 cm were sterilized by autoclaving at 121 °C for 20 min. Each implant was placed in a 0.5 ml tube with $8x10^5$ hMSCs in 400 µl α-Minimum Essential Medium (Invitrogen, Thermo Fisher Scientific, Waltham, MA, United States) supplemented with 10% v/v Fetal Bovine Serum, 50 g/ml Gentamycin, 1.5 g/ml Fungizone/AmphotericinB (all Invitrogen), 1 ng/ml fibroblast growth factor 2 (FGF-2; Bio-Rad, Hercules, California, United States) and 10^{-4} M vitamin C (Sigma-Aldrich). The samples were incubated at 37 °C and 5% CO_2, and turned 180° every 10 min three times. After 40 min, the implants were placed in a 6 well plate and fresh medium was added to each well (2 ml/well). The samples were incubated for 24 hr (37 °C, 5% CO_2) and the medium refreshed after 1 and 6 hr. After incubation, the samples were rinsed 3 times in 0.9% w/v NaCl (saline), stained with Calcein AM and Ethidium homodimer-1 (CyQuant kit) and incubated for 40 min at 37 °C and 5% CO_2. Thereafter, the samples were rinsed 3 times with saline and imaged by confocal microscopy using a Zeiss LSM510 Meta (Carl Zeiss Microscopy, Jena, Germany). Samples were placed in a glass bottomed petri dish (MatTek, Ashland, MA, United States) and imaged using 488 and 543 nm lasers with a bandpass filter (505-530 nm) for the green channel and a 560 nm long pass filter used for the red channel.

MTT assay

The hMSCs were seeded on the implants as described in the live/dead assay with 3 specimens for each experimental group at every time point (*i.e.*, 1, 4 and 7 days). Prior to the measurement, the implants were placed in a new well plate, rinsed 3 times with PBS and then incubated for 3.5 hr in 250 µg/ml MTT in serum free α-Minimum Essential Medium (Invitrogen, Thermo Fisher Scientific, Landsmeer, the Netherlands) at 37 °C and 5% CO_2. Subsequently, the medium was removed and purple MTT formazan crystals were dissolved in 100% ethanol. Thereafter, the optical density ($OD_{570\text{-}670}$) was measured with a Versmax 96 Wells plate reader (Versamax, Molecular devices, Workingham, United Kingdom).

3.2.6 Statistical analysis

All data are expressed as mean ± standard deviation. Statistical analysis was performed with GraphPad Prism (GraphPad Software, La Jolla, California, United States) using one-way and repeated measures ANOVA. The differences between the groups were considered statistically significant when $p < 0.05$.

3.3 RESULTS

3.3.1 Additive manufacturing of implants

The repeating unit cell used in the design of implant together with the resulting porous structures with different aspect ratios of the unit cell are presented in **Figure 1A**. The porosity and surface area of the porous structures with different aspect ratios are also indicated. The porosity of the implant is a function of the aspect ratio. The aspect ratio with the largest surface area (*i.e.* 1.0) was chosen for further processing by SLM. The nominal value of the porosity of these implants was 14.4%. The manufactured SLM implants (**Figure 1B**) demonstrated a clear porous structure with a rough surface (**Figure 1C**). The spherical shape of a number of unmolten or partially molten particles was observed with SEM (**Figure 1D,E**). These particles further increase the surface area of the implants.

3.3.2 Surface biofunctionalization and resulting morphology

The V-t curves recorded for SLM PEO, SLM PEO+Ag, solid PEO, and solid PEO+Ag implants show similar characteristics (**Figure 2A**). Initially, the voltage during the PEO process rapidly increased at a rate of 16 ± 2 V/s. The slope of the V-t curves inflected when plasma discharging started at 115 ± 5 V after 6 ± 1 s, indicating that dielectric breakdown had occurred. After about

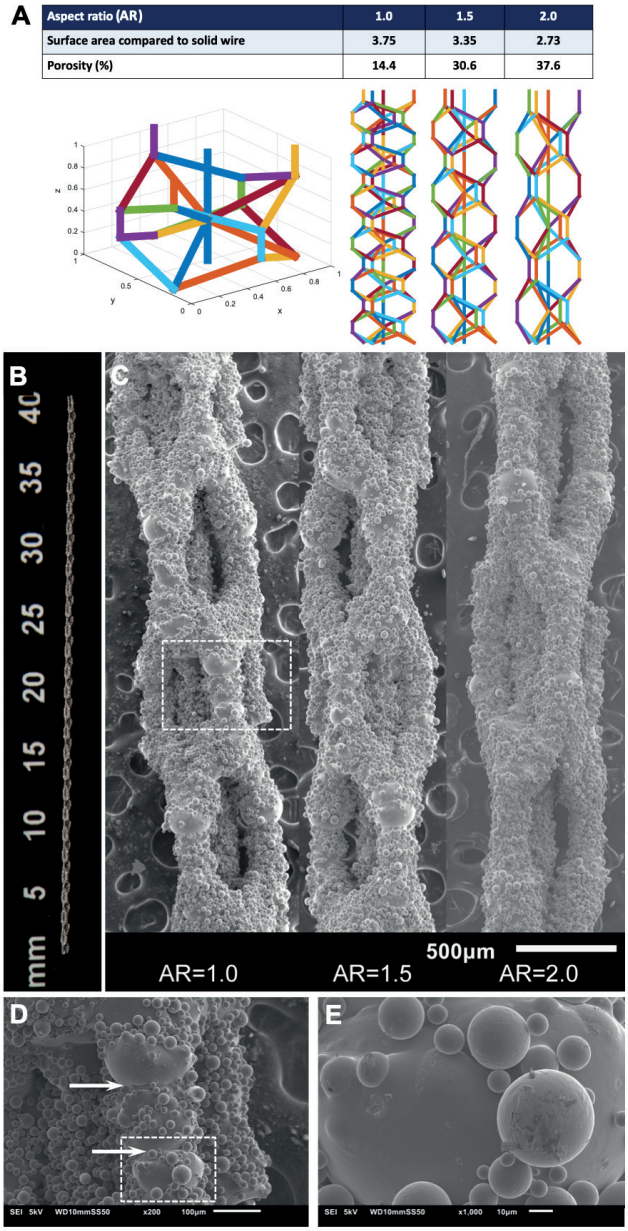

Figure 1. The design and morphology of SLM Ti6Al4V porous implants. (A) the repeating unit cell together with the resulting SLM porous structures with different aspect ratios (AR=1.0, 1.5 and 2.0), as well as their corresponding porosities and surface areas; (B) The macro-scale view of an SLM implant with an aspect ratio of 1.0; (C) SEM micrographs revealing the surface morphology of the SLM implants with the different aspect ratios; (D) Enlargement of the selected area in (C) showing the fully molten Ti6Al4V particles (arrows) following the SLM process; and (E) Detailed view of the selected area in (D) presenting partially molten and unmolten Ti6Al4V particles.

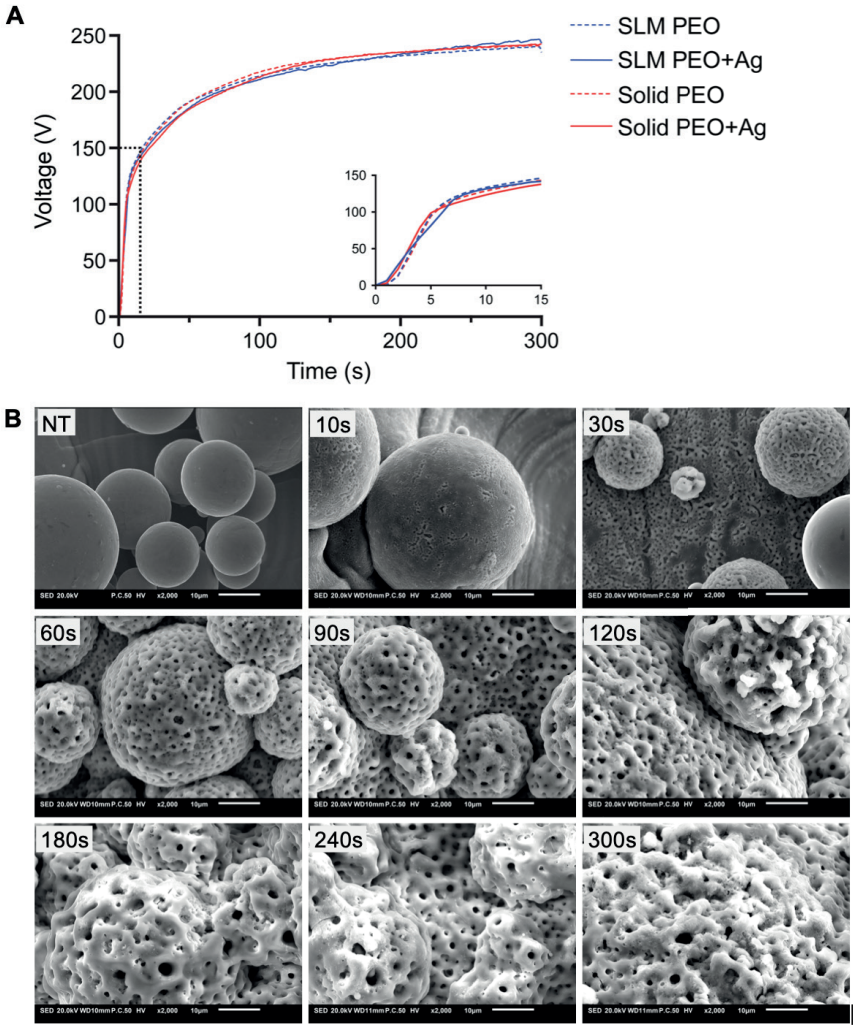

Figure 2. (A) The voltage-time transients recorded during the PEO process of different implants, *i.e.* SLM PEO, SLM PEO+Ag, solid PEO and solid PEO+Ag. (B) The evolution of surface morphology of the SLM PEO implants as a function of different (10-300 s) oxidation times (NT = non-treated surface), recorded by SEM (scale bar = 10 μm).

180 s, the voltage was increasing almost linearly with the final voltage of 245 ± 5 V being reached after 300 s. The SEM images of implants revealed the gradual growth of the oxide layer and the formation of an interconnected micro-/nano-porous structure (**Figure 2B**). After 10 s, non-uniformly distributed nanopores with elongated morphology were observed. This corresponds with dielectric breakdown after 6 ± 1 s observed in the V-t curves. Both the

bulk material and some (but not all) of the spherical titanium particles showed formation of the nanoporous structures. The porous structure seemed to have followed the laser scanning lines originating from the SLM process (**Figure 2B**, 10 and 30s).

As oxidation continued, the number of pores increased and pores grew in size. After 30 s, some spherical particles were still smooth without surface porosity. After 60 s, the surface was completely covered with a structure of micro- and nano-pores and the overall shape of the pores tended to be circular. Continued oxidation resulted in fusion of micropores and formation of bigger circular pores. In addition, pores started to protrude from the surface and the TiO_2 layer was thickening after 90-120 s. As the oxidation time reached 180 s, the protruding pores had grown in size up to several μm, which coincided with the observation of larger plasma discharges. This morphology was maintained until the end of the oxidation process at 300 s. The specific PEO morphology was developed throughout the 3D porous structure of the SLM PEO implant, as shown in **Figures 1-3** [47]. PEO in the presence of AgNPs indicated similar results with the entire surface of the SLM PEO+Ag and solid PEO+Ag implants uniformly covered by the micro-/nano-porous oxide layer (**Figure 3A,B**). However, the SLM PEO+Ag implants (**Figure 3A**) showed clearly higher levels of surface micro-/nano-porosity as compared to the solid PEO+Ag implants (**Figure 3B**).

3.3.3 Surface chemistry of Ag based implants

The presence of AgNPs incorporated during the PEO process after 300 s has been studied for both solid and SLM implants by SEM+EDS analysis. As revealed by both secondary and backscattered SEM images, the AgNPs were fully embedded in the grown oxide layer after 300 s and uniformly distributed throughout the surface area of the implants (**Figure 3C**). EDS point analysis showed the presence of Ag in the areas of the oxide layer appearing to embody AgNPs while no Ag EDS peaks were revealed in the TiO_2 matrix where Ag was not present (**Figure 3D**). Furthermore, Ca, P, O, Ti, Al, and V were observed on the surface of the implants. Ca and P are incorporated species from the PEO electrolyte whereas Ti, Al and V are alloying elements of the metallic implants.

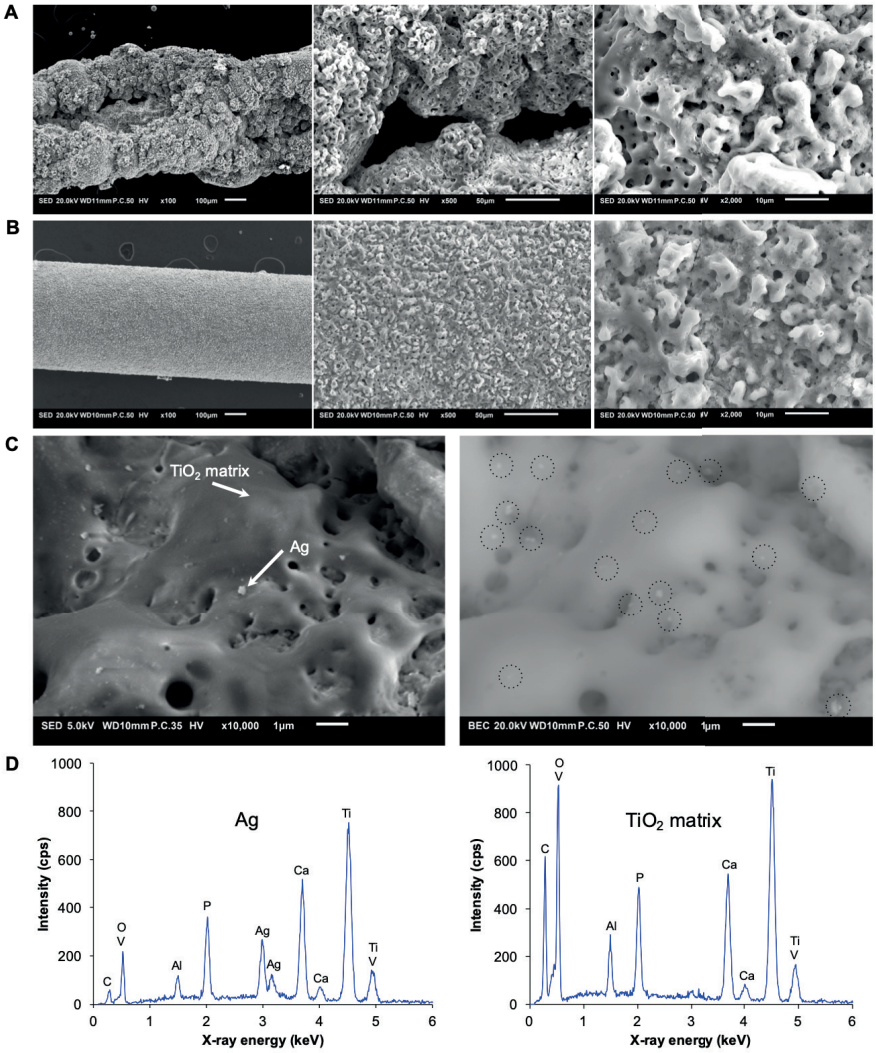

Figure 3. Comparison between the surface morphology of (A) SLM PEO+Ag and (B) solid PEO+Ag implants after 300 s oxidation, recorded by SEM. (C) Secondary (left) and backscattered (right) SEM images presenting the location and distribution of AgNPs – indicated by dotted circles – on SLM PEO+Ag implants. (D) EDS spectra of areas of Ag (left) and TiO_2 matrix (right; arrows in C) of SLM PEO+Ag implants revealing the presence of Ag, Ca and P elements.

3.3.4 Surface phase composition of implants

XRD analysis of the PEO implants (**Figure 4**) revealed a highly crystalline oxide layer with high levels of rutile and relatively lower levels of anatase phases in both solid and SLM implants, after 300 s of PEO treatment. While the oxide layer grown on the surface of solid

implants did not show any peaks of hydroxyapatite, this phase was present on the oxide layer created during the biofunctionalization process of the SLM implants. Hydroxyapatite phase was already present in the oxide layer of SLM implants after 120 s of PEO treatment and continued to grow at longer treatment time (*i.e.* 240 and 300 s). Along with hydroxyapatite phase, Ca-based phases such as $CaTiO_3$ (perovskite) and $Ca_3(PO_4)_2$ (calcium phosphate) were also found in the XRD patterns after 120, 240 and 300 s of oxidation.

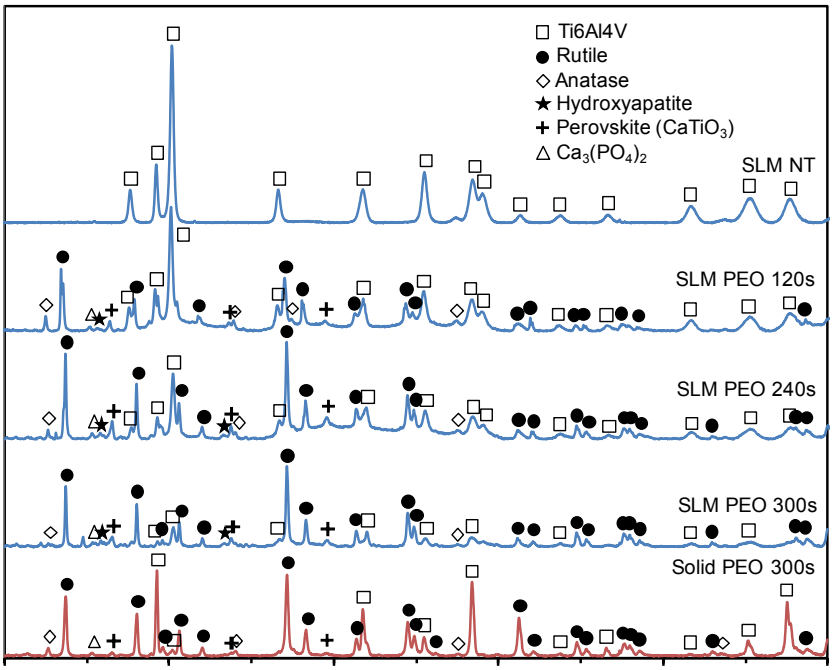

Figure 4. XRD patterns of SLM NT, SLM PEO (after different oxidation times: 120, 240 and 300 s) and the solid PEO after 300 s.

3.3.5 Silver release and antimicrobial activity

Silver release kinetics

Both SLM PEO+Ag and solid PEO+Ag implants continued to release Ag ions at least up to 28 days (**Figure 5A**). The cumulative release rate of Ag ions was highest in the first 3-4 days and decreased to a more or less constant level after 4 days. At all time points, SLM PEO+Ag showed a significantly higher ($p < 0.001$) release, up to 4.35 times higher, than the solid PEO+Ag implants.

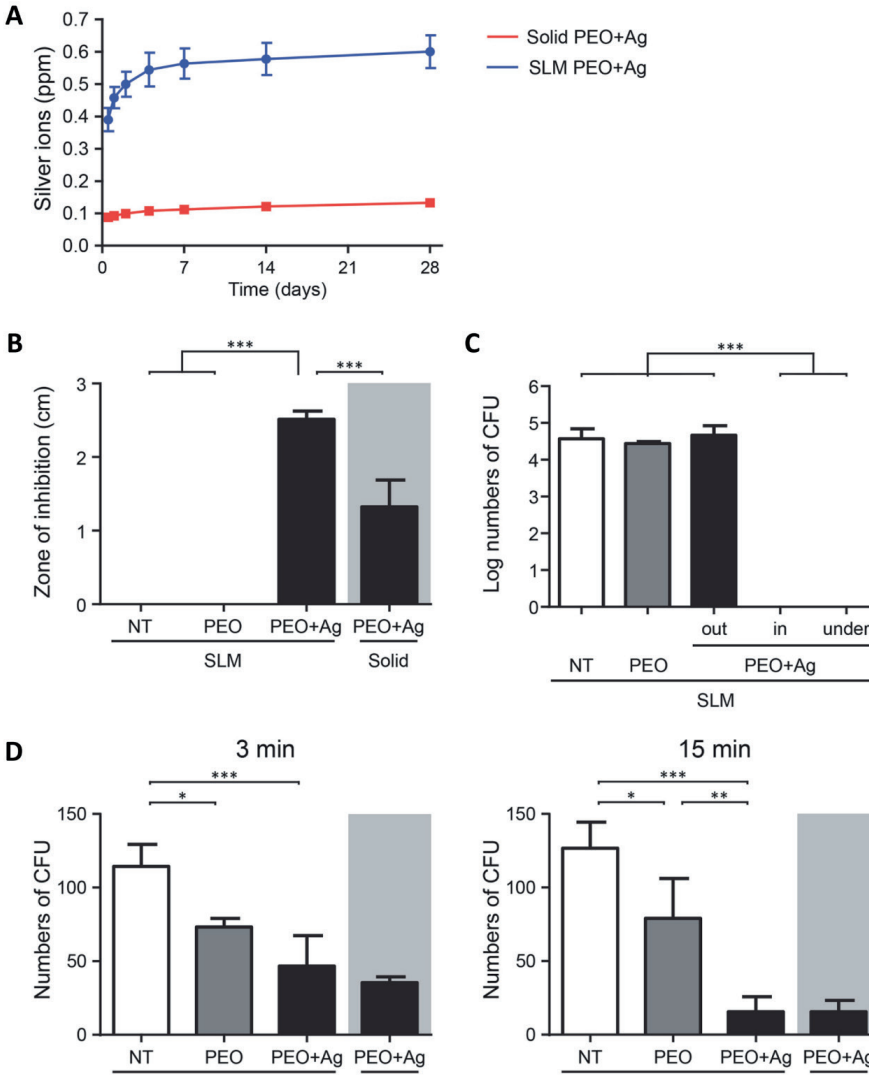

Figure 5. Cumulative silver ion release and antimicrobial activity of SLM PEO+Ag implants against MRSA AMC201. (A) Ag release profiles (n=3) of SLM PEO+Ag and solid PEO+Ag implants measured by ICP-OES. Silver release of SLM PEO+Ag was higher than of solid PEO+Ag implants at all time points ($p < 0.001$). (B) Inhibition zones around implants in a Petrifilm assay. The diameters of the zones of inhibition of SLM NT, SLM PEO and SLM PEO+Ag were statistically compared with each other, and the zones around SLM PEO+Ag were compared to those of solid PEO+Ag (n=3; ***, $p < 0.001$). (C) Assessment of viability of MRSA AMC201 at 24h after incubation in an agar around SLM NT, SLM PEO, SLM PEO+Ag and solid PEO+Ag implants. Agar was sampled under all implants and in- and outside the zones of inhibition (SLM PEO+Ag) (n=2; ***, $p < 0.001$). (D) Surface microbicidal activity after 3 and 15 min against an inoculum of 200 CFU of MRSA AMC201. Numbers of CFU cultured from SLM NT, SLM PEO and SLM PEO+Ag implants were statistically compared with each other, and those from SLM PEO+Ag to those from solid PEO+Ag implants (n=3; *, $p < 0.05$; **, $p < 0.01$; ***, $p < 0.001$).

Released antimicrobial activity, inhibition zones

Released antimicrobial activity was assessed in a zone of inhibition assay using MRSA as the target bacteria (**Figure 5B**). The diameter of the inhibition zone around SLM PEO+Ag implants was approximately twice the diameter around the solid PEO+Ag implants (*i.e.* 2.5 mm as compared to 1.3 mm, $p < 0.001$). The SLM NT and SLM PEO implants did not show any zone of inhibition. Large numbers of CFU were cultured from agar under the SLM NT and SLM PEO implants as well as from agar originating from outside the inhibition zone of the PEO+Ag implants (**Figure 5C**). Cultures of agar originating from the inhibition zone, either around or under the SLM PEO+Ag implants, were all negative, proving that the released Ag ions were bactericidal to the MRSA.

Surface microbicidal activity

A surface microbicidal activity assay was performed, with short term exposure of MRSA to the implant surfaces. Contact with the SLM PEO ($p < 0.05$) and SLM PEO+Ag ($p < 0.001$) implants significantly reduced the numbers of MRSA CFU as compared to SLM NT implants after 3 and 15 min of exposure (**Figure 5D**). Moreover, SLM PEO+Ag implants performed significantly better ($p < 0.01$) than SLM PEO implants after 15 min. After 3 min there was a significant reduction of the numbers of CFU on the SLM PEO implants relative to those on the SLM NT implants, but the numbers at 15 min were not reduced any further. In case of the SLM PEO+Ag implants, the numbers of CFU did decline further between 3 and 15 minutes, indicating a continuing antimicrobial effect. The decrease in numbers of CFU on the solid PEO+Ag implants was similar to the decrease observed on SLM PEO+Ag implants, indicating a similarly rapid bactericidal capacity for both types of implants.

Anti-biofilm activity

To assess the effect of the surface microbicidal activity on biofilm formation, the implants were incubated with MRSA for 24 and 48 hr under conditions inducing biofilm formation and analyzed by SEM (**Figure 6**). After 24 hr of incubation the SLM NT implants demonstrated bacterial adhesion on a substantial part of the surface. Bacteria were grouped in large clusters varying from dozens to hundreds of bacterial cells per cluster. Furthermore, these bacteria had grown in up to 3-4 layers of cells. In addition, dividing cells were observed and identified by an inclined septation plane. After 48 hr of incubation, biofilms had formed on SLM NT implants and an increased area of the surface was covered by bacteria as compared to 24 hr. Furthermore, bacteria were increasingly stacked on top of each other for up to 4-5 layers. Moreover, an extracellular matrix covering the bacteria could be observed, indicating multiplication of the bacteria and the formation of a biofilm.

After 24 hr, the SLM PEO implants demonstrated less bacterial adhesion than those from the SLM NT group. Bacteria were grouped in small clusters of up to approximately 10 cells and were found to penetrate into the micro-pores of the PEO TiO_2 surface layer. After 48 hr, fewer bacteria were attached to the surface and were grouped in similar clusters as compared to 24 hr. No sign of biofilm formation was observed.

The SLM PEO+Ag implants demonstrated reduced numbers of adherent bacteria as compared to SLM NT implants after 24 hr. Furthermore, bacteria were attached to the surface in smaller clusters. Occasionally, bacteria on the surface were observed in clusters, while individual bacteria were found to be dwelling in the micropores present on the surface. After 48 hr, this distribution had not changed, and no biofilm formation was observed.

Ex vivo microbicidal activity

To assess microbicidal activity in a model representing the *in vivo* situation, we used an *ex vivo* implant infection model, utilizing freshly explanted mouse cadaver femurs. In this *ex vivo*

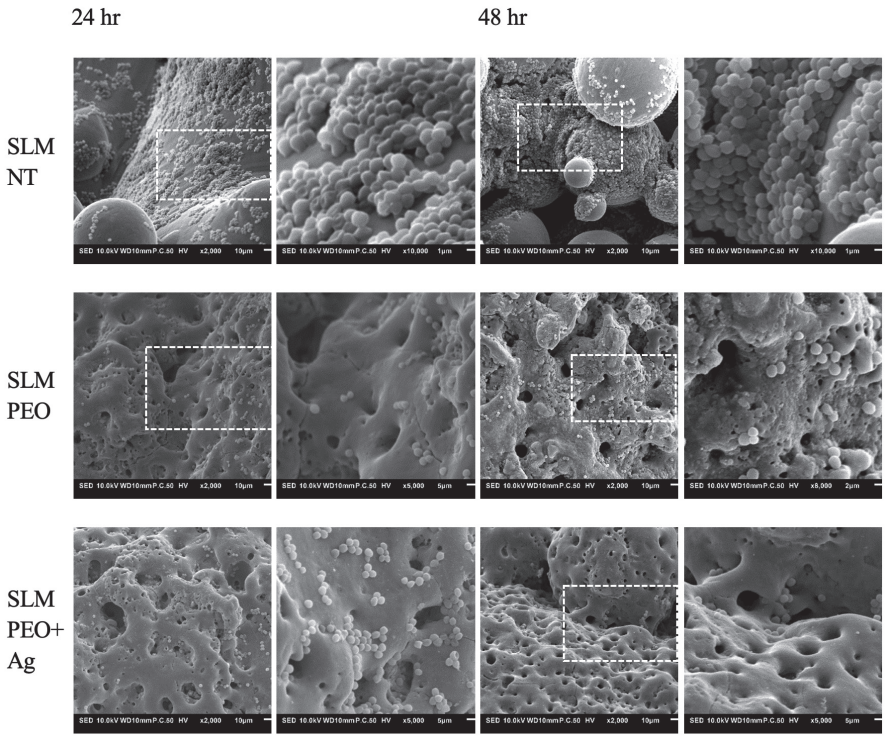

Figure 6. Low (2,000×) and high (5,000-10,000×) magnification SEM images of MRSA AMC201 biofilm formation on SLM NT, SLM PEO and SLM PEO+Ag implants (n=2) after 24 and 48 hr of incubation in TSB 1% glucose.

model, the SLM PEO and SLM PEO+Ag implants caused a significant ($p < 0.001$) reduction of the numbers of CFU as compared to the SLM NT implants of approximatively 2- and 4-logs, respectively (**Figure 7**). Two out of 3 femurs with SLM PEO+Ag implants were entirely culture negative. None of the femurs carrying solid PEO+Ag implants were culture negative.

3.3.6 Cytotoxicity of the SLM implants for hMSCs

Live/dead staining indicated that neither of the SLM NT, SLM PEO and SLM PEO+Ag specimens showed signs of cytotoxicity for hMSCs after 24 hours (**Figure 8A**). Cells attached uniformly on the entire surface of these porous SLM implants and only very few dead cells were observed in any of the samples compared to the number of live cells. In addition, the MTT assay demonstrated an enhanced metabolic activity of hMSCs after 7 days on both SLM PEO and SLM PEO+Ag implants relative to the SLM NT implants ($p < 0.001$), suggestive of cell proliferation on these surfaces over time (**Figure 8B**). Furthermore, no significant differences have been detected between the SLM PEO and SLM PEO+Ag groups. These findings indicate that incorporation of AgNPs in the oxide layer did not induce cytotoxic effects for hMSCs.

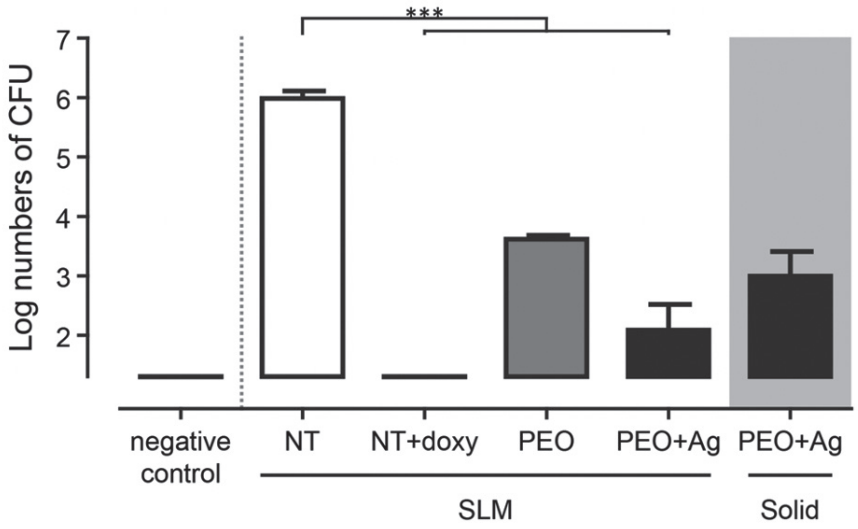

Figure 7. Microbicidal activity of implants against MRSA in the *ex vivo* mouse femur model. Mouse femurs were inoculated with 200 CFU of MRSA AMC201 in 2 µl PT prior to implantation. Log CFU of MRSA on SLM NT was statistically compared to SLM PEO and SLM PEO+Ag implants, and SLM PEO+Ag to solid PEO+Ag implants. To assess efficacy of the sterilization procedure a femur without implant or MRSA bacteria was processed and cultured (sterilization control). To validate the model 2 µl of doxycycline was injected into the femur cavity prior to implantation of an MRSA inoculated SLM NT implant (positive control; SLM NT+doxy). Femurs were homogenized and quantitatively cultured after 24 hr of incubation (n=3; ***, $p < 0.001$).

3.4 DISCUSSION

Additive manufacturing is a major breakthrough in medical device manufacturing with high potential of application, particularly in the field of orthopedics. There is however a strong need for antimicrobial strategies to prevent IAI when these implants are produced with high porosity and concomitant increased surface area. The results of our current study clearly show the strong *in vitro* and *ex vivo* antimicrobial activity of the porous implants that were rationally designed, additively manufactured by SLM, and biofunctionalized through PEO treatment to grow a firmly adherent oxide layer that incorporated AgNPs and released Ag ions over time. The SLM PEO+Ag implants had bactericidal activity against MRSA, one of the most challenging bacterial pathogens causing IAI. They prevented biofilm formation of these bacteria *in vitro*, as well as bacterial survival and growth in an *ex vivo* mouse femur implant infection model. Moreover, the implants produced in this study were not cytotoxic for hMSCs.

3.4.1 Antimicrobial activity of porous SLM PEO+Ag implants

The SLM PEO+Ag implants caused a clear zone of inhibition of MRSA, which was larger than the zone observed around solid PEO+Ag implants. This correlated with the higher release of Ag ions by the SLM PEO+Ag implants. Cultures from the zone of inhibition, and surface microbicidal assays showed that the implants not only inhibited bacterial growth but killed the bacteria. Indeed, biofilm formation *in vitro* was prevented and *ex vivo* antimicrobial assays using a mouse femur implant infection model confirmed an over time bactericidal effect of the solid PEO+Ag as well as the SLM PEO+Ag implants, the latter being superior in clearing the MRSA. It is important to note that *ex vivo* experiments do not benefit from the performance of an active immune system that could be instrumental in even further reducing the number of bacteria in *in vivo* experiments. The *ex vivo* setup in this study did not clarify whether MRSA adhered to the implant's surface or migrated into the bone tissue. Nevertheless, the results of the current study unequivocally demonstrate a strong antimicrobial activity of SLM PEO+Ag implants. Considering that Ag tends to work against many different bacterial species [48], testing with a wider panel of bacteria would strengthen the general protective capacity observed in this study. The strong antibacterial activity of SLM PEO+Ag implants is a result of several factors including the presence of AgNPs, the increased surface area due to additive manufacturing, and the effects of PEO treatment.

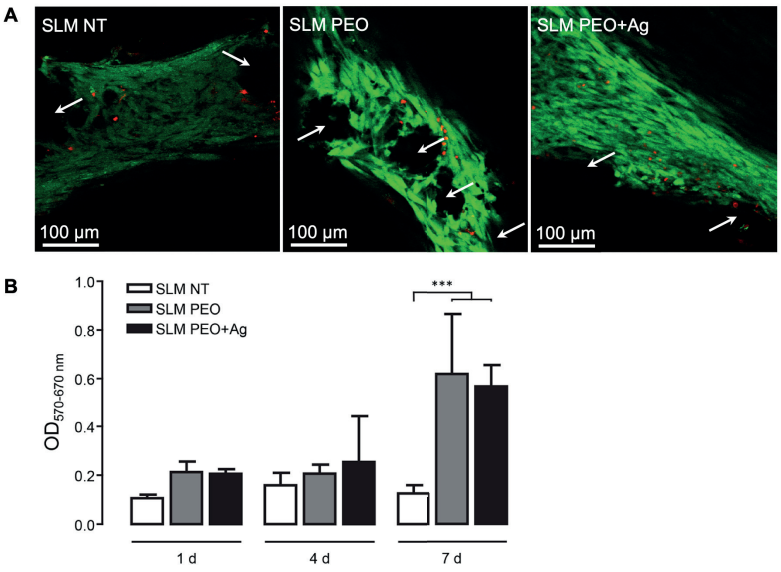

Figure 8. Cytotoxicity of the SLM NT, SLM PEO and SLM PEO+Ag implants (n=3) on human mesenchymal stem cells (hMSCs): (A) live/dead staining demonstrating viable cells in green and dead cells in red after 24 hr; (B) MTT assay showing the metabolic activity of the hMSCs expressed as optical density ($OD_{570\text{-}670\ nm}$) after 1, 4 and 7 days of *in vitro* culture (***, $p < 0.001$).

3.4.2 The effects of additive manufacturing and increased surface area

The effects of increased surface area created through rational design of the porous structure and additive manufacturing of the designed structure can be separated from those of the PEO treatment and AgNPs when comparing the implants from the SLM PEO+Ag group with those from the solid PEO+Ag group. The SLM PEO+Ag implants released more than four times larger amounts of Ag ions, caused zones of inhibition of MRSA with a two times larger diameter and showed a more pronounced decrease in number of CFU of MRSA in the *ex vivo* experiments, as compared to the solid PEO+Ag implants. This clearly shows the importance of the more than 3-fold increase of the surface area in the SLM porous implants, and highlights the utility of rational design and advanced additive manufacturing techniques in creating advanced functionalities such as strong antimicrobial activity. This can easily be combined with other functionalities such as improved bone regeneration performance to achieve multifunctional implants. In this context, it is important to underline that in addition to providing pore space for bone regeneration, the geometrical parameters of the porous structure of the implants were designed taking into account established requirements for bone regeneration performance of porous biomaterials, such as using appropriate range of pore sizes.

Another important difference between solid and SLM implants is the presence of hydroxyapatite phases in the oxide layer of the additively manufactured porous implants revealed by the XRD analysis, which were not present in the XRD patterns of the solid implants. Many studies have shown hydroxyapatite could improve the bone regeneration performance of biomaterials and improve osseointegration of the implants [46-49]. The presence of hydroxyapatite phases is therefore important as these implants are aimed for orthopedic applications. The presence of the hydroxyapatite phases cannot be directly explained by the larger surface area of additively manufactured implants. A more likely reason for development of hydroxyapatite phases in our porous implants is the higher temperatures during the plasma discharges of the PEO process, as the internal surfaces of the implants have different states of fluid flow, with the velocity of cooled electrolyte expected to be lower within the internal pores of the additively manufactured porous implants, resulting in momentarily higher local temperatures during and right after plasma discharges. Higher temperature could work similar to thermal treatments and cause formation of hydroxyapatite phases [50,51].

3.4.3 The effects of PEO treatment

The results of various antimicrobial assays including the *ex vivo* assay, surface microbicidal assay, and biofilm formation assay show certain levels of antimicrobial activity for the SLM PEO implants. Since these implants lack AgNPs in their oxide layers, the observed antimicrobial effects might be associated to their surface characteristics rather than to release of any type of antimicrobial agent. The PEO treatment creates a micro-/nano-porous structure on the surface of implants with specific nanotopographical features [47]. A few pioneering studies have recently reported that nanotopographical features can influence bacterial adhesion and biofilm formation and that surfaces with high aspect ratio show bactericidal behavior [52-55]. In concert with the results of the current study, it has been recently shown that the antimicrobial effect of nanotopographical features is limited to adherent bacteria and does not include free living (*i.e.* planktonic) bacteria [52]. The antimicrobial activity of surface nanotopographies are, however, expected to diminish over time [52].

Another factor possibly contributing to the antimicrobial activity of the SLM PEO implants is the presence of crystalline titanium oxide layers in the form of anatase and rutile phases, which can decrease bacterial adhesion and cause formation of reactive ion species [56,57]. If the antimicrobial activity of the SLM PEO implants is, indeed, caused by the nanotopographical features and anatase/rutile phases created through the PEO treatment, it is important that the rationally designed porous structure used in the current study increases the surface area of the implants by a factor of 3.75. As mentioned above, the PEO treatment in the presence of AgNPs maximized the surface antimicrobial activity and showed released activity through the release

of Ag ions thus providing antimicrobial function in the peri-implant area. This is essential as the tissue around the implant represents a niche for bacteria colonization [58,59].

3.4.4 Cytotoxicity

Titanium implants with a large surface area have shown to be cytotoxic [55]. In addition, AgNPs may also be associated with toxicity, caused either by high levels of Ag ions or by the small size of AgNPs (nanotoxicity [39,40]). The biofunctionalization process developed here was designed to minimize both these types of cytotoxicity. Embedding the AgNPs in the oxide layer grown through PEO minimizes the risk that they would freely circulate and cause nanotoxicity. The embedding of the AgNPs in the oxide layer is also the reason behind the gradual nature of Ag ion release, which results in a sustained release profile. Indeed, both SLM PEO and SLM PEO+Ag implants in this study did not induce cytotoxicity to hMSCs but rather supported an increase in their metabolic activity with time relative to the SLM NT implants, suggestive of cell proliferation on these samples. The maximum cumulative release of 0.6 ppm silver ions from SLM PEO+Ag implants over 28 days is far below the mean half maximal inhibitory concentration (IC_{50}) of osteoblasts viability of 10 ppm [63]. In general, mammalian cells with their larger size, superior structural and functional organization, and ability to produce extracellular matrix are more tolerable to silver than the bacterial cells [64]. Nevertheless, over-doses may induce cytotoxicity through mechanisms comparable to bacterial cells involving AgNPs uptake and interactions of released silver ions with intracellular biomolecules leading to impairment of cell membrane permeability, various metabolic pathways and cellular functions [65-67]. PEO surfaces with their specific morphology and Ca/P chemistry are known to support cellular functions such as adhesion, as also observed in this study, but also osteogenic differentiation and matrix mineralization [31,60-62]. The presence of hydroxyapatite on our PEO surfaces will likely further increase the potential of our surfaces for optimal host cell interaction.

3.4.5 Clinical implications

Preventing infections associated with orthopedic implants is often complicated by the fact that prevention of early (*i.e.* peri-operative [10]) infections requires a different strategy as compared to late, hematogenous or contiguous infections [10]. Preventing peri-operative infections may require release of high doses of antimicrobial agents in the first few hours to first few days after surgery. In contrast, preventing late infections requires sustained release of limited doses of antimicrobial agents, but sufficiently high to prevent resistance development. Biomaterials that combine a high dose release in the first few hours/days with sustained release of limited dosages of antimicrobial agents are however rare.

The additively manufactured porous implants developed in the current study release high doses of Ag ions within the first 12-24 hr and much smaller doses for up to one month. The release of the Ag ions is expected to continue past the first month as the AgNPs are embedded in the oxide layer of the implant and are gradually oxidized, as opposed to other biomaterials that release the AgNPs themselves and may therefore rapidly deplete their reservoir of antimicrobial agents.

From the practical viewpoint, the PEO process is a single step and fast process (5 min in the current study) that could cover the internal surface areas of additively manufactured porous implants. The biomaterial selected (*i.e.* Ti6Al4V) is also widely [63-68] used for manufacturing of orthopedic implants. The above-mentioned aspects of the developed implant make it attractive for clinical application, as practical barriers are relatively limited. Moreover, the implants developed in the current study have the potential of addressing the other important challenge in orthopedic implants, namely improved bone regeneration performance and implant osseointegration. Previous studies have shown the huge potential of combining additively manufactured porous biomaterials with mechanical design [69-71], biofunctionalizing surface treatments [72,73], and drug delivery approaches [74] for improving the bone regeneration performance and biomechanical stability of orthopedic implants. The results of the current study show that using an additively manufactured porous biomaterial stimulates formation of hydroxyapatite phases in the PEO layer that are considered beneficial for improving bone tissue regeneration and implant fixation. Moreover, it has been shown by biomechanical and quantitative histomorphometric analyses that the micro-/nano-porous structure created through PEO can stimulate bone regeneration performance of the implants when compared to non-treated implants [61,75,76]. Finally, similar to the way AgNPs were incorporated in the oxide layer of the implants developed in the current study, inorganic particles such as some of the trace elements [77-82] could be added to stimulate bone tissue regeneration and osseointegration of the implants. One could therefore use additively manufactured porous biomaterials biofunctionalized through PEO to simultaneously address both major challenges in design and manufacturing of orthopedic implants, namely IAI and implant loosening.

3.5 CONCLUSIONS

To address the problem of IAI, additively manufactured porous titanium implants with large surface areas were rationally designed, manufactured by SLM, and biofunctionalized using the PEO surface treatment to incorporate immobilized AgNPs in the grown oxide layer and to create a micro-/nano-porous structure on the surface of the implants. Biomaterial characterization techniques, *in vitro* and *ex vivo* antimicrobial assays, and cytotoxicity assays

were used to evaluate the performance of the developed implants. Antimicrobial assays consistently showed strong antimicrobial activity of the developed implants against MRSA including released activity, surface antimicrobial activity and prevention of biofilm formation. Furthermore, XRD analysis revealed formation of hydroxyapatite phase in the oxide layer of additively manufactured porous implants, whereas no such phase was detected in the oxide layer of the corresponding solid implants. The novel implants had no cytotoxic effects for hMSCs. Moreover, the porous implants showed four times larger amount of released Ag ions, two times larger zones of inhibition, and one additional order of magnitude of reduction in the number of CFU in the *ex vivo* antimicrobial assay compared to solid PEO+Ag. Based on these data we consider the novel implants promising for further (pre)clinical development.

ACKNOWLEDGEMENTS

The valuable technical contribution of our colleague Sander Leeflang (Additive Manufacturing Lab, TU Delft) in manufacturing the implants used in this study is gratefully acknowledged. In addition, our special thanks to Matty Wijnen from AHC Benelux for the ICP-OES analyses, to Leonie de Boer (AMC, Medical Microbiology) for assistance with the microbiological analyses, and to the Animal Research Institute AMC (ARIA) for mouse femur preparation.

REFERENCES

[1] Goodman, S. B., Yao, Z., Keeney, M. & Yang, F. The future of biologic coatings for orthopaedic implants. *Biomaterials* **34**, 3174-3183 (2013).

[2] Du, Z., Xiao, Y., Hashimi, S., Hamlet, S. M. & Ivanovski, S. The effects of implant topography on osseointegration under estrogen deficiency induced osteoporotic conditions: Histomorphometric, transcriptional and ultrastructural analysis. *Acta Biomaterialia* (2016).

[3] Gittens, R. A., Olivares-Navarrete, R., Schwartz, Z. & Boyan, B. D. Implant osseointegration and the role of microroughness and nanostructures: lessons for spine implants. *Acta biomaterialia* **10**, 3363-3371 (2014).

[4] von Wilmowsky, C., Moest, T., Nkenke, E., Stelzle, F. & Schlegel, K. A. Implants in bone: Part II. Research on implant osseointegration. *Oral and maxillofacial surgery* **18**, 355-372 (2014).

[5] Busscher, H. J. *et al.* Biomaterial-associated infection: locating the finish line in the race for the surface. *Science translational medicine* **4**, 153rv110-153rv110 (2012).

[6] Campoccia, D., Montanaro, L. & Arciola, C. R. The significance of infection related to orthopedic devices and issues of antibiotic resistance. *Biomaterials* **27**, 2331-2339 (2006).

[7] Campoccia, D., Montanaro, L. & Arciola, C. R. A review of the clinical implications of anti-infective biomaterials and infection-resistant surfaces. *Biomaterials* **34**, 8018-8029 (2013).

[8] Hickok, N. J. & Shapiro, I. M. Immobilized antibiotics to prevent orthopaedic implant infections. *Advanced drug delivery reviews* **64**, 1165-1176 (2012).

[9] Kazemzadeh-Narbat, M. *et al.* Antimicrobial peptides on calcium phosphate-coated titanium for the prevention of implant-associated infections. *Biomaterials* **31**, 9519-9526 (2010).

[10] Trampuz, A. & Widmer, A. F. Infections associated with orthopedic implants. *Current opinion in infectious diseases* **19**, 349-356 (2006).

[11] Zhao, L., Chu, P. K., Zhang, Y. & Wu, Z. Antibacterial coatings on titanium implants. *Journal of Biomedical Materials Research Part B: Applied Biomaterials* **91**, 470-480 (2009).

[12] Agarwal, R. & García, A. J. Biomaterial strategies for engineering implants for enhanced osseointegration and bone repair. *Advanced drug delivery reviews* **94**, 53-62 (2015).

[13] de Wild, M. *et al.* Bone regeneration by the osteoconductivity of porous titanium implants manufactured by selective laser melting: a histological and micro computed tomography study in the rabbit. *Tissue Engineering Part A* **19**, 2645-2654 (2013).

[14] Harada, N. *et al.* Bone regeneration in a massive rat femur defect through endochondral ossification achieved with chondrogenically differentiated MSCs in a degradable scaffold. *Biomaterials* **35**, 7800-7810 (2014).

[15] Castilho, M. *et al.* Direct 3D powder printing of biphasic calcium phosphate scaffolds for substitution of complex bone defects. *Biofabrication* **6**, 015006 (2014).

[16] Nieminen, J., Pakarinen, T.-K. & Laitinen, M. Orthopaedic reconstruction of complex pelvic bone defects. Evaluation of various treatment methods. *Scandinavian Journal of Surgery* **102**, 36-41 (2013).

[17] DiCaprio, M. R. & Friedlaender, G. E. Malignant bone tumors: limb sparing versus amputation. *Journal of the American Academy of Orthopaedic Surgeons* **11**, 25-37 (2003).

[18] Hardes, J. *et al.* Characteristics and outcome of infections associated with tumor endoprostheses. *Archives of orthopaedic and trauma surgery* **126**, 289-296 (2006).

[19] Lee, S., Oh, J., Lee, K., Yoo, K. & Kim, H. Infection after prosthetic reconstruction in limb salvage surgery. *International orthopaedics* **26**, 179-184 (2002).

[20] Sim, I.-W., Tse, L., Ek, E., Powell, G. & Choong, P. Salvaging the limb salvage: management of complications following endoprosthetic reconstruction for tumours around the knee. *European Journal of Surgical Oncology (EJSO)* **33**, 796-802 (2007).

[21] Ahmadi, S. M. *et al.* Additively manufactured open-cell porous biomaterials made from six different space-filling unit cells: The mechanical and morphological properties. *Materials* **8**, 1871-1896 (2015).

[22] Karageorgiou, V. & Kaplan, D. Porosity of 3D biomaterial scaffolds and osteogenesis. *Biomaterials* **26**, 5474-5491 (2005).

[23] Van Bael, S. *et al.* The effect of pore geometry on the in vitro biological behavior of human periosteum-derived cells seeded on selective laser-melted Ti6Al4V bone scaffolds. *Acta biomaterialia* **8**, 2824-2834 (2012).

[24] Bidan, C. M. *et al.* How linear tension converts to curvature: geometric control of bone tissue growth. *PloS one* **7**, e36336 (2012).

[25] Rumpler, M., Woesz, A., Dunlop, J. W., van Dongen, J. T. & Fratzl, P. The effect of geometry on three-dimensional tissue growth. *Journal of the Royal Society Interface* **5**, 1173-1180 (2008).

[26] Zadpoor, A. A. Bone tissue regeneration: the role of scaffold geometry. *Biomaterials science* **3**, 231-245 (2015).

[27] Amin Yavari, S. *et al.* Bone regeneration performance of surface-treated porous titanium. *Biomaterials* **35**, 6172-6181 (2014).

[28] Chung, C. J. *et al.* Plasma electrolytic oxidation of titanium and improvement in osseointegration. *Journal of Biomedical Materials Research Part B: Applied Biomaterials* **101**, 1023-1030 (2013).

[29] Lara Rodriguez, L., Sundaram, P., Rosim-Fachini, E., Padovani, A. & Diffoot-Carlo, N. Plasma electrolytic oxidation coatings on γTiAl alloy for potential biomedical applications. *Journal of Biomedical Materials Research Part B: Applied Biomaterials* **102**, 988-1001 (2014).

[30] Robinson, H., Markaki, A., Collier, C. & Clyne, T. Cell adhesion to plasma electrolytic oxidation (PEO) titania coatings, assessed using a centrifuging technique. *Journal of the mechanical behavior of biomedical materials* **4**, 2103-2112 (2011).

[31] Whiteside, P., Matykina, E., Gough, J. E., Skeldon, P. & Thompson, G. E. In vitro evaluation of cell proliferation and collagen synthesis on titanium following plasma electrolytic oxidation. *Journal of Biomedical Materials Research Part A* **94**, 38-46 (2010).

[32] Eby, D. M., Luckarift, H. R. & Johnson, G. R. Hybrid antimicrobial enzyme and silver nanoparticle coatings for medical instruments. *ACS applied materials & interfaces* **1**, 1553-1560 (2009).

[33] Kim, J. S. *et al.* Antimicrobial effects of silver nanoparticles. *Nanomedicine: Nanotechnology, Biology and Medicine* **3**, 95-101 (2007).

[34] Nanda, A. & Saravanan, M. Biosynthesis of silver nanoparticles from Staphylococcus aureus and its antimicrobial activity against MRSA and MRSE. *Nanomedicine: Nanotechnology, Biology and Medicine* **5**, 452-456 (2009).

[35] Panáček, A. *et al.* Silver colloid nanoparticles: synthesis, characterization, and their antibacterial activity. *The Journal of Physical Chemistry B* **110**, 16248-16253 (2006).

[36] Rai, M., Yadav, A. & Gade, A. Silver nanoparticles as a new generation of antimicrobials. *Biotechnology advances* **27**, 76-83 (2009).

[37] Saravanan, M. & Nanda, A. Extracellular synthesis of silver bionanoparticles from Aspergillus clavatus and its antimicrobial activity against MRSA and MRSE. *Colloids and Surfaces B: Biointerfaces* **77**, 214-218 (2010).

[38] Rizzello, L. & Pompa, P. P. Nanosilver-based antibacterial drugs and devices: mechanisms, methodological drawbacks, and guidelines. *Chemical Society Reviews* **43**, 1501-1518 (2014).

[39] AshaRani, P., Low Kah Mun, G., Hande, M. P. & Valiyaveettil, S. Cytotoxicity and genotoxicity of silver nanoparticles in human cells. *ACS Nano* **3**, 279-290 (2008).

[40] Asharani, P., Wu, Y. L., Gong, Z. & Valiyaveettil, S. Toxicity of silver nanoparticles in zebrafish models. *Nanotechnology* **19**, 255102 (2008).

[41] Necula, B., Apachitei, I., Tichelaar, F., Fratila-Apachitei, L. & Duszczyk, J. An electron microscopical study on the growth of TiO 2–Ag antibacterial coatings on Ti6Al7Nb biomedical alloy. *Acta biomaterialia* **7**, 2751-2757 (2011).

[42] Necula, B. *et al.* In vitro cytotoxicity evaluation of porous TiO 2–Ag antibacterial coatings for human fetal osteoblasts. *Acta biomaterialia* **8**, 4191-4197 (2012).

[43] Necula, B. S., Fratila-Apachitei, L. E., Zaat, S. A., Apachitei, I. & Duszczyk, J. In vitro antibacterial activity of porous TiO 2–Ag composite layers against methicillin-resistant Staphylococcus aureus. *Acta biomaterialia* **5**, 3573-3580 (2009).

[44] Kwakman, P. H. *et al.* How honey kills bacteria. *The FASEB Journal* **24**, 2576-2582 (2010).

[45] Kwakman, P. H., Te Velde, A. A., De Boer, L., Vandenbroucke-Grauls, C. M. & Zaat, S. A. Two major medicinal honeys have different mechanisms of bactericidal activity. *PloS one* **6**, e17709 (2011).

[46] Kusakabe, H. *et al.* Osseointegration of a hydroxyapatite-coated multilayered mesh stem. *Biomaterials* **25**, 2957-2969 (2004).

[47] Lakstein, D. *et al.* Enhanced osseointegration of grit-blasted, NaOH-treated and electrochemically hydroxyapatite-coated Ti–6Al–4V implants in rabbits. *Acta biomaterialia* **5**, 2258-2269 (2009).

[48] Tami, A. E. *et al.* Hydroxyapatite particles maintain peri-implant bone mantle during osseointegration in osteoporotic bone. *Bone* **45**, 1117-1124 (2009).

[49] Yang, G.-l., He, F.-m., Hu, J.-a., Wang, X.-x. & Zhao, S.-f. Effects of biomimetically and electrochemically deposited nano-hydroxyapatite coatings on osseointegration of porous titanium implants. *Oral Surgery, Oral Medicine, Oral Pathology, Oral Radiology, and Endodontology* **107**, 782-789 (2009).

[50] Durdu, S., Deniz, Ö. F., Kutbay, I. & Usta, M. Characterization and formation of hydroxyapatite on Ti6Al4V coated by plasma electrolytic oxidation. *Journal of Alloys and Compounds* **551**, 422-429 (2013).

[51] Han, Y., Sun, J. & Huang, X. Formation mechanism of HA-based coatings by micro-arc oxidation. *Electrochemistry Communications* **10**, 510-513 (2008).

[52] Amin Yavari, S. *et al.* Antibacterial behavior of additively manufactured porous titanium with nanotubular surfaces releasing silver ions. *ACS applied materials & interfaces* **8**, 17080–17089 (2016).

[53] Hasan, J., Crawford, R. J. & Ivanova, E. P. Antibacterial surfaces: the quest for a new generation of biomaterials. *Trends in biotechnology* **31**, 295-304 (2013).

[54] Hochbaum, A. I. & Aizenberg, J. Bacteria pattern spontaneously on periodic nanostructure arrays. *Nano letters* **10**, 3717-3721 (2010).

[55] Ivanova, E. P. *et al.* Bactericidal activity of black silicon. *Nature communications* **4** (2013).

[56] Del Curto, B. *et al.* Decreased bacterial adhesion to surface-treated titanium. *International journal of artificial organs* **28**, 718-730 (2005).

[57] Suresh, A. K., Pelletier, D. A. & Doktycz, M. J. Relating nanomaterial properties and microbial toxicity. *Nanoscale* **5**, 463-474 (2013).

[58] Broekhuizen, C. A. *et al.* Tissue around catheters is a niche for bacteria associated with medical device infection. *Critical care medicine* **36**, 2395-2402 (2008).

[59] Zaat, S., Broekhuizen, C. & Riool, M. Host tissue as a niche for biomaterial-associated infection. *Future microbiology* **5**, 1149-1151 (2010).

[60] Park, T.-E., Choe, H.-C. & Brantley, W. Bioactivity evaluation of porous TiO 2 surface formed on titanium in mixed electrolyte by spark anodization. *Surface and Coatings Technology* **235**, 706-713 (2013).

[61] Wu, J. *et al.* Improved biological performance of microarc-oxidized low-modulus Ti-24Nb-4Zr-7.9 Sn alloy. *Journal of Biomedical Materials Research Part B: Applied Biomaterials* **92**, 298-306 (2010).

[62] Zhao, L. *et al.* Initial osteoblast functions on Ti-5Zr-3Sn-5Mo-15Nb titanium alloy surfaces modified by microarc oxidation. *Journal of biomedical materials research Part A* **92**, 432-440 (2010).

[63] Heinl, P., Müller, L., Körner, C., Singer, R. F. & Müller, F. A. Cellular Ti–6Al–4V structures with interconnected macro porosity for bone implants fabricated by selective electron beam melting. *Acta biomaterialia* **4**, 1536-1544 (2008).

[64] Hollander, D. A. *et al.* Structural, mechanical and in vitro characterization of individually structured Ti–6Al–4V produced by direct laser forming. *Biomaterials* **27**, 955-963 (2006).

[65] Ku, C.-H., Pioletti, D. P., Browne, M. & Gregson, P. J. Effect of different Ti–6Al–4V surface treatments on osteoblasts behaviour. *Biomaterials* **23**, 1447-1454 (2002).

[66] Murr, L. *et al.* Microstructure and mechanical behavior of Ti–6Al–4V produced by rapid-layer manufacturing, for biomedical applications. *Journal of the mechanical behavior of biomedical materials* **2**, 20-32 (2009).

[67] Neoh, K. G., Hu, X., Zheng, D. & Kang, E. T. Balancing osteoblast functions and bacterial adhesion on functionalized titanium surfaces. *Biomaterials* **33**, 2813-2822 (2012).

[68] Wu, C. *et al.* Novel sphene coatings on Ti–6Al–4V for orthopedic implants using sol–gel method. *Acta biomaterialia* **4**, 569-576 (2008).

[69] Ahmadi, S. *et al.* Mechanical behavior of regular open-cell porous biomaterials made of diamond lattice unit cells. *Journal of the mechanical behavior of biomedical materials* **34**, 106-115 (2014).

[70] Van der Stok, J. *et al.* Selective laser melting-produced porous titanium scaffolds regenerate bone in critical size cortical bone defects. *Journal of Orthopaedic Research* **31**, 792-799 (2013).

[71] Wauthle, R. *et al.* Additively manufactured porous tantalum implants. *Acta biomaterialia* **14**, 217-225 (2015).

[72] Amin Yavari, S. *et al.* Effects of bio-functionalizing surface treatments on the mechanical behavior of open porous titanium biomaterials. *Journal of the mechanical behavior of biomedical materials* **36**, 109-119 (2014).

[73] Amin Yavari, S. *et al.* Crystal structure and nanotopographical features on the surface of heat-treated and anodized porous titanium biomaterials produced using selective laser melting. *Applied Surface Science* **290**, 287-294 (2014).

[74] van der Stok, J. *et al.* Full regeneration of segmental bone defects using porous titanium implants loaded with BMP-2 containing fibrin gels. *European cells & materials* **2015**, 141-154 (2015).

[75] Park, K. *et al.* Osseointegration of anodized titanium implants under different current voltages: a rabbit study. *Journal of oral rehabilitation* **34**, 517-527 (2007).

[76] Sul, Y.-T. The significance of the surface properties of oxidized titanium to the bone response: special emphasis on potential biochemical bonding of oxidized titanium implant. *Biomaterials* **24**, 3893-3907 (2003).

[77] Bonnelye, E., Chabadel, A., Saltel, F. & Jurdic, P. Dual effect of strontium ranelate: stimulation of osteoblast differentiation and inhibition of osteoclast formation and resorption in vitro. *Bone* **42**, 129-138 (2008).

[78] Kue, R., Sohrabi, A., Nagle, D., Frondoza, C. & Hungerford, D. Enhanced proliferation and osteocalcin production by human osteoblast-like MG63 cells on silicon nitride ceramic discs. *Biomaterials* **20**, 1195-1201 (1999).

[79] Lin, K. *et al.* Enhanced osteoporotic bone regeneration by strontium-substituted calcium silicate bioactive ceramics. *Biomaterials* **34**, 10028-10042 (2013).

[80] Paul, W. & Sharma, C. P. Effect of calcium, zinc and magnesium on the attachment and spreading of osteoblast like cells onto ceramic matrices. *Journal of Materials Science: Materials in Medicine* **18**, 699-703 (2007).

[81] Yang, F. *et al.* Strontium enhances osteogenic differentiation of mesenchymal stem cells and in vivo bone formation by activating Wnt/catenin signaling. *Stem cells* **29**, 981-991 (2011).

[82] Zhao, L. *et al.* The osteogenic activity of strontium loaded titania nanotube arrays on titanium substrates. *Biomaterials* **34**, 19-29 (2013).

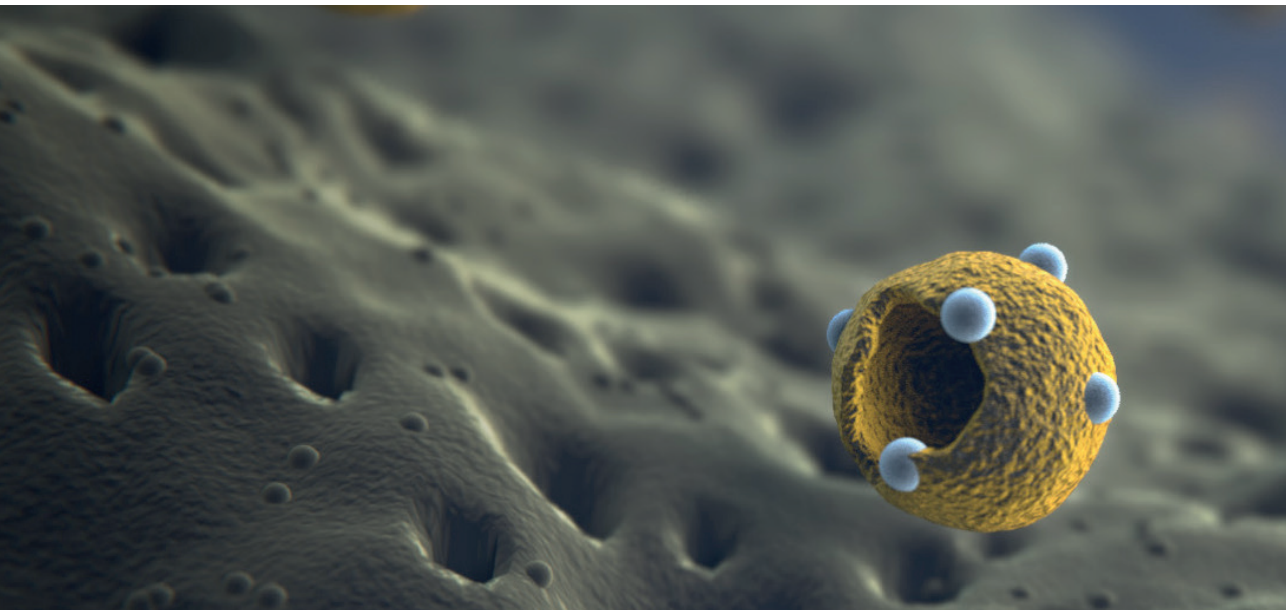

CHAPTER 04

Multifunctional implants with silver and copper

I.A.J. van Hengel, M.W.A.M. Tierolf, V.P.M. Valerio, M. Minneboo, A.C. Fluit, L.E. Fratila-Apachitei, I. Apachitei, A.A. Zadpoor, Self-defending additively manufactured bone implants bearing silver and copper nanoparticles, Journal of Materials Chemistry B 8 (2020) 1589-1602.

Effective preventive measures against implant-associated infection (IAI) are desperately needed. Therefore, the development of self-defending implants with intrinsic antibacterial properties has gained significant momentum. Biomaterials biofunctionalized with silver (Ag) have resulted in effective antibacterial biomaterials, yet regularly induce cytotoxicity. In this study, the use of both Ag and copper (Cu) nanoparticles (NPs) on TiO_2 surfaces was investigated to generate antibacterial and osteoconductive biomaterials. Hence, additively manufactured Ti6Al4V volume-porous implants were biofunctionalized with plasma electrolytic oxidation (PEO) through the incorporation of varying ratios of Ag and/or Cu NPs in the TiO_2 layer covering the implant surface. For all experimental groups, the surface morphology, chemical composition, ion release profile, generation of reactive ion species, antibacterial activity against methicillin-resistant *Staphylococcus aureus* (MRSA) *in vitro* and *ex vivo*, as well as the response of pre-osteoblastic MC3T3-E1 cells in metabolic activity and differentiation assays were determined. PEO biofunctionalization resulted in rough and highly porous surfaces that released Ag and Cu ions for 28 days and generated hydroxyl as well as methyl radicals. A strong synergistic bactericidal behavior between Ag and Cu ions was detected, which allowed to decrease the concentration of Ag ions by 10-fold, while maintaining the same level of antibacterial activity. Antibacterial agar diffusion and quantitative assays indicated strong antibacterial activity *in vitro* for the implants containing Ag and Ag/Cu, while no antibacterial activity was observed for implants bearing only Cu NPs. Moreover, the biofunctionalized implants with ratios of up to 75% Ag and 25% Cu NP totally eradicated all bacteria in an *ex vivo* model using murine femora. Meanwhile, the biofunctionalized implants did not show any signs of cytotoxicity, while implants bearing only Cu NPs improved the metabolic activity after 7 and 11 days. The biomaterials developed here, therefore, exploit the synergistic behavior of Ag and Cu to simultaneously offer strong antibacterial behavior while fully mitigating the cytotoxicity of Ag against mammalian cells.

4.1 INTRODUCTION

Implant-associated infection (IAI) is one of the most devastating complications for patients with orthopedic implants. Despite extensive preventive methods and antibiotic prophylaxis, up to 2.5% of primary hip and knee replacements and 10% of revision surgeries are complicated by IAI [1]. The prevalence of IAI is anticipated to increase, given an aging and progressively obese population that requires joint replacement surgeries at younger age as well as a rapid development of bacterial resistance against antibiotics, leading to persistent and difficult-to-treat infections [2]. Moreover, IAI accounts for extremely high healthcare costs, which are projected to be $1.62 billion in the US alone by 2020 [3]. The development of orthopedic implants that minimize the risk of IAI are, therefore, of utmost importance.

To prevent the bacterial colonization of the implant surface, orthopedic implants with intrinsic antibacterial properties are being developed [4]. Since in this case the antibacterial agents are applied directly at the implantation site, the required dose is lower as compared to systemic intake, thereby decreasing the side effects [5]. Inorganic nanoparticles (NPs), such as silver (Ag) and copper (Cu) have been explored as alternatives to antibiotics that suffer from ever increasing bacterial resistance [6, 7]. The large surface area of NPs leads to their amplified oxidation on the implant surface while the accompanying release of metallic ions induces strong bactericidal effects [8].

To incorporate antibacterial agents, the surface of the metallic implant needs to be biofunctionalized. While the modification of the surface chemistry and morphology may be used to prevent bacterial adhesion, the incorporation of antibacterial agents on the implant surface allows for actively targeting the bacteria residing in the adjacent tissues [9, 10]. To produce an antibacterial surface, the antibacterial agent is either embedded on the implant surface, incorporated in a conversed surface layer, or applied as a coating [11]. Through these approaches, functional, and antibacterial biomaterials have been synthesized containing antibiotics, inorganic NPs, or antimicrobial peptides [12-14].

Among surface biofunctionalization techniques, plasma electrolytic oxidation (PEO) is a single-step, electrochemical process that is particularly suited for the biofunctionalization of highly porous metallic biomaterials, such as additively manufactured porous titanium implants [8]. The use of additive manufacturing (AM) facilitates the fabrication of novel implant designs that allow for the fine-tuning of the mechanical properties such that stress shielding is prevented and bony ingrowth is enhanced [15-17]. However, due to their vast surface area, these porous implants are prone to bacterial adhesion, and, therefore, require surface biofunctionalization.

During PEO, the native metallic oxide layer (*i.e.*, TiO_2) is vastly expanded, resulting in a bioactive surface with high levels of nano/micro-porosity, enhanced roughness, and

crystalized (*i.e.*, rutile or anatase) TiO_2 phase compositions [18, 19]. Addition of inorganic NPs during PEO results in a firmly attached and homogeneous layer of immobilized NPs on the implants surface, thereby preventing the free circulation of the NPs and associated adverse effects. Furthermore, the incorporation of NPs in the growing TiO_2 layer during PEO enables the sustained release of metallic ions, contributing to prolonged antibacterial effects [20, 21].

Previous studies have demonstrated that PEO treatment using Ag NPs, indeed, results in highly effective antibacterial biomaterials [22-24]. Ag NPs are potent against a wide range of bacterial strains including methicillin-resistant strains that are often involved in IAI [25, 26]. Moreover, bacterial resistance against Ag is uncommon and rarely develops during treatment [27]. However, Ag NPs may induce cytotoxicity against host cells including mesenchymal stromal cells and neutrophils [28-31]. Meanwhile, Cu NPs have demonstrated antibacterial properties while simultaneously stimulating osteogenesis and angiogenesis [32]. Moreover, there are reports in the literature regarding the synergistic effects of Ag and other antibacterial agents [33-35]. We, therefore, hypothesized that there is a synergistic effect between Ag and Cu and that by exploiting those effects the antibacterial properties of implants can be enhanced, ultimately resulting in a reduced amount of the required Ag NPs and, thus, the mitigation of the cytotoxic effects.

4.2 EXPERIMENTAL

4.2.1 Implant design and additive manufacturing

Volume-porous Ti6Al4V implants were designed and fabricated according to a protocol and design rationale that we have presented elsewhere [8]. Briefly, the implants of 4 cm in length and a diameter of 0.5 mm were manufactured by a selective laser melting (SLM) printer (SLM-125, Realizer, Borchem, Germany) using a YLM-400-AC Ytterbium fiber laser (IPG Photonics Corporation, Oxford, United States) in an argon atmosphere with less than 0.2% oxygen content. Medical-grade (grade 23, ELI) Ti6Al4V powder particles (AP&C, Boisbriand, Quebec, Canada) with spherical morphology, particle sizes ranging from 10 to 45 μm, and a layer thickness of 50 μm were used. SLM laser processing was performed with a laser power of 96 W, a wavelength of 1070 ± 10 nm, and an exposure time of 300 μs, resulting in a laser spot size of 145 μm. Subsequently, loose powder particles were removed by vacuum cleaning and the implants were ultrasonicated at 35 kHz in acetone, 96% ethanol, and demineralized water for 5 min each.

4.2.2 Surface biofunctionalization

The surface of Ti6Al4V implants was modified by PEO, resulting in a uniform and highly porous superficial titanium oxide layer. The PEO electrolyte contained 0.15 M calcium acetate (≥ 99%, Sigma-Aldrich, St. Louis, Missouri, United States) and 0.02 M calcium

glycerophosphate (≥ 99%, Dr. Paul Lohmann GmbH, Emmerthal, Germany) dissolved in demineralized water in which Ag NPs (65 – 75% Ag, Sigma-Aldrich, St. Louis, Missouri, United States) and/or Cu NPs (99.8% Cu, SkySpring Nanomaterials, Houston, Texas, United States) were dispersed at varying ratios with 3.0 g/L designated as 100 %, generating different experimental groups. SLM implants that did not receive any PEO biofunctionalization were designated as non-treated (NT). PEO biofunctionalization was performed without any NPs (PT), 3.0 g/L or 1.5 g/L Ag NPs (PT – Ag, PT – Ag 50), 3.0 g/L Cu NPs (PT – Cu), and varying ratios of both Ag and Cu NPs (PT – Ag Cu, PT – Ag Cu 75 25 and PT – Ag Cu 50 50).

The particle sizes of the NPs ranged between 7 and 25 nm for Ag NPs and 40 and 60 nm for Cu NPs while both particles displayed a spherical morphology. The PEO electrolyte was sonicated 2 times for 3 min and stirred in between for 5 min at 500 rpm with a magnetic stirrer (IKA-Werke GmbH & Co. KG, Staufen, Germany) and a stir bar of 40×8 mm (VWR, Radnor, Pennsylvania, United States).

The implants were biofunctionalized by PEO using a custom-made laboratory setup that consisted of an AC power supply (50 Hz, type ACS 1500, ET powder Systems Ltd., Chesterfield, United Kingdom), a data acquisition board (SCXI, National Instruments, Austin, Texas, United States) that connected the computer interface and power supply, and an electrolytic cell consisting of double-walled glass with two electrodes. PEO processing was performed under galvanostatic conditions at a current density of 20A/dm^2 for 5 min in 800 ml electrolyte. In this process, the implant functioned as the anode and a ring-shaped stainless steel formed the cathode. The electrolytic cell was cooled with a thermostatic bath and the temperatures ranged between 6 and 8°C at the beginning and the end of the PEO process. To ensure homogeneous distribution of the particles, the electrolyte was stirred continuously at 500 rpm. During PEO processing, the voltage-time (V-t) transients were recorded every second.

Following PEO biofunctionalization, the implants were rinsed in running tap water for 1 min. Thereafter, the implants were sterilized by 30 s ultrasonication in ethanol, 5 min immersion and 30 s ultrasonication in demineralized water, and subsequently heat treated for 1 h at 110°C in an oven (Nabertherm TR60, New Castle, United States).

4.2.3 Characterization of the surface morphology and chemical composition

The surface morphology of the biofunctionalized implants was analyzed using scanning electron microscopy (SEM, JSM-IT100LV, JEOL, Tokyo, Japan). The electron beam energy ranged between 5 – 20 kV and working distance of 10 mm was used. Prior to imaging, the specimens were sputtered with a gold layer of 5 ± 2 nm to enhance their electrical conductivity. To analyze the chemical composition, spot analysis was performed with energy dispersive X-ray spectroscopy (EDS).

4.2.4 Ion release kinetics

To study the release kinetics of Ag and Cu ions, biofunctionalized specimens (n = 3/group) were submerged in 1 ml phosphate-buffered saline (PBS) in dark Eppendorf tubes. The specimens were kept in a water bath at 37°C under static conditions. The PBS was collected and replaced after 12 h and 1, 2, 4, 7, 14, and 28 days. The collected PBS was acidified with 5% nitric acid to dissolve all the ion species entirely. Subsequently, the ion concentrations were detected using inductively coupled plasma – optical emission spectrometry (ICP-OES) using a PerkinElmer Optima 3000DV (PerkinElmer, Zaventem, Belgium).

4.2.5 Electron paramagnetic resonance

To elucidate whether the implants generated reactive oxygen species (ROS) that contribute to contact-killing of adhesive bacteria, the ROS formation from the implant surfaces was measured using an electron paramagnetic resonance (EPR) spectrometer (Bruker EMX Plus, Billerica, Massachusetts, United States). The implants (n = 2/group, length = 0.5 cm) were inserted inside a quartz capillary tube and were placed inside the EPR spectrometer. First, the baseline spectrum of the implants itself was measured followed by the detection of the formed radicals, which was performed through the submersion of the implants in 10 µl PBS containing 20 mM spin trap 5,5-dimethyl-pyrroline N-oxide (DMPO, Sigma-Aldrich, St.Louis, United States). The EPR measurements were performed using a frequency of 9.78 GHz, a sweep width of 100 G, a time constant of 163.8 ms, a conversion time of 160 ms, a modulation amplitude of 1 G, a modulation frequency of 100 kHz, a receiver gain of 60 dB, an attenuation of 10 dB, and a power of 20 mW. The radical generation was analyzed every 10 min for 2.5 h.

4.2.6 Antibacterial assays

4.2.6.1 Preparation of the bacterial inoculum

The bactericidal properties of the biofunctionalized biomaterials were evaluated *in vitro* and *ex vivo* against methicillin-resistant *Staphylococcus aureus* (MRSA, strain USA300) [36]. Bacterial inocula were prepared by the addition of a single colony into 3 ml tryptic soy broth (TSB) or cation-adjusted Mueller Hinton broth (CAMH) and incubated for 2 h at 37°C while shaking at 120 rpm. Subsequently, the optical density at 600 nm (OD_{600}) was measured and the desired bacterial inoculum was prepared. The inoculum was quantified by plating 10-fold serial dilutions of 10 µl triplicates on blood agar plates (Becton Dickinson, Franklin Lakes, United States) followed by overnight incubation and colony forming unit (CFU) quantification.

4.2.6.2 Agar diffusion assay

The antibacterial leaching activity of the implants was tested in an agar diffusion assay. Agar plates were poured from Luria broth (LB) containing 200 g tryptone, 100 g yeast powder, 240 g Agar No.1 (all from Oxoid, ThermoFisher Scientific, Massachusetts, United States), and 200 g NaCl dissolved in 20 L ultrapure water. A bacterial inoculum of 10^7 CFU/ml was prepared in TSB. Subsequently, bacteria were distributed over the agar plates using a cotton swab. Thereafter, 1.5 cm implants were pressed onto the agar surface and incubated at 37°C in a humid environment for 24 h. Following incubation, the area of the zone of inhibition was analysed using an image processing program (Photoshop CS6, Adobe, California, United States) to determine the antibacterial leaching activity (n = 3/group).

4.2.6.3 Minimal inhibitory concentration (MIC) and minimal bactericidal concentration (MBC)

In order to determine the MIC and MBC of Ag^+ and/or Cu^{2+} ions, Ag nitrate and Cu nitrate (both from Sigma-Aldrich, St. Louis, United States) were dissolved in CAMH broth. A bacterial inoculum of OD_{600} 0.09 was prepared from which 65 µl was transferred to 10 ml of CAMH. Subsequently, two-fold serial dilutions were prepared in 96-well plates starting at initial concentrations of 2 mM for Ag^+ and 80 mM for Cu^{2+} respectively. Next, 50 µl of bacterial inoculum and 50 µl of both Ag^+ and Cu^{2+} dilutions were added to a 96-well plate and were incubated overnight at 37°C under static conditions. The following day, the MIC was determined as the lowest concentration of Ag^+ and/or Cu^{2+} where no turbidities were present. To determine the MBC, 10 µl aliquots of each well were plated on blood agar plates, incubated overnight at 37°C, and the numbers of CFU were determined. The MBC was defined as the lowest concentration of Ag^+ or Cu^{2+} ions without any bacterial colonies.

4.2.6.4 Bactericidal CFU count

The bactericidal activity of the biofunctionalized implants against adherent and planktonic bacteria was assessed by inserting 4 implants of 1 cm in a 200 µl MicroAmp® Fast Reaction Tube (Life Technologies, Carlsbad, California, United States) with a bacterial inoculum of 2×10^3 CFU in 100 µl TSB + 1% glucose. Subsequently, the specimens (n = 3/group) were incubated overnight under static conditions at 37°C. To quantify the number of the adherent CFU, the implants were rinsed 3 times in PBS, ultrasonicated in 200 µl PBS for 3 min. Subsequently, 10-fold serial dilutions of 10 µl aliquots were plated on blood agar plates. The numbers of the non-adherent CFU present in the incubation medium were quantified by plating 10 µl of the incubation medium of 10-fold dilutions on blood agar plates. Following overnight incubation at 37°C, the number of CFUs was quantified.

4.2.6.5 Biofilm formation and characterization

The biofilm formation on the implants (n = 2/group) was determined through static incubation at 37°C in 100 µl TSB + 1% glucose with 2 x 10^3 CFU/ml for 24 h. Subsequently, the implants were rinsed in PBS and fixated in McDowels fixative (4% paraformaldehyde and 1% glutaraldehyde in 10 mM phosphate buffer at pH 7.4). Prior to SEM imaging, the fixated implants were cleaned in demineralized water for 5 min, dehydrated in 50% ethanol for 15 min, 70% ethanol for 20 min, 96% ethanol for 20 min, and hexamethyldisilazane for 15 min. Next, the implants were left to dry in air for 2 h, sputtered with a gold layer of 5 ± 2 nm, and inspected by SEM.

4.2.6.6 Ex vivo experiments

The *ex vivo* antibacterial properties of the biofunctionalized implants were studied using murine femurs provided by the Central Laboratory Animal Institute (Utrecht University). The surrounding tissue was removed from the femurs, which were subsequently sterilized in 70% ethanol for 10 min and submerged in demineralized water for 10 min. To insert the implants into the femur, a hole (Ø 0.5 mm) was drilled through the epicondyle into the intramedullary canal of the femur. Subsequently, the bone marrow was extracted using a syringe followed by 2 µl injection of PBS into the medullary cavity. Then, the implants were inoculated with an inoculum of 200 CFU in 2 µl demineralized water, left to dry in air for 15 min, and inserted into the femora.

To validate the system, 2 µl tetracycline (50 mg/ml, Sigma-Aldrich, St.Louis, Missouri, United States) was inserted into the intramedullary cavity after implantation with an inoculated NT implant. To verify the proper sterilization of the femora, one femur was not implanted with an implant (negative control). Following implantation, the femora were incubated in 0.5 ml Eppendorf tubes on a rotating platform at 37°C for 24 h to simulate intraosseous fluid flow. Subsequently, the femora were homogenized in 800 µl PBS using 15 zirconia beads (Ø 2mm, BioSpec, Bartlesville, Oklahoma, United States) with a MagNA Lyser (Roche Diagnostics, Risch-Rotkreuz, Switzerland) at 7000 rpm for 2 cycles of 30 s and cooling on ice in between. Consequently, 10-fold serial dilutions of the homogenate were plated on blood agar plates, incubated overnight at 37°C, and the CFU numbers were quantified.

4.2.7 Cytotoxicity assays

4.2.7.1 Cell seeding and culturing

Osteoblast-like cells (MC3T3-E1, Sigma-Aldrich) were pre-cultured for 7 days in α-MEM supplemented with 1% penicillin-streptomycin and 10% fetal bovine serum (all from ThermoFisher, Waltham, Massachusetts, United States). The culture medium was refreshed

every 2–3 days. The cells were seeded on 1 cm implants in 0.2 ml tubes containing 1.5 x 10^5 MC3T3-E1 cells in 100 µl culture medium. The implants were then tilted every 20 min (for 2 h in total) at 37°C in 5% CO_2 and were placed in a 48 well plate with 200 µl of fresh medium. Following 2 days of culturing, osteogenic differentiation was induced by the addition of 50 µg/µl ascorbid acid and 4 mM β-glycerophosphate (both from Sigma-Aldrich). Thereafter, the medium was refreshed every 2 – 3 days.

4.2.7.2 Presto blue assay

The metabolic activity of the MC3T3-E1 cells was determined by a PrestoBlue assay (Thermofisher, Waltham, MA, United States) after 1, 3, 7, and 11 days. The implants were incubated in 200 µl fresh culture medium with 20 µl PrestoBlue cell viability reagent for 1 h at 37°C. Thereafter, the absorbance was measured at a wavelength of 530 – 595 nm with a Wallac plate reader (Victor X4, PerkinElmer, Massachusetts, United States).

4.2.7.3 Alkaline Phosphatase (ALP) assay

The ALP activity of MC3T3-E1 cells on the implant was determined after 11 days. As such, the implants (n = 4/group) were rinsed with PBS and inserted in 250 µl PBS-Triton (8% NaCl, 0.2% KCl, 1.44% Na_2HPO_4, 0.24% KH_2PO_4, and 0.1% Triton X-100). Subsequently, the implants were ultrasonicated for 10 s to dissociate the cells and were incubated with 100 µl p-nitrophenyl phosphate (pNPP, Sigma-Aldrich) for 10 min at 37°C. Thereafter, the reaction was stopped by the addition of 250 µl NaOH. The absorbance was then measured at a wavelength of 405 nm with a Wallac plate reader (PerkinElmer). A standard curve was prepared by the addition of 100 µl PBS-Triton and 250 µl NaOH to each well to determine the ALP activity and the total protein content was determined using a bovine serum albumin (BSA) protein assay kit (Invitrogen, California, United States). Subsequently, the ALP levels were normalized to the total protein content.

4.2.7.4 Cell morphology

To assess cell morphology on the implant's surface, the implants were fixated after 11 days in McDowels fixative and kept at 4°C. Prior to SEM imaging, the implants were rinsed twice in demineralized water for 5 min and dehydrated in ethanol (for 15 min in 50%, for 20 min in 70%, and for 20 min in 96%). Subsequently, the implants were left to dry in air for 2 h, sputtered with a gold layer (5 ± 2 nm) and analyzed by SEM (n = 2/group).

4.2.8 Statistical analysis

All data are expressed as mean ± standard deviation. The statistical analyses were performed using GraphPad Prism (GraphPad Software, La Jolla, California, United States) with one-way ANOVA and Bonferroni *post hoc* test. Differences between groups were considered statistically significant at $p < 0.05$.

4.3 RESULTS

4.3.1 Surface morphology and PEO biofunctionalization

Following SLM, SEM analysis demonstrated that the highly porous implants had partially molten or unmolten powder particles attached to the implant surface, which further enhanced the surface area of the implants (**Figure 1A**). PEO biofunctionalization (**Figure 1B**) resulted in similar V-t curves recorded for all experimental groups (**Figure 1C**). Up to the point of dielectric breakdown, the voltage increased with a rate of 14 ± 1 V/s after which the ascent of the curve decreased to 0.49 V/s and plasma discharging started at 115 ± 5 V, resulting in a final voltage of 249 ± 6 V. SEM analysis demonstrated homogenous coverage of the implants surfaces with a micro-/nano-porous oxide layer (**Figure 1D**). The addition of Ag and/or Cu NPs did not alter the surface morphology as compared to the PT implants.

4.3.2 Surface chemistry and phase composition of biofunctionalized implants

The presence of Ag and Cu NPs on the implants after PEO biofunctionalization was demonstrated by EDS analysis (**Figure 2**). Secondary electron and backscattering mode indicated a wide spread of Ag and/or Cu NPs on the surface which were fully embedded into the TiO_2 surface layer. Point analysis demonstrated the presence of Ti, Al, V, Ca and P in the surface layer for all biofunctionalized implants as well as Ag, Cu, and both Ag and Cu NPs for the PT – Ag, PT – Cu, and PT – Ag Cu implants, respectively.

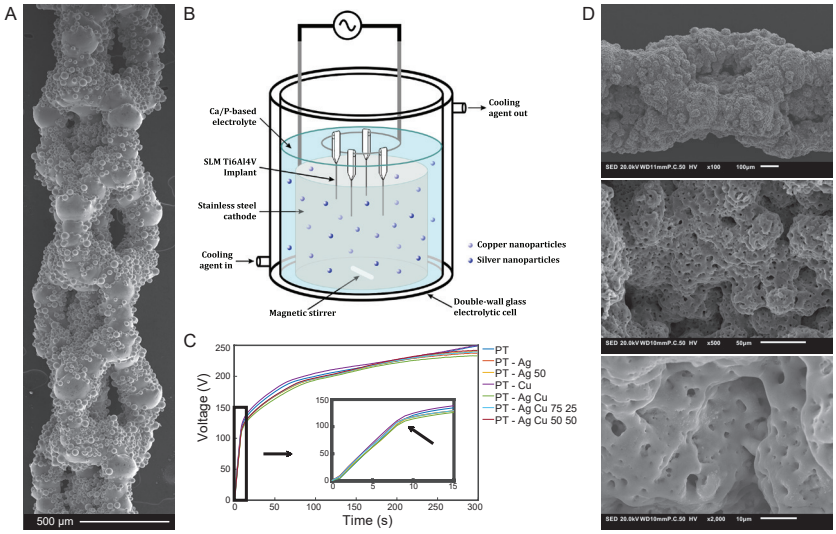

Figure 1. (A) The surface morphology of a selective laser melted Ti6Al4V implant visualized using SEM imaging. (B) A schematic drawing of the electrolytic cell used for PEO biofunctionalization depicting the electrolyte species, silver and copper nanoparticles, and the arrangement of the implants and the cathode. (C) The recorded V-t transients during the PEO biofunctionalization process of the selective laser melted implants with different electrolytes containing varying ratios of Ag and/or CuNPs. (D) The SEM images of the surface morphology following 300 s of PEO biofunctionalization with 100x (top), 500x (middle) and 2000x (bottom) magnifications.

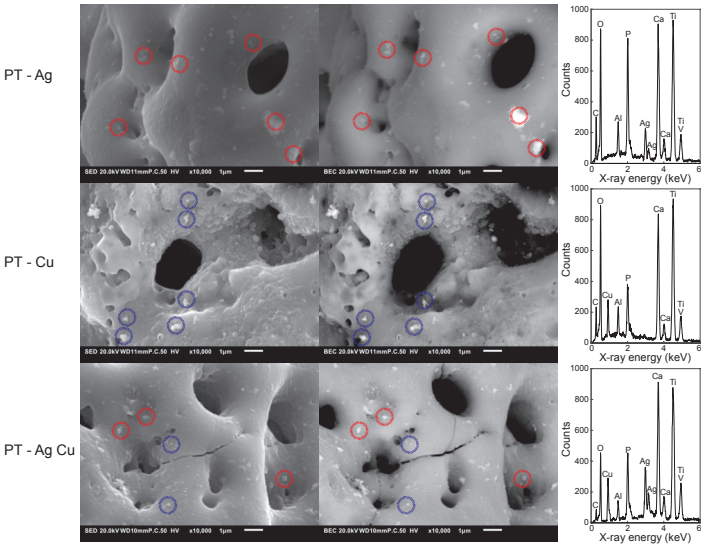

Figure 2. The EDS analysis of the biofunctionalized implants containing Ag and/or CuNPs. The locations of the AgNPs (red circles) and CuNPs (blue circles) on the implant surface were demonstrated by SEM using secondary (left) and backscattered (right) modes. Spot analysis confirmed the presence of Ag and Cu NPs as part of a surface layer containing Ti, Al, V, C, O, Ca, and P.

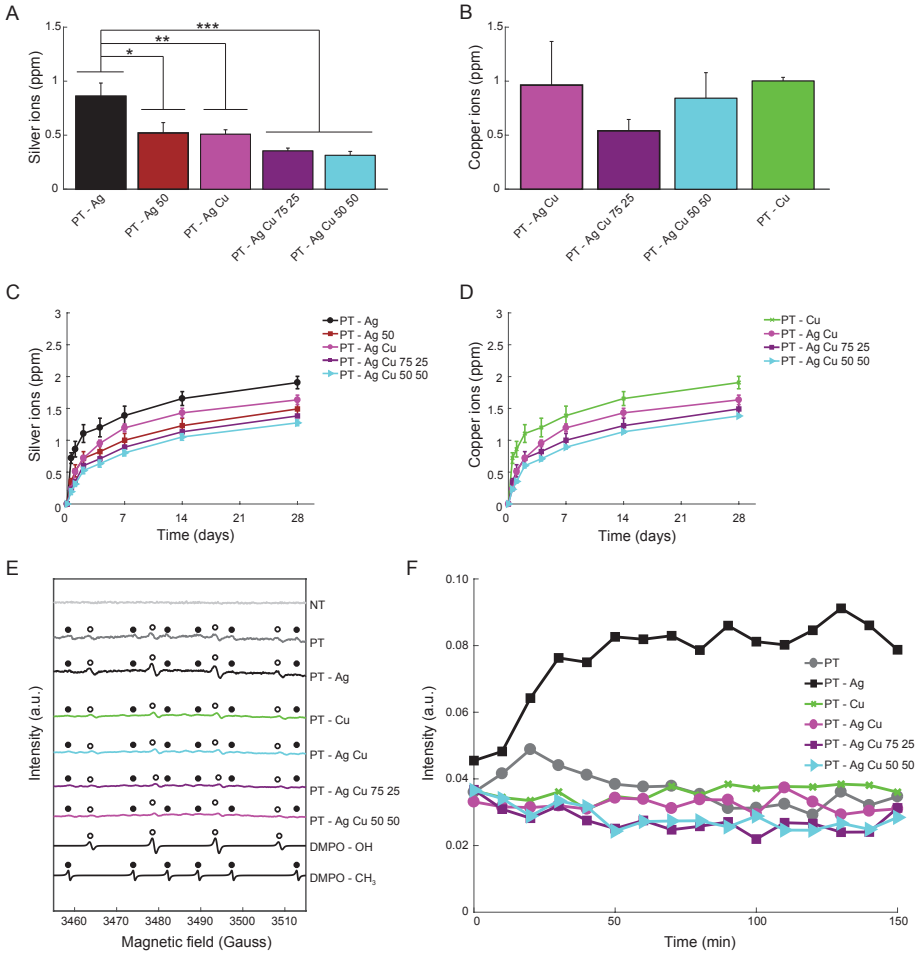

Figure 3. The ion release profile and the generation of oxygen radicals. (A) The Ag and (B) Cu ions released from the biofunctionalized implants (n=3) after 24 h in PBS were detected by ICP-OES. The cumulative release profiles of (C) Ag and (D) Cu ions for up to 28 days. (E) The generation of oxygen radicals by the implants measured using electron paramagnetic resonance and DMPO spin traps. Simulations of OH and CH_3 radical spectra are depicted by DMPO – OH and DMPO – CH_3 respectively. (F) 2D electron paramagnetic resonance spectrum demonstrating the oxygen radical formation for 150 min. *, p<0.05, **, p<0.01, ***, p<0.001.

4.3.3 Ion release and formation of reactive oxygen species

In the first 24 h, combined application of Ag and Cu NPs reduced the release of Ag^+ for the PT – Ag 50, PT – Ag Cu, PT – Ag Cu 75 25, and PT – Ag Cu 50 50 groups as compared to the PT – Ag group ($p < 0.05$, $p < 0.01$, $p < 0.001$ and $p < 0.001$, respectively; **Figure 3A**). Meanwhile, the release of Cu^{2+} was not affected by the presence of Ag NPs in the implant surface (**Figure 3B**). The ion release continued for the entire duration of our measurements (*i.e.*, 4 weeks).

When the entire duration of the release experiment is considered, combining Ag and Cu NPs reduced the Ag^+ release from the PT – Ag Cu, PT – Ag Cu 75 25, and PT – Ag Cu 50 50 groups as compared to the PT – Ag specimens ($p < 0.05$, $p < 0.01$ and $p < 0.01$, respectively; **Figure 3C**) while the release of Cu^{2+} was enhanced for the PT – Cu group as compared to the PT – Ag Cu 50 50 specimens ($p < 0.05$; **Figure 3D**).

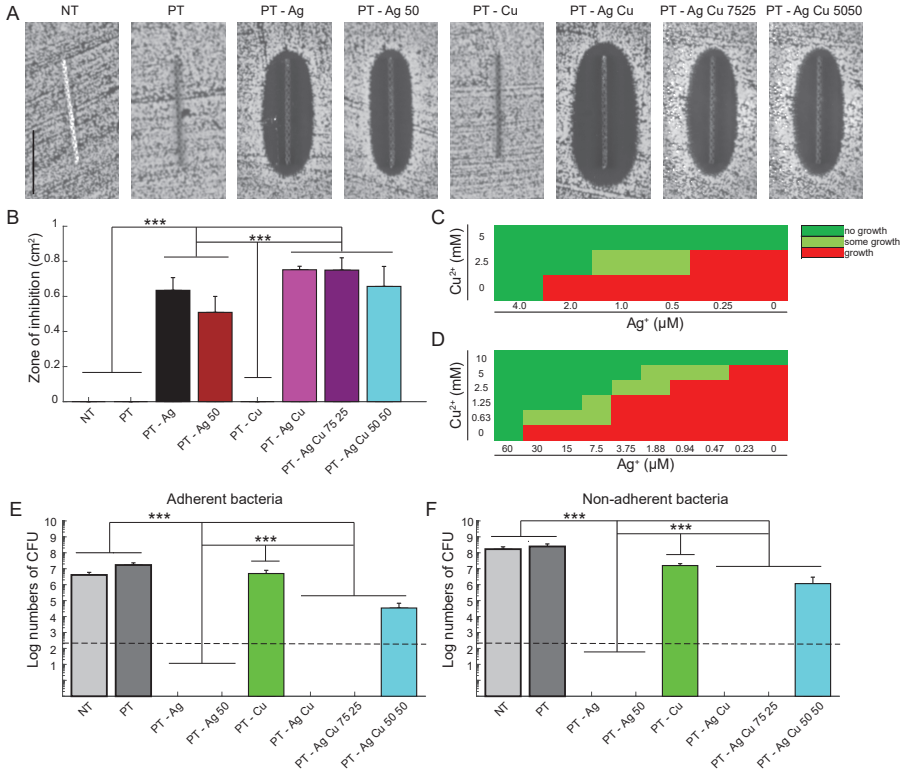

Figure 4. The antibacterial leaching activity and quantification of bactericidal activity *in vitro* against MRSA USA300. (A) The images of the antibacterial inhibition zones around implants after 24 hours on agar plates using an inoculum of 10^7 CFU/ml. (B) Quantification of the area of the inhibition zones. (C) The minimum inhibitory and (D) bactericidal concentrations for the different concentrations of Ag^+ and/or Cu^{2+} ions. The bactericidal activity against (E) the Adherent and (F) planktonic bacteria. Dashed line represents the inoculum. *, $p<0.05$, **, $p<0.01$, ***, $p<0.001$. $n=3$ per group for all experiments. Scale bar = 1 cm.

All biofunctionalized implants did generate both hydroxyl and methyl radicals, while the NT implants did not generate any oxygen radicals (**Figure 3E**). Following the hydroxyl radical formation up to 2.5 h, the groups containing Ag NPs demonstrated enhanced radical formation as compared to all other groups (**Figure 3F**).

4.3.4 Antibacterial assays

After 24 h incubation, all the specimens containing Ag NPs demonstrated a zone of inhibition whereas the specimens from the groups NT, PT, and PT – Cu did not (**Figure 4A**). The size of the inhibition zones did not differ significantly between all the groups containing Ag NPs (**Figure 4B**). To explore the synergistic antibacterial behavior between Ag^+ and Cu^{2+} ions, we determined the MIC and MBC for Ag^+ and Cu^{2+} against MRSA USA300. The MIC for Ag^+ was 4 µM and 5 mM for Cu^{2+} while combining 2 µM Ag^+ and 2.5 mM Cu^{2+} prevented bacterial growth (**Figure 4C**). Similarly, the MBC was 60 µM and 10 mM for Ag^+ and Cu^{2+} respectively while combining 30 – 0.47 µM Ag^+ with 0.63 – 5 mM Cu^{2+} resulted in total eradication of the bacterial inoculum (**Figure 4D**).

The specimens from the PT – Ag, PT – Ag 50, PT – Ag Cu, and PT – Ag Cu 75 25 groups totally prevented bacterial adhesion, whereas those from the PT – Ag Cu 50 50 group (3.4×10^4 CFU) showed a 3-log reduction in the number of the adherent CFUs as compared to the specimens from the NT, PT, and PT – Cu groups (1.7×10^8, 2.5×10^8 and 5.0×10^6 CFU respectively; $p < 0.001$; **Figure 4E**). Similar results were obtained for the planktonic bacteria with PT – Ag Cu 50 50 (1.2×10^7 CFU) demonstrating a 2-log reduction in the number of CFUs as compared to the NT, PT, and PT – Cu groups (4.1×10^6, 1.7×10^8 and 1.6×10^7 CFU respectively; $p < 0.001$; **Figure 4F**). The NT, PT, and PT – Cu groups did not prevent biofilm formation on the implants where bacteria had stacked on top of each other in multiple layers (**Figure 5**). The PT – Ag and PT – Ag Cu implants only showed sparsely attached bacteria, which were mostly entrapped inside the micropores.

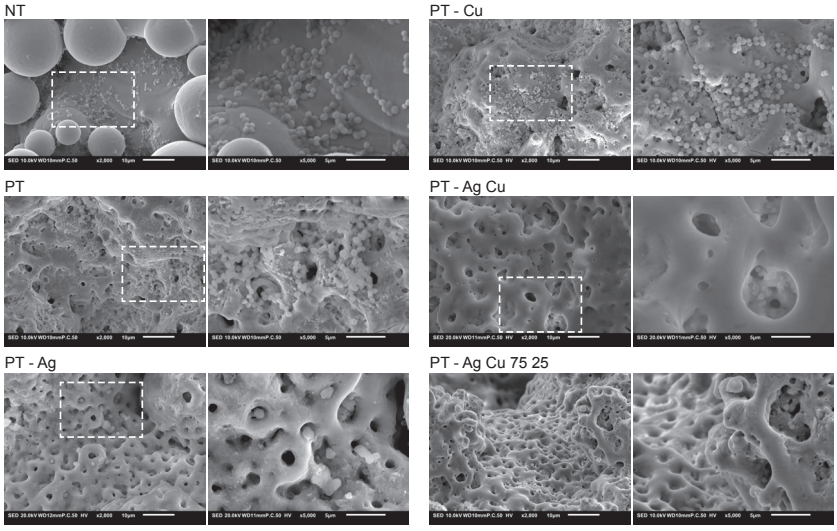

Figure 5. Biofilm formation on the implants (n=2) after incubation in TSB 1% glucose for 24 h visualized using low- (2000x) and high-magnification (8000x) SEM images.

To determine the *ex vivo* bactericidal activity, the implants were inserted into a murine femoral infection model (**Figure 6A**). After 24 h of incubation, the specimens from the PT – Ag, PT – Ag Cu, and PT – Ag Cu 75 25 groups fully eradicated the bacterial inoculum while those from the PT – Ag 50 group (3.7×10^5 CFU) reduced the bacterial growth by two orders of magnitude as compared to the NT and PT specimens (5.4×10^7 and 6.1×10^6 CFU respectively; $p < 0.001$; **Figure 6B**).

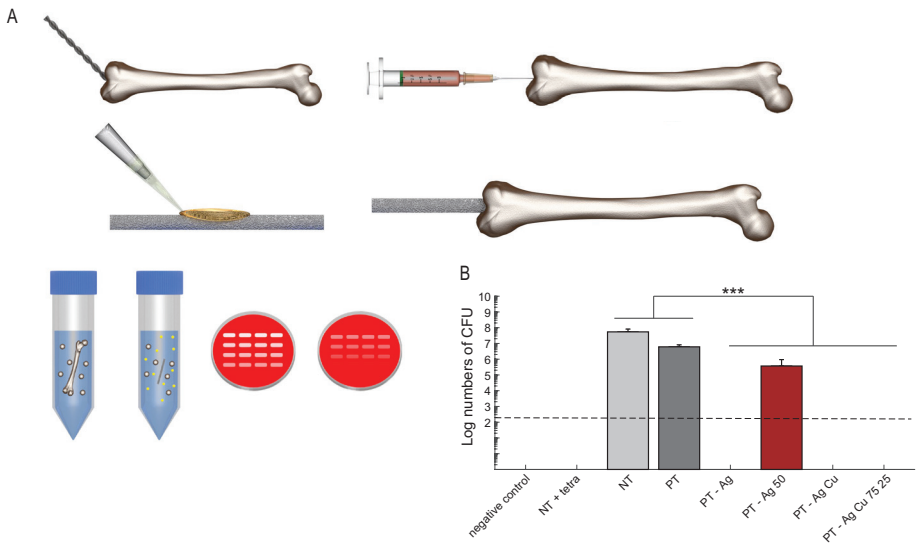

Figure 6. The bactericidal capacity of implants in an *ex vivo* femoral mouse model against MRSA USA300. (A) A 0.5 mm hole was created to access the intramedullary cavity of mouse femora. Thereafter, the bone marrow was extracted and 2 µl PBS injected. The implants were inoculated with 2×10^2 CFU and implanted intramedullary. After 24 h incubation, the femora were homogenized and 10-fold serial dilutions of the homogenate were plated on blood agar plates. (B) The quantification of the number of CFU following 24 h incubation *ex vivo*. To confirm proper sterilization of the femors, one femur without implant and bacterial inoculum was prepared and analyzed (negative control). To validate the system, 2 µl tetracycline was inserted into the femoral canal before implantation (NT+tetra). Dashed line represents the bacterial inoculum. n=3, ***, p <0.001.

4.3.5 Cytocompatibility

At day 1 and 3, the specimens from all groups demonstrated similar metabolic activity while after 7 days PT, PT – Ag 50, PT – Cu and PT – Ag Cu 75 25 exhibited enhanced metabolic activity as compared to the NT specimens ($p < 0.001$, $p < 0.05$, $p < 0.001$ and $p < 0.001$, respectively; **Figure 7A**). Furthermore, the PT implants had enhanced metabolic activity as compared to the specimens from the PT – Ag, PT – Ag 50, and PT – Ag Cu 75 25 groups ($p < 0.001$, $p < 0.001$ and $p < 0.01$, respectively). The same held for the PT – Cu implants as compared to those from the PT – Ag and PT – Ag 50 groups ($p < 0.05$ and $p < 0.01$, respectively;). After 11 days, the PT

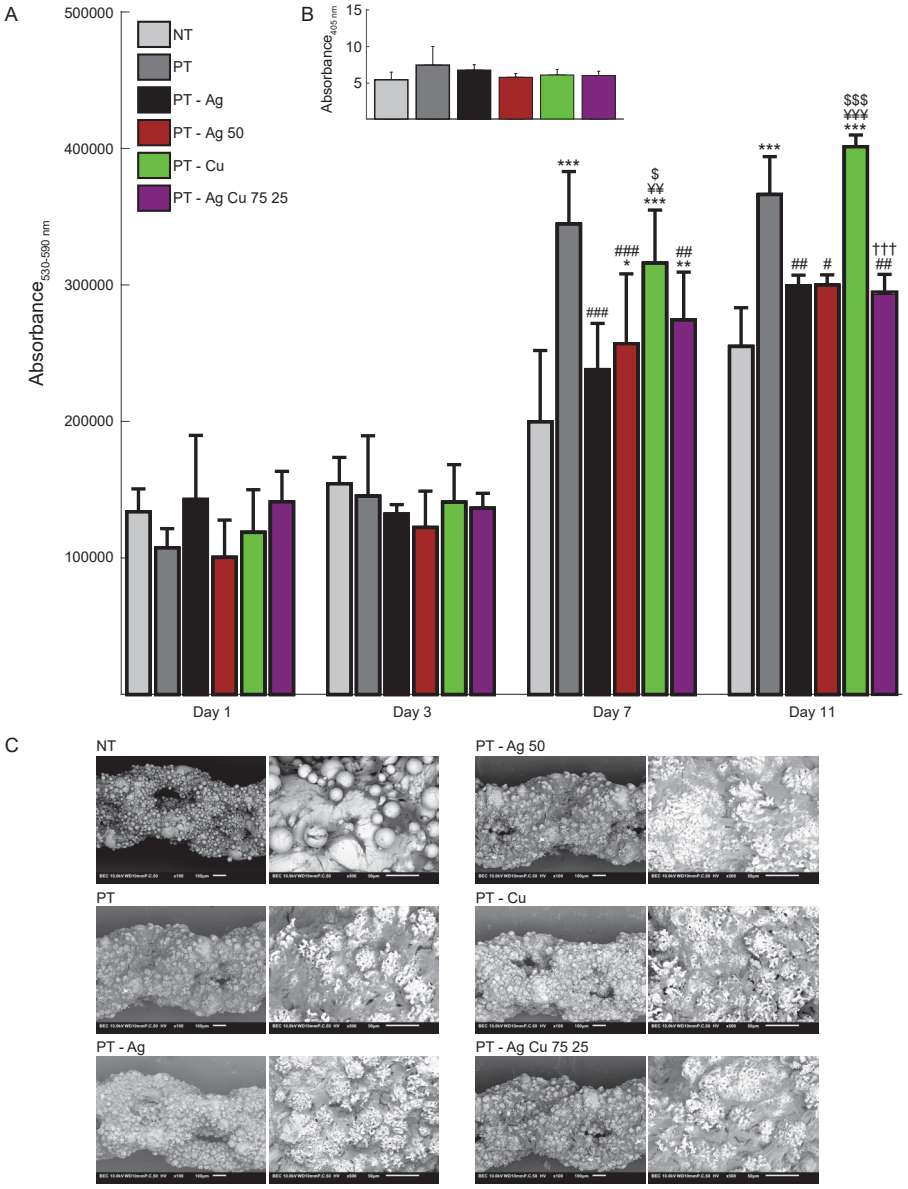

Figure 7. The cytotoxicity assessment of the implants (n=4) were performed using the MC3T3-E1 pre-osteoblasts. The osteogenic capacity of MC3T3-E1 cells cultured on the NT and biofunctionalized implants were determined as well (n=4 per group). (A) The metabolic activity of MC3T3-E1 cells indicated in terms of the optical density ($OD_{530-590nm}$) determined by Presto blue assay after 1, 3, 7, and 11 days of culture. (B) The ALP activity and (C) SEM images demonstrating the cell morphology and the spread of the MC3T3-E1 cells on the implants after 11 days of culture. Cell covered areas appear dark gray, while the implant substrate has a bright appearance. *, p<0.05, **, p<0.01 ***, p<0.001. * vs NT, # vs PT, ¥ vs PT – Ag, $ vs PT – Ag 50, † vs PT – Cu.

and PT – Cu implants displayed enhanced metabolic activity as compared to the NT implants ($p < 0.001$). The same held for the PT group as compared to PT – Ag, PT – Ag 50, and PT – Ag Cu 75 25 groups ($p < 0.01$, $p < 0.05$ and $p < 0.01$, respectively) as well as for the PT – Cu group as compared to the PT – Ag, PT – Ag 50, and PT – Ag Cu 75 25 groups ($p < 0.001$). Furthermore, the ALP activity after 11 days did not differ significantly between the different groups (**Figure 7B**). The cell morphology after 11 days demonstrated that all surfaces had cell attachment on significant parts of their surfaces (**Figure 7C**). Cells showed an elongated morphology and were found to span large surface areas.

4.4 DISCUSSION

Given the widespread research into and the increasing demand for highly porous orthopedic implants manufactured by AM, there is an ever increasing need for implant surfaces with intrinsic antibacterial activity. While targeting adherent and surrounding bacteria, antibacterial agents should not induce adverse effects in the surrounding host tissue. Therefore, we explored the use of combining Ag and Cu NPs, incorporated onto the surface of AM Ti6Al4V implants through PEO biofunctionalization, to produce potent antibacterial surfaces. We report here that Ag and Cu NP bearing implant surfaces with ratios of up to 75% Ag and 25% Cu NPs display leaching and direct-contact bactericidal activity against MRSA *in vitro* and *ex vivo*, while not inducing cytotoxicity to pre-osteoblastic MC3T3-E1 cells.

To prevent IAI, immediate antibacterial activity is required as most infections arise at an early stage after implantation [37, 38]. In this study, the PT – Ag and PT – Ag Cu implants with ratios of up to 75% Ag and 25% Cu NPs fully eradicated adherent and planktonic bacteria *in vitro* and *ex vivo* within 24 h. The prevention of bacterial adherence is essential to prevent biofilm formation, which gives rise to untreatable infections as the dose required to remove bacteria within a biofilm may be up to 1000-fold higher as compared to planktonic bacteria [39]. The fact that the biofunctionalized implants demonstrated strong antibacterial activity against MRSA is of clinical significance, since *Staphylococci* account for over 60% of IAI [29]. Furthermore, IAI caused by MRSA are more difficult to treat resulting in a reduced number of cured patients after 1 year, as compared to methicillin-susceptible *Staphylococcus aureus* [40].

To enhance the antibacterial activity of the implant, reduce cytotoxicity, and reduce the likelihood of bacterial resistance, we incorporated both Ag and Cu NPs onto the implant surfaces of our biofunctionalized implants. Combining Ag^{+} and Cu^{2+} resulted in synergistic effects in the MIC and MBC assays by up to 2 and 10-fold respectively. The same synergistic behavior resulted in the antibacterial results of the PT – Ag Cu 75 25 group being comparable to those of the PT – Ag and PT – Ag Cu groups whereas the specimens from the PT – Ag Cu 50 50 group resulted in 3-log and 2-log inhibition of the adherent and planktonic bacteria,

respectively. Our results concur with previous studies where combining Ag and Cu enhanced the bactericidal activity against MRSA compared to either Ag or Cu [41, 42]. The underlying mechanism causing this synergistic effect remains to be elucidated [43].

The sensitivity of bacteria to Cu is generally lower as compared to Ag [44], as reflected by the MIC-values obtained in this study. Cu is a cofactor in enzymatic reactions [45], required for proper bacterial cell metabolism, and therefore present in most bacterial culture media [46]. At the same time, elevated levels of freely circulating Cu are toxic to bacterial cells as they interfere with iron-sulfur cofactors [47], prevent other metals from binding to specific protein sites [48], and result in the generation of ROS [49]. Therefore, bacteria have developed several Cu defense mechanisms [50] including Cu exporting ATPases, multi-Cu oxidases, and resistance-nodulation-cell division efflux pumps that contributed to the development of highly Cu-resistant bacterial strains [51].

Contrary to Cu, Ag is not required for proper bacterial cell metabolism. Bacteria are, therefore, highly sensitive to Ag as is evident from 50 to 8000 times lower MIC-values as compared to Cu [44]. Ag targets a wide spectrum of bacteria by disturbing protein function, disruption of the cell membrane, generation of ROS, and blocking iron-sulfur clusters resulting in disturbed bacterial homeostasis and DNA damage [28]. Furthermore, Ag has demonstrated to make antibiotic-resistant Gram-negative bacteria, both in biofilms and planktonic cells, susceptible to antibiotic treatment again [52]. Therefore, the synthesis of Ag-containing antibacterial biomaterials has been studied intensively and has been demonstrated to reduce the clinical infection rates in patients receiving large limb salvaging prostheses [53-55].

However, mammalian cells are also susceptible to Ag, meaning that cytotoxicity is a concern too [31]. In this study, the PEO biofunctionalized implants containing Ag NPs did not show any signs of cytotoxicity against pre-osteoblastic cells and even demonstrated enhanced metabolic activity as compared to the NT implants after 7 days, while the PT and PT – Cu implants outperformed the Ag-containing implants after 7 and 11 days. Furthermore, no significant differences were observed on the ALP expression after 11 days of culture. All these results indicate that our surface biofunctionalized implants induce no cytotoxic effects against the pre-osteoblast cells. Indeed, the incorporation of Ca and P species onto the TiO_2 implant surface layer during the PEO biofunctionalization process results in the formation of hydroxyapatite [8] that together with the nano-/micro-porous structure of the created oxide layer enhance the osteogenic properties of the implants [56, 57]. Furthermore, the addition of Cu to titanium surfaces stimulates the ALP activity, the expression of the osteogenic and angiogenic markers, such as osteopontin, osteoprotegerin, hypoxia-inducible factor-1α, and vascular endothelial growth factor, and the matrix mineralization of mesenchymal stromal cells [32, 58]. In this study, we did not observe any effect on osteogenic differentiation nor

antibacterial activity by PT – Cu implants, probably because the Cu^{2+} ion release from our biofunctionalized implants is substantially lower as compared to other studies that applied PEO [59, 60]. The results presented in the current study suggest that the synergistic effects of Ag and Cu make it possible to reduce the amount of the Ag released from the antibacterial surfaces while maintaining similar levels of antibacterial properties, thereby minimizing the potential adverse effects of Ag on the host cells. Moreover, given the fact that the Ag and Cu NPs are tightly embedded inside the oxide layer during the PEO process, the circulation of the NPs and, thus, any adverse effects associated with that can be prevented.

In addition to the above-mentioned advantage, combining Ag and Cu on titanium surfaces reduces the likelihood of bacteria developing resistance against such antibacterial agents [61]. Even though bacterial resistance to either Ag or Cu is not regarded currently as a threat for their clinical application, Ag-resistant MRSA strains have been isolated from nasal and wound sources in patients [62] and mobile elements carrying Ag resistance are widely spread among pathogenic bacteria [63]. Moreover, *Staphylococcus aureus* has demonstrated increased levels of resistance against Ag in a polymicrobial environment due to the presence of Ag-reducing factors secreted by other bacterial species [64]. In addition, Cu-resistance inducing genes have been reported in *Staphylococci*, including MRSA, resulting in hyper-resistant strains [65, 66]. Therefore, preventing further development of resistance against Ag or Cu is essential for the extensive usability of these antibacterial agents. This further underlines the importance of exploiting the synergistic effects between multiple inorganic NPs.

Apart from immediate bactericidal activity, long-term antibacterial leaching activity is desired, as IAI may arise even years after surgery stemming from a haematogenous origin [67]. It is, therefore, of interest to create a reservoir of antibacterial agents on the surface of orthopedic biomaterials. In this study, the Ag and Cu NPs were firmly embedded and immobilized in the biofunctionalized TiO_2 layer during the PEO process, thereby forming a reservoir that released significant levels of Ag and Cu ions for at least one month. We confirmed the purity of the NPs as well as preservation of shape and composition of the NPs after PEO biofunctionalization by transmission electron microscopy [18] and EDS analysis. The Ag^+ and Cu^{2+} ion release was responsible for the clearance of planktonic bacteria *in vitro* and is important as the surrounding peri-implant tissue may form a niche for bacteria to infect the implant surface at later time points and generate systemic infections [12]. The combination of Ag and Cu NPs affected the ion release profile of both Ag and Cu ions compared to implants that possessed either Ag or Cu NPs. The underlying mechanism for the altered Ag and Cu ion release was not studied, but may stem from the micro-galvanic coupling processes at the implant surface [68].

Next to antibacterial leaching activity, antibacterial surfaces require contact-killing properties to extinguish adherent bacteria. ROS are known to play an important role in this process due to their extremely reactive nature, which also results in a short life-span. Previous studies have indicated the importance of ROS in bacterial killing by antibacterial surfaces containing either Ag or Cu [68-71]. We, therefore, investigated the generation of ROS from the implants with EPR and observed that PEO biofunctionalization resulted in the formation of both hydroxyl and methyl radicals. Furthermore, Ag incorporated into the implant surface enhanced the generation of hydroxyl radicals even further, whereas Cu NPs did not. Previously, we observed rutile and anatase TiO_2 phases in the surface layer of the implants by X-ray diffraction [8]. Anatase and rutile have shown to generate ROS and subsequent antibacterial activity [72, 73]. Therefore, ROS formed on the implant surfaces are likely to contribute to the observed antibacterial behavior in this study.

Given the fact that bacteria may infect both the implant surface and surrounding tissue, it is important to test multiple antibacterial properties *in vitro* such as the antibacterial leaching activity and contact killing. However, such studies lack the presence of the surrounding tissue. Therefore, we tested the implants in an *ex vivo* infection model consisting of murine femurs [8]. In this model, specimens from both PT – Ag and PT – Ag Cu groups with ratios of up to 75% Ag and 25% Cu demonstrated complete eradication of a bacterial inoculum, while those from the PT – Ag 50 group reduced the bacterial growth by two orders of magnitude. In the applied *ex vivo* setup, no distinction was made between the bacteria adhering to the implant or those that evaded into the adjacent bone tissue. In addition, in this model, no immune system is active that may aid in the eradication of the bacteria. Nonetheless, the results demonstrate a strong antibacterial behavior of all Ag NP-bearing implants.

The aforementioned antibacterial functionalities *in vitro* and *ex vivo* are generated through a single-step incorporation of both Ag and Cu NPs, and Ca and P elements in the electrolyte during the PEO process. PEO is highly suitable for the biofunctionalization of the surface of AM porous biomaterials, as it ensures a homogenous modification of the surface all over the implant surface, while not altering their mechanical properties [74]. These properties make PEO highly suitable for the modification of AM meta-biomaterials, that are currently under development and may in the future significantly improve the fixation of bone scaffolds and orthopedic implants [75]. Assigning antibacterial properties to these highly porous structures will be crucial to fight off IAI. Thus far, some studies have indicated that the enormous surface area of AM porous biomaterials allows for enhanced antibacterial performance of biofunctionalized implants bearing Ag NPs alone [8] or in combination with antibiotics [14, 31].

4.5 CONCLUSIONS

To develop novel antibacterial biomaterials that prevent IAI, Ti6Al4V implants were rationally designed, fabricated by SLM, and subsequently biofunctionalized by PEO with varying ratios of Ag and Cu NPs from 0 to 100%. The material and morphological properties, release profiles, generation of reactive ion species, antibacterial behavior, and biocompatibility of the developed biomaterials were assessed using various material characterization techniques, antibacterial assays, and cytotoxicity tests. ICP-OES and EPR analysis revealed a sustained release of Ag and Cu ions up to 28 days and the generation of hydroxyl radicals in the first 2.5 h, respectively resulting in strong antibacterial leaching and direct-contact activity against MRSA as well as a synergistic behavior between Ag^{+} and Cu^{2+}. Very strong antibacterial behaviors against both planktonic and adherent bacteria were also observed *in vitro*. Furthermore, the biofunctionalized implants containing both Ag and Cu NPs with ratios of up to 75% Ag and 25% Cu fully eradicated a bacterial inoculum in a murine *ex vivo* infection model. The synthesized implants did not induce cytotoxicity in pre-osteoblastic cells. Therefore, PEO biofunctionalization with Ag and Cu NPs is a promising strategy for preventing the infections associated with AM porous implants.

ACKNOWLEDGEMENTS

The research for this paper was financially supported by the Prosperos project, funded by the Interreg VA Flanders – The Netherlands program, CCI grant no. 2014TC16RFCB046.

REFERENCES

[1] C.L. Romano, S. Scarponi, E. Gallazzi, D. Romano, L. Drago, Antibacterial coating of implants in orthopaedics and trauma: a classification proposal in an evolving panorama, J Orthop Surg Res 10 (2015) 157.

[2] D. Culliford, J. Maskell, A. Judge, C. Cooper, D. Prieto-Alhambra, N.K. Arden, C.O.S. Group, Future projections of total hip and knee arthroplasty in the UK: results from the UK clinical practice research datalink, Osteoarthritis Cartilage 23 (2015) 594-600.

[3] S.M. Kurtz, E. Lau, H. Watson, J.K. Schmier, J. Parvizi, Economic burden of periprosthetic joint infection in the United States, J Arthroplasty 27 (2012) 61-67.

[4] D. Campoccia, L. Montanaro, C.R. Arciola, A review of the biomaterials technologies for infection-resistant surfaces, Biomaterials 34 (2013) 8533-54.

[5] T.F. Moriarty, R. Kuehl, T. Coenye, W.J. Metsemakers, M. Morgenstern, E.M. Schwarz, M. Riool, S.A.J. Zaat, N. Khana, S.L. Kates, R.G. Richards, Orthopaedic device-related infection: current and future interventions for improved prevention and treatment, EFORT Open Rev 1 (2016) 89-99.

[6] N. Stobie, B. Duffy, D.E. McCormack, J. Colreavy, M. Hidalgo, P. McHale, S.J. Hinder, Prevention of Staphylococcus epidermidis biofilm formation using a low-temperature processed silver-doped phenyltriethoxysilane sol-gel coating, Biomaterials 29 (2008) 963-9.

[7] K.Y. Yoon, J. Hoon Byeon, J.H. Park, J. Hwang, Susceptibility constants of Escherichia coli and Bacillus subtilis to silver and copper nanoparticles, Sci Total Environ 373 (2007) 572-5.

[8] I.A.J. van Hengel, M. Riool, L.E. Fratila-Apachitei, J. Witte-Bouma, E. Farrell, A.A. Zadpoor, S.A.J. Zaat, I. Apachitei, Selective laser melting porous metallic implants with immobilized silver nanoparticles kill and prevent biofilm formation by methicillin-resistant Staphylococcus aureus, Biomaterials 140 (2017) 1-15.

[9] S.B. Goodman, Z. Yao, M. Keeney, F. Yang, The future of biologic coatings for orthopaedic implants, Biomaterials 34 (2013) 3174-83.

[10] K.G. Neoh, X. Hu, D. Zheng, E.T. Kang, Balancing osteoblast functions and bacterial adhesion on functionalized titanium surfaces, Biomaterials 33 (2012) 2813-22.

[11] J.P. Celis, D. Drees, M.Z. Huq, P.Q. Wu, M. De Bonte, Hybrid processes — a versatile technique to match process requirements and coating needs, Surface and Coatings Technology 113 (1999) 165-181.

[12] M. Riool, L. de Boer, V. Jaspers, C.M. van der Loos, W.J.B. van Wamel, G. Wu, P.H.S. Kwakman, S.A.J. Zaat, Staphylococcus epidermidis originating from titanium implants infects surrounding tissue and immune cells, Acta Biomater 10 (2014) 5202-5212.

[13] S.K. Nandi, A. Shivaram, S. Bose, A. Bandyopadhyay, Silver nanoparticle deposited implants to treat osteomyelitis, J Biomed Mater Res B Appl Biomater 106 (2018) 1073-1083.

[14] S. Bakhshandeh, Z. Gorgin Karaji, K. Lietaert, A.C. Fluit, C.H.E. Boel, H.C. Vogely, T. Vermonden, W.E. Hennink, H. Weinans, A.A. Zadpoor, S. Amin Yavari, Simultaneous delivery of multiple antibacterial agents from additively manufactured porous biomaterials to fully eradicate planktonic and adherent staphylococcus aureus, ACS Appl Mater Interfaces 9 (2017) 25691-25699.

[15] N. Taniguchi, S. Fujibayashi, M. Takemoto, K. Sasaki, B. Otsuki, T. Nakamura, T. Matsushita, T. Kokubo, S. Matsuda, Effect of pore size on bone ingrowth into porous titanium implants fabricated by additive manufacturing: An in vivo experiment, Mater Sci Eng C Mater Biol Appl 59 (2016) 690-701.

[16] R. Hedayati, S.M. Ahmadi, K. Lietaert, B. Pouran, Y. Li, H. Weinans, C.D. Rans, A.A. Zadpoor, Isolated and modulated effects of topology and material type on the mechanical properties of additively manufactured porous biomaterials, J Mech Behav Biomed Mater 79 (2018) 254-263.

[17] S.M. Ahmadi, R. Hedayati, Y. Li, K. Lietaert, N. Tumer, A. Fatemi, C.D. Rans, B. Pouran, H. Weinans, A.A. Zadpoor, Fatigue performance of additively manufactured meta-biomaterials: The effects of topology and material type, Acta Biomater 65 (2018) 292-304.

[18] B.S. Necula, I. Apachitei, F.D. Tichelaar, L.E. Fratila-Apachitei, J. Duszczyk, An electron microscopical study on the growth of TiO2-Ag antibacterial coatings on Ti6Al7Nb biomedical alloy, Acta Biomater 7 (2011) 2751-7.

[19] I.A.J. van Hengel, M. Riool, L.E. Fratila-Apachitei, J. Witte-Bouma, E. Farrell, A.A. Zadpoor, S.A.J. Zaat, I. Apachitei, Data on the surface morphology of additively manufactured Ti6Al4V implants during processing by plasma electrolytic oxidation, Data Brief 13 (2017) 385-389.

[20] A. Shivaram, S. Bose, A. Bandyopadhyay, Understanding long-term silver release from surface modified porous titanium implants, Acta Biomater 58 (2017) 550-560.

[21] S.-H. Uhm, J.-S. Kwon, D.-H. Song, E.-J. Lee, W.-S. Jeong, S. Oh, K.-N. Kim, E.H. Choi, K.-M. Kim, Long-Term antibacterial performance and bioactivity of plasma-engineered Ag-NPs/TiO2 nanotubes for bio-implants, Journal of Biomedical Nanotechnology 12 (2016) 1890-1906.

[22] B.S. Necula, L.E. Fratila-Apachitei, S.A. Zaat, I. Apachitei, J. Duszczyk, In vitro antibacterial activity of porous TiO2-Ag composite layers against methicillin-resistant Staphylococcus aureus, Acta Biomater 5 (2009) 3573-80.

[23] Z. Gorgin Karaji, M. Speirs, S. Dadbakhsh, J.-P. Kruth, H. Weinans, A. Zadpoor, S. Amin Yavari, Additively manufactured and surface biofunctionalized porous nitinol, ACS Applied Materials & Interfaces 9 (2017) 1293-1304.

[24] K.R. Shin, Y.S. Kim, G.W. Kim, H.W. Yang, Y.G. Ko, D.H. Shin, Effects of concentration of Ag nanoparticles on surface structure and in vitro biological responses of oxide layer on pure titanium via plasma electrolytic oxidation, Applied Surface Science 347 (2015) 574-582.

[25] A. Nanda, M. Saravanan, Biosynthesis of silver nanoparticles from Staphylococcus aureus and its antimicrobial activity against MRSA and MRSE, Nanomedicine 5 (2009) 452-6.

[26] H.H. Lara, N.V. Ayala-Núñez, L.d.C. Ixtepan Turrent, C. Rodríguez Padilla, Bactericidal effect of silver nanoparticles against multidrug-resistant bacteria, World Journal of Microbiology and Biotechnology 26 (2009) 615-621.

[27] S.L. Percival, P.G. Bowler, D. Russell, Bacterial resistance to silver in wound care, J Hosp Infect 60 (2005) 1-7.

[28] J.A. Lemire, J.J. Harrison, R.J. Turner, Antimicrobial activity of metals: mechanisms, molecular targets and applications, Nat Rev Microbiol 11 (2013) 371-84.

[29] D. Campoccia, L. Montanaro, C.R. Arciola, The significance of infection related to orthopedic devices and issues of antibiotic resistance, Biomaterials 27 (2006) 2331-9.

[30] R.Y. Pelgrift, A.J. Friedman, Nanotechnology as a therapeutic tool to combat microbial resistance, Adv Drug Deliv Rev 65 (2013) 1803-15.

[31] M. Croes, S. Bakhshandeh, I.A.J. van Hengel, K. Lietaert, K.P.M. van Kessel, B. Pouran, B.C.H. van der Wal, H.C. Vogely, W. Van Hecke, A.C. Fluit, C.H.E. Boel, J. Alblas, A.A. Zadpoor, H. Weinans, S. Amin Yavari, Antibacterial and immunogenic behavior of silver coatings on additively manufactured porous titanium, Acta Biomater 81 (2018) 315-327.

[32] I. Burghardt, F. Luthen, C. Prinz, B. Kreikemeyer, C. Zietz, H.G. Neumann, J. Rychly, A dual function of copper in designing regenerative implants, Biomaterials 44 (2015) 36-44.

[33] L. Zou, J. Wang, Y. Gao, X. Ren, M.E. Rottenberg, J. Lu, A. Holmgren, Synergistic antibacterial activity of silver with antibiotics correlating with the upregulation of the ROS production, Sci Rep 8 (2018) 11131.

[34] G. Jin, H. Qin, H. Cao, S. Qian, Y. Zhao, X. Peng, X. Zhang, X. Liu, P.K. Chu, Synergistic effects of dual Zn/Ag ion implantation in osteogenic activity and antibacterial ability of titanium, Biomaterials 35 (2014) 7699-713.

[35] J.A. Garza-Cervantes, A. Chavez-Reyes, E.C. Castillo, G. Garcia-Rivas, O. Antonio Ortega-Rivera, E. Salinas, M. Ortiz-Martinez, S.L. Gomez-Flores, J.A. Pena-Martinez, A. Pepi-Molina, M.T. Trevino-Gonzalez, X. Zarate, M. Elena Cantu-Cardenas, C. Enrique Escarcega-Gonzalez, J.R. Morones-Ramirez, Synergistic antimicrobial effects of silver/transition-metal combinatorial treatments, Sci Rep 7 (2017) 903.

[36] F.C. Tenover, R.V. Goering, Methicillin-resistant Staphylococcus aureus strain USA300: origin and epidemiology, J Antimicrob Chemother 64 (2009) 441-6.

[37] K.L. Ong, S.M. Kurtz, E. Lau, K.J. Bozic, D.J. Berry, J. Parvizi, Prosthetic joint infection risk after total hip arthroplasty in the Medicare population, J Arthroplasty 24 (2009) 105-9.

[38] H. Dale, A.M. Fenstad, G. Hallan, L.I. Havelin, O. Furnes, S. Overgaard, A.B. Pedersen, J. Karrholm, G. Garellick, P. Pulkkinen, A. Eskelinen, K. Makela, L.B. Engesaeter, Increasing risk of prosthetic joint infection after total hip arthroplasty, Acta Orthop 83 (2012) 449-58.

[39] A.W. Smith, Biofilms and antibiotic therapy: is there a role for combating bacterial resistance by the use of novel drug delivery systems?, Adv Drug Deliv Rev 57 (2005) 1539-50.

[40] D. Teterycz, T. Ferry, D. Lew, R. Stern, M. Assal, P. Hoffmeyer, L. Bernard, I. Uçkay, Outcome of orthopedic implant infections due to different staphylococci, International Journal of Infectious Diseases 14 (2010) 913-918.

[41] S. Rtimi, D.D. Dionysiou, S.C. Pillai, J. Kiwi, Advances in catalytic/photocatalytic bacterial inactivation by nano Ag and Cu coated surfaces and medical devices, Applied Catalysis B: Environmental 240 (2019) 291-318.

[42] M.K. Ballo, S. Rtimi, C. Pulgarin, N. Hopf, A. Berthet, J. Kiwi, P. Moreillon, J.M. Entenza, A. Bizzini, In vitro and in vivo effectiveness of an innovative silver-copper nanoparticle coating of catheters to prevent methicillin-resistant staphylococcus aureus infection, Antimicrob Agents Chemother 60 (2016) 5349-56.

[43] B. Joshi, C. Regmi, D. Dhakal, G. Gyawali, S.W. Lee, Efficient inactivation of Staphylococcus aureus by silver and copper loaded photocatalytic titanate nanotubes, Progress in Natural Science: Materials International 28 (2018) 15-23.

[44] S. Ferraris, S. Spriano, Antibacterial titanium surfaces for medical implants, Mater Sci Eng C Mater Biol Appl 61 (2016) 965-78.

[45] D. Karlin, Metalloenzymes, structural motifs, and inorganic models, Science 261 (1993) 701-8.

[46] J.T. Trevors, C.M. Cotter, Copper toxicity and uptake in microorganisms, Journal of Industrial Microbiology 6 (1990) 77-84.

[47] S. Chillappagari, A. Seubert, H. Trip, O.P. Kuipers, M.A. Marahiel, M. Miethke, Copper stress affects iron homeostasis by destabilizing iron-sulfur cluster formation in Bacillus subtilis, J Bacteriol 192 (2010) 2512-24.

[48] L. Macomber, J.A. Imlay, The iron-sulfur clusters of dehydratases are primary intracellular targets of copper toxicity, PNAS 106 (2009) 8344-8349.

[49] A. Hiniker, J.F. Collet, J.C. Bardwell, Copper stress causes an in vivo requirement for the Escherichia coli disulfide isomerase DsbC, J Biol Chem 280 (2005) 33785-91.

[50] C. Rademacher, B. Masepohl, Copper-responsive gene regulation in bacteria, Microbiology 158 (2012) 2451-64.

[51] F. Altimira, C. Yanez, G. Bravo, M. Gonzalez, L.A. Rojas, M. Seeger, Characterization of copper-resistant bacteria and bacterial communities from copper-polluted agricultural soils of central Chile, BMC Microbiology 12 (2012).

[52] J.R. Morones-Ramirez, J.A. Winkler, C.S. Spina, J.J. Collins, Silver enhances antibiotic activity against gram-negative bacteria, Sci Transl Med 5 (2013).

[53] H. Wafa, R.J. Grimer, K. Reddy, L. Jeys, A. Abudu, S.R. Carter, R.M. Tillman, Retrospective evaluation of the incidence of early periprosthetic infection with silver-treated endoprostheses in high-risk patients, Bone Join J 97-B (2015) 252-7.

[54] J. Hardes, M.P. Henrichs, G. Hauschild, M. Nottrott, W. Guder, A. Streitbuerger, Silver-coated megaprosthesis of the proximal tibia in patients with sarcoma, J Arthroplasty 32 (2017) 2208-2213.

[55] F. Donati, G. Di Giacomo, S. D'Adamio, A. Ziranu, S. Careri, M. Rosa, G. Maccauro, Silver-coated hip megaprosthesis in oncological limb savage surgery, Biomed Res Int 2016 (2016).

[56] C.J. Chung, R.T. Su, H.J. Chu, H.T. Chen, H.K. Tsou, J.L. He, Plasma electrolytic oxidation of titanium and improvement in osseointegration, J Biomed Mater Res B Appl Biomater 101 (2013) 1023-30.

[57] P. Whiteside, E. Matykina, J.E. Gough, P. Skeldon, G.E. Thompson, In vitro evaluation of cell proliferation and collagen synthesis on titanium following plasma electrolytic oxidation, J Biomed Mater Res A 94 (2010) 38-46.

[58] C. Wu, Y. Zhou, M. Xu, P. Han, L. Chen, J. Chang, Y. Xiao, Copper-containing mesoporous bioactive glass scaffolds with multifunctional properties of angiogenesis capacity, osteostimulation and antibacterial activity, Biomaterials 34 (2013) 422-33.

[59] W. Zhu, Z. Zhang, B. Gu, J. Sun, L. Zhu, Biological activity and antibacterial property of nano-structured TiO2 coating incorporated with Cu prepared by micro-arc oxidation, Journal of Materials Science & Technology 29 (2013) 237-244.

[60] D. Zhao, Y. Lu, X. Zeng, Z. Wang, S. Liu, T. Wang, Antifouling property of micro-arc oxidation coating incorporating Cu2O nanoparticles on Ti6Al4V, Surface Engineering 33 (2017) 796-802.

[61] B. Khameneh, R. Diab, K. Ghazvini, B.S. Fazly Bazzaz, Breakthroughs in bacterial resistance mechanisms and the potential ways to combat them, Microb Pathog 95 (2016) 32-42.

[62] J.V. Loh, S.L. Percival, E.J. Woods, N.J. Williams, C.A. Cochrance, Silver resistance in MRSA isolated from wound and nasal sources in humans and animals, International Wound Journal 6 (2009) 32-38.

[63] K. Mijnendonckx, N. Leys, J. Mahillon, S. Silver, R. Van Houdt, Antimicrobial silver: uses, toxicity and potential for resistance, Biometals 26 (2013) 609-21.

[64] M. Muller, Bacterial silver resistance gained by cooperative interspecies redox behavior, Antimicrobial Agents and Chemotherapy 62 (2018).

[65] A.T. Fessler, Q. Zhao, S. Schoenfelder, K. Kadlec, G. Brenner Michael, Y. Wang, W. Ziebuhr, J. Shen, S. Schwarz, Complete sequence of a plasmid from a bovine methicillin-resistant Staphylococcus aureus harbouring a novel ica-like gene cluster in addition to antimicrobial and heavy metal resistance genes, Vet Microbiol 200 (2017) 95-100.

[66] J. Purves, J. Thomas, G.P. Riboldi, M. Zapotoczna, E. Tarrant, P.W. Andrew, A. Londono, P.J. Planet, J.A. Geoghegan, K.J. Waldron, J.A. Morrissey, A horizontally gene transferred copper resistance locus confers hyper-resistance to antibacterial copper toxicity and enables survival of community acquired methicillin resistant Staphylococcus aureus USA300 in macrophages, Environ Microbiol 20 (2018) 1576-1589.

[67] K. Huotari, M. Peltola, E. Jamsen, The incidence of late prosthetic joint infections: a registry-based study of 112,708 primary hip and knee replacements, Acta Orthop 86 (2015) 321-5.

[68] G. Wang, W. Jin, A.M. Qasim, A. Gao, X. Peng, W. Li, H. Feng, P.K. Chu, Antibacterial effects of titanium embedded with silver nanoparticles based on electron-transfer-induced reactive oxygen species, Biomaterials 124 (2017) 25-34.

[69] H.J. Park, J.Y. Kim, J. Kim, J.H. Lee, J.S. Hahn, M.B. Gu, J. Yoon, Silver-ion-mediated reactive oxygen species generation affecting bactericidal activity, Water Res 43 (2009) 1027-32.

[70] G. Applerot, J. Lellouche, A. Lipovsky, Y. Nitzan, R. Lubart, A. Gedanken, E. Banin, Understanding the antibacterial mechanism of CuO nanoparticles: revealing the route of induced oxidative stress, Small 8 (2012) 3326-37.

[71] S. Meghana, P. Kabra, S. Chakraborty, N. Padmavathy, Understanding the pathway of antibacterial activity of copper oxide nanoparticles, RSC Advances 5 (2015) 12293-12299.

[72] X. Lin, J. Li, S. Ma, G. Liu, K. Yang, M. Tong, D. Lin, Toxicity of TiO2 nanoparticles to Escherichia coli: effects of particle size, crystal phase and water chemistry, PLoS One 9 (2014) e110247.

[73] H.N. Pantaroto, A.P. Ricomini-Filho, M.M. Bertolini, J.H. Dias da Silva, N.F. Azevedo Neto, C. Sukotjo, E.C. Rangel, V.A.R. Barao, Antibacterial photocatalytic activity of different crystalline TiO2 phases in oral multispecies biofilm, Dent Mater 34 (2018) e182-e195.

[74] Z. Gorgin Karaji, R. Hedayati, B. Pouran, I. Apachitei, A.A. Zadpoor, Effects of plasma electrolytic oxidation process on the mechanical properties of additively manufactured porous biomaterials, Mater Sci Eng C Mater Biol Appl 76 (2017) 406-416.

[75] H.M.A. Kolken, S. Janbaz, S.M.A. Leeflang, K. Lietaert, H.H. Weinans, A.A. Zadpoor, Rationally designed meta-implants: a combination of auxetic and conventional meta-biomaterials, Materials Horizons 5 (2018) 28-35.

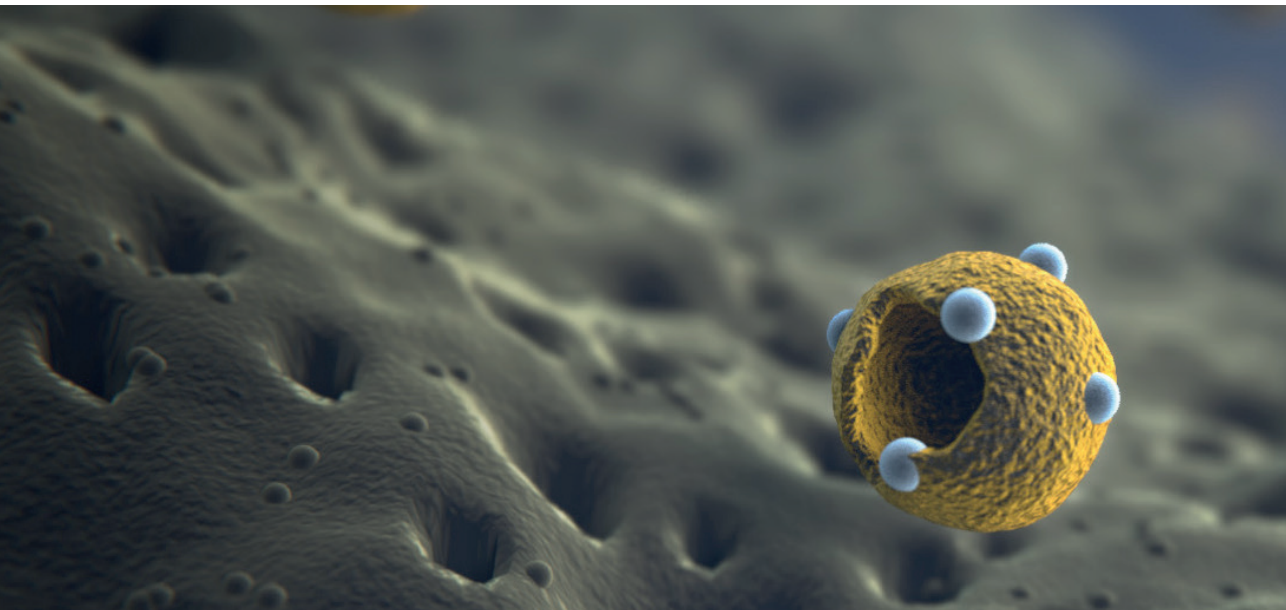

CHAPTER 05

Multifunctional implants with silver and zinc

I.A.J. van Hengel, N.E. Putra, M.W.A.M. Tierolf, M. Minneboo, A.C. Fluit, L.E. Fratila-Apachitei, I. Apachitei, A.A. Zadpoor, Biofunctionalization of selective laser melted porous titanium using silver and zinc nanoparticles to prevent infections by antibiotic-resistant bacteria, Acta Biomaterialia 107 (2020) 325-337.

Antibiotic-resistant bacteria are frequently involved in implant-associated infections (IAI), making the treatment of these infections even more challenging. Therefore, multifunctional implant surfaces that simultaneously possess antibacterial activity and induce osseointegration are highly desired in order to prevent IAI. The incorporation of multiple inorganic antibacterial agents onto the implant surface may aid in generating synergistic antibacterial behavior against a wide microbial spectrum while reducing the occurrence of bacterial resistance. In this study, porous titanium implants synthesized by selective laser melting (SLM) were biofunctionalized with plasma electrolytic oxidation (PEO) using electrolytes based on Ca/P species as well as silver and zinc nanoparticles in ratios from 0 to 100% that were tightly embedded into the growing titanium oxide layer. After the surface biofunctionalization process, silver and zinc ions were released from the implant surfaces for at least 28 days resulting in antibacterial leaching activity against methicillin-resistant *Staphylococcus aureus* (MRSA). Furthermore, the biofunctionalized implants generated reactive oxygen species, thereby contributing to antibacterial contact-killing. While implant surfaces containing up to 75% silver and 25% zinc nanoparticles fully eradicated both adherent and planktonic bacteria *in vitro* as well as in an *ex vivo* experiment performed using murine femora, solely zinc-bearing surfaces did not. The minimum inhibitory and bactericidal concentrations determined for different combinations of both types of ions confirmed the presence of a strong synergistic antibacterial behavior, which could be exploited to reduce the amount of required silver ions by two orders of magnitude (*i.e.*, 120 folds). At the same time, the zinc bearing surfaces enhanced the metabolic activity of pre-osteoblasts after 3, 7, and 11 days. Altogether, implant biofunctionalization by PEO with silver and zinc nanoparticles is a fruitful strategy for the synthesis of multifunctional surfaces on orthopedic implants and the prevention of IAI caused by antibiotic-resistant bacteria.

5.1 INTRODUCTION

Implant-associated infections (IAI) are one of the main causes of implant failure [1, 2]. IAI are initiated by bacterial invasion of the wound cavity and the subsequent adherence of bacteria onto the implant surface [3]. This is usually followed by the formation of bacterial biofilms that make it extremely difficult to eradicate bacteria from the implant surface, as they become largely insusceptible to the antibacterial agents that, in order to be effective, would have to penetrate through the protective biofilm layer [4, 5]. This is particularly concerning given the ongoing development of antibiotic resistance in bacterial species such as methicillin-resistant *Staphylococcus aureus* (MRSA) that has resulted in an increasing number of untreatable infections and significant patient mortality [6-10]. There is, therefore, an urgent need for the development of novel antibacterial strategies that minimize the risk of such infections.

There are two major strategies that could be used to minimize the risk of IAI caused by antibiotic-resistant strains. The first strategy is to minimize the risk of biofilm formation by stimulating the fast regeneration of bony tissue. Driven by host cells that cover the implant surface at an early stage, the formation of *de novo* bone could result in full integration of the implant inside the host tissue. The additive manufacturing (AM) of geometrically complex and highly ordered porous implants can be particularly useful in enhancing the bone tissue regeneration performance of biomaterials by offering both an interconnected porous structure [11] and bone-mimicking mechanical properties [12, 13]. Furthermore, such porous structures significantly increase the surface area that is available for the biofunctionalization of the implants. This increased surface area boosts the efficacy of the second strategy where the surface of the implant is biofunctionalized using combinations of potent antibacterial agents against which bacteria cannot easily develop resistance.

Here, we merged both of the aforementioned strategies to design and manufacture porous metallic implants to maximize the likelihood of preventing IAI caused by antibiotic-resistant strains. Our approach consists of AM porous titanium using a rationally designed porous structure [14], which is then surface-biofunctionalized using plasma electrolytic oxidation (PEO) to create multifunctional surfaces that promote the osseointegration of the implants while exhibiting a potent antibacterial behavior against antibiotic-resistant bacteria. More specifically, the electrolyte used in the PEO process contained both Ca/P species that are known to elicit an osteogenic response [15] and two types of inorganic nanoparticles (*i.e.*, silver and zinc). The choice of the nanoparticles (NPs) is of crucial importance in this regard. Silver ions are highly potent agents against a very wide spectrum of bacterial strains [16-18]. Moreover, resistance against silver is rare and difficult to acquire [19]. Combining silver with zinc offers several advantages. First, we hypothesized that silver and zinc exhibit a synergistic

behavior, providing the same level of bactericidal behavior with a much lower concentration of silver ions. This is particularly important given the concerns that high concentrations of silver ions could lead to cytotoxicity against host cells [20]. Second, combining several antibacterial agents that target the different components of bacterial cells [21, 22] could further reduce the risk of bacterial resistance. Finally, certain concentrations of zinc ions are known to give rise to osteogenic behavior [23, 24]. This could further reinforce the multifunctional performance of the implants.

During PEO, both Zn and Ag nanoparticles are tightly embedded in a growing TiO_2 surface layer that covers the entire surface of the porous titanium implants. Moreover, the PEO process generates a highly porous oxide layer that further expands the already vast surface area of the implants and enhances the release of ions from the incorporated elements [25-27].

In this study, we synthesized multifunctional AM implants and studied their surface characteristics, chemical composition and their performance against antibiotic-resistant bacteria using both *in vitro* and *ex vivo* assays. Moreover, we explored the mechanisms of their antibacterial behavior by evaluating the ion release kinetics and the generation of reactive oxygen species (ROS). Finally, we investigated the response of host cells to the implants through *in vitro* cultures of pre-osteoblasts and the assessment of their metabolic and alkaline phosphatase (ALP) activities.

5.2 MATERIALS AND METHODS

5.2.1 Implant design and additive manufacturing

We aimed to manufacture titanium implants suitable for testing in an *ex vivo* murine infection model. Therefore, we designed a hexagonal unit cell that was subsequently stacked to create implants with a length of 4 cm and a diameter of 5 mm. Subsequently, the implants were produced at the Additive Manufacturing Laboratory (TU Delft, Delft, The Netherlands) using a selective laser melting (SLM) printer (SLM-125, Realizer, Borchem, Germany) that operated with a YLM-400-AC Ytterbium fiber laser (IPG Photonics Corporation, Oxford, United States) under an argon atmosphere with less than 0.2% oxygen. The parameters of the SLM process were as follows: a wavelength of 1070 ± 10 nm, an exposure time of 300 μs and a laser power of 96 W, resulting in a laser spot size of 145 μm. We used a layer thickness of 50 μm and medical-grade (grade 23, ELI) Ti-6AL-4V powder (AP&C, Boisbriand, Quebec, Canada), which had a spherical morphology with particle sizes of 10 – 45 μm. After SLM, the loose powder particles were removed by vacuum cleaning and the implants were ultrasonicated subsequently in acetone, 96% ethanol, and demineralized water for 5 min each.

5.2.2 Plasma electrolytic oxidation

The surface of the implants was biofunctionalized by PEO in an electrolyte containing 0.15 M calcium acetate (Dr. Paul Lohmann GmbH, Emmerthal, Germany) and 0.02 M calcium glycerophosphate (Sigma-Aldrich, St. Louis, Missouri, United States) dissolved in demineralized water. In addition, Ag NPs and/or Zn NPs (both from Sigma-Aldrich, St. Louis, Missouri, United States) were dispersed in varying ratios with 3.0 g/l indicated as 100% in the electrolyte. This resulted in PEO biofunctionalized implants without NPs (PT), with 3.0 and 1.5 g/L Ag NPs (PT – Ag and PT – Ag 50, respectively), with 3.0 g/L Zn NPs (PT – Zn), and with both Ag and Zn NPs (PT – Ag Zn, PT – Ag Zn 75 25, and PT – Ag Zn 50 50). The as-manufactured implants (NT) served as a control group. Both Ag and Zn NPs displayed a spherical morphology with particle sizes ranging between 7 and 25 nm for Ag NPs and between 40 and 60 nm for Zn NPs. The PEO electrolyte was sonicated 2 times for 3 min and stirred in between for 5 min at 500 rpm on a magnetic stirrer (IKA-Werke GmbH & Co. KG, Staufen, Germany) using a stir bar of 40×8 mm (VWR, Radnor, Pennsylvania, United States).

The PEO process was performed using a custom-made laboratory setup that comprised an AC power supply (50Hz, type ACS 1500, ET powder Systems Ltd., Chesterfield, United Kingdom), a data acquisition board (SCXI, National Instruments, Austin, Texas, United States), and two electrodes inside a double-walled glass electrolytic cell. During the PEO process, a ring-shaped piece made from stainless steel served as the cathode while the implant was the anode. The voltage-time (*V-t*) transients were recorded every second. PEO processing took place at a current density of 20 A/dm^2 under galvanostatic conditions in 800 ml electrolyte for 5 min while the electrolytic cell was cooled with a thermostatic bath to keep the temperature between 6 – 8 °C throughout the PEO process. A homogeneous distribution of particles inside the electrolyte was established by continuously stirring at 500 rpm. Following PEO biofunctionalization, the implants were cleansed in running tap water for 1 min, sterilized at 110 °C for 1 h in an oven (Nabertherm TR60, New Castle, United States), and stored under sterile conditions.

5.2.3 Zeta potential of nanoparticles in PEO electrolyte

The stability of the Ag and/or Zn nanoparticles in the PEO electrolyte was determined by measurement of the zeta potential using a Zetasizer Nano ZS (Malvern Analytical, United Kingdom). The PEO electrolytes containing ratios of Ag and/or Zn nanoparticles from 0 – 100% were diluted 10 times and subsequently 1 ml was injected into a DTS1060 capillary cell (n = 3/condition). Thereafter, the zeta potential was determined at room temperature with 10 runs for each measurement.

5.2.4 Analysis of surface morphology, chemical composition and titanium oxide layer

The surface morphology of the biofunctionalized implants was imaged using scanning electron microscopy (SEM, JSM-IT100LV, JEOL, Tokyo, Japan). Prior to that, the implants were covered with a gold layer of 5 ± 2 nm to enhance their electrical conductivity. During SEM imaging an electron beam intensity ranged between 5 – 20 kV and working distance of 10 mm were used. By means of energy dispersive X-ray spectroscopy (EDS), the chemical composition on the surface of the implants was determined using spot analyses.

In addition, a cross-sectional analysis was performed to analyze the titanium oxide layer on the implant surface. Therefore, implants were sectioned perpendicular towards the longitudinal axis and embedded in a conductive resin with carbon filler (PolyFast, Struers, Copenhagen, Denmark). Subsequently, the specimens were grounded with sandpapers of 4000, 2000, 800, 320, 180 and 80 grit (Struers) under running tap water. Thereafter, the specimens were ultrasonicated for 5 min in isopropanol, dried in air, polished with 3 and 1 µm diamond suspension DiaDuo-2 (Struers) and analyzed by SEM. Furthermore, the chemical composition of the titanium layer was determined by EDS (n = 5).

5.2.5 Ion release kinetics

The release kinetics of Ag and Zn ions were determined by inductively coupled plasma – optical emission spectrometry (ICP-OES). Biofunctionalized implants of 1 cm in length were placed in dark Eppendorf tubes (n = 3/group) containing 1 ml phosphate-buffered saline (PBS). During the experiments, the specimens were kept at 37 °C using a water bath under static conditions. The PBS was collected and replenished after 0.5, 1, 2, 4, 7, 14, and 28 days. To dissolve all ions in the liquid, the collected PBS was acidified with 5% nitric acid. Subsequently, the ion concentration was detected by ICP-OES using a PerkinElmer Optima 3000DV (PerkinElmer, Zaventem, Belgium).

5.2.6 Electron paramagnetic resonance

The formation of ROS by the implants was determined through an electron paramagnetic resonance (EPR) spectrometer (Bruker EMX Plus, Billerica, Massachusetts, United States). The implants (n = 2/group) of 0.5 cm in length were inserted in a quartz capillary tube and placed inside the EPR spectrometer. Thereafter, the baseline spectra of the implants were determined followed by a measurement of the spectra corresponding to the radicals formed as a result of submerging the implants in 10 µl PBS containing 20 mM spin trap 5,5-dimethyl-pyrroline N-oxide (DMPO, Sigma-Aldrich, St.Louis, United States). The radical generation

was analyzed every 10 min for 2.5 h with the following EPR settings: a frequency of 9.78 GHz, a sweep width of 100 G, a time constant of 163.8 ms, a conversion time of 160 ms, a modulation amplitude of 1 G, a modulation frequency of 100 kHz, a receiver gain of 60 dB, an attenuation of 10 dB, and a power of 20 mW.

5.2.7 Antibacterial assays

5.2.7.1 Preparation of the bacterial inoculum

The bactericidal properties of the biofunctionalized implants were assessed against MRSA USA300 [28] using *in vitro* and *ex vivo* assays. The bacterial inocula were prepared by resuspending a single colony into 3 ml tryptic soy broth (TSB) or cation-adjusted Mueller Hinton broth (CAMH) followed by incubation for 2 h at 37 °C while shaking at 120 rpm. Thereafter, the optical density at 600 nm (OD_{600}) was measured and the required bacterial inoculum was prepared. The inoculum was verified by plating 10 µl triplicates of 10-fold serial dilutions on blood agar plates (Becton Dickinson, Franklin Lakes, United States) followed by overnight incubation at 37 °C and colony forming unit (CFU) quantification.

5.2.7.2 Inhibition zone

The antibacterial leaching activity of the implants was determined using an inhibition zone assay. Luria broth (LB) containing 200 g tryptone, 100 g yeast powder, 240 g Agar No.1 (all from Oxoid, ThermoFisher Scientific, Massachusetts, United States) and 200 g NaCl dissolved in 20 L ultrapure water was used to pour agar plates. A bacterial inoculum of 10^7 CFU/ml in TSB was distributed over the agar plates using a cotton swab and subsequently 1.5 cm implants (n = 3/group) were pressed onto the agar surface and incubated in a humid environment at 37°C for 24 h. Following incubation, the area of the inhibition zones was determined by an image processing program (Photoshop CS6, Adobe, California, United States) to determine the antibacterial leaching activity of the specimens.

5.2.7.3 Minimal inhibitory concentration (MIC) and minimal bactericidal concentration (MBC)

The MIC and MBC of Ag^+ and Zn^{2+} ions, as well as combinations thereof, against MRSA USA300 were determined using Ag nitrate and Zn nitrate (both from Sigma-Aldrich, St. Louis, United States) dissolved in CAMH broth. Next, two-fold serial dilutions were prepared in 96-well plates starting at initial concentrations of 2 mM for Ag^+ and 80 mM for Zn^{2+}, respectively. Subsequently, an inoculum at OD_{600} 0.09 was prepared of which 65 µl was transferred to 10 ml

of CAMH. Next, 50 µl of the bacterial inoculum and 50 µl of both Ag^{+} and Zn^{2+} dilutions were added to a 96-well plate and incubated overnight at 37 °C under static conditions. Following incubation, the MIC was denoted as the lowest concentration of Ag^{+} and/or Zn^{2+} where no turbidities were observed. The MBC was determined using 10 µl aliquots of each well plated on blood agar plates and overnight incubation at 37 °C. The MBC was determined as the lowest concentration of Ag^{+} and/or Zn^{2+} ions without any bacterial colonies present.

5.2.7.4 Quantification of adherent and planktonic bacteria on implants

The bactericidal activity of the biofunctionalized implants was quantified for both adherent and planktonic bacteria against a bacterial inoculum of 2×10^3 CFU MRSA USA300 in 100 µl TSB + 1% glucose in a 200 µl MicroAmp® Fast Reaction Tube (Life Technologies, Carlsbad, California, United States) to which 4 implants of 1 cm in length were added. The specimens (n = 3/group) were incubated overnight under static conditions at 37 °C. Subsequently, the number of the adherent CFU was quantified by rinsing the specimens 3 times in PBS and ultrasonication in 200 µl PBS for 3 min of which 10 µl aliquots of subsequent 10-fold serial dilutions were plated on blood agar plates. The non-adherent bacteria present in the culture medium were quantified by plating 10 µl of 10-fold dilutions onto blood agar plates followed by CFU quantification after overnight incubation at 37 °C.

5.2.7.5 Biofilm formation and characterization

The ability of the implants to prevent biofilm formation (n = 2/group) was determined through static incubation in 100 µl TSB + 1% glucose with 2×10^3 CFU/ml MRSA USA300 at 37 °C for 24 h. After 24 h, the implants were rinsed in PBS and fixated in McDowels fixative (4% paraformaldehyde and 1% glutaraldehyde in 10 mM phosphate buffer at pH 7.4). Subsequently, the fixated implants were dehydrated using the following procedure: rinsing in demineralized water for 5 min, dehydrating in 50% ethanol for 15 min, 70% ethanol for 20 min, 96% ethanol for 20 min, and hexamethyldisilazane for 15 min. Thereafter, the implants were left to dry in air for 2 h, sputtered with a gold layer of 5 ± 2 nm, and analyzed by SEM.

5.2.7.6 Ex vivo infection model

The antibacterial properties of the specimens were also studied in an *ex vivo* infection model using murine femurs provided by the Central Laboratory Animal Institute (Utrecht University). First, the tissues surrounding the femurs were removed. Then, the femurs were sterilized using 70% ethanol for 10 min and were subsequently submerged in demineralized

water for 10 min. A hole of 0.5 mm was drilled through the epicondyle into the intramedullary canal. The bone marrow was removed with a syringe, and 2 µl of PBS was inserted into the medullary cavity. Prior to implantation, the implants were inoculated with 200 CFU MRSA USA300 in 2 µl demineralized water, dried in air for 15 min, and press-fitted into the femur.

To verify the proper sterilization, one femur was not implanted with an implant (negative control). The model was validated by injecting 2 µl tetracycline (50 mg/ml, Sigma-Aldrich, St. Louis, Missouri, United States) intramedullary before implantation with an inoculated NT implant. Following the implantation procedure, the femurs were inserted in 0.5 ml Eppendorf tubes and were incubated on a dynamic platform to simulate intraosseous fluid flow at 37 °C for 24 h. After overnight incubation, the femurs were homogenized using 15 zirconia beads (Ø 2 mm, BioSpec, Bartlesville, Oklahoma, United States) in 800 µl PBS with a MagNA Lyser (Roche Diagnostics, Risch-Rotkreuz, Switzerland) at 7000 rpm for 2 rounds of 30 s each while being cooled on ice in between. To quantify the number of CFU, 10-fold serial dilutions of the homogenate were plated on blood agar plates and incubated overnight at 37°C.

5.2.8 Cytocompatibility of MC3T3-E1 cells on implants

5.2.8.1 Pre-culture of cells and cell seeding

Pre-osteoblast MC3T3-E1 cells (Sigma-Aldrich) were cultured for 7 days in α-MEM supplemented with 1% penicillin-streptomycin and 10% fetal bovine serum (all from ThermoFisher, Waltham, Massachusetts, United States). The medium was refreshed every 2 – 3 days. For cell seeding on 1 cm implants, 1.5 x 10^5 MC3T3-E1 cells were added to 100 µl culture medium in 0.2 ml tubes. To stimulate cell adhesion, the implants were tilted every 20 min for 2 h in total (37 °C, 5% CO_2) and were thereafter placed in a 48 well plate with 200 µl fresh medium. After 2 days, osteogenic differentiation was initiated by the addition of 50 µg/µl ascorbic acid and 4 mM β-glycerophosphate (both from Sigma-Aldrich). During the experiments, the culture medium was refreshed every 2 – 3 days.

5.2.8.2 Presto blue assay

The metabolic activity of the MC3T3-E1 cells was determined after 1, 3, 7, and 11 days using a PrestoBlue assay (Thermofisher, Waltham, MA, United States). The implants were incubated in 200 µl fresh culture medium for 1 h at 37 °C with 20 µl PrestoBlue cell viability reagent. Subsequently, the absorbance was measured at a wavelength of 530 – 590 nm with a Wallac plate reader (Victor X4, PerkinElmer, Massachusetts, United States).

5.2.8.3 Alkaline Phosphatase (ALP) assay

The ALP activity of the MC3T3-E1 cells was determined after 11 days by rinsing the implants (n = 4/group) with PBS and submersion in 250 µl PBS-Triton (8% NaCl, 0.2% KCl, 1.44% Na_2HPO_4, 0.24% KH_2PO_4, and 0.1% Triton X-100 in H_2O). To dissociate the cells, the implants were ultrasonicated for 10 s and incubated for 10 min at 37 °C in 100 µl p-nitrophenyl phosphate (pNPP, Sigma-Aldrich). The enzymatic reaction was blocked with the addition of 250 µl NaOH. The absorbance at a wavelength of 405 nm was then measured with a Wallac plate reader (Perkin Elmer). To determine the ALP activity, a standard curve was prepared through the addition of 100 µl PBS-Triton and 250 µl NaOH to each well. The total protein content was determined with a BSA protein assay kit (Invitrogen). Subsequently, the ALP levels were normalized to the total protein content.

5.2.8.4 Morphology of MC3T3-E1 cells on implants

The implants with MC3T3-E1 cells were fixated after 11 days in McDowels fixative (4% paraformaldehyde and 1% glutaraldehyde in 10 mM phosphate buffer at pH 7.4) and were stored at 4 °C. Subsequently, the implants were cleansed twice for 5 min in demineralized water and were dehydrated using an ethanol dilution series of 15 min in 50%, 20 min in 70%, and 20 min in 96%. Next, the implants were dried in air for 2 h, sputtered with a gold layer of 5 ± 2 nm, and analyzed by SEM (n = 2/group).

5.2.9 Statistical analysis

All data are expressed as mean ± standard deviation. The statistical analyses were performed using GraphPad Prism (GraphPad Software, La Jolla, California, United States) with one-way ANOVA and Bonferroni *post hoc* test. The differences between groups were considered statistically significant at $p < 0.05$.

5.3 RESULTS

5.3.1 PEO biofunctionalization and surface morphology of Ti6Al4V implants

Following SLM, the porous implants displayed partially molten or unmolten Ti-6Al-4V powder particles tightly attached to their surface (**Figure 1A**). Subsequently, the implants were biofunctionalized in a PEO setup (**Figure 1B**) using Ca/P-based electrolytes with Ag and/or Zn NPs. The addition of NPs to the PEO electrolyte did not affect the *V-t* curves obtained during the PEO process (**Figure 1C**). Prior to dielectric breakdown, the voltage increased with 14 ± 1 V/s followed by an inflection of the curve and a decreased rate of growth of 0.49

V/s. From 115 ± 5 V, plasma discharges were observed until a final voltage of 249 ± 6 V was reached. The zeta potential of Ag and/or Zn NPs in the PEO electrolyte varied between -11 to -20 mV, demonstrating a negative charge of the NPs in the electrolyte (**Figure 1D**). Surface characterization by SEM revealed a homogenous micro-/nano-porous oxide layer on the outer surface of the implants (**Figure 1E**). Furthermore, the surface morphology of implants bearing Ag and/or Zn NPs did not differ from the PT implants. Cross-sectional analysis of the implants by SEM demonstrated the presence of a titanium oxide layer on both the inner and the outer surface of the implants (**Figure 1F**). In the oxide layer the presence of Ti, Al, V, O, Ca, P and C elements was confirmed by EDS (**Figure 1G**).

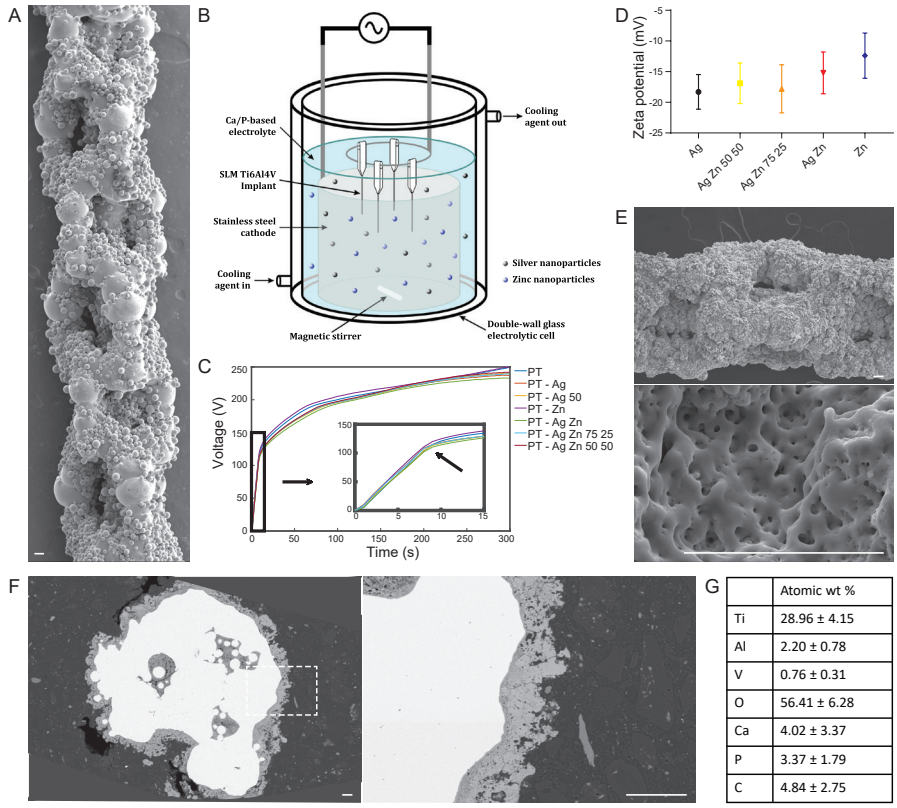

	Atomic wt %
Ti	28.96 ± 4.15
Al	2.20 ± 0.78
V	0.76 ± 0.31
O	56.41 ± 6.28
Ca	4.02 ± 3.37
P	3.37 ± 1.79
C	4.84 ± 2.75

Figure 1. (A) The surface morphology of selective laser melted Ti-6Al-4V implants imaged using SEM. (B) An illustration of the electrolytic cell used for PEO biofunctionalization depicting the electrolyte, Ag and Zn nanoparticles, the arrangement of the implants, and cathode. (C) The *V-t* curves recorded during the PEO biofunctionalization of the SLM implants with different electrolytes containing the varying ratios of Ag and/or Zn NPs. (D) Zeta potential measurements of Ag and/or Zn NP ratios dispersed in the PEO electrolyte. (E) SEM images of the surface morphology of a PT implant following 300 s of PEO biofunctionalization. (F) Cross-sectional analysis of a biofunctionalized implant by SEM. (G) Chemical composition of the titanium oxide layer determined by EDS (n=5). Scale bar = 50 µm.

5.3.2 Surface chemistry and phase composition

Following PEO processing, Ag and Zn NPs were observed on the implant surfaces as demonstrated by EDS analysis (**Figure 2**). Ag and/or Zn NPs were fully embedded onto the TiO_2 surface layer and were widely spread. EDS point analysis indicated the presence of Ca, P, Ti, Al, and V on the surface of all biofunctionalized implants while Ag and/or Zn NPs were found for PT – Ag, PT – Zn, and PT – Ag Zn implant surfaces, respectively.

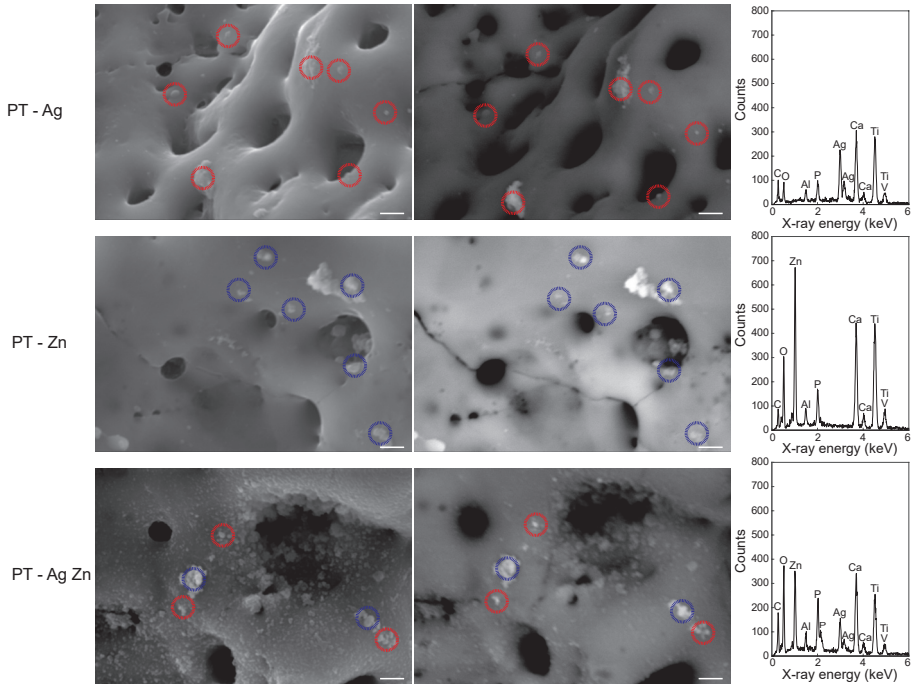

Figure 2. EDS analysis of the biofunctionalized implants containing Ag and/or Zn NPs. The locations of the Ag NPs (red circles) and Zn NPs (blue circles) on the implant surface were demonstrated using secondary (left) and backscattered (right) SEM images. EDS spot analysis confirmed the presence of Ag and Zn NPs as part of a surface layer consisting of Ti, Al, V, C, O, Ca, and P. Scale bar = 1 µm.

5.3.3 Ion release kinetics and formation of reactive oxygen species

5.3.3.1 Ion release kinetics

Combining Ag and Zn NPs resulted in a reduced rate of Ag ion release in the first 24 h for the PT – Ag Zn, PT – Ag Zn 50 50, and PT – Ag 50 groups as compared to the PT – Ag implants ($p < 0.001$; **Figure 3A**). The release of Zn ions was not affected by the incorporation of Ag NPs onto the implant surface (**Figure 3B**). The release of the ions persisted up to at least 28 days.

Combining Ag and Zn NPs reduced the release of Ag ions from the PT – Ag Zn, PT – Ag Zn 75 25, and PT – Ag Zn 50 50 groups as compared to the PT – Ag implants ($p < 0.001$, $p < 0.05$, and $p < 0.001$, respectively; **Figure 3C**) while the release of Zn ions was enhanced for the PT – Zn implants as compared to the PT – Ag Zn 50 50 group ($p < 0.05$; **Figure 3D**).

5.3.3.2 Reactive oxygen species formation

Both hydroxyl and methyl radicals were generated by all of the biofunctionalized implant groups, while NT implants did not generate any ROS (**Figure 3E**). Following the hydroxyl radical formation for up to 2.5 h, the PT – Zn group exhibited a higher level of radical formation as compared to all other groups (**Figure 3F**).

5.3.4 Antibacterial assays

5.3.4.1 Antibacterial leaching activity and minimal inhibitory and bactericidal concentration

Following 24 h incubation, the implants bearing Ag NPs demonstrated zones of inhibition whereas the NT, PT, PT – Zn and PT – Zn implants showed no such zones (**Figure 4A**). The size of the inhibition zones was similar between the implants indicating that the antibacterial leaching activity did not differ significantly (**Figure 4B**). The synergistic effects on antibacterial activity between Ag^+ and Zn^{2+} ions were studied by determining the MIC and MBC for Ag^+ and Zn^{2+} against MRSA USA300. The MIC was 4 μM for Ag^+ and 630 μM for Zn^{2+} while combining 2 μM Ag^+ and 310 μM Zn^{2+} fully prevented bacterial growth (**Figure 4C**). Similarly, the MBC was respectively 60 μM and 5000 μM for Ag^+ and Zn^{2+} while combining 30 – 0.47 μM Ag^+ with 160 – 2500 μM Zn^{2+} resulted in total eradication of the bacterial inoculum (**Figure 4D**).

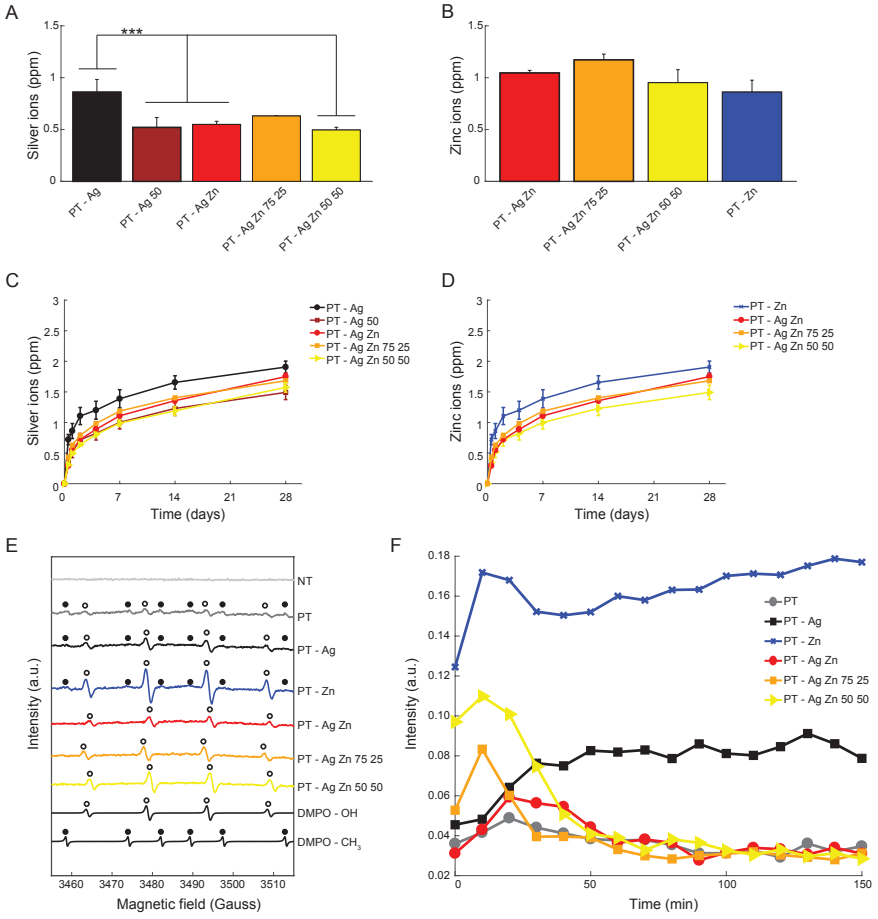

Figure 3. The ion release profile and the generation of ROS. (A) The Ag and (B) Zn ions released from the biofunctionalized implants (n=3) after 24 h in PBS as measured by ICP-OES. The cumulative release profile of (C) Ag and (D) Zn ions measured during a period of 28 days. (E) The generation of ROS by the implants as measured by electron paramagnetic resonance using DMPO spin trap. DMPO – OH and DMPO – CH_3 depict a simulation of OH and CH_3 radical spectra respectively. (F) The 2D electron paramagnetic resonance spectrum measured for the hydroxyl radical formation for up to 150 min. *, $p < 0.05$, **, $p < 0.01$, ***, $p < 0.001$.

5.3.4.2 Quantification of bactericidal activity and biofilm prevention

The specimens from the PT – Ag, PT – Ag 50, PT – Ag Zn, and PT – Ag Zn 75 25 groups totally prevented bacterial adhesion whereas those from the PT – Ag Zn 50 50 group showed a four-log inhibition ($p < 0.001$) as compared to the specimens from the NT, PT, and PT – Zn groups (**Figure 4E**). Similar results were obtained for planktonic bacteria with the PT – Ag Zn 50 50 group demonstrating a two-log inhibition ($p < 0.001$) as compared to the NT, PT,

and PT – Zn implants (**Figure 4F**). The NT, PT, and PT - Zn implants did not prevent biofilm formation on the implants where bacteria were observed to be on top of each other in multiple layers (**Figure 5**). The PT – Ag and PT – Ag Zn implants, on the other hand, rarely displayed any attached bacteria. In the rare occasions where bacteria were found on the surface of the PT – Ag and PT – Ag Zn implants, they were primarily observed inside the PEO micropores.

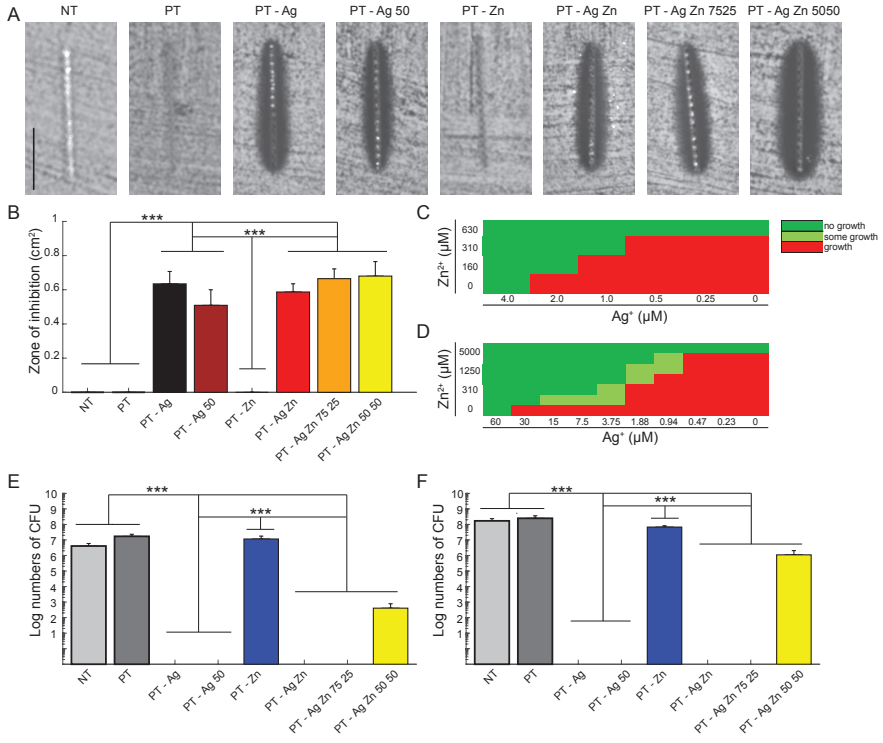

Figure 4. The antibacterial leaching activity and quantification of bactericidal activity *in vitro* against MRSA USA300. (A) The images of the antibacterial inhibition zones around the specimens after 24 h on agar with an inoculum of 10^7 CFU/ml. (B) The quantification of the area of the inhibition zones. (C) The minimum inhibitory and (D) bactericidal concentration for the different concentrations of Ag^+ and/or Zn^{2+} ions. (E) The adherent and (F) planktonic bactericidal activity against an inoculum of 2×10^3 CFU/ml after 24 h. *, $p < 0.05$, **, $p < 0.01$, ***, $p < 0.001$. All experiments were performed in triplicates. Scale bar = 1 cm.

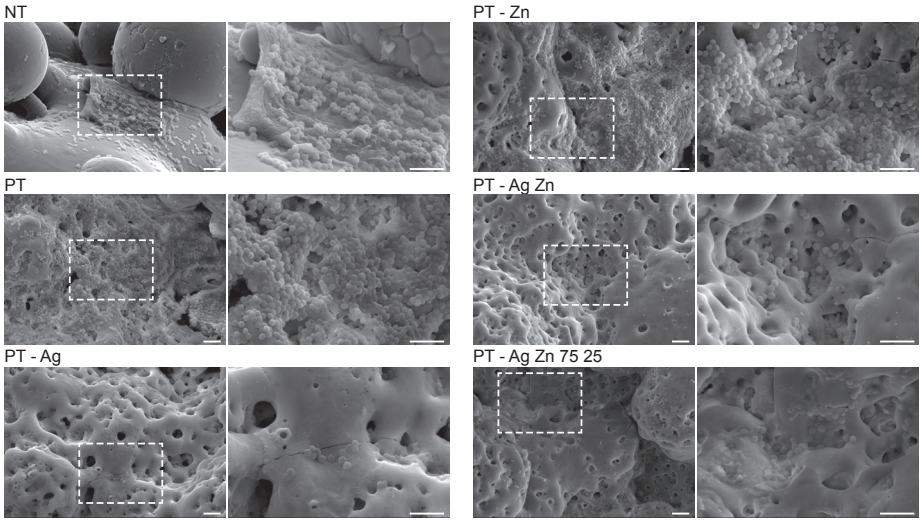

Figure 5. Biofilm formation on the implants (n=2) following 48 h incubation in TSB 1% glucose as visualized using low (2000x) and high (8000x) magnification SEM images. Scale bar = 5 µm.

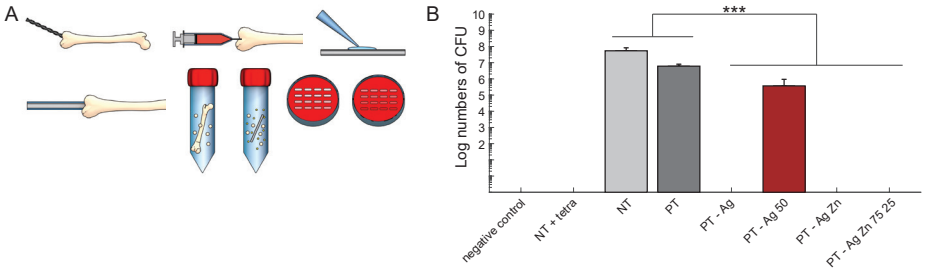

Figure 6. The bactericidal activity of the implants against MRSA USA300 in an *ex vivo* femoral mouse model. (A) A 0.5 mm hole was created into the intramedullary canal of mouse femurs by drilling through the epicondyle. Thereafter, the bone marrow was removed and 2 µl PBS was injected. The mouse femurs were inoculated with 2×10^2 CFU and were implanted intramedullary. After 24 h of incubation, the femurs were homogenized and 10-fold serial dilutions of the homogenate were plated on blood agar plates. (B) The quantification of the number of CFU following 24 h incubation *ex vivo*. To confirm proper sterilization, one femur without implant and bacterial inoculum was processed and analyzed (negative control). For validation of the model, 2 µl of tetracycline was injected intramedullary prior to implantation with an inoculated implant (NT+tetra). n=3, ***, $p < 0.001$.

5.3.4.3 Ex vivo antibacterial activity

The *ex vivo* bactericidal activity of the implants was evaluated in a murine femoral infection model (**Figure 6A**). After 24 h of incubation, the PT – Ag, PT – Ag Zn and PT – Ag Zn 75 25 implants fully eradicated the bacterial inoculum while the specimens from the PT – Ag 50 group reduced the bacterial growth by 2-log ($p < 0.001$) as compared to the NT and PT implants (**Figure 6B**).

5.3.5 Cytocompatibility of MC3T3-E1 cells on biofunctionalized implants

At day 1, the MC3T3-E1 cells cultured on all implants demonstrated similar metabolic activities while after day 3 the metabolic activity was enhanced for cells on the PT – Zn implants as compared to the PT – Ag, PT – Ag 50, and PT Ag Zn 75 25 implants ($p < 0.05$, $p < 0.05$ and $p < 0.01$, respectively; **Figure 7A**). After 7 days, the metabolic activities of the cells present on the PT and PT – Zn implants were significantly higher than those of the NT implants ($p < 0.001$). Similarly, the metabolic activity of cells on the PT group was significantly higher than that of the PT – Ag, PT – Ag 50, and PT – Ag Zn 75 25 groups ($p < 0.001$, $p < 0.01$ and $p < 0.01$, respectively). The same held for the PT – Zn implants as compared to the PT – Ag, PT – Ag 50, and PT – Ag Zn 75 25 implants ($p < 0.001$). After 11 days, cells on the PT and PT – Zn groups displayed enhanced metabolic activity as compared to the NT group ($p < 0.001$). The same was observed for PT as compared to PT – Ag, PT – Ag 50, and PT – Ag Zn 75 25 ($p < 0.05$) and PT – Zn as compared to PT – Ag, PT – Ag 50, and PT – Ag Zn 75 25 ($p < 0.001$). The ALP activity did not differ significantly between the different groups after 11 days (**Figure 7B**). The cell morphology after 11 days demonstrated that all surfaces had cell attachment on significant parts of their surface **(Figure 7C**). The cells showed elongated morphologies and were found to span large areas.

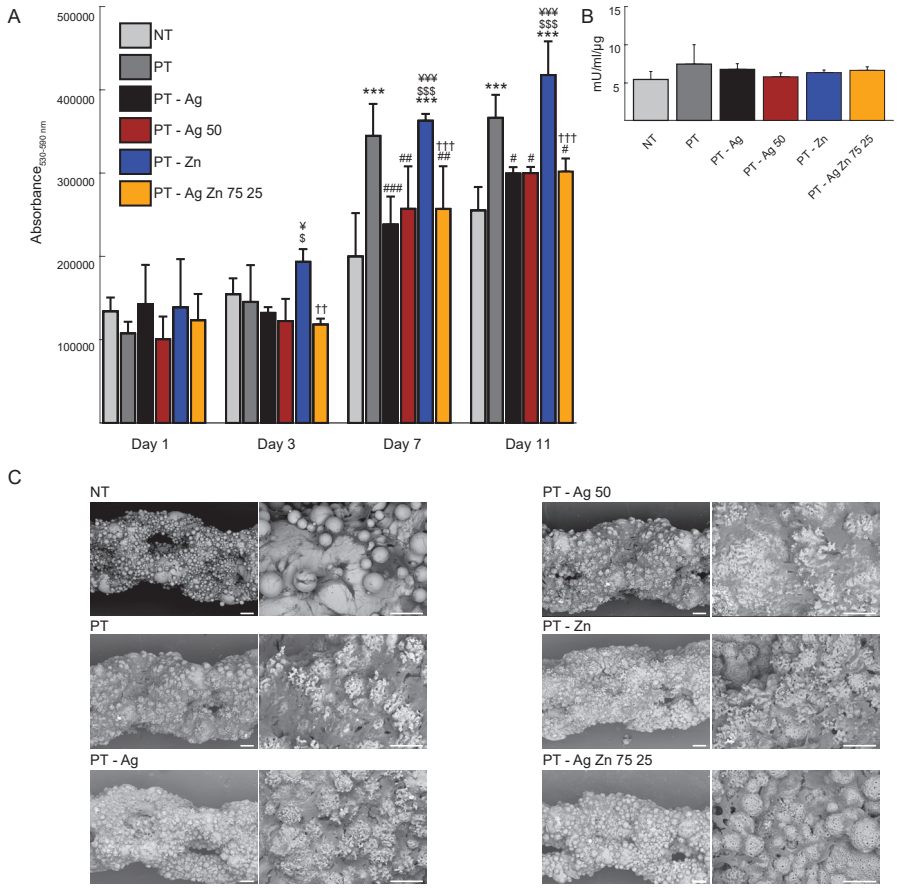

Figure 7. Cytocompatibility assessment using MC3T3-E1 pre-osteoblasts cultured on the implants (n=4). (A) The metabolic activity of the MC3T3-E1 cells indicated as the optical density ($OD_{530\text{-}590nm}$) determined by the Presto blue assay after 1, 3, and 7 days of culture. (B) The ALP activity and (C) SEM images demonstrating the cell morphology and the spread of the MC3T3-E1 cells on the implants after 11 days of culture. *, $p < 0.05$, **, $p < 0.01$ ***, $p < 0.001$. *vs NT, # vs PT, ¥ vs PT – Ag, $ vs PT – Ag 50, † vs PT – Zn. Scale bar = 50 µm.

5.4 DISCUSSION

To improve implant longevity, the prevention of IAI induced by antibiotic-resistant bacteria is essential. Multifunctional implant surfaces that possess antibacterial activity and stimulate bony ingrowth are important tools in our quest to achieve that goal. AM enables the fabrication of highly porous implants that could benefit the most from these multifunctional surfaces, as bacteria could adhere to the internal surfaces of such porous structures and more easily survive the sterilization process. On the other hand, however, the much larger internal surface area

of AM porous biomaterials amplifies the effects of the applied surface biofunctionalization. In this study, PEO biofunctionalized SLM porous titanium implants bearing Ag and Zn NPs demonstrated multifunctional behavior including the prevention of colonization by MRSA both *in vitro* as well as *ex vivo* without inducing cytotoxicity, while PT – Zn implants further enhanced the metabolic activity of pre-osteoblast cells.

Currently, IAI account for 20% of orthopedic implant failures [29]. Most strains involved in IAI displayed resistance to at least one antibiotic [30] reducing treatment rates to 48% [31] and enhancing patient morbidities [32]. With the number of patients anticipated to increase up to 600% by 2030 [33] due to an aging and increasingly obese population, these complications will continue to increase the burden for patients and society [34]. Although the need for multifunctional implant surfaces has been recognized for some time, the synthesis of surfaces that possess antibacterial efficacy and osteogenic behavior has proven to be challenging. Both properties go hand in hand, as proper bone ingrowth limits the space for bacteria to cause infection while adherent bacteria on the implant surfaces impair the proper adherence and differentiation of osteogenic cells [35]. Therefore, multifunctional surfaces should contain multiple elements to induce both antibacterial and osteogenic properties [36]. Ideally, a multifunctional surface would promote rapid osseointegration and provide both immediate and long-term protection against bacteria adhering to the implant surface as well as those present in the tissue surrounding the implant. The development of such types of surfaces in a time- and cost-efficient manner requires a single-step process that provides strong adhesion between the surface and implant substrate and is applicable to complex geometries without altering the mechanical properties of the implant. The use of PEO with Ca/P-based electrolytes containing Ag and Zn NPs does comply with all of the abovementioned criteria [14, 37, 38].

While the antibacterial properties of Ag have been known for some time, there are some concerns regarding the cytotoxicity of silver-based agents [39]. Meanwhile, Zn has been applied in various forms on biofunctionalized biomaterials [40, 41] and has demonstrated bactericidal activity against a wide spectrum of Gram-positive and Gram-negative bacteria [22, 42-44] as well as osteogenic properties including the stimulation of the adhesion, proliferation, and osteogenic differentiation of mesenchymal stem cells (MSCs) [45-47]. Furthermore, Zn is five times less toxic for human MSCs as compared to Ag [48, 49]. However, Ag and Zn NPs have, thus far, not been incorporated collectively onto the surface of porous AM titanium implants with vast surface areas to fully exploit the aforementioned properties of Ag and Zn NPs.

The biofunctionalized implants in this study released Zn^{2+} and Ag^{+} ions for up to 28 days. The addition of Zn NPs to the PEO electrolyte resulted in a reduced rate of Ag^{+} released from the PT – Ag Zn implants as compared to the PT – Ag group. This observation may originate from a reduced incorporation of Ag NP onto the implant surface or a reduced rate of Ag^{+} oxidation and

subsequent release due to galvanic coupling [46, 50]. Since Zn has a lower standard electrode potential as compared to both Ag and the TiO_2 surface layer [51], the Zn NPs will function as local anodes, Ag NP as local cathodes, and the TiO_2 surface layer as the electron pathway, ultimately resulting in the oxidation of the Zn NP and subsequent Zn^{2+} release. The oxidation of Ag NP and, thus, the release of Ag^+ is, however, inhibited. Simultaneously, H^+ will be consumed from the surrounding environment during the micro-galvanic coupling process, which disturbs the ATP synthesis and ion transportation inside bacteria, thereby contributing to the creation of an antibacterial zone in the proximity of the implant surface [51].

The ion release from the implant surface results in an antibacterial leaching behavior, which in this study is reflected by the zone of inhibition. We observed that the PT – Ag and PT – Ag Zn implants exhibited a significant zone of inhibition, whereas the PT – Zn implants did not, which concurs with the fact that the MIC of Zn^{2+} is 100 to 150 times higher than that of Ag^+ [52]. We also observed that combining Zn^{2+} and Ag^+ allowed to reduce the Ag^+ concentration by up to 120 folds while keeping similar MIC and MBC values, respectively.

Zn is less toxic for bacteria than Ag. That is because Zn is crucial in various bacterial metabolic processes, such as ATP synthesis, and has been shown to play a role in inter-bacterial communication between *Staphylococci* resulting in enhanced bacterial adhesion and biofilm formation [53, 54]. In contrast, Ag is not vital for bacterial cells and irreversibly targets cytoplasmic proteins, enzymatic functioning, and the DNA replication machinery resulting in cell death [55-57]. The exact mechanism underlying the synergistic antibacterial behavior between Zn and Ag is not fully understood. However, ROS may play a role in the observed synergistic antibacterial behavior between Zn^{2+} and Ag^+ [58, 59].

Due to their short-life time, however, ROS do not enhance the leaching activity of the implants. Instead, they ward off bacteria that attach to the surface. All PEO biofunctionalized implants in this study generated hydroxyl radicals whereas NT implants did not. This suggests that the formation of rutile and anatase TiO_2 phases during the PEO process contributes to ROS generation [14], which has been shown to prevent bacterial adhesion [60]. The PT – Zn implants generated the highest levels of hydroxyl and methyl radical generation, followed by the PT – Ag implants whereas the combinations of Ag and Zn ratios reduced the amount of the hydroxyl radical formed and annihilated the formation of methyl radicals. Ag doping of Zn photocatalytic microspheres has demonstrated to enhance the formation of hydroxyl radicals [61, 62]. However, the exact mechanisms through which the biofunctionalization of SLM titanium implants with both Ag and Zn NPs affects the formation of ROS as compared to either nanoparticles species alone are not clear and need to be elucidated.

Infection with MRSA worsens the patient's prognosis compared to methicillin-susceptible *Staphylococcus aureus* strains [63]. It is, therefore, relevant to test biofunctionalized implants

in an adequate model against MRSA. Therefore, we investigated the antibacterial activity in a murine *ex vivo* model to simulate *in vivo* conditions. Although *ex vivo* models lack an active immune system and the ability of bony ingrowth, the bone extracellular matrix has shown to greatly support the adhesion of *Staphylococcus aureus* and, thus, affect the infection process [64]. In this model, the PT – Ag, PT – Ag Zn, and PT – Ag Zn 75 25 implants fully eradicated a bacterial inoculum within 24 h, whereas the PT – Ag 50 implants induced a two-log reduction in the number of CFU as compared to the PT and PT – Zn groups.

In addition to improving the antibacterial properties of the implants, the addition of Zn to Ag-bearing surfaces is important to reduce the cytotoxicity caused by Ag. In our study, the PT – Zn implants enhanced the metabolic activity of the MC3T3-E1 cells after 3, 7, and 11 days as compared to NT and Ag-biofunctionalized implants, while no difference in the ALP expression was detected after 11 days. Our results are partially in line with previous studies that have demonstrated the effects of such ions on both cell adhesion and osteogenic differentiation *in vitro* [65, 66] and have been shown to correlate with enhanced bone ingrowth *in vivo* [24]. Taken together, the results of the current study suggest that the dose of Zn^{2+} on our implants might have been too low to initiate a clear effect on the ALP activity or that these effects may be present at other time points. Meanwhile, the cytotoxicity of Ag has shown to differ between *in vitro* and *in vivo* experiments and can affect the proper functioning of neutrophils [20, 67]. Combining Ag and Zn in a plasma sprayed hydroxyapatite coating has resulted in enhanced bone regeneration in orthopedic and dental *in vivo* models [68]. Titanium biomaterials biofunctionalized by PEO through the addition of Ag NPs have thus far not been investigated *in vivo* while PEO-biofunctionalized biomaterials with Ca/P electrolyte [15, 69] as well as with Zn [70, 71] have both shown to stimulate osseointegration. Further *in vivo* studies are, therefore, required to take the next steps in translating the results of the current study to clinical settings.

Altogether, the number of AM porous implants is anticipated to increase substantially. The prevention of infection associated with such types of implants is, therefore, crucial. Given that over 60% of IAI are induced by *Staphylococci* [6], and *S. aureus* and *S. epidermidis* strains exhibit ever increasing levels of antibiotic-resistance [72-74], the current prophylaxis regimes are becoming less effective [7], thereby putting patients at risk and warranting the development of novel strategies to prevent IAI by resistant bacteria. One of the most important strategies in this regard is the surface biofunctionalization of AM implants with Ag and Zn NPs. Combining Ag and Zn results in synergistic antibacterial behavior [50, 75, 76], which allows for reducing the required concentration of Ag ions by two orders of magnitude and is likely caused by a combination of ion release and ROS formation on the implant surface. This will make the development of bacterial resistance unlikely, which is crucial to prevent future infections on AM porous implants.

5.5 CONCLUSIONS

To improve the longevity of orthopedic implants, multifunctional implant surfaces that both prevent bacterial infection and strengthen the fixation of the implant inside the host bony tissue are being developed. Here, we designed and synthesized highly porous SLM titanium bone implants that were biofunctionalized using PEO with Ag and Zn NPs in ratios from 0 to 100%. The biofunctionalized implants with ratios of up to 75% Ag and 25% Zn fully eradicated bacterial inocula within 24 h in both *in vitro* and *ex vivo* experiments. Combining Ag and Zn NPs on the implant surface resulted in reduced rates of Ag ion release and ROS formation. Furthermore, the Zn-biofunctionalized implants enhanced the metabolic activity of pre-osteoblast cells as compared to the NT and Ag-biofunctionalized implants. Therefore, the implants biofunctionalized with Ag and Zn NPs hold great promise as candidates for further development towards multifunctional bone implants.

ACKNOWLEDGEMENTS

The research for this paper was financially supported by the Prosperos project, funded by the Interreg VA Flanders – The Netherlands program, CCI grant no. 2014TC16RFCB046.

REFERENCES

[1] M. Khan, K. Osman, G. Green, F.S. Haddad, The epidemiology of failure in total knee arthroplasty, The Bone & Joint Journal 98-B (2016) 105-112.

[2] E. Lenguerrand, M.R. Whitehouse, A.D. Beswick, S.A. Jones, M.L. Porter, A.W. Blom, Revision for prosthetic joint infection following hip arthroplasty, Bone & Joint Research 6 (2017) 391-398.

[3] B.H. Kapadia, R.A. Berg, J.A. Daley, J. Fritz, A. Bhave, M.A. Mont, Periprosthetic joint infection, The Lancet 387 (2016) 386-394.

[4] C.R. Arciola, D. Campoccia, G.D. Ehrlich, L. Montanaro, Biofilm-based implant infections in orthopaedics, Advances in Experimental Medicine and Biology 1 (2015) 29-46.

[5] L. Hall-Stoodley, J.W. Costerton, P. Stoodley, Bacterial biofilms: from the natural environment to infectious diseases, Nature Reviews Microbiology 2 (2004) 95-108.

[6] D. Campoccia, L. Montanaro, C.R. Arciola, The significance of infection related to orthopedic devices and issues of antibiotic resistance, Biomaterials 27 (2006) 2331-2339.

[7] B. Li, T.J. Webster, Bacteria antibiotic resistance: new challenges and opportunities for implant-associated orthopedic infections, Journal of Orthopaedic Research 36 (2017) 22-32.

[8] K.L. Garvin, S.H. Hinrichs, U. J.A., Emerging antibiotic-resistant bacteria. Their treatment in total joint arthroplasty, Clinical Orthopaedics and Related Research 369 (1999) 110-123.

[9] J. Parvizi, I.M. Pawasarat, K.A. Azzam, A. Joshi, E.N. Hansen, K.J. Bozic, Periprosthetic joint infection, The Journal of Arthroplasty 25 (2010) 103-107.

[10] K.R. Berend, A.V. Lombardi, M.J. Morris, A.G. Bergeson, J.B. Adams, M.A. Sneller, Two-stage treatment of hip periprosthetic joint infection is associated with a high rate of infection control but high mortality, Clinical Orthopaedics and Related Research 471 (2012) 510-518.

[11] A. Zadpoor, Design for additive bio-manufacturing: from patient-specific medical devices to rationally designed meta-biomaterials, International Journal of Molecular Sciences 18 (2017).

[12] S. Ahmadi, S. Yavari, R. Wauthle, B. Pouran, J. Schrooten, H. Weinans, A. Zadpoor, Additively manufactured open-cell porous biomaterials made from six different space-filling unit cells: the mechanical and morphological properties, Materials 8 (2015) 1871-1896.

[13] F.S.L. Bobbert, K. Lietaert, A.A. Eftekhari, B. Pouran, S.M. Ahmadi, H. Weinans, A.A. Zadpoor, Additively manufactured metallic porous biomaterials based on minimal surfaces: A unique combination of topological, mechanical, and mass transport properties, Acta Biomaterialia 53 (2017) 572-584.

[14] I.A.J. van Hengel, M. Riool, L.E. Fratila-Apachitei, J. Witte-Bouma, E. Farrell, A.A. Zadpoor, S.A.J. Zaat, I. Apachitei, Selective laser melting porous metallic implants with immobilized silver nanoparticles kill and prevent biofilm formation by methicillin-resistant Staphylococcus aureus, Biomaterials 140 (2017) 1-15.

[15] C.-J. Chung, R.-T. Su, H.-J. Chu, H.-T. Chen, H.-K. Tsou, J.-L. He, Plasma electrolytic oxidation of titanium and improvement in osseointegration, Journal of Biomedical Materials Research Part B: Applied Biomaterials 101B (2013) 1023-1030.

[16] J.S. Kim, E. Kuk, K.N. Yu, J.-H. Kim, S.J. Park, H.J. Lee, S.H. Kim, Y.K. Park, Y.H. Park, C.-Y. Hwang, Y.-K. Kim, Y.-S. Lee, D.H. Jeong, M.-H. Cho, Antimicrobial effects of silver nanoparticles, Nanomedicine: Nanotechnology, Biology and Medicine 3 (2007) 95-101.

[17] A. Nanda, M. Saravanan, Biosynthesis of silver nanoparticles from Staphylococcus aureus and its antimicrobial activity against MRSA and MRSE, Nanomedicine: Nanotechnology, Biology and Medicine 5 (2009) 452-456.

[18] G. Franci, A. Falanga, S. Galdiero, L. Palomba, M. Rai, G. Morelli, M. Galdiero, Silver nanoparticles as potential antibacterial agents, Molecules 20 (2015) 8856-8874.

[19] A. Panacek, L. Kvitek, M. Smekalova, R. Vecerova, M. Kolar, M. Roderova, F. Dycka, M. Sebela, R. Prucek, O. Tomanec, R. Zboril, Bacterial resistance to silver nanoparticles and how to overcome it, Nat Nanotechnol 13 (2018) 65-71.

[20] M. Croes, S. Bakhshandeh, I.A.J. van Hengel, K. Lietaert, K.P.M. van Kessel, B. Pouran, B.C.H. van der Wal, H.C. Vogely, W. Van Hecke, A.C. Fluit, C.H.E. Boel, J. Alblas, A.A. Zadpoor, H. Weinans, S. Amin Yavari, Antibacterial and immunogenic behavior of silver coatings on additively manufactured porous titanium, Acta Biomater 81 (2018) 315-327.

[21] N. Duran, M. Duran, M.B. de Jesus, A.B. Seabra, W.J. Favaro, G. Nakazato, Silver nanoparticles: a new view on mechanistic aspects on antimicrobial activity, Nanomedicine 12 (2016) 789-799.

[22] A. Sirelkhatim, S. Mahmud, A. Seeni, N.H.M. Kaus, L.C. Ann, S.K.M. Bakhori, H. Hasan, D. Mohamad, Review on zinc oxide nanoparticles: antibacterial activity and toxicity mechanism, Nanomicro Lett 7 (2015) 219-242.

[23] X. Shen, Y. Hu, G. Xu, W. Chen, K. Xu, Q. Ran, P. Ma, Y. Zhang, J. Li, K. Cai, Regulation of the biological functions of osteoblasts and bone formation by Zn-incorporated coating on microrough titanium, ACS Appl Mater Interfaces 6 (2014) 16426-40.

[24] Y. Qiao, W. Zhang, P. Tian, F. Meng, H. Zhu, X. Jiang, X. Liu, P.K. Chu, Stimulation of bone growth following zinc incorporation into biomaterials, Biomaterials 35 (2014) 6882-97.

[25] B.S. Necula, J.P.T.M. van Leeuwen, L.E. Fratila-Apachitei, S.A.J. Zaat, I. Apachitei, J. Duszczyk, In vitro cytotoxicity evaluation of porous TiO2–Ag antibacterial coatings for human fetal osteoblasts, Acta Biomaterialia 8 (2012) 4191-4197.

[26] L. Lara Rodriguez, P.A. Sundaram, E. Rosim-Fachini, A.M. Padovani, N. Diffoot-Carlo, Plasma electrolytic oxidation coatings on γTiAl alloy for potential biomedical applications, Journal of Biomedical Materials Research Part B: Applied Biomaterials 102 (2014) 988-1001.

[27] B.S. Necula, L.E. Fratila-Apachitei, S.A.J. Zaat, I. Apachitei, J. Duszczyk, In vitro antibacterial activity of porous TiO2–Ag composite layers against methicillin-resistant Staphylococcus aureus, Acta Biomaterialia 5 (2009) 3573-3580.

[28] F.C. Tenover, R.V. Goering, Methicillin-resistant Staphylococcus aureus strain USA300: origin and epidemiology, J Antimicrob Chemother 64 (2009) 441-6.

[29] K.J. Bozic, S.M. Kurtz, E. Lau, K. Ong, T.P. Vail, D.J. Berry, The epidemiology of revision total hip arthroplasty in the United States, J Bone Joint Surg Am 91 (2009) 128-33.

[30] C.R. Arciola, D. Campoccia, Y.H. An, L. Baldassarri, V. Pirini, M.E. Donati, F. Pegreffi, L. Montanaro, Prevalence and antibiotic resistance of 15 minor staphylococcal species colonizing orthopedic implants, The International Journal of Artificial Organs 29 (2006) 395-401.

[31] D.J. Kilgus, D.J. Howe, A. Strang, Results of periprosthetic hip and knee infections caused by resistant bacteria, Clinical Orthopaedics and Related Research 404 (2002) 116-124.

[32] S. Inoue, T. Moriyama, Y. Horinouchi, T. Tachibana, F. Okada, K. Maruo, S. Yoshiya, Comparison of clinical features and outcomes of Staphylococcus aureus vertebral osteomyelitis caused by methicillin-resistant and methicillin-sensitive strains, Springerplus 2 (2013) 1-7.

[33] S. Kurtz, K. Ong, E. Lau, F. Mowat, M. Halpern, Projections of primary and revision hip and knee arthroplasty in the United States from 2005 to 2030, J Bone Joint Surg Am 89 (2007) 780-5.

[34] S.M. Kurtz, E. Lau, H. Watson, J.K. Schmier, J. Parvizi, Economic burden of periprosthetic joint infection in the United States, J Arthroplasty 27 (2012) 61-65.

[35] A.G. Gristina, P. Naylor, Q. Myrvik, Infections from biomaterials and implants: a race for the surface, Med Prog Technol 14 (1989) 205-224.

[36] J. Raphel, M. Holodniy, S.B. Goodman, S.C. Heilshorn, Multifunctional coatings to simultaneously promote osseointegration and prevent infection of orthopaedic implants, Biomaterials 84 (2016) 301-314.

[37] B.S. Necula, I. Apachitei, F.D. Tichelaar, L.E. Fratila-Apachitei, J. Duszczyk, An electron microscopical study on the growth of TiO2–Ag antibacterial coatings on Ti6Al7Nb biomedical alloy, Acta Biomaterialia 7 (2011) 2751-2757.

[38] Z. Gorgin Karaji, R. Hedayati, B. Pouran, I. Apachitei, A.A. Zadpoor, Effects of plasma electrolytic oxidation process on the mechanical properties of additively manufactured porous biomaterials, Mater Sci Eng C Mater Biol Appl 76 (2017) 406-416.

[39] C.E. Albers, W. Hofstetter, K.A. Siebenrock, R. Landmann, F.M. Klenke, In vitro cytotoxicity of silver nanoparticles on osteoblasts and osteoclasts at antibacterial concentrations, Nanotoxicology 7 (2013) 30-6.

[40] Y. Su, K. Wang, J. Gao, Y. Yang, Y.X. Qin, Y. Zheng, D. Zhu, Enhanced cytocompatibility and antibacterial property of zinc phosphate coating on biodegradable zinc materials, Acta Biomater (2019) 174-185.

[41 R. Zhang, X. Liu, Z. Xiong, Q. Huang, X. Yang, H. Yan, J. Ma, Q. Feng, Z. Shen, Novel micro/nanostructured TiO2/ZnO coating with antibacterial capacity and cytocompatibility, Ceramics International 44 (2018) 9711-9719.

[42] N. Jones, B. Ray, K.T. Ranjit, A.C. Manna, Antibacterial activity of ZnO nanoparticle suspensions on a broad spectrum of microorganisms, FEMS Microbiol Lett 279 (2008) 71-6.

[43] A. Jesline, N.P. John, P.M. Narayanan, C. Vani, S. Murugan, Antimicrobial activity of zinc and titanium dioxide nanoparticles against biofilm-producing methicillin-resistant Staphylococcus aureus, Applied Nanoscience 5 (2014) 157-162.

[44] U. Kadiyala, E.S. Turali-Emre, J.H. Bahng, N.A. Kotov, J.S. VanEpps, Unexpected insights into antibacterial activity of zinc oxide nanoparticles against methicillin resistant Staphylococcus aureus (MRSA), Nanoscale 10 (2018) 4927-4939.

[45] H. Hu, W. Zhang, Y. Qiao, X. Jiang, X. Liu, C. Ding, Antibacterial activity and increased bone marrow stem cell functions of Zn-incorporated TiO2 coatings on titanium, Acta Biomater 8 (2012) 904-15.

[46] G. Jin, H. Cao, Y. Qiao, F. Meng, H. Zhu, X. Liu, Osteogenic activity and antibacterial effect of zinc ion implanted titanium, Colloids Surf B Biointerfaces 117 (2014) 158-65.

[47] Y. Yu, G. Jin, Y. Xue, D. Wang, X. Liu, J. Sun, Multifunctions of dual Zn/Mg ion co-implanted titanium on osteogenesis, angiogenesis and bacteria inhibition for dental implants, Acta Biomater 49 (2017) 590-603.

[48] S. Hackenberg, A. Scherzed, M. Kessler, S. Hummel, A. Technau, K. Froelich, C. Ginzkey, C. Koehler, R. Hagen, N. Kleinsasser, Silver nanoparticles: evaluation of DNA damage, toxicity and functional impairment in human mesenchymal stem cells, Toxicol Lett 201 (2011) 27-33.

[49] P. Ickrath, M. Wagner, A. Scherzad, T. Gehrke, M. Burghartz, R. Hagen, K. Radeloff, N. Kleinsasser, S. Hackenberg, Time-dependent toxic and genotoxic effects of zinc oxide nanoparticles after long-term and repetitive exposure to human mesenchymal stem cells, Int J Environ Res Public Health 14 (2017).

[50] G. Jin, H. Qin, H. Cao, S. Qian, Y. Zhao, X. Peng, X. Zhang, X. Liu, P.K. Chu, Synergistic effects of dual Zn/Ag ion implantation in osteogenic activity and antibacterial ability of titanium, Biomaterials 35 (2014) 7699-713.

[51] H. Cao, X. Liu, F. Meng, P.K. Chu, Biological actions of silver nanoparticles embedded in titanium controlled by micro-galvanic effects, Biomaterials 32 (2011) 693-705.

[52] S. Ferraris, S. Spriano, Antibacterial titanium surfaces for medical implants, Mater Sci Eng C Mater Biol Appl 61 (2016) 965-78.

[53] D. He, C.J. Miller, T.D. Waite, Fenton-like zero-valent silver nanoparticle-mediated hydroxyl radical production, Journal of Catalysis 317 (2014) 198-205.

[54] D.G. Conrady, C.C. Brescia, K. Horii, A.A. Weiss, D.J. Hassett, A.B. Herr, A zinc-dependent adhesion module is responsible for intercellular adhesion in staphylococcal biofilms, Proceedings of the National Academy of Sciences of the United States of America 105 (2008) 19456-19461.

[55] T.C. Dakal, A. Kumar, R.S. Majumdar, V. Yadav, Mechanistic basis of antimicrobial actions of silver nanoparticles, Front Microbiol 7 (2016) 1831.

[56] L. Wang, C. Hu, L. Shao, The antimicrobial activity of nanoparticles: present situation and prospects for the future, Int J Nanomedicine 12 (2017) 1227-1249.

[57] M. Rai, A.P. Ingle, R. Pandit, P. Paralikar, I. Gupta, M.V. Chaud, C.A. Dos Santos, Broadening the spectrum of small-molecule antibacterials by metallic nanoparticles to overcome microbial resistance, Int J Pharm 532 (2017) 139-148.

[58] T. Wei, Q. Yu, H. Chen, Responsive and synergistic antibacterial coatings: fighting against bacteria in a smart and effective way, Adv Healthc Mater 8 (2019).

[59] X. Wang, S. Liu, M. Li, P. Yu, X. Chu, L. Li, G. Tan, Y. Wang, X. Chen, Y. Zhang, C. Ning, The synergistic antibacterial activity and mechanism of multicomponent metal ions-containing aqueous solutions against Staphylococcus aureus, J Inorg Biochem 163 (2016) 214-220.

[60] B. Del Curto, M.F. Brunella, C. Giordano, M.P. Pedeferri, V. Valtulina, L. Visai, A. Cigada, Decreased bacterial adhesion to surface-treated titanium, The International Journal of Artificial Organs 28 (2005) 718-730.

[61] W. Lu, S. Gao, J. Wang, One-pot synthesis of Ag/ZnO self-assembled 3D hollow microspheres with enhanced photocatalytic performance, J. Phys. Chem. C 112 (2008) 16792–16800.

[62] O. Bechambi, M. Chalbi, W. Najjar, S. Sayadi, Photocatalytic activity of ZnO doped with Ag on the degradation of endocrine disrupting under UV irradiation and the investigation of its antibacterial activity, Applied Surface Science 347 (2015) 414-420.

[63] D. Teterycz, T. Ferry, D. Lew, R. Stern, M. Assal, P. Hoffmeyer, L. Bernard, I. Uckay, Outcome of orthopedic implant infections due to different staphylococci, Int J Infect Dis 14 (2010) 913-918.

[64] M.C. Hudson, W.K. Ramp, K.P. Frankenburg, Staphylococcus aureus adhesion to bone matrix, FEMS Microbiology Letters 173 (1999) 279-284.

[65] K. Yusa, O. Yamamoto, M. Fukuda, S. Koyota, Y. Koizumi, T. Sugiyama, In vitro prominent bone regeneration by release zinc ion from Zn-modified implant, Biochem Biophys Res Commun 412 (2011) 273-8.

[66] Z. Zhang, B. Gu, W. Zhang, G. Kan, J. Sun, The enhanced characteristics of osteoblast adhesion to porous Zinc–TiO2 coating prepared by plasma electrolytic oxidation, Applied Surface Science 258 (2012) 6504-6511.

[67] S. Bakhshandeh, Z. Gorgin Karaji, K. Lietaert, A.C. Fluit, C.H.E. Boel, H.C. Vogely, T. Vermonden, W.E. Hennink, H. Weinans, A.A. Zadpoor, S. Amin Yavari, Simultaneous delivery of multiple antibacterial agents from additively manufactured porous biomaterials to fully eradicate planktonic and adherent Staphylococcus aureus, ACS Applied Materials & Interfaces 9 (2017) 25691-25699.

[68] A.A. Vu, S.F. Robertson, D. Ke, A. Bandyopadhyay, S. Bose, Mechanical and biological properties of ZnO, SiO2, and Ag2O doped plasma sprayed hydroxyapatite coating for orthopaedic and dental applications, Acta Biomater 92 (2019) 325-335.

[69] A. Santos-Coquillat, E. Martínez-Campos, M. Mohedano, R. Martínez-Corriá, V. Ramos, R. Arrabal, E. Matykina, In vitro and in vivo evaluation of PEO-modified titanium for bone implant applications, Surface and Coatings Technology 347 (2018) 358-368.

[70] J. He, W. Feng, B.H. Zhao, W. Zhang, Z. Lin, In vivo effect of titanium implants with porous zinc-containing coatings prepared by plasma electrolytic oxidation method on osseointegration in rabbits, Int J Oral Maxillofac Implants 33 (2018) 298-310.

[71] Q. Zhao, L. Yi, L. Jiang, Y. Ma, H. Lin, J. Dong, Surface functionalization of titanium with zinc/strontium-doped titanium dioxide microporous coating via microarc oxidation, Nanomedicine 16 (2019) 149-161.

[72] S. Ravi, M. Zhu, C. Luey, S.W. Young, Antibiotic resistance in early periprosthetic joint infection, ANZ J Surg 86 (2016) 1014-1018.

[73] A.M. Malhas, R. Lawton, M. Reidy, D. Nathwani, B.A. Clift, Causative organisms in revision total hip & knee arthroplasty for infection: Increasing multi-antibiotic resistance in coagulase-negative Staphylococcus and the implications for antibiotic prophylaxis, Surgeon 13 (2015) 250-5.

[74] A. Bogut, J. Niedzwiadek, D. Strzelec-Nowak, J. Blacha, T. Mazurkiewicz, W. Marczynski, M. Koziol-Montewka, Infectious prosthetic hip joint loosening: bacterial species involved in its aetiology and their antibiotic resistance profiles against antibiotics recommended for the therapy of implant-associated infections, New Microbiol. 37 (2014) 209-218.

[75] G. Jin, H. Qin, H. Cao, Y. Qiao, Y. Zhao, X. Peng, X. Zhang, X. Liu, P.K. Chu, Zn/Ag micro-galvanic couples formed on titanium and osseointegration effects in the presence of S. aureus, Biomaterials 65 (2015) 22-31.

[76] L. Zhang, Q. Gao, Y. Han, Zn and Ag Co-doped anti-microbial TiO2 coatings on Ti by micro-arc oxidation, Journal of Materials Science & Technology 32 (2016) 919-924.

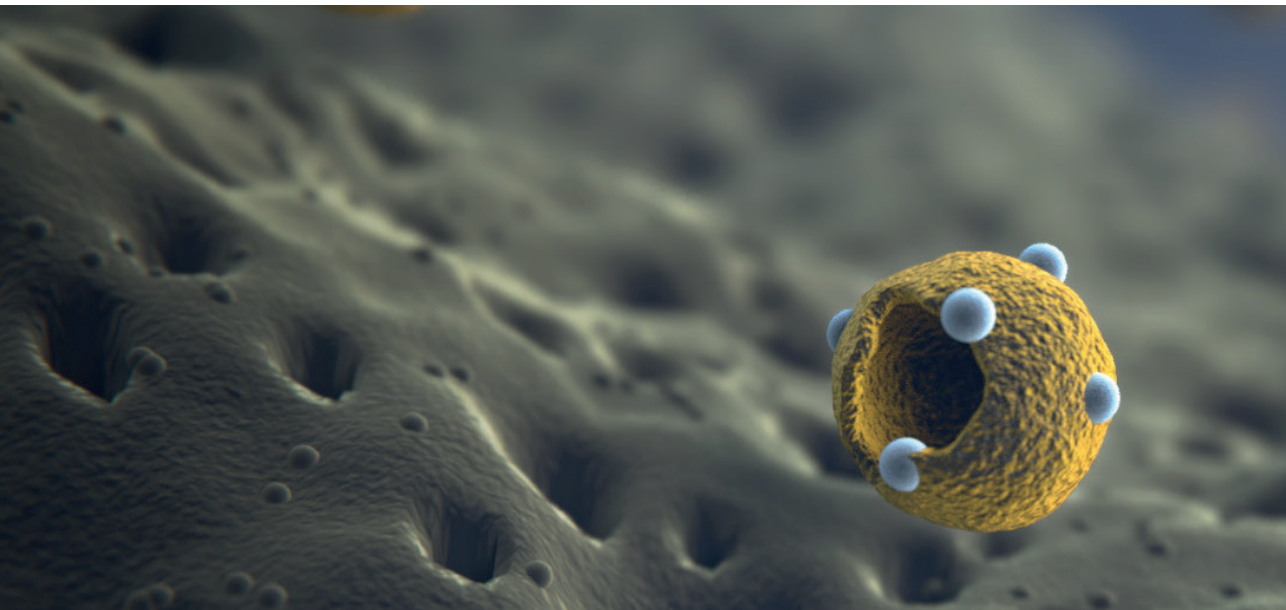

CHAPTER 06

Multifunctional implants with silver and strontium

I.A.J. van Hengel, F.S.A. Gelderman, S. Athanasiadis, M. Minneboo, H. Weinans, A.C. Fluit, B.C.J. van der Eerden, L.E. Fratila-Apachitei, I. Apachitei, A.A. Zadpoor, Functionality-packed additively manufactured porous titanium implants, Materials Today Bio 7 (2020) 100060.

The holy grail of orthopedic implant design is to ward off both aseptic and septic loosening for long enough that the implant outlives the patient. Questing this holy grail is feasible only if orthopedic biomaterials possess a long list of functionalities that enable them to discharge the onerous task of permanently replacing the native bone tissue. Here, we present a rationally designed and additively manufactured (AM) topologically ordered porous metallic biomaterial that is made from Ti6Al4V using selective laser melting and packs most (if not all) of the required functionalities into a single implant. In addition to presenting a fully interconnected porous structure and form-freedom that enables realization of patient-specific implants, the biomaterials developed here were biofunctionalized using plasma electrolytic oxidation to locally release both osteogenic (*i.e.*, strontium) and antibacterial (*i.e.*, silver ions) agents. The same single-step biofunctionalization process also incorporated hydroxyapatite into the surface of the implants. Our measurements verified the continued release of both types of active agents up to 28 days. Assessment of the antibacterial activity *in vitro* and in an *ex vivo* murine model demonstrated extraordinarily high levels of bactericidal effects against a highly virulent and multi-drug resistant *Staphylococcus aureus* (MRSA) strain (*i.e.*, USA300) with total eradication of both planktonic and adherent bacteria. This strong antibacterial behavior was combined with a significantly enhanced osteogenic behavior, as evidenced by significantly higher levels of alkaline phosphatase (ALP) activity compared to non-biofunctionalized implants. Finally, we discovered synergistic antibacterial behavior between strontium and silver ions, meaning that 4-32 folds lower concentrations of silver ions were required to achieve growth inhibition and total killing of bacteria. The functionality-packed biomaterial presented here demonstrates a unique combination of functionalities that make it an advanced prototype of future orthopedic biomaterials where implants will outlive patients.

6.1 INTRODUCTION

Orthopedic implants are the jewels of the medical device industry: they help keep tens of millions of people mobile. Like all other functional devices, however, they too have a limited service life. Generally, loosening marks the end of the lifespan of orthopedic implants when debilitating pain sets in and the patient's mobility diminishes to the point of complete evanescence.

Implant loosening can generally be categorized as being either aseptic or septic. The holy grail of orthopedic implant design is to ward off both aseptic and septic loosening for long enough that the implant outlives the patient. Researchers have been questing for this holy grail using a host of methodological approaches such as the synthesis of new biomaterials [1], the surface biofunctionalization of implants [2, 3], conceiving implants with bone-mimicking mechanical properties [4-7], and the local delivery of active agents [8, 9].

Frequently, however, these developments fall short of the ultimate goal, as the strenuous task of permanently replacing biological tissues requires mustering more than one single craft. Therefore, multiple functionalities need to be packed into one single piece of implant. To prevent aseptic loosening for as long as possible, one should improve the primary stability of the implant [10, 11], minimize stress shielding through bone-mimicking mechanical properties [12-15], provide a fully-interconnected volume-porous structure to allow for optimal bony ingrowth [16, 17], and stimulate the osteogenic differentiation of stem cells [18, 19]. As for septic loosening, both short-term and long-term implant-associated infections (IAIs) should be staved off through obliteration of the bacteria reaching the implant surface post-operatively, hematogenously, or contiguously [20]. This lengthy list of design objectives necessitates a re-interpretation of the term "multi-functional biomaterials" as biomaterials that are packed with many multi-domain functionalities that have been traditionally considered difficult to obtain and at times even contradictory.

A number of recent developments in additive manufacturing (AM) technologies [21-25], rational design processes [26, 27], and surface biofunctionalization techniques [28-30] have, however, made it feasible to incorporate many or all of the above-mentioned functionalities into one single piece of orthopedic implant. Here, we present an advanced prototype of such functionality-packed biomaterials that has the potential of meeting most (if not all) of our design objectives. First, we used rational design principles and AM for fabrication of topologically ordered porous titanium that present a fully interconnected porous micro-architecture to allow for optimal bony ingrowth [21, 22, 31], while exhibiting highly adjustable bone-mimicking mechanical properties [32-34] that minimize stress shielding. We also used the form-freedom offered by AM [35] to create bespoke implants that maximize

their primary stability. In the case of the present study, the bespoke geometry is that of the murine femora used for our *ex vivo* animal experiments. These miniaturized geometries also demonstrate the potential of our approach for fabrication of implants with fine geometrical details. These three functionalities are not the only advantages of our complex topological design: it was also optimized to increase the surface area of our implants by more than threefold as compared to a corresponding solid implant [36]. This multi-fold increase in the surface area amplifies the effects of the unique surface biofunctionalization technique used for addressing the remaining design objectives.

In addition to being functionality-packed, much of the novelty of the biomaterials presented here originates from the surface biofunctionalization technique applied to simultaneously prevent aseptic loosening through stimulation of the osteogenic differentiation of stem cells as well as septic loosening through both short- and long-term delivery of antibacterial agents from the entire volume of the AM porous biomaterials. Although the osteogenic [37-40] and antibacterial [29, 41-43] properties of the locally delivered active agents (*i.e.*, strontium and silver nanoparticles, respectively) are known, we explored the use of both agents simultaneously to generate multi-functional properties on the complex geometry of our highly porous AM implants.

6.2 MATERIALS AND METHODS

6.2.1 Topological design and AM

We used a hexagonal unit cell with an ultra-high surface to volume ratio [36] to design the micro-architecture of our topologically ordered porous structures. Miniaturized implants with a geometry optimized for implantation in murine femora were designed with a length of 4 cm and a diameter of 0.5 mm, resulting in a 35.6 surface to volume ratio. The specimens were AM using a customized selective laser melting (SLM) equipment (SLM-125, Realizer, Borchem, Germany) at the Additive Manufacturing Laboratory (TU Delft, Delft, The Netherlands) employing a YLM-400-AC Ytterbium fiber laser (IPG Photonics Corporation, Oxford, United States) operated inside an argon atmosphere with less than 0.2% oxygen content. Medical-grade (grade 23, ELI) Ti6Al4V powder (AP&C, Boisbriand, Quebec, Canada) with a spherical morphology, particles sizes between 10 and 45 μm, and a layer thickness of 50 μm was used. Laser processing was performed with an exposure time of 300 μs, a wavelength of 1070 ± 10 nm, and a laser power of 96 W, resulting in a laser spot size of 145 μm. Following SLM manufacturing, the loose powder particles were removed by vacuum cleaning. The specimens were subsequently ultrasonicated in acetone followed by immersion in 96% ethanol and demineralized water for 5 min each.

6.2.2 Surface biofunctionalization

The surface of AM porous implants was biofunctionalized using plasma electrolytic oxidation (PEO) in a custom-made setup consisting of an AC power source (50 Hz, type ACS 1500, ET Power Systems Ltd, Eyam, United Kingdom), a data acquisition board (SCXI, National Instruments, Austin, Texas, United States), a computer interface, and a double-walled glass electrolytic cell containing 800 ml electrolyte [44, 45]. The PEO electrolyte contained 0.15 M calcium acetate, 0.02 M calcium glycerophosphate, 0.3 M strontium acetate, and 3.0 g/L silver nanoparticles (AgNPs) (Sigma-Aldrich, St. Louis, Missouri, United States). AgNPs with a spherical morphology and a size distribution of 7 – 25 nm were dispersed in the PEO electrolyte by ultrasonication of 2 times 3 min to obtain a homogenous suspension in the electrolyte. In between the sonication steps, the electrolyte was stirred for 5 min at 500 rpm with a magnetic stirrer (IKA-Werke GmBH & Co. KG, Staufen, Germany) and stir bar of 40 x 8 mm (VWR, Radnor, Pennsylvania, United States).

PEO processing was performed under galvanostatic conditions with a current density of 20 A/dm^2. The implant served as the anode whereas a stainless-steel cylinder placed against the inner wall of the electrolytic cell formed the cathode. To maintain the homogeneity of the electrolyte, it was continuously stirred at 500 rpm. Furthermore, the temperature of the electrolyte was kept in a range of 6 ± 2 °C through a thermostatic bath (Thermo Haake, Karlsruhe, Germany) connected to the electrolytic cell. During the PEO process, the voltage-time (V-t) transients were recorded at a sampling rate of 1 Hz. After surface biofunctionalization, the implants were rinsed in running tap water for 1 min and sterilized by heat treatment for 1 h at 110 °C in an oven (Nabertherm GmbH, Lilienthal, Germany).

As-manufactured implants without any surface biofunctionalization were designated as the non-treated (NT) group. Additional experimental groups included PEO-treated implants without strontium or silver (PT), as well as those with strontium (PT-Sr), AgNPs (PT-Ag), or both (PT-AgSr).

6.2.3 Biomaterial characterization

6.2.3.1 Scanning electron microscopy (SEM)

The surface morphology of the specimens was studied using a SEM (JSM-IT100LA, JEOL, Tokyo, Japan) with electron beam energies in the range of 5 – 20 kV and a working distance of 10 mm. Prior to imaging, the implants (n = 3/group) were coated with a gold layer of 5 ± 2 nm to enhance electrical conductivity. To analyze the chemical composition of the implant surface, energy-dispersive X-ray spectroscopy (EDS) was performed.

6.2.3.2 X-ray diffraction (XRD)

The phase compositions of the specimens from the NT, PT, and PT-Sr groups were studied with a D8 advanced diffractometer (Bruker, Billerica, Massachusetts, United States) with Bragg-Brentano geometry and Lynxeye position sensitive detectors. The following settings were applied: CuKα radiation detector = LL 0.11 W 0.14, divergence slit = V6, scatter screen height = 5 mm, current = 40 mA, and voltage = 45kV. No sample spinning was applied during the experiments. The specimens were measured using a coupled θ - 2θ scan from 20 – 120°, a step size of 0.034° 2θ, and a counting speed of 10 s/step. The obtained data was analyzed using the DiffracSuite.Eva (version 4.1) software (Bruker).

6.2.3.3 Inductively coupled plasma optical emission spectroscopy (ICP-OES)

The release kinetics of strontium and silver ions were analyzed using ICP-OES. Biofunctionalized specimens (n = 3 per experimental group, length =1.5 cm) were submerged in 1 ml phosphate buffered saline (PBS) in a brown glass vial and kept at 37 °C in a water bath. The medium was sampled after 0.5, 1, 2, 4, 7, 14 and 28 days to measure the concentrations of silver and strontium ions using a spectrometer (Spectro Arcos, Kleve, Germany).

6.2.4 Antibacterial assays

6.2.4.1 Preparation bacterial inoculum

To prepare a bacterial inoculum, a single colony of methicillin-resistant *Staphylococcus aureus* (MRSA; strain = USA300 [46-48]) was suspended in either 3 ml tryptic soy broth (TSB) or cation-adjusted Mueller Hinton broth (CAMH) and incubated for 2 h at 37°C while shaking at 120 rpm. Following incubation, the optical density at 600 nm (OD_{600}) was measured and the required bacterial inoculum was prepared based on the OD_{600} value. The prepared inoculum was quantified by plating 10 µl triplicates of 10-fold serial dilutions on blood agar plates (Becton Dickinson, Franklin Lakes, United States) followed by overnight incubation at 37 °C and quantification of colony forming units (CFU).

6.2.4.2 Minimal inhibitory concentration (MIC) and minimal bactericidal concentration (MBC)

The MIC and MBC of Ag^+ and Sr^{2+} ions as well as combinations thereof were determined in CAMH broth using silver nitrate and strontium acetate (both from Sigma-Aldrich, St. Louis, United States). An MRSA USA300 inoculum of OD_{600} 0.09 was prepared of which 65 µl was transferred to 10 ml of CAMH. Two-fold serial dilutions were prepared in a 96-well plate starting

from 2 mM for Ag^+ and 80 mM for Sr^{2+}. Subsequently, 50 µl of bacterial inoculum and 50 µl of both Ag^+ and Sr^{2+} dilutions were added together in a 96-well plate and incubated overnight at 37 °C under static conditions. The following day, the MIC was scored as the lowest concentration of Ag^+ and Sr^{2+} where no turbidities were present. To determine the MBC, 10 µl aliquots of each well were plated on blood agar plates and incubated overnight at 37 °C, followed by CFU counting. The MBC was noted as the lowest concentration of Ag^+ and Sr^{2+} where no colonies were observed.

6.2.4.3 Leachable antibacterial assay

To determine the antibacterial leaching activity, agar plates were prepared from Luria broth (LB) consisting of 200 g tryptone, 100 g yeast powder, 240 g Agar No.1 (all from Oxoid, ThermoFisher Scientific, Massachusetts, United States), and 200 g NaCl dissolved in 20 L ultrapure water. A bacterial inoculum of OD_{600} 0.01 was prepared in TSB and bacterial suspensions were evenly distributed over the surface of the agar plates using a sterile swab. Subsequently, 1.5 cm implants were placed on the agar surface and incubated at 37 °C in a humid environment for 24 h. After incubation, the area of the zone of inhibition was measured with image processing software (Photoshop CS6, Adobe, California, United States) to determine the antibacterial leaching activity (n = 3 per group).

6.2.4.4 Quantitative bactericidal assay

To quantify the bactericidal activity, the numbers of adherent and non-adherent (*i.e.*, planktonic) CFU were quantified. Therefore, 4 implants of 1 cm were inserted in 200 µl MicroAmp® Fast Reaction Tubes (Life Technologies, Carlsbad, California, United States) with a bacterial inoculum of 2×10^3 CFU MRSA USA300 in 100 µl TSB + 1% glucose and incubated overnight at 37 °C under static conditions (n = 3 per group). To determine the number of adherent CFU, the implants were washed 3 times in PBS, ultrasonicated for 3 min in 200 µl PBS, and 10 µl aliquots of 10-fold serial dilutions were plated on blood agar plates. The number of non-adherent CFU were quantified from the inoculation medium by plating 10 µl aliquots of 10-fold dilutions on blood agar plates. Following overnight incubation at 37 °C, the number of CFU were quantified.

6.2.4.5 Biofilm formation and characterization

To evaluate the formation of biofilms, implants (n = 2 per group) were statically incubated at 37 °C in 1 ml TSB + 1% glucose and inoculated with 10^8 CFU/ml MRSA USA300. After 48 h, the implants were washed with PBS and fixated in McDowels fixative (4% paraformaldehyde

and 1% glutaraldehyde in 10 mM phosphate buffer at pH 7.4). Biofilm formation was analyzed by dehydrating the fixated implants according to the following procedure: rinsing in demineralized water for 5 min and dehydration in 50% ethanol for 15 min, 70% ethanol for 20 min, 96% ethanol for 20 min and hexamethyldisilazane for 15 min. Subsequently, the implants were dried in air for 2 h and coated with a gold layer of 5 ± 2 nm.

6.2.4.6 Ex vivo animal experiments

To assess the intraosseous antibacterial properties, the biofunctionalized implants were evaluated *ex vivo* in murine femora explanted from mouse cadavers by the Central Laboratory Animal Institute (Utrecht University). Following removal of the surrounding tissue, the femora were sterilized in 70% ethanol for 10 min and subsequently submerged in demineralized water for 10 min. A hole of 0.5 mm was drilled through the epicondyle into the intramedullary canal and bone marrow was removed with a syringe. To simulate *in vivo* conditions, 2 µl of PBS was inserted into the medullary cavity. Prior to implantation, the implants were inoculated with an inoculum of 200 CFU MRSA USA300 in 2 µl PBS, left to dry in air for 15 min, and implanted into the femur.

As a control for the ethanol sterilization of the femora, one femur did not receive an implant (negative control). To validate the model, 2 µl of tetracycline (50 mg/ml, Sigma-Aldrich, St.Louis, Missouri, United States) was injected into the bone cavity after implantation with an inoculated NT implant. Following implantation, the femora were incubated in 0.5 ml tubes at 37 °C on a rotating platform to simulate intraosseous fluid flow. After 24 h, the femora were submersed in 800 µl PBS with 15 zirconia beads (Ø 2mm, BioSpec, Bartlesville, Oklahoma, United States) and homogenized using a MagNA Lyser (Roche Diagnostics, Risch-Rotkreuz, Switzerland) at 7000 rpm for 2 cycles of 30 s and cooled on ice in between. From the resulting homogenate, 10-fold serial dilutions were prepared on blood agar plates, incubated overnight at 37 °C, and the numbers of CFU were quantified.

6.2.5 Osteogenic cell assays

6.2.5.1 Cell seeding and culturing

Osteoblastic murine MC3T3-E1cells (Sigma-Aldrich) were cultured for 7 days in culture medium consisting of α Minimum Essential Medium (αMEM), supplemented with 1% penicillin-streptomycin and 10% fetal bovine serum (all from ThermoFisher Scientific). The medium was refreshed every 2 – 3 days. Prior to cell seeding, the implants were cut to 1 cm length and sterilized at 110 °C for 1 h in an oven (Nabertherm GmbH, Lilienthal, Germany). Cell seeding was performed by inserting an implant in a 0.2 ml tube with 1.5×10^5 MC3T3-E1

cells in 100 µl culture medium. Subsequently, the implants were incubated at 37 °C and 5% CO_2 in a horizontal position and tilted every 20 min for 2 h in total. After seeding, the implants were placed in a 48 well plate with 200 µl fresh medium. After 2 days of culturing, osteogenic differentiation was induced by the addition of 50 µg/ml ascorbic acid and 4 mM β-glycerophosphate (all from Sigma-Aldrich). Thereafter, the medium was refreshed every 2 – 3 days. Two independent experiments were performed (each time in quadruplicates).

6.2.5.2 Presto blue assay

The metabolic activity of the MC3T3-E1 cells was determined by a PrestoBlue assay (Thermofisher, Waltham, MA, United States) after 1, 3, 7 and 11 days of culture. The same replicates were used for all time points. The implants (n = 4 per group) were incubated in 200 µl fresh culture medium supplemented by 20 µl PrestoBlue cell viability reagent for 1 h at 37°C. Thereafter, the fluorescence was measured at an excitation wavelength of 530 nm and an emission wavelength of 595 nm with a **Victor X3 microplate reader (PerkinElmer, Nederland B.V., Groningen, The Netherlands)**. Furthermore, we determined the cell seeding efficiency on the implants (n = 4 per group) immediately after seeding by deducting the number of live cells present in the culture medium from the total number of seeded cells.

6.2.5.3 Alkaline phosphate (ALP) assay

The ALP activity of the differentiated MC3T3-E1 cells was determined 11 days after cell seeding. The implants (n = 4 per group) were rinsed with PBS and 250 µl PBS-Triton added (8% NaCl, 0.2% KCl, 1.44% Na_2HPO_4, 0.24% KH_2PO_4 and 0.1% Triton X-100 in H_2O). The cells were dissociated from the implants by ultrasonication for 10 min and incubated with 100 µl p-nitrophenyl phosphate (pNPP, Sigma-Aldrich) at 37 °C for 10 min. Subsequently, 250 µl NaOH was added to stop the reaction. The absorbance was then measured at a wavelength of 405 nm with the same Victor X3 microplate reader. To determine the ALP activity, a standard curve was prepared by addition of 100 µl PBS-Triton and 250 µl NaOH to each well and the total protein content was determined with a BCA protein assay kit (Invitrogen). Subsequently, the ALP levels were normalized to the total protein content.

6.2.5.4 Cell morphology

The number and morphology of MC3T3-E1 cells on the surface of the implants were assessed by SEM after 5 days of incubation. The implants were fixed in McDowels fixative (4% paraformaldehyde and 1% glutaraldehyde in 10 mM phosphate buffer at pH 7.4) and stored at

4 °C. Prior to SEM imaging, the implants were rinsed twice in demineralized water for 5 min and dehydrated in ethanol (15 min in 50%, 20 min in 70% and 20 min in 96%). Subsequently, the implants were dried in air for 2 h, coated with a gold layer of 5 ± 2 nm, and analyzed by SEM (n = 2 per group).

6.2.6 Statistical analysis

All data are presented as mean ± standard deviation. Statistical analysis was performed with GraphPad Prism (GraphPad Software, La Jolla, California, United States) using one-way and repeated-measured ANOVA tests. The differences between various experimental groups were considered as statistically significant when $p < 0.05$.

6.3 RESULTS

6.3.1 Surface morphology and PEO biofunctionalization

AM porous biomaterial presented highly porous structures with various partially molten Ti6Al4V powder particles attached to the surfaces (**Figure 1A**). The V-t curves (**Figure 1B**) recorded for the specimens from the PT and PT-Ag groups demonstrated similar transients whereas those of the PT-Sr and PT-AgSr groups had a much lower final voltage. Up until dielectric breakdown, the voltage increased with 14 ± 1 V/s for the PT and PT-Ag implants after which the slope of the curve reduced to 0.49 V/s and plasma discharging started at 115 ± 5 V, resulting in a final voltage of 249 ± 6 V. For the PT-Sr and PT-AgSr implants, the voltage rose slower with a rate of 11.3 ± 1 V/s. Furthermore, the increase rate of the voltage was lower (*i.e.*, 0.28 V/s) as compared to the specimens from the PT and PT-Ag groups resulting in final voltages of 170 ± 4 for the PT-Sr and PT-AgSr groups. SEM analysis demonstrated uniform coverage of the implant surfaces with a micro-/nano-porous oxide layer (**Figure 1C**). The addition of strontium acetate in the PEO electrolyte resulted in smaller pore sizes for the PT-Sr group as compared to the PT group. The addition of AgNPs did not alter the surface morphology of the biofunctionalized implants compared to PT and PT-Sr implants.

6.3.2 Surface chemistry and phase composition of biofunctionalized implants

Spot EDS measurements demonstrated the presence of Ca, P, Ti, Al, and V on the surface of all biofunctionalized specimens (**Figure 2A**). Sr was detected on the surface of the specimens from the PT-Sr and PT-AgSr groups. Furthermore, backscattered SEM images as well as EDS measurements verified the presence of AgNP on the surface of PT-Ag and PT-AgSr implants. AgNPs were spread homogenously over the surface and fully embedded in the TiO_2 layer.

Phase analysis with XRD demonstrated a crystalline TiO_2 layer consisting of mainly rutile as well as lesser extents of anatase phases (**Figure 2B**). Moreover, the hydroxyapatite phase ($Ca_{10}(PO_4)_{5.64}(CO_3)_{0.66}(OH)_{3.03}$) and strontium apatite ($Sr_5(PO_4)_3(O_2)_{0.24}(OH)_{1.52}$) were detected on PT and PT-Sr specimens, respectively. In addition, strontium titanium oxide ($SrTiO_3$) and strontium-Ca/P ($Sr_2Ca(PO_4)_2$) were observed on the surface of the PT-Sr implants.

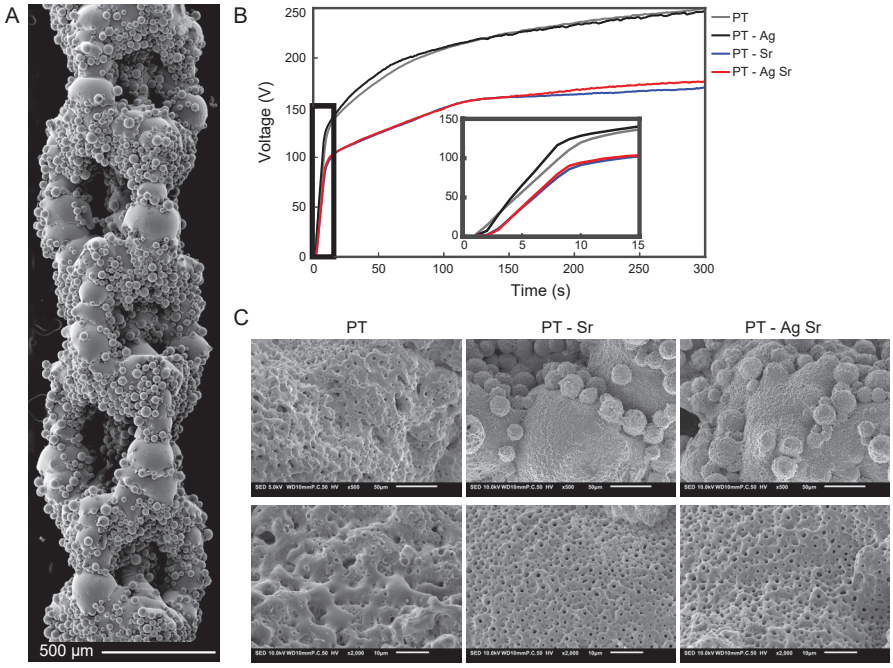

Figure 1. (A) SEM micrograph demonstrating the surface morphology of the implants after SLM. (B) The V-t transients recorded during the PEO processing of the SLM implants with different electrolytes. (C) Low (500×) and high (2000×) magnification SEM images of the PT, PT-Sr and PT-AgSr implants after 300 s of oxidation.

6.3.3 Ion release and antibacterial activity

6.3.3.1 Ion release kinetics

Sr and Ag ions were released from the biofunctionalized specimens up to 28 days (**Figure 3A,3B**). Ion release was highest in the first 4 days followed by a gradual release profile. Sr ion release was up to 1.15 times higher ($p < 0.01$) for the PT-Sr specimens as compared to those from the PT-AgSr group while the release of Ag ions was 1.23 times higher for the PT-Ag group compared to the PT-AgSr implants ($p < 0.01$).

6.3.3.2 Minimal inhibitory concentration and zone of inhibition

The MIC values for Ag^{+} and Sr^{2+} were 16 μM and 20 mM respectively while combining 4 μM of Ag^{+} and 2.5 mM of Sr^{2+} prevented bacterial growth altogether (**Figure 3C**). Similarly, the MBC values of Ag^{+} and Sr^{2+} were respectively 256 μM and 80 mM while combining 128 – 16 μM of Ag^{+} with 5 – 40 mM of Sr^{2+} resulted in total absence of bacterial growth (**Figure 3D**). After 24 h incubation, PT-AgSr implants demonstrated a significantly enhanced zone of inhibition (1.52 versus 1.12 cm^2, $p < 0.05$) as compared to the specimens from the PT-Ag group while no inhibition zones were detected for the NT, PT, and PT-Sr implants (**Figure 3E**).

6.3.3.3 Quantification of bactericidal activity and prevention of biofilm formation

Both PT-Ag and PT-AgSr completely prevented bacteria from adhering onto the surface after 24 h (**Figure 3F**). Furthermore, PT-Ag and PT-AgSr implants eradicated all non-adherent bacteria (**Figure 3G**). The NT, PT and PT-Sr implants did not prevent the growth of either adherent or non-adherent bacteria after 24 h. After 48 h, the specimens from the NT, PT and PT-Sr groups demonstrated bacterial adhesion on a substantial part of their surface area, while PT-Ag and PT-AgSr demonstrated almost no attached bacteria, save for a few found after substantial effort (**Figure 4**). On the surface of the NT implants, these clusters of bacteria had grown into multiple layers of bacterial cells. After 48 h, no instances of stacked bacterial clusters were found on the surfaces of the PT-Ag and PT-AgSr implants.

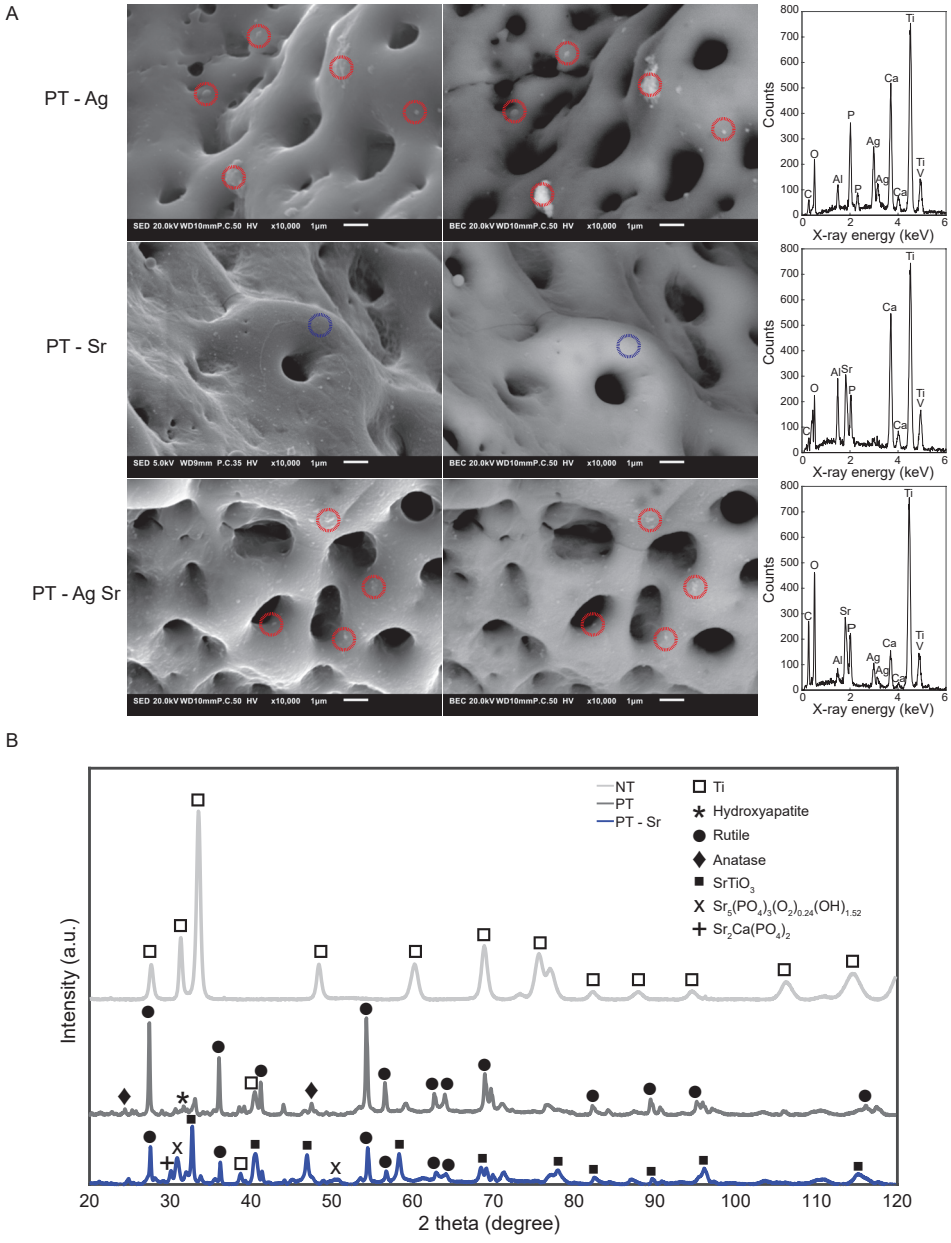

Figure 2. (A) Secondary (left) and backscattered (right) SEM images demonstrating the location and chemical composition of silver nanoparticles (red dotted circles) and the TiO_2 matrix (blue dotted circles) on PT-Ag, PT-Sr and PT-AgSr implant surfaces. (B) The XRD spectra of NT, PT, and PT-Sr specimens.

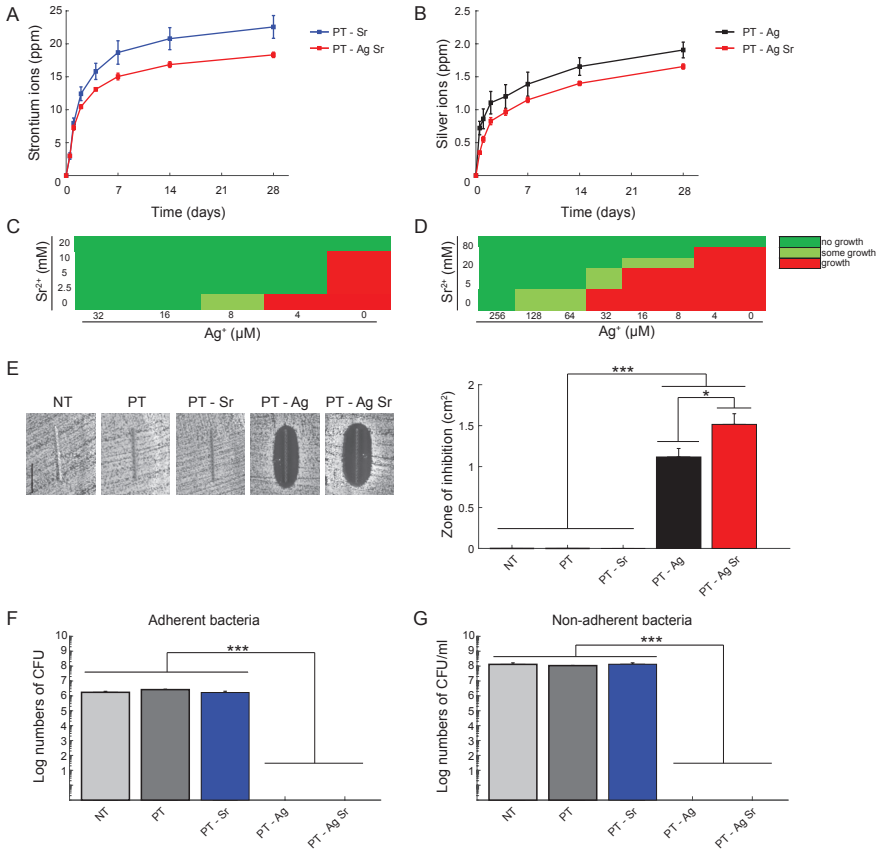

Figure 3. The ion release profile and *in vitro* antibacterial activity against MRSA USA300. The cumulative ion release of (A) Sr^{2+} and (B) Ag^{+} ions released from biofunctionalized implants in PBS as determined by ICP-OES. (C) The results of the minimum inhibitory and (D) bactericidal concentration tests demonstrating the level of bacterial growth for different concentrations of Ag^{+} and/or Sr^{2+} ions. (E) The photographs (left) and size (right) of the inhibition zones formed around the specimens after 24 hours of incubation on an agar plate with an inoculum of 10^7 CFU/ml. (F) The number of adherent and (G) non-adherent bacteria following the incubation of the implants with an inoculum of 2×10^3 CFU/ml for 24 h. *, $p<0.05$, **, $p<0.01$, ***, $p<0.001$. $n=3$ per group for all experiments.

6.3.3.4 Ex vivo antibacterial activity

The antibacterial activity was determined *ex vivo* using an intraosseous infection model consisting of murine femora (**Figure 5A**). The specimens from the PT-Ag and PT-AgSr groups fully eradicated the bacterial inoculum while those from the NT, PT, and PT-Sr did not prevent bacterial growth *ex vivo* (**Figure 5B**).

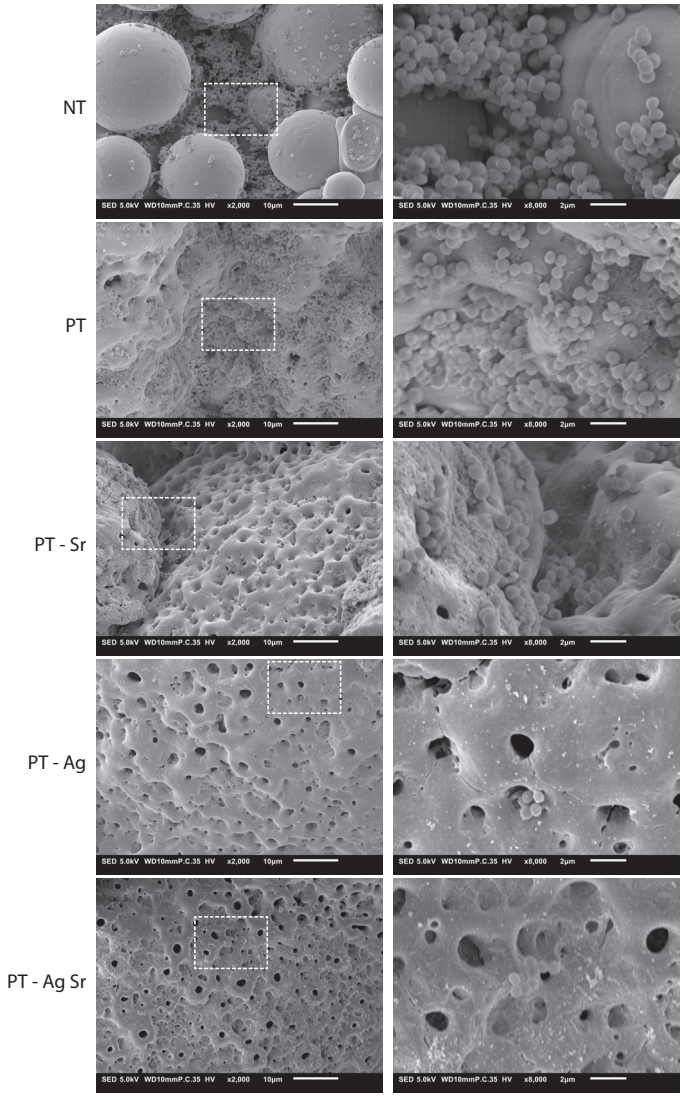

Figure 4. Low (2000×) and high (8000×) magnification SEM images of the MRSA USA300 bacteria and their biofilm formation on the specimens after 48 h of incubation in TSB 1% glucose.

6.3.4 Osteogenic activity of MC3T3-E1 cells on biofunctionalized implants

After 1 and 3 days the metabolic activity of the MC3T3-E1 cells on all specimens was similar while after 7 and 11 days the metabolic activity on specimens from the PT, PT-Sr and PT-AgSr groups was significantly enhanced as compared to the NT implants ($p < 0.001$ and $p <$

0.01, respectively; **Figure 6A**). In addition, after 7 days metabolic activity of the PT implants was higher as compared to those from the PT-Ag and PT-AgSr groups ($p < 0.001$ and $p < 0.05$ respectively) as well as PT-Sr compared to PT-Ag ($p < 0.001$). Furthermore, after 11 days the metabolic activity of PT-Sr, PT-AgSr and PT implants was enhanced compared to PT-Ag implants ($p < 0.001$, $p < 0.01$ and $p < 0.05$ respectively). The efficiency of the cell seeding was 83 ± 6 % and did not differ significantly between experimental groups (**Figure 6B**). After 11 days, the ALP activities of the specimens from the PT-Sr and PT-AgSr groups were significantly higher as compared to the NT implants ($p < 0.01$ and $p < 0.05$ respectively) as well as PT-Sr compared to PT-Ag ($p < 0.05$; **Figure 6C**). While all surfaces demonstrated cell attachment on substantial parts of their surfaces, the surface of all biofunctionalized implants was almost fully covered by the cells (**Figure 6D**). Cells demonstrated elongated morphologies and were attached onto and into the micropores. Furthermore, the cells crossed the gaps in between the 3D morphology of the implant surfaces.

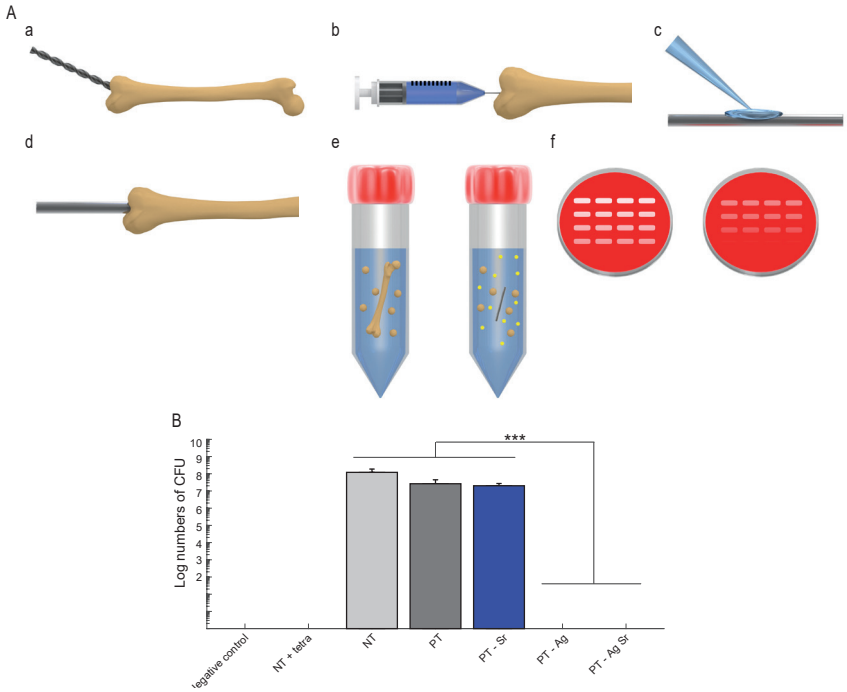

Figure 5. Bactericidal activity of implants in an *ex vivo* femoral mouse model against MRSA USA300. (A) (a) A hole was drilled through the epicondyle of the femur starting under an angle of 45° and lowering to the longitudinal axis of the femur. (b) Subsequently bone marrow was removed and (c) implants were inoculated with 2×10^2 CFU prior to (d) implantation. (e) After 24 h incubation, the femora were homogenized and (f) the number of CFU was determined. (B) Number of CFU in murine femurs after 24 h incubation *ex vivo*. To confirm sterilization, a femur without implant and bacterial inoculum was processed and analyzed (negative control). To validate the model, 2 µl of tetracycline was injected into the femoral cavity prior to implantation (NT+tetra). n=3, ***, p <0.001.

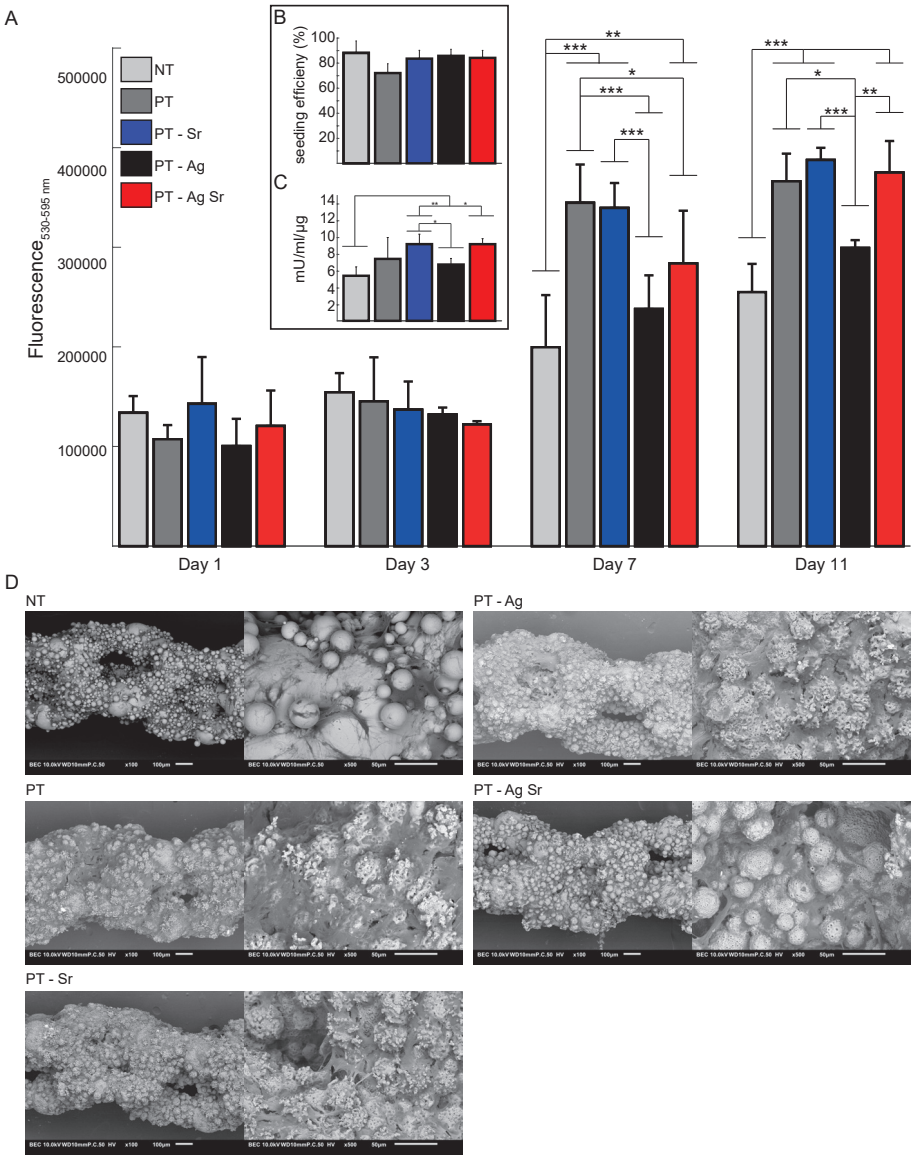

Figure 6. The osteogenic activity of MC3T3-E1 cells cultured on NT and biofunctionalized implants (n=4 per group). (A) The metabolic activity of MC3T3-E1 cells determined by the Presto blue assay after 1, 3, 7 and 11 days of culture. (B) Cell seeding efficiency defined as % of cells present on the implants after cell seeding compared to the total number of seeded cells. (C) The ALP activity of MC3T3-E1 cells after 11 days of culture. (D) SEM images revealing the cell morphology and spread of MC3T3-E1 cells on the specimens after 11 days of culture (magnification: 100× and 500×). *, p<0.05, **, p<0.01, ***, p<0.001.

6.4 DISCUSSION

We presented an advanced prototype of a functionality-packed porous metallic biomaterial made through AM and surface biofunctionalized to stimulate its bone regeneration performance and to prevent IAIs. The results presented here clearly verified the presence of all intended functionalities and revealed a number of unique features that this biomaterial possesses. In particular, we showed that these functionality-packed porous biomaterials are extremely potent against the multi-drug resistant strain MRSA USA300 that is resistant against various antibacterial agents including erythromycin, levofloxacin, mupirocin and tetracycline [48]. In fact, we observed total eradication of planktonic and adherent bacteria both in our *in vitro* experiments as well as in our *ex vivo* murine femoral model.

Antibacterial surfaces based on silver that exhibit strong antibacterial activities are usually extremely cytotoxic against host cells to the point that very few to no viable host cells could be found *in vitro* [49]. The biomaterials biofunctionalized with silver nanoparticles presented here, however, exhibit a combination of significantly increased osteogenic activity with unusually high levels of bactericidal behavior against a potent multi-drug resistant bacterial strain. On top of these unique multi-functional properties, we reported for the first time the synergistic antibacterial behavior of silver and strontium ions, which could be used to decrease the required concentration of silver ions by 4-32 folds. Such a huge decrease in the required concentration of silver ions (corresponding to the synergistic levels of MIC and MBC) allows for minimizing cytotoxicity against host cells while fully eradicating multi-drug resistant bacterial strains that form severe infection burdens for patients and for healthcare systems worldwide.

Combined with other functionalities such as a fully interconnected porous structure, bone-mimicking mechanical properties, form-freedom allowing for the design of patient-specific implants, and highly increased surface area that amplifies the effects of biofunctionalized surfaces, the functionality-packed AM porous biomaterials presented here constitute a very promising candidate for fabrication of a new generation of orthopedic implants.

Morphological assessment of the AM porous implants confirmed that a number of design objectives that were set out to obtain the required functionalities have been achieved. The results of this study clearly show a fully interconnected porous structure with a regular, ordered topology that closely matches the design, an increased surface area, micro/nanotopographical features that are known to improve cell attachment [50-52], the formation of hydroxyapatite ($Ca_{10}(PO_4)_{5.64}(CO_3)_{0.66}(OH)_{3.03}$) and strontium apatite ($Sr_5(PO_4)_3(O_2)_{0.24}(OH)_{1.52}$) that stimulate bone tissue regeneration as a result of the same one-step biofunctionalization process [36, 53-55], and continuous release of both Sr^{2+} and Ag^{+} for up to 4 weeks. This confirms the functionality-packed nature of the presented porous biomaterial.

Permanent protection against both septic and aseptic loosening requires that the release of active agents continues for several years particularly in the case of antibacterial agents. That is because bacteria may be able to reach the implant surface even years after the surgery through the blood stream or as a consequence of infection in a nearby organ [20]. Such long-term release of antibacterial agents is, first of all, not easily achieved using most biofunctionalization techniques and may not be even desired in the case of antibiotics. That is because the depletion of the reservoir of antibacterial agents will gradually result in lower concentrations being released. Long-term exposure of bacteria to sublethal doses of antibiotics is widely confirmed to result in the development of antibacterial resistance and appearance of multi-drug resistant bacteria that are not easily treated.

The biomaterials developed in the current study offer three advantages in this regard. First, immobilization of the silver nanoparticles within the firmly attached oxide layer that grows from the bulk of the biomaterial itself ensures very long term delivery of the active agents [23, 56]. Second, it is known that, as opposed to antibiotics, bacteria do not easily acquire resistance against silver ions [57]. Indeed, long term delivery may be only advisable for the antibacterial agents against which bacteria do not easily acquire resistance such as silver ions. Finally, the synergistic behavior resulting from simultaneous release of silver and strontium ions results in an unusually strong antibacterial behavior, which is expected to be even more difficult for the bacteria to acquire resistance against.

While a beneficial osteogenic effect of silver addition to strontium-containing surfaces has been described [58], in this study, for the first time ever a synergistic antibacterial behavior between silver and strontium is reported. The underlying mechanism of this behavior is not clear, yet our MIC and MBC measurements clearly show that between 4- and 32-folds lower concentrations of silver are required to inhibit growth and kill bacteria depending on the concentration of strontium ions available in the solution. The release of strontium ions at concentrations of about 10-fold higher than silver ions may change the peri-cellular environment locally (*e.g.*, increase in pH, osmotic pressure [59, 60]) and influence molecular interactions with the cell wall, potentially favoring the ingress of silver ions, in addition to their own inhibitory effects on bacteria via inactivation of ATP synthesis and induced oxidative stress [61]. Similar types of synergistic behavior have been previously shown when silver has been combined with antibiotics (*e.g.*, vancomycin [28]) or other inorganic materials such as zinc [62] or copper [63]. However, the synergistic behavior observed here has a major advantage over all those reported previously: strontium is not known to cause bacterial resistance such as those caused by antibiotics nor does it cause cytotoxicity at doses reported for other metallic ions [64]. Indeed, our results demonstrate an improved cell response and an osteogenic behavior which is beneficial for improving the bone tissue regeneration performance of our biomaterials.

To fully exhibit the functionality of the developed biofunctionalized AM porous implants, *in vivo* studies are to be conducted that include an active immune system which apart from preventing infection strongly affects bone regeneration [65]. Prior studies on silver-bearing biomaterials demonstrated strong antibacterial behavior *in vitro* [28, 66, 67] yet showed varying results *in vivo* where silver was capable to prevent bacterial adhesion [68, 69] while it may also hamper the immune response to infection [29]. Meanwhile, strontium has shown to compensate for the observed cytotoxic effects of silver [70, 71] and promote bone formation in critical-sized defects [72]. Furthermore, strontium reduces osteoclastogenesis and modulates the macrophage response towards enhanced bone formation [73, 74].

Evidence is mounting in support of the osteogenic behavior of strontium [75-79]. Although the exact mechanisms are not yet fully understood, it is known that strontium enhances osteoblast activity and inhibits bone resorption via activation of the calcium-sensing receptor, upregulation of osteoprotegerin and downregulation of RANKL expression [80, 81]. A local and sustained release of therapeutic levels of strontium in the peri-implant area can stimulate bone formation while eliminating the adverse side effects associated with a systemic treatment.

Next to its osteogenic effect, strontium may stimulate angiogenesis which is essential for osteogenesis [82]. Our results also support the osteogenic behavior of strontium including significantly increased ALP activity. This enhanced osteogenic response means that our biomaterials satisfy one of the other design objectives, required for secondary fixation of orthopedic implants.

6.5 CONCLUSIONS

In summary, we presented an AM porous biomaterial with the full range of the functionalities that are required to enhance the longevity of orthopedic implants to the point that neither septic nor aseptic loosening will occur throughout their expected service life. The AM porous biomaterials were biofunctionalized using PEO to incorporate multiple active agents (*i.e.*, silver nanoparticles and strontium) into the micro- and nanotopographical structure that uniformly covered their entire surface. Moreover, the same single-step process also integrated hydroxyapatite into the biofunctionalized oxide layer. Our results confirm that this biomaterial satisfies all the design criteria set out and is packed with the full range of intended functionalities including a much larger surface area, a fully interconnected porous structure and most importantly a combination of strong antibacterial and osteogenic behaviors. The data resulting from both our *in vitro* experiments and *ex vivo* murine model show total eradication of both planktonic and adherent MRSA within 24 h. Furthermore,

our biomaterials resulted in significantly higher level of ALP activity compared to non-biofunctionalized implants, confirming their osteogenic response. Finally, we discovered an unexpected synergistic antibacterial behavior between silver ions and strontium that is of tremendous potential utility, given that it allows for simultaneously reducing the required dose of silver ions by 4-32 folds while inducing osteogenic behavior. The functionality-packed biomaterials presented here therefore have a unique potential for clinical applications and prolonging the longevity of orthopedic implants.

ACKNOWLEDGEMENTS

The research for this paper was financially supported by the Prosperos project, funded by the Interreg VA Flanders – The Netherlands program, CCI grant no. 2014TC16RFCB046.

REFERENCES

[1] M. Niinomi, M. Nakai, J. Hieda, Development of new metallic alloys for biomedical applications, Acta Biomaterialia 8 (2012) 3888-3903.

[2] H. Ao, J. Zhou, T. Tang, B. Yue, Biofunctionalization of titanium with bacitracin immobilization shows potential for anti-bacteria, osteogenesis and reduction of macrophage inflammation, Colloids and Surfaces B: Biointerfaces 145 (2016) 728-739.

[3] S. Yavari, B. Necula, L. Fratila-Apachitei, J. Duszczyk, I. Apachitei, Biofunctional surfaces by plasma electrolytic oxidation on titanium biomedical alloys, Surface Engineering 32 (2016) 411-417.

[4] M. Dallago, V. Fontanari, E. Torresani, M. Leoni, C. Pederzolli, C. Potrich, M. Benedetti, Fatigue and biological properties of Ti-6Al-4V ELI cellular structures with variously arranged cubic cells made by selective laser melting, Journal of the Mechanical Behavior of Biomedical Materials 78 (2018) 381-394.

[5] E. Sallica-Leva, A. Jardini, J. Fogagnolo, Microstructure and mechanical behavior of porous Ti–6Al–4V parts obtained by selective laser melting, Journal of the Mechanical Behavior of Biomedical Materials 26 (2013) 98-108.

[6] V. Weißmann, R. Bader, H. Hansmann, N. Laufer, Influence of the structural orientation on the mechanical properties of selective laser melted Ti6Al4V open-porous scaffolds, Materials & Design 95 (2016) 188-197.

[7] A.A. Zadpoor, Mechanics of additively manufactured biomaterials, Journal of the Mechanical Behavior of Biomedical Materials 70 (2017) 1-6.

[8] N. Harmankaya, J. Karlsson, A. Palmquist, M. Halvarsson, K. Igawa, M. Andersson, P. Tengvall, Raloxifene and alendronate containing thin mesoporous titanium oxide films improve implant fixation to bone, Acta Biomaterialia 9 (2013) 7064-7073.

[9] D.-W. Lee, Y.-P. Yun, K. Park, S.E. Kim, Gentamicin and bone morphogenic protein-2 (BMP-2)-delivering heparinized-titanium implant with enhanced antibacterial activity and osteointegration, Bone 50 (2012) 974-982.

[10] I.C. Chou, S.Y. Lee, C.P. Jiang, Effects of implant neck design on primary stability and overload in a type IV mandibular bone, International Journal for Numerical Methods in Biomedical Engineering 30 (2014) 1223-1237.

[11] A. Falco, M. Berardini, P. Trisi, Correlation Between Implant Geometry, Implant Surface, Insertion Torque, and Primary Stability: In Vitro Biomechanical Analysis, International Journal of Oral & Maxillofacial Implants 33 (2018).

[12] R. Hedayati, M. Sadighi, M. Mohammadi-Aghdam, A. Zadpoor, Mechanical properties of regular porous biomaterials made from truncated cube repeating unit cells: Analytical solutions and computational models, Materials Science and Engineering: C 60 (2016) 163-183.

[13] R. Hedayati, M. Sadighi, M. Mohammadi-Aghdam, A. Zadpoor, Mechanical behavior of additively manufactured porous biomaterials made from truncated cuboctahedron unit cells, International Journal of Mechanical Sciences 106 (2016) 19-38.

[14] S. Limmahakhun, A. Oloyede, K. Sitthiseripratip, Y. Xiao, C. Yan, Stiffness and strength tailoring of cobalt chromium graded cellular structures for stress-shielding reduction, Materials & Design 114 (2017) 633-641.

[15] A.A. Zadpoor, R. Hedayati, Analytical relationships for prediction of the mechanical properties of additively manufactured porous biomaterials, Journal of Biomedical Materials Research Part A

104 (2016) 3164-3174.

[16] Z. Li, C. Liu, B. Wang, C. Wang, Z. Wang, F. Yang, C. Gao, H. Liu, Y. Qin, J. Wang, Heat treatment effect on the mechanical properties, roughness and bone ingrowth capacity of 3D printing porous titanium alloy, RSC Advances 8 (2018) 12471-12483.

[17] J. Van der Stok, M. Koolen, M. De Maat, S.A. Yavari, J. Alblas, P. Patka, J. Verhaar, E. Van Lieshout, A.A. Zadpoor, H. Weinans, Full regeneration of segmental bone defects using porous titanium implants loaded with BMP-2 containing fibrin gels, European Cells & Materials 2015 (2015) 141-154.

[18] J. Lv, P. Xiu, J. Tan, Z. Jia, H. Cai, Z. Liu, Enhanced angiogenesis and osteogenesis in critical bone defects by the controlled release of BMP-2 and VEGF: implantation of electron beam melting-fabricated porous Ti6Al4V scaffolds incorporating growth factor-doped fibrin glue, Biomedical Materials 10 (2015) 035013.

[19] H. Zhang, F. Migneco, C.-Y. Lin, S.J. Hollister, Chemically-conjugated bone morphogenetic protein-2 on three-dimensional polycaprolactone scaffolds stimulates osteogenic activity in bone marrow stromal cells, Tissue Engineering Part A 16 (2010) 3441-3448.

[20] A. Trampuz, A.F. Widmer, Infections associated with orthopedic implants, Current Opinion in Infectious Diseases 19 (2006) 349-356.

[21] T.-X. Han, B. Chang, X. Ding, G.-N. Yue, W. Song, H.-P. Tang, L. Jia, L.-Z. Zhao, Y.-M. Zhang, Improved bone formation and ingrowth for additively manufactured porous Ti 6 Al 4 V bone implants with strontium laden nanotube array coating, RSC Advances 6 (2016) 13686-13697.

[22] N. Taniguchi, S. Fujibayashi, M. Takemoto, K. Sasaki, B. Otsuki, T. Nakamura, T. Matsushita, T. Kokubo, S. Matsuda, Effect of pore size on bone ingrowth into porous titanium implants fabricated by additive manufacturing: an in vivo experiment, Materials Science and Engineering: C 59 (2016) 690-701.

[23] S.-H. Uhm, J.-S. Kwon, D.-H. Song, E.-J. Lee, W.-S. Jeong, S. Oh, K.-N. Kim, E.H. Choi, K.-M. Kim, Long-term antibacterial performance and bioactivity of plasma-engineered Ag-NPs/TiO2 nanotubes for bio-implants, Journal of Biomedical Nanotechnology 12 (2016) 1890-1906.

[24] D. Xiao, Y. Yang, X. Su, D. Wang, J. Sun, An integrated approach of topology optimized design and selective laser melting process for titanium implants materials, Bio-medical Materials and Engineering 23 (2013) 433-445.

[25] C. Yan, L. Hao, A. Hussein, P. Young, Ti–6Al–4V triply periodic minimal surface structures for bone implants fabricated via selective laser melting, Journal of the Mechanical Behavior of Biomedical Materials 51 (2015) 61-73.

[26] F. Bobbert, A. Zadpoor, Effects of bone substitute architecture and surface properties on cell response, angiogenesis, and structure of new bone, Journal of Materials Chemistry B 5 (2017) 6175-6192.

[27] H.M. Kolken, S. Janbaz, S.M. Leeflang, K. Lietaert, H.H. Weinans, A.A. Zadpoor, Rationally designed meta-implants: a combination of auxetic and conventional meta-biomaterials, Materials Horizons 5 (2018) 28-35.

[28] S. Bakhshandeh, Z. Gorgin Karaji, K. Lietaert, A.C. Fluit, C.E. Boel, H.C. Vogely, T. Vermonden, W.E. Hennink, H. Weinans, A.A. Zadpoor, Simultaneous delivery of multiple antibacterial agents from additively manufactured porous biomaterials to fully eradicate planktonic and adherent Staphylococcus aureus, ACS Applied Materials & Interfaces 9 (2017) 25691-25699.

[29] M. Croes, S. Bakhshandeh, I. van Hengel, K. Lietaert, K. van Kessel, B. Pouran, B. van der Wal, H. Vogely, W. Van Hecke, A. Fluit, C.E. Boel, J. Albas, A.A. Zadpoor, H. Weinans, S. Amin Yavari, Antibacterial and immunogenic behavior of silver coatings on additively manufactured porous titanium, Acta Biomaterialia 81 (2018) 315-327.

[30] Z. Gorgin Karaji, M. Speirs, S. Dadbakhsh, J.-P. Kruth, H. Weinans, A. Zadpoor, S. Amin Yavari, Additively manufactured and surface biofunctionalized porous nitinol, ACS Applied Materials & Interfaces 9 (2017) 1293-1304.

[31] Z. Wang, C. Wang, C. Li, Y. Qin, L. Zhong, B. Chen, Z. Li, H. Liu, F. Chang, J. Wang, Analysis of factors influencing bone ingrowth into three-dimensional printed porous metal scaffolds: A review, Journal of Alloys and Compounds 717 (2017) 271-285.

[32] S.M. Ahmadi, R. Hedayati, Y. Li, K. Lietaert, N. Tümer, A. Fatemi, C. Rans, B. Pouran, H. Weinans, A.A. Zadpoor, Fatigue performance of additively manufactured meta-biomaterials: the effects of topology and material type, Acta Biomaterialia 65 (2018) 292-304.

[33] R. Hedayati, S. Ahmadi, K. Lietaert, B. Pouran, Y. Li, H. Weinans, C. Rans, A. Zadpoor, Isolated and modulated effects of topology and material type on the mechanical properties of additively manufactured porous biomaterials, Journal of the Mechanical Behavior of Biomedical Materials 79 (2018) 254-263.

[34] R. Wauthle, S.M. Ahmadi, S.A. Yavari, M. Mulier, A.A. Zadpoor, H. Weinans, J. Van Humbeeck, J.-P. Kruth, J. Schrooten, Revival of pure titanium for dynamically loaded porous implants using additive manufacturing, Materials Science and Engineering: C 54 (2015) 94-100.

[35] I.A.J. van Hengel, M. Riool, L.E. Fratila-Apachitei, J. Witte-Bouma, E. Farrell, A.A. Zadpoor, S.A.J. Zaat, I. Apachitei, Data on the surface morphology of additively manufactured Ti-6Al-4V implants during processing by plasma electrolytic oxidation, Data Brief 13 (2017) 385-389.

[36] I.A.J. Van Hengel, M. Riool, L.E. Fratila-Apachitei, J. Witte-Bouma, E. Farrell, A.A. Zadpoor, S.A.J. Zaat, I. Apachitei, Selective laser melting porous metallic implants with immobilized silver nanoparticles kill and prevent biofilm formation by methicillin-resistant Staphylococcus aureus, Biomaterials 140 (2017) 1-15.

[37] K. Lin, L. Xia, H. Li, X. Jiang, H. Pan, Y. Xu, W.W. Lu, Z. Zhang, J. Chang, Enhanced osteoporotic bone regeneration by strontium-substituted calcium silicate bioactive ceramics, Biomaterials 34 (2013) 10028-10042.

[38] S. Peng, G. Zhou, K.D. Luk, K.M. Cheung, Z. Li, W.M. Lam, Z. Zhou, W.W. Lu, Strontium promotes osteogenic differentiation of mesenchymal stem cells through the Ras/MAPK signaling pathway, Cellular Physiology and Biochemistry 23 (2009) 165-174.

[39] C. Wu, Y. Zhou, C. Lin, J. Chang, Y. Xiao, Strontium-containing mesoporous bioactive glass scaffolds with improved osteogenic/cementogenic differentiation of periodontal ligament cells for periodontal tissue engineering, Acta Biomaterialia 8 (2012) 3805-3815.

[40] F. Yang, D. Yang, J. Tu, Q. Zheng, L. Cai, L. Wang, Strontium enhances osteogenic differentiation of mesenchymal stem cells and in vivo bone formation by activating Wnt/catenin signaling, Stem Cells 29 (2011) 981-991.

[41] Q.L. Feng, J. Wu, G. Chen, F. Cui, T. Kim, J. Kim, A mechanistic study of the antibacterial effect of silver ions on Escherichia coli and Staphylococcus aureus, Journal of Biomedical Materials Research 52 (2000) 662-668.

[42] C. Marambio-Jones, E.M. Hoek, A review of the antibacterial effects of silver nanomaterials and potential implications for human health and the environment, Journal of Nanoparticle Research 12 (2010) 1531-1551.

[43] Z.-m. Xiu, Q.-b. Zhang, H.L. Puppala, V.L. Colvin, P.J. Alvarez, Negligible particle-specific antibacterial activity of silver nanoparticles, Nano Letters 12 (2012) 4271-4275.

[44] B. Necula, I. Apachitei, F. Tichelaar, L. Fratila-Apachitei, J. Duszczyk, An electron microscopical study on the growth of TiO2–Ag antibacterial coatings on Ti6Al7Nb biomedical alloy, Acta Biomaterialia 7 (2011) 2751-2757.

[45] B. Necula, J. Van Leeuwen, L. Fratila-Apachitei, S. Zaat, I. Apachitei, J. Duszczyk, In vitro cytotoxicity evaluation of porous TiO2–Ag antibacterial coatings for human fetal osteoblasts, Acta Biomaterialia 8 (2012) 4191-4197.

[46] N.S. Harik, G. Com, X. Tang, M.M. Castro, M.E. Stemper, J.L. Carroll, Clinical characteristics and epidemiology of methicillin-resistant Staphylococcus aureus (MRSA) in children with cystic fibrosis from a center with a high MRSA prevalence, American Journal of Infection Control 44 (2016) 409-415.

[47] G. Nimmo, USA300 abroad: global spread of a virulent strain of community-associated methicillin-resistant Staphylococcus aureus, Clinical Microbiology and Infection 18 (2012) 725-734.

[48] F.C. Tenover, R.V. Goering, Methicillin-resistant Staphylococcus aureus strain USA300: origin and epidemiology, Journal of Antimicrobial Chemotherapy 64 (2009) 441-446.

[49] S. Amin Yavari, L. Loozen, F.L. Paganelli, S. Bakhshandeh, K. Lietaert, J.A. Groot, A.C. Fluit, C. Boel, J. Alblas, H.C. Vogely, Antibacterial behavior of additively manufactured porous titanium with nanotubular surfaces releasing silver ions, ACS Applied Materials & Interfaces 8 (2016) 17080-17089.

[50] P. Whiteside, E. Matykina, J.E. Gough, P. Skeldon, G.E. Thompson, In vitro evaluation of cell proliferation and collagen synthesis on titanium following plasma electrolytic oxidation, J Biomed Mater Res A 94 (2010) 38-46.

[51] J. Wu, Z.M. Liu, X.H. Zhao, Y. Gao, J. Hu, B. Gao, Improved biological performance of microarc-oxidized low-modulus Ti-24Nb-4Zr-7.9Sn alloy, J Biomed Mater Res B Appl Biomater 92 (2010) 298-306.

[52] L. Zhao, Y. Wei, J. Li, Y. Han, R. Ye, Y. Zhang, Initial osteoblast functions on Ti-5Zr-3Sn-5Mo-15Nb titanium alloy surfaces modified by microarc oxidation, J Biomed Mater Res A 92 (2010) 432-40.

[53] H. Kusakabe, T. Sakamaki, K. Nihei, Y. Oyama, S. Yanagimoto, M. Ichimiya, J. Kimura, Y. Toyama, Osseointegration of a hydroxyapatite-coated multilayered mesh stem, Biomaterials 25 (2004) 2957-69.

[54] S. Durdu, Ö.F. Deniz, I. Kutbay, M. Usta, Characterization and formation of hydroxyapatite on Ti6Al4V coated by plasma electrolytic oxidation, Journal of Alloys and Compounds 551 (2013) 422-429.

[55] Y. Han, J. Sun, X. Huang, Formation mechanism of HA-based coatings by micro-arc oxidation, Electrochemistry Communications 10 (2008) 510-513.

[56] A. Shivaram, S. Bose, A. Bandyopadhyay, Understanding long-term silver release from surface modified porous titanium implants, Acta Biomater 58 (2017) 550-560.

[57] S.L. Percival, P.G. Bowler, D. Russell, Bacterial resistance to silver in wound care, J Hosp Infect 60 (2005) 1-7.

[58] X. He, X. Zhang, L. Bai, R. Hang, X. Huang, L. Qin, X. Yao, B. Tang, Antibacterial ability and osteogenic activity of porous Sr/Ag-containing TiO2 coatings, Biomed Mater 11 (2016) 045008.

[59] A. Moghanian, S. Firoozi, M. Tahriri, Characterization, in vitro bioactivity and biological studies of sol-gel synthesized SrO substituted 58S bioactive glass, Ceramics International 43 (2017) 14880-14890.

[60] J. Liu, S.C. Rawlinson, R.G. Hill, F. Fortune, Strontium-substituted bioactive glasses in vitro osteogenic and antibacterial effects, Dent Mater 32 (2016) 412-22.

[61] J. Tan, D. Wang, H. Cao, Y. Qiao, H. Zhu, X. Liu, Effect of local alkaline microenvironment on the behaviors of bacteria and osteogenic cells, ACS Appl Mater Interfaces 10 (2018) 42018-42029.

[62] G. Jin, H. Qin, H. Cao, S. Qian, Y. Zhao, X. Peng, X. Zhang, X. Liu, P.K. Chu, Synergistic effects of dual Zn/Ag ion implantation in osteogenic activity and antibacterial ability of titanium, Biomaterials 35 (2014) 7699-713.

[63] L.V. Jankauskait, L.A. Vitkauskien, A. Lazauskas, J. Baltrusaitis, I. ProsyLevas, M. AndruleviLius, Bactericidal effect of graphene oxide/Cu/Ag nanoderivatives against Escherichia coli, Pseudomonas aeruginosa, Klebsiella pneumoniae, Staphylococcus aureus and Methicillin-resistant Staphylococcus aureus, Int J Pharm 511 (2016) 90-97.

[64] S. Ferraris, S. Spriano, Antibacterial titanium surfaces for medical implants, Mater Sci Eng C Mater Biol Appl 61 (2016) 965-78.

[65] H. Takayanagi, Osteoimmunology: shared mechanisms and crosstalk between the immune and bone systems, Nat Rev Immunol 7 (2007) 292-304.

[66] Z. Jia, P. Xiu, P. Xiong, W. Zhou, Y. Cheng, S. Wei, Y. Zheng, T. Xi, H. Cai, Z. Liu, C. Wang, W. Zhang, Z. Li, Additively manufactured macroporous titanium with silver-releasing micro-/nanoporous surface for multipurpose infection control and bone repair - a proof of concept, ACS Appl Mater Interfaces 8 (2016) 28495-28510.

[67] A. Gao, R. Hang, X. Huang, L. Zhao, X. Zhang, L. Wang, B. Tang, S. Ma, P.K. Chu, The effects of titania nanotubes with embedded silver oxide nanoparticles on bacteria and osteoblasts, Biomaterials 35 (2014) 4223-35.

[68] C.M. Tilmaciu, M. Mathieu, J.P. Lavigne, K. Toupet, G. Guerrero, A. Ponche, J. Amalric, D. Noel, P.H. Mutin, In vitro and in vivo characterization of antibacterial activity and biocompatibility: a study on silver-containing phosphonate monolayers on titanium, Acta Biomater 15 (2015) 266-77.

[69] A. Devlin-Mullin, N.M. Todd, Z. Golrokhi, H. Geng, M.A. Konerding, N.G. Ternan, J.A. Hunt, R.J. Potter, C. Sutcliffe, E. Jones, P.D. Lee, C.A. Mitchell, Atomic layer deposition of a silver nanolayer on advanced titanium orthopedic implants inhibits bacterial colonization and supports vascularized de novo bone ingrowth, Adv Healthc Mater 6 (2017).

[70] Z. Geng, R. Wang, X. Zhuo, Z. Li, Y. Huang, L. Ma, Z. Cui, S. Zhu, Y. Liang, Y. Liu, H. Bao, X. Li, Q. Huo, Z. Liu, X. Yang, Incorporation of silver and strontium in hydroxyapatite coating on titanium surface for enhanced antibacterial and biological properties, Mater Sci Eng C Mater Biol Appl 71 (2017) 852-861.

[71] H. Cheng, W. Xiong, Z. Fang, H. Guan, W. Wu, Y. Li, Y. Zhang, M.M. Alvarez, B. Gao, K. Huo, J. Xu, N. Xu, C. Zhang, J. Fu, A. Khademhosseini, F. Li, Strontium (Sr) and silver (Ag) loaded nanotubular structures with combined osteoinductive and antimicrobial activities, Acta Biomaterialia 31 (2016) 388-400.

[72] A. Henriques Lourenco, N. Neves, C. Ribeiro-Machado, S.R. Sousa, M. Lamghari, C.C. Barrias, A. Trigo Cabral, M.A. Barbosa, C.C. Ribeiro, Injectable hybrid system for strontium local delivery promotes bone regeneration in a rat critical-sized defect model, Sci Rep 7 (2017) 5098.

[73] W. Zhang, F. Zhao, D. Huang, X. Fu, X. Li, X. Chen, Strontium-substituted submicrometer bioactive glasses modulate macrophage responses for improved bone regeneration, ACS Appl Mater Interfaces 8 (2016) 30747-30758.

[74] X. Yuan, H. Cao, J. Wang, K. Tang, B. Li, Y. Zhao, M. Cheng, H. Qin, X. Liu, X. Zhang, Immunomodulatory Effects of Calcium and Strontium Co-Doped Titanium Oxides on Osteogenesis, Front Immunol 8 (2017) 1196.

[75] E. Gentleman, Y.C. Fredholm, G. Jell, N. Lotfibakhshaiesh, M.D. O'Donnell, R.G. Hill, M.M. Stevens, The effects of strontium-substituted bioactive glasses on osteoblasts and osteoclasts in vitro, Biomaterials 31 (2010) 3949-56.

[76] L. Cianferotti, F. D'Asta, M.L. Brandi, A review on strontium ranelate long-term antifracture efficacy in the treatment of postmenopausal osteoporosis, Ther Adv Musculoskelet Dis 5 (2013) 127-39.

[77] L. Kyllonen, M. D'Este, M. Alini, D. Eglin, Local drug delivery for enhancing fracture healing in osteoporotic bone, Acta Biomaterialia 11 (2015) 412-34.

[78] M. Yamaguchi, M.N. Weitzmann, The intact strontium ranelate complex stimulates osteoblastogenesis and suppresses osteoclastogenesis by antagonizing NF-kappaB activation, Mol Cell Biochem 359 (2012) 399-407.

[79] J.Y. Reginster, J.M. Kaufman, S. Goemaere, J.P. Devogelaer, C.L. Benhamou, D. Felsenberg, M. Diaz-Curiel, M.L. Brandi, J. Badurski, J. Wark, A. Balogh, O. Bruyere, C. Roux, Maintenance of antifracture efficacy over 10 years with strontium ranelate in postmenopausal osteoporosis, Osteoporos Int 23 (2012) 1115-22.

[80] T.C. Brennan, M.S. Rybchyn, W. Green, S. Atwa, A.D. Conigrave, R.S. Mason, Osteoblasts play key roles in the mechanisms of action of strontium ranelate, Br J Pharmacol 157 (2009) 1291-300.

[81] J. Coulombe, H. Faure, B. Robin, M. Ruat, In vitro effects of strontium ranelate on the extracellular calcium-sensing receptor, Biochem Biophys Res Commun 323 (2004) 1184-90.

[82] W. Zhang, H. Cao, X. Zhang, G. Li, Q. Chang, J. Zhao, Y. Qiao, X. Ding, G. Yang, X. Liu, X. Jiang, A strontium-incorporated nanoporous titanium implant surface for rapid osseointegration, Nanoscale 8 (2016) 5291-301.

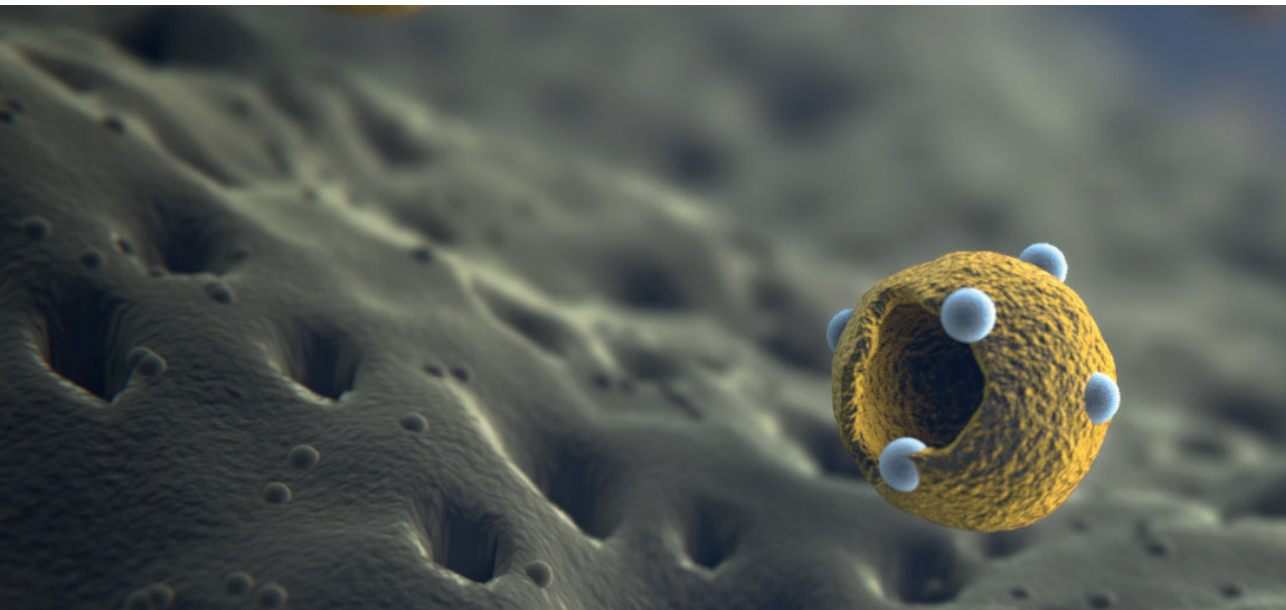

CHAPTER 07

Using processing parameters to optimize surface morphology and osteogenic properties

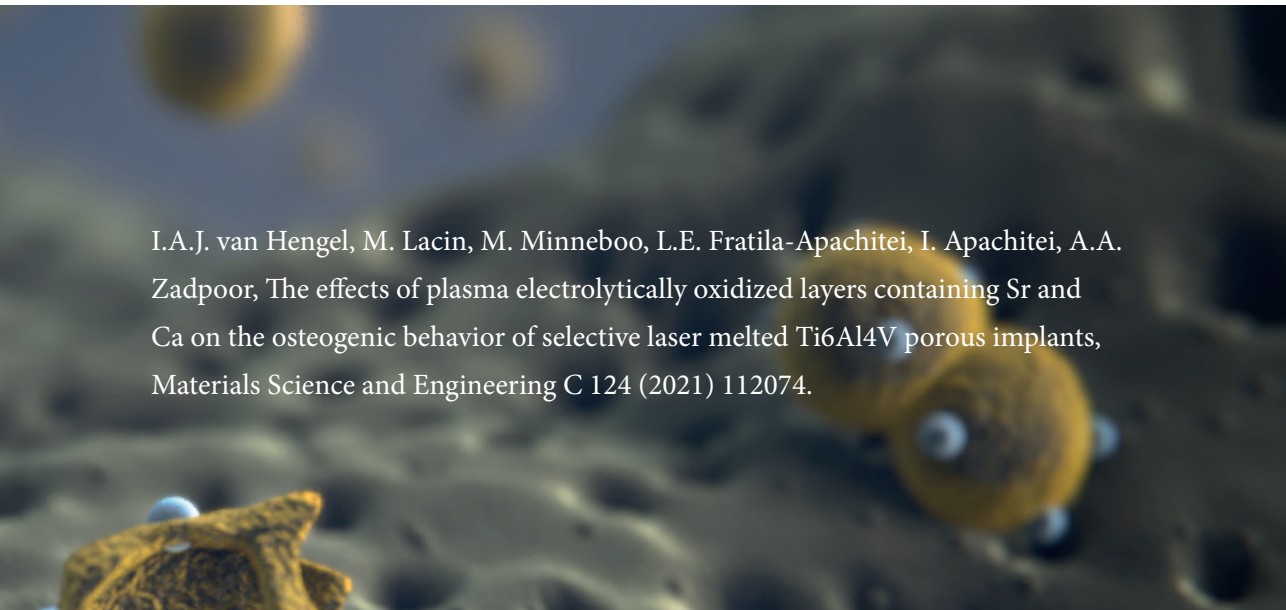

I.A.J. van Hengel, M. Lacin, M. Minneboo, L.E. Fratila-Apachitei, I. Apachitei, A.A. Zadpoor, The effects of plasma electrolytically oxidized layers containing Sr and Ca on the osteogenic behavior of selective laser melted Ti6Al4V porous implants, Materials Science and Engineering C 124 (2021) 112074.

Surface biofunctionalization is frequently applied to enhance the functionality and longevity of orthopedic implants. Here, we investigated the osteogenic effects of additively manufactured porous Ti6Al4V implants whose surfaces were biofunctionalized using plasma electrolytic oxidation (PEO) in Ca/P-based electrolytes with or without strontium. Various levels of Sr and Ca were incorporated in the oxide layers by using different current densities and oxidation times. Increasing the current density and oxidation time resulted in thicker titanium oxide layers and enhanced the release of Ca^{2+} and Sr^{2+}. Biofunctionalization with strontium resulted in enhanced pore density, a thinner TiO_2 layer, four-fold reduced release of Ca^{2+}, and mainly anatase phases as compared to implants biofunctionalized in electrolytes containing solely Ca/P species under otherwise similar conditions. Different current densities and oxidation times significantly increased the osteogenic differentiation of MC3T3-E1 cells on implants biofunctionalized with strontium, when the PEO treatment was performed with a current density of 20 A/dm^2 for 5 and 10 min as well as for a current density of 40 A/dm^2 for 5 min. Therefore, addition of Sr in the PEO electrolyte and control of the PEO processing parameters represent a promising way to optimize the surface morphology and osteogenic activity of future porous AM implants.

7.1 INTRODUCTION

The demand for orthopedic bone implants that last for extensive lifetimes is increasing [1]. To support the longevity of cementless bone implants, proper fixation between implant and bone tissue is of utmost importance. Such implants are increasingly made using additive manufacturing (AM), as it allows for the free-form fabrication of customized (titanium) implants for a variety of purposes including the treatment of large bony defects [2-4]. The mechanical behavior of AM porous implants can be controlled through geometrical design to further enhance the longevity of such implants [5, 6]. The highly porous nature of such implants means that they possess vast surface areas, which make these implants prone to infection. Surface biofunctionalization of these AM implants has been, therefore, used to not only prevent implant-associated infections but also to stimulate osteogenic properties [7] of AM porous implants. Such biofunctionalization procedures, however, have been found to be challenging.

Plasma electrolytic oxidation (PEO) is an electrochemical surface treatment that has been shown to enhance the bioactivity of titanium implants [8-10]. PEO transforms the native amorphous titanium oxide surface layer into a surface consisting of nanocrystalline titanium oxide phases in a single-step process [11, 12]. At the start of the PEO process, the voltage rises steadily until dielectric breakdown occurs, resulting in local spark discharges at the interface between substrate and electrolyte [13]. As the surface layer grows, the spark discharges decrease in number, but increase in intensity. With increasing oxidation time, gas bubbles arise at the surface contributing to the development of large, protruding pores. At the same time, nanocrystalline phases form as a result of the locally high temperatures that are experienced during the spark discharges and the accompanying pressures. During layer growth, species from the electrolytes as well as from the titanium substrates are incorporated in the porous oxide layer.

PEO is suitable for the surface biofunctionalization of complex, porous geometries [14], does not alter the mechanical behavior of the substrate due to limited heat input [15], and results in strong bonding between the titanium oxide layer and the substrate [16-19]. The bioactivity of the implant surface can be adjusted through the composition of the PEO electrolyte. The use of Ca/P-based electrolytes results in the formation of crystalline Ca/P phases including hydroxyapatite [20-22], which can stimulate bone tissue regeneration. Through the addition of inorganic nanoparticles, such as Ag, Cu, and/or Zn, the implant surfaces are endowed with antibacterial properties [23, 24].

Strontium has been used to treat osteoporotic patients effectively due to its initiation of bone formation and its simultaneous reduction of bone resorption, thereby reducing the

risk of fracture [25, 26]. However, systemic strontium intake may induce cardiac events [27]. Therefore, local administration at low, yet effective doses, is necessary to prevent the side effects associated with the medicinal use of strontium [28]. As such, strontium has been applied on the surface of titanium biomaterials and has been shown to enhance the osteogenic differentiation of mesenchymal stromal cells *in vitro* [29, 30] and repair bone defects *in vivo* [31, 32]. Titanium biomaterials treated with strontium using PEO have been shown to result in enhanced osteogenic properties [33-35].

Apart from altering the chemical composition of the PEO electrolyte, the electrical processing parameters can change the surface morphology of the implants and the phase composition. For example, increasing the current density and oxidation time will result in thicker oxide layers, larger surface pores and increased formation of crystalline phases [36, 37].

The contributions of these processing parameters to the osteogenic properties of the resulting surfaces have not yet been investigated. The characterization of the surface morphology and osteogenic properties is required to understand the missing link between the surface biofunctionalization process and the resulting bioactivity. Insight into these effects will contribute to an optimized performance of future orthopedic implants. In previous research [38], we have observed a synergistic effect of the incorporated Sr and Ag on the antibacterial activity of PEO-treated porous AM titanium implants highlighting the potential of further optimization of the incorporated elements for achieving the desired biofunctionalities. Therefore, in this study, we incorporated different levels of Sr into the titanium implants by modifying the PEO processing parameters including the current density and oxidation time, and assessed their effects on the surface morphology and the osteogenic properties of porous AM titanium implants.

7.2 MATERIALS AND METHODS

7.2.1 Implant manufacturing and surface biofunctionalization

Porous implants were rationally designed and manufactured by AM as previously described [14]. Biofunctionalization of these implants was performed by PEO using a customized setup which included an AC power source (ACS 1500, 50 Hz, ET power Systems Ltd., Chesterfield, United Kingdom), connected to a data acquisition board through a computer interface (SCXI, National Instruments, Austin, Texas, United States), and an electrolytic cell consisting of double-walled glass. During PEO processing, the implant functioned as the anode while a stainless steel cylinder formed the cathode. The PEO electrolyte was continuously stirred at 500 rpm and voltage-time (V-t) transients were sampled at a rate of 1 Hz.

The PEO electrolyte was prepared by dissolving 0.15 M calcium acetate (Sigma-Aldrich, St. Louis, Missouri, United States) and 0.02 M calcium glycerophosphate (Dr. Paul Lohmann GmbH, Emmerthal, Germany) in 800 ml demineralized water supplemented with 1.0 M strontium acetate (Sigma-Aldrich). The conductivity of the electrolytes was measured in three-fold using a conductivity meter (Consort, Topac Inc., Cohasset, Massachusetts, United States). The experimental groups included implants without any PEO biofunctionalization and were labelled non-treated (NT), implants that were treated with PEO but without strontium acetate (PT), and PEO-treated implants with strontium acetate (PT – Sr). The PEO processing was conducted galvanostatically using RMS current densities of 20, 30, and 40 A/dm^2 for 5 and 10 min with sinusoidal input signals. After PEO biofunctionalization, the implants were rinsed under running tap water for 1 min, sonicated in 70% ethanol for 30 s, rinsed in demineralized water for 5 min, sonicated in demineralized water for 30 s and sterilized in an oven at 110 °C for 1 h.

7.2.2 Assessment of titanium oxide layer and surface morphology

In order to investigate the titanium oxide layer surrounding the implant, cross-sections were prepared (n = 3/group). Therefore, perpendicular sections were made along the longitudinal axis of the implant and fixed in a conductive resin (Polyfast, Struers, Copenhagen, Denmark). Then, the specimens were successively ground for 2 min each with 80, 180, 320, 800, 1200, 2000 and 4000 SiC abrasive paper successively (Struers, Copenhagen, Denmark) using tap water for lubrication. The grinding steps were followed by ultrasonication in isopropanol for 5 min and air drying. Finally, the specimens were polished with DiaDuo-2 suspension (Struers) containing diamonds of 3 µm, rinsed with isopropanol and tap water, and then polished with DiaDuo-2 diamonds of 1 µm.

To characterize the morphology of the implant surfaces, scanning electron microscopy (SEM, JSM-IT100LV, JEOL, Tokyo, Japan) was used. In order to increase the electrical conductivity, a gold layer of 5 ± 2 nm was sputtered onto the surface. SEM imaging was performed at a working distance of 10 mm and an electron beam energy between 5 and 20 kV. The thickness and porosity were measured at 5 different spots on 3 implants for each experimental group. Pore diameter and pore density were determined using ImageJ. Chemical analysis was performed by energy-dispersive X-ray spectroscopy (EDS) at 6 different spots for each experimental group.

7.2.3 Inductively coupled plasma optical emission spectrometry

The ion release profiles of Ca^{2+} and Sr^{2+} were evaluated using inductively coupled plasma – optical emission spectrometry (ICP-OES). The ion release of the biofunctionalized implants

(n = 3/group) was studied through the immersion of 1 cm implants in 1 ml phosphate-buffered saline (PBS) in light-shielding 1.5 ml Eppendorf tubes at 37 °C under static conditions. The PBS was sampled and refilled after ½, 1, 2, 4, 7, 15, and 30 days. Subsequently, the sampled PBS was diluted in 5% nitric acid. The chemical element levels were measured by ICP-OES (Spectro Arcos, Kleve, Germany).

7.2.4 X-ray diffraction

To investigate the composition of phases present on the implant surfaces, X-ray diffraction (XRD) analysis was conducted using a D8 advanced diffractometer (Bruker, Billerica, Massachusetts, United States). For XRD analysis, the following settings were used: voltage = 45kV, current = 40 mA, scatter screen height = 5 mm, and CuKα radiation detector = LL 0.11 W 0.14. The specimens were analyzed statically with a coupled θ - 2θ scan ranging from 20 to 120°, a counting rate of 5 s/step, and a step size of 0.030° 2θ. Subsequently, the collected data was evaluated using DiffracSuite.Eva (version 5.0, Bruker).

7.2.5 Osteogenic cell response

7.2.5.1 Cell seeding and culturing

The osteogenic properties of the implant surfaces were evaluated using preosteoblast cells (MC3T3-E1, Sigma-Aldrich). We tested the osteogenic capacity of NT, PT – 20 A/dm^2 – 5 min, and all PT – Sr implants. The cells were pre-cultured for 7 days in α-MEM supplemented with 10% fetal bovine serum and 1% penicillin-streptomycin (both from ThermoFisher, Waltham, Massachusetts, United States). During experimentation, the cell culture medium was renewed every 2–3 days. In order to seed the cells, implants of 1.0 cm length were placed in 0.2 ml tubes together with 100 µl culture medium containing 1.5×10^5 cells. Subsequently, the tubes were kept in an incubator (at 37 °C, 5% CO_2) and tilted every 20 min for 2 h. Thereafter, the samples were transferred into a 48 well plate with 200 µl fresh medium. We performed the experiments under two conditions: either in standard culture medium throughout the entire experiment or switching after 2 days of culture to osteogenic medium through supplementation of the standard culture medium with 50 µg/ml ascorbic acid and 4 mM β-glycerophosphate (all from Sigma-Aldrich).

7.2.5.2 Metabolic activity assay

To determine the metabolic activities of the MC3T3-E1 cells on the implants, a Presto Blue assay (Thermofisher, Waltham, MA, United States) was performed after 1, 3, 7, 11, and 14 days. At

these time points, 20 µl Presto Blue reagent and 180 µl fresh culture medium were added to the implants, which were subsequently kept in the incubator for 1 h at 37 °C. Finally, the absorbance of the supernatant was determined at 530 nm excitation wavelength and 590 nm emission wavelength using a micro-plate reader (Victor X3, PerkinElmer, Groningen, The Netherlands).

7.2.5.3 Alkaline Phosphatase assay

Osteogenic differentiation was investigated after 11 and 14 days by measuring the alkaline phosphatase (ALP) activity of the MC3T3-E1 cells. Therefore, the specimens (n = 4/group) were cleansed in PBS, submerged in 250 µl of PBS-Triton (containing 0.1% Triton X-100) and subsequently the specimens were ultrasonicated for 10 min, to dissociate the cells from the implant. Then, the specimens were kept in 100 µl p-nitrophenyl phosphate (pNPP, Sigma-Aldrich) at 37 °C for 10 min after which 250 µl of NaOH was supplemented to halt the process. The ALP activity was determined using a standard curve with 0 – 100 µl of pNPP, with 100 µl of PBS-Triton as well as 250 µl of NaOH in every well. Subsequently, the absorbance measurement was performed at a wavelength of 405 nm with a Victor X3 plate reader (PerkinElmer). Finally, using a bicinchoninic acid (BCA) kit (Invitrogen, California, United States), the overall protein content of every specimen was measured, followed by the normalization of the ALP activity to the overall protein content.

7.2.5.4 Cell morphology

The morphology of the cells cultured on the implant surfaces was analyzed by SEM after 7 days of culture (n = 2/group). To that end, the specimens were fixated for 20 min in McDowels fixative consisting of 4% paraformaldehyde and 1% glutaraldehyde in 10 mM phosphate buffer at pH 7.4 and kept in demineralized water at 4 °C. Then, the specimens were rinsed two times in demineralized water for 5 min, dehydrated in diluted ethanol series of 50% for 15 min, 70% for 20 min, and 96% for 20 min, and air-dried for 2 h. Subsequently, the specimens were sputtered with a 5 ± 2 nm gold layer and investigated by SEM.

7.2.6 Statistical analysis

All statistical analyses were performed using GraphPad Prism (GraphPad Software, La Jolla, California, United States) applying one-way and repeated-measures ANOVA and Bonferroni *post hoc* tests. Data are reported as mean ± standard deviation. The differences between the groups were considered statistically significant at $p < 0.05$.

7.3 RESULTS

7.3.1 Voltage transients

The recorded V-t curves demonstrated that implant biofunctionalization by PEO resulted in higher voltages for the PT implants in comparison with PT–Sr implants (**Figure 1A**). Initially, the voltage rose sharply until the dielectric breakdown with a rate of 12, 15, and 18 V/s for PT–20 A/dm^2, PT–30 A/dm^2 and PT–40 A/dm^2, respectively. The dielectric breakdown occurred after 10 ± 2 s at 117 ± 2 V for PT–20 A/dm^2, after 8 ± 1 s at 119 ± 2 V for PT–30 A/dm^2, and after 7 ± 1 s at 129 ± 2 V for PT–40 A/dm^2. For the PT–Sr groups, the dielectric breakdown occurred after 8 ± 1 s at 80 ± 1 V, after 6 ± 1 s at 80 ± 3 V, and after 5 ± 1 s at 81 ± 4 V for 20 A/dm^2, 30 A/dm^2 and 40 A/dm^2, respectively. After the dielectric breakdown, the slope of the V-t curve inflected resulting in a final voltage (after 10 min of oxidation) of 261 ± 3 V, 278 ± 6 V, and 283 ± 3 V for the PT–20 A/dm^2, PT–30 A/dm^2, and PT–40 A/dm^2 groups, respectively while the voltage rose to 127 ± 2 V for PT–Sr–20 A/dm^2, 139 ± 5 V for PT–Sr–30 A/dm^2 and 144 ± 3 V for PT–Sr–40 A/dm^2. The electrical conductivity of the PT – Sr electrolyte was enhanced more than three-fold compared to that of the PT electrolyte (**Figure 1B**).

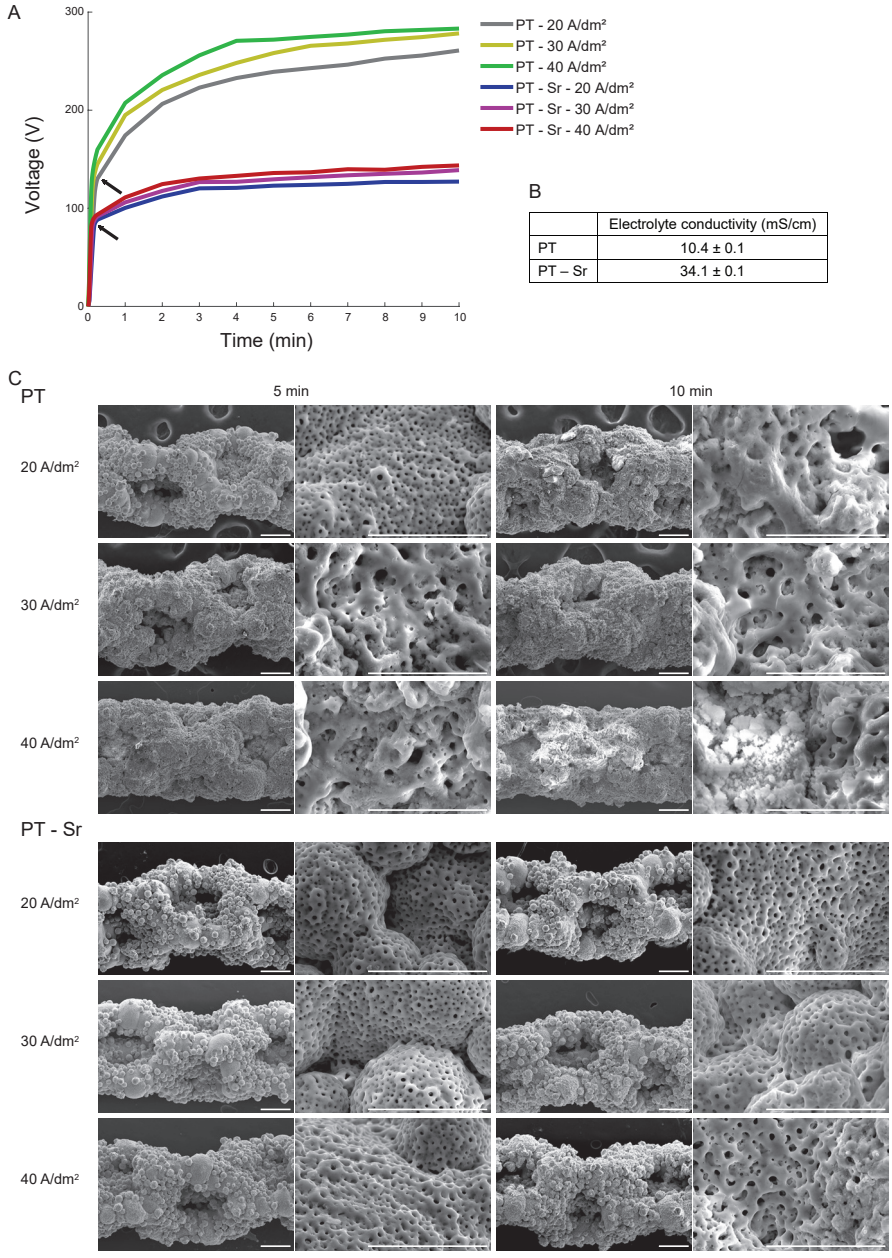

	Electrolyte conductivity (mS/cm)
PT	10.4 ± 0.1
PT – Sr	34.1 ± 0.1

Figure 1. (A) The V-t transients registered during the PEO processing of AM implants. Arrows indicate dielectric breakdown. (B) The electrolyte conductivity of PT and PT – Sr electrolytes (n = 3). (C) The SEM images showing the surface morphology of the implants after PEO biofunctionalization. Scale bars are 200 μm (low magnifications) and 40 μm (high magnifications).

7.3.2 Implant surface morphology after PEO biofunctionalization

Following PEO biofunctionalization, the implant surface morphology was analyzed by SEM (**Figure 1C**). All conditions displayed a homogenous coverage of the titanium oxide layer over the entire implant as identified by a highly interconnected microporous surface, which is characteristic for PEO biofunctionalization. Oxidation of the PT implants for 5 min with 20 A/dm^2 resulted in the highest pore density with the smallest pore sizes while PEO biofunctionalization with increased current densities resulted in relatively rougher surfaces with fewer pores and larger pore sizes (**Table 1**). Enhancing the oxidation time from 5 to 10 min resulted in an even further enlargement of pore sizes and the roughening of the surface except for 10 min with 40 A/dm^2 which showed reduced pore sizes compared to 10 min with 30 A/dm^2. In the case of the PT–Sr implants, the changes in morphology were less prominent. Increasing the current density did not result in a change in the surface morphology of the implants after 5 min. After 10 min, however, the PT–Sr–30 A/dm^2 and PT–Sr–40 A/dm^2 groups revealed a less circular pore shape and the roughening of their surfaces. EDS analysis demonstrated the presence of Ti, Al, O, C, P, Ca and Sr species and indicated that Ca was largely replaced by Sr when comparing PT and PT–Sr implants (**Table 1**).

Table 1. Porosity and chemical analysis of the implant surfaces. The proportion of chemical elements is indicated as at%.

	Pore density (%)	Pore diameter (µm)	Ca (at%)	Sr (at%)
PT – 5min – 20A/dm^2	2.6 ± 0.1	2.7 ± 1.1	9.8 ± 2.9	-
PT – 5min – 30A/dm^2	2.2 ± 0.7	3.3 ± 1.7	7.1 ± 2.0	-
PT – 5min – 40A/dm^2	1.6 ± 0.5	5.2 ± 1.9	7.8 ± 2.2	-
PT – 10min – 20A/dm^2	0.8 ± 0.4	4.5 ± 3.2	9.1 ± 2.5	-
PT – 10min – 30A/dm^2	0.6 ± 0.2	4.9 ± 2.4	9.7 ± 2.9	-
PT – 10min – 40A/dm^2	0.4 ± 0.2	2.0 ± 1.5	8.1 ± 1.4	-
PT – Sr – 5min – 20A/dm^2	1.2 ± 0.5	1.3 ± 0.3	0.5 ± 0.1	3.0 ± 0.5
PT – Sr – 5min – 30A/dm^2	1.2 ± 0.1	1.5 ± 0.4	0.7 ± 0.3	3.5 ± 1.4
PT – Sr – 5min – 40A/dm^2	2.0 ± 0.4	1.7 ± 0.4	0.7 ± 0.1	3.8 ± 0.4
PT – Sr – 10min – 20A/dm^2	1.3 ± 0.9	1.4 ± 0.3	1.8 ± 0.8	11.9 ± 5.5
PT – Sr – 10min – 30A/dm^2	2.5 ± 0.3	2.3 ± 0.6	1.1 ± 0.3	7.2 ± 2.5
PT – Sr – 10min – 40A/dm^2	3.6 ± 0.8	2.0 ± 0.4	1.0 ± 0.2	3.5 ± 0.6

7.3.3 Cross-section morphology and thickness of the biofunctionalized TiO_2 layers

The morphology and thickness of the titanium oxide surface layers were analyzed through cross-section analysis by SEM (**Figure 2A**). For the PT implants, the oxide layer morphology differed across their thickness. At the interface with the substrate (inner side), a fully dense and uniform layer with an intact interface with the substrate was observed for all the implant groups. This barrier layer had a thickness of ca. 2 µm. Moving outwards, a porous morphology was visible while the surface oxide layer was found to be dense in all the groups except for the PT– 10min–40 A/dm² group, which only displayed a porous outer layer. The PT–Sr implant groups also displayed a fully dense oxide layer at the implant substrate interface, followed by a middle porous layer, and a denser surface layer on top. Increasing the current density and oxidation time resulted in enhanced cross-sectional pore sizes up to an oxidation time of 10 min with 40 A/dm² (**Figure 2B**).

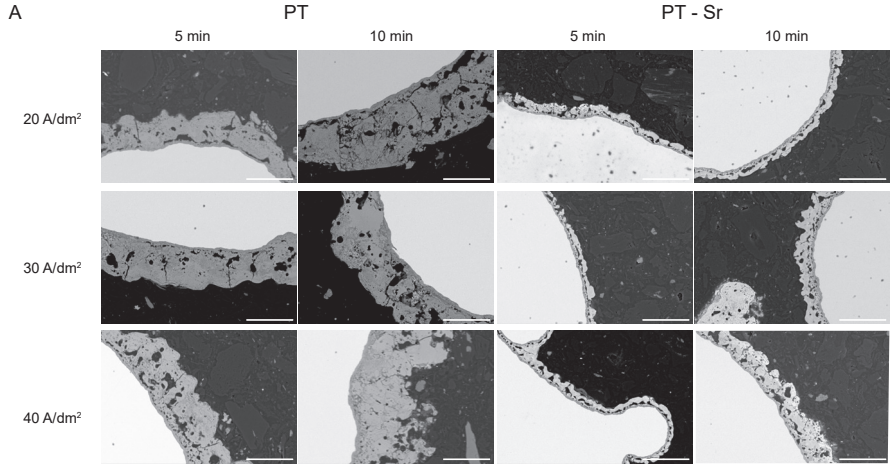

B

	Pore diameter (µm)
PT – 5min – 20A/dm²	2.7 ± 1.3
PT – 5min – 30A/dm²	4.2 ± 1.7
PT – 5min – 40A/dm²	4.3 ± 1.5
PT – 10min – 20A/dm²	3.9 ± 1.2
PT – 10min – 30A/dm²	5.1 ± 2.0
PT – 10min – 40A/dm²	4.5 ± 2.5
PT – Sr – 5min – 20A/dm²	1.8 ± 0.9
PT – Sr – 5min – 30A/dm²	2.3 ± 1.2
PT – Sr – 5min – 40A/dm²	2.5 ± 0.8
PT – Sr – 10min – 20A/dm²	2.6 ± 1.7
PT – Sr – 10min – 30A/dm²	3.1 ± 1.4
PT – Sr – 10min – 40A/dm²	3.4 ± 1.6

C

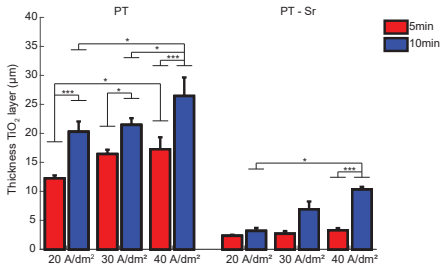

Figure 2. The thickness of the surface layer of TiO_2 implants. (A) The SEM images of the surface layer in backscattering mode. (B) Cross-sectional pore-size analysis by SEM ($n = 3$). (C) A quantitative analysis of the thickness of the implant surface layers ($n = 3$). * $p < 0.05$, *** $p < 0.001$. Scale bar = 10 µm.

The thickness of the implant oxide layer was enhanced both by an increased current density and an increased oxidation time (**Figure 2C**). For the PT implants, the thickness of the oxide layer increased after 10 min as compared to 5 min for treatments with current densities of 20, 30, and 40 A/dm^2 ($p < 0.001$, $p < 0.05$ and $p < 0.001$, respectively), after 5 min with 40 A/dm^2 as compared to 20 A/dm^2 ($p < 0.05$), and after 10 min with 40 A/dm^2 as compared to 20 A/dm^2 and 30 A/dm^2 ($p < 0.05$). For the PT–Sr implants, the oxide layer was enhanced after oxidation for 10 min with 40 A/dm^2 as compared to 5 min with 40 A/dm^2 and as compared to 10 min with 20 A/dm^2 ($p < 0.001$). The thickness of the titanium oxide layer was significantly larger for the PT implants in comparison with the PT–Sr implants under similar current densities and oxidation times, varying between 12 and 26 µm for the PT implants and between 2 and 10 µm for the PT–Sr implants.

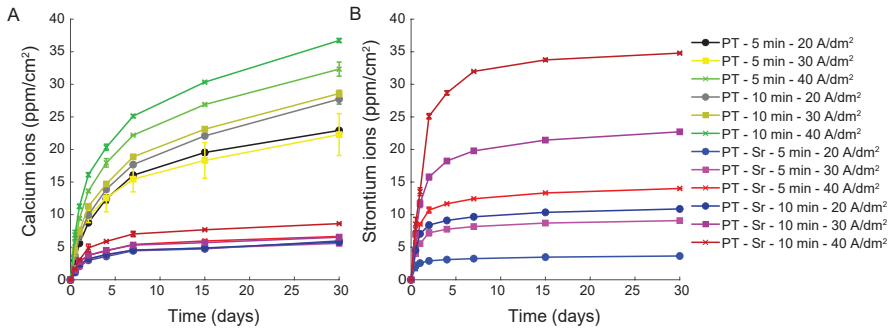

Figure 3. The cumulative ion release profiles. (A) The calcium and (B) strontium ion release from the implant surfaces ($n = 3$) measured by ICP-OES.

7.3.4 Ion release kinetics

The Ca and Sr ion release kinetics were analyzed by ICP-OES for up to 30 days. For the PT implants, the Ca^{2+} release was increased 1.37 fold for treatment with a current density of 40 A/dm^2 as compared to a current density of 30 A/dm^2 (**Figure 3A**). Comparing 5 and 10 min of oxidation time resulted in 1.21, 1.28, and 1.14 fold increase in the Ca^{2+} release for the PT implants treated with current densities of 20, 30, and 40 A/dm^2, respectively. For the PT–Sr implants, the Ca^{2+} released increased by 1.26 fold for the implants treated with a current density of 40 A/dm^2 as compared to those subjected to a current density of 30 A/dm^2 while treatment with 10 min as compared to 5 min resulted in 0.97, 1.16, and 1.30 fold increase in the Ca^{2+} release for the PT–Sr implants treated with current densities of 20, 30, and 40 A/dm^2, respectively. The Ca^{2+} release was at least 4-fold higher for all the PT implants as compared to the PT–Sr implants. Furthermore, for both the PT and PT–Sr implants, the Ca^{2+} release was highest for 10 min and a current density of 40 A/dm^2.

The Sr^{2+} release was the highest for 10 min oxidation with 40 A/dm^2 and increased with both the oxidation time and current density **(Figure 3B)**. The Sr^{2+} release was 2.49 and 2.09 fold higher when the current density increased from 20 to 30 A/dm^2 for 5 and 10 min oxidation time, respectively. The implants treated with 40 A/dm^2 further increased the Sr^{2+} release by 1.54 fold. Elongating the oxidation time from 5 to 10 min, resulted in 2.98, 2.50, and 2.48 fold increase in the Sr^{2+} release for the PT–Sr implants treated with current densities of 20, 30, and 40 A/dm^2, respectively. The PT–Sr implants released between 0.63 and 2.11 fold higher levels of Sr^{2+} as compared to Ca^{2+} after 5 min and between 1.87 and 4.04 fold after 10 min.

7.3.5 Phase composition of the titanium oxide layer

The phase composition of the implants' oxide layer was evaluated by XRD (**Figure 4**). While differences in the phase composition were frequently observed between 5 and 10 min of oxidation time, few phase changes were observed between the current densities of 20, 30, and 40 A/dm^2. For the PT implants, mainly the rutile TiO_2 phase was observed, while anatase was exclusively observed for 5 min of oxidation time. Both after 5 and 10 min of PEO processing, the $Ca_{10}(PO_4)_6(OH)_2$ (hydroxyapatite) phase as well as $CaTiO_3$ and $Ca_3(PO_4)_2$ were present. $CaTiO_3$ and hydroxyapatite were not detected on the PT–Sr implants, while $Ca_4H_2(P_3O_{10})_2$ and $Sr_8Ca_{2.5}(PO_4)_7$ phases were detected exclusively on the PT–Sr implants after 10 min of oxidation with current densities of 30 and 40 A/dm^2. Furthermore, $SrTiO_3$ and $Sr_{10}(PO_4)_6(OH)_2$ were detected on all the PT–Sr implants, with $Sr_{10}(PO_4)_6(OH)_2$ being observed more frequently with current densities of 30 and 40 A/dm^2. On the PT–Sr implants, primarily the phases pertaining to the base metal were observed with scarce rutile phases for current densities of 30 and 40 A/dm^2. After 10 min of PEO processing with current densities of 30 and 40 A/dm^2 anatase was detected.

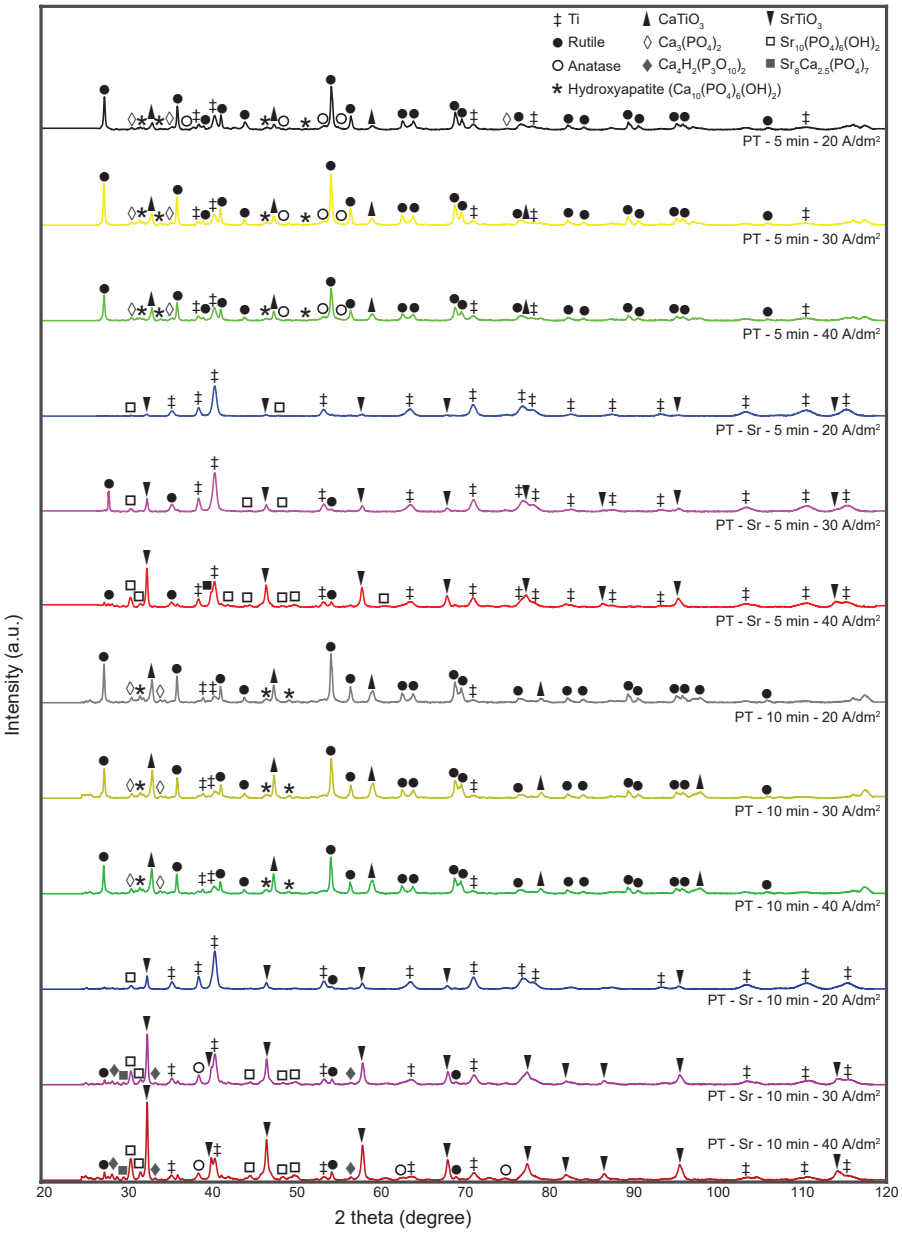

Figure 4. The X-ray diffraction spectra of the implants after PEO biofunctionalization.

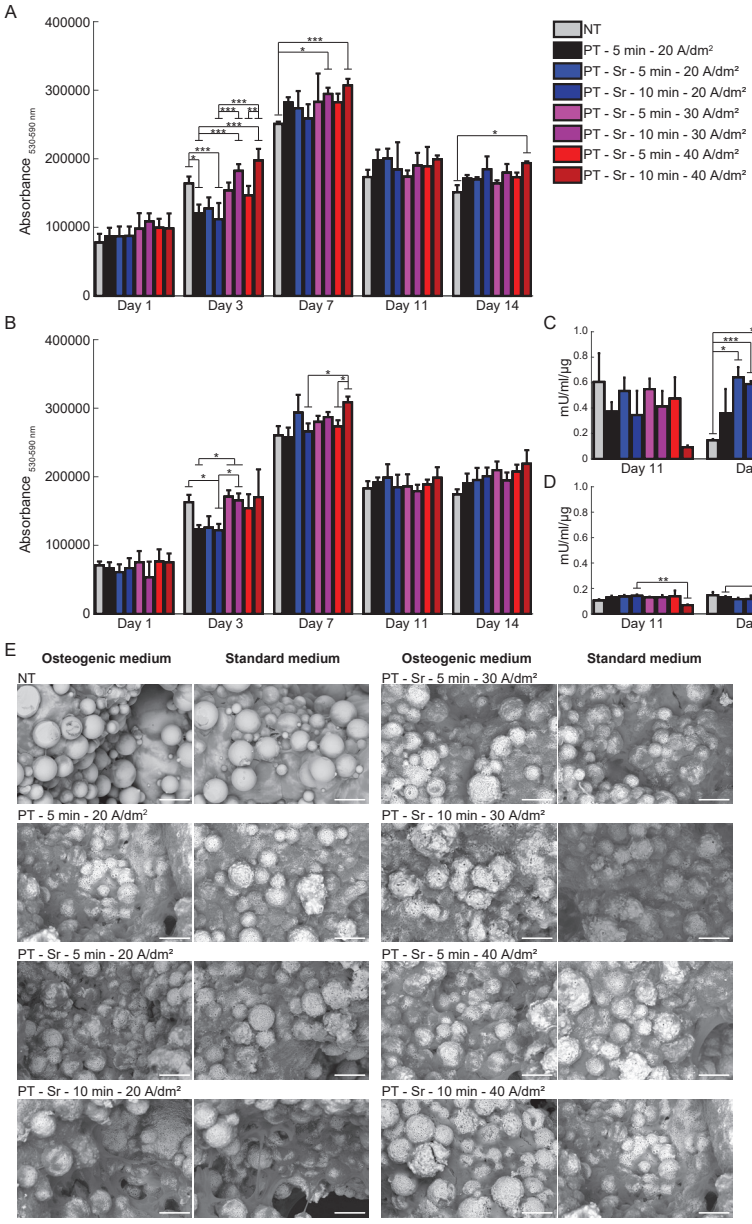

Figure 5. The osteogenic capacity of the MC3T3-E1 cells cultured on the implant surfaces (n = 4). Determination of the metabolic activity by the Presto Blue assay of MC3T3-E1 cells cultured on the implants after 1, 3, 7, 11, and 14 days of culture (A) with and (B) without the addition of the osteogenic differentiation medium after 2 days. The measurement of the ALP activity after 11 and 14 days (C) with and (D) without the addition of the osteogenic differentiation medium. (E) The SEM images of the cells on the implants after 7 days of culture in osteogenic and standard culture medium. * $p < 0.05$, ** $p < 0.01$, *** $p < 0.001$. Scale bar = 50 µm.

7.3.6 Bioactivity of biofunctionalized implants

In general, the surface of the PT–Sr implants resembled the surface of the PT implants oxidized for 5 min at 20 A/dm^2. Therefore, the metabolic activity of MC3T3-E1 cells cultured on the implants in standard and osteogenic media was determined using a Presto Blue assay on NT, PT implants biofunctionalized for 5 min at 20 A/dm^2 and all PT–Sr implants. With the osteogenic medium and after 3 days of culture (**Figure 5A**) the metabolic activity differed significantly between the NT and PT ($p < 0.05$) and PT–Sr 20 A/dm^2 implants for 10 min ($p < 0.001$), PT and PT–Sr 30 A/dm^2 for 10 min ($p < 0.001$) and PT–Sr 40 A/dm^2 for 10 min ($p < 0.001$). After 7 days of culture, significant differences were observed between the NT and PT–Sr 30 A/dm^2 for 10 min ($p < 0.05$) and PT–Sr 40 A/dm^2 for 10 min ($p < 0.001$) as well as between PT–Sr 20 A/dm^2 and PT–Sr 40 A/dm^2 for 10 min ($p < 0.01$). After 14 days, there was a significant difference between NT and PT–Sr 40 A/dm^2 for 10 min ($p < 0.05$). Without the osteogenic medium and after 3 days of cell culture, the metabolic activity differed significantly (**Figure 5B**) between NT and PT–Sr 20 A/dm^2 for 10 min ($p < 0.05$), PT and PT–Sr 30 A/dm^2 for 5 min ($p < 0.05$), PT and PT–Sr 30 A/dm^2 for 10 min ($p < 0.05$) and PT–Sr 20 A/dm^2 and PT–Sr 30 A/dm^2 for 10 min ($p < 0.05$). After 7 days, there were significant differences between PT–Sr 20 A/dm^2 and PT–Sr 40 A/dm^2 for 10 min ($p < 0.05$) as well as PT–Sr 40 A/dm^2 for 5 and 10 min ($p < 0.05$). Comparing the metabolic activity in the presence of or without osteogenic medium, the results did not differ significantly.

The levels of ALP activity in osteogenic medium (**Figure 5C**), differed significantly after 14 days between NT and PT–Sr 20 A/dm^2 for 5 min ($p < 0.05$), PT–Sr 20 A/dm^2 for 10 min ($p < 0.001$) and PT–Sr 40 A/dm^2 for 5 min ($p < 0.05$). Without the osteogenic medium (**Figure 5D**), there were significant differences in the ALP activity after 11 days between PT–Sr 20 A/dm^2 and PT–Sr 40 A/dm^2 for 10 min ($p < 0.01$). After 14 days, there was only a significant difference between PT and PT–Sr 40 A/dm^2 for 10 min ($p < 0.01$). Without the osteogenic medium, the levels of the ALP activity were on average 4-fold lower than in the presence of the osteogenic medium. SEM analysis of the cultured cells on the implant surface for 7 days demonstrated a wide coverage of the surface by the MC3T3-E1 cells under all conditions (**Figure 5E**).

7.4 DISCUSSION

Given the enhanced need for orthopedic implants, the surface biofunctionalization of AM porous titanium implants has gained significant momentum. However, the biofunctionalization of porous structures remains challenging. While PEO has been successfully applied to create bioactive surfaces with osteogenic and antibacterial behavior on highly porous AM titanium

implants [14, 38], there is limited understanding of the contribution of individual PEO processing parameters to the generation of bioactivity on titanium biomaterials. Therefore, the possibilities to maximize the bioactivity of titanium implants by this versatile process are not fully explored and harnessed.

During PEO processing, ionic species present in the PEO electrolyte can become part of the titanium oxide layer. The composition of the electrolyte, therefore, directly governs the bioactivity of the biofunctionalized implant surfaces. In this study, we used Ca/P-based PEO electrolytes as they have been shown to generate osteogenic surfaces, partly due to hydroxyapatite formation during the PEO process [14]. In addition, strontium was added as this has been shown to further enhance the osteogenic capacity [33, 39] and, more recently, to possibly boost the antibacterial potential of AgNPs incorporated in such layers [38]. To incorporate different levels of Sr, various current densities (namely 20, 30 and 40 A/dm^2) and oxidation time (namely 5 and 10 minutes) were used. Altering the PEO electrolyte affects the PEO process, which in turn changes the surface morphology [20]. The SEM analysis of the surface of the PT–Sr implants revealed a porous surface with smaller pores as compared to the PT implants. An oxidation time of 10 min with current densities of 30 and 40 A/dm^2 resulted in reduced porosity due to a partial destruction of the top surface layer. The smaller pore size of the PT-Sr implants may be associated with the lower voltage stems from a higher electrolyte conductivity for the PT–Sr electrolytes compared to the PT electrolytes.

Both enhancing the current density and oxidation time affected the surface morphology of the PT implants, as the pore density was reduced while the pore size increased. This continued until 10 min oxidation with 40 A/dm^2 which resulted in destruction of the oxide layer and subsequent reduction of pore sizes. The changes were more pronounced for longer oxidation times, which is in line with the findings of other studies [40, 41]. This increased pore diameter is caused by the rising spark size and intensity and the accompanying buildup of pressures, causing an expansion in the pore diameter and making pores increasingly interconnected [42]. However, the surface morphology of the PT–Sr implants was barely affected by the current density or oxidation time, due to the small and less intense spark discharges caused by the presence of strontium to the PEO electrolyte. Notably, the surface morphology of the PT-Sr implants resembled the morphology of the PT implants oxidized at the lowest current density and shortest time (*i.e.*, 20 A/dm^2 and 5 minutes).

Since the current density and oxidation time alter the growth of the TiO_2 layer during PEO processing, we also explored the thickness and cross-section morphology of the TiO_2 surface layer. For all experimental groups, three different sections were observed in the TiO_2 layer: a thin, fully dense, and continuous barrier layer at the interface between oxide layer and implant substrate, followed by a layer with large pores, and on top a denser outer layer.

This layer build-up is the result of different phases during the PEO process. The barrier layer is formed before dielectric breakdown by the inwards migration of the O^{2-} and the migration of titanium ions outwards [43]. After dielectric breakdown, the continuous build up and destruction of the layer occurs, leading to the outwards expansion of the oxide layer and intensified spark discharging resulting in the formation of larger, protruding pores that are increasingly interconnected [12]. The oxide layer was thinner for all the PT–Sr implants as compared to the PT implants. In addition, the pore size of the PT–Sr implants was smaller, reflecting the surface pore analysis. The thickness of the oxide layer was enhanced to a large extent by extending the oxidation time and to smaller extents by increasing the current density, which is in line with the results of previous studies [44].

An analysis of the ion release kinetics indicated that both the oxidation time and current density enhanced the release of the Ca and Sr ions, which correlated with the enhanced thickness of the oxide layer that functions as a reservoir for ions to be released. Due to increased current densities and prolonged oxidation times, the electrical field between anode and cathode is increased, thereby enhancing the migration of the Ca and Sr ions into the growing oxide layer [45]. The release of Ca was reduced for the PT–Sr implants in comparison with the PT implants, reflecting the observation that Ca is largely replaced by strontium in the case of PT–Sr implants, as confirmed by EDS analysis. This phenomenon has also been observed in other studies [46]. For all the PT–Sr implants, except for 5 min of oxidation with a current density of 20 A/dm^2, the release rate of Sr^{2+} was higher than that of Ca^{2+}.

During PEO processing, spark discharges may lead to local temperatures of up to 3500 K [47], resulting in the mixing of the species that originate from the substrate and those present in the electrolyte. Nanocrystalline phases are formed due to the increasing temperatures and their formation increases with the applied energy input [48]. Initially, anatase is formed during the PEO process, followed by increased rutile formation over time due to more intense spark discharges with concurring rise in local temperature and pressure [49]. These nanocrystalline phases are known to induce photocatalytic activity and contribute to antibacterial activity [50]. In this study, we observed that enhanced oxidation time and current densities induced numerous phase changes. The composition of the electrolyte affects the crystallinity of the TiO_2 layer due to altered spark discharge formation and the incorporation of the species present in the PEO electrolyte [51]. We observed that the PT–Sr implants demonstrated more intense Ti peaks from the substrate, indicating a thinner oxide layer in comparison with the PT implants. Furthermore, less rutile was observed in comparison with the PT implants. This is due to a less intense spark discharging and concurring lower temperatures during the PEO process.

The formation of both rutile and anatase phases has been shown to stimulate the formation of hydroxyapatite and other Ca/P phases on titanium surfaces [52]. Furthermore,

the photocatalytic activity of anatase and rutile increases with the hydroxyl density at the implant surface during spark discharging [53, 54]. As a result, Ti-OH is formed that, together with Ca^{2+} and PO_4^{3-} delivered by the electrolyte, induce the nucleation and formation of hydroxyapatite crystals [55, 56]. We observed higher numbers of crystalline Ca/P and strontium-Ca/P phases on the implant surfaces which were treated for longer oxidation times and also displayed higher levels of rutile and anatase. Interestingly, we observed hydroxyapatite on the PT implants, but not on the PT–Sr implants. Therefore, altering the oxidation time and composition of the PEO electrolyte directly affected the formation of crystalline TiO_2 and Ca/P phases on the implant surface. In previous work [14], we have observed that the growth rate observed during the PEO process is not affected by the different microstructure of additively manufactured implants in comparison with that of solid implants made from annealed Ti6Al4V. However, the complex micro-architecture of selective laser melted implants is likely to affect the internal fluid flow, resulting in altered local cooling of the electrolyte and potentially increased temperature during plasma discharging. These local increases of temperature in turn could contribute to the formation of hydroxyapatite phases.

Surface biofunctionalization by PEO has been shown to improve cellular behavior including cell adhesion, osteogenic differentiation, and matrix mineralization, which is generally attributed to the microporous surface morphology [57, 58] and the presence of Ca/P as well as strontium on the implant surface [59-61]. Moreover, the presence of hydroxyapatite has been shown to enhance the osseointegration of titanium implants [62-64]. We, therefore, investigated whether the observed changes in the implant surface morphology and phase composition due to the addition of strontium to the PEO electrolyte as well as the variation of the current density and oxidation time affected the osteogenic behavior of preosteoblast MC3T3-E1 cells cultured on the implant surfaces.

We performed those experiments both in standard culture medium and in an osteogenic medium. The metabolic activity was analyzed up to 14 days and was not significantly different between the specimens cultured in standard and osteogenic medium. Moreover, after 7 days, the metabolic activity decreased for all surfaces and culture conditions and this is likely caused by a stop in cell proliferation as the implant surface was increasingly covered. The osteogenic medium enhanced the ALP activity, which is a differentiation marker, of the MC3T3-E1 cells on any implant at each time point as compared to the specimens cultured in the standard medium. After 14 days, the ALP activity of the PT–Sr implants biofunctionalized with a current density of 20 A/dm^2 for both 5 and 10 min as well as a current density of 40 A/dm^2 for 5 min was enhanced in comparison with the NT implants. The trend also indicates higher average ALP activities of these PT–Sr implants relative to the PT implants oxidized at 20 for 5 minutes, although not statistically significant. These PT–Sr implants had a surface

morphology comparable with the PT implants oxidized at 20 A/dm^2 for 5 minutes and released the lower amounts of Sr ions compared to the other PT–Sr implants.

Our results suggest that the osteogenic behavior of the implants may be determined by a combination of surface morphology and Sr ion release, since an unfavorable surface morphology and too high doses of strontium may hamper the osteogenic differentiation of cells and induce apoptosis [65-67]. Surface characteristics including porosity [57], pore size [68], pore shape [69], and the presence of TiO_2 [70] and Ca/P/Sr-based phases [21, 33, 60] all have been shown to affect osteogenesis. On the macroscale, a lower porosity has been shown to enhance osteogenic differentiation *in vitro*, while a higher porosity and larger pore size has been found to result in greater bone ingrowth *in vivo* due to enhanced vascularization [68]. The PEO-biofunctionalized implants with increased microporosity have exhibited enhanced peri-implant bone formation *in vivo* [57]. Furthermore, both hydroxyapatite- and strontium hydroxyapatite-containing PEO-biofunctionalized implants are found to stimulate osteogenic differentiation *in vitro* and result in a higher bonding strength *in vivo* [33]. Finally, previous studies have reported an association between an increased microporosity and enhanced cell adhesion, cell proliferation, and ALP activity *in vitro* [59]. To fully pinpoint the contribution of each individual surface characteristic in our study, an extensive investigation of each separate characteristic needs to be performed, which is suggested for future studies.

In this study PEO processing was performed in AC mode, however also other PEO processing parameters can be explored, including the use of DC mode, pulsed uni- or bipolar current, different frequencies and varying duty cycles. The use of DC mode may result in difficulties to control the surface discharge kinetics [18]. Therefore, unipolar or bipolar pulse current regimes are used to control the spark duration [71]. Thereby the heat conditions during PEO are regulated and as such the surface morphology and chemical composition. Surfaces produced in pulsed bipolar mode possess a higher porosity due to enhanced spark discharges compared to unipolar mode [72]. In addition, with pulsed bipolar mode a larger proportion of the oxidized implant surface was composed of elements from the PEO electrolyte, rather than from the implant substrate [73]. However, when the cathode pulse was increased over a certain optimum the thickness of the titanium oxide layer was decreased [74].

The properties of the surfaces can be influenced by the duty cycles of the unipolar and bipolar pulsed modes, *i.e.* varying the time of current during each period. In this way the power of the plasma discharge can be enhanced by shorter pulse durations and increased voltages or currents [75]. As a result enhanced duty cycles will lead to increased heat generation and spark energy, thereby generating larger pores [76]. In addition, the frequency of the pulses can be changed, with higher frequencies leading to enhanced porosity and corrosion resistance [77]. Furthermore, the fraction of anatase and rutile phases can be affected by varying the

frequencies [78]. Moreover, long duty cycles combined with high frequencies have shown to support the apatite forming capacity of the implant surfaces [79]. However, the effects of these PEO processing parameters on the osteogenic capacity of the implant surface remain to be elucidated.

Further exploration of the effects of the concentration of strontium in the PEO electrolyte and the electrical parameters is needed to fully optimize the ratio of strontium and Ca release on an implant with osteogenic surface morphology. Combined with antibacterial agents [7, 14], such as antibiotics or inorganic nanoparticles, this will generate potent multifunctional surfaces on future AM porous titanium implants. The next evaluation steps should include *in vivo* experiments.

7.5 CONCLUSIONS

In this study, we investigated the effects of the composition of calcium and strontium-based electrolytes, current density, and oxidation time on the surface morphology, phase formation, ion release, metabolic activity, and osteogenic properties of AM porous titanium implants. The implants biofunctionalized with strontium displayed smaller pore sizes, a thinner TiO_2 layer thickness, four-fold lower rate of Ca^{2+} release, predominantly anatase TiO_2 phases and Sr-containing phases as compared to the implants biofunctionalized in electrolytes containing only Ca/P species. Increasing the oxidation time resulted in a rougher surface with bigger pores, up to 4.4 fold thickening of the TiO_2 surface layer, and enhanced formation of Ca/P and TiO_2 phases to a further extent than increasing the current density. The rate of the Ca^{2+} release was enhanced by up to 1.3 and 1.2 folds and that of the Sr^{2+} release by up to 3.5 and 2.7 folds when the higher values of the current density and oxidation time were used, respectively. The different current densities and oxidation times resulted in varying metabolic activities after 3 and 7 days of the culture of MC3T3-E1 cells while the ALP activity was enhanced after 14 days for PEO biofunctionalization in Sr-containing electrolytes with a current density of 20 A/dm^2 for both 5 and 10 min, as well as with a current density of 40 A/dm^2 for 5 min. Altogether, changing the oxidation time and current density caused significant changes in the surface morphology, Sr incorporation and bioactivity of AM porous titanium implants.

ACKNOWLEDGEMENTS

The research for this paper was financially supported by the Prosperos project, funded by the Interreg VA Flanders – The Netherlands program, CCI grant no. 2014TC16RFCB046.

REFERENCES

[1] H. Maradit Kremers, D.R. Larson, C.S. Crowson, W.K. Kremers, R.E. Washington, C.A. Steiner, W.A. Jiranek, D.J. Berry, Prevalence of total hip and knee replacement in the United States, J Bone Joint Surg Am 97 (2015) 1386-97.

[2] K. Willemsen, R. Nizak, H.J. Noordmans, R.M. Castelein, H. Weinans, M.C. Kruyt, Challenges in the design and regulatory approval of 3D-printed surgical implants: a two-case series, The Lancet Digital Health 1 (2019) e163-e171.

[3] E.D. Sheha, S.D. Gandhi, M.W. Colman, 3D printing in spine surgery, Ann Transl Med 7 (2019) S164.

[4] K.C. Wong, 3D-printed patient-specific applications in orthopedics, Orthop Res Rev 8 (2016) 57-66.

[5] H.M.A. Kolken, S. Janbaz, S.M.A. Leeflang, K. Lietaert, H.H. Weinans, A.A. Zadpoor, Rationally designed meta-implants: a combination of auxetic and conventional meta-biomaterials, Materials Horizons 5 (2018) 28-35.

[6] A.A. Zadpoor, Additively manufactured porous metallic biomaterials, J Mater Chem B 7 (2019) 4088-4117.

[7] S. Bakhshandeh, Z. Gorgin Karaji, K. Lietaert, A.C. Fluit, C.H.E. Boel, H.C. Vogely, T. Vermonden, W.E. Hennink, H. Weinans, A.A. Zadpoor, S. Amin Yavari, Simultaneous delivery of multiple antibacterial agents from additively manufactured porous biomaterials to fully eradicate planktonic and adherent Staphylococcus aureus, ACS Appl Mater Interfaces 9 (2017) 25691-25699.

[8] L. Lara Rodriguez, P.A. Sundaram, E. Rosim-Fachini, A.M. Padovani, N. Diffoot-Carlo, Plasma electrolytic oxidation coatings on gammaTiAl alloy for potential biomedical applications, J Biomed Mater Res B Appl Biomater 102 (2014) 988-1001.

[9] B.S. Necula, I. Apachitei, L.E. Fratila-Apachitei, E.J. van Langelaan, J. Duszczyk, Titanium bone implants with superimposed micro/nano-scale porosity and antibacterial capability, Applied Surface Science 273 (2013) 310-314.

[10] S.A. Yavari, B.S. Necula, L.E. Fratila-Apachitei, J. Duszczyk, I. Apachitei, Biofunctional surfaces by plasma electrolytic oxidation on titanium biomedical alloys, Surface Engineering 32 (2016) 411-417.

[11] T.W. Clyne, S.C. Troughton, A review of recent work on discharge characteristics during plasma electrolytic oxidation of various metals, International Materials Reviews 64 (2018) 127-162.

[12] B.S. Necula, I. Apachitei, F.D. Tichelaar, L.E. Fratila-Apachitei, J. Duszczyk, An electron microscopical study on the growth of TiO2-Ag antibacterial coatings on Ti6Al7Nb biomedical alloy, Acta Biomater 7 (2011) 2751-7.

[13] E. Matykina, P. Skeldon, G.E. Thompson, Fundamental and practical evaluations of PEO coatings of titanium, International Heat Treatment and Surface Engineering 3(1-2) (2013) 45-51.

[14] I.A.J. van Hengel, M. Riool, L.E. Fratila-Apachitei, J. Witte-Bouma, E. Farrell, A.A. Zadpoor, S.A.J. Zaat, I. Apachitei, Selective laser melting porous metallic implants with immobilized silver nanoparticles kill and prevent biofilm formation by methicillin-resistant Staphylococcus aureus, Biomaterials 140 (2017) 1-15.

[15] Z. Gorgin Karaji, R. Hedayati, B. Pouran, I. Apachitei, A.A. Zadpoor, Effects of plasma electrolytic oxidation process on the mechanical properties of additively manufactured porous biomaterials, Mater Sci Eng C Mater Biol Appl 76 (2017) 406-416.

[16] S. Aliasghari, A. Němcová, P. Skeldon, G.E. Thompson, Influence of coating morphology on adhesive bonding of titanium pre-treated by plasma electrolytic oxidation, Surface and Coatings Technology 289 (2016) 101-109.

[17] H. Sharifi, M. Aliofkhazraei, G.B. Darband, S. Shrestha, A Review on Adhesion Strength of Peo Coatings by Scratch Test Method, Surface Review and Letters 25(03) (2018).

[18] A.L. Yerokhin, X. Nie, A. Leyland, A. Matthews, S.J. Dowey, Plasma electrolysis for surface engineering, Surface and Coatings Technology 122 (1999) 73-93.

[19] Y. Wang, T. Lei, B. Jiang, L. Guo, Growth, microstructure and mechanical properties of microarc oxidation coatings on titanium alloy in phosphate-containing solution, Applied Surface Science 233 (2004) 258-267.

[20] E. Ahounbar, S.M. Mousavi Khoei, H. Omidvar, Characteristics of in-situ synthesized hydroxyapatite on TiO2 ceramic via plasma electrolytic oxidation, Ceramics International 45 (2019) 3118-3125.

[21] Y.W. Lim, S.Y. Kwon, D.H. Sun, H.E. Kim, Y.S. Kim, Enhanced cell integration to titanium alloy by surface treatment with microarc oxidation: a pilot study, Clin Orthop Relat Res 467 (2009) 2251-8.

[22] S. Marques Ida, N.C. da Cruz, R. Landers, J.C. Yuan, M.F. Mesquita, C. Sukotjo, M.T. Mathew, V.A. Barao, Incorporation of Ca, P, and Si on bioactive coatings produced by plasma electrolytic oxidation: The role of electrolyte concentration and treatment duration, Biointerphases 10 (2015) 041002.

[23] X. Lu, M. Mohedano, C. Blawert, E. Matykina, R. Arrabal, K.U. Kainer, M.L. Zheludkevich, Plasma electrolytic oxidation coatings with particle additions – A review, Surface and Coatings Technology 307 (2016) 1165-1182.

[24] I.A.J. van Hengel, N.E. Putra, M. Tierolf, M. Minneboo, A.C. Fluit, L.E. Fratila-Apachitei, I. Apachitei, A.A. Zadpoor, Biofunctionalization of selective laser melted porous titanium using silver and zinc nanoparticles to prevent infections by antibiotic-resistant bacteria, Acta Biomater 107 (2020) 325-337.

[25] L. Cianferotti, F. D'Asta, M.L. Brandi, A review on strontium ranelate long-term antifracture efficacy in the treatment of postmenopausal osteoporosis, Ther Adv Musculoskelet Dis 5(3) (2013) 127-39.

[26] J.Y. Reginster, J.M. Kaufman, S. Goemaere, J.P. Devogelaer, C.L. Benhamou, D. Felsenberg, M. Diaz-Curiel, M.L. Brandi, J. Badurski, J. Wark, A. Balogh, O. Bruyere, C. Roux, Maintenance of antifracture efficacy over 10 years with strontium ranelate in postmenopausal osteoporosis, Osteoporos Int 23(3) (2012) 1115-22.

[27] J.Y. Reginster, Cardiac concerns associated with strontium ranelate, Expert Opin Drug Saf 13(9) (2014) 1209-13.

[28] L. Kyllonen, M. D'Este, M. Alini, D. Eglin, Local drug delivery for enhancing fracture healing in osteoporotic bone, Acta Biomater 11 (2015) 412-34.

[29] E. Gentleman, Y.C. Fredholm, G. Jell, N. Lotfibakhshaiesh, M.D. O'Donnell, R.G. Hill, M.M. Stevens, The effects of strontium-substituted bioactive glasses on osteoblasts and osteoclasts in vitro, Biomaterials 31(14) (2010) 3949-56.

[30] M. Yamaguchi, M.N. Weitzmann, The intact strontium ranelate complex stimulates osteoblastogenesis and suppresses osteoclastogenesis by antagonizing NF-kappaB activation, Mol Cell Biochem 359(1-2) (2012) 399-407.

[31] Y. Dang, L. Zhang, W. Song, B. Chang, T. Han, Y. Zhang, L. Zhao, In vivo osseointegration of Ti implants with a strontium-containing nanotubular coating, Int J Nanomedicine 11 (2016) 1003-11.

[32] A. Henriques Lourenco, N. Neves, C. Ribeiro-Machado, S.R. Sousa, M. Lamghari, C.C. Barrias, A. Trigo Cabral, M.A. Barbosa, C.C. Ribeiro, Injectable hybrid system for strontium local delivery promotes bone regeneration in a rat critical-sized defect model, Sci Rep 7(1) (2017) 5098.

[33] C.J. Chung, R.T. Su, H.J. Chu, H.T. Chen, H.K. Tsou, J.L. He, Plasma electrolytic oxidation of titanium and improvement in osseointegration, J Biomed Mater Res B Appl Biomater 101 (2013) 1023-30.

[34] J.-M. Yu, H.-C. Choe, Morphology changes and bone formation on PEO-treated Ti-6Al-4V alloy in electrolyte containing Ca, P, Sr, and Si ions, Applied Surface Science 477 (2019) 121-130.

[35] I.A.J. van Hengel, F.S.A. Gelderman, S. Athanasiadis, M. Minneboo, H. Weinans, A.C. Fluit, B.C.J. van der Eerden, L.E. Fratila-Apachitei, I. Apachitei, A.A. Zadpoor, Functionality-packed additively manufactured porous titanium implants, Materials Today Bio 7 (2020).

[36] M. Montazeri, C. Dehghanian, M. Shokouhfar, A. Baradaran, Investigation of the voltage and time effects on the formation of hydroxyapatite-containing titania prepared by plasma electrolytic oxidation on Ti–6Al–4V alloy and its corrosion behavior, Applied Surface Science 257 (2011) 7268-7275.

[37] A. Kossenko, S. Lugovskoy, N. Astashina, A. Lugovskoy, M. Zinigrad, Effect of time on the formation of hydroxyapatite in PEO process with hydrothermal treatment of the Ti-6Al-4V alloy, Glass Physics and Chemistry 39 (2013) 639-642.

[38] I.A.J. van Hengel, M. Tierolf, V.P.M. Valerio, M. Minneboo, A.C. Fluit, L.E. Fratila-Apachitei, I. Apachitei, A.A. Zadpoor, Self-defending additively manufactured bone implants bearing silver and copper nanoparticles, J Mater Chem B 8 (2020) 1589-1602.

[39] H.-P. Teng, H.-Y. Lin, Y.-H. Huang, F.-H. Lu, Formation of strontium-substituted hydroxyapatite coatings on bulk Ti and TiN-coated substrates by plasma electrolytic oxidation, Surface and Coatings Technology 350 (2018) 1112-1119.

[40] M. Shokouhfar, C. Dehghanian, M. Montazeri, A. Baradaran, Preparation of ceramic coating on Ti substrate by plasma electrolytic oxidation in different electrolytes and evaluation of its corrosion resistance: Part II, Applied Surface Science 258(7) (2012) 2416-2423.

[41] X. Zhang, Z. Yao, Z. Jiang, Y. Zhang, X. Liu, Investigation of the plasma electrolytic oxidation of Ti6Al4V under single-pulse power supply, Corrosion Science 53(6) (2011) 2253-2262.

[42] S. Durdu, S. Bayramoğlu, A. Demirtaş, M. Usta, A.H. Üçışık, Characterization of AZ31 Mg Alloy coated by plasma electrolytic oxidation, Vacuum 88 (2013) 130-133.

[43] H. Habazaki, M. Uozumi, H. Konno, K. Shimizu, P. Skeldon, G.E. Thompson, Crystallization of anodic titania on titanium and its alloys, Corrosion Science 45(9) (2003) 2063-2073.

[44] E. Erfanifar, M. Aliofkhazraei, H.F. Nabavi, A.S. Rouhaghdam, Growth kinetics and morphology of microarc oxidation coating on titanium, Surface and Coatings Technology 315 (2017) 567-576.

[45] H. Hu, X. Liu, F. Meng, C. Ding, Formation and bioactivity of porous and nanostructured TiO2/beta-TCP coating on titanium, J Nanosci Nanotechnol 11(12) (2011) 10913-6.

[46] C.J. Chung, H.Y. Long, Systematic strontium substitution in hydroxyapatite coatings on titanium via micro-arc treatment and their osteoblast/osteoclast responses, Acta Biomater 7 (2011) 4081-7.

[47] C.S. Dunleavy, I.O. Golosnoy, J.A. Curran, T.W. Clyne, Characterisation of discharge events during plasma electrolytic oxidation, Surface and Coatings Technology 203(22) (2009) 3410-3419.

[48] X. Liu, P.K. Chu, C. Ding, Surface nano-functionalization of biomaterials, Materials Science and Engineering: R: Reports 70(3-6) (2010) 275-302.

[49] Y. Mizukoshi, N. Masahashi, Photocatalytic Activities and Crystal Structures of Titanium Dioxide by Anodization: Their Dependence upon Current Density, Materials Transactions 51(8) (2010) 1443-1448.

[50] M. Lilja, K. Welch, M. Astrand, H. Engqvist, M. Stromme, Effect of deposition parameters on the photocatalytic activity and bioactivity of TiO2 thin films deposited by vacuum arc on Ti-6Al-4V substrates, J Biomed Mater Res B Appl Biomater 100(4) (2012) 1078-85.

[51] Z. Su, L. Zhang, F. Jiang, M. Hong, Formation of crystalline TiO2 by anodic oxidation of titanium, Progress in Natural Science: Materials International 23(3) (2013) 294-301.

[52] M. Lilja, A. Genvad, M. Astrand, M. Stromme, H. Enqvist, Influence of microstructure and chemical composition of sputter deposited TiO2 thin films on in vitro bioactivity, J Mater Sci Mater Med 22(12) (2011) 2727-34.

[53] Y. Han, S.-H. Hong, K. Xu, Structure and in vitro bioactivity of titania-based films by micro-arc oxidation, Surface and Coatings Technology 168(2-3) (2003) 249-258.

[54] Y. Han, K. Xu, Photoexcited formation of bone apatite-like coatings on micro-arc oxidized titanium, J Biomed Mater Res A 71(4) (2004) 608-14.

[55] T. Kokubo, H.-M. Kim, M. Kawashita, Novel bioactive materials with different mechanical properties, Biomaterials 24(13) (2003) 2161-2175.

[56] T. Akatsu, Y. Yamada, Y. Hoshikawa, T. Onoki, Y. Shinoda, F. Wakai, Multifunctional porous titanium oxide coating with apatite forming ability and photocatalytic activity on a titanium substrate formed by plasma electrolytic oxidation, Mater Sci Eng C Mater Biol Appl 33(8) (2013) 4871-5.

[57] K.H. Park, S.J. Heo, J.Y. Koak, S.K. Kim, J.B. Lee, S.H. Kim, Y.J. Lim, Osseointegration of anodized titanium implants under different current voltages: a rabbit study, J Oral Rehabil 34 (2007) 517-27.

[58] Y. Sul, The significance of the surface properties of oxidized titanium to the bone response: special emphasis on potential biochemical bonding of oxidized titanium implant, Biomaterials 24(22) (2003) 3893-3907.

[59] T.-E. Park, H.-C. Choe, W.A. Brantley, Bioactivity evaluation of porous TiO2 surface formed on titanium in mixed electrolyte by spark anodization, Surface and Coatings Technology 235 (2013) 706-713.

[60] P. Whiteside, E. Matykina, J.E. Gough, P. Skeldon, G.E. Thompson, In vitro evaluation of cell proliferation and collagen synthesis on titanium following plasma electrolytic oxidation, J Biomed Mater Res A 94 (2010) 38-46.

[61] L. Zhao, Y. Wei, J. Li, Y. Han, R. Ye, Y. Zhang, Initial osteoblast functions on Ti-5Zr-3Sn-5Mo-15Nb titanium alloy surfaces modified by microarc oxidation, J Biomed Mater Res A 92(2) (2010) 432-40.

[62] H. Kusakabe, T. Sakamaki, K. Nihei, Y. Oyama, S. Yanagimoto, M. Ichimiya, J. Kimura, Y. Toyama, Osseointegration of a hydroxyapatite-coated multilayered mesh stem, Biomaterials 25(15) (2004) 2957-69.

[63] G.L. Yang, F.M. He, J.A. Hu, X.X. Wang, S.F. Zhao, Effects of biomimetically and electrochemically deposited nano-hydroxyapatite coatings on osseointegration of porous titanium implants, Oral Surg Oral Med Oral Pathol Oral Radiol Endod 107(6) (2009) 782-9.

[64] A.E. Tami, M.M. Leitner, M.G. Baucke, T.L. Mueller, G.H. van Lenthe, R. Muller, K. Ito, Hydroxyapatite particles maintain peri-implant bone mantle during osseointegration in osteoporotic bone, Bone 45(6) (2009) 1117-24.

[65] Z. Xu, J. Long, N. Zhang, H. Cao, W. Tang, K. Shi, X. Wang, S. Moya, L. Duan, H. Pan, Y. Lai, D. Wang, G. Wang, Strong mineralization ability of strontium zinc silicate: Formation of a continuous biomorphic mineralized layer with enhanced osteogenic activity, Colloids Surf B Biointerfaces 176 (2019) 420-430.

[66] A. Aimaiti, A. Maimaitiyiming, X. Boyong, K. Aji, C. Li, L. Cui, Low-dose strontium stimulates osteogenesis but high-dose doses cause apoptosis in human adipose-derived stem cells via regulation of the ERK1/2 signaling pathway, Stem Cell Res Ther 8(1) (2017) 282.

[67] X. Guo, S. Wei, M. Lu, Z. Shao, J. Lu, L. Xia, K. Lin, D. Zou, Dose-dependent Effects of Strontium Ranelate on Ovariectomy Rat Bone Marrow Mesenchymal Stem Cells and Human Umbilical Vein Endothelial Cells, Int J Biol Sci 12(12) (2016) 1511-1522.

[68] V. Karageorgiou, D. Kaplan, Porosity of 3D biomaterial scaffolds and osteogenesis, Biomaterials 26 (2005) 5474-91.

[69] S. Van Bael, Y.C. Chai, S. Truscello, M. Moesen, G. Kerckhofs, H. Van Oosterwyck, J.P. Kruth, J. Schrooten, The effect of pore geometry on the in vitro biological behavior of human periosteum-derived cells seeded on selective laser-melted Ti6Al4V bone scaffolds, Acta Biomaterialia 8 (2012) 2824-34.

[70] X. Pan, Y. Li, A.O. Abdullah, W. Wang, M. Qi, Y. Liu, Micro/nano-hierarchical structured TiO2 coating on titanium by micro-arc oxidation enhances osteoblast adhesion and differentiation, R Soc Open Sci 6 (2019) 182031.

[71] L. Casanova, L. Vicentini, M. Pedeferri, M. Ormellese, Unipolar plasma electrolytic oxidation: Waveform optimisation for corrosion resistance of commercially pure titanium, Materials and Corrosion (2020).

[72] R.O. Hussein, X. Nie, D.O. Northwood, A spectroscopic and microstructural study of oxide coatings produced on a Ti–6Al–4V alloy by plasma electrolytic oxidation, Materials Chemistry and Physics 134 (2012) 484-492.

[73] Z. Yao, Y. Jiang, F. Jia, Z. Jiang, F. Wang, Growth characteristics of plasma electrolytic oxidation ceramic coatings on Ti–6Al–4V alloy, Applied Surface Science 254 (2008) 4084-4091.

[74] Z. Yao, Y. Xu, Z. Jiang, F. Wang, Effects of cathode pulse at low frequency on the structure and composition of plasma electrolytic oxidation ceramic coatings, Journal of Alloys and Compounds 488 (2009) 273-278.

[75] S.V. Gnedenkov, S.L. Sinebryukhov, A.M. Puz, A.S. Gnedenkov, I.E. Vyaliy, D.V. Mashtalyar, V. Egorkin, Plasma electrolytic oxidation coatings on titanium formed with microsecond current pulses, Solid State Phenomena 213 (2014) 149-153.

[76] I.H. Han, J.H. Choi, B.H. Zhao, H.K. Baik, I.S. Lee, Effects of electrical wave form on pore size of micro-arc oxidized TiO2 film, Key Engineering Materials 309-311 (2006) 375-378.

[77] B.-Z. Hassan, E. Saebnoori, H. Hassannejad, A. Hassanzadeh-Tabrizi, Comparing morphology and corrosion behavior of nanostructured coatings obtained via plasma electrolytic oxidation with direct and pulse currents on commercial titanium substrate, Surface Engineering and Applied Electrochemistry 55 (2020) 667-678.

[78] H.-Y. Wang, R.-F. Zhu, Y.-P. Lu, G.-Y. Xiao, J.I.E. Ma, Y.F. Yuan, Preparation and mechanism of controllable micropores on bioceramic TiO2 coatings by plasma electrolytic oxidation, Surface Review and Letters 20 (2013) 1350051.

[79] S. Gowtham, T. Arunnellaiappan, N. Rameshbabu, An investigation on pulsed DC plasma electrolytic oxidation of cp-Ti and its corrosion behaviour in simulated body fluid, Surface and Coatings Technology 301 (2016) 63-73.

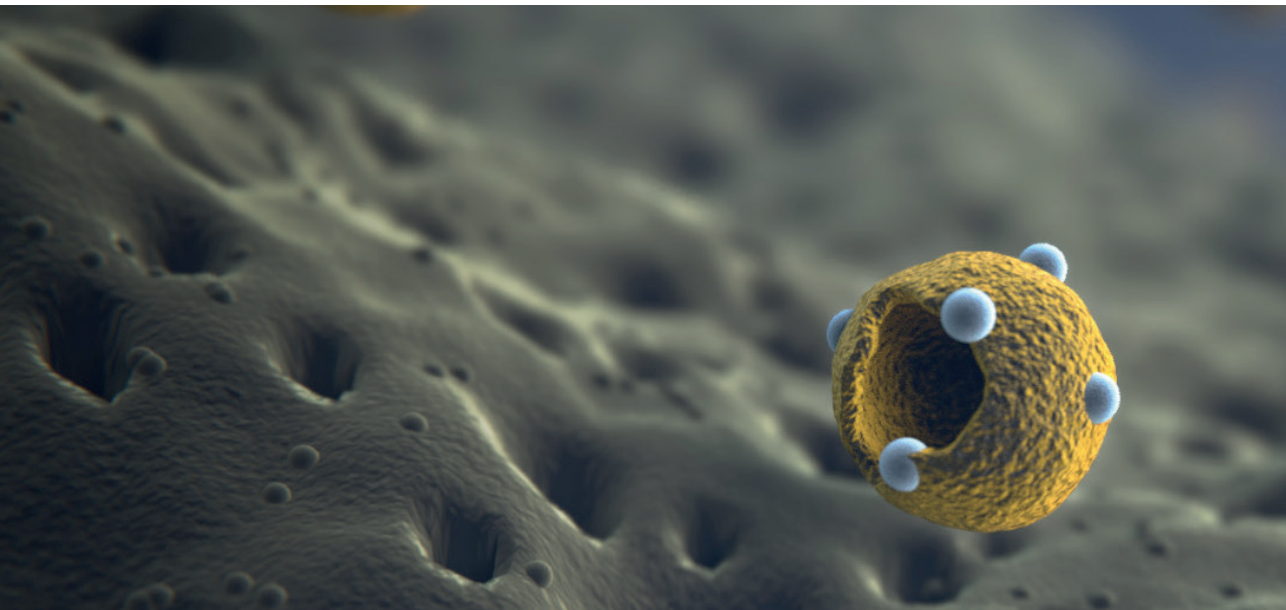

CHAPTER 08

Inorganic elements to enhance angiogenesis of orthopedic implants

M. Salandova, I.A.J. van Hengel, I. Apachitei, A.A. Zadpoor, B.C.J. van der Eerden, L.E. Fratila-Apachitei, Inorganic agents for enhanced angiogenesis of orthopedic biomaterials, Advanced Healthcare Materials (2021) e2002254.

Aseptic loosening of a permanent prosthesis remains one of the most common reasons for bone implant failure. To improve the fixation between implant and bone tissue as well as enhance blood vessel formation, bioactive agents are incorporated into the surface of the biomaterial. This study reviews and compares five bioactive elements (copper, magnesium, silicon, strontium, and zinc) with respect to their effect on the angiogenic behaviour of endothelial cells (ECs) when incorporated on the surface of biomaterials. Moreover, it provides an overview of the state-of-the-art methodologies used for the *in vitro* assessment of the angiogenic properties of these elements. Two databases were searched using keywords containing endothelial cells and copper, magnesium, silicon, strontium, and zinc. After applying the defined inclusion and exclusion criteria, 59 articles were retained for the final assessment. Here, we present an overview of the angiogenic properties of five bioactive elements and the methods used for assessment of their *in vitro* angiogenic potential. The findings showed that silicon and strontium can effectively enhance osseointegration through the simultaneous promotion of both angiogenesis and osteogenesis. Therefore, their integration onto the surface of biomaterials could ultimately decrease the incidence of implant failure due to aseptic loosening.

8.1 INTRODUCTION

Despite the great technological advancements in total joint replacements over the past decades, implant failure remains a concern for approximately 10% of patients undergoing primary total hip arthroplasty (THA) [1,2]. Many of the causes leading to failures are attributed to poor or delayed osseointegration of the permanent implants [2,3], as it has been established that achieving osseointegration is a key prerequisite for implant stability and proper loading of the implant [2,4,5]. Unsatisfactory osseointegration is often associated with the formation of fibrous tissue between the biomaterial and the bone, which represents a soft interlayer not able to sufficiently anchor the implant. Moreover, an unsecured attachment can result in micromovements and subsequent generation of wear debris, which may elicit an inflammatory reaction and excessive bone resorption, eventually leading to the loosening of the prosthesis [6–10].

Presently, metallic and ceramic biomaterials are used for the majority of load-bearing orthopaedic implants due to their high strength [11,12]. Bioinert alumina and zirconia ceramics demonstrate superiority in hardness and wear resistance among available biomaterials resulting in minimal immune response, which makes them extremely suitable for the fabrication of the articulating components of total joint replacements (TJRs), such as femoral heads [10,12]. Among metallic biomaterials, titanium alloys are increasingly used for TJRs. They are often praised for their high corrosion resistance and moderate elastic modulus, the latter reducing the stress shielding effect and preventing undesired bone resorption [6,7,9]. Even though these biomaterials exhibit an exemplary chemical and mechanical stability, their bioinert nature does not encourage the establishment of a stronger and more physiological connection between the implant and the new bone, thus necessitating further surface treatment of the implants [2,10,11]. Many of the approaches currently used to promote osseointegration are based on the attraction of mesenchymal stem cells (MSCs) and the stimulation of their osteogenic differentiation, leading to new bone tissue formation on the implant surface. This can be achieved through the adjustment of the chemical and physical surface properties of the used biomaterial [2,4,6].

Given the highly vascularized nature of the bone [13,14] and the importance of blood supply in the bone repair process [15], angiogenesis plays a crucial role and remains a major challenge in bone tissue engineering and regeneration. Furthermore, the research on the effects of inorganic elements on angiogenesis is relatively scarce when compared to the research on osteogenic agents [16]. Due to their vital role, damaged blood vessels are repaired through the angiogenic process in the initial stages of bone regeneration [5,17,18]. This restores the blood flow, thereby ensuring delivery of oxygen, nutrients, signalling and molecules as

well as facilitating the supply of cells to the affected site and enabling the removal of waste products [19–21]. Implants with both osteogenic and angiogenic surface biofunctionalities are, therefore, highly desirable to enhance osseointegration [22].

Among the available methods used for the modulation of cellular responses by an implant, modification of the chemical composition of the biomaterials is an approach that enables the incorporation of multiple agents with different action mechanisms, thereby yielding a biomaterial with versatile surface properties. Essential and trace elements are known for their inherent role in many molecular mechanisms in the human body, and the increased understanding of their signalling and structural functions associated with bone metabolism has led to their utilization in therapeutic applications for bone (*e.g.*, osteoporotic treatments, promoting osseointegration) [5,13,14,23]. The calcium (Ca) and phosphorus (P) essential elements, which are constituting the hydroxyapatite crystals found in bone, were among the first elements with osteogenic potential and recognized suitability for orthopaedic applications [14,23]. Nowadays, trace elements such as copper (Cu), magnesium (Mg), silicon (Si), strontium (Sr), and zinc (Zn), which may additionally enhance angiogenesis, are also incorporated into bulk biomaterials or onto their surfaces, delivering their stimulatory effect to the intended site through tunable release kinetics. They can modulate the activity of stem/progenitor cells, thereby inducing new bone and/or blood vessel formation and enhancing osseointegration [5,13,23–25].

Due to its biodegradable nature and mechanical properties comparable to the bone, Mg is an attractive metallic biomaterial for resorbable scaffolds intended for bone regeneration [13,26]. The presence of Mg may favour osseointegration through the recruitment of bone marrow stromal stem cells [13] and more recent research has indicated its angiogenic potential through the upregulated expression of angiogenic factors [14]. Sr is used as strontium ranelate (Protelos) for treating osteoporotic patients [23,27]. The superiority of strontium ranelate over other osteoporotic drugs is related to its ability to decouple the various processes involved in bone remodelling by promoting osteogenesis while simultaneously suppressing bone resorption [28–30]. The antimicrobial activity of Cu has been utilized in the medical field for decades [31]. However, this metal is also gaining increasing recognition for its wide range of catalytic and structural functions in other biological processes [23,32], such as tissue regeneration [33,34]. As far as orthopaedic applications are concerned, Cu can not only decrease the incidence of implant-associated infections, but it could also improve bone quality around the implant by increasing its mineral density [32,35] and promoting the formation of a new vascular network [36]. The majority of Zn found in the human body is stored within bone [13,23,32], reflecting its essential involvement in bone homeostasis. Zn promotes osteogenesis by regulating the activity of osteoblasts and osteoclasts [23,27,32] and

similar to Cu, it could also be employed as an antibacterial agent [13]. Si is involved in bone metabolism through both anabolic and catabolic processes, it promotes bone homeostasis, regeneration, and increases its mineral density [37,38]. One of the introduced osteogenic mechanisms of silicon is the promotion of collagen 1 deposition and stabilization [32,38], as well as the recruitment of progenitor cells through immunomodulation of monocytes [37].

This review aims to provide the reader with a state-of-the-art overview on the angiogenic properties of trace elements incorporated on the surfaces of permanent orthopaedic biomaterials with a focus on the *in vitro* assays used to evaluate the response of endothelial cells (ECs) to such biomaterials, the comparative angiogenic potential of the trace elements for bone implants, and the mechanisms underlying the observed angiogenic activity.

8.2 METHODS

PubMed and Web of Science were used as the primary search databases. The search terms and strategy are summarized in **Table 1** and supplementary **Figure S1**. First, the databases were screened for the general term endothelial cells and the selected elements. The search terms were further specified by the addition of angiogenic components and the intended applications while the period was set to the time window between 2010 and 2020. The search from both databases yielded 465 articles. After removal of duplicates, 419 articles were individually screened. Based on the relevance of the title and abstract, 109 articles were selected and further classified with consideration to the application requirements mentioned in the motivation section above. Finally, 75 articles were included for full-text assessment out of which 58 were included in the final comparison of the five inorganic elements.

All included articles discussed the effects of one or more of the selected ions/nanoparticles (Cu, Mg, Si, Sr, or Zn) on endothelial cells. The composition of the tested materials, concentrations of the potential angiogenic agent (in the form of ions or nanoparticle), and the reported effects on ECs were summarized and compared. The articles were also screened for the different assessment methods of the angiogenic properties of the agents to evaluate their widespread use whilst critically reviewing their suitability, with consideration of the reliability of the output data, costs, and other general (dis)advantages (*e.g.*, duration, complexity level, etc.). The findings were compared and completed with the results of several review articles on *in vitro* angiogenic assessment methods, yielding the final overview.

Table 1.*Summary of inclusion and exclusion criteria.*

Screening	**Inclusion criteria**	
	Web of Science	PubMed
Initial search term:	TS=((endothelial cells) AND (angiogen*) AND (magnesium OR mg OR copper OR Cu OR silicon OR Si OR zinc OR Zn OR strontium OR Sr) AND (implant OR scaffold OR material))	endothelial cells AND angiogen* AND (magnesium OR Mg OR copper OR Cu OR silicon OR Si OR zinc OR Zn OR strontium OR Sr) AND (implant OR scaffold OR material)
Year:	2010-2020	
First screening:	Relevance of title and abstract; discussing effect of the ions/particles on endothelial cells/angiogenesis	
Second screening:	Bone related field of application (orthopaedic/dental)	
Full-text screening:	Effect of one of the ions on angiogenic behaviour of endothelial cells	

8.3 ANGIOGENESIS AND ITS ROLE IN FRACTURE HEALING

After a bone replacement surgery, the body suffers local tissue damage analogous to that of a fracture. The blood supply is disrupted and the local environment loses mechanical stability [18,39]. New bone and vascular tissue must both be generated to restore homeostasis and to secure a strong tissue-biomaterial interface, which is vital for the success of cementless permanent implants. The mutual dependence of angiogenesis and osteogenesis has been recognized by many studies as being critical for achieving successful bone repair, as impaired angiogenic ability or significantly damaged vasculature has been associated with increased occurrence of nonunions or delayed repair [20,21,40–42]. The fracture healing process is illustrated in **Figure 1**.

In the immediate aftermath of tissue damage, the wound elicits inflammatory and haemostatic reactions, defined by orchestrated molecular cascades, blood vessel constriction, blood coagulation, and the formation of a fibrin-rich blood clot at the affected site [20,41,43]. The clot is characterized by hypoxia and low pH and serves as a temporary scaffold at the wounded site [20]. It is also a source for cytokines and signalling molecules, which together with environmental factors (hypoxia) are responsible for the recruitment of MSCs, endothelial progenitor cells (EPCs), and inflammatory cells from their local sources [15,19,39,43,44].

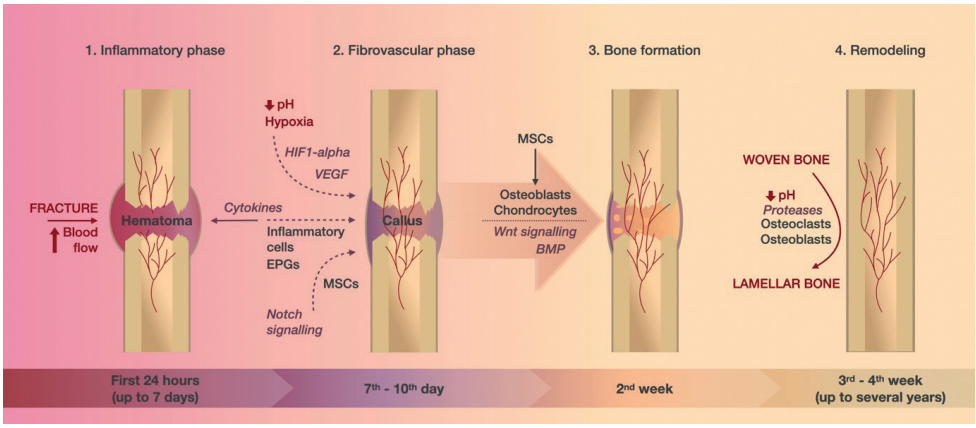

Figure 1. An illustration depicting the stages of fracture healing: 1) In the initial inflammatory phase (lasting up to 7 days after injury), the increased blood delivery to the affected site results in the formation of hematoma with a high content of cytokines; 2) Cells attracted by cytokines and environmental factors (hypoxia, low pH, HIF1-alpha, VEGF) are responsible for the repair of damaged vessels and formation of provisional fibrous tissue called callus (7-10 days after injury); 3) At around two weeks after injury, MSCs undergo differentiation into osteoblasts and chondrocytes governed by Wnt and BMP signalling and provisional woven bone is generated; 4) In the final phase starting 3-4 weeks after injury and lasting up to several years, the woven bone is replaced by lamellar bone.

The initial inflammatory reaction has a substantial influence on the formation of a callus, *i.e.* a fibrovascular tissue that provides a more stable support/matrix for the further development of blood vessels and bone tissue [18,39,42]. Through reciprocal signalling, vasculature and bone mature side by side. Hypertrophic chondrocytes and cells of the osteoblastic lineage contribute to the secretion of vascular endothelial growth factor (VEGF) [45], a pro-angiogenic factor that, in synergy with several bone morphogenic proteins (BMPs), increases the recruitment of MSCs and encourages their differentiation towards osteoblasts [18]. Stimulated ECs proliferate, migrate, and develop into structures to form new vessels and restore the blood flow in the callus. The vasculature surrounding and growing into the provisional fibrous tissue is vital for its replacement by the hard callus, as it enables sufficient delivery of oxygen and nutrients required for this endochondral ossification and helps to convey osterix-positive osteoprogenitor cells from the perichondrium into the metaphysis, contributing to osteoblastogenesis inside the bone [15,18,21,39,40,45–47]. Finally, the provisional woven bone is remodelled through repetitive tissue resorption and deposition cycles and replaced by a functional lamellar bone [15,39,40].

The vascular network can be formed via two processes, angiogenesis and vasculogenesis, which are often incorrectly interchanged despite their substantial differences. Vasculogenesis employs the endothelial progenitor cells (EPCs), which are obtained from different sources.

The recruitment of EPCs is governed by molecular (cytokines) and environmental (hypoxic) factors. These cells then further differentiate into mature endothelial cells and develop *de novo* (new) blood vessels [17–19,43]. The importance of vasculogenesis in the onset of vascularization during embryonic development has been known for decades, but recent studies confirmed its role also postnatally [17]. Angiogenesis, on the other hand, utilizes the existing vasculature and is the dominant vessel formation process in tissue repair and tumour growth. It differentiates between two mechanisms of network growth: sprouting and splitting of the blood vessels [17–19,43]. The latter process, also called intussusceptive angiogenesis, is usually observed in well-perfused regions undergoing morphological changes, such as remodelling or growth. In contrast, areas with no or very little blood supply, such as wounds, are characterised by proliferative branching (sprouts) from the remaining vasculature, thus forming a new capillary network [17,48,49]. Sprouting angiogenesis, the prevailing revascularization mechanism for fracture healing, is defined by the following stages which are also illustrated in **Figure 2**.

1. Firstly, the basement membrane of the blood vessels, which together with mural cells (vascular smooth muscle cells and pericytes) prevents ECs from leaving their designated location in the vascular wall, must be degraded to liberate the ECs. Major biomolecular factors of this phase include matrix metalloproteinases, which define the extent of the membrane degradation and at the same time are responsible for the secretion of angiogenic factors, such as VEGF, fibroblast growth factor (FGF), and transforming growth factor beta (TGF-β), as well as activation of relevant angiogenic chemokines [17,22,50].
2. The sprouting angiogenesis is characterized by endothelial cells of distinct (but reversible) function and morphology. The new branches comprise of tip and stalk cells. The establishing capillaries are guided by mildly proliferative tip cells, contain many filopodia and navigate the new vessels toward a relevant (angiogenic) stimulus (hypoxia, biochemical gradient) [17,22].
3. The new endothelial branch is initially formed as a solid cord without a lumen. The growth and branching of the new vessel are mainly determined by the proliferation of stalk cells, which, in contrast to tip cells, are characterized by fewer filopodia [17]. Moreover, they are responsible for the production of the basement membrane and the establishment of junctions with neighbouring cells [17,50].
4. Stalk cells are responsible not only for the elongation of the branches but also for lumen formation, which is achieved by the tubular arrangement of these cells. Past studies introduced two mechanisms, in which the lumen is formed either by "cell

hollowing" or "cord hollowing". The "cell hollowing" theory works on the assumption that the intracellular vacuoles of adjacent endothelial cells connect, thus creating inner space. The more recent "cord hollowing" theory, on the other hand, explains the lumen formation with cells acquiring a distinct phenotype, subsequent rearrangement of neighbouring cells, and lumen opening as a result of repulsive forces on the established inner membrane [17,50,51].

5. Once the lumen is established, the blood flow initiates. The contiguous tubular branches are then coalesced, forming an interconnected network. The new vasculature is then corrected through remodelling and pruning; the nutritional demands give rise to small and large vessels, whereas local levels of oxygen and VEGF determine apoptosis of some ECs to accomplish the optimal vascular density [17,50].

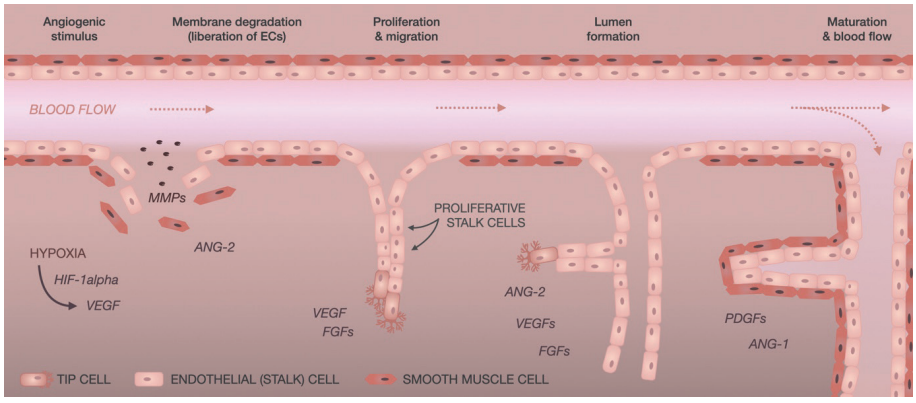

Figure 2. An illustration of sprouting angiogenesis. The presence of different factors (hypoxia, HIF1-alpha, VEGF) can initiate angiogenesis, which is divided into 4 stages: 1) In the first stage, the membrane degrades resulting in the liberation of ECs; 2) The cells proliferate and migrate, thereby establishing new branches of the vascular network; 3) The new branches are initially formed without a lumen and are hollowed in a subsequent stage; 4) The new endothelium matures, and blood flow is established through the new vessels.

The blood vessel formation process is governed by several biomolecular factors. The hypoxic conditions and increased lactate levels, characteristic for the hematoma and callus at the site of an injury, stabilize expression of hypoxia-inducible factor 1 alpha (HIF1-α) [15,19,20,44]. According to some studies conducted in mice, the increased expression of HIF1-α was associated with hyper-vascularisation, while its depletion resulted in delayed callus formation [19]. HIF1-α drives expression of VEGF, which promotes both the angiogenic and vasculogenic processes [19,20], and more than 60 factors related to adaptation in hypoxic conditions [51]. VEGF is secreted by many cells, including MSCs, osteoblasts, hypertrophic chondrocytes,

but also inflammatory cells [18]. It stimulates proliferation and sprouting of endothelial cells and its expression attracts EPCs towards the site of injury. Studies have shown that inhibition or deficiency of VEGF is reflected in the reduced angiogenic potential, healing ability, and quality of the newly formed tissue [15,19,20,39,44]. Platelet endothelial cell adhesion molecule (PECAM1), also known as cluster of differentiation 31 (CD31), is an adhesion and signalling molecule expressed by vascular cells. In coordination with other molecules, it has been demonstrated to promote the migration of endothelial cells while also ensuring maintenance of cellular integrity in terms of proper barrier function (permeability) and cell-cell junctions [52].

8.4 FREQUENTLY USED *IN VITRO* METHODS FOR ASSESSMENT OF SPROUTING ANGIOGENESIS INDUCED BY INORGANIC AGENTS

In vitro assays are usually the starting point of an investigation and often represent a very simple setup lacking many physiological cues (such as mechanical strain and chemotaxis) and interaction with other cell types. Although this is considered a hindrance while aiming to simulate an accurate *in vivo* situation, those simple *in vitro* assays are advantageous for examining a direct effect of an agent on an isolated cellular system and studying individual mechanisms found in complex tissues.

The *in vitro* angiogenic assays are designed to emulate the process of blood vessel formation and to investigate the effect of new stimuli on the behaviour of endothelial cells at the different stages of angiogenesis. The cellular response is tested for the proliferative, migrating, and sprouting capacity, attachment, morphology, viability, and phenotype commitment. The angiogenic assessment should cover multiple stages of the vessel formation process and consider the biomolecular complexity and selectivity, in which only specific factors and/or behavioural aspects are promoted/suppressed and how those events are coupled [53].

The articles yielded from the literature were also screened for the different angiogenic assessment methods, which were summarized and compared in terms of their approach (direct (D) culturing of cells on the material's surface, indirect (I) culturing of cells in the material's extract) usability, reliability, costs, and general (dis)advantages (**Table 2**).

The next subsections provide an overview of the different types of endothelial cells and describe the *in vitro* assays that study endothelial behaviour and the different stages of angiogenesis.

8.4.1 Type of endothelial cells

Together with smooth muscle cells, ECs represent the fundamental structural units of the vascular system. They line the lumen of blood vessels and are therefore employed in the *in vitro* models

for angiogenic assessment. There are several types of endothelial cells that can be used in *in vitro* models intended to study angiogenesis. Naturally, their origin (human or animal) determines their phenotype, size (10-20 μm in diameter), and morphology; the cells differ in expression and release of biomolecular factors and in the tendency to form tissue-specific structures, such as sprouting ability [54–57]. Therefore, the cell type should be selected according to the desired outcome of the experiment, and results should be interpreted with care [57].

Primary cells are strongly preferred for assessment of angiogenesis, albeit the use of immortalized cell lines is also possible. Primary cells are isolated from a donor tissue without being subjected to any modifications and therefore represent a more accurate approximation of the actual tissue. They pose some disadvantages such as differences between individual batches and limited passage-dependent proliferation capacity. The most commonly used human primary cells are human umbilical vein endothelial cells (HUVECs). HUVECs are relatively large cells obtained from the endothelium of an umbilical vein. They are easy to isolate and harvest, highly proliferative, and capable of forming capillaries. For those reasons, they are frequently chosen for studying the angiogenic behaviour of endothelial cells, although they are not of microvascular origin [53–57]. Besides HUVECs, human arterial endothelial cells (HAECs) are another type of macrovascular ECs, suitable for models studying pathological vascular disorders [57]. Among other commonly used primary ECs are human microvascular endothelial cells (HMECs) [57], which are suitable for studying endothelium and neoangiogenesis in the surroundings of tumorous tissue, bovine aortic endothelial cells (BAECs) [53,54], and human dermal microvascular endothelial cells (HDMECs) [53–55].

An immortalized cell line, on the other hand, is mostly established from a single cell where all cells possess identical genetic information [58,59]. Cell lines can be used for initial experiments assessing cytotoxicity and chemical biocompatibility of various molecules, however, due to their atypical behaviour, which must be taken into consideration during experiments, they are not suitable for advanced steps of the research process [60]. Unlike primary cells, they do not lose their proliferative ability after several passages. Therefore, they are not a representative sample for assessing cellular proliferation [58,61]. An example of an immortalized cell line is EA.hy926, a human umbilical vein cell line with a differentiation profile suitable for angiogenic *in vitro* models [62,63].

The conditions for the culture of endothelial cells are specified by the manufacturer who usually supplies or advices appropriate culturing media. Cell line EA.hy926 can be cultured in Dulbecco's Modified Eagle Medium (DMEM, Lonza) supplemented with fetal bovine serum, streptomycin and penicillin [64,65]. Primary HUVECs supplied from Lonza, however, require use of specific media (Endothelial Cell Basal Medium) enriched by a number of growth factors such as VEGF, FGF and epidermal growth factor (hEGF), also offered by Lonza.

8.4.2 Assessment of basal membrane degradation

Degradation of the basal membrane is a critical step, which liberates the endothelial cells from the tightly ordered monolayer and allows for proceeding with proliferation and migration, and the eventual generation of a new capillary network. Methods for assessment of the first stage of angiogenesis, the degradation of the basal membrane, are based on measuring the activity of matrix metalloproteinases (MMPs) produced by the endothelial cells. Those enzymes are responsible for digestion of the membrane and liberating the endothelial cells from the blood vessel wall [17,54].

In a gel zymogen assay, a gelatinous substrate, such as collagen, fibrinogen, or gelatine, is embedded (co-polymerized) in a polyacrylamide gel. Collected supernatants from the endothelial cells, cultured for a defined period of time, are then electrophoresed through the prepared gel. For evaluation of the protease activity, Coomassie staining is utilized to detect remaining protein, with the proteolyzed regions in the gel appearing clear against the dark background [53,54].

Another assay enabling to assess the degradative capability of ECs is the matrix invasion assay. Cells are placed in a transwell system. The chamber membrane, which normally permits the permeation of cells through its pores, is occluded with an extract of the basal membrane; cells cannot migrate through unless they degrade the extract and thereby free the pores. The quantification of cells migrated into the lower chamber is proportional to the proteolytic activity of the cellular enzymes [54,66]. Both assays are relatively time-consuming and were not found among the most frequently used assays in the reviewed papers.

8.4.3 Cell proliferation

The reproductive capacity of stalk cells determines the growth rate of establishing capillaries. Hence, it is fundamental to analyse the effects of the biomaterial and/or its extract on the proliferative capacity of endothelial cells. There are many assays available, which can deliver information about cell proliferation. They can be divided into categories, based on the principle they utilize to determine the cell proliferative capacity.

8.4.3.1 Cell staining and counting

Cells are usually cultured for several hours/days in the presence of the investigated (potential) stimulus. Upon reaching the defined time points, a suitable staining technique can be chosen based on the desired information.

The most commonly employed fluorescent stain is 4',6-diamidino-2-phenylindole

(DAPI) [67], which binds to adenine-thymine-rich regions and is dependent on the permeability of the cellular membrane (fixed/dead cells). DAPI can be used for quantification of all cells present in individual wells, in which case it requires fixing of the cell culture with an appropriate fixative (*e.g.* formaldehyde). An alternative to DAPI is propidium iodide (PI) [68], which also binds to the DNA of all fixed/dead cells, with little sequence preference.

Without fixing, DAPI or PI can permeate dead cells only. In combination with another fluorescent dye, that can stain live cells (*e.g.* Hoechst, calcein), DAPI or PI can be used for Live/Dead staining.

The quantification of the stained cultures can be completed by automated/manual analysis of images obtained from a microscope, or by using a flow cytometer. Another option is labelling the cells with Trypan Blue and counting them in a haemocytometer or an automated cell counter [54].

8.4.3.2 Quantification of DNA synthesis

More advanced albeit more time consuming and costly techniques use fluorescent or radioactive labels to monitor the mitotic division of cells. A labelling agent ([^{3}H] thymidine [57], bromodeoxyuridine (BrdU) [69,70], 5-ethynyl-2'-deoxyuridine (EdU) [71]) is added to the culture and during subsequent cellular divisions, it becomes incorporated into the DNA. The output signal can then be monitored throughout a defined period of time in a device with an appropriate detector. The quantification of incorporated thymidine requires the use of radiation, which is proportional to the division rate and can be measured in a scintillation counter. BrdU is a newer analogue of thymidine and uses immunochemical detection methods. The most advanced EdU incorporation technique uses click chemistry instead of an antibody and unlike BrdU does not require denaturation of the DNA for detection of the signal. Both a flow cytometer and a fluorescent microscope can be used for the detection and evaluation of the proliferative capacity of cells [53,54,57,71,72].

8.4.3.3 Colorimetric assays

Colorimetric assays employ specific compounds that can be modified by chemical reduction through mitochondria of active cells and of which their fluorescently reduced products can be measured using spectrophotometry. The output signal is often correlated with the number of active cells and is used to reflect the proliferation rate of the culture. The compound is added to the cell culture at the end of a defined cultivation period. It is usually incubated with the cells for about 1-2 hours (could be more in case of slowly dividing cells), and the intensity can then be analysed on an absorbance- or a fluorescent-based plate reader. The

most commonly used colorimetric assays are MTT [73,74] (reduction of yellow tetrazolium salt to purple formazan), AlamarBlue, and PrestoBlue [68,75] (reduction of blue resazurin to red resorufin) [53,54,72].

8.4.4 Cell migration

Assays reflecting the motility and guidance of tip cells during sprouting angiogenesis can be divided into two categories: (a) response and attraction of endothelial cells towards an environmental factor along its concentration gradient (chemotaxis), (b) general cellular motility (chemokinesis), and ability of cells to restore a disrupted monolayer (heal the emulated wound) after being introduced to a (potentially) proangiogenic agent.

One of the most frequently employed experimental setups of the first group is the transwell [76,77]: a two-chamber system with a separative cell-permeable membrane. Precultured cells are placed in the upper chamber (the well insert), while the medium containing the active agent is in the lower chamber. The cells are then incubated for several hours. The size of the pores in the membrane requires active adjustment of cell morphology to allow the cells to pass through. Afterward, the cells are fixed, stained and the number of cells migrated through the membrane is analysed [54,55,57,72]. Another assay intended for the evaluation of cellular chemotaxis is the under-agarose assay. In this experimental setup, the cells migrate from one well towards a well with an attractant under the agarose gel, which separates the wells [54].

The general cellular motility can be assessed through a wound-healing/scratch assay [78,79]. First, cells are cultured until confluence is reached after which the monolayer is scratched. The cells are usually monitored for several hours and pictures are taken at defined time points. The wound healing capacity can then be evaluated from the pictures using an ImageJ plugin (*MRI Wound Healing Tool*).

Cell starvation in a serum-free medium prior to those experiments is a common practice to maximise the migratory and motility response of endothelial cells [54,80,81].

8.4.5 Tube formation/Sprouting

The ability of endothelial cells to organize into tube-like structures is the first visual indication of establishing capillary lumen and the new vascular network. In principle, it can be tested in several gel-containing models [82,83].

Generally, wells intended for cell seeding are coated with one of several available substrates (collagen, laminin, fibrin, Matrigel) and allowed to solidify. Subsequently, cells are seeded onto the gel and their sprouting behaviour is monitored for several hours. Microscope imaging can then be used for evaluation of the ECs sprouting ability. The most common

methods for quantification are counting the number of nodes/branches/sprouts or the length of rings/tubes formed. Such an analysis can be done either manually or fully automated [84].

Unlike other substrates, Matrigel contains many growth factors, enhances attachment, and highly stimulates migration and differentiation of cells. The potential overstimulation has been demonstrated by seeding other non-vascular cell types (*e.g.* fibroblasts) into Matrigel, which were also able to form tubular structures, although it does not belong to their normal behavioural features. Hence, the use of growth factor-reduced Matrigel is strongly recommended for the assessment of sprouting.

To approximate the 3D *in vivo* conditions and allow for both horizontal and vertical migration and sprouting of cells, the thickness of the coated layer can be increased, cells can be mixed with the gel or seeded between gel layers [53,54,57,72].

8.4.6 Gene/protein expression

The type and concentration of specific biomolecules expressed by ECs reflect their angiogenic behaviour. In addition, the maturity and phenotype specificity of ECs can be determined through the detection of specific types of gene and protein expression. When assessing the angiogenic capacity of endothelial cells, the most frequently tested angiogenic factors are VEGF, HIF1—α, and PECAM1 (CD31).

To determine the types and quantities of activated genes, reverse transcription-quantitative polymerase chain reaction (RT-qPCR) is performed [85,86]. In this method, extracted and reversely transcribed genetic information is multiplied, bound to a detectable molecule (a fluorescent marker), and analysed in a qPCR machine.

Enzyme-linked immunosorbent assay (ELISA) is a commonly used diagnostic tool capable of detecting synthesized or secreted proteins *in vitro* [87]. The method utilizes protein-specific antibodies and fluorescent substrates (added in defined order) that enable quantification of the existing proteins using a spectrophotometer. Protein concentration and/or its subcellular localization can be quantified using Western Blotting [69], where proteins are denatured prior to their loading into an electrophoretic gel setup [55,56].

8.4.7 Other assays

8.4.7.1 Attachment, morphology, viability

Although evaluation of the cellular attachment is not directly assigned to any of the stages of sprouting angiogenesis, it is often included in the angiogenic assessments, as proper attachment and morphology are considered to be pivotal for further angiogenic development stages [88]. Monitoring of cells cultured with (extracts of) a given biomaterial can provide

information about their response to its (bio)chemical composition. To observe and evaluate the behaviour of cells influenced by both chemical and physical properties, cells can be seeded directly onto the biomaterial surface. The most common methods to assess the morphology, spreading, and viability of ECs include scanning electron microscopy (SEM) and confocal laser scanning microscopy (CLSM) [83,87,89].

8.4.7.2 NO production

Nitric oxide (NO) is the most important substance produced by the endothelium. Proper functioning of ECs is dependent on balanced levels of NO, and their disruption is associated with severe impairments of the vascular system (vasoconstriction, inflammation, atherosclerosis) [51,90].

Measuring the produced NO is a good way to gain information about the quality of the established endothelium [91,92]. Its very short half-life led to the development of methods based on colorimetric or fluorometric detection. They utilize the rapid oxidation of NO and subsequent enzymatic conversion of the nitrate to nitrite by nitrate reductase to form a coloured quantifiable product (Griess test), which can be analysed on a plate reader or other suitable detector [93].

8.4.7.3 Coculture with other cell types

Depending on the intended application, ECs are often cultured in the presence of other cells to emulate the *in vivo* conditions and the mutual biological interactions.

For bone tissue engineering purposes, ECs are most frequently cultured with MSCs or osteoblasts, which secrete VEGF and other specific proteins to facilitate the differentiation of ECs (increased expression of CD31) towards angiogenesis [94–96].

Various approaches taken for the evaluation of the interactions were identified. The response of ECs to the growth factors secreted by other cell types, such as MSCs, can be studied in a simple culture setup combining the endothelial culture medium with the conditioned medium from the other cell type [16]. Introducing a second cell type significantly increases the complexity of the experimental setup [67]. The additional challenges encountered in these models are mostly related to the seeding protocol, establishment of a proper media composition required for the survival of included cells and the ratio of seeded cells.

Many publications have established protocols with recommended cell number ratios and temporal order in which ECs and MSCs/osteoblasts should be seeded. The readers are advised to seek detailed guidance for those assays elsewhere (*e.g.* [96–98]) as it is beyond the scope of this review.

Table 2. *Overview and comparison of methods frequently used for assessment of angiogenic behaviour of ECs*

Examined property	Methods	Assays	Description of the assay	Advantages/Disadvantages	Reference
Matrix degradation	Assessing MMP activity	*Zymogen assay*	The MMPs activity is assessed through their ability to degrade/digest gel; after staining the hydrolysed areas appear clear in contrast to the dark background.	Inexpensive; time-consuming	[54]
		Matrix invasion assay	Using a transwell with basal membrane occulated pores.	Time-consuming	[66]
Proliferation	Direct cell count (staining)	*DAPI*	The stain labels all cells and the cell number can be evaluated from images.	Inexpensive; time-consuming; operator errors.	[67]
		Trypan Blue	Labelling all cells with a fluorescent dye and counting in a haemocytometer or trypsinized and counted in a cell counter.	Possible machine errors depending on the cell density.	[54]
		Propidium iodide	PI labels all cells which can be then counted in a flow cytometer.	Simple; it does not indicate the ratio of live/dead cells.	[68]
	DNA synthesis quantification through mitotic divisions	*[^{3}H] thymidine*	Incorporation of a labelling compound into the DNA strings and measuring the output signal (intensity) in a device with an adequate detector.	Radioactive; slow.	[57]
		BrdU		Not radioactive (environmentally friendly); more costly.	[69,70]
		EdU		Click chemistry - no degradation needed for detection.	[71]
	Colorimetric assays	*MTT*	Detecting the intensity of a compound product reduced by active mitochondria.	Simple; ambiguous interpretation of data - need for an additional assay to validate the results.	[73,74]
		Alamar Blue/ Presto Blue			[68,75]

Examined property	Methods	Assays	Description of the assay	Advantages/Disadvantages	Reference
Migration	Migration along a gradient (chemotaxis)	*Transwell assay*	Monitoring cells migrating through a porous membrane towards a stimulus; standard use of 8 µm pores for HUVECs.	Easy quantification; higher costs.	[76,77]
		Under-agarose assay	A well with cells separated from a well with chemoattractant; the cells migrate under agarose gel towards the attractant.	Less sensitive; cheap; difficult to quantify.	[54]
	Wound closure capacity (chemokinesis)	*Wound healing/ scratch assay*	Scraping a confluent layer and monitoring the closure capacity of cells.	Difficult quantification (uneven size and boundaries of the scratch).	[78,79]
Tube formation/ Sprouting	Sprouting in 2D	*Sprouting in Matrigel/ collagen/ laminin/fibrin*	Plating wells with an appropriate gel and seeding cells on top; assessing length and number of sprouts/ tubes/ rings in a microscope.	Matrigel is relatively expensive; 2D is not an accurate representation of the *in vivo* situation; simple method.	[82,83]
	Sprouting in 3D	*Sprouting in a thicker basement membrane*	Use of a thicker or multi-layer setup allowing both horizontal and vertical migration; assessing length and number of sprouts/ tubes/ rings in a microscope.	More accurate to *in vivo* situation; difficult quantification.	[72]
Phenotype differentiation	mRNA expression	*RT-qPCR*	Quantitative detection of coding sequences of angiogenesis related proteins in the DNA (VEGF, HIF1-alpha, PECAM1/CD31).	Time-consuming; less sensitive.	[85,86]
	Protein expression	*ELISA, Western blot*	Quantification of angiogenesis-related proteins detected in the culture supernatant (VEGF, HIF1-alpha) or on the membrane (PECAM1/CD31).	Sensitive methods; ELISA is simpler and cheaper than Western blot.	[69,87]
	Other	*NO release*	Detection of nitric oxide, which is indicative of well-functioning endothelium.	Quick; difficult detection due to short half-life of NO.	[91,92]
Indirect effect	Coculture	*MSCs, osteoblasts, chondrocytes*	Culturing multiple cell types together and observing their interaction and response to different agents introduced in the culture.	Challenging culturing technique; a more accurate representation of the *in vivo* interactions.	[16,67]
Adhesion/ Morphology	Observation of cells	*Morphology & Spreading*	Observing cellular response to the substrate extracts/surface.	Simple and quick.	[88]

8.5 INTERACTION OF ENDOTHELIAL CELLS WITH INORGANIC ANGIOGENIC AGENTS

8.5.1 Copper

Copper is known for its antibacterial activity and angiogenic potential [13,87]. An optimal concentration of copper has been also shown to stimulate normal bone metabolism and reduce the bone resorption rate [99,100]. Therefore, the element represents nowadays an attractive choice for general tissue engineering solutions, including bone regeneration.

Seventeen articles were identified in the literature and included in the comparison (**Table 3**) The largest group of biomaterials that incorporated copper were bioceramics [67,74,82,91,101–103]. Titanium was found to be the most common metallic material used in combination with copper, due to its superior mechanical properties and excellent suitability for orthopaedic applications [64,73,79,87,104]. Mg-Cu alloy represented a group of biodegradable metals and a solution for long-lasting antibacterial effects [83].

Generally, the addition of copper to different materials resulted in increased proliferative, migration and tube formation capability, secretion of angiogenesis dependant factors (VEGF) by ECs *in vitro,* and favourable vessel formation, also in *in vivo* models. Some studies reported morphological alteration of the materials surface with the additions of different concentrations of the agent [64,67,74,79,87,89,91,103]. Along with the chemical stimulatory agents, surface morphology in the form of nanostructures, or wettability can also favour angiogenic capacity of ECs and their adhesion and spreading on the material [103].

The investigation of the effect of medium-supplemented Cu on the angiogenic behaviour of HUVECs yielded data of the cellular response to various doses of the pure ion [78,104]. The stimulatory effects on proliferation were observed with a concentration of up to 14.1 mg/l, while migration was enhanced only up to 0.06 mg/l of copper in the medium [78]. Cu-Zn supplemented medium with Cu concentration of 6.3 mg/l showed improved migration activity, while increased amount of Cu (31.5 mg/l) was associated with cytotoxic effects on ECs [104]. Similarly, the effect of $CuSO_4$ on endothelial cells was investigated [105]. Those findings showed improvement in endothelial activity with 19.9 mg/l of Cu^{2+} (equivalent to 50 mg/l of $CuSO_4$), which is somewhat higher than the above-mentioned findings [78]. The optimal concentration of Cu ions released from the materials indicated in the publications also differed. The effective range of Cu^{2+} released from the majority of bioceramics was between 0.7 and 1.2 mg/l [67,82,101]. However, lower concentrations of ions leading to a positive endothelial response were also reported, such as 0.098 mg/l of Cu^{2+} released (on day 7) from a Cu-modified calcium phosphate cement [91]. Similar release profiles favouring the ECs were detected in the case of N/Cu doped titanium where the concentration of Cu^{2+} was

0.10 mg/l [79]. Much higher doses of Cu^{2+} have been reported from Zn/Cu-doped calcium phosphate [67] and Cu-crosslinked alginate with bioactive glass nanoparticles [102], with concentrations of 1.0 and 5.0 mg/l (day 7), respectively.

8.5.2 Magnesium

Magnesium is a very light and biocompatible metal. Its essential role in bone metabolism and degradability make it a promising solution for some areas of regenerative medicine demanding a new type of degradable metallic medical devices [14].

Nine articles discussing the effect of Mg on ECs were identified in the search and the summary of the findings can be found in **Table 4**. Unlike copper or strontium, magnesium was much more often incorporated within metallic materials [69,75,83,106,107] rather than in bioglasses or bioceramics [108]. The response of ECs to the magnesium-containing materials varied and greatly depended on the concentration. Several studies showed improvement in angiogenic capacity in terms of proliferation, migration, tube formation, and expression of angiogenic genes, after introducing the culture to magnesium [69,107–109]. The effective concentrations reported were usually much higher compared to the other elements being mostly in the range of 60-122 mg/l [75,76,83], although endothelial activation was also observed at a much lower concentration of 0.015 mg/l Mg^{2+} released from Zn/Mg-coated titanium [107]. Concentration-dependent cytotoxicity was studied using a tricalcium phosphate (TCP) material [108]. The TCP doped with 1.0 wt.% Mg stimulated ECs, while a TCP scaffold with 4.0 wt.% Mg had an inhibitory effect on their proliferative activity and growth. Similarly, the cytotoxic effects of untreated Mg-Ca alloy due to excessive generation of corrosion products were discussed in another study [75]. To mitigate the adverse inhibitory activity, the alloy was subjected to plasma electrolytic oxidation (PEO) treatment. Similarly, alkali heat treatment was adopted to achieve a more moderate release profile of the Mg-Ca alloy [106].

8.5.3 Silicon

Silicon is a major component of bioglasses and bioceramics. For its capacity to stimulate both MSCs/osteoblasts towards osteogenesis and ECs towards angiogenesis, silicon is utilized for many tissue engineering applications [14,110].

Within this review, 16 articles were identified and included in the comparison presented in **Table 5**. The findings showed that silicon was often used in combination with a titanium alloy and incorporated within its surface [65,73,92,111–115]. Such a solution exhibits good mechanical properties imparted by titanium and utilizes bioactive osteogenic/angiogenic component in the form of silicon ions/particles [7]. The addition of silicon often resulted in

an alteration of the surface morphology. Decreasing roughness with the addition of silicon was reported [92,112] as well as improved wettability [65,113]. Bioceramics often incorporate silicon directly in their matrices. A frequently reported bioceramic was Ca-Mg-Si [116,117], a combination of three known bioactive components, or silicon-containing hydroxyapatite [118].

The literature findings showed that silicon is capable to effectively promote the angiogenic behaviour of ECs by increasing their proliferation, migration capacity, enhancing the tube formation process, and upregulating the expression of angiogenesis-related genes (VEGF, HIF1—α). The optimal concentration varied among the studies but could generally be divided into a low concentration and a high concentration group. Favourable concentrations between 1.0 and 7.0 mg/l were reported [65,75,77,115–117], while enhanced ECs activity in a concentration range of 17-27 mg/l was also observed [73,111,118–120].

8.5.4 Strontium

Strontium and its role in the bone formation process have been addressed by many studies. The robust capacity of this element to stimulate osteoblast differentiation and promote formation of new bone tissue represents a promising solution for orthopaedic implants, granting a stronger attachment between to the implant [16,28,121–123]. However, despite the importance of angiogenesis in the fracture healing process, the effect of strontium on endothelial cells has not been widely investigated.

This review yielded 14 articles discussing the effect of strontium on endothelial cells (**Table 6**). The employed materials ranged from ceramics and metals to polymer matrices. Strontium was incorporated either in the bulk material or on its surface (either as an ion or nanoparticle), which determines its release profile characteristics.

The effect of strontium ranelate (SrR), commercially known as Protelos/Protos, an antiosteoporotic drug, on endothelial cells was discussed in [124]. The group reported a stimulatory capability of strontium on migration and tube formation properties of HUVECs with concentrations of around 7.5 mg/l Sr^{2+}. However, they also addressed concerns about the increased incidence of cardiovascular events associated with the systemic use of SrR, which were also discussed in other studies [125]. Nevertheless, they concluded that locally administered doses of the agent, smaller than those required by the oral intake of Protelos, should not be regarded as high risk.

Several publications discussed the effect of strontium incorporated in calcium-polyphosphate scaffolds (CPP) [86,126,127]. Their findings, which complied with other strontium containing bioceramics [85,121,128–130], generally implied enhanced proliferative and migration capacity, and higher tube formation ability of ECs in the presence of strontium.

Titanium-based alloys with strontium incorporated on their surface yielded similar results [16,131,132]. The studies reported improved adhesive, migration, and tube formation properties *in vitro*, suggesting likely enhanced vessel formation *in vivo*.

A group of researchers reported varying surface morphologies between calcium-polyphosphate-doped with strontium (SCPP) and without (CPP) and discussed their possible effect on ECs activity. The SCPP presented larger and more interconnected pores, resulting in a smoother surface with greater amounts of Ca^{2+} and $(PO4)^{3-}$, and appeared to be favourable for ECs [86,126,127].

The concentration of Sr^{2+} improving the angiogenic behaviour from studies that included the ion release profiles ranged from less than 1.0 to several milligrams per litre. Most findings on optimal Sr^{2+} concentrations for ECs were within the range of 0.1 – 6.0 mg/l (cumulative release after 7 days or extract with constant concentration) [16,77,86,128,130]. Higher concentrations between 13-27 mg/l, released from a bioceramic material, were reported by Zhu at al [85].

8.5.5 Zinc

Another abundant trace element found in the human body is zinc. Zinc is important for many biological reactions and plays an essential role in the metabolic processes of bone. Next to magnesium, it is another biocompatible biodegradable metal, with its corrosion rate being somewhat lower than that of magnesium [70].

Ten articles identified within the literature search have been summarized in **Table 7**. The findings showed that Zn can be incorporated in coatings on metallic substrates [69,104,107,133] as well as in bioglass and other ceramic materials [14,67,68]. Similar to magnesium and copper, the angiogenic ability of zinc is strongly dependent on its concentration and high doses can have adverse effects on the viability of endothelial cells. An investigation of the effect of pure metal zinc on endothelial cells showed that low concentrations of zinc of up to 3.92 mg/l (60 μM) promoted the angiogenic behaviour of endothelial cells, while higher doses inhibited their activity [70]. This was in line with other observations of positive effects on ECs at concentrations of 1.4 mg/l after 7 days of culture [67], although even higher concentration of up to 32.5 mg/l favouring the migration activity of ECs was reported [104].

Owing to its high corrosion rate, supplementary surface modification was often adopted to control the ion release and improve the cytocompatibility of zinc [133]. Zinc was often found as a co-doped agent in combination with other bioactive elements such as copper [67], magnesium [69,107], phosphorus/calcium [67,133,134] or silicon [14,68], which also reported improved viability of endothelial cells *in vitro* [14,135] and formation of blood vessels *in vivo* [134]. However, the positive effects were often attributed to the synergistic effect of zinc and the other element.

Table 3. *Literature overview of the effects of copper on ECs.*

Tested material	Effective conc./ Ion release Cu^{2+}	*In vitro* cell line/ *In vivo* species	Assays - Direct (D)/Indirect (I)	Incubation time	Other material properties	Results	Ref
Cu-Ti-O-titanium	SC: 4.62 at%; No IRP	EA.hy926	Cell adhesion (D); Live/Dead viability (D); MTT proliferation (D); NO release (D); ELISA (D); Tube formation in ECMatrix (I)	0.5, 1, 4 24 h; 1, 3, 5 d; 1, 3, 5 d; 24 h; 1 d; 4, 8, 18 h	The nanotube structure became less organized with increasing Cu content and tubular length decreased.	The Cu-doped nanotubes increased proliferation, VEGF secretion and tube formation.	[64]
Sr/Cu-bioactive glass	SC: 0.14 at%; IRP: 0.0025 mM/mg	HUVECs	MTT viability (I); Tube formation in Matrigel (I)	24, 48 h; 16 h	The fibre diameter increased with Sr content.	The Cu-dopant promoted angiogenic behaviour of HUVECs.	[74]
Cu-bioglass	MC: 1 wt%; IRP: ~0.95-1.15 mg/l	HDMECs	Staining for ECs surface markers (I); Tube formation in Matrigel (I)	7, 14 d; 24 h	-	The Cu-enriched scaffold stimulated ECs towards angiogenesis through increased VEGF expression by MSCs.	[82]
Mg-Cu alloy	MC: 0.03 wt%; IRP: 0.15 mg/l (after 5 d)	HUVECs; SD rats	MTT proliferation (I); Cell morphology (I); Scratch migration (I); Tube formation in Matrigel (I); RT-qPCR (I); Western blot (I); Aortic ring model	1, 3, 5 d; 12 h; 6, 12 h; 4, 8, 16 h; 3 d; 3 d; 7, 14 d	-	The Mg-Cu alloy (especially with 0.03 wt.%) showed stimulation towards angiogenesis, possibly owing to both Mg and Cu.	[83]
Cu^{2+}	-	Endothelial cells	-	-	-	Enhanced proliferation of ECs by the Cu ions.	[100]

Cu-bioactive glass	MC: 1.6 mol%; IRP: ~0.7 mg/l	HUVECs; Chicken embryos	Tube formation in Matrigel (I); Chicken chorioallantoic membrane assay	36 h; 5 d	-	The extracts with Cu improved tubule formation *in vivo* and vessel formation in the *ex vivo* model.	[101]
Cu-calcium phosphate	MC: 0.1 mol% (Cu/(Cu+Ca)); IRP: 0.098 mg/l (after 7 d)	HUVECs	CCK-8 proliferation (D); Cell attachment and morphology (D); Live/Dead viability (D); NO release (D); RT-qPCR (D)	2, 4 d; 24 h; 24 h; 2 d; 7 d	Crystal size increased with Cu concentration.	The samples with 0.05 and 0.1 mol% improved the angiogenic capacity of HUVECs.	[91]
Cu/Si-TiO_2 coating	SC: 0.76 at%; IRP: 0.01 mg/l (after 7 d)	EA.hy926	Live/Dead viability (D); MTT proliferation (D); Cell morphology (D); ELISA (D); Tube formation in ECMatrix (I)	1, 3, 5 d; 1, 4, 7 d; 1 d; 24 h; 4, 8, 18 h	-	The M-CuSi5 alloy with 0.76 at% Cu presented the best pro-angiogenic properties.	[73]
Cu/Zn-calcium phosphate	MC: 0.02 mol/l; IRP: 0.9 mg/l (after 7 d)	Vascular ECs (in cc w. BMSCs)	Cell morphology (D); DAPI staining (D); CCK-8 proliferation (D); ELISA (D)	5 d; 5 d; 1, 4, 7 d; 14 d	Addition of dopant resulted in cubical nano-/microparticles on the surface, depending on the concentration.	Cu/Zn co-dopant system improved angiogenic capacity of HUVECs in cc with BMSCs.	[67]
Cu^{2+}	0.06-14.1 mg/l	HUVECs	Alamar Blue viability (D); Scratch migration (D); Intracellular ROS levels (D)	3 d; 6 h; 24 h	-	Improved proliferation of ECs Cu of up to 222 µM improved proliferation and up to 1 µM also migration of ECs.	[78]
Cu-Ti6Al4V	MC: 6 wt%; IRP: 0.75 µg/cm^2 (after 7 d)	EA.hy926	Cell attachment and morphology (D); CCK-8 proliferation (D); RT-qPCR (D); ELISA (D)	1, 3 d; 1, 3, 5, 7 d; 3, 7 d; 3, 7 d	The presence of Cu resulted in micropores.	The Ti6Al4V-6Cu alloy enhanced angiogenic properties of ECs.	[87]

Cu-eluting graphene	MC: 0.36 g; IRP: 7 % (missing units; after 3 d)	SVEC4-10	Proliferation (DNA quantification) (D); Cell morphology (D); Tube formation in Matrigel (I); RT-qPCR (D)	3, 7 d; 24 h; 4 h; 3 d	The samples present different roughness (R_a=0.75-2.18 μm)	The sustained Cu release from PCL/RGO Cu enhances proliferation, migration, tube formation of ECs.	[89]
Cu/Ca-bioglass-alginate	IRP: ~5 mg/l (after 7 d)	HUVECs; HDMECs	MTT viability (I); Tube formation in Matrigel (I)	24 h; 24 h (1-2 w preculture)	-	The presence of bioglass nanoparticles (combined with Cu^{2+}) enhances the angiogenic capacity of HUVECs.	[102]
Cu-HA	MC: 3.15 wt%; No IRP	Human ECs; New Zealand white rabbits	Cell adhesion and spreading (D); Alamar Blue viability (D); Subcutaneous implantation	5 d; 1, 3, 5 d; 1, 4, 8 w	Addition of Cu through hydrothermal treatment resulted in micro/nanostructured surface.	The surface architecture of Cu5-HA supported the spreading and proliferation of ECs *in vitro* and vessel formation *in vivo*.	[103]
N/Cu-titanium	SC: 23 at%; IRP: 0.1 mg/l (after 7 d)	HUVECs	Alamar Blue proliferation (D); Scratch migration (D)	1, 4, 7 d; 6 h (3 d preculture)	The surfaces of implanted samples were evenly smooth.	The greater number of Cu^{2+} ions released from N/Cu-Ti promotes angiogenic behaviour of HUVECs.	[79]
$CuSO_4$	19.9 mg/l	HUVECs; CD1 mice	Tube formation in Fibrin gel; Subcutaneous scaffold implantation	12 d; 30 d	-	50 μg/ml of $CuSO_4$ improved the tube formation of ECs *in vitro* and in combination with GFs might be a good option for *in vivo* solutions.	[105]
Ca-P-Zn-Cu coating on Ti	6.3 mg/l (supplemented media)	HUVECs	Tube formation in collagen gels Transwell migration	24, 48 h 4 h		Improved migration activity with Cu (6.3 mg/l) in combination with Zn, while cytotoxic effects were observed with higher Cu concentration (31.5 mg/l).	[104]

MAGNESIUM

Table 4. *Literature overview of the effects of magnesium on ECs.*

Tested material	Effective conc./ Ion release Mg^{2+}	*In vitro* cell line/ *In vivo* species	Assays - Direct (D)/Indirect (I)	Incubation time	Other material properties	Results	Ref
(Si-)Mg-Ca alloy	SC: 37-64 at%; IRP: 70 mg/l (after 5 d)	C166-GFP endothelial cell line	Cell morphology (D); Alamar Blue cytocompatibility (I)	30 min; 5 d	The samples differed in surface roughness (0.7-4.3 μm), thickness and porosity.	The untreated surface of Mg-Ca alloy disabled the growth and proliferation of ECs.	[75]
Mg-TCP scaffolds	MC: 0.6 wt%; IRP: 56 mg/l (after 1 d)	HUVECs	CCK-8 proliferation (I); Live/Dead viability (I); Cell morphology visualisation (I); NO release (I); RT-qPCR (I)	1, 4, 7 d; 24 h; 24 h; 48 h; 7, 14 d	-	The scaffold with 0.6 wt% of Mg promoted angiogenic behaviour of HUVECs, while 2.4 wt% inhibited them.	[108]
Mg-alloy w. NO nanofibres	MC: 94 wt.%; No IRP	HUVECs	WST-1 proliferation (I); Tube formation in Matrigel (I)	1, 2, 3 d; 12 h	-	The rapid degradation of Mg did not match with the healing progress; here NO is incorporated to improve the healing process.	[136]
Mg-Zn-Mn alloy	MC: 97 wt.%; No IRP	HUVECs	DNA synthesis capacity (BrdU) (I); MTT viability (I); Tube formation in Matrigel (I); Western blot (I); RT-qPCR (I)	24, 48 h; 24, 48, 72, 96, 120 h; 16 h; N/A; N/A	-	The 6.25% Mg-Zn-Mn alloy extract could improve the angiogenic behaviour of HUVECs, most likely owing to Mg.	[69]
Mg^{2+}	61-122 mg/l	ECs (not specified); Nude mice; SD rats	Transwell migration (I); Subcutaneous implantation; Cranial defects	24 h; 1, 3, 7, 14 d; 4 w	-	Mg improved angiogenic behaviour of HUVECs through VEGF secretion of MSCs, and vascularization in *in vivo* models.	[76]

Mg-acrylic bone cement	MC: 5.3 wt%; IRP: 50 mg/l (after 1 d)	HUVECs; SD rats	Tube formation in Matrigel (I); Femoral defects	18 h; 2 m	-	The Mg-induced degradation improved tube formation of HUVECs.	[109]
Mg-Ca alloy	SC: 10-12 at%; No IRP	ECV304	Cell adhesion and morphology (D); CCK-8 proliferation (D)	6, 24 h; 24 h	-	The modification improved the corrosion rate and cytocompatibility of the Mg alloy.	[106]
Zn/Mg-titanium	IRP: 0.015 mg/l (after 7 d)	HUVECs	CCK-8 proliferation (D); RT-qPCR (D); Immunofluorescence analysis (D); Intracellular Zn detection	1, 4, 7 d; 10 d; 10 d; 10 d	-	The presence of Mg showed proangiogenic effects (proliferation, gene expression).	[107]
Mg-Cu alloy	MC: 99 wt.%; IRP: ~190 mg/l (after 5 d)	HUVECs; SD rats	MTT proliferation (I); Cell morphology (I); Scratch migration (I); Tube formation in Matrigel (I); RT-qPCR (I); Western blot (I); Aortic ring model	1, 3, 5 d; 12 h; 6, 12 h; 4, 8, 16 h; 3 d; 3 d; 7, 14 d	-	The Mg-Cu alloy showed stimulation towards angiogenesis, possibly owing to both Mg and Cu.	[83]

SILICON

Table 5. *Literature overview of the effects of silicon on ECs.*

Tested material	Effective conc./ Ion release Si^{4+}	*In vitro* cell line/ *In vivo* species	Assays - Direct (D)/Indirect (I)	Incubation time	Other material properties	Results	Ref
Ti-Si-N coating on Ti6Al4V	SC: 20 at%; No IRP	EA.hy926	CCK proliferation (D); Cell morphology and spreading (D); NO release (D)	1, 5 d; 5 d; 5 d	Decreasing nanoroughness with increasing Si content may affect the attachment properties.	Better morphology and greater spreading, increased proliferation and endothelialisation.	[92]
Si-micro/nano-structured titanium	SC: 0.86 at%; IRP: 23 mg/l; (after 7 d)	EA.hy926	Cell adhesion (D); Actin assay (D); Cell morphology (D); Live/dead viability (D); MTT proliferation (D); ELISA (D); Tube formation in EC Matrix (I); RT-qPCR (D)	0.5, 1, 4 h; 1, 4, 24 h; 1 d; 1, 3, 5 d; 1, 4, 7 d 24 h; 4, 8, 15 h; 3 d	Micro- and nanostructures from MAO and HT treatment respectively influenced the cell adhesion and the Si release profile.	Nanostructures secured a more constant Si release profile and improved the angiogenic behaviour of HUVECs.	[111]
Ti-Si-N coating on Ti6Al4V	SC: 12 at%; No IRP	EA.hy926	NO release (D); Cell morphology and spreading (D)	3 d; 24 h	Decreasing nanoroughness with increasing Si content.	Enhanced adhesion of endothelial cells on the coating.	[112]
Silk fiber w. Zn+Si-BrC brushite	MC: 0.5 wt%; No IRP	Porcine ECs; New Zealand white rabbits	Tube formation in collagen (D); Alamar Blue proliferation (D); Viability assay with PI (D); NO release (D); Femur defect	N/A; 1, 3, 7 d; 7 d; 1, 7 d; 1, 3 m	-	Positive effect of Si (and synergistic effect of Si/Zn) on angiogenesis.	[68]
Bioactive glass nanoporous structure	MC: 40 mol% (85 mol% SiO_2); IRP: 21 mg/l (after 7 d)	HUVECs; SD rats	Scratch migration (I); Tube formation in Matrigel (I); Subcutaneous implantation	24 h; 3, 6 h; 2, 4 w	Nanofibrous structure enhances neo-blood vessel formation.	Stable delivery of Ca and Si and their synergistic effect with the nano-sites of improve angiogenesis.	[120]

Si-DLC coating on Ti6Al7Nb	SC: 14–22 at%; No IRP	EA.hy926	Live/Dead viability (D); XTT viability (I,D)	48 h; 48 h	Increasing wettability with higher Si content.	Si is tolerated by cells up to the limit between 14 and 22 at%.	[113]
Si-TiO_2 nanotubes	SC: 2.8 at%; IRP: 7 mg/l (after 1 d)	EA.hy926	Live/Dead viability (D); Tube formation in ECMatrix (I); NO release (I); ELISA (I)	1, 3, 5 d; 4, 7, 17 h; 24 h; 24 h	Increase of Si content increases the hydrophilicity.	The incorporation of Si into the material boosted the angiogenic capacity of ECs.	[65]
Strontium-HT-Gahnite	1.6-6.6 mg/l (diluted extracts)	HUVECs	MTT proliferation (I); Transwell migration (I); RT-qPCR (I); Calvarial defect	1, 4, 7 d; 18 h (7 d preculture); 4 d; 4-6 w	-	Increased metabolic activity at day 7, migration capacity and mRNA expression of HUVECs with the dissolution products.	[77]
Ti-Si-N coating on titanium	SC: ~11-13 at%; No IRP	EA.hy926	Cell morphology and spreading (D); CCK-8 proliferation (D); NO release (D); RT-qPCR (D); Western blotting (D)	24 h; 1, 6 d; 6 d; 6 d; N/A	-	Si promoted endothelial proliferation and upregulates VEGF in ECs.	[114]
Si-TiO_2	SC: 1.8 wt%; IRP: 3.5 mg/l (after 7 d)	HUVECs	Alamar Blue proliferation (D); Cell morphology, Live/Dead viability (D); Scratch migration (D); Tube formation in Matrigel (I); ELISA (D); RT-qPCR (D)	1, 4, 7 d; 7 d; 8h (1 d preculture) 12 h 1, 3, 5, 7 d 4, 7, 14 d	-	The coating with 1.8 wt% of Si improved the proliferation, migration, VEGF, tube formation of HUVECs.	[115]
Mesoporous silica microspheres	IRP: ~22 mg/l (after 7 d)	HUVECs; Domestic chicken embryos	CCK-8 proliferation (I); RT-qPCR (I); Western blotting (I); Immunohistochemistry (I); Tube formation in Matrigel (I); Scratch migration (I); Transwell migration (I); Angiogenesis in chick chorioallantoic membrane (CAM)	1, 3, 7 d; 24 h; 24 h; 24 h; 0, 4, 6, 12 h; 12, 24 h; 12 h; 11 d	-	The presence of Si promoted angiogenic capacity of HUVECs through stimulating expression of HIF1-alpha, especially in combination with the delivery of VEGF.	[119]

Si-oxynitro-phosphide coating	SC: 53-62 at%; No IRP	HUVECs	Cell attachment (D); MTS viability (D); MTS growth (D); Proliferation with Calcein-AM (I); Transwell migration (I); Matrix deposition (D); Tube formation in Matrigel (D); RT-qPCR (D)	4 h; 24 h; 1, 3, 7 d; 24, 48 h; 24 h; 5 d; 6 h; 24, 72 h	Surface wettability correlated with the number of attached cells.	The silica-based coatings enhanced proliferation, migration, matrix deposition, tube formation VEGF expression of HUVECs.	[137]
Cu/Si-TiO_2	SC: 16 at%; IRP: ~27 mg/l (after 7 d)	EA.hy926	Live/Dead viability (D); MTT proliferation (D); Cell morphology (D); ELISA (D); Tube formation in ECMatrix (I); RT-qPCR (I)	1, 3, 5 d; 1, 4, 7 d; 1 d; 24 h; 4, 8, 18 h; 3 d	-	The implant with 16 at% of Si showed the best proangiogenic property by stimulating the proliferation, favourable morphology and gene expression of ECs.	[73]
Ca–Mg–Si bioceramics	1.18-4.44 mg/l (diluted extracts)	HAECs	WST-1 proliferation assay (I); NO release (I); Tube formation in ECMatrix (I); RT-qPCR (I)	4 d; 24 h; 2.5, 5.5, 17 h; 4 d	-	Ceramics releasing higher amount of Si had greater stimulatory effect on angiogenic behaviour of ECs.	[116]
Ca–Mg–Si bioceramics	0.6-2.1 mg/l (diluted extracts)	HAECs; New Zealand rabbits	WST-1 proliferation (I); Tube formation in ECMatrix (I); RT-qPCR (I) NO release (I); Scaffold implantation near distal femur	4 d; 2.5, 5.5, 17 h; 4 d 24 h; 8, 16 w	-	Presence of Si stimulated angiogenic behaviour of ECs *in vitro* and neovascularization *in vivo*.	[117]

Si-HA	SC: 6.15 at%; IRP: 17 mg/l (after 7 d)	HUVECs; White leghorn chicken eggs; Wistar rats	Viability with Calcein AM (D); Cell adhesion (D); Proliferation with PicoGreen (D); NO release (D); ELISA (D); Chicken Chorioallantoic Membrane Assay; Subcutaneous implantation	24 h; 24 h; 1, 7 d; 1, 7 d; 1, 7 d; 4 d; 2 w	-	Scaffold with Si had stimulatory effects on functionality and viability of ECs.	[118]
(Si-)Mg-Ca alloy	SC: 10 at%; IRP: 2.0 mg/l (after 5 d)	C166-GFP EC line	Cell morphology (D); Alamar Blue cytocompatibility (I)	30 min; 5 d	The samples differed in surface roughness (0.7-4.3 µm), thickness and porosity.	The Si topography promoted the cellular organisation.	[75]

STRONTIUM

Table 6. *Literature overview of the effects of strontium on ECs.*

Tested material	Effective conc./ Ion release Sr^{2+}	*In vitro* cell line/ *In vivo* species	Assays - Direct (D)/Indirect (I)	Incubation time	Other material properties	Results	Ref
SCPP	MC: 8 mol%; No IRP	HUVECs (cc w. OB); New Zealand white rabbits	MTT proliferation (D); Tube formation (I); ELISA (D); *In vivo* implantation (D)	7, 14, 21, 28, 35 d N/A 28 d 4, 8, 16 w	SCPP (presence of Sr) demonstrated much smoother surface than CPP and HA.	Better angiogenic properties of SCPP than CPP and HA.	[126]
Sr-TiO_2 nanoporous surface	IRP: 0.6 mg/l (after 7 d)	HUVECs (CM from BMSCs); Beagle dogs	Transwell migration (I); Tube formation in ECMatrix(I); *In vivo* implantation (D)	24 h; 24 h; 6 w	-	TiO_2 coating promoted angiogenic potential of BMSCs and HUVECs (conditioned medium from BMSCs).	[16]
Sr-TiO_3 nanotubes	SC: 12.5 at%; IRP: 1.4-1.5 mg/l (after 1 d)	EA.hy926 (CM from OB)	NO release (I); Tube formation ECMatrix (I)	24 h; 4, 8, 18 h		More NO production and tube formation with strontium.	[131]
Sr-graphene ox.-collagen scaffold	IRP: 45 % (no units)	HUVECs (CM from hADSC); Rats	Viability, morphology, adhesion (D); Transwell migration (I); Tube formation in Matrigel (I); Cranial defect	24 h; 24 h; 6 h; 4, 12 w	Sr-GO-Col exhibited rougher surface than collagen.	Vascularization potential improved by Sr-GO-Col.	[88]
Strontium ranelate	7.47 mg/l (medium with Sr)	HUVECs	Transwell migration (D); Tube formation in Matrigel (D); Western blotting (D); RT-qPCR (D)	24 h; 4-12 h (48 h preculture); 0, 15, 30, 60, 90 min	-	Better migration and more branching points and loops detected with SrR.	[124]

Strontium-HT-Gahnite	0.24-0.96 mg/l (diluted extracts)	HUVECs; SD rats	MTT proliferation (I); Transwell migration (I); RT-qPCR (I); Calvarial defect	1, 4, 7 d; 18h (7 days preculture); 4 d 4-6 w	Angiogenic Si incorporated in the material.	Increased metabolic activity at day 7, migration capacity and mRNA expression of HUVECs with the dissolution products.	[77]
Sr-calcium silicate	~1.1-4.2 mg/l (diluted extracts)	HUVECs; Fisher 344 rats	MTT proliferation (I); Tube formation in ECMatrix (I); Calvarial defects	1, 3, 7 d; 4, 8, 12 h; 4 w	-	Greater proliferation after 7 days and higher stimulation towards tube formation with SrCS. Better vascularization of newly formed bone.	[130]
Sr-TiO_2	SC: 25-34 wt%; IRP: 1.3-1.6 mg/l (after 1 d)	HUVECs; SD rats	Cell morphology (D); MTT cellular activity (D); Scratch migration (D); Tube formation in Matrigel (I); Tibiofibular fracture	1, 3 d; 1, 3 d; 2 d (1 d preculture); 16 h; 4 w	Nano-gridding in combination with Sr promotes angiogenic behaviour of HUVECs.	The addition of Sr to the nano-gridded surface enhanced the adhesion, migration and tube formation of HUVECs, and vascularization of newly formed bone.	[132]
Sr-bioactive glass microspheres	6.227 mg/l (extract)	HUVECs; SD rats	Immunofluorescent staining (I); RT-qPCR (I); Calvarial defect	3 d; 3 d; 1, 6 w	The material contained Si which is a known direct proangiogenic stimulant.	SrBGM can enhanced angiogenesis through regulation of an immune reaction.	[128]
SCPP	MC: 8 mol%; No IRP	HUVECs	MTT proliferation assay (D); Cell morphology in SEM (D); ELISA (D); RT-qPCR (D)	1, 3, 5, 7 d; 7 d; 7 d; 7 d	SCPP presented smoother surface than CPP; presence of Sr prevented formation of hydrogel.	SCPP resulted in higher proliferation rate, secretion of angiogenic genes, and better adhesion and spread of HUVECs.	[127]
Sr-doped bioactive glass nanoparticles	MC: 8.5 mol%; No IRP	HUVECs	Alamar Blue cellular activity (D); Cell distribution (D);	1, 3, 7 d; 1, 3, 7 d	Nanoparticles favoured the spread and attachment of HUVECs.	Sr had a positive effect on the behaviour of HUVECs.	[121]

$Sr_5(PO_4)2SiO_4$	13-27 mg/ml (extract);	HUVECs	MTT proliferation (I,D); Cell morphology (I); RT-qPCR (I); Cell attachment (D)	1, 3, 7 d; 1 d; 7 d; 1, 3, 7 d	Angiogenic Si was incorporated in the material. As a control, TCP was used.	The SPS scaffold enhanced angiogenic differentiation, attachment and proliferation of HUVECs.	[85]
SCPP	MC: 8 mol%; IRP: 0.08 mg/l (after 7 d)	HUVECs (cc with OB); New Zealand white rabbits	MTT cellular activity (D); Cell morphology (D); RT-qPCR (D); ELISA (D); Calvarial defect	1, 3, 7, 10, 14 d; 7 d; 7 d; 7 d; 8 w	SCPP presented a more compact surface in contrast to CPP and HA.	The SCPP scaffold promoted angiogenic behaviour of both cell types *in vitro* and also *in vivo* in newly formed bone.	[86]
Sr-doped bioactive glass	MC: 0.1 wt%; No IRP	Eahy926; Wistar rats	SulfoRhodamin B proliferation (I); Femoral defect	1, 3, 6 d 4, 7, 15, 30, 60 d	Incorporation of Sr into the BG decreased the oxidative stress thus contributing to bone repair.	Stimulated proliferation of ECs.	[129]

Table 7. Literature overview of the effects of zinc on ECs.

Tested material	Effective conc./ Ion release Zn^{2+}	*In vitro* cell line/ *In vivo* species	Assays - Direct (D)/Indirect (I)	Incubation time	Other material properties	Results	Ref
Zn-P coating on Zn	SC: 25 at%; 30 mg/l (extract)	EA.hy926	MTT viability (I); Cell adhesion and morphology (D)	1, 3, 5 days; 3 d	-	The ZnP coating improved the cytocompatibility of pure Zn and enhanced the attachment and viability of ECs.	[133]
PCL-nHA-nZnO	N/A	HUVECs (cc with OB); Chicken embryos	MTT proliferation (D); Cell morphology (D); Migration into the scaffolds (D); RT-qPCR (D); Chick embryo chorioallantoic membrane assay	1-7 d; 3 d; 7 d; 7 d; 2 d	Secondary pores resulting from the surface modification with ZnO.	The *in vivo* assay in chicken embryo showed increased blood vessel formation in the presence of ZnO on the surface.	[134]
Silk fiber w. Zn+Si-BrC brushite	MC: 0.25 wt%; No IRP	Porcine endothelial cells; New Zealand white rabbits	Tube formation in collagen (I); Alamar Blue proliferation (D); Viability assay with PI (D); NO release (D); Femur defect	N/A; 1, 3, 7 d; 7 d; 1, 7 d; 1, 3 m	-	Positive synergistic effect of Si/Zn on angiogenesis.	[68]
Mg-Zn-Mn alloy	MC: 1 wt% Zn; No IRP	HUVECs	DNA synthesis capacity (BrdU) (I); MTT viability assay (I); Tube formation in Matrigel (I); Western blot (I); RT-qPCR (I)	24, 48 h; 24, 48, 72, 96, 120 h; 16 h; N/A; N/A	-	The 6.25% Mg-Zn-Mn-alloy extract could improve the angiogenic behaviour of HUVECs, however no direct effect of Zn is discussed.	[69]

Cu/Zn-calcium phosphate	MC: 1.3 g/l; IRP: 1.4 mg/l (after 7 d)	Vascular endothelial cells (cc with BMSCs)	Cell morphology (D); DAPI staining (D); CCK-8 Proliferation assay (D); ELISA (VEGF) (D)	5 d; 5 d; 1, 4, 7 d; 14 d	Addition of dopant resulted in cubical nano-/microparticles on the surface, depending on the concentration.	Cu/Zn co-dopant system improved angiogenic capacity of HUVECs in cc with BMSCs.	[67]
ZnO-polymer nanocomposite	MC: 0.8-1.6 wt%; No IRP	HUVECs; Wistar rats	Cell attachment evaluation in SEM (D); MTT cell viability assay (D); LDH assay (D); Subcutaneous implantation	24 h; 24 h; 24 h; 7, 21 d	-	Scaffolds with of 1 and 2 wt.% of ZnO resulted in better angiogenic behaviour of HUVECs and blood vessel formation *in vivo*.	[135]
Zn/Mg-titanium	IRP: ~0.02 mg/l (after 7 d)	HUVECs	CCK-8 Proliferation assay (D); RT-qPCR (D); Immunofluorescence analysis (D); Intracellular zinc detection	1, 4, 7 d; 10 d; 10 d; 10 d	-	Zn ions alone did not show significant improvement in angiogenesis, however, when combined with Mg, it has a positive effect.	[107]
Zn^{2+}	3.9 mg/l	HCECs (artery ECs)	MTT viability; BrdU proliferation; Cell adhesion; Centrifugation assay; Cell spreading; Scratch migration; Cell morphology; RT-qPCR	24 h; 24 h; 2, 6 h; 2, 6 h; 0, 2, 4, 6, 8 h; 0, 6 h; 24 h; 24 h		Low concentration of Zn (up to 60 µM = 3.9 mg/l) promoted angiogenic behaviour of HUVECs.	[70]
Bioactive glasses with Zn	N/A	N/A	N/A REVIEW	N/A	-	Zn in certain concentration promoted angiogenic behaviour of HUVECs.	[14]
Ca-P-Zn-Cu coating on Ti	6.5 – 32.5 mg/l (supplemented media)	HUVECs	Tube formation in collagen gels Transwell migration	24, 48 h 4 h		Improved migration ability with Zn of up to 32.5 mg/l.	[104]

Direct (D) assay = culturing cells directly on the material's surface; Indirect (I) assay = culturing cells with the material's extract; Abbreviations: MC = material composition; SC = surface composition; IRP = ion release profile; h = hours; d = days; w = weeks; cc = coculture; ECs = endothelial cells; OB = osteoblasts

8.6 DISCUSSION

Aseptic loosening is recognized as one of the leading causes of implant failure after primary THA. Through ion and particle doping, angiogenesis and osteogenesis boosting agents can be introduced onto the surfaces of bioinert biomaterials (such as titanium) and thereby strengthen the attachment at the interface and very likely improve the failure odds. The results summarized in the previous section (section 5) showed that all reviewed elements (copper, magnesium, silicon, strontium, and zinc) present a concentration-dependent angiogenic potential. In this section, the properties of these elements will be further discussed with respect to the methodological approach used for angiogenic assessment. Furthermore, the elements will be compared based on their angiogenic mechanism of action and their effect on other cell types engaged in the bone repair process. Finally, the acquired knowledge will be utilized to propose a solution, which could improve osseointegration of a permanent implant through the effective delivery of dual angiogenic and osteogenic promoters from the biomaterial's surface.

8.6.1 Assessment methods for angiogenesis induced by inorganic agents

For this review, publications discussing the interaction of one or multiple of the selected elements with endothelial cells are compared. Direct (D) and indirect (I) testing strategies of the materials were identified; the cells were either seeded directly on the surface or cultured with extracts (also referred to as degradation fluid or conditioned medium) of the respective biomaterial on a standard culture dish. Depending on the biomaterial, the two approaches can yield different results and their mutual comparison may not be accurate [14]. Extracts obtained from the material stimulate the cell only via released ions/particles (chemical composition) from the biomaterials. On the other hand, the cells in direct contact with the biomaterial will be also affected by its surface morphology, wettability, or surface energy [138–141]. Several studies have discussed the morphological changes of the biomaterial's surface and its potential effect on the ECs. For example, the changes of the surface of the biomaterial achieved by the incorporation of silicon were reported to be substantial for attachment, spreading, and further activity of cells [92,111]. However, they did not provide both sets of data (from direct and indirect testing of the biomaterial), which could clarify the hierarchy of the chemical and physical stimuli, *i.e.* which one is primary for initiation of the desired cellular response. Generally, treating cells with extracts is relatively simple while seeding, detaching and collecting cells from a biomaterial with complex surface morphology require optimized protocols which are methodologically more challenging and laborious.

The vast majority of biomaterials found in this review were very complex with multiple (bioactive) elements in their composition. Despite the rigorous testing of different concentrations of the studied elements, the other bioactive agents present in the biomaterials and the possible additive/synergistic effect must always be taken into consideration and ideally should be compared with studies examining the effect of pure ions [70,78] or very simple molecules separately [124].

The incubation time of the ECs with the various biomaterials/ions varied per study, but was generally in the range of several days (some studies reported incubation of only a few hours). This experimental variable also affects the results as short incubations might not be sufficient to take any/the full effect and elicit response whereas long incubations may lead to undesired effects as well, such as toxicity.

Focusing on methodologies, the most frequently studied cell properties related to angiogenesis are proliferation, migration, and sprouting. Due to their simple protocol, colorimetric assays are often chosen for the determination of cellular proliferative activity. For the ambiguous character of the output data and their potential misinterpretation [72,142], the number of studies included in this review which interpreted the results of colorimetric metabolic assays as proliferation data rather than metabolic activity was concerning. The highly reducing environment does not necessarily reflect the higher number of cells as this may also be the result of increased metabolic activity due to stimulating biochemical cues. Therefore, careful data interpretation is essential and the use of another assay (such as DAPI cell count) for validation of the obtained results is strongly recommended [53,54,72]. An obstacle that can be encountered using DAPI and other fluorescent imaging methods is autofluorescence of certain materials (such as some polymers) [143].

A weakness of the scratch/wound healing assay, assessing the cell motility, is its reproducibility, as the size of the scratch is not always uniform. Additionally, it should be noted that the wound closure is not necessarily accomplished by migration alone, and the contribution of proliferation should be considered as well [53,54,57,72]. Finally, the transwell assay allows for testing with extracts or conditioned media only, while the wound healing assay can be performed also on substrates with smooth surfaces allowing to create a scratch in the cellular monolayer.

The tube formation assays were mostly performed in Matrigel-coated wells. Despite its relatively high price, its batch-to-batch composition variation, and the fact that it is derived from murine breast tumour tissue, it seems to be the standard material for this assay. However, its high growth factor content has been demonstrated to induce an atypical tendency towards the formation of tubular structures by non-endothelial cells.

Phenotype commitment is most frequently assessed using RT-qPCR and ELISA methods (quantification of VEGF, HIF1-α, PECAM1 expression) and detection of released

NO ions. Besides the already discussed angiogenesis-related growth factors and molecules (HIF1-α, VEGF, PECAM1), the process is also guided by a number of other signalling pathways involved in transcriptional and post-translational regulation. Wnt pathways are groups of signalling proteins mediating cellular proliferation, migration, differentiation, survival, and apoptosis, and they are potent guides for bone healing and vessel remodelling. With regards to angiogenesis, *Wnt/ß-catenin* is one of the known Wnt pathways governing the transcription of genes associated with vascular growth (VEGF) [144–147]. Notch signalling ligands and receptors are involved in vascular homeostasis [148–150], regulating phenotype commitment of endothelial tip and stalk cells responsible for migration and proliferation, respectively, during vascular sprouting [148].

None of the studies included in this review investigated the effect of ions on the first stage of angiogenesis, which is the basal membrane degradation. A possible explanation could be that researchers consider an already broken/damaged basement membrane in their models and do not feel the need to address it. Those assays may, however, be highly relevant for assessment of osteoconductive scaffolds supporting large defects/injuries and requiring regeneration of greater portion of bone and its vasculature.

Studies testing the response of cells seeded directly on the biomaterials often included observation of the cellular morphology. This simple experiment grants direct (although not quantitative) feedback about the biomaterial cytocompatibility for ECs.

All in all, there is a wide spectrum of available methods for assessment of angiogenic behaviour of endothelial cells in 2D. The recommended approach drawn from the findings of this review is in favour of testing multiple behavioural features of endothelial cells in the presence of a potential angiogenic stimulus in order to evaluate its angiogenic potential. Moreover, it is advisable to perform cell cultures in extracts obtained from the biomaterials (indirect test), and on biomaterial's surfaces (direct test) to decouple and distinguish between effects of chemical composition and physical properties of the used biomaterial, as they both play a significant role in the cellular response. Considering the growing trend of porous and degradable biomaterials necessitating proper bone ingrowth, relevant angiogenic models with transition from 2D to 3D will become a fundamental aspect of research dealing with osteoconductive biomaterials. The 3D methodologies lay ground for closer approximation of intercellular interactions and their innate matrices which as well are pivotal for tissue regeneration [146,151].

8.6.2 Role of ions in angiogenesis at the implant-bone interface

An ideal element should feature a dual incentive towards angiogenic and osteogenic commitment of endothelial cells and MSCs/osteoblasts respectively, and thereby simultaneously promote

blood vessel and bone matrix formation. All reviewed elements (copper, magnesium, silicon, strontium, and zinc) demonstrated pro-angiogenic characteristics at certain concentrations (discussed in section 5). Considering the relatively wide range of effective concentrations reported in the different studies, the obtained responses of ECs to the elements were very likely conditioned by additional factors, such as other released ions from the biomaterials or physical properties of the substrates.

The role of zinc in blood vessel formation has been ascribed to its regulatory actions towards VEGF secretion through its high affinity to zinc proteins [152], and other zinc sensing receptors [153], which can additionally promote survival and growth of ECs through activation of intracellular signalling pathways. The enhancing effects of magnesium on migratory properties of ECs, on the other hand, have been associated with its chemoattractant role [154] and increased integrin function [155]. Both magnesium and zinc show auspicious potential for scaffolds in bone tissue engineering applications for their biodegradable properties. However, according to the current research, their degradation process has not been well contained yet. This may be reflected by the concentrations of released magnesium and zinc ions, which were usually much higher than concentrations detected with copper, silicon, or strontium. The high corrosion rate of both reviewed metals (magnesium and zinc) can result in adverse effects on bone regeneration: in the case of magnesium scaffolds, uncontrollable development of hydrogen bubbles and alkaline environment have been shown to severely inhibit the osteogenic process [13]. In addition, such a scaffold might not ensure the required mechanical stability throughout the healing process until the new bone tissue is formed [136]. The current attempts to moderate the negative effects of the rapid corrosion include alloying with other more stable metals or surface modifications, possibly making the fabrication process excessively complex. Incorporation of Mg on the surface of a permanent orthopaedic implant needs further scrutiny regarding surface design, taking into account the effects on both the osteogenic and angiogenic processes [75,106].

The clear superiority of copper for bone tissue engineering and vascular applications is attributed to its dual antibacterial and angiogenic capacity. Even in relatively small concentrations, copper can mitigate the risks of fatal peri-implant bacterial infection, leading to septic loosening of a prosthesis [13,87,101]. Besides its antibacterial activity, copper could potentially accelerate bone healing through enhanced angiogenesis. The mechanism by which copper promotes the formation of new blood vessels is based on the stabilization of HIF1-α and further stimulation of VEGF expression [13,36,91]. Despite the inherent role of copper in the bone metabolic processes, several publications reported severe sensitivity and possible inhibitory effects of copper on MSCs and osteoblasts at concentrations which, at the same time, were found to be beneficial for ECs [78,156]. Regarding orthopaedic applications, an

appropriate amount of copper favouring both cell types must be carefully chosen to avoid compromising the bone healing process. Alternatively, fabricating a coating with a properly tuned ion release profile could systematically stimulate the most relevant cells in the individual stages of the healing process and thereby effectively promote bone regeneration.

Another element with a dual character is silicon. Owing to its favourable properties for endothelial and osteoblastic cells, which have been known for years, it is being employed for applications in tissue engineering, including solutions for bone regeneration, where positive interactions with both cell types are crucial [65,111,115]. Silicon is a stable element and unlike copper, magnesium, or zinc, it does not exhibit as many risks regarding possible cytotoxicity and it is the only element in this study that is well accepted by tissues even in large concentrations (it is present in the majority of active bioceramic materials). Its mechanism of action is analogous to that of copper: it increases expression of proangiogenic molecules, such as VEGF and FGF, it activates kinase insert domain receptor (KDR) and stimulates the production of nitric oxide [157,158].

Strontium is currently known for its excellent capacity to encourage the formation of new bone and represents a new generation of promising orthopaedic solutions [27,30]. Due to its mechanism of action, it can promote bone formation more effectively than calcium, and most likely, it also surpasses the capacity of silicon to secure a strong attachment with the implant. Despite the intensive research, little has been reported regarding its effect on ECs. The data from the reviewed literature indicate that strontium can favour the viability of ECs and also promote angiogenesis by stimulating MSCs to produce VEGF [124,127]. The exact mechanism by which strontium activates ECs and guides their angiogenic behaviour is not yet fully known, however, the involvement of the calcium-sensing receptor (CaSR) has been discussed [159]. This receptor is inherently involved in the mechanism of strontium-facilitated osteogenesis. It can bind strontium instead of calcium due to its similar atomic and ionic properties [28,123]. Confirming the role of CaSR in the strontium-mediated angiogenic commitment of ECs would introduce a new and possibly very effective system for the early development of well-vascularized bone.

Taken together, the comparison of the five elements and requirements for the intended application (**Table 8**) suggests that strontium and silicon could be a superior choice to the other three elements with the currently available processing methods. The aims to utilize zinc and magnesium are challenged by their rapid corrosion (unproperly controlled ion release could result in adverse effects), while copper may hamper the osteogenic process at concentrations beneficial for ECs. Strontium is known for its tremendous potential to promote osteogenesis, for which it has been utilized in osteoporotic treatments in the past, and the findings of this study imply promising results for the endothelial interaction as well. Silicon is utilized across many tissue engineering areas and presents a dual angiogenic and osteogenic activity.

Table 8. *Overview of the criteria assessment per element.*

	Intended use	Tolerable ion content for ECs	Angiogenic properties	Osteogenic properties	Other properties	Current biocompatibility for bone applications
Cu	Cardio. and ortho. applications	20 mg/l	Excellent	Inhibitory effect at high conc.	Antibacterial properties	Good
Mg	Degradable scaffolds	190 mg/l	Good	Good	Biodegradability	Low due to high corrosion rate and cytotoxicity due to degradation products
Si	All tissue engineering	27 mg/l	Good	Good	Applicability for various tissues	Excellent
Sr	Ortho. applications	27 mg/l	Good	Excellent	Antiosteoporotic drug	Good
Zn	Degradable ortho. scaffolds	32 mg/l	Good	Good	Biodegradability	Low due to high corrosion rate (the same consideration as for Mg)

8.6.3 Angiogenic response of ECs mediated through other cell types

Indirect cellular interactions with materials, mediated via other cell types, are certainly of great importance as they represent a closer approximation of the *in vivo* situation in *in vitro* models. Although they were not the main focus of this review, some included publications [16,67,86,126,131] discussed these interactions and therefore will be briefly addressed in this section.

The mutual interaction of MSCs, osteoblasts, chondrocytes, fibroblasts, and immune cells with endothelial cells is certainly vital for proper fracture repair. Although a coculture of MSCs/osteoblasts with ECs is the most commonly used model for bone fracture-related angiogenesis, these cells do not interact until later in the healing process. The initial inflammatory reaction, with the onset of angiogenesis, is guided by immune cells. The description of the relationship between macrophages and ECs showed an improved angiogenic response of ECs cultured in conditioned medium from stimulated mouse monocytes [128].

Endothelial cells thrive in the presence of MSCs/osteoblasts and vice versa. The angiogenic and osteogenic differentiation potentials are higher in comparison to respective monocultures, leading to successful bone regeneration [96,97]. MSCs belong to a group of cell types capable of VEGF secretion. Via paracrine signalling pathways, this cytokine can mediate the activity of ECs, including their differentiation, proliferation, and migration [16,94,160].

The performed experiments showed that cocultures of ECs and MSCs were beneficial for differentiation of endothelial phenotype and expression of specific markers, such as CD31 and von Willebrand factor, likely due to the delivery of VEGF to endothelial cells [94]. The symbiotic relationship of the coculture has also been illustrated by the mutual attachment of MSCs and ECs (particularly endothelial progenitor cells), which augments the pluripotency of MSCs and simultaneously promotes angiogenesis [95,161].

Under optimal conditions, VEGF production by MSCs can be increased. The use of strontium-containing titanium material was reported to stimulate MSCs towards higher secretion of VEGF and platelet-derived growth factor (PDGF)-BB, which are both essential for angiogenesis [16]. In their experiments, much higher concentrations of those molecules were detected in conditioned medium obtained from MSCs cultured with strontium, which subsequently ensured greater recruitment and tube formation capacity of HUVECs. An experiment yielding similar findings was described in other studies, using conditioned media from MSCs stimulated by Sr [131] and Mg [76] ions, respectively and, for EC cultures.

These findings support the arguments, that despite their importance in the initial stages of research, monocultures are not an optimal representation of the *in vivo* interactions, and they further imply that the angiogenic function should be assessed from a broader angle. Generally, it also suggests that elements, which do not necessarily trigger endothelial cells could still (strongly) boost the blood vessel formation *indirectly* through stimulation of other cell types and subsequent activation of endothelial cells. The relationship between MSCs and ECs, which has proven to serve as an example, is critical for angiogenesis and most likely determines the outcome.

8.6.4 Future perspectives

Considering the causes leading to failures of permanent hip implants, promoting bone formation and strengthening the attachment at the interface could potentially reduce their aseptic loosening, which is usually attributed to the insufficient bioactivity of those biomaterials.

The fracture healing model is used to emulate the bone repair process after replacement surgeries. This complex set of events, which is governed by many molecular cascades and environmental factors, can be modulated by various physical or biochemical agents interfering in individual of multiple stages of this process. The scientific evidence for the mutual dependency between bone matrix deposition and blood vessel formation, and its role in the fracture healing process, has commenced the development of biomaterials, which could promote both processes simultaneously through relevant agents, and thereby ensure early deposition of well-vascularized bone and secure a stronger connection with the implant [15,22].

The current strategies to improve angiogenesis usually rely on the favourable environment created by structures with pores of appropriate volumetric ratio, which allow for vessel ingrowth [11,18]. Those, however, must ensure complete interconnectivity, else they hinder the cellular invasion and formation of a new vascular network [162]. Local delivery of proangiogenic factors such as VEGF is limited by natural properties of those molecules, including low protein stability and short circulating half-life and therefore their therapeutic use compels advanced engineering methods [22,163–165]. Angiogenic stimulation through inorganic ions [25] offers another approach with a potentially tunable release profile of the active element adapted to the needs of the different stages in the healing process.

In this review, five inorganic elements (copper, magnesium, silicon, strontium, and zinc) were analysed and compared with respect to their angiogenic capacity. Taking into account the currently available surface biofunctionalisation methods, the properties of silicon and strontium showed the best match with the defined criteria. Both elements present low or no risk of cytotoxicity, effectively promote osteogenesis, and this review confirmed also their angiogenic potential. Therefore, a suitable approach would be to design titanium-based implants with silicon and/or strontium-doped surfaces, which could deliver angiogenic and osteogenic stimuli simultaneously and in a controlled manner.

The incorporation of such agents can be achieved through various processes, *e.g.* chemical and physical vapour deposition, electrochemical deposition, or plasma spraying [6,166]. Electrochemical methods are often preferred for their relatively short procedure, applicability for large and complex titanium substrates, and a wide range of elements/molecules, which can be incorporated on the surface [167,168]. Moreover, by altering the input parameters, such as time, applied potential, and electrolyte composition, the methods can produce a surface with desired (tailored) topography. One of the available electrochemical methods is plasma electrolytic oxidation (PEO; also known as micro-arc oxidation - MAO), which generates a porous oxide layer through local plasma discharges [169,170]. Silicon and strontium can be both incorporated into the surface of titanium-based alloys through the PEO process [75,171,172] and a gradual release of ionic products from the formed layer may lead to desired angiogenic and osteogenic effects at the affected site. Such a bioactive system should be firstly tested *in vitro* using the most relevant and accurate assays, as presented in this review. In addition, the cellular response to such biomaterials should be tested not only in monocultures of ECs, but also in cocultures of ECs and MSCs/osteoblastic cells to approximate the biomolecular interactions occurring during the mutually dependent processes, namely the vessel and bone formation. Only with a rigorous set of *in vitro* experiments as described above, followed by relevant *in vivo* studies, will any given biomaterial containing Cu, Mg, Si, Sr, or Zn prove itself as a superior implant in THA.

8.7 CONCLUSIONS

The role of angiogenesis in the fixation of permanent orthopaedic implants in bone tissue has remained underinvestigated. Therefore, we have conducted a review of the angiogenic properties of trace elements (Cu, Mg, Si, Sr, and Zn) incorporated in the biomaterials' surfaces. We have evaluated the assays used to study the response of endothelial cells to these surfaces, made a comparative analysis of the angiogenic properties of the elements investigated, and evidenced the mechanism underlying their angiogenic properties.

The results described in this review showed that the methodological approach for angiogenic assessment comprised of similar *in vitro* 2D assays among the reviewed studies. Differences were identified in the incubation period of cells with the bioactive agent(s). The most frequently used assays included proliferation, migration, and sprouting assays followed by gene expression methods. All five reviewed elements (Cu, Mg, Si, Sr, Zn) displayed *in vitro* pro-angiogenic capacity, but were in some cases strongly concentration-dependent. Silicon and strontium appear to be superior for orthopaedic implants as agents with dual angiogenic and osteogenic properties, considering the currently available processing containment of those materials. They are known for their robust potential to promote osteogenic capacity and the findings in this study suggest promising results for the early development of vascularized bone.

ACKNOWLEDGEMENTS

The research for this paper was financially supported by the Prosperos project, funded by the Interreg VA Flanders – The Netherlands program, CCI grant no. 2014TC16RFCB046.

ABBREVIATIONS

ANG-1/2	Angiopoietin 1/2
BAECs	Bovine aorta endothelial cells
(B)MSCs	(Bone marrow-derived) mesenchymal stem cells
BrdU	Bromodeoxyuridine
CaSR	Calcium sensing receptor
cc	Coculture
CD31	Cluster of differentiation 31
CLSM	Confocal laser scanning microscopy
CM	Conditioned medium
d	Days
DAPI	4',6-diamidino-2-phenylindole
ECs	Endothelial cells
EdU	5-ethynyl-2'-deoxyuridine
ELISA	Enzyme-linked immunosorbent assay
EPCs	Endothelial progenitor cells
FGF	Fibroblast growth factor
h	Hours
HA	Hydroxyapatite
hADSC	Human adipose-derived stem cells
HAECs	Human aortic endothelial cells
HCECs	Human coronary artery endothelial cells
HDMECs	Human dermal microvascular endothelial cells
HIF1-α	Hypoxia inducible factor 1 alpha
HMECs	Human microvascular endothelial cells
HUVECs	Human umbilical vein endothelial cells
IRP	Ion release profile
MAO	Microarc oxidation
MC	Material composition
MMPs	Matrix metallopeptidases/ metalloproteinases
NO	Nitric oxide
OB	Osteoblasts/osteoblastic cells
PDGFs	Platelet-derived growth factor
PECAM1	Platelet endothelial cell adhesion molecule
PEO	Plasma electrolytic oxidation
PI	Propidium iodide
ROS	Reactive oxygen species
RT-qPCR	Reverse transcription-quantitative polymerase chain reaction
SC	Surface composition
(S)CPP	(Strontium) calcium polyphosphate
SD rats	Sprague Dawley rats
SEM	Scanning electron microscopy
TCP	Tricalcium phosphate
TGF-β	Transforming growth factor beta
VEGF	Vascular endothelial growth factor
w	weeks

REFERENCES

[1] Karachalios, T.; Komnos, G.; Koutalos, A. Total Hip Arthroplasty: Survival and Modes of Failure. *EFORT Open Rev.*, **2018**, *3*, 232–239.

[2] Raphel, J.; Holodniy, M.; Goodman, S.B.; Heilshorn, S.C. Multifunctional Coatings to Simultaneously Promote Osseointegration and Prevent Infection of Orthopaedic Implants. *Biomaterials*, **2016**, *84*, 301–314.

[3] Delaunay, C.; Hamadouche, M. What Are the Causes for Failures of Primary Hip Arthroplasties in France ? **2013**, 3863–3869.

[4] Parithimarkalaignan, S.; Padmanabhan, T. V. Osseointegration: An Update. *J. Indian Prosthodont. Soc.*, **2013**, *13*, 2–6.

[5] Yu, X.; Tang, X.; Gohil, S. V; Laurencin, C.T. Biomaterials for Bone Regenerative Engineering. *Adv. Healthc. Mater.*, **2015**, *4*, 1268–1285.

[6] Awad, N.K.; Edwards, S.L.; Morsi, Y.S. A Review of TiO2 NTs on Ti Metal: Electrochemical Synthesis, Functionalization and Potential Use as Bone Implants. *Mater. Sci. Eng. C*, **2017**, *76*, 1401–1412.

[7] Sumner, D.R. Long-Term Implant Fixation and Stress-Shielding in Total Hip Replacement. *J. Biomech.*, **2015**, *48*, 797–800.

[8] Kulkarni, M.; Mazare, A.; Schmuki, P.; Iglič, A. Biomaterial Surface Modification of Titanium and Titanium Alloys for Medical Applications. *Nanomedicine*, 111–136.

[9] Jones, L.C.; Timmie Topoleski, L.D.; Tsao, A.K. *Biomaterials in Orthopaedic Implants*; Elsevier Ltd., **2017**.

[10] Li, B.; Webster, T. *Orthopedic Biomaterials 2009*; **2009**.

[11] Sidhu, S.S. *Biomaterials in Orthopaedics and Bone Regeneration*; **2019**.

[12] Im, G. Il. Biomaterials in Orthopaedics: The Past and Future with Immune Modulation. *Biomater. Res.*, **2020**, *24*, 7–10.

[13] Lin, S.H.; Zhang, W.J.; Jiang, X.Q. Applications of Bioactive Ions in Bone Regeneration. *Chinese J. Dent. Res.*, **2019**, 93–104.

[14] Hoppe, A.; Güldal, N.S.; Boccaccini, A.R. A Review of the Biological Response to Ionic Dissolution Products from Bioactive Glasses and Glass-Ceramics. *Biomaterials*, **2011**, *32*, 2757–2774.

[15] Marsell, R.; Einhorn, T.A. The Biology of Fracture Healing. *Injury*, **2011**, *42*, 551–555.

[16] Zhang, W.; Cao, H.; Zhang, X.; Li, G.; Chang, Q.; Zhao, J.; Qiao, Y.; Ding, X.; Yang, G.; Liu, X.; Jiang, X. A Strontium-Incorporated Nanoporous Titanium Implant Surface for Rapid Osseointegration. *Nanoscale*, **2016**, 5291–5301.

[17] Kolte, D.; Mcclung, J.A.; Aronow, W.S. Chapter 6. Vasculogenesis and Angiogenesis. In: *Translational Research in Coronary Artery Disease*; Elsevier Inc., **2016**; pp. 49–66.

[18] Shrivats, A.R.; Alvarez, P.; Schutte, L.; Hollinger, J.O. Bone Regeneration. In: *Principles of Tissue Engineering*; Elsevier, **2014**; pp. 1201–1221.

[19] Bahney, C.S.; Zondervan, R.L.; et al. Cellular Biology of Fracture Healing. *J. Orthop. Res.*, **2019**, *37*, 35–50.

[20] Kolar, P.; Gaber, T.; Perka, C. Human Early Fracture Hematoma Is Characterized by Inflammation and Hypoxia. *Clin. Orthop. Relat. Res.*, **2011**, *469*, 3118–3126.

[21] Hankenson, K.D.; Dishowitz, M.; Gray, C.; Schenker, M. Angiogenesis in Bone Regeneration. *Injury*, **2012**, *42*, 556–561.

[22] Stegen, S.; Gastel, N. Van; Carmeliet, G. Bringing New Life to Damaged Bone: The Importance of Angiogenesis in Bone Repair and Regeneration. *Bone*, **2015**, *70*, 19–27.

[23] Lakhkar, N.J.; Lee, I.; Kim, H.; Salih, V.; Wall, I.B.; Knowles, J.C. Bone Formation Controlled by Biologically Relevant Inorganic Ions: Role and Controlled Delivery from Phosphate-Based Glasses. *Adv. Drug Deliv. Rev.*, **2013**, *65*, 405–420.

[24] Bellucci, D.; Braccini, S.; Chiellini, F.; Balasubramanian, P.; Boccaccini, A.R.; Cannillo, V. Bioactive Glasses and Glass-Ceramics versus Hydroxyapatite : Comparison of Angiogenic Potential and Biological Responsiveness. **2019**, 2601–2609.

[25] Andrea, L.D.D.; Romanelli, A.; Stasi, D.; Pedone, C.; Andrea, L.D. Bioinorganic Aspects of Angiogenesis. **2010**, 7625–7636.

[26] Walker, J.; Shadanbaz, S.; Woodfield, T.B.F.; Staiger, M.P.; Dias, G.J. Magnesium Biomaterials for Orthopedic Application: A Review from a Biological Perspective. *J. Biomed. Mater. Res. - Part B Appl. Biomater.*, **2014**, *102*, 1316–1331.

[27] Jimenez, M.; Abradelo, C.; Roman, J.S.; Rojo, L. Bibliographic Review on the State of the Art of Strontium and Zinc Based Regenerative Therapies. Recent Developments and Clinical Applications. *J. Mater. Chem. B*, **2019**, *7*, 1974–1985.

[28] Stepan, J.J. Strontium Ranelate : In Search for the Mechanism of Action. *J. Bone Miner. Metab.*, **2013**, *31*, 606–612.

[29] Marie, P.J.; Felsenberg, D.; Brandi, M.L. How Strontium Ranelate , via Opposite Effects on Bone Resorption and Formation, Prevents Osteoporosis. *Osteoporos. Int.*, **2011**, *22*, 1659–1667.

[30] Tan, S.; Zhang, B.; Zhu, X.; Ao, P.; Guo, H.; Yi, W.; Zhou, G. Deregulation of Bone Forming Cells in Bone Diseases and Anabolic Effects of Strontium-Containing Agents and Biomaterials. *Biomed Res. Int.*, **2014**, *2014*, 1–12.

[31] Goh, E.T.; Kirby, G.; Rajadas, J.; Liang, X.J.; Tan, A. Accelerated Wound Healing Using Nanoparticles. In: *Nanoscience in Dermatology*; Elsevier Inc., **2016**; pp. 287–306.

[32] Della Pepa, G.; Brandi, M.L. Microelements for Bone Boost: The Last but Not the Least. *Clin. Cases Miner. Bone Metab.*, **2016**, *13*, 181–185.

[33] Kornblatt, A.P.; Nicoletti, V.G.; Travaglia, A. The Neglected Role of Copper Ions in Wound Healing. *J. Inorg. Biochem.*, **2016**, *161*, 1–8.

[34] Borkow, G.; Gabbay, J.; Dardik, R.; Eidelman, A.I.; Lavie, Y.; Grunfeld, Y.; Ikher, S.; Huszar, M.; Zatcoff, R.C.; Marikovsky, M. Molecular Mechanisms of Enhanced Wound Healing by Copper Oxide-Impregnated Dressings. *Wound Repair Regen.*, **2010**, *18*, 266–275.

[35] Qu, X.; He, Z.; Qiao, H.; Zhai, Z.; Mao, Z.; Yu, Z.; Dai, K. Serum Copper Levels Are Associated with Bone Mineral Density and Total Fracture. *J. Orthop. Transl.*, **2018**, *14*, 34–44.

[36] Wang, H.; Zhao, S.; Zhou, J.; Shen, Y.; Huang, W. Evaluation of Borate Bioactive Glass Scaffolds as a Controlled Delivery System for Copper Ions in Stimulating Osteogenesis and Angiogenesis in Bone Healing. *J. Mater. Chem. B*, **2014**, *2*, 8547–8557.

[37] Sun, J.; Jiao, K.; Niu, L.; Jiao, Y.; Song, Q.; Shen, L.; Tay, F.R.; Chen, J. Intrafibrillar Silicified Collagen Scaffold Modulates Monocyte to Promote Cell Homing, Angiogenesis and Bone Regeneration. *Biomaterials*, **2017**, *113*, 203–216.

[38] Götz, W.; Tobiasch, E.; Witzleben, S.; Schulze, M. Effects of Silicon Compounds on Biomineralization, Osteogenesis, and Hard Tissue Formation. *Pharmaceutics*, **2019**, *11*, 1–27.

[39] Li, J.; Kacena, M.A.; Stocum, D.L. *Fracture Healing*; Second Edi.; Elsevier Inc., **2019**.

[40] Einhorn, T.A.; Gerstenfeld, L.C.; Surgery, O.; Avenue, H.; Surgery, O. Fracture Healing : Mechanisms and Interventions. *Nat. Rev. Rheumatol.*, **2015**, *11*, 45–54.

[41] Loi, F.; Cordova, L.A.; Pajarinen, J.; Lin, T.; Yao, Z.; Goodman, S.B. Inflammation, Fracture and Bone Repair. *Bone*, **2016**, *86*, 119–130.

[42] Bahney, C.S.; Zondervan, R.L.; Allison, P.; Theologis, A.; Ashley, J.W.; Ahn, J.; Miclau, T.; Marcucio, R.S.; Hankenson, K.D. Cellular Biology of Fracture Healing. *J. Orthop. Res.*, **2019**, *37*, 35–50.

[43] Claes, L.; Recknagel, S.; Ignatius, A. Fracture Healing under Healthy and Inflammatory Conditions. *Nat. Rev. Rheumatol.*, **2012**, *8*, 133–143.

[44] Oryan, A.; Monazzah, S.; Bigham-sadegh, A. Bone Injury and Fracture Healing Biology. *Biomed. Environ. Sci.*, **2015**, *28*, 57–71.

[45] Sivaraj, K.K.; Adams, R.H. Blood Vessel Formation and Function in Bone. *Development*, **2016**, 2706–2715.

[46] Maes, C.; Kobayashi, T.; Selig, M.K.; Torrekens, S.; Roth, S.I.; Mackem, S.; Carmeliet, G.; Kronenberg, H.M. Osteoblast Precursors, but Not Mature Osteoblasts, Move into Developing and Fractured Bones along with Invading Blood Vessels. *Dev. Cell*, **2010**, *19*, 329–344.

[47] Maes, C.; Clemens, T.L. Angiogenic–Osteogenic Coupling: The Endothelial Perspective. *Bonekey Rep.*, **2014**, *3*, 1–4.

[48] Ackermann, M.; Houdek, J.P.; Gibney, B.C.; Ysasi, A. Sprouting and Intussusceptive Angiogenesis in Postpneumonectomy Lung Growth : Mechanisms of Alveolar Neovascularization. *Angiogenesis*, **2014**, 541–551.

[49] Djukic, T.; Kim, J.; Zuber, B.; Makanya, A. Synergistic Interaction of Sprouting and Intussusceptive Angiogenesis during Zebrafish Caudal Vein Plexus Development. *Sci. Rep.*, **2018**, *8*, 1–15.

[50] Potente, M.; Gerhardt, H.; Carmeliet, P. Basic and Therapeutic Aspects of Angiogenesis. *Cell*, **2011**, *146*, 873–887.

[51] Milkiewicz, M.; Ispanovic, E.; Doyle, J.L.; Haas, T.L. Regulators of Angiogenesis and Strategies for Their Therapeutic Manipulation. *Int. J. Biochem. Cell Biol.*, **2006**, *38*, 333–357.

[52] Lertkiatmongkol, P.; Liao, D.; Mei, H.; Hu, Y.; Peter, J.; Hospital, U. Endothelial Functions of PECAM-1 (CD31). *Curr. Opin. Hematol.*, **2017**, *23*, 253–259.

[53] Stryker, Z.I.; Rajabi, M.; Davis, P.J. Evaluation of Angiogenesis Assays. *Biomedicines*, **2019**, 1–13.

[54] Goodwin, A.M. In Vitro Assays of Angiogenesis for Assessment of Angiogenic and Anti-Angiogenic Agents. *Microvasc. Res.*, **2007**, *74*, 172–183.

[55] Khan, G.J.; Shakir, L.; Khan, S.; Naeem, H.S. Assessment Methods of Angiogenesis and Present Approaches for Its Quantification. *Cancer Res. J.*, **2014**, *2*, 47–62.

[56] Almalki, W.H.; Shahid, I.; Mehdi, A.Y.; Hafeez, M.H. Assessment Methods for Angiogenesis and Current Approaches for Its Quantification. *Indian J. Pharmacol.*, **2014**, *46*, 251–256.

[57] Brien, T.O.; Sanz-nogue, C. In Vitro Models for Assessing Therapeutic Angiogenesis. *Drug Discov. Today*, **2016**, *21*, 1495–1503.

[58] Carter, M.; Shieh, J. Cell Culture Techniques. In: *Guide to Research Techniques in Neuroscience*; **2015**; pp. 295–310.

[59] Montano, M. Model Systems. In: *Translational Biology in Medicine*; **2014**; pp. 9–33.

[60] Kaur, G.; Dufour, J.M. Cell Lines: Valuable Tools or Useless Artifacts. *Spermatogenesis*, **2012**, *2*, 1–5.

[61] Skardal, A. Bioprinting Essentials of Cell and Protein Viability. In: *Essentials of 3D Biofabrication and Translation*; Elsevier Inc., **2015**; pp. 1–17.

[62] Edgell, C.J.S.; Haizlip, J.E.; Bagnell, C.R.; Packenham, J.P.; Harrison, P.; Wilbourn, B.; Madden, V.J. Endothelium Specific Weibel-Palade Bodies in a Continuous Human Cell Line, EA.Hy926. *Vitr. Cell. Dev. Biol.*, **1990**, *26*, 1167–1172.

[63] Wang, T.C.; Kimura, S.; Rawers, J.C. Permanent Cell Line Expressing Human Factor VIII-Related Antigen Established by Hybridization. *Cell Biol.*, **1983**, *80*, 3734–3737.

[64] Zong, M.; Bai, L.; Liu, Y.; Wang, X.; Zhang, X.; Huang, X.; Hang, R.; Tang, B. Antibacterial Ability and Angiogenic Activity of Cu-Ti-O Nanotube Arrays. *Mater. Sci. Eng. C*, **2017**, *71*, 93–99.

[65] Bai, L.; Wu, R.; Wang, Y.; Wang, X.; Zhang, X.; Huang, X.; Qin, L.; Hang, R.; Zhao, L.; Tang, B. Osteogenic and Angiogenic Activities of Silicon-Incorporated TiO2 Nanotube Arrays. *J. Mater. Chem. B*, **2016**, *4*, 5548–5559.

[66] Thermo Fisher Scientific. Protocol: Matrix Invasion Assay. https://www.thermofisher.com/nl/en/home/references/protocols/cell-and-tissue-analysis/cell-profilteration-assay-protocols/angiogenesis-protocols/matrix-invasion-assay.html (Accessed Mar 19, **2020**).

[67] Xiao, D.; Yang, F.; Zhao, Q.; Chen, S.; Shi, F.; Xiang, X.; Deng, L.; Sun, X.; Weng, J.; Feng, G. Fabrication of a Cu/Zn Co-Incorporated Calcium Phosphate Scaffold-Derived GDF-5 Sustained Release System with Enhanced Angiogenesis and Osteogenesis Properties. *RSC Adv.*, **2018**, *8*, 29526–29534.

[68] Moses, J.C.; Dey, M.; Devi, K.B.; Roy, M.; Nandi, S.K.; Mandal, B.B. Synergistic Effects of Silicon/Zinc Doped Brushite and Silk Scaffolding in Augmenting the Osteogenic and Angiogenic Potential of Composite Biomimetic Bone Grafts. *ACS Biomater. Sci. Eng.*, **2019**, *5*, 1462–1475.

[69] Li, D.; Yuan, Q.; Yu, K.; Xiao, T.; Liu, L.; Dai, Y. Mg-Zn-Mn Alloy Extract Induces the Angiogenesis of Human Umbilical Vein Endothelial Cells via FGF / FGFR Signaling Pathway. *Biochem. Biophys. Res. Commun.*, **2019**, *514*, 618–624.

[70] Zhao, N.; Zhu, D. Endothelial Cellular Responses to Biodegradable Metal Zinc. *Biomater. Sci. Eng.*, **2015**, *1*, 1174–1182.

[71] Merck Millipore. EdU Cell Proliferation Assay. https://www.merckmillipore.com/CZ/cs/product/EdU-Cell-Proliferation-Assay-EdU-647,MM_NF-17-10528?ReferrerURL=https%3A%2F%2Fwww.google.com%2F (Accessed Apr 6, **2020**).

[72] Staton, C.A.; Stribbling, S.M.; Tazzyman, S.; Hughes, R.; Brown, N.J.; Lewis, C.E. Current Methods for Assaying Angiogenesis in Vitro and in Vivo. *Int. J. Exp. Pathol.*, **2004**, *85*, 233–248.

[73] He, X.; Zhang, G.; Zhang, H.; Hang, R.; Huang, X. Cu and Si Co-Doped Microporous TiO2 Coating for Osseointegration by the Coordinated Stimulus Action. *Appl. Surf. Sci.*, **2020**, *503*, 144072–144087.

[74] Weng, L.; Boda, S.K.; Teusink, M.J.; Shuler, F.D.; Li, X.; Xie, J. Binary Doping of Strontium and Copper Enhancing Osteogenesis and Angiogenesis of Bioactive Glass Nanofibers While Suppressing Osteoclast Activity. *Appl. Mater. Interfaces*, **2017**, *9*, 24484–24496.

[75] Santos-Coquillat, A.; Esteban-Lucia, M.; Martinez-Campos, E.; Mohedano, M.; Arrabal, R. PEO Coatings Design for Mg-Ca Alloy for Cardiovascular Stent and Bone Regeneration Applications. *Mater. Sci. Eng. C*, **2019**, *105*, 110026–110044.

[76] Lin, S.; Yang, G.; Jiang, F.; Zhou, M.; Yin, S.; Tang, Y. A Magnesium-Enriched 3D Culture System That Mimics the Bone Development Microenvironment for Vascularized Bone Regeneration. *Adv. Sci.*, **2019**, *6*, 1900209–1900220.

[77] Wang, G.; Zhang, W.; Lv, K. Effects of Sr-HT-Gahnite on Osteogenesis and Angiogenesis by Adipose Derived Stem Cells for Critical-Sized Calvarial Defect Repair. *Sci. Rep.*, **2017**, *7*, 41135–41145.

[78] Li, K.; Xia, C.; Qiao, Y.; Liu, X. Dose-Response Relationships between Copper and Its Biocompatibility/Antibacterial Activities. *J. Trace Elem. Med. Biol.*, **2019**, *55*, 127–135.

[79] Xia, C.; Cai, D.; Tan, J.; Li, K.; Qiao, Y.; Liu, X. Synergistic Effects of N/Cu Dual Ions Implantation on Stimulating Antibacterial Ability and Angiogenic Activity of Titanium. *Biomater. Sci. Eng.*, **2018**, *4*, 3185–3193.

[80] Xu, L.; Willumeit-römer, R.; Luthringer-feyerabend, B.J.C. Effect of Magnesium-Degradation Products and Hypoxia on the Angiogenesis of Human Umbilical Vein Endothelial Cells Q. **2019**, *98*, 269–283.

[81] Nie, F.Q.; Yamada, M.; Kobayashi, J.; Yamato, M.; Kikuchi, A.; Okano, T. On-Chip Cell Migration Assay Using Microfluidic Channels. *Biomaterials*, **2007**, *28*, 4017–4022.

[82] Rath, S.N.; Brandl, A.; Hiller, D.; Hoppe, A. Bioactive Copper-Doped Glass Scaffolds Can Stimulate Endothelial Cells in Co-Culture in Combination with Mesenchymal Stem Cells. *PLoS One*, **2014**, *9*, 1–24.

[83] Liu, C.; Fu, X.; Pan, H.; Wan, P.; Wang, L.; Tan, L.; Wang, K. Biodegradable Mg-Cu Alloys with Enhanced Osteogenesis, Angiogenesis, and Long-Lasting Antibacterial Effects. *Sci. Rep.*, **2016**, *6*, 1–17.

[84] Carpentier, G.; Berndt, S.; Ferratge, S.; Rasband, W.; Cuendet, M.; Uzan, G.; Albanese, P. Angiogenesis Analyzer for ImageJ — A Comparative Morphometric Analysis of "Endothelial Tube Formation Assay" and "Fibrin Bead Assay." *Sci. Rep.*, **2020**, *10*, 1–13.

[85] Zhu, H.; Zhai, D.; Lin, C.; Zhang, Y.; Huan, Z.; Chang, J.; Wu, C. 3D Plotting of Highly Uniform Sr5(PO4)2SiO4 Bioceramic Scaffolds for Bone Tissue Engineering. *J. Mater. Chem. B*, **2016**, 6200–6212.

[86] Gu, Z.; Xie, H.; Huang, C.; Peng, H.; Tan, H. Effects of Strontium-Doped Calcium Polyphosphate on Angiogenic Growth Factors Expression of Co-Culturing System in Vitro and of Host Cell in Vivo. *RSC Adv.*, **2014**, *4*, 2783–2792.

[87] Xu, X.; Lu, Y.; Li, S.; Guo, S.; He, M.; Luo, K.; Lin, J. Copper-Modified Ti6Al4V Alloy Fabricated by Selective Laser Melting with pro-Angiogenic and Anti-Inflammatory Properties for Potential Guided Bone Regeneration Applications. *Mater. Sci. Eng. C*, **2018**, *90*, 198–210.

[88] Chen, Y.; Zheng, Z.; Zhou, R.; Zhang, H.; Chen, C.; Xiong, Z.; Liu, K.; Wang, X. Developing a Strontium-Releasing Graphene Oxide- / Collagen-Based Organic – Inorganic Nanobiocomposite for Large Bone Defect Regeneration via MAPK Signaling Pathway. *ACS Appl. Mater. Interfaces*, **2019**, *11*, 15986–15997.

[89] Jaidev, L.R.; Kumar, S.; Chatterjee, K. Multi-Biofunctional Polymer Graphene Composite for Bone Tissue Regeneration That Elutes Copper Ions to Impart Angiogenic , Osteogenic and Bactericidal Properties. *Colloids Surfaces B Biointerfaces*, **2017**, *159*, 293–302.

[90] Tousoulis, D.; Kampoli, A.; Tentolouris, C.; Papageorgiou, N. The Role of Nitric Oxide on Endothelial Function. *Curr. Vasc. Pharmacol.*, **2012**, *10*, 4–18.

[91] Zhang, J.; Wu, H.; He, F.; Wu, T.; Zhou, L.; Ye, J. Concentration-Dependent Osteogenic and Angiogenic Biological Performances of Calcium Phosphate Cement Modified with Copper Ions. *Mater. Sci. Eng. C*, **2019**, *99*, 1199–1212.

[92] Zhang, M.; Ma, S.; Xu, K.; Chu, P.K. Vascular Endothelial Cell Compatibility of Superhard Ternary Ti-Si-N Coatings with Different Si Contents. *Vaccum*, **2014**, *106*, 53–63.

[93] Enzo Life Sciences. Nitric Oxide (total), detection kit. https://www.enzolifesciences.com/ADI-917-020/nitric-oxide-total-detection-kit/ (Accessed Mar 19, **2020**).

[94] Ge, Q.; Zhang, H.; Hou, J.; Wan, L.; Cheng, W.; Wang, X.; Dong, D.A.N.; Chen, C.; Xia, J.I.E.; Guo, J.U.N.; Chen, X.; Wu, X. VEGF Secreted by Mesenchymal Stem Cells Mediates the Differentiation of Endothelial Progenitor Cells into Endothelial Cells via Paracrine Mechanisms. *Mol. Med. Rep.*, **2018**, *17*, 1667–1675.

[95] Kocherova, I.; Bryja, A.; Mozdziak, P.; Volponi, A.A.; Piotrowska-kempisty, H.; Antosik, P.; Dyszkiewicz-konwi, M. Human Umbilical Vein Endothelial Cells (HUVECs) Co-Culture with Osteogenic Cells: From Molecular Communication to Engineering Prevascularised Bone Grafts. *J. Clin. Med.*, **2019**, *8*, 1602–1622.

[96] Simunovic, F.; Winninger, O.; Strassburg, S.; Koch, H.G.; Finkenzeller, G.; Stark, G.B.; Lampert, F.M. Increased Differentiation and Production of Extracellular Matrix Components of Primary Human Osteoblasts after Cocultivation with Endothelial Cells: A Quantitative Proteomics Approach. *J. Cell. Biochem.*, **2019**, 396–404.

[97] Paul, D.; Herzog, E.; Dohle, E.; Bischoff, I.; Kirkpatrick, C.J. Cell Communication in a Coculture System Consisting of Outgrowth Endothelial Cells and Primary Osteoblasts. *Biomed. Res. Int.*, **2014**, *2014*, 1–15.

[98] Wu, L.; Zhao, X.; He, B.; Jiang, J.; Xie, X.; Liu, L. The Possible Roles of Biological Bone Constructed with Peripheral Blood Derived EPCs and BMSCs in Osteogenesis and Angiogenesis. *Biomed Res. Int.*, **2016**, *2016*, 1–11.

[99] Wilson, T.; Katz, J.M.; Gray, D.H. Inhibition of Active Bone Resorption by Copper. *Calcif. Tissue Int.*, **1981**, *39*, 35–39.

[100] Cacciotti, I. Bivalent Cationic Ions Doped Bioactive Glasses: The Influence of Magnesium, Zinc, Strontium and Copper on the Physical and Biological Properties. *J. Mater. Sci.*, **2017**, *52*, 8812–8831.

[101] Ryan, E.J.; Ryan, A.J.; González-vázquez, A.; Philippart, A.; Ciraldo, F.E.; Hobbs, C.; Nicolosi, V.; Boccaccini, A.R.; Kearney, C.J.; Brien, F.J.O.; Engineering, T.; College, R. Collagen Scaffolds Functionalised with Copper-Eluting Bioactive Glass Reduce Infection and Enhance Osteogenesis and Angiogenesis Both in Vitro and in Vivo. *Biomaterials*, **2019**, *197*, 405–416.

[102] Cattalini, J.P.; Hoppe, A.; Pishbin, F.; Roether, J.; Boccaccini, A.R. Novel Nanocomposite Biomaterials with Controlled Copper/Calcium Release Capability for Bone Tissue Engineering Multifunctional Scaffolds. *Interface*, **2015**, *12*, 1–13.

[103] Elrayah, A.; Zhi, W.; Feng, S.; Al-Ezzi, S.; Lei, H.; Weng, J. Preparation of Micro / Nano-Structure Copper-Substituted Hydroxyapatite Scaffolds with Improved Angiogenesis Capacity for Bone Regeneration. *Materials (Basel).*, **2018**, *11*, 1516–1531.

[104] Wolf-Brandstetter, C.; Beutner, R.; Hess, R.; Bierbaum, S.; Wagner, K.; Scharnweber, D.; Gbureck, U.; Moseke, C. Multifunctional Calcium Phosphate Based Coatings on Titanium Implants with Integrated Trace Elements. *Biomed. Mater.*, **2020**, *15*.

[105] Bordeleau, L.; Barralet, J.; Doillon, C.J.; Ge, C. The Stimulation of Angiogenesis and Collagen Deposition by Copper. *Biomaterials*, **2010**, *31*, 824–831.

[106] Zhang, L.; Xu, M.; Hu, Y.; Gao, F.; Gong, T.; Liu, T.; Li, X.; Pan, C. Biofunctionization of Biodegradable Magnesium Alloy to Improve the in Vitro Corrosion Resistance and Biocompatibility. *Appl. Surf. Sci.*, **2018**, *451*, 20–31.

[107] Yu, Y.; Jin, G.; Xue, Y.; Wang, D.; Liu, X.; Sun, J. Multifunctions of Dual Zn / Mg Ion Co-Implanted Titanium on Osteogenesis , Angiogenesis and Bacteria Inhibition for Dental Implants. *Acta Biomater.*, **2017**, *49*, 590–603.

[108] Gu, Y.; Zhang, J.; Zhang, X.; Liang, G.; Xu, T. Three-Dimensional Printed Mg-Doped b -TCP Bone Tissue Engineering Scaffolds : Effects of Magnesium Ion Concentration on Osteogenesis and Angiogenesis In Vitro. *Tissue Eng. Regen. Med.*, **2019**, *16*, 415–429.

[109] Lin, X.; Ge, J.; Wei, D.; Liu, C.; Tan, L. Surface Degradation-Enabled Osseointegrative, Angiogenic and Antiinfective Properties of Magnesium- Modified Acrylic Bone Cement. *J. Orthop. Transl.*, **2019**, *17*, 121–132.

[110] Ali, M.; Asatourian, A.; Orangi, J.; Sorenson, C.M.; Sheibani, N. Functional Role of Inorganic Trace Elements in Angiogenesis — Part II : Cr , Si , Zn , Cu , and S. *Crit. Rev. Oncol. / Hematol.*, **2015**, *96*, 143–155.

[111] He, X.; Zhang, X.; Li, J.; Hang, R.; Huang, X.; Yao, X.; Qin, L.; Tang, B. Titanium-Based Implant Comprising a Porous Microstructure Assembled with Nanoleaves and Controllable Silicon-Ion Release for Enhanced Osseointegration. *J. Mater. Chem. B*, **2018**, *6*, 5100–5114.

[112] Zhang, M.; Ma, S.; Xu, K.; Bai, L.; Chu, P.K. Bio-Tribological Properties and Cytocompatibility of Ti-Si-N Coatings. *Vaccum*, **2015**, *115*, 50–57.

[113] Bociaga, D.; Sobczyk-guzenda, A.; Komorowski, P.; Balcerzak, J. Surface Characteristics and Biological Evaluation of Si-DLC Coatings Fabricated Using Magnetron Sputtering Method on Ti6Al7Nb Substrate. *Nanomaterials*, **2019**, *9*, 812–826.

[114] Zhang, M.; Gao, A.; Ma, S.; Xu, K.; Chu, P.K. Corrosion Resistance of Ti-Si-N Coatings in Blood and Cytocompatibility with Vascular Endothelial Cells. *Vaccum*, **2016**, *128*, 45–55.

[115] Ding, Z.; Qiao, Y.; Peng, F.; Xia, C.; Qian, S.; Wang, T.; Sun, J.; Liu, X. Si-Doped Porous TiO2 Coatings Enhanced in Vitro Angiogenic Behavior of Human Umbilical Vein Endothelial Cells. *Colloids Surfaces B Biointerfaces*, **2017**, *159*, 493–500.

[116] Zhai, W.; Lu, H.; Wu, C.; Chen, L.; Lin, X.; Naoki, K.; Chen, G.; Chang, J. Stimulatory Effects of the Ionic Products from Ca–Mg–Si Bioceramics on Both Osteogenesis and Angiogenesis in Vitro. *Acta Biomater.*, **2013**, *9*, 8004–8014.

[117] Zhai, W.; Lu, H.; Chen, L.; Lin, X.; Huang, Y.; Dai, K.; Naoki, K.; Chen, G.; Chang, J. Silicate Bioceramics Induce Angiogenesis during Bone Regeneration. *Acta Biomater.*, **2012**, *8*, 341–349.

[118] Anitha, A.; Menon, D.; Sivanarayanan, T.B.; Koyakutty, M.; Mohan, C.C.; Nair, S. V; Nair, M.B. Bioinspired Composite Matrix Containing Hydroxyapatite – Silica Core – Shell Nanorods for Bone Tissue Engineering. *Appl. Mater. Interfaces*, **2017**, *9*, 26707–26718.

[119] Dashnyam, K.; Jin, G.; Kim, J.; Perez, R.; Jang, J.; Kim, H. Promoting Angiogenesis with Mesoporous Microcarriers through a Synergistic Action of Delivered Silicon Ion and VEGF. *Biomaterials*, **2017**, *116*, 145–157.

[120] Kim, J.; El-fiqi, A.; Kim, H. Synergetic Cues of Bioactive Nanoparticles and Nanofibrous Structure in Bone Scaffolds to Stimulate Osteogenesis and Angiogenesis. *Appl. Mater. Interfaces*, **2017**, *9*, 2059–2073.

[121] Rodrigues, T.; Gomes, M.E.; Leite, A.J.; Gonc, A.I.; Mano, F. Strontium-Doped Bioactive Glass Nanoparticles in Osteogenic Commitment. *Appl. Mater. Interfaces*, **2018**, *10*, 23311–23320.

[122] Hamdy, N.A.T. Strontium Ranelate Improves Bone Microarchitecture in Osteoporosis. *Rheumatology*, **2009**, *48*, 9–13.

[123] Saidak, Z.; Marie, P.J. Strontium Signaling : Molecular Mechanisms and Therapeutic Implications in Osteoporosis. *Pharmacol. Ther.*, **2012**, *136*, 216–226.

[124] Guo, X.; Wei, S.; Lu, M.; Shao, Z.; Lu, J.; Xia, L.; Lin, K. Dose-Dependent Effects of Strontium Ranelate on Ovariectomy Rat Bone Marrow Mesenchymal Stem Cells and Human Umbilical Vein Endothelial Cells. *Int. J. Biol. Sci.*, **2016**, *12*, 1511–1522.

[125] Reginster, J. Cardiac Concerns Associated with Strontium Ranelate. *Expert Opin. Drug Saf.*, **2014**, *13*, 1209–1213.

[126] Gu, Z.; Xie, H.; Li, L.; Zhang, X. Application of Strontium-Doped Calcium Polyphosphate Scaffold on Angiogenesis for Bone Tissue Engineering. *J. Mater. Sci. Mater. Med.*, **2013**, *24*, 1251–1260.

[127] Wang, X.; Wang, Y.; Li, L.; Gu, Z.; Xie, H.; Yu, X. Stimulations of Strontium-Doped Calcium Polyphosphate for Bone Tissue Engineering to Protein Secretion and MRNA Expression of the Angiogenic Growth Factors from Endothelial Cells in Vitro. *Ceram. Int.*, **2014**, *40*, 6999–7005.

[128] Zhao, F.; Lei, B.; Li, X.; Mo, Y.; Wang, R. Promoting in Vivo Early Angiogenesis with Sub-Micrometer Strontium- Contained Bioactive Microspheres through Modulating Macrophage Phenotypes. *Biomaterials*, **2018**, *178*, 36–47.

[129] Jebahi, S.; Oudadesse, H.; Feki, H.; Rebai, T.; Keskes, H.; Pellen, P. Antioxidative / Oxidative Effects of Strontium-Doped Bioactive Glass as Bone Graft . In Vivo Assays in Ovariectomised Rats. *J. Appl. Biomed.*, **2012**, *10*, 195–209.

[130] Lin, K.; Xia, L.; Li, H.; Jiang, X.; Pan, H.; Xu, Y.; Lu, W.W.; Zhang, Z.; Chang, J. Enhanced Osteoporotic Bone Regeneration by Strontium-Substituted Calcium Silicate Bioactive Ceramics. *Biomaterials*, **2013**, *34*, 10028–10042.

[131] Chen, Y.; Gao, A.; Bai, L.; Wang, Y.; Wang, X.; Zhang, X.; Huang, X.; Hang, R.; Tang, B.; Chu, P.K. Antibacterial, Osteogenic, and Angiogenic Activities of SrTiO3 Nanotubes Embedded with Ag2O Nanoparticles. *Mater. Sci. Eng. C*, **2017**, *75*, 1049–1058.

[132] Gong, Z.; Cheng, H.; Zhang, M.; Liu, X.; Zeng, Y.; Xiang, K.; Xu, Y.; Wang, Y.; Zhu, Z. Osteogenic Activity and Angiogenesis of a SrTiO3 Nano-Gridding Structure on Titanium Surface. *J. Mater. Chem. B*, **2017**, *5*, 537–552.

[133] Su, Y.; Wang, K.; Gao, J.; Yang, Y.; Qin, Y.; Zheng, Y.; Zhu, D. Enhanced Cytocompatibility and Antibacterial Property of Zinc Phosphate Coating on Biodegradable Zinc Materials. *Acta Biomater.*, **2019**, *98*, 174–185.

[134] Hashemi-najafabadi, A.R.S. The Effect of Modified Electrospun PCL-NHA-NZnO Scaffolds on Osteogenesis and Angiogenesis. *J. Biomed. Mater. Res.*, **2019**, *107A*, 2040–2052.

[135] Augustine, R.; Dan, P.; Sosnik, A.; Kalarikkal, N.; Tran, N. Electrospun Poly (Vinylidene Fluoride-Trifluoroethylene)/Zinc Oxide Nanocomposite Tissue Engineering Scaffolds with Enhanced Cell Adhesion and Blood Vessel Formation. *Nano Res.*, **2017**, *10*, 3358–3376.

[136] Kyung, J.; Hyunseon, J.; Jimin, S.; Ji, S.; Yeong, S.; Kim, R.; Shil, E.; Jong, K.; Park, W.; Gyo, W.; Hojeong, J.; Chan, Y.; Hyun, K.; Seok, K.; Shin, J.H.; Ok, M.R. Conceptual Study for Tissue - Regenerative Biodegradable Magnesium Implant Integrated with Nitric Oxide - Releasing Nanofibers. *Met. Mater. Int.*, **2019**, *25*, 1098–1107.

[137] Monte, F.A.; Awad, K.R.; Ahuja, N.; Kim, H.K.W.; Aswath, P.; Brotto, M.; Varanasi, V.G. Amorphous Silicon Oxynitrophosphide-Coated Implants Boost Angiogenic Activity of Endothelial Cells. *Tissue Eng. Part A*, **2020**, *26*, 15–27.

[138] McLucas, E.; Moran, M.T.; Rochev, Y.; Carroll, W.M.; Smith, T.J. An Investigation into the Effect of Surface Roughness of Stainless Steel on Human Umbilical Vein Endothelial Cells. *Endothelium*, **2006**, *13*, 35–41.

[139] Mohan, C.C.; Sreerekha, P.R.; Divyarani, V. V; Nair, S.; Chennazhi, K. Influence of Titania Nanotopography on Human Vascular Cell Functionality and Its Proliferation in Vitro †. *J. Mater. Chem.*, **2012**, *22*, 1326–1340.

[140] Lai, M.; Yang, X.; Liu, Q.; Li, J.; Hou, Y.; Chen, X. The Surface Nanostructures of Titanium Alloy Regulate the Proliferation of Endothelial Cells. *AIMS Mater. Sci.*, **2014**, *1*, 45–58.

[141] Huang, L.; Cui, L.; Kim, D.H.; Joo, H.J.; Seo, H.; Choi, S.; Noh, J.; Lee, K.B.; Hong, S.J. Regulating Response and Leukocyte Adhesion of Human Endothelial Cell by Gradient Nanohole Substrate. *Sci. Rep.*, **2019**, *9*, 1–11.

[142] Quent, V.M.C.; Loessner, D.; Friis, T.; Reichert, J.C.; Hutmacher, D.W. Discrepancies between Metabolic Activity and DNA Content as Tool to Assess Cell Proliferation in Cancer Research. *J. Cell. Mol. Med.*, **2010**, *14*, 1003–1013.

[143] Chiu, Y.C.; Brey, E.M.; Pérez-Luna, V.H. A Study of the Intrinsic Autofluorescence of Poly (Ethylene Glycol)-Co-(L-Lactic Acid) Diacrylate. *J. Fluoresc.*, **2012**, *22*, 907–913.

[144] Kuo, A.; Lee, M.Y.; Sessa, W.C.; Olsen, J.J.; Pohl, S. öther G.; Deshmukh, A.; Visweswaran, M.; Ward, N.C.; Arfuso, F.; Agostino, M.; Dharmarajan, A. The Role of Wnt Signalling in Angiogenesis. *Clin. Biochem. Rev.*, **2017**, *38*, 131–142.

[145] Reis, M.; Liebner, S. Wnt Signaling in the Vasculature. *Exp. Cell Res.*, **2013**, *319*, 1317–1323.

[146] Cai, X.; Xie, J.; Yao, Y.; Cun, X.; Lin, S.; Tian, T.; Zhu, B.; Lin, Y. Angiogenesis in a 3D Model Containing Adipose Tissue Stem Cells and Endothelial Cells Is Mediated by Canonical Wnt Signaling. *Bone Res.*, **2017**, *5*, 1–13.

[147] Newman, A.C.; Hughes, C.C.W. Macrophages and Angiogenesis: A Role for Wnt Signaling. *Vasc. Cell*, **2012**, *4*, 1–7.

[148] Xie, Q.; Cheng, Z.; Chen, X.; Lobe, C.G.; Liu, J. The Role of Notch Signalling in Ovarian Angiogenesis. *J. Ovarian Res.*, **2017**, *10*, 1–8.

[149] Ramasamy, S.K.; Kusumbe, A.P.; Wang, L.; Adams, R.H. Endothelial Notch Activity Promotes Angiogenesis and Osteogenesis in Bone. *Nature*, **2014**, *507*, 376–380.

[150] Pitulescu, M.E.; Schmidt, I.; Giaimo, B.D.; Antoine, T.; Berkenfeld, F.; Ferrante, F.; Park, H.; Ehling, M.; Biljes, D.; Rocha, S.F.; Langen, U.H.; Stehling, M.; Nagasawa, T.; Ferrara, N.; Borggrefe, T.; Adams, R.H. Dll4 and Notch Signalling Couples Sprouting Angiogenesis and Artery Formation. *Nat. Cell Biol.*, **2017**, *19*, 915–927.

[151] Zucchelli, E.; Majid, Q.A.; Foldes, G. New Artery of Knowledge: 3D Models of Angiogenesis. *Vasc. Biol.*, **2020**, *1*, H135–H143.

[152] Lian, L. shan; Yang, Y. guo; Liu, W.; Guo, L. long; Guan, H.; Liu, C. wei; Li, Y. jun. Zinc Finger Protein-Activating Transcription Factor Up-Regulates Vascular Endothelial Growth Factor-A Expression in Vitro. *Chinese Med. Sci. J.*, **2012**, *27*, 171–175.

[153] Zhu, D.; Su, Y.; Zheng, Y.; Fu, B.; Tang, L.; Qin, Y.X. Zinc Regulates Vascular Endothelial Cell Activity through Zinc-Sensing Receptor ZnR/GPR39. *Am. J. Physiol. - Cell Physiol.*, **2018**, *314*, C404–C414.

[154] Lapidos, K.A.; Woodhouse, E.C.; Kohn, E.C.; Masiero, L. Mg++-Induced Endothelial Cell Migration: Substratum Selectivity and Receptor-Involvement. *Angiogenesis*, **2001**, *4*, 21–28.

[155] Maier, J.A.M.; Bernardini, D.; Rayssiguier, Y.; Mazur, A. High Concentrations of Magnesium Modulate Vascular Endothelial Cell Behaviour in Vitro. *Biochim. Biophys. Acta - Mol. Basis Dis.*, **2004**, *1689*, 6–12.

[156] Li, S.; Wang, M.; Chen, X.; Li, S.; Xie, H. Inhibition of Osteogenic Differentiation of Mesenchymal Stem Cells by Copper Supplementation. *Cell Prolif.*, **2014**, *47*, 81–90.

[157] Dashnyam, K.; El-fiqi, A.; Buitrago, J.O.; Perez, R.A.; Knowles, J.C.; Kim, H. A Mini Review Focused on the Proangiogenic Role of Silicate Ions Released from Silicon-Containing Biomaterials. *J. Tissue Eng.*, **2017**, *8*, 1–13.

[158] Li, H.; Chang, J. Bioactive Silicate Materials Stimulate Angiogenesis in Fibroblast and Endothelial Cell Co-Culture System through Paracrine Effect. *Acta Biomater.*, **2013**, *9*, 6981–6991.

[159] Chen, Y.W.; Shi, G.Q.; Ding, Y.L.; Yu, X.X.; Zhang, X.H.; Zhao, C.S.; Wan, C.X. In Vitro Study on the Influence of Strontium-Doped Calcium Polyphosphate on the Angiogenesis-Related Behaviors of HUVECs. *J. Mater. Sci. Mater. Med.*, **2008**, *19*, 2655–2662.

[160] Yang, X.; Jiang, J.; Zhou, L.; Wang, S.; He, M.; Luo, K.; Chen, Y.; Xu, X. Osteogenic and Angiogenic Characterization of Mandible and Femur Osteoblasts. *J. Mol. Histol.*, **2019**, *50*, 105–117.

[161] Xia, J.; Zhang, H.; Gao, X.; Guo, J.; Hou, J.; Wang, X.; Wang, S.; Yang, T.; Zhang, X.; Ge, Q.; Wan, L.; Cheng, W.; Zheng, J. E-Cadherin-Mediated Contact of Endothelial Progenitor Cells with Mesenchymal Stem Cells through b -Catenin Signaling. **2016**, *40*, 407–418.

[162] Xiao, X.; Wang, W.; Liu, D.; Zhang, H.; Gao, P.; Geng, L.; Yuan, Y.; Lu, J.; Wang, Z. The Promotion of Angiogenesis Induced by Three-Dimensional Porous Beta-Tricalcium Phosphate Scaffold with Different Interconnection Sizes via Activation of PI3K/Akt Pathways. *Sci. Rep.*, **2015**, *5*, 1–11.

[163] Prakasam, M.; Locs, J.; Salma-ancane, K.; Loca, D. Biodegradable Materials and Metallic Implants — A Review. *J. Funct. Biomater.*, **2017**, 1–15.

[164] Mitchell, A.C.; Briquez, P.S.; Hubbell, J.A.; Cochran, J.R. Engineering Growth Factors for Regenerative Medicine Applications. *Acta Biomater.*, **2016**, *30*, 1–12.

[165] Wang, Z.; Wang, Z.; Lu, W.W.; Zhen, W.; Yang, D.; Peng, S. Novel Biomaterial Strategies for Controlled Growth Factor Delivery for Biomedical Applications. *NPG Asia Mater.*, **2017**, *9*, e435-17.

[166] Singh, T.R.R.; Mcmillan, H.; Mooney, K.; Alkilani, A.Z.; Donnelly, R.F. Microneedles for Drug Delivery and Monitoring. In: *Microfluidic devices for biomedical applications*; Woodhead Publishing Limited, **2013**; pp. 185–230.

[167] Guan, Y. Nanotubular Surface Modification of Metallic Implants via Electrochemical Anodization Technique. *Int. J. Nanomedicine*, **2014**, *9*, 4421–4435.

[168] Kulkarni, M. Titanium Nanostructures for Biomedical Applications. *Nanotechnology*, **2015**, *26*, 1–18.

[169] Echeverry-Rendón, M.; Galvis, O.; Giraldo, D.Q.; López-lacomba, J.L. Osseointegration Improvement by Plasma Electrolytic Oxidation of Modified Titanium Alloys Surfaces. *J. Mater. Sci. Mater. Med.*, **2015**, *26*, 1–18.

[170] Hartjen, P.; Hoffmann, A.; Henningsen, A.; Barbeck, M.; Kopp, A.; Kluwe, L.A.N.; Precht, C.; Quatela, O.; Gaudin, R.; Heiland, M.A.X.; Friedrich, R.E.; Knipfer, C.; Grubeanu, D.; Smeets, R.; Jung, O.L.E. Plasma Electrolytic Oxidation of Titanium Implant Surfaces : Microgroove-Structures Improve. *Int. J. Exp. Clin. Pathophysiol. Drug Res.*, **2018**, *247*, 241–247.

[171] Teng, H.P.; Lin, H.Y.; Huang, Y.H.; Lu, F.H. Formation of Strontium-Substituted Hydroxyapatite Coatings on Bulk Ti and TiN-Coated Substrates by Plasma Electrolytic Oxidation. *Surf. Coatings Technol.*, **2018**, *350*, 1112–1119.

[172] van Hengel, I.A.J.; Gelderman, F.S.A.; Athanasiadis, S.; Minneboo, M.; Weinans, H.; Fluit, A.C.; van der Eerden, B.C.J.; Fratila-Apachitei, L.E.; Apachitei, I.; Zadpoor, A.A. Functionality-Packed Additively Manufactured Porous Titanium Implants. *Mater. Today Bio*, **2020**, *7*, 100060–100071.

SUPPLEMENTARY FIGURES

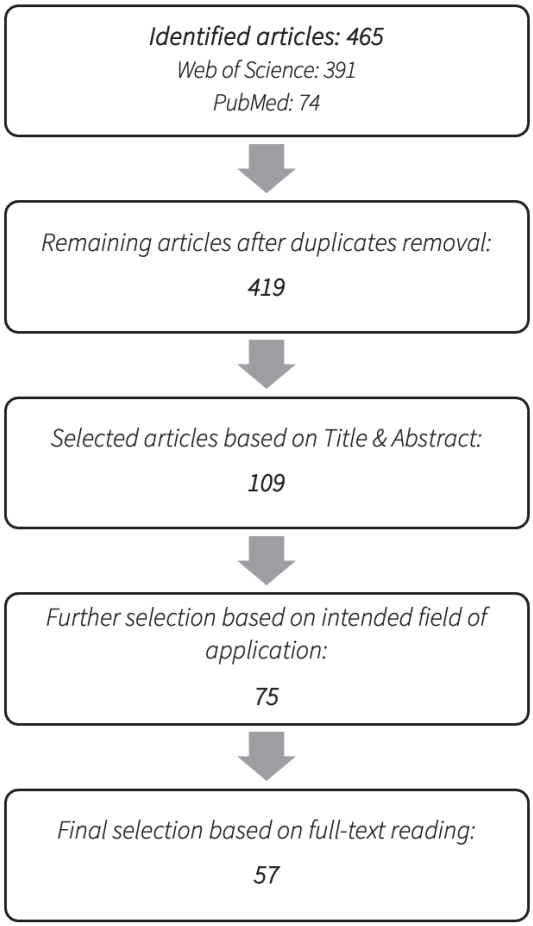

***Figure S1**. Flowchart presenting the literature screening process.*

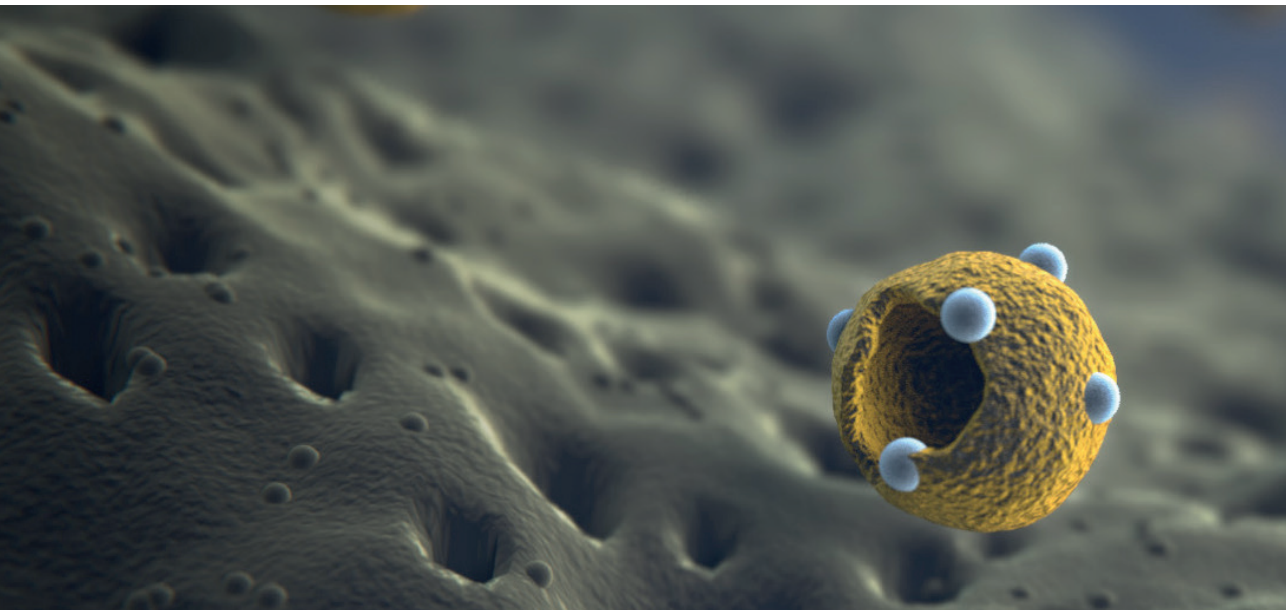

CHAPTER 09

Preclinical testing of multifunctional implants

I.A.J. van Hengel, B. van Dijk, K. Modaresifar, J.F.F. Hooning van Duyvenbode, F. Ruben H.A. Nurmohamed, M.A. Leeflang, A.C. Fluit, L.E. Fratila-Apachitei, I. Apachitei, H. Weinans, A.A. Zadpoor, In vivo prevention of implant-associated infections caused by antibiotic resistant bacteria through biofunctionalization of additively manufactured porous titanium, submitted.

The high human and financial burdens of implant-associated infections (IAI) as well as the ever-growing problem of antibiotic-resistant bacteria have underscored the importance of IAI prevention. Additively manufactured (AM) porous titanium implants that are increasingly used in clinical practice are of particular interest in this regard, because they may cause an increased risk of infection due to their huge, internal surfaces. However, the same huge surface, when biofunctionalized, can be used to prevent IAI. Here, we used a rat implant infection model to evaluate both the biocompatibility and infection-prevention performance of AM porous titanium against bioluminescent methicillin-resistant Staphylococcus aureus (MRSA). The specimens were biofunctionalized with Ag nanoparticles (NPs) through plasma electrolytic oxidation (PEO). Infection was initiated using either intramedullary injection *in vivo* or through *in vitro* inoculation of the implant prior to implantation. The course of infection was followed at days 1, 3, 5, and 7 using bioluminescent imaging. Non-treated (NT) implants were compared with PEO-treated implants with Ag NPs (PT-Ag), without Ag NPs (PT) and infection without an implant. After 7 days, the bacterial load and bone morphological changes were evaluated. When the infection was initiated through *in vivo* injection, the presence of the implant did not enhance infection, indicating that this technique may not assess the prevention but rather the treatment of IAI. Following *in vitro* inoculation, the bacterial load after 7 days on the PT-Ag implants was significantly reduced as compared to the PT implants. Moreover, we found that the bacterial load of the peri-implant bony tissue was decreased with 90% as compared to both NT and PT implants. All infected groups had enhanced osteomyelitis scores as compared to non-infected controls. These findings demonstrate the potential of PEO-biofunctionalized AM porous titanium for further development, testing, and eventually use in clinical settings.

9.1 INTRODUCTION

Implant-associated infections (IAI) are a devastating complication for patients who experienced total joint replacement, trauma and bone tumor resection surgeries [1-3]. These infections also form a tremendous societal and financial burden for our societies in general and our healthcare systems in particular. As the number of implantations continues to increase [4], the urgency of addressing IAI further increases. Moreover, an increasing incidence of antibiotic resistant bacteria [5] has only intensified this urgency. Given that the treatment of IAI, particularly those caused by multi-drug resistant bacteria, is associated with extremely high human and monetary costs, the focus has shifted towards the prevention of IAI through the development of self-defending implants [6, 7].

While infection prevention is important for all types of orthopedic implants, it is even more so for additively manufactured (AM) porous implants that are increasingly used in clinical settings due to their favorable mechanical properties [8, 9] and high potential for bony ingrowth [10]. That is because of two main reasons. First, the huge, internal surfaces of such implants may increase the risk of IAI. Second, the treatment of infections associated with such types of implants is extremely difficult as the substantial amount of bony ingrowth complicates the implant removal procedure in the event of high-grade infections. On the other hand, the vast internal surface area of such implants, when biofunctionalized, can be used to prevent IAI.

The surface biofunctionalization of orthopedic implants has received much attention including antibiotic-releasing coatings that have been studied for some time and are shown to reduce infections *in vivo* [11, 12]. Such coatings are, however, ineffective against antibiotic resistant bacteria. In fact, a widespread use of such coatings may even trigger the emergence of new antibiotic resistant strains. Alternative approaches are, therefore, needed to combat IAI [13].

Inorganic nanoparticles (NPs), such as Ag, are among the most effective antibacterial agents against antibiotic resistant bacteria, because they exhibit strong antibacterial activity against a wide microbial spectrum with very limited risk of resistance [14]. Clinically, Ag-coated mega-prostheses have been demonstrated to reduce infection rates in oncology patients receiving an implant following tumor resection [15-17]. However, some concerns have been raised about the cytotoxicity caused by Ag-coated surfaces [18].

Here, we study the *in vivo* biocompatibility and infection prevention performance of biofunctionalized AM porous titanium against methicillin-resistant *Staphylococcus aureus* (MRSA). The surface biofunctionalization of such implants is challenging due to the difficulties associated with the homogeneous treatment of their entire surface area and the creation of

a durable protective layer. Electrochemical surface modifications have been particularly successful in producing antibacterial surfaces on porous biomaterials [19]. Among those, plasma electrolytic oxidation (PEO) is a single-step process that transforms the native titanium oxide layer into a bioactive surface in a matter of minutes. PEO biofunctionalization with Ag has resulted in implant surfaces with strong antibacterial activity *in vitro* [20-23]. Furthermore, PEO biofunctionalization has resulted in osteogenic implants *in vivo* [24-26]. More recently, we have applied PEO and Ag NPs to produce multifunctional surfaces on AM porous implants [27]. These implants demonstrated antibacterial activity *in vitro* and *ex vivo* against MRSA without inducing any cytotoxicity. However, the antibacterial properties of implants biofunctionalized by PEO with Ag have never been tested *in vivo*.

In this *in vivo* study, we investigated the infection-prevention capacity of AM implants biofunctionalized by PEO with Ag NPs, by implanting the implants in the intramedullary canal of rat tibiae. We explored the use of bioluminescent bacteria to follow the course of infection in this model. These bacteria are genetically modified to emit light while living. The development of infection in the same animal can, thus, be monitored in real-time and non-invasively, thereby increasing the number of time points at which the infection metrics can be measured [28-30]. We then analyzed the development of the infections and bone morphology, associated with each implant type.

9.2 MATERIALS AND METHODS

9.2.1 Study design

Volume-porous Ti-6Al-4V implants were manufactured with selective laser melting (SLM) and were subsequently biofunctionalized with PEO using Ag NPs as the active antibacterial agent, resulting in three different types of implants: non-treated implants without any surface modification (NT), PEO-treated implants without Ag NPs (PT), and PEO-treated implants with Ag NPs (PT-Ag). Thereafter, infections were initiated and the implants were implanted into the intramedullary cavity of rat tibia. The infections were initiated in two different ways: either through *in vivo* injection of the MRSA bacteria into the intramedullary cavity and the subsequent implantation of the implant or by *in vitro* inoculation of the implant with MRSA prior to implantation into the intramedullary cavity. Altogether, seven different experimental groups can be identified (**Table 1**): In the first three groups, the *in vivo* injection of bacteria into the intramedullary cavity was immediately followed by the implantation of the NT implants (inject-NT, $n = 9$), PT-Ag implants (inject-PT-Ag, $n = 5$), or no implants (inject-no-implant, $n = 3$). In the 4 remaining groups, the *in vitro* inoculation of the implant prior to the implantation was performed with MRSA bacteria for the first 3 groups, including NT

implants (ino-NT, n = 6), PT implants (ino-PT, n = 6), and PT-Ag implants (ino-PT-Ag, n = 6), and without bacteria for the last group, *i.e.* NT implants (ino-NT-no-infection, n = 2).

Table 1. The experimental groups used in this study.

Bacterial inoculation method	Bacterial infection	Implant	PEO treatment (PT)	Ag NPs	Label
In vivo injection of bacteria into intramedullary cavity	Yes	Yes	-	-	inject-NT (no treatment)
	Yes	Yes	Yes	Yes	inject-PT-Ag
	Yes	-	-	-	inject-no-implant
In vitro inoculation of implant prior to implantation	Yes	Yes	-	-	ino-NT
	Yes	Yes	Yes	-	ino-PT
	Yes	Yes	Yes	Yes	ino-PT-Ag
	No (PBS)	Yes	-	-	ino-NT-no-inf

9.2.2 Implant design and additive manufacturing

The rationale behind the implant design has been presented elsewhere [27]. The geometry of the implant was adapted to make it befit the intramedullary tibial rat model. The final design of the implant was 1.1 mm in diameter and 15 mm in length (total). It had a solid proximal part of 3 mm to prevent the leakage of fluids from the intramedullary cavity into the knee joint. The implants were additively manufactured in-house using a selective laser melting (SLM) machine (SLM-125, Realizer, Borchem, Germany) with a LM-400-AC Ytterbium laser (IPG Photonics Corporation, Oxford, United States). The laser power was 96 W with a wavelength of 1070 ± 10 nm and an exposure time of 300 µs. The implants were fabricated under argon flow, resulting in an oxygen content < 0.2%. Medical-grade (grade 23, ELI) Ti-6Al-4V powder (AP&C, Boisbriand, Quebec, Canada) with spherical particle morphology and particle sizes ranging from 10 to 45 µm was used as the feedstock. Following SLM, loose powder particles were cleared by vacuum cleaning. The specimens were subsequently ultrasonicated in acetone, 96% ethanol, and demineralized water for 5 min each.

9.2.3 Surface biofunctionalization

The implant surface was biofunctionalized by PEO using electrolytes consisting of 0.15 M calcium acetate and 0.02 M calcium glycerophosphate (both from Sigma-Aldrich, St. Louis, Missouri, United States) dissolved in demineralized water. In the case of the PT-Ag implants, 3.0 g/L Ag NPs (Sigma-Aldrich) with a spherical morphology and particles sizes between 7 – 25 nm were dispersed into the PEO electrolyte. The PEO electrolytes were sonicated twice for 3 min and were stirred in between at 500 rpm for 5 min with a magnetic stirrer (IKA-

Werk GmbH & Co. KG, Staufen, Germany) using a stir bar of 40×8 mm (VWR, Radnor, Pennsylvania, United States).

The PEO biofunctionalization process was performed using a custom-made setup consisting of an AC power source (50Hz, ACS 1500, ET powder Systems Ltd., Chesterfield, United Kingdom), a data acquisition board (SCXI, National Instruments, Austin, Texas, United States) that connected the computer interface to the power supply, and two electrodes placed in a double-walled glass electrolytic cell that contained 800 ml of the electrolyte. The implants served as the anode while a cylindrical shaped stainless-steel ring placed against the inner wall of the electrolytic cell formed the cathode. PEO processing was performed with a constant current density of 20 A/dm^2 for 5 min. Homogeneous particle distribution was ensured through continuous stirring of the electrolyte at 500 rpm. During biofunctionalization, the voltage-time (V-t) transients were recorded every second and the temperature was kept constant at 5 ± 2 °C using a thermostatic bath (Thermo Haake, Karlsruhe, Germany). The PEO treatment was followed by 1 min of rinsing the implants in running tap water and autoclaving for sterilization.

9.2.4 Characterization of the surface morphology and chemical composition

The surface morphology of the implants prior to and after the PEO treatment was characterized using a scanning electron microscope (SEM, JSM-IT100LV, JEOL, Tokyo, Japan). Before imaging, a gold layer of 5 ± 2 nm was sputtered onto the specimens. The chemical composition of the implants was determined using energy dispersive X-ray spectroscopy (EDS).

9.2.5 Ion release kinetics

To investigate the release kinetics of Ag ions from the PT-Ag implants, 3 specimens from each group were immersed in 1 ml phosphate buffered saline (PBS) in a dark Eppendorf tube and were kept at 37 °C in a water bath under static conditions. Subsequently, the specimens were extracted after 0.5, 1, 2, 4, and 7 days of immersion. The concentration of the elements was then measured through inductively coupled plasma optical emission spectroscopy (ICP-OES) (PerkinElmer Optima 3000DV, PerkinElmer, Zaventem, Belgium).

9.2.6 X-ray diffraction

The phase composition of the implants was analyzed by X-ray diffraction (XRD) using a D8 advanced diffractometer (Bruker, Billerica, Massachusetts, United States). The settings were as

follows: voltage = 45 kV, current = 40 mA, scatter screen height = 5 mm, divergence slit = V6, and CuKα radiation detector = LL 0.11 W 0.14. The specimens were analyzed with a coupled θ - 2θ scan ranging between 20 and 120°, a counting rate of 5 s/step, and a step size of 0.030° 2θ. Thereafter, the acquired data was analyzed using DiffracSuite.Eva (version 5.0, Bruker).

9.2.7 Preparation of bacterial culture and implant inoculation

The antibacterial properties of the implants were tested *in vivo* in a rat tibial infection model against the MRSA strain AH4802 [31]. Preparation of the bacterial inoculum was initiated one day prior to surgery by suspending a single colony into 3 ml of tryptic soy broth (TSB) and incubating it overnight at 37 °C. Thereafter, the bacteria were washed and centrifuged twice in PBS at 14,000 rpm for 2 min and the optical density was measured at a wavelength of 600 nm. For intramedullary injection, the inoculum was diluted to a concentration of 10^6 CFU / 10 µl. For the inoculation of the implant, an inoculum of 108 / ml was prepared in Eppendorf tubes and the implants were incubated statically in the horizontal position for 1 min. To determine the number of CFUs present on the implants after the inoculation process and prior to implantation, the implants (n = 3/group) were sonicated in PBS and the inoculum was quantified by plating 10-fold serial dilutions in quadruplicates onto blood agar plates followed by overnight incubation at 37 °C and CFU quantification.

9.2.8 Animal experiment

The animal experiment was approved by the local ethics committee for animal experiments (Utrecht University, The Netherlands) and the central authority for scientific procedures on animals (approved protocol AVD115002017446). This study was conducted according to the ARRIVE guidelines for reporting animal research [32]. For the experiment, 14-week-old male Sprague Dawley rats (Charles River, L'Arbresle, France) were housed in groups of three in individually ventilated cages at the central laboratory of the animal institute (Utrecht University). Food and water were available ad libitum. Animals were housed in the animal facility one week prior to the experiment to acclimatize and were randomly allocated to an experimental group using the RAND function in Microsoft Excel.

Prior to surgery, the animals were given 0.03 mg/kg of buprenorphine (Temgesic®, RB Pharmaceuticals Limited, Slough, United Kingdom) and 4 mg/kg of carprofen (Rymadil®, Pfizer Animal Health, Capelle aan den IJssel, The Netherlands) subcutaneously as well as Carprofen post-operatively after 24 h. The surgery was performed under general anesthesia with 2 – 3% isoflurane. The left hind leg was shaved and soaked in iodine to disinfect the skin. Subsequently, a para-patellar incision was made to open the skin and fascia. The patella

tendon was dissected laterally and was dislocated medially. Next, a hole was drilled through the cortical bone into the intramedullary canal of the tibia. Infection was induced either through the *in vivo* injection of 10 µl bacterial inoculum into the medullary cavity using a micro syringe (Hamilton, Reno, Nevada, United States) or through 1 min incubation *in vitro* of the specimens in 1 ml of the prepared bacterial inoculum (static, horizontal position). Thereafter, the implant was inserted into the intramedullary canal. If no implant was inserted, the hole was sealed with bone wax. Subsequently, wound closure was performed using PDS II and Monocryl sutures (both from Ethicon, Somerville, New Jersey, United States). The rats were euthanized after 7 days with CO2.

The surgery was performed by two surgeons in a laminar flow cabinet, assisted by one assistant to guarantee sterile conditions throughout the surgery. In total, 43 animals were used. Based on a previous study using this model [33], we anticipated a bacterial load of 2×10^6 CFU on the NT implants after 1 week with a standard deviation of 60%. A reduction of 90% in the bacterial load was considered clinically significant. Assuming an 80% power, the required sample size was 6 per group. Considering the risk of dropouts, we decided to use 7 animals per group. The inject-NT group included 10 animals to obtain an accurate estimate of the infection rate. Furthermore, the inject-no-implant group had 3 animals, as this was merely a control group for the presence of an implant. In addition, the ino-NT-no-inf group has 2 animals as it had to simply confirm that we had conducted the surgery under sterile conditions. Due to the misalignment of the implant with the intramedullary canal, 6 specimens were excluded from the analysis, including 1 inject-NT, 2 inject-PT-Ag, 1 ino-NT, 1 ino-PT, and 1 ino-PT-Ag specimens.

9.2.9 Bioluminescence measurement

At the day of surgery and 1, 3, 5 and 7 days after surgery, the bioluminescent signal of the bacteria was measured for 5 min using the optical imaging system of MIlabs (Utrecht, the Netherlands) while the animals were under general anesthesia with 2% isoflurane. The bioluminescent images were processed using the optical imaging unit of the MIlabs software (version 2.3.5). A square-shaped region of interest (ROI) with a size of 260×260 pixels was used to measure the integrated density of the determinant leg. Subsequently, an ROI of the same size was used to measure the integrated density of the background. Ultimately, the integrated density of the luminescent area was determined by subtracting the background signal from the ROI of the concerned leg.

9.2.10 Micro-CT

Tibiae were harvested and cleansed from their surrounding tissue under sterile conditions. Subsequently, micro-CT scanning was performed with a Quantum FX scanner (PerkinElmer, Waltham, Massachusetts, United States) using a tube current of 180 mA, a tube voltage of 90 kV, and a 20 mm field of view. The images were stacked with a resolution of 20 μm and were analyzed using the BoneJ plugin (version 1.3.12) of ImageJ (version 1.48).

The implant was excluded from the analysis based on a global threshold. To cover the same bone area in all the specimens, the proximal fusion point between the tibia and fibula served as an anatomical reference. The total bone volume (BV) was determined for 600 slices distally (1.2 cm) from the point of reference. The bone was segmented by applying an adaptive threshold based on the mean local grayscale distribution. The peri-implant BV was defined as the volume of the bone tissue present in the region of interest (ROI) within the inner cortical perimeter, while the cortical BV represented the BV present outside the ROI. Both peri-implant and cortical BVs were determined for 10 slides at 3 mm (proximal) and 9 mm (distal) from the point of reference. The porosity of the cortical bone tissue was also determined. In addition, the outer perimeter of the harvested tibiae was measured as a sign of cortical expansion.

9.2.11 Osteomyelitis score

Bone changes indicating osteomyelitis were scored twice by 2 blinded observers using the raw micro-CT scans with the following criteria: 0 (no abnormalities), 1 (mild osteolysis and/or periosteal response), 2 (significant osteolysis and/or cortical thickening), 3 (focal loss of cortex with extensive osteolysis), and 4 (complete loss of cortical morphology).

9.2.12 CFU count

To quantify the CFU count, a 1 cm long bone sample was obtained from the proximal part of the tibia with a sterilized saw (Dremel rotary saw, Breda, The Netherlands). Subsequently, the implant and the bony tissue were separated. The bony tissue was weighed and homogenized (Polytron PT3100, Kinetic Benelux, Best, The Netherlands). The implants were rinsed three times in PBS and were subsequently sonicated for 1 min. Thereafter, the implants were weighed, serial dilutions were prepared on blood agar plates, and the number of CFU was counted after overnight incubation. The CFU count was normalized to the weight of the bones and the full length of the implants to determine the normalized CFU counts of the bone tissue and the implants, respectively. The assessment of the contralateral (*i.e.*, right) tibiae did not demonstrate any bacterial infection in any of the animals.

9.2.13 Biofilm formation

The ability of the implants to prevent biofilm formation (n = 2/group) was analyzed on the distal part of the implant. Using a sterilized saw (Dremel rotary saw, Breda, The Netherlands), a 0.5 mm thick bone slice was cut. The implant and the bony tissue were subsequently separated. The bony tissue was used for histology. The implant was rinsed twice in PBS and was subsequently fixated in 4% paraformaldehyde. Thereafter, the implants were rinsed with demineralized water for 5 min and were dehydrated in 50% ethanol for 15 min, in 70% ethanol for 20 min, in 96% ethanol for 20 min and in hexamethyldesilizane for 15 min. Finally, the implants were air-dried for 2 h and were inspected using SEM.

9.2.14 Statistical analysis

All data are expressed as mean ± standard deviation. Statistical analyses were performed with GraphPad Prism (GraphPad Software, version 9.3.0, La Jolla, California, United States) using one and two-way ANOVA followed by Bonferroni post-hoc test. The differences between the groups were considered statistically significant when $p < 0.05$.

9.3 RESULTS

9.3.1 Implant synthesis and surface biofunctionalization

The 3D implant design with repetitive unit cell structure is presented in **Figure 1A**. The implants synthesized by SLM displayed a highly porous structure with partially molten particles attached to the implant surface (**Figure 1B**). The V-t transients of the PEO process showed similar characteristics for PT and PT-Ag implants (**Figure 1C**). At the initial stage, the voltage rose sharply to 93 ± 3 V after 10 s until dielectric breakdown occurred followed by a gradual increase of the voltage until a final voltage of 220 ± 5 V and 229 ± 4 V was reached for the PT-Ag and PT implants, respectively. The PEO processing markedly altered the macroscopic appearance of the implants (**Figure 1D**).

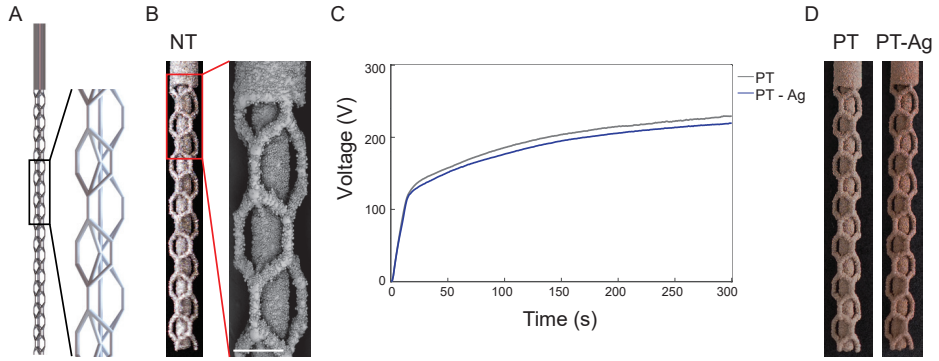

Figure 1. The design, surface morphology, and V-t transients of AM porous titanium implants. (A) The design and (B) macroscopic as well as microscopic images of the AM porous implants designed using a repetitive unit cell with a diameter of 0.5 mm, and a solid and porous part of 3 and 12 mm length respectively. (C) The V-t transients recorded during the surface biofunctionalization of the PT and PT-Ag implants using PEO. (D) The macroscopic images of the PT and PT-Ag implants after the PEO biofunctionalization process. Scale bar = 500 µm.

9.3.2 Biomaterial characterization

SEM imaging demonstrated a highly porous surface with interconnected pores, which homogeneously spanned the entire surface of the PEO-biofunctionalized implants (**Figure 2A**). EDS analysis confirmed the presence of Ag NPs (**Figure 2B**). Ti, Al, and V were detected as the alloying elements of the implants. Ca, P, O, and C, which were present in the PEO electrolyte, were also detected. Ag ions were continuously released from the PT-Ag implants, resulting in a cumulative ion release of 1.83 ± 0.06 ppm/cm^2 after 7 days (**Figure 2C**). XRD analysis demonstrated that the phase composition of the NT implants consisted entirely of Ti phase, while this phase was transformed into primarily rutile as well as anatase TiO_2 phases on the PT implants (**Figure 2D**). Furthermore, $CaTiO_3$, $Ca_5(VO_4)_3OH$, $CCaO_3$ and hydroxyapatite were detected on the surface of the PT implants. The phase composition of the PT-Ag implants was identical to that of the PT implants and is, therefore, not presented.

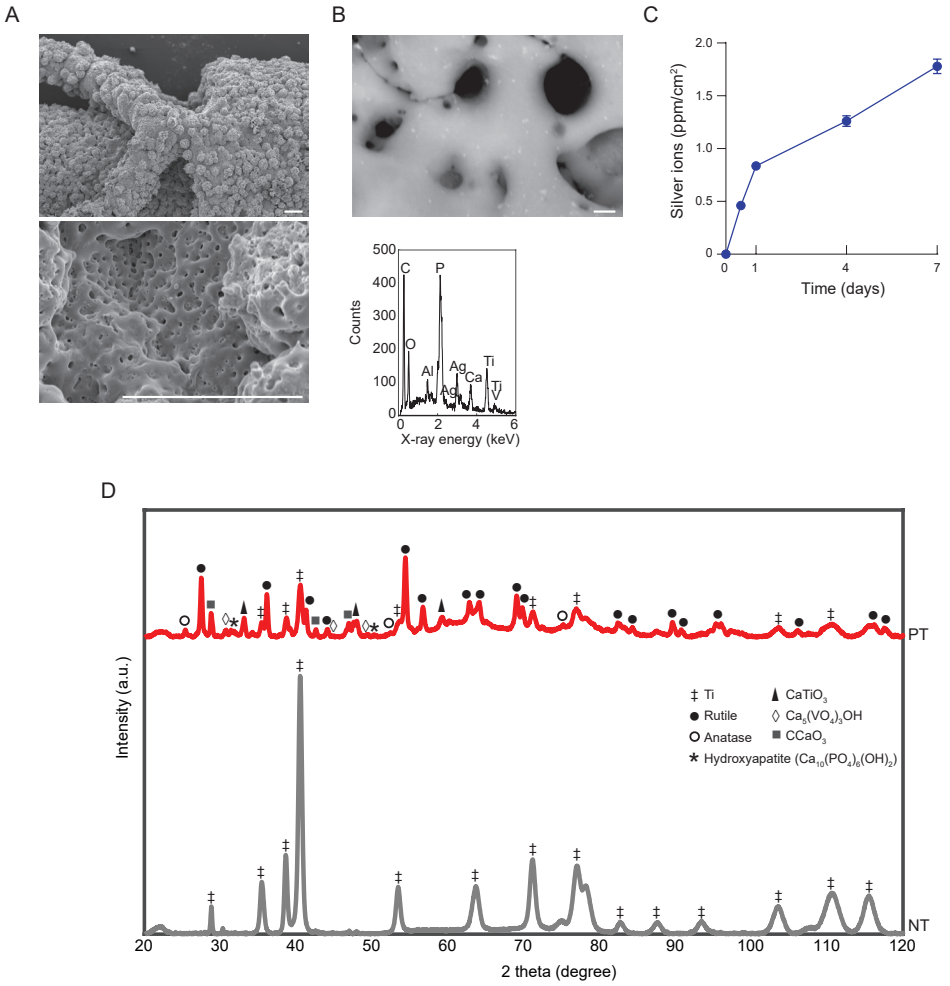

Figure 2. The surface characterization of the PEO-biofunctionalized implants. (A) The SEM imaging of the surface of the PT implants. Scale bar = 100 µm. (B) The EDS analysis of the PT-Ag implant surfaces with EDS. Scale bar = 1 µm. (C) The Ag ion release kinetics of the PT-Ag implants (n = 3) over 7 days as measured by ICP-OES. (D) The X-ray diffraction spectra of the NT and PT implants.

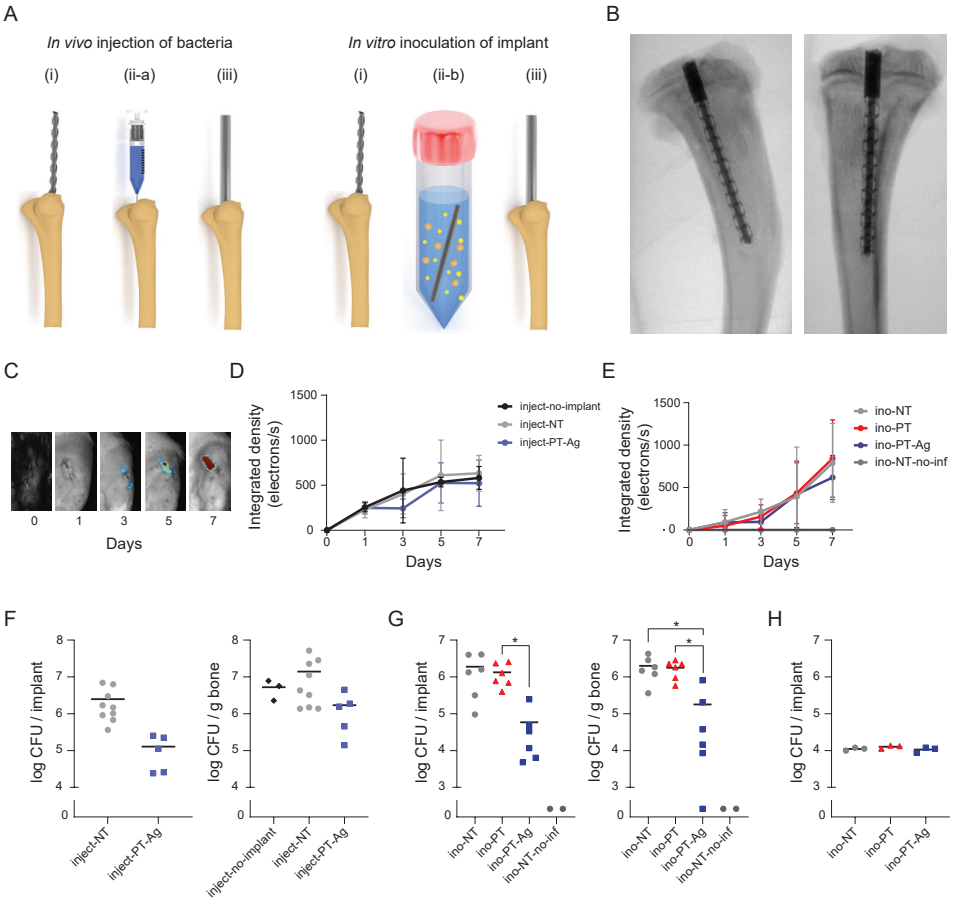

Figure 3. Antibacterial activity of the implants against MRSA. (A) Both ways of initiating the infection: *in vivo* intramedullary injection of bacteria into the intramedullary cavity (left) and *in vitro* inoculation of the implant prior to implantation (right). The surgical procedure consisted of (i) drilling a hole through the tibial plateau followed by either (ii-a) *in vivo* injection of bacteria or (ii-b) *in vitro* inoculation of the implant, and (iii) the implantation of the implant into the intramedullary canal. (B) The Micro-CT images of the implant in the tibia from medial (left) and posterior (right) positions. (C) The bioluminescence images and spectra of the bioluminescent MRSA AH4802 *in vivo* over 7 days in the intramedullary cavity for the infections initiated through (D) *in vivo* intramedullary injection or (E) through *in vitro* inoculation prior to implantation. The quantification of the bacterial load after 7 days (F) after the *in vivo* injection of the bacteria and (G) after *in vitro* inoculation on the implant prior to the implantation. (H) CFU count following the *in vitro* inoculation of the implants and before their implantation into the tibia. $n = 10$ for inject-NT, $n = 7$ for all other implants, $n = 3$ for inject-no-implant and $n = 2$ for ino-NT-no-inf. * $p < 0.05$.

9.3.3 Antibacterial properties

Infection was initiated either through the *in vivo* injection of bacteria into the intramedullary canal (inject-implants) or the *in vitro* inoculation of the implant prior to implantation (ino-implants; **Figure 3A**). After 7 days, the implants in the tibia were visualized using micro-CT (**Figure 3B**). Bioluminescence imaging (**Figure 3C**) demonstrated the bioluminescent signal for all the groups at all time points, except for the ino-NT-no-infection group and day 0 of all the inject-implants (**Figure 3D**) and ino-implants (**Figure 3E**). No significant differences were observed between the groups at any time point. The quantification of the number of CFU after 7 days on the implants and in the peri-implant bone indicated that there were no differences between the groups in which the bacteria were injected into the intramedullary canal *in vivo* (**Figure 3F**), although the bacterial load on inject-PT-Ag implants was nearly significantly lower compared to inject-NT implants ($p = 0.0576$). For the groups in which the infection was induced through the *in vitro* inoculation of the implants, the number of the CFU associated with ino-PT-Ag implants was significantly lower than that of the ino-NT implants ($p < 0.05$). Furthermore, the CFU count of the bony tissue surrounding the ino-PT-Ag implants was significantly lower as compared to the ino-NT and ino-PT implants ($p < 0.05$; **Figure 3G**). The number of CFU on the ino-implants prior to the implantation did not differ following bacterial inoculation (**Figure 3H**). SEM imaging demonstrated biofilm formation on the NT and PT implants, with bacterial cells stacked on top of each other in multiple layers, while there were no signs of biofilm formation on the PT-Ag implants, but only a few individual bacteria (**Figure 4**).

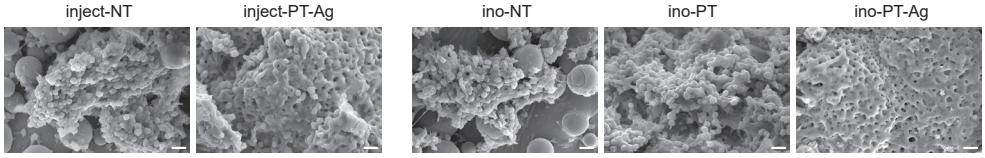

Figure 4. The biofilm formation on the implants visualized by SEM after 7 days. Scale bar = 5 μm.

9.3.4 Bone changes

Micro-CT analysis demonstrated osteomyelitis on infected tibiae as indicated by osteolysis and cortical thickening (**Figure 5A**). The radiological scoring of the osteomyelitis indicated that the inject-NT ($p < 0.01$), inject-PT-Ag ($p < 0.001$), ino-NT ($p < 0.0001$), ino-PT ($p < 0.001$), and ino-PT-Ag ($p < 0.05$) groups had significantly higher osteomyelitis scores as compared to the control group, while the osteomyelitis scores of the inject-no-implant and ino-NT-no-infection groups were not significantly different from that of the control group

(**Figure 5B**). The total BV of the infected left tibia of the inject-NT ($p < 0.05$), inject-PT-Ag ($p < 0.001$) and inject-no-implant ($p < 0.01$) groups were different from that of the inject-control group (*i.e.*, right tibia) while no significant differences were observed between the groups in which the implants were inoculated *in vitro* (**Figure 5C**). The cortical BV and peri-implant BV were determined both proximally and distally to indicate the location of the changes in the bone morphology. The proximal cortical BV was enhanced for the inject-NT ($p < 0.001$), inject-PT-Ag ($p < 0.0001$), and inject-no-implant ($p < 0.001$) groups as compared to the inject-control group. The same held for the ino-NT group as compared to the ino-control ($p < 0.05$) group, and for the inject-PT-Ag group as compared to the ino-PT-Ag group both proximally ($p < 0.05$) and distally ($p < 0.0001$; **Figure 5D**). The peri-implant BV did not differ significantly between the groups (**Figure 5E**). The outer perimeter was significantly increased for the inject-NT group as compared to the ino-NT group ($p < 0.001$). The same observation was made for the inject-PT-Ag group as compared to the ino-PT-Ag group ($p < 0.001$; **Figure 5F**) while the inner perimeter was similar between all the groups (**Figure 5G**). The cortical bone porosity of the *in vivo* injection groups did not differ while it was significantly enhanced proximally for the ino-NT ($p < 0.05$), ino-PT ($p < 0.0001$), and ino-PT-Ag ($p < 0.001$) groups as compared to the ino-control group. The same observation was made for the ino-PT group as compared to the ino-NT-no-infection ($p < 0.05$) group and distally for the ino-PT group as compared to the ino-control group ($p < 0.01$; **Figure 5H**).

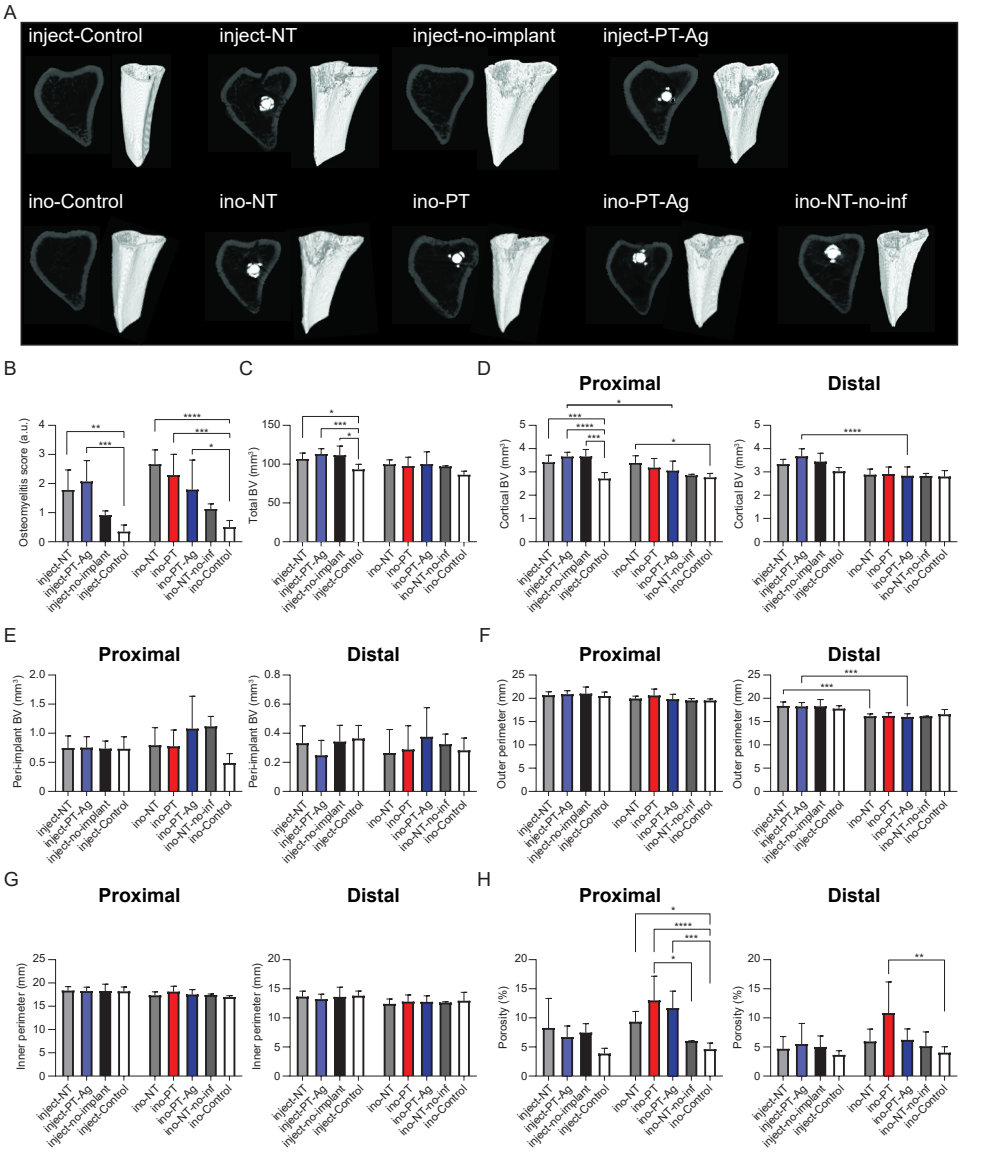

Figure 5. Changes in the bone morphology after 7 days. (A) The micro-CT images of the rat tibiae. (B) Radiographic osteomyelitis scores. The quantification of several bone morphometric parameters using micro-CT, including (C) total BV, (D) cortical BV, (E) peri-implant BV, (F) outer perimeter, (G) inner perimeter, and (H) porosity. * $p < 0.05$, ** $p < 0.01$, *** $p < 0.001$, **** $p < 0.0001$. BV; bone volume.

9.4 DISCUSSION

Implants with intrinsic antibacterial properties are urgently needed to prevent IAI, thereby increasing the longevity of orthopedic implants. Over the last few years, AM porous titanium implants biofunctionalized by PEO have demonstrated promising results in that direction. However, the antibacterial properties of such implants had, thus far, not been assessed *in vivo*. Here, we used a rat implant infection model to evaluate the *in vivo* biocompatibility and infection prevention performance of AM titanium biofunctionalized by PEO using Ag NPs. We observed that the PT-Ag implants reduced the bacterial load as compared to the NT and PT implants. Furthermore, the method used for inducing the infection affected the course of infection and the relative performance of the different experimental groups.

9.4.1 *In vivo* implant infection models: prevention vs. treatment and the role of the inoculation method

It is important to note that the PEO-biofunctionalized implants are primarily designed for infection prevention and not infection treatment. An implant infection model that faithfully represents the actual clinical conditions, with low infection rates, would need a prohibitively large number of animals, rendering such an experiment infeasible due to practical, ethical, and financial considerations. Researchers have, therefore, explored alternative approaches to mimic the clinical situation as closely as possible while limiting the required number of animals. While there are late-onset infections caused by hematological pathogens, the majority of IAI cases arise during the first 3 weeks after surgery and are caused by the bacteria entering the wound area [34]. While the number of bacteria entering the wound peri-operatively are generally limited [35], a much higher bacterial load should be used in animal experiments to demonstrate an antibacterial effect using a limited number of animals. The biofunctionalized implants would then have to demonstrate antibacterial activity against a much higher bacterial load than is needed in clinical settings [36]. That would translate to a higher required dose of the antibacterial agent, which may increase the risk of cytotoxicity [37].

IAI can be initiated by the bacteria present on improperly sterilized implants [38] or by those reaching the wound area through the surgeon's hands [39], migrating from the tissues adjacent to the wound area [40], or, in the case of late-onset IAI by pathogens, originating from the bloodstream [41]. As we were primarily interested in the prevention of early-onset IAI, we investigated the first two ways of infection: either through the *in vivo* injection of bacteria into the intramedullary canal or by the *in vitro* inoculation of the implants with bacteria prior to implantation.

In vivo injection of bacteria into the intramedullary cavity has the disadvantage that a

very high bacterial load is already present inside the bone before the implant is inserted and that bacteria may infect the bony tissue rather than adhering onto the implant surface. As a result, the implant may need to possess a strong antibacterial activity to clear bacteria from the infected tissue. This model, therefore, mimics the clinical situation where a (severe) infection is already present in the surrounding tissues and the implant should be capable of treating that infection. Here, we did not observe a difference in the bacterial load after 1 week between inject-no implant, inject-NT, and inject-PT-Ag in the bone tissue, while the bacterial load on the implant was nearly significantly reduced for inject-PT-Ag implants compared to inject-NT implants. The comparison between the inject-no implant and inject-NT is particularly important in this regard. It is known that the presence of an implant frustrates the immune system, thereby decreasing the required infection dose by up to 10^6 fold [42]. It is, therefore, expected that infection clearance is less effective in the inject-NT group as compared to the inject-no-implant group. The fact that there are no significant differences between these two groups suggest that the course of infection is primarily driven by the bacteria infecting the surrounding tissues upon injection and not the presence of the implant.

The *in vitro* inoculation of the implant mimics the situation where an unsterile implant is implanted. This situation is suitable to study the prevention of IAI as the bacteria are in the vicinity of the implant and are, thus, more likely to proliferate on or near the implant surface than in the bony tissue. The results of this study support this hypothesis as the ino-PT-Ag implants reduced the bacterial load in the bony tissue with 90% as compared to the ino-NT and ino-PT implants as well as the bacterial load on the implant for the ino-PT-Ag implants as compared to the ino-PT implants.

There were no differences between the ino-PT and ino-NT, indicating that the PEO biofunctionalization process does not increase the risk of infection. Furthermore, ino-NT-no-infection had no bacteria, showing that the surgery had been, indeed, taken place under sterile conditions. In addition, all controls (*i.e.*, right tibiae) were culture-negative, indicating that the infection was localized at the site of contamination.

In addition to the way the infection is initiated, the animal species affects the outcome of the experiment. Rat models are versatile and low-cost, making them appropriate for screening before pre-clinical tests using full-sized implants are performed in larger animals [43]. However, rats have a strong immune system which requires a high bacterial load, as compared to *e.g.* rabbits that are very sensitive to infection [44]. On the other hand, mice are much smaller, rendering both the surgery and the fabrication of the implants excessively challenging.

We implanted the implant intramedullary into the tibia as this more closely resembles the clinical situation as compared to subcutaneous implantation. The local environment

does play a role in the infection as different type of immune cells may be present at different anatomical sites. Moreover, the tissue micro-environments are different and the cytotoxicity levels differ between the bony and skin tissue, making it difficult to study the specific aspects that are relevant for bone-related infections [45]. Furthermore, the intramedullary insertion of the implant mimics the implantation of an implant in orthopedic patients.

9.4.2 Bioluminescence imaging

In this study, we used bioluminescence imaging to track the course of infection in real-time. We continued to receive the bioluminescent signal at all-time points, except for the ino-NT-no-infection group and the day 0 of all the groups. While we observed no differences in the bioluminescent signal between the different groups, we detected differences in the bacterial load on day 7 in terms of the CFU count. The strength of the bioluminescent signal and the resolution of the scanner are likely not sensitive enough to pick up these differences in the bacterial load within the reduction range found [30, 46], as there is still a number of bacteria within the studied region of interest and, thus, a bioluminescence saturation effect might have been reached. Nevertheless, we do detect an increase in bioluminescence signal from day 0 onwards. Further optimization should make it possible to use bioluminescent bacteria as a powerful tool to track the course of infection in this intramedullary tibial infection model, as it enhances the number of data points and is likely to reduce the number of required animals.

9.4.3 Surface biofunctionalization of AM porous implants

The implants developed in this study were volume-porous implants produced by AM. Previous research has indicated that highly porous materials are more prone to infection as compared to fully dense materials, although this difference disappears when the implant is overgrown with the surrounding tissue [47]. It is important to assess the infection risk of highly porous AM implants, since the use of AM is expected to increase vastly due to the customization opportunities offered by free-form fabrication and the possibility to optimize the mechanical properties of such geometrically-ordered porous implants [48]. The design objective often is to enhance the bony ingrowth [49, 50] while reducing the risk of IAI [51].

The surface biofunctionalization of porous implants is challenging. PEO has been applied frequently to generate multifunctional implants that possess both antibacterial and osteogenic properties [52-55]. While the antibacterial properties have been evaluated extensively *in vitro*, the antibacterial properties of implants biofunctionalized by PEO had, thus far, not been assessed *in vivo*. However, the osteogenic properties have been analyzed in various animal models and have resulted in 1. enhanced osseointegration and push-out

bonding strength in the femora of a rabbit model after 12 weeks [56], 2. strong bone matrix deposition and enhanced bone-to-implant contact in pig mandibles after 8 weeks [24], and 3. shortened osseointegration time, increased bone mineral deposition, and enhanced bone-implant contact in rabbit mandibles over 12 weeks [25]. On the other hand, the use of Ag on titanium implants has been shown to result in potent antibacterial implants *in vivo* as evidenced by the prevention of the infections caused by *S. epidermidis* in a murine tissue cage model [57], a reduction in the bacterial loads when the implants were implanted into rat femora [58], and a 2-log reduction in the bacterial load in a rabbit tibial infection model [59].

Apart from the antibacterial activity, there are some concerns regarding cytotoxicity of Ag-based surface treatments, as Ag is both more antibacterial yet also more cytotoxic as compared to other antibacterial agents, such as Cu and Zn [37]. Therefore, the key is to find the balance between the antibacterial activity and osteogenic activity. The toxicity of Ag NPs depends on their size and subsequent Ag ion release [60]. Furthermore, low doses of Ag NPs have been found to support bone fracture healing *in vivo* [61] and are demonstrated to enhance bone regeneration especially when combined with Ca/P or hydroxyapatite containing surface layers [62, 63]. In this regard, it is important to stress that Ag is more likely to be suitable for infection prevention rather than treatment since treatment would require high Ag doses.

9.4.4 Bone morphology

Apart from the CFU count, we studied the changes in the bone morphology as the inflammatory reaction to *S. aureus* infection is characterized by dynamic bone changes resulting in quiescent, resorbed, and new bone [64]. Novel bone formation precedes cortical osteolysis [65, 66] since it is a direct response to the inflammatory environment, while cortical osteolysis is partially initiated by bacterial presence in the cortical Haversian and Volkmann canals [67]. This can be monitored by scoring the radiographic appearance on micro-CT images. This scoring is capable of distinguishing between infected and non-infected bone, but there is no direct relationship between the bacterial load and the radiographic scores. That is because bone requires several weeks to remodel back to its native architecture [68] and the bone remodeling caused by infection has been shown to be strain-dependent due to the different immune responses they elicit [69, 70] and the varying levels of the secretion of toxins that modulate bone regeneration [71].

We observed an increased osteomyelitis score among all of the infected groups as compared to the control conditions. Furthermore, the total BV and proximal cortical BV were enhanced for all infected inject-implants as compared to inject-control, while bone porosity was enhanced for all the infected ino-implants as compared to the ino-control group as well

as for the ino-PT group as compared to the ino-NT-no-inf group. Moreover, there were no differences in the bone morphology between the ino-NT-no-inf and ino-control groups, indicating that the observed changes in the bone morphology were due to the presence of infection, and not due to the surgical procedure. In addition, the proximal cortical BV and distal outer perimeter were enhanced for the inject-PT-Ag group as compared to the ino-PT-Ag group, indicating that the PT-Ag implants were less able to prevent bone changes when the infection was initiated through *in vivo* intramedullary injection as compared to the *in vitro* inoculation of the implant prior to implantation. While the PT-Ag implants reduced the bacterial load, they did not eradicate all the signs of infection, including bone morphology changes. To achieve this, the infection should have been completely eradicated for several weeks to allow the bony tissue to regenerate [72].

9.4.5 Future work

The potential of AM porous titanium implants with Ag NPs can be further improved by instigating osteogenic properties and enhancing their antibacterial activity through the addition of other inorganic NPs, such as Cu, Zn, and Sr that give rise to synergistic antibacterial behavior while also enhancing bone regeneration [23, 52, 55]. Furthermore, the long-term antibacterial properties of these implants need to be investigated particularly because silver-biofunctionalized implants have shown some promise in terms of long-term antibacterial properties [62]. Finally, the *in vivo* evaluation of the different variants of PEO-biofunctionalized AM porous titanium implants needs to be continued in (large) animal models and clinical trials before translation to clinical settings is possible.

9.5 CONCLUSIONS

In this *in vivo* study, we investigated the infection-prevention capacity of AM implants biofunctionalized by PEO with Ag, by implanting the implants in the intramedullary canal of rat tibia. Bioluminescence imaging showed no significant differences between the experimental groups. In the groups where the infections were induced through *in vivo* intramedullary injection of bacteria, the presence of the implant did not affect the course of infection. This suggests that this model is more suitable for assessing infection treatment rather than evaluating the infection prevention performance of the implants. When infections was induced through the *in vitro* inoculation of the implants prior to implantation, the bacterial load on the PT-Ag implants was significantly lower as compared to the PT implants. Furthermore, the CFU count of the bony tissue surrounding the PT-Ag implants was significantly smaller (90-95% reduction) than those of the tissue specimens associated

with the NT and PT implants (day 7). Osteomyelitis scores were enhanced on all the infected implants as compared to the non-infected controls. Taken together, the results of this study warrant further preclinical and clinical studies on PEO biofunctionalized AM implants.

ACKNOWLEDGEMENTS

The research for this paper was financially supported by the Prosperos project, funded by the Interreg VA Flanders – The Netherlands program, CCI grant no. 2014TC16RFCB046. The authors would like to acknowledge Jelle Scharringa and Mattie van Rijen for their technical assistance.

REFERENCES

[1] S.M. Kurtz, K.L. Ong, E. Lau, K.J. Bozic, D. Berry, J. Parvizi, Prosthetic joint infection risk after TKA in the Medicare population, Clin Orthop Relat Res 468 (2010) 52-6.

[2] A. Trampuz, W. Zimmerli, Diagnosis and treatment of infections associated with fracture-fixation devices, Injury (2006) S59-66.

[3] C. Graci, G. Maccauro, F. Muratori, M.S. Spinelli, M.A. Rosa, C. Fabbriciani, Infection following bone tumor resection and reconstruction with tumoral prostheses, International Journal of Immunopathology and pharmacology 23 (2010) 1005-1013.

[4] A.M. Schwartz, K.X. Farley, G.N. Guild, T.L. Bradbury, Jr., Projections and Epidemiology of Revision Hip and Knee Arthroplasty in the United States to 2030, J Arthroplasty 35(6S) (2020) S79-S85.

[5] A. Manesh, G.M. Varghese, Rising antimicrobial resistance: an evolving epidemic in a pandemic, The Lancet Microbe 2(9) (2021) e419-e420.

[6] H. Wafa, R.J. Grimer, K. Reddy, L. Jeys, A. Abudu, S.R. Carter, R.M. Tillman, Retrospective evaluation of the incidence of early periprosthetic infection with silvertreated endoprostheses in high-risk patients, Bone Joint J 97-B (2015) 252-7.

[7] T. Shirai, H. Tsuchiya, H. Nishida, N. Yamamoto, K. Watanabe, J. Nakase, R. Terauchi, Y. Arai, H. Fujiwara, T. Kubo, Antimicrobial megaprostheses supported with iodine, J Biomater Appl 29(4) (2014) 617-23.

[8] G. Huang, S.T. Pan, J.X. Qiu, The Clinical Application of Porous Tantalum and Its New Development for Bone Tissue Engineering, Materials (Basel) 14(10) (2021).

[9] C. Gao, C. Wang, H. Jin, Z. Wang, Z. Li, C. Shi, Y. Leng, F. Yang, H. Liu, J. Wang, Additive manufacturing technique-designed metallic porous implants for clinical application in orthopedics, RSC Advances 8(44) (2018) 25210-25227.

[10] N. Taniguchi, S. Fujibayashi, M. Takemoto, K. Sasaki, B. Otsuki, T. Nakamura, T. Matsushita, T. Kokubo, S. Matsuda, Effect of pore size on bone ingrowth into porous titanium implants fabricated by additive manufacturing: An *in vivo* experiment, Mater Sci Eng C Mater Biol Appl 59 (2016) 690-701.

[11] V. Hegde, H.Y. Park, E. Dworsky, S.D. Zoller, W. Xi, D.O. Johansen, A.H. Loftin, C.D. Hamad, T. Segura, N.M. Bernthal, The use of a novel antimicrobial implant coating *in vivo* to prevent spinal implant infection, Spine 45 (2020) E305-E311.

[12] C.C. Yang, C.C. Lin, J.W. Liao, S.K. Yen, Vancomycin-chitosan composite deposited on post porous hydroxyapatite coated Ti6Al4V implant for drug controlled release, Mater Sci Eng C Mater Biol Appl 33 (2013) 2203-12.

[13] B. Li, T.J. Webster, Bacteria antibiotic resistance: new challenges and opportunities for implant-associated orthopedic infections, J Orthop Res 36 (2018) 22-32.

[14] S.L. Percival, P.G. Bowler, D. Russell, Bacterial resistance to silver in wound care, J Hosp Infect 60 (2005) 1-7.

[15] J. Hardes, M.P. Henrichs, G. Hauschild, M. Nottrott, W. Guder, A. Streitbuerger, Silver-Coated Megaprosthesis of the Proximal Tibia in Patients With Sarcoma, J Arthroplasty 32(7) (2017) 2208-2213.

[16] F. Donati, G. Di Giacomo, S. D'Adamio, A. Ziranu, S. Careri, M. Rosa, G. Maccauro, Silver-coated hip megaprosthesis in oncological limb savage surgery, Biomed Res Int 2016 (2016) 9079041.

[17] M.C. Wyatt, M. Foxall-Smith, A. Roberton, A. Beswick, D.C. Kieser, M.R. Whitehouse, The use of silver coating in hip megaprostheses: a systematic review, Hip Int 29 (2019) 7-20.

[18] M. Bottagisio, A.B. Lovati, F. Galbusera, L. Drago, G. Banfi, A precautionary approach to guide the use of transition metal-based nanotechnology to prevent orthopedic infections, Materials (Basel) 12 (2019).

[19] J. Gallo, M. Holinka, C.S. Moucha, Antibacterial surface treatment for orthopaedic implants, Int J Mol Sci 15 (2014) 13849-80.

[20] B.S. Necula, L.E. Fratila-Apachitei, S.A. Zaat, I. Apachitei, J. Duszczyk, *In vitro* antibacterial activity of porous TiO2-Ag composite layers against methicillin-resistant Staphylococcus aureus, Acta Biomater 5 (2009) 3573-80.

[21] K.R. Shin, Y.S. Kim, G.W. Kim, H.W. Yang, Y.G. Ko, D.H. Shin, Effects of concentration of Ag nanoparticles on surface structure and *in vitro* biological responses of oxide layer on pure titanium via plasma electrolytic oxidation, Applied Surface Science 347 (2015) 574-582.

[22] S.H. Uhm, J.S. Kwon, D.H. Song, E.J. Lee, W.S. Jeong, S. Oh, K.N. Kim, E.H. Choi, K.M. Kim, Long-term antibacterial performance and bioactivity of plasma-engineered Ag-NPs/TiO(2), J Biomed Nanotechnol 12 (2016) 1890-1906.

[23] I.A.J. van Hengel, N.E. Putra, M. Tierolf, M. Minneboo, A.C. Fluit, L.E. Fratila-Apachitei, I. Apachitei, A.A. Zadpoor, Biofunctionalization of selective laser melted porous titanium using silver and zinc nanoparticles to prevent infections by antibiotic-resistant bacteria, Acta Biomater 107 (2020) 325-337.

[24] A. Santos-Coquillat, E. Martínez-Campos, M. Mohedano, R. Martínez-Corriá, V. Ramos, R. Arrabal, E. Matykina, *In vitro* and *in vivo* evaluation of PEO-modified titanium for bone implant applications, Surface and Coatings Technology 347 (2018) 358-368.

[25] J. He, W. Feng, B.H. Zhao, W. Zhang, Z. Lin, *In vivo* effect of titanium implants with porous zinc-containing coatings prepared by plasma electrolytic oxidation method on osseointegration in rabbits, Int J Oral Maxillofac Implants 33 (2018) 298-310.

[26] T.-E. Park, H.-C. Choe, W.A. Brantley, Bioactivity evaluation of porous TiO2 surface formed on titanium in mixed electrolyte by spark anodization, Surface and Coatings Technology 235 (2013) 706-713.

[27] I.A.J. van Hengel, M. Riool, L.E. Fratila-Apachitei, J. Witte-Bouma, E. Farrell, A.A. Zadpoor, S.A.J. Zaat, I. Apachitei, Selective laser melting porous metallic implants with immobilized silver nanoparticles kill and prevent biofilm formation by methicillin-resistant Staphylococcus aureus, Biomaterials 140 (2017) 1-15.

[28] J.A. Niska, J.A. Meganck, J.R. Pribaz, J.H. Shahbazian, E. Lim, N. Zhang, B.W. Rice, A. Akin, R.I. Ramos, N.M. Bernthal, K.P. Francis, L.S. Miller, Monitoring bacterial burden, inflammation and bone damage longitudinally using optical and muCT imaging in an orthopaedic implant infection in mice, PLoS One 7 (2012) e47397.

[29] H. Funao, K. Ishii, S. Nagai, A. Sasaki, T. Hoshikawa, M. Aizawa, Y. Okada, K. Chiba, S. Koyasu, Y. Toyama, M. Matsumoto, Establishment of a real-time, quantitative, and reproducible mouse model of Staphylococcus osteomyelitis using bioluminescence imaging, Infect Immun 80 (2012) 733-41.

[30] R.J. Miller, J.M. Thompson, J. Zheng, M.C. Marchitto, N.K. Archer, B.L. Pinsker, R.V. Ortines, X. Jiang, R.A. Martin, I.D. Brown, Y. Wang, R.S. Sterling, H.Q. Mao, L.S. Miller, *In vivo* bioluminescence imaging in a rabbit model of orthopaedic implant-associated infection to monitor efficacy of an antibiotic-releasing coating, J Bone Joint Surg Am 101 (2019) e12.

[31] R.J. Miller, H.A. Crosby, K. Schilcher, Y. Wang, R.V. Ortines, M. Mazhar, D.A. Dikeman, B.L. Pinsker, I.D. Brown, D.P. Joyce, J. Zhang, N.K. Archer, H. Liu, M.P. Alphonse, J. Czupryna, W.R. Anderson, N.M. Bernthal, L. Fortuno-Miranda, J.W.M. Bulte, K.P. Francis, A.R. Horswill, L.S. Miller, Development of a Staphylococcus aureus reporter strain with click beetle red luciferase for enhanced *in vivo* imaging of experimental bacteremia and mixed infections, Sci Rep 9(1) (2019) 16663.

[32] N. Percie du Sert, A. Ahluwalia, S. Alam, M.T. Avey, M. Baker, W.J. Browne, A. Clark, I.C. Cuthill, U. Dirnagl, M. Emerson, P. Garner, S.T. Holgate, D.W. Howells, V. Hurst, N.A. Karp, S.E. Lazic, K. Lidster, C.J. MacCallum, M. Macleod, E.J. Pearl, O.H. Petersen, F. Rawle, P. Reynolds, K. Rooney, E.S. Sena, S.D. Silberberg, T. Steckler, H. Wurbel, Reporting animal research: Explanation and elaboration for the ARRIVE guidelines 2.0, PLoS Biol 18 (2020) e3000411.

[33] M. Croes, S. Bakhshandeh, I.A.J. van Hengel, K. Lietaert, K.P.M. van Kessel, B. Pouran, B.C.H. van der Wal, H.C. Vogely, W. Van Hecke, A.C. Fluit, C.H.E. Boel, J. Alblas, A.A. Zadpoor, H. Weinans, S. Amin Yavari, Antibacterial and immunogenic behavior of silver coatings on additively manufactured porous titanium, Acta Biomater 81 (2018) 315-327.

[34] A. Trampuz, W. Zimmerli, Diagnosis and treatment of implant-associated septic arthritis and osteomyelitis, Current Infectiouns Disease Reports 10 (2008) 394-403.

[35] K. Saleh, A. Sonesson, B. Persson, K. Riesbeck, A. Schmidtchen, A descriptive study of bacterial load of full-thickness surgical wounds in dermatologic surgery, Dermatol Surg 37(7) (2011) 1014-22.

[36] B. Friberg, S. Friberg, L.G. Burman, Inconsistent correlation between aerobic bacterial surface and air counts in operating rooms with ultra clean laminar air flows: proposal of a new bacteriological standard for surface contamination, Journal of Hospital Infection 42 (1999) 287-293.

[37] I.A.J. van Hengel, M.W.A.M. Tierolf, L.E. Fratila-Apachitei, I. Apachitei, A.A. Zadpoor, Antibacterial titanium implants biofunctionalized by plasma electrolytic oxidation with silver, zinc, and copper: a systematic review, Int J Mol Sci 22 (2021) 3800.

[38] F. Schomig, C. Perka, M. Pumberger, R. Ascherl, Implant contamination as a cause of surgical site infection in spinal surgery: are single-use implants a reasonable solution? - a systematic review, BMC Musculoskelet Disord 21 (2020) 634.

[39] D. Pittet, B. Allegranzi, H. Sax, S. Dharan, C.L. Pessoa-Silva, L. Donaldson, J.M. Boyce, Evidence-based model for hand transmission during patient care and the role of improved practices, The Lancet Infectious Diseases 6 (2006) 641-652.

[40] M. Riool, L. de Boer, V. Jaspers, C.M. van der Loos, W.J.B. van Wamel, G. Wu, P.H.S. Kwakman, S.A.J. Zaat, Staphylococcus epidermidis originating from titanium implants infects surrounding tissue and immune cells, Acta Biomater 10 (2014) 5202-5212.

[41 E. Sheehan, J. McKenna, K.J. Mulhall, P. Marks, D. McCormack, Adhesion of Staphylococcus to orthopaedic metals, an *in vivo* study, Journal of Orthopaedic Research 22 (2004) 39-43.

[42] W. Zimmerli, F.A. Waldvogel, P. Vaudaux, U.E. Nydegger, Pathogenesis of foreign body infection description and characteristics of an animal model, The Journal of Infectious Diseases 146 (1982) 487-497.

[43] W. Reizner, J.G. Hunter, N.T. O'Malley, R.D. Southgate, E.M. Schwarz, S.L. Kates, A systematic review of animal models for Staphylococcus aureus osteomyelitis, Eur Cell Mater 27 (2014) 196-212.

[44] Y.H. An, R.J. Friedman, Animal models of orthopedic implant infection, J Invest Surg 11 (1998) 139-46.

[45] J. Nowakowska, R. Landmann, N. Khanna, Foreign body infection models to study host-pathogen response and antimicrobial tolerance of bacterial biofilm, Antibiotics (Basel) 3 (2014) 378-97.

[46] N.M. Bernthal, A.I. Stavrakis, F. Billi, J.S. Cho, T.J. Kremen, S.I. Simon, A.L. Cheung, G.A. Finerman, J.R. Lieberman, J.S. Adams, L.S. Miller, A mouse model of post-arthroplasty Staphylococcus aureus joint infection to evaluate *in vivo* the efficacy of antimicrobial implant coatings, PLoS One 5(9) (2010) e12580.

[47] K. Merritt, J.W. Shafer, S.A. Brown, Implant site infection rates with porous and dense materials. pdf, Journal of Biomedical Materials Research 13 (1979) 101-108.

[48] H.M.A. Kolken, S. Janbaz, S.M.A. Leeflang, K. Lietaert, H.H. Weinans, A.A. Zadpoor, Rationally designed meta-implants: a combination of auxetic and conventional meta-biomaterials, Materials Horizons 5 (2018) 28-35.

[49] J.Y. Hong, S.Y. Ko, W. Lee, Y.Y. Chang, S.H. Kim, J.H. Yun, Enhancement of bone ingrowth into a porous titanium structure to improve osseointegration of dental implants: a pilot study in the canine model, Materials (Basel) 13 (2020).

[50] L.M. Reis de Vasconcellos, D.O. Leite, F. Nascimento de Oliveira, Y.R. Carvalho, C.A.A. Cairo, Evaluation of bone ingrowth into porous titanium implant: histomorphometric analysis in rabbits, Braz Oral Res 24 (2010) 399-405.

[51] E.A. Lewallen, S.M. Riester, C.A. Bonin, H.M. Kremers, A. Dudakovic, S. Kakar, R.C. Cohen, J.J. Westendorf, D.G. Lewallen, A.J. van Wijnen, Biological strategies for improved osseointegration and osteoinduction of porous metal orthopedic implants, Tissue Eng Part B Rev 21 (2015) 218-30.

[52] I.A.J. van Hengel, F.S.A. Gelderman, S. Athanasiadis, M. Minneboo, H. Weinans, A.C. Fluit, B.C.J. van der Eerden, L.E. Fratila-Apachitei, I. Apachitei, A.A. Zadpoor, Functionality-packed additively manufactured porous titanium implants, Mater Today Bio 7 (2020) 100060.

[53] A. Santos-Coquillat, R. Gonzalez Tenorio, M. Mohedano, E. Martinez-Campos, R. Arrabal, E. Matykina, Tailoring of antibacterial and osteogenic properties of Ti6Al4V by plasma electrolytic oxidation, Applied Surface Science 454 (2018) 157-172.

[54] M. Thukkaram, R. Coryn, M. Asadian, P.S. Esbah Tabaei, P. Rigole, N. Rajendhran, A. Nikiforov, J. Sukumaran, T. Coenye, P. Van Der Voort, G. Du Laing, R. Morent, A. Van Tongel, L. De Wilde, P. De Baets, K. Verbeken, N. De Geyter, Fabrication of microporous coatings on titanium implants with improved mechanical, antibacterial, and cell-interactive properties, ACS Appl Mater Interfaces 12 (2020) 30155-30169.

[55] I.A.J. van Hengel, M. Tierolf, V.P.M. Valerio, M. Minneboo, A.C. Fluit, L.E. Fratila-Apachitei, I. Apachitei, A.A. Zadpoor, Self-defending additively manufactured bone implants bearing silver and copper nanoparticles, J Mater Chem B 8 (2019) 1589--1602.

[56] C.J. Chung, R.T. Su, H.J. Chu, H.T. Chen, H.K. Tsou, J.L. He, Plasma electrolytic oxidation of titanium and improvement in osseointegration, J Biomed Mater Res B Appl Biomater 101 (2013) 1023-30.

[57] R. Kuehl, P.S. Brunetto, A.K. Woischnig, M. Varisco, Z. Rajacic, J. Vosbeck, L. Terracciano, K.M. Fromm, N. Khanna, Preventing implant-associated infections by silver coating, Antimicrob Agents Chemother 60 (2016) 2467-75.

[58] D.L. Cavanaugh, Z.G. Tan, J.P.t. Norris, A. Hardee, P.S. Weinhold, L.E. Dahners, P.E. Orndorff, R.A. Shirwaiker, Evaluation of silver-titanium implants activated by low intensity direct current for orthopedic infection control: An *in vitro* and *in vivo* study, J Biomed Mater Res B Appl Biomater 104 (2016) 1023-31.

[59] M. Fabritius, A.A. Al-Munajjed, C. Freytag, H. Julke, M. Zehe, T. Lemarchand, J.J. Arts, D. Schumann, V. Alt, K. Sternberg, Antimicrobial Silver Multilayer Coating for Prevention of Bacterial Colonization of Orthopedic Implants, Materials (Basel) 13 (2020).

[60] S. Kim, D.Y. Ryu, Silver nanoparticle-induced oxidative stress, genotoxicity and apoptosis in cultured cells and animal tissues, J Appl Toxicol 33 (2013) 78-89.

[61] R. Zhang, P. Lee, V.C. Lui, Y. Chen, X. Liu, C.N. Lok, M. To, K.W. Yeung, K.K. Wong, Silver nanoparticles promote osteogenesis of mesenchymal stem cells and improve bone fracture healing in osteogenesis mechanism mouse model, Nanomedicine 11 (2015) 1949-59.

[62] A. Shivaram, S. Bose, A. Bandyopadhyay, Understanding long-term silver release from surface modified porous titanium implants, Acta Biomater 58 (2017) 550-560.

[63] T. Akiyama, H. Miyamoto, Y. Yonekura, M. Tsukamoto, Y. Ando, I. Noda, M. Sonohata, M. Mawatari, Silver oxide-containing hydroxyapatite coating has *in vivo* antibacterial activity in the rat tibia, J Orthop Res 31 (2013) 1195-200.

[64] V.A. Stadelmann, I. Potapova, K. Camenisch, D. Nehrbass, R.G. Richards, T.F. Moriarty, *In vivo* microCT monitoring of osteomyelitis in a rat model, Biomed Res Int 2015 (2015) 587857.

[65] S.M. Shiels, K.M. Bedigrew, J.C. Wenke, Development of a hematogenous implant-related infection in a rat model, BMC Musculoskelet Disord 16 (2015) 255.

[66] J.C.E. Odekerken, J.J.C. Arts, D.A.M. Surtel, G.H.I.M. Walenkanmp, T.J.M. Welting, A rabbit osteomyelitis model for the longitudinal assessment of early post-operative implant infections, Journal of Orthopaedic Surgery and Research 8 (2013) 38.

[67] C. Pineda, R. Espinosa, A. Pena, Radiographic imaging in osteomyelitis: the role of plain radiography, computed tomography, ultrasonography, magnetic resonance imaging, and scintigraphy, Semin Plast Surg 23 (2009) 80-9.

[68] M. Croes, M.C. Kruyt, W. Boot, B. Pouran, M.V. Braham, S.A. Pakpahan, H. Weinans, H.C. Vogely, A.C. Fluit, W.J. Dhert, J. Alblas, F.C. Oner, The role of bacterial stimuli in inflammation-driven bone formation, Eur Cell Mater 37 (2019) 402-419.

[69] T. Krisher, Z. Bar-Shavit, Regulation of osteoclastogenesis by integrated signals from toll-like receptors, J Cell Biochem 115 (2014) 2146-54.

[70] O. Reikeras, J.E. Wang, S.J. Foster, S.E. Utvag, Staphylococcus aureus peptidoglycan impairs fracture healing: an experimental study in rats, J Orthop Res 25 (2007) 262-6.

[71] J.E. Cassat, N.D. Hammer, J.P. Campbell, M.A. Benson, D.S. Perrien, L.N. Mrak, M.S. Smeltzer, V.J. Torres, E.P. Skaar, A secreted bacterial protease tailors the Staphylococcus aureus virulence repertoire to modulate bone remodeling during osteomyelitis, Cell Host Microbe 13 (2013) 759-72.

[72] M. Croes, B.C.H. van der Wal, H.C. Vogely, Impact of bacterial infections on osteogenesis: evidence from *in vivo* studies, J Orthop Res 37 (2019) 2067-2076.

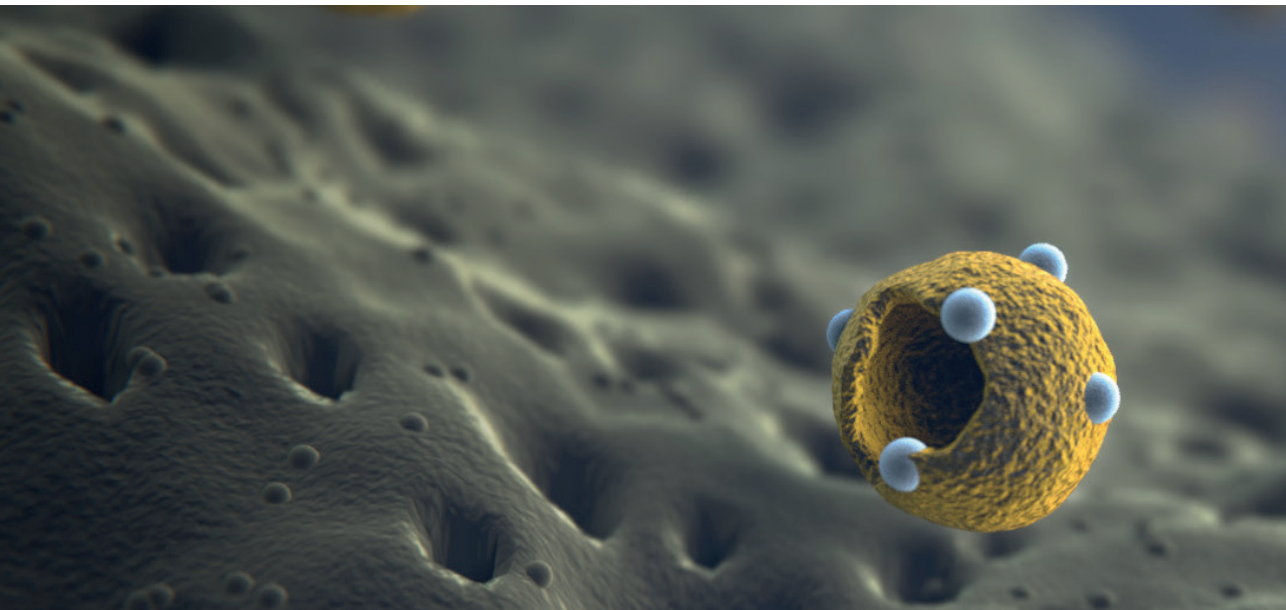

CHAPTER 10

Discussion

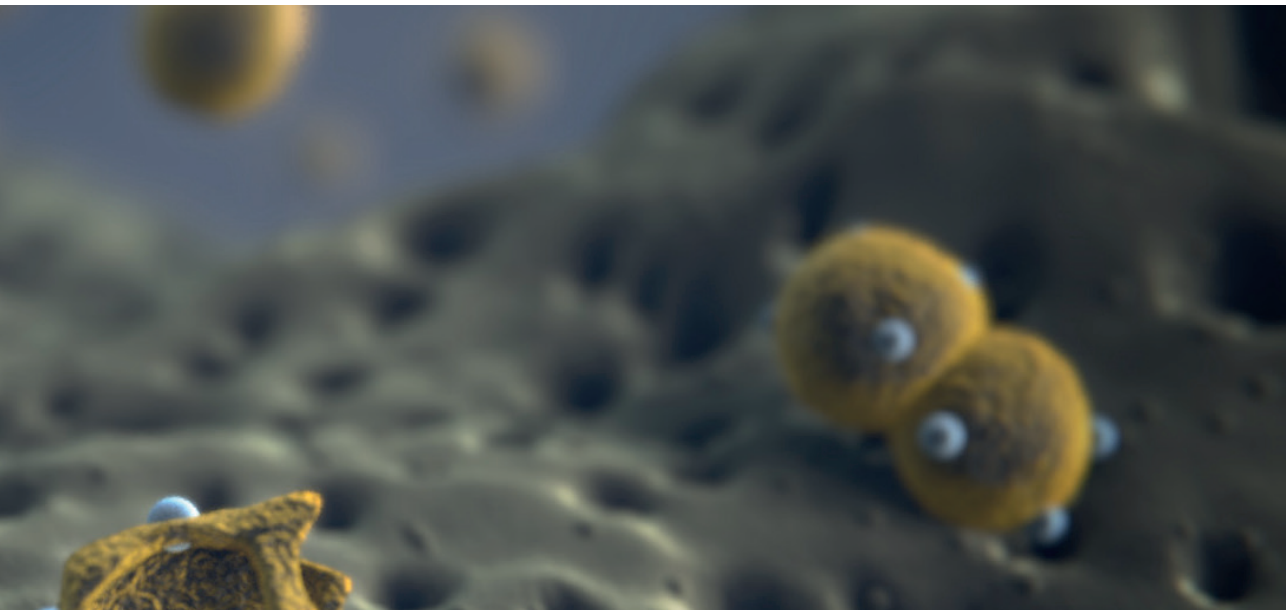

10 DISCUSSION

The aim of this thesis was to synthesize multifunctional implants that prevent complications and guarantee lifelong implant functioning. This topic involves a wide range of research areas including, biomaterials science, biomechanics, microbiology, and tissue engineering. This combination of topics makes this field of research simultaneously highly challenging and intriguing. In this discussion, we will summarize the main findings of this thesis, reflect on the results, and provide a future outlook. The discussion is closed with some concluding remarks.

10.1 Main findings of this thesis

In this thesis, surface biofunctionalization using PEO was applied to AM volume-porous titanium implants to generate multifunctional implants with antibacterial and osteogenic properties. We set out to provide an overview of the progress made on antibacterial titanium implants biofunctionalized by PEO with silver, copper and/or zinc. We first conducted a systematic literature review (Chapter 2). A substantial (*i.e.*, >50%) reduction in the bacterial load was reported by 100% of the studies that used Ag, by 93% of those that used Cu, by 73% of those that Zn, and by 100% of those using a combination of silver, copper and/or zinc. Cytocompatibility was tested in only 71% of the studies. Very few studies observed cytotoxicity, including 13% of the studies using silver, 10% of those using copper, 0% of those using zinc, and 0% of those using a combination of two elements. Combining Ag, Cu, and Zn is a promising strategy since the antibacterial activity was enhanced without the induction of any cytotoxic effects. A majority of the studies used *S. aureus* to test the antibacterial activity, which reflects the fact that *Staphylococci* are the main inflictors of IAI. Considering Gram-negative bacteria, 31% of the included studies used *E. coli*. To prevent IAI, it is important to not only prevent the bacteria from adhering onto the implant surface, but to also kill the bacteria present in the surroundings of the implant, as these may cause future infections. As such, it is crucial to test the antibacterial activity against both adherent and planktonic bacteria. This was done in only 23% of the studies, while 42% of the included studies only tested the performance of the biomaterials against adherent bacteria and 35% only against planktonic bacteria. All the included studies were performed *in vitro*, with a few studies also exploring *ex vivo* models to determine the antibacterial activity. To date, no *in vivo* studies has been performed. Therefore, the research on titanium implants biofunctionalized by PEO with the help of Ag, Cu, and/or Zn has not yet entered the preclinical phase.

Subsequently, the biofunctionalization of AM volume-porous implants by PEO with the help of silver NPs was investigated and the antibacterial activity of the resulting implants were compared with those of solid implants (Chapter 3). The rationally designed volume-porous

implants that were fabricated by AM had a 3.75 times larger surface area as compared to solid implants with similar dimensions. The biofunctionalized implants demonstrated antibacterial activity against MRSA both *in vitro* and *ex vivo*, and this activity was enhanced for porous implants compared to solid implants. Furthermore, PEO biofunctionalization with silver NPs resulted in hydroxyapatite formation on the implant surface of porous implants and enhanced the metabolic activity of human mesenchymal stem cells.

Thereafter, the multifunctional properties of similarly designed AM implants with surfaces containing a combination of silver NPs and other inorganic agents, including copper, zinc, or strontium, were explored. Combining silver with copper or zinc NPs resulted in synergistic antibacterial behaviors (Chapters 4 and 5). Ratios of up to 75% silver and 25% copper or zinc NPs resulted in the full eradication of MRSA *ex vivo*. Furthermore, no signs of cytotoxicity against preosteoblasts were observed. Combining silver NPs with strontium resulted in an unexpected synergistic antibacterial behavior (Chapter 6). Furthermore, the addition of strontium enhanced the osteogenic differentiation of preosteoblasts. Combining silver NPs with copper NPs, zinc NPs, or strontium is, therefore, a fruitful strategy to improve both the antibacterial activity and osteogenic potential of PEO biofunctionalized titanium implants.

PEO is a versatile process that can be adapted to obtain the desired implant surface morphology and chemical composition. Therefore, the effects of the processing parameters of PEO and the electrolyte composition on the surface morphology and accompanying osteogenic properties of the resulting implants were investigated (Chapter 7). Changing the processing parameters, including the oxidation time, current density, and electrolyte composition (*e.g.*, with or without strontium) altered the surface morphology, oxide layer thickness, ion release kinetics, chemical composition, and phase composition of the biofunctionalized implants. Furthermore, a specific set of parameters (*i.e.*, PEO biofunctionalization for 5 and 10 min with 20A/dm^2 and 5 min with 40A/dm^2) enhanced the osteogenic differentiation of preosteoblasts.

To date, the focus of the research performed on titanium implants has primarily been on osteogenesis. Another important aspect in the bone tissue regeneration process, namely angiogenesis, needs to be more thoroughly studied. We, therefore, conducted a literature review to explore the potential applications of various inorganic elements (*i.e.*, copper, magnesium, silicon, strontium, and zinc) for enhancing angiogenesis through the surface biofunctionalization of titanium implants (Chapter 8). The methodology and results of various studies regarding the ion release kinetics, endothelial cell characteristics, use of direct and indirect assays, incubation time, and material properties were analyzed and *in vitro* assays to investigate angiogenesis were described. Based on this analysis, silicon and strontium were highlighted as the most promising candidates to enhance angiogenesis in titanium implants.

Finally, we tested the efficacy of AM volume-porous implants biofunctionalized by PEO with silver NPs against MRSA in an *in vivo* bone infection model (Chapter 9). The implants were positioned in the intramedullary tibial canal. Infection was initiated either through intramedullary injection with bacteria or through the *in vitro* inoculation of the implant prior to implantation. The course of infection was tracked throughout 7 days using bioluminescent bacteria, after which the bacterial load, bone morphological changes, and immune response were evaluated. When infection was initiated through intramedullary injection, no differences in bacterial load were observed between the implants with or without silver NPs. However, when infection was initiated through *in vitro* inoculation, the bacterial load was reduced on the PEO-treated implants treated with silver NPs compared to non-treated implants or PEO biofunctionalized implants without silver NPs. All the infected groups had enhanced radiographic osteomyelitis scores as compared to non-infected controls while the immune response did not differ between the different groups. The results of this study confirmed the antibacterial activity of the PEO-biofunctionalized implants *in vivo* and clearly showed that proper models are required to study the prevention of IAI.

In this thesis, it was demonstrated that AM volume-porous implants could be biofunctionalized through PEO with silver, copper, and/or zinc NPs as well as strontium, resulting in implants with multifunctional properties. The fabricated implants exhibited potent antibacterial activity *in vitro*, *ex vivo*, and *in vivo* without any signs of cytotoxicity against human mesenchymal stem cells. Porous implants also demonstrated superior antibacterial activity as compared to solid implants. This advantage of porous implants is expected to be even clearer when large-scale implants are used. Moreover, combining silver NPs with copper or zinc NPs, or strontium resulted in synergistic antibacterial behavior and, in some cases, also enhanced the osteogenic response. We also found that adjusting the processing parameters of the PEO process is a powerful tool to optimize the surface morphology and strengthen the bioactivity of the implants. Altogether, the presented results indicate that the presented multifunctional implants are promising candidates for further preclinical development.

10.2 General discussion

The increasing number of orthopedic implants underlines the need for implants that can guarantee a lifelong service life. Complications, such as IAI and aseptic loosening, threaten this goal. Since the treatment of infections has become more challenging due to antibiotic-resistant bacteria, the focus has shifted towards the prevention of complications. In order to preserve the implant, it should be properly anchored. Bony ingrowth into the implant and the prevention of infections are, therefore, essential. To fulfil both criteria, implants with

multifunctional properties are required.

The next generation of orthopedic implants are likely to be increasingly produced by AM, which allows for the fabrication of highly porous structures. The form-freedom offered by AM techniques means that the implants can be designed such that they fill the bony defect and fulfil the load-bearing properties together with a high resistance to fatigue [1]. The design of the implant can be optimized to minimize the stress shielding while stimulating the bony ingrowth [2]. Furthermore, the porous structures allow the bone cells to migrate into the implant, initiating the formation of bone tissue and forming a tight connection between the implant and its surrounding bone tissue [3]. In addition, the porous structures facilitate the mass transport and, thus, the supply of nutrients and oxygen, while facilitating the outbound transport of metabolism byproducts [4, 5].

However, AM porous implants present some new challenges too. For example, the enhanced bony ingrowth into the porous structure makes it more difficult to remove the implant during a revision surgery [6]. In addition, the porous structure that allows the bone cells to migrate into the structure may also facilitate the adherence of bacteria to the internal surfaces of the implant [7]. Therefore, the surfaces of AM volume-porous implants need to be biofunctionalized to prevent IAI and enhance bony ingrowth through both osteogenesis and angiogenesis. However, surface biofunctionalization of porous structures is challenging [8]. Electrochemical surface techniques, such as PEO are capable of biofunctionalizing porous structures because the implant is submerged into the electrolyte during the process, allowing the electrolyte to reach all the internal surfaces of the fully-interconnected porous structure. PEO is a highly suitable technique for the synthesis of multifunctional surfaces as the use of calcium and phosphate-based electrolytes generates an implant surface with osteogenic properties [9, 10]. Furthermore, inorganic elements can be added to the electrolyte to generate antibacterial properties [11, 12]. PEO does not modify the bulk material and only modifies the outer surface layer. As a result, the mechanical properties of the implant are only minimally affected by PEO treatment [13].

Given that bacterial resistance steadily increases, and is by some even called the 'silent pandemic' [14], the search for novel antibacterial agents is in full swing. One class of promising antibacterial agents are inorganic NPs, such as silver, copper, and zinc [15]. The nanoscale dimensions of those particles results in a high surface area to volume ratio, making them highly effective against bacteria [16, 17]. Indeed, these NPs are highly effective against a wide range of bacterial species, including resistant bacterial strains [18-20]. Moreover, limited resistance against silver, copper, or zinc has been reported to date [21-23]. To further reduce the likelihood of the development of resistance, various combination of multiple of these agents may be used to kill bacteria early on before they get the chance to develop resistance [24, 25].

This will ultimately ensure the prolonged application of these highly effective antibacterial agents [26]. The simultaneous use of multiple agents also enhances the antibacterial activity, meaning that lower concentrations of each element are needed. The potential cytotoxicity due to a high concatenation of specific elements is, therefore, less likely to manifest.

These inorganic NPs are suitable for embedding into the surface of the implants by PEO [27-30]. In addition, these NPs have shown to kill bacteria in various ways, primarily through ion release, but also through contact killing and the formation of reactive oxygen species [31-34]. That said, how exactly inorganic NPs kill bacteria when they are embedded onto implant surfaces is not yet fully understood. Improved knowledge on the mechanism may pave the way for more efficient use of inorganic NPs. This is particularly important when multiple elements are combined because the presence of multiple antibacterial mechanisms would make it more difficult to develop resistance against these antibacterial agents.

In addition to antibacterial properties, multifunctional implants need to enhance bony ingrowth and, thus, the secondary fixation of the implants. The PEO processing of titanium implants using electrolytes based on calcium and phosphate results in implants with osteogenic properties. Interestingly, we observed that hydroxyapatite was formed on porous implants, which constitutes up to 70% of the bone volume [35]. This is most likely due to the altered circulation of the electrolyte and less rapid cooling that can facilitate the local heat treatment during plasma discharges and contribute to the formation of hydroxyapatite [36]. To further improve the osteogenic behavior of PEO biofunctionalized implants, strontium can be added to the PEO electrolyte. Strontium ranelate has been used to treat osteoporotic patients, as it simultaneously stimulates bone formation by osteoblasts and reduces bone resorption by osteoclasts [37-40]. Due to potential adverse cardiac events, systemic treatment with strontium ranelate was terminated [41]. Nonetheless, local administration of strontium requires much lower doses than the systemic intake. The incorporation of strontium onto the implant surface, therefore, represents a promising strategy to take advantage of strontium while preventing the potential side effects [42].

An essential part of osteogenesis is angiogenesis [43]. Without the formation of blood vessels, no mature bone tissue can be formed. The effects of biofunctionalized implants on angiogenesis is a relatively novel research area. That is partially due to the fact that it is relatively difficult to study angiogenesis using regular 2D cell culture systems, and 3D culture systems are still not the gold standard for angiogenic research [44, 45]. Although there are multiple elements known to possess angiogenic properties, not all of them may be suitable for implant biofunctionalization because bony ingrowth needs to be supported as well and infections should be averted [46]. Once again, a combination of multiple elements may be an elegant solution to this challenge.

This thesis focusses on the prevention of IAI. However, most assays and methods to study IAI are focused on the treatment rather than the prevention of infection. This is because it is relatively difficult to study infection prevention. In clinical settings, only 1-9% of implants should become infected [47]. Studying such a rare event would require a formidably large number of specimens to achieve sufficient statistical power. That is why antibacterial assays usually use much higher bacterial loads to establish infections. These conditions are more representative of established infections that need treatment but can be studied using a limited number of specimens. The other limitations of most *in vitro* assays is that the immune system is usually not incorporated into the *in vitro* experiments, meaning that there is no limit for bacterial growth. Furthermore, *in vitro* experiments are usually conducted in growth medium or agar, which is completely different from the actual bone tissue. Although co-culture systems have been developed [48-51], it is still difficult to completely resemble the native bone environment. In this respect, *ex vivo* models may be of interest because the bony matrix, which has shown to affect the bacterial adhesion and pathology [52, 53], is present in such models. However, these models lack an active immune component. Nonetheless, these experiments are much easier and faster to perform than *in vivo* experiments and can, therefore, be used to screen the antibacterial activity of biofunctionalized implants before *in vivo* testing.

The *in vivo* infection models are also generally focused on the treatment rather than the prevention of infections. In order to limit the number of required animals while preserving the statistical power of the experiments, it is necessary to work with controlled and settled infections. Such experimental conditions do not reflect the actual clinical situations faced when trying to prevent (rather than treat) IAI. Creating controlled, settled infections requires much higher doses of bacteria, while also requiring much higher doses of antibacterial agents, which in turn increase the chance of creating cytotoxic effects. Indeed, ethical, financial, and practical concerns make it nearly impossible to directly evaluate the prevention of IAI *in vivo*.

However, to enhance the knowledge gained from a single experiment, additional tools, such as bioluminescent bacteria may be of interest, as they will allow for a much more detailed tracking of infections [54-56]. This may provide a way to study the course of infection also when low numbers of bacteria are present, although the spatial resolution of this method needs to be improved to allow for tracking low numbers or even individual bacteria [57]. Advances in proper infection prevention models are required to accelerate the development of future multifunctional implants.

Prior to the application of multifunctional implants in clinical settings, the implants will need to be tested in larger animal models with physiological and anatomical conditions that are more comparable to those of the human. Then, the implant biofunctionalization needs to be embedded into the implant manufacturing process. PEO is a swift and single-

step process, which can be optimized to require even shorter times than used in this thesis. Keeping in mind that every year 4-12% of the patients receiving implants suffer from some type of complications [58, 59] and given that at least part of these complications may be prevented by using multifunctional implants, it is imperative to further develop such implants to simultaneously improve the treatment of the patients, save healthcare expenses, and reduce the societal burden [60]. Ultimately, the benefits of these implants need to outweigh their costs. The increased cost of manufacturing such multi-functional implants is likely to be more than compensated for by the savings made on the expensive treatments required for addressing the complications arising from implant failures. For example, revision surgeries for aseptic loosening cost €11,000 on average while revision due to infections cost €35-45,000 with some cases surpassing €100,000 of direct costs [61-63]. This results in annual spending of $1.62 billion in the US alone [64], which is projected to increase to $1.85 billion by 2030. These financial and societal costs have motivated urgent calls for effective preventive strategies to reduce IAI [65]. In summary, a wide range of stake-holders including patients, healthcare systems and the society at large would benefit from the prevention of implant complications and lifelong-serving multifunctional implants.

10.3 Future outlook

Scientific research may provide some answers, but above all it leads to more questions. This thesis is no exception. As the topic of this thesis spans a wide range of disciplines, so do the remaining questions. They range from in-depth material research and antibacterial mechanisms to the scalability of the presented approach and how to get the developed implants to patients.

Rational design and additive manufacturing

In this thesis, we demonstrated that porous implants outperform solid implants after surface biofunctionalization. More porous designs and larger implants are expected to enhance this effect even further.

Computer modeling and simulation may be helpful in the rational design of the ideal implant structure and surface. Topology optimization has been used extensively to optimize the design of load-bearing structures. However, the optimal implant shape is not yet known, partially because several factors (*e.g.*, mechanical, mass transport, and biological properties as well as the patient anatomy) need to be simultaneously considered in the design of optimal implants and partially because bone ingrowth changes the mechanical conditions around the implant over time. The next generation of computer models should include the

chemical composition, surface morphology, antibacterial behavior, osteogenic response, and angiogenic properties of the implants to better predict the performance of multifunctional implants. Such models can then be coupled with computational models of the PEO process to optimize the parameters of the surface treatment process.

PEO electrolyte and processing parameters

PEO is a versatile process that can be tailored to obtain the desired properties. The effects of the composition of the electrolyte and processing parameters on the thickness, morphology, and chemical composition, and biological properties of the resulting oxide layer need to be studied in more detail. In addition, PEO biofunctionalization in the DC mode can be investigated to enhance control over the morphology of the oxide layer.

Infection risk of untreated porous implants

Future titanium implants are likely to be much more porous. There are reasons to believe that such volume-porous implants may be at an enhanced risk of infection. However, more (clinical) studies are required to determine whether any such effects actually exist. As many patients may eventually receive volume-porous implants, it is crucial to assess their infection risk beforehand.

Mechanism of antibacterial effect and prevention of bacterial resistance

Understanding the antibacterial mechanism may lead to enhanced antibacterial functionality. Although the underlying working mechanisms of inorganic nanoparticles have been explored, the exact ways through which they kill bacteria when embedded onto implant surfaces are not fully understood. Furthermore, it is unclear how different inorganic elements employ different bacterial mechanisms. A better understanding of these mechanisms may help in preventing the development of bacterial resistance and in securing the prolonged use of such antibacterial agents.

Host response: osteogenesis, angiogenesis, and immune cells

In this thesis, the surface treatments performed in the presented studies did not cause cytotoxicity against human mesenchymal stem cells. Indeed, surfaces bearing strontium stimulated the osteogenic differentiation of mammalian cells. This was primarily investigated within two weeks of cell culture, whereas the effects on late-stage differentiation, matrix mineralization, and maturation of bone tissue are unknown. In addition, the effects of the

generated surfaces on angiogenesis should be studied. Finally, the effects of the presented PEO surfaces on the other types of cells particularly the immune cells need to be further studied. These aspects are also interesting for *in vivo* studies.

Follow-up *in vivo* experiments

Given the *in vivo* results presented in this thesis using the implants biofunctionalized with silver NPs, it remains to be determined whether combinations of silver with copper, zinc, and/or strontium result in synergistic effects *in vivo*. Moreover, the immune response and bone regeneration should be studied in more detail, for instance, through fluorescent labeled-calcium injections and bioluminescent immune cells.

Towards clinical applications

To bring the implants generated in this thesis from the bench to the bedside, several other steps need to be taken. The AM process need to be further developed to increase the speed and decrease the costs associated with the fabrication of large, volume-porous implants. As for the PEO processing, the oxidation time needs to be optimized, since shorter times and parallel treatment of multiple implants are required for scaling up the production capacity and making the PEO process less time-consuming and more cost-effective. Moreover, the multifunctional implants need to be tested in large animal models, such as sheep and dogs, with more human-like physiology, anatomy, and load-bearing conditions. When used in clinical settings, sterilization procedures need to be thoroughly investigated to make sure AM volume-porous implants can be efficiently sterilized. The final designs of antibacterial and osteogenic implants should be initially used in patients who are at a higher risk of infection, such as immunocompromised patients, or in procedures with high infection rates, such as trauma procedures and revision surgeries.

10.4 Concluding remarks

The use of orthopedic implants and, thus, the complications associated with their use, such as aseptic loosening and IAI, are expected to increase. Given the rapid development of antibiotic-resistant bacterial strains, the need for multifunctional implants is higher than ever. Rational design, AM, and surface biofunctionalization form a powerful toolset to create multifunctional implants with a much-increased service life. In this thesis, a framework is presented for the synthesis of potent multifunctional implants that may serve as the first prototypes for the future generation of implants.

REFERENCES

[1] S.M. Ahmadi, R. Hedayati, Y. Li, K. Lietaert, N. Tumer, A. Fatemi, C.D. Rans, B. Pouran, H. Weinans, A.A. Zadpoor, Fatigue performance of additively manufactured meta-biomaterials: The effects of topology and material type, Acta Biomater 65 (2018) 292-304.

[2] R. Huiskes, H. Weinans, B. van Rietbergen, The relationship between stress shielding and bone resorption around total hip stems and the effects of flexible materials, Clinical Orthopaedics and Related Research 274 (1992) 124-134.

[3] P. Rider, Ž. Kačarević, S. Alkildani, S. Retnasingh, R. Schnettler, M. Barbeck, Additive Manufacturing for Guided Bone Regeneration: A Perspective for Alveolar Ridge Augmentation, International Journal of Molecular Sciences 19 (2018).

[4] S. Van Bael, Y.C. Chai, S. Truscello, M. Moesen, G. Kerckhofs, H. Van Oosterwyck, J.P. Kruth, J. Schrooten, The effect of pore geometry on the in vitro biological behavior of human periosteum-derived cells seeded on selective laser-melted Ti6Al4V bone scaffolds, Acta Biomater 8(7) (2012) 2824-34.

[5] S. Truscello, G. Kerckhofs, S. Van Bael, G. Pyka, J. Schrooten, H. Van Oosterwyck, Prediction of permeability of regular scaffolds for skeletal tissue engineering: A combined computational and experimental study, Acta Biomaterialia 8(4) (2012) 1648-1658.

[6] J.M. Laffosse, Removal of well-fixed fixed femoral stems, Orthopaedics & Traumatology: Surgery & Research 102(1) (2016) S177-S187.

[7] K. Merritt, J.W. Shafer, S.A. Brown, Implant site infection rates with porous and dense materials, Journal of Biomedical Materials Research 13 (1979).

[8] L.F. Dumée, L. He, B. Lin, F.-M. Ailloux, J.-B. Lemoine, L. Velleman, F. She, M.C. Duke, J.D. Orbell, G. Erskine, P.D. Hodgson, S. Gray, L. Kong, The fabrication and surface functionalization of porous metal frameworks – a review, Journal of Materials Chemistry A 1(48) (2013).

[9] R. Chaharmahali, A. Fattah-alhosseini, K. Babaei, Surface characterization and corrosion behavior of calcium phosphate (Ca-P) base composite layer on Mg and its alloys using plasma electrolytic oxidation (PEO): A review, Journal of Magnesium and Alloys 9(1) (2021) 21-40.

[10] A. Santos-Coquillat, E. Martínez-Campos, M. Mohedano, R. Martínez-Corriá, V. Ramos, R. Arrabal, E. Matykina, In vitro and in vivo evaluation of PEO-modified titanium for bone implant applications, Surface and Coatings Technology 347 (2018) 358-368.

[11] K. Leśniak-Ziółkowska, A. Kazek-Kęsik, K. Rokosz, S. Raaen, A. Stolarczyk, M. Krok-Borkowicz, E. Pamuła, W. Simka, Plasma electrolytic oxidation as an effective tool for production of copper incorporated bacteriostatic coatings on Ti-15Mo alloy, Applied Surface Science 563 (2021).

[12] M. Rizwan, R. Alias, U.Z. Zaidi, R. Mahmoodian, M. Hamdi, Surface modification of valve metals using plasma electrolytic oxidation for antibacterial applications: A review, J Biomed Mater Res A 106(2) (2018) 590-605.

[13] Z. Gorgin Karaji, R. Hedayati, B. Pouran, I. Apachitei, A.A. Zadpoor, Effects of plasma electrolytic oxidation process on the mechanical properties of additively manufactured porous biomaterials, Mater Sci Eng C Mater Biol Appl 76 (2017) 406-416.

[14] A.R. Mahoney, M.M. Safaee, W.M. Wuest, A.L. Furst, The silent pandemic: Emergent antibiotic resistances following the global response to SARS-CoV-2, iScience 24(4) (2021).

[15] G. Vimbela, S.M. Ngo, C. Fraze, L. Yang, D.A. Stout, Antibacterial properties and toxicity from metallic nanomaterials, International Journal of Nanomedicine Volume 12 (2017) 3941-3965.

[16] A. Díez-Pascual, Antibacterial Activity of Nanomaterials, Nanomaterials 8(6) (2018).

[17] L. Wang, C. Hu, L. Shao, The antimicrobial activity of nanoparticles: present situation and prospects for the future, Int J Nanomedicine 12 (2017) 1227-1249.

[18] S.L. Percival, J. Thomas, S. Linton, T. Okel, L. Corum, W. Slone, The antimicrobial efficacy of silver on antibiotic-resistant bacteria isolated from burn wounds, International Wound Journal 9 (2011) 488-493.

[19] F. Pietsch, A.J. O'Neill, A. Ivask, H. Jenssen, J. Inkinen, A. Kahru, M. Ahonen, F. Schreiber, Selection of resistance by antimicrobial coatings in the healthcare setting, Journal of Hospital Infection 106(1) (2020) 115-125.

[20] L. Sibleyras, M. Vos, L. Sibleyras, L.K. Lo, E. Hesse, W. Gaze, U. Klümper, Zinc can counteract selection for ciprofloxacin resistance, FEMS Microbiology Letters 367(3) (2020).

[21] M. Muller, Bacterial silver resistance gained by cooperative interspecies redox behavior, Antimicrobial Agents and Chemotherapy 62 (2018) e00672-18.

[22] S.L. Percival, P.G. Bowler, D. Russell, Bacterial resistance to silver in wound care, J Hosp Infect 60(1) (2005) 1-7.

[23] B.M. Staehlin, J.G. Gibbons, A. Rokas, T.V. O'Halloran, J.C. Slot, Evolution of a heavy metal homeostasis/resistance island reflects increasing copper stress in Enterobacteria, Genome Biology and Evolution (2016).

[24] J.W. Mouton, Combination therapy as a tool to prevent emergence of bacterial resistance, Infection 27 (1999) S24-S28.

[25] R.J. Worthington, C. Melander, Combination approaches to combat multidrug-resistant bacteria, Trends Biotechnol 31(3) (2013) 177-84.

[26] G. Courtemanche, R. Wadanamby, A. Kiran, L.F. Toro-Alzate, M. Diggle, D. Chakraborty, A. Blocker, M. van Dongen, Looking for Solutions to the Pitfalls of Developing Novel Antibacterials in an Economically Challenging System, Microbiology Research 12(1) (2021) 173-185.

[27] O. Oleshko, I. Liubchak, Y. Husak, V. Korniienko, A. Yusupova, T. Oleshko, R. Banasiuk, M. Szkodo, I. Matros-Taranets, A. Kazek-Kesik, W. Simka, M. Pogorielov, In Vitro Biological Characterization of Silver-Doped Anodic Oxide Coating on Titanium, Materials (Basel) 13(19) (2020).

[28] X. Yao, X. Zhang, H. Wu, L. Tian, Y. Ma, B. Tang, Microstructure and antibacterial properties of Cu-doped TiO2 coating on titanium by micro-arc oxidation, Applied Surface Science 292 (2014) 944-947.

[29] X. Zhang, J. Li, X. Wang, Y. Wang, R. Hang, X. Huang, B. Tang, P.K. Chu, Effects of copper nanoparticles in porous TiO2 coatings on bacterial resistance and cytocompatibility of osteoblasts and endothelial cells, Mater Sci Eng C Mater Biol Appl 82 (2018) 110-120.

[30] O. Oleshko, Y. Husak, V. Korniienko, R. Pshenychnyi, Y. Varava, O. Kalinkevich, M. Pisarek, K. Grundsteins, O. Pogorielova, O. Mishchenko, W. Simka, R. Viter, M. Pogorielov, Biocompatibility and Antibacterial Properties of ZnO-Incorporated Anodic Oxide Coatings on TiZrNb Alloy, Nanomaterials 10(12) (2020).

[31] J. Wang, J. Li, G. Guo, Q. Wang, J. Tang, Y. Zhao, H. Qin, T. Wahafu, H. Shen, X. Liu, X. Zhang, Silver-nanoparticles-modified biomaterial surface resistant to staphylococcus: new insight into the antimicrobial action of silver, Sci Rep 6 (2016) 32699.

[32] G. Applerot, A. Lipovsky, R. Dror, N. Perkas, Y. Nitzan, R. Lubart, A. Gedanken, Enhanced antibacterial activity of nanocrystalline ZnO due to increased ROS-mediated cell injury, Adv. Funct. Mater. 19 (2009) 842-852.

[33] A. Nagy, A. Harrison, S. Sabbani, R.S. Munson, P. Dutta, W.J. Waldman, Silver nanoparticles embedded in zeolite membranes: release of silver ions and mechanism of antibacterial action, International Journal of Nanomedicine (2011).

[34] G. Applerot, J. Lellouche, A. Lipovsky, Y. Nitzan, R. Lubart, A. Gedanken, E. Banin, Understanding the antibacterial mechanism of CuO nanoparticles: revealing the route of induced oxidative stress, Small 8(21) (2012) 3326-37.

[35] A.L. Boskey, Bone composition: relationship to bone fragility and antiosteoporotic drug effects, BoneKEy Reports 2 (2013).

[36] I.M. Pohrelyuk, R.V. Proskurnyak, O.V. Tкachuk, Y.V. Obukh, Formation of Hydroxyapatite Coatings on Titanium by Plasma-Electrolytic Oxidation in Alkaline Electrolytes, Materials Science 55(4) (2020) 563-568.

[37] J.-Y. Reginster, D. Felsenberg, S. Boonen, A. Diez-Perez, R. Rizzoli, M.-L. Brandi, T.D. Spector, K. Brixen, S. Goemaere, C. Cormier, A. Balogh, P.D. Delmas, P.J. Meunier, Effects of long-term strontium ranelate treatment on the risk of nonvertebral and vertebral fractures in postmenopausal osteoporosis: Results of a five-year, randomized, placebo-controlled trial, Arthritis & Rheumatism 58(6) (2008) 1687-1695.

[38] W. Querido, M. Farina, K. Anselme, Strontium ranelate improves the interaction of osteoblastic cells with titanium substrates: Increase in cell proliferation, differentiation and matrix mineralization, Biomatter 5(1) (2015).

[39] M. Pilmane, K. Salma-Ancane, D. Loca, J. Locs, L. Berzina-Cimdina, Strontium and strontium ranelate: Historical review of some of their functions, Materials Science and Engineering: C 78 (2017) 1222-1230.

[40] A.D. Bakker, B. Zandieh-Doulabi, J. Klein-Nulend, Strontium Ranelate affects signaling from mechanically-stimulated osteocytes towards osteoclasts and osteoblasts, Bone 53(1) (2013) 112-119.

[41] J.Y. Reginster, Cardiac concerns associated with strontium ranelate, Expert Opin Drug Saf 13(9) (2014) 1209-13.

[42] O.Z. Andersen, V. Offermanns, M. Sillassen, K.P. Almtoft, I.H. Andersen, S. Sørensen, C.S. Jeppesen, D.C.E. Kraft, J. Bøttiger, M. Rasse, F. Kloss, M. Foss, Accelerated bone ingrowth by local delivery of strontium from surface functionalized titanium implants, Biomaterials 34(24) (2013) 5883-5890.

[43] A. Grosso, M.G. Burger, A. Lunger, D.J. Schaefer, A. Banfi, N. Di Maggio, It Takes Two to Tango: Coupling of Angiogenesis and Osteogenesis for Bone Regeneration, Frontiers in Bioengineering and Biotechnology 5 (2017).

[44] C.A. Staton, M.W.R. Reed, N.J. Brown, A critical analysis of current in vitro and in vivo angiogenesis assays, International Journal of Experimental Pathology 90(3) (2009) 195-221.

[45] V. Mastrullo, W. Cathery, E. Velliou, P. Madeddu, P. Campagnolo, Angiogenesis in Tissue Engineering: As Nature Intended?, Frontiers in Bioengineering and Biotechnology 8 (2020).

[46] M. Salandova, I.A.J. van Hengel, I. Apachitei, A.A. Zadpoor, B.C.J. van der Eerden, L.E. Fratila-Apachitei, Inorganic Agents for Enhanced Angiogenesis of Orthopedic Biomaterials, Adv Healthc Mater (2021) e2002254.

[47] W. Zimmerli, Clinical presentation and treatment of orthopaedic implant-associated infection, J Intern Med 276(2) (2014) 111-9.

[48] B.L. Foss, N. Ghimire, R. Tang, Y. Sun, Y. Deng, Bacteria and osteoblast adhesion to chitosan immobilized titanium surface: A race for the surface, Colloids and Surfaces B: Biointerfaces 134 (2015) 370-376.

[49] V.T.H. Pham, V.K. Truong, A. Orlowska, S. Ghanaati, M. Barbeck, P. Booms, A.J. Fulcher, C.M. Bhadra, R. Buividas, V. Baulin, C.J. Kirkpatrick, P. Doran, D.E. Mainwaring, S. Juodkazis, R.J. Crawford, E.P. Ivanova, "Race for the Surface": Eukaryotic Cells Can Win, ACS Applied Materials & Interfaces 8(34) (2016) 22025-22031.

[50] S. Zaatreh, K. Wegner, M. Strauß, J. Pasold, W. Mittelmeier, A. Podbielski, B. Kreikemeyer, R. Bader, Co-Culture of S. epidermidis and Human Osteoblasts on Implant Surfaces: An Advanced In Vitro Model for Implant-Associated Infections, Plos One 11(3) (2016).

[51] S.D. Zoller, V. Hegde, Z.D.C. Burke, H.Y. Park, C.R. Ishmael, G.W. Blumstein, W. Sheppard, C. Hamad, A.H. Loftin, D.O. Johansen, R.A. Smith, M.M. Sprague, K.R. Hori, S.J. Clarkson, R. Borthwell, S.I. Simon, J.F. Miller, S.D. Nelson, N.M. Bernthal, Evading the host response: Staphylococcus "hiding" in cortical bone canalicular system causes increased bacterial burden, Bone Research 8(1) (2020).

[52] M.C. Hudson, W.K. Ramp, K.P. Frankenburg, Staphylococcus aureus adhesion to bone matrix and bone-associated biomaterials, FEMS Microbiology Letters 173 (1999) 2790284.

[53] K.L. Urish, J.E. Cassat, K.M. Ottemann, Staphylococcus aureus Osteomyelitis: Bone, Bugs, and Surgery, Infection and Immunity 88(7) (2020).

[54] J.A. Niska, J.A. Meganck, J.R. Pribaz, J.H. Shahbazian, E. Lim, N. Zhang, B.W. Rice, A. Akin, R.I. Ramos, N.M. Bernthal, K.P. Francis, L.S. Miller, Monitoring bacterial burden, inflammation and bone damage longitudinally using optical and muCT imaging in an orthopaedic implant infection in mice, PLoS One 7(10) (2012) e47397.

[55] R.J. Miller, J.M. Thompson, J. Zheng, M.C. Marchitto, N.K. Archer, B.L. Pinsker, R.V. Ortines, X. Jiang, R.A. Martin, I.D. Brown, Y. Wang, R.S. Sterling, H.Q. Mao, L.S. Miller, In Vivo Bioluminescence Imaging in a Rabbit Model of Orthopaedic Implant-Associated Infection to Monitor Efficacy of an Antibiotic-Releasing Coating, J Bone Joint Surg Am 101(4) (2019) e12.

[56] J.M. Thompson, L.S. Miller, Preclinical Optical Imaging to Study Pathogenesis, Novel Therapeutics and Diagnostics Against Orthopaedic Infection, Journal of Orthopaedic Research 37(11) (2019) 2269-2277.

[57] P. Avci, M. Karimi, M. Sadasivam, W.C. Antunes-Melo, E. Carrasco, M.R. Hamblin, In-vivo monitoring of infectious diseases in living animals using bioluminescence imaging, Virulence 9(1) (2017) 28-63.

[58] S.M. Heo, I. Harris, J. Naylor, A.M. Lewin, Complications to 6 months following total hip or knee arthroplasty: observations from an Australian clinical outcomes registry, BMC Musculoskelet Disord 21(1) (2020) 602.

[59] P.J. Belmont, Jr., G.P. Goodman, B.R. Waterman, J.O. Bader, A.J. Schoenfeld, Thirty-day postoperative complications and mortality following total knee arthroplasty: incidence and risk factors among a national sample of 15,321 patients, J Bone Joint Surg Am 96(1) (2014) 20-6.

[60] M.T. Trentinaglia, C. Van Der Straeten, I. Morelli, N. Logoluso, L. Drago, C.L. Romanò, Economic Evaluation of Antibacterial Coatings on Healthcare Costs in First Year Following Total Joint Arthroplasty, The Journal of Arthroplasty 33(6) (2018) 1656-1662.

[61] R.F. Kallala, I.S. Vanhegan, M.S. Ibrahim, S. Sarmah, F.S. Haddad, Financial analysis of revision knee surgery based on NHS tariffs and hospital costs, The Bone and Joint Journal 97-B (2014) 197-201.

[62] T. Puhto, A.P. Puhto, M. Vielma, H. Syrjala, Infection triples the cost of a primary joint arthroplasty, Infect Dis (Lond) 51(5) (2019) 348-355.

[63] S.M. Kurtz, E. Lau, J. Schmier, K.L. Ong, K. Zhao, J. Parvizi, Infection burden for hip and knee arthroplasty in the United States, J Arthroplasty 23(7) (2008) 984-91.

[64] S.M. Kurtz, E. Lau, H. Watson, J.K. Schmier, J. Parvizi, Economic burden of periprosthetic joint infection in the United States, J Arthroplasty 27(8 Suppl) (2012) 61-5 e1.

[65] A. Premkumar, D.A. Kolin, K.X. Farley, J.M. Wilson, A.S. McLawhorn, M.B. Cross, P.K. Sculco, Projected Economic Burden of Periprosthetic Joint Infection of the Hip and Knee in the United States, J Arthroplasty 36(5) (2021) 1484-1489 e3.

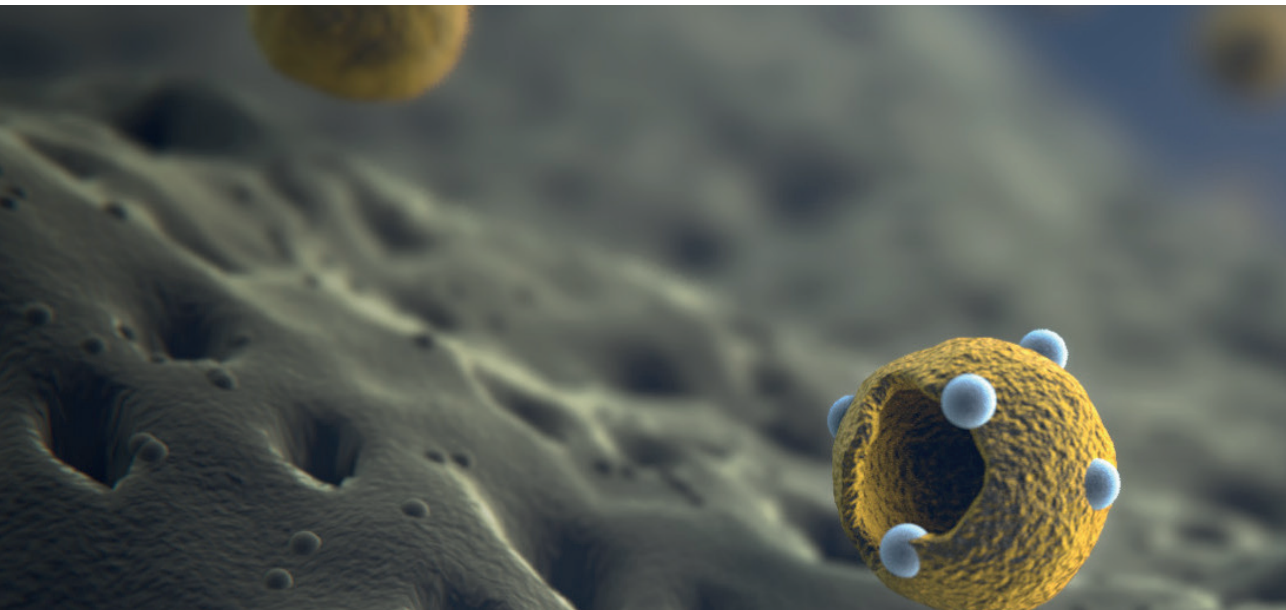

ADDENDA

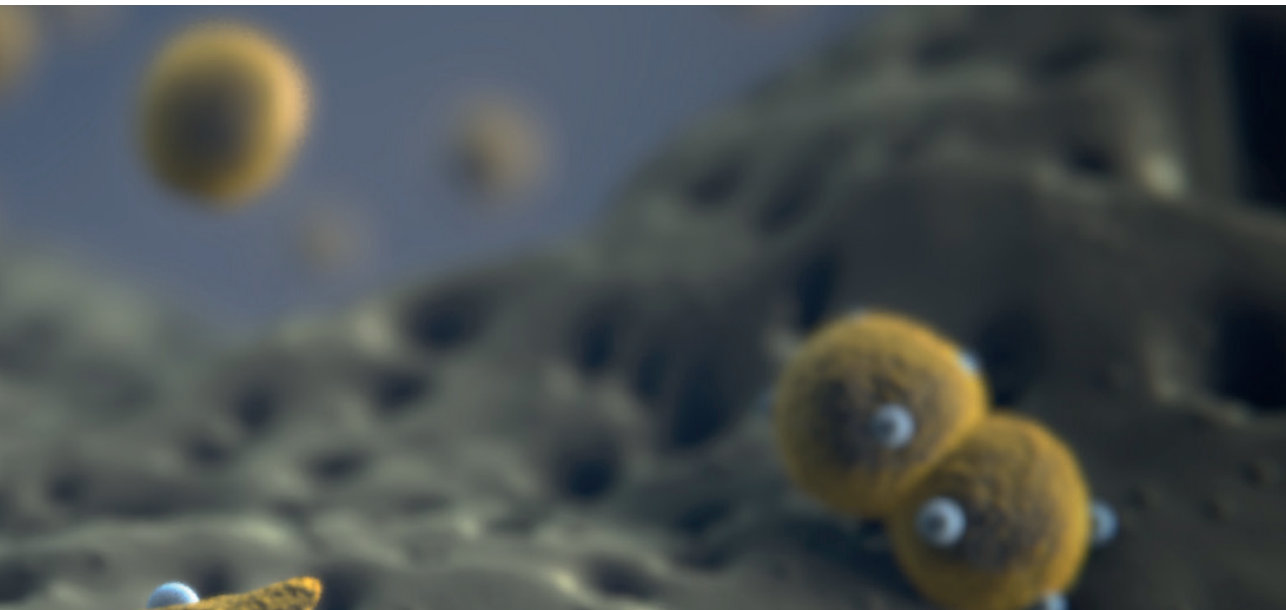

Acknowledgements

During my PhD I have had help from numerous people, without whom I would not have been able to accomplish this work.

Allereerst ben ik prof. **Amir Zadpoor** dankbaar die mij deze promotieplek heeft aangeboden. Beste Amir, dank voor je begeleiding en onvoorwaardelijke support. Toen ik aangaf dat ik het leuk zou vinden om studenten te begeleiden kreeg ik al op dag 1 van mijn promotietraject studenten van je doorgestuurd. Het onderstreept je mentaliteit van doorpakken, wat ook blijkt uit het feit dat we altijd in het Nederlands gecommuniceerd hebben. Je gaf aan dat je goede mensen aannam en die verder vrij liet om te doen wat zij dachten dat goed was. Dit heb ik als ontzettend prettig ervaren. Ik hoefde daarbij nooit te introduceren waar ik mee bezig was, zelfs niet als het om kleine details ging. Daarnaast heb ik ook enorm veel van je geleerd, bijvoorbeeld wat betreft het publiceren van artikelen en creatief denken bij het opzetten van experimenten.

I owe enormous gratitude to my co-promotor dr. **Iulian Apachitei**. Dear Iulian, we got to know each other a long time ago when I started the master program in Biomedical Engineering. Thanks to your enthusiasm I decided to start the master thesis in this field and follow-up with a PhD project. You are one of the kindest persons I know and you always supported me in any way possible. I appreciated the long discussions we had in your office both on scientific topics and daily life in general. I benefitted greatly from your wide scientific knowledge and you kept me focused when it was necessary. Your door was always open, even though you were extremely busy, which is something I appreciated tremendously. I also greatly enjoyed supervising students together with you, we always had fruitful and fun meetings, and thanks to your help many students have conducted a great master thesis under our supervision. Thank you for everything you have done for me in all those years.

Where there is Iulian, dr. **Lidy Fratila-Apachitei** is never far away. Dear Lidy, thank you for the many ways that you have helped me during my PhD research. You have done a tremendous job with facilitating the cell culture lab and helping me with my cell culture experiments. You have a good eye for setting up experiments and also provided me with highly talented students for our projects. I enjoyed the discussions we had about ongoing projects and the meetings we had outside our research group. Also, you gave great feedback on my manuscripts and helped many papers pass the revisions. In addition you encouraged me to present my work at scientific conferences and involved me in teaching activities. I very much enjoyed working with you.

During my PhD I was also supported by highly skilled technical personnel. **Sander**, dank voor al je hulp bij het uitvoeren van mijn experimenten. Ik heb enorm genoten van het ontwerpproces, waarbij een simpele schets uiteindelijk leidde tot een mooi implantaat.

Je droge humor hielp om de meetings luchtig te houden. **Michelle**, dank voor al je hulp bij het uitvoeren en plannen van de cel experimenten. Het was altijd gezellig en heel erg prettig samenwerken. Het was fijn om 'biologie' te kunnen praten in een technische groep en frustraties over bepaalde assays en experimenten te kunnen delen. **Ruud**, bedankt voor de XRD analyses. **Michel**, dank voor het uitvoeren van de ICP-OES metingen. **Sabrina, Angelique, Marjolijn, Adinda, Hanneke** en **Mirjam** bedankt voor jullie organisatorische ondersteuning en leuke verhalen in jullie kantoor. Dank aan prof. **Dirk-Jan Veeger** voor de ondersteuning en hulp tijdens de coronapandemie in het laatste jaar.

Parts of the research in this thesis have been conducted outside the TU Delft. The antibacterial experiments were conducted at the UMC Utrecht in the department of medical microbiology in collaboration with the department of orthopedics in collaboration with dr. **Ad Fluit** and prof. **Harrie Weinans**. Beste Ad, zelden heb ik zo'n relaxt en humoristisch persoon in de wetenschap ontmoet als jij. Jouw inzet heeft enorm bijgedragen aan de antibacteriële resultaten in dit onderzoek. Beste Harrie, dank voor de interessante meetings en hulp bij het uitvoeren van de *in vivo* experimenten in Utrecht. Thanks to dr. **Saber Amin Yavari** for involving me early on with the experiments in the UMCU and the good company at the EORS conference and prosperos meetings. **Michiel**, **Bruce, Fred** en **Ruben**, bedankt voor jullie hulp bij de operaties. Zonder jullie inbreng was het laatste hoofdstuk van dit proefschrift er niet gekomen. De goede gesprekken en discussies maakten de lange dagen op de OK een stuk lichter. Daarnaast wil ik **Barry**, **Wilco** en **Daphne** bedanken voor hun technische ondersteuning. **Marco**, bedankt voor de hulp met de magnalyzer en de ondersteuning van studenten die op het lab aan het werk waren. **Jelle**, het werk is veel aangenamer als je een goede gesprekspartner naast je hebt zitten op de bench. Dank ook aan dr. **Sebastian Zaat**, **Martijn** en **Leonie** van het AMC voor hun hulp bij het uitvoeren van de microbiologische experimenten aldaar.

Another part was performed at the Erasmus MC in Rotterdam in the department of internal medicine with dr. **Bram van der Eerden**. Beste Bram, dank voor al die jaren samenwerking. Met veel plezier ging ik altijd naar onze meetings en ik ben ook dankbaar dat je altijd maar plek en tijd had voor de talloze studenten die vanuit Delft naar jullie lab in het Erasmus MC kwamen. Je enorme wetenschappelijke kennis heeft bijgedragen aan vele artikelen in dit proefschrift. Dank ook aan **Marijke** voor het trainen en technische ondersteuning van studenten. Thanks to dr. **Eric Farrell** and **Janneke** for their efforts and help with cytotoxicity and histology experiments. Your help and clear analysis were greatly appreciated.

During my PhD I have greatly enjoyed the company of fellow people in our group. First of all I would like to thank my office buddies for the many hours we spent behind our desks

talking, laughing, discussing, complaining and occasionally working. We were fortunate enough to have an office at the end of the corridor and I think many envied us for the relatively large office we had. **Costanza**, we started at the same day and became office buddies from the second month. It was nice to share happiness and complaints about whatever topic, and I have had so many good laughs, often about our misunderstandings. **Bob**, je was een hele prettige kantoorgenoot die rust bracht in het kantoor maar ook altijd in was voor een praatje. We konden lang discussiëren over de wetenschap in het algemeen en je hebt kennis van vele zaken. Ik heb bewondering hoe je hebt doorgezet en hoop dat je nog vele jaren prettig zult kunnen werken in ons kantoor. **Steven**, je was er niet vaak, maar als je er was dan was dat te merken. Zelden heb ik zoveel gelachen met iemand. Je bent een bijzonder persoon en ik heb veel respect dat je hebt doorgezet en met succes je promotietraject hebt afgesloten. Thanks also to my first roommates **Mohammad Ahmadi** and **Nazli** for giving me a warm welcome in the group. Mohammad, it was interesting to follow your story about combining entrepreneurship and science. Nazli, it was always great to meet you in the corridor, "hellloooooooo", and talk with you in good spirits about whatever topic.

Over the years our group has expanded enormously and it has been great to be part of such a fun group of people. Thanks to **Eric, Fabian, Helda, Jiahui, Katerina, Kirsten, Livia, Mahdiyeh, Mahya, Marike, Maryam, Mauricio, Merle, Pedro, Pier, Sara** and **Teunis** for the many lunches, coffees, cakes, drinks, dinners, parties and random encounters in the hallways of the faculty during the years. **Sebastien**, mijn scientific twin, ik ken denk ik niemand die zo gepassioneerd is voor de wetenschap als jij. Je bent ontzettend gezellig, meelevend en bevlogen en we hebben altijd leuk kunnen praten over van alles en nog wat. Het was geweldig om met jou presentaties te mogen geven bij Bessensap en Universiteit van Nederland. **Eline**, mijn Prosperos buddy, we hebben samen vele meetings bezocht en dat was altijd gezellig. We hebben doorgezet om naar buitenlandse conferenties te mogen en het was leuk dat we naar de MRS meeting in Phoenix ("Arizeuna!") gingen, waar we killerbees en onverstaanbare presentaties met ongelofelijk lelijke layouts en kauwgom kauwende presentatoren doorstaan hebben. **Françoise**, je bent een van de meest zorgzame mensen die ik ken. Als er wat geregeld moest worden voor een collega dan stond jij altijd als eerste klaar. Ik vond het altijd erg gezellig om even je kantoor binnen te lopen en een praatje te maken, waar ik dan vaak heel lang bleef hangen. **Khashayar**, ik schrijf dit in het Nederlands om je dit al erg goed kunt. Ik vind het heel knap hoe je je deze taal eigen hebt gemaakt. We hebben vele gesprekken gehad over Bergkamp, Iraanse en Nederlandse gewoonten maar ook over onze promotieonderwerpen die dicht bij elkaar lagen. Dankzij jouw voorspellingen ga je nu als "het Orakel" door het leven, "in Koeman we trust." Niet te vergeten, dank voor je hulp bij het voltooien van de experimenten in Utrecht. **Niko**, I got to know you when you did a master thesis under

supervision of Iulian and me. When I first met you I thought you were Dutch and it took me a while before I understood that you did not get a word of what I had been saying. You were always positive and never bothered by the cold, even when everyone else was. **Juan**, it was great fun to visit football games and go to parties, although I am not sure you remember all of them. Thank you also for the invitation for the football matches at the sport center. **Yageng**, it was nice to hang around with you in the lab. You are the biggest fan of krentenbollen I know. Thank you for organizing a delicious Chinese dinner, sharing good beers and playing some pingpong matches. I hope you will get the chance to visit Yangshuo soon. **Shahram**, mijn allerbeste vriend, toch? **Mohammad Mirzaali**, you are by far the most cheeky colleague. You always had interesting stories to share and I greatly enjoyed our random encounters in the corridor. Thanks to the exchange PhD and master students **Ezgi, Andrea** and **Mohammad** for the good times. **Niklas**, thanks for the great company, teaching us unspeakable Danish words and of course the evenings in Doerak.

The 3ME faculty is a great place to randomly run into people. **Remko**, we hebben tijdens de afgelopen jaren heel wat loopjes gedaan en dankzij jou heb ik zelfs mijn debuut kunnen maken voor Feijenoord. **Pavlo**, I do not remember during which graduate course we met exactly, because there have been many. I still do not know how you manage to combine being a serious triathlete and many, many travels with performing research, and even doing it well. **Jinne** and **Akash**, it was nice to catch up with you during chill coffee breaks.

During my PhD I participated in multiple conferences and summer schools. Thanks to team Continue!, **Stefan, Karina, Samzon, Pierre, Julian** and **prof**. **Martin Heinze** for an amazing experience in Berlin and Grenoble during the ClinMed summer school. **Stefano**, great to have met you at the Advanced Leadership workshop in Lecco and share experiences about USA and Italy.

During my PhD I have been given the opportunity to supervise master students during their thesis projects. **Stefanos**, you did a great job with performing cell culture experiments at the Erasmus MC without having any prior experience. **Vito,** ik herinner me nog de hilarische vraag van een van je vrienden bij het afstuderen of we niet bang waren dat die implantaten met zilver gestolen zouden worden, waar jij vervolgens een keurig wetenschappelijk antwoord op gaf. **Francisca,** jij had een enorme drive om onderzoek te doen en ik hoop dat je in de toekomst verder kunt in het onderzoek. **Niko,** you were very independent and extremely skilled in the lab. I was very happy that you were offered a PhD position in our group during the master thesis ceremony. **Melissa,** jij was niet op je mondje gevallen en was enorm goed in het managen van je eigen master thesis, met geweldig resultaat, was gezellig! **Munzur,** je hebt geweldig snel de methoden in ons lab eigen gemaakt en grotendeels zelfstandig je afstuderen gedaan. Ben benieuwd hoe je nu reageert als iemand vraagt hoe je weekend was. **Raisa,**

jouw onderzoek was geen makkelijk onderwerp, maar dat heb je knap tot een geheel weten te vormen. **Monika**, you were very passionate about research and did a tremendous job by publishing the literature review. It is great that you will continue as a PhD student in our group. **Noa**, jouw project was zeer uitdagend dankzij de uitbraak van de pandemie. Desondanks heb je doorgezet en heb je uiteindelijk afgerond met een fantastische verdediging. It was a great experience for me to supervise all of you during your thesis projects and I am happy that your contributions have resulted in co-authorship on multiple journal and conference publications.

,

List of publications

Publications

I.A.J. van Hengel, M. Riool, L.E. Fratila-Apachitei, J. Witte-Bouma, E. Farrell, A.A. Zadpoor, S.A.J. Zaat, I. Apachitei, Selective laser melting porous metallic implants with immobilized silver nanoparticles kill and prevent biofilm formation by methicillin-resistant *Staphylococcus aureus*, Biomaterials 140 (2017) 1-15.

I.A.J. van Hengel, M. Riool, L.E. Fratila-Apachitei, J. Witte-Bouma, E. Farrell, A.A. Zadpoor, S.A.J. Zaat, I. Apachitei, Data on the surface morphology of additively manufactured Ti-6Al-4V implants during processing by plasma electrolytic oxidation, Data in Brief 13 (2017) 385-389.

M. Baroncelli, B.C.J. van der Eerden, S. Chatterji, E. Rull Trinidad, Y.Y. Kan, M. Koedam, **I.A.J. van Hengel**, R. Alves, L.E. Fratila-Apachitei, J.A.A. Demmers, J. van de Peppel, J. van Leeuwen, Human Osteoblast-Derived Extracellular Matrix with High Homology to Bone Proteome Is Osteopromotive, Tissue Engineering Part A 24 (2018) 1377-1389.

M. Croes, S. Bakhshandeh, **I.A.J. van Hengel**, K. Lietaert, K.P.M. van Kessel, B. Pouran, B.C.H. van der Wal, H.C. Vogely, W. Van Hecke, A.C. Fluit, C.H.E. Boel, J. Alblas, A.A. Zadpoor, H. Weinans, S. Amin Yavari, Antibacterial and immunogenic behavior of silver coatings on additively manufactured porous titanium, Acta Biomaterialia 81 (2018) 315-327.

I.A.J. van Hengel, M.W.A.M. Tierolf, V.P.M. Valerio, M. Minneboo, A.C. Fluit, L.E. Fratila-Apachitei, I. Apachitei, A.A. Zadpoor, Self-defending additively manufactured bone implants bearing silver and copper nanoparticles, J Mater Chem B 8(8) (2020) 1589-1602.

I.A.J. van Hengel, N.E. Putra, M.W.A.M. Tierolf, M. Minneboo, A.C. Fluit, L.E. Fratila-Apachitei, I. Apachitei, A.A. Zadpoor, Biofunctionalization of selective laser melted porous titanium using silver and zinc nanoparticles to prevent infections by antibiotic-resistant bacteria, Acta Biomaterialia 107 (2020) 325-337.

I.A.J. van Hengel, F.S.A. Gelderman, S. Athanasiadis, M. Minneboo, H. Weinans, A.C. Fluit, B.C.J. van der Eerden, L.E. Fratila-Apachitei, I. Apachitei, A.A. Zadpoor, Functionality-packed additively manufactured porous titanium implants, Materials Today Bio 7 (2020) 100060.

M. Fazel, H.R. Salimijazi, M. Shamanian, M. Minneboo, K. Modaresifar, **I.A.J. van Hengel**, L.E. Fratila-Apachitei, I. Apachitei, A.A. Zadpoor, Osteogenic and antibacterial surfaces on additively manufactured porous Ti-6Al-4V implants: Combining silver nanoparticles with hydrothermally synthesized HA nanocrystals, Materials Science & Engineering C 120 (2021) 111745.

I.A.J. van Hengel, M. Laçin, M. Minneboo, L.E. Fratila-Apachitei, I. Apachitei, A.A. Zadpoor, The effects of plasma electrolytically oxidized layers containing Sr and Ca on the osteogenic behavior of selective laser melted Ti6Al4V porous implants, Materials Science & Engineering C 124 (2021) 112074.

I.A.J. van Hengel, M. Tierolf, L.E. Fratila-Apachitei, I. Apachitei, A.A. Zadpoor, Antibacterial Titanium Implants Biofunctionalized by Plasma Electrolytic Oxidation with Silver, Zinc, and Copper: A Systematic Review, International Journal of Molecular Sciences 22 (2021).

M. Šalandová, **I.A.J. van Hengel**, I. Apachitei, A.A. Zadpoor, B.C.J. van der Eerden, L.E. Fratila-Apachitei, Inorganic Agents for Enhanced Angiogenesis of Orthopedic Biomaterials, Advanced Healthcare Materials (2021) e2002254.

S.J.P. Callens, D. Fan, **I.A.J. van Hengel**, M. Minneboo, L.E. Fratila-Apachitei, A.A. Zadpoor, Emergent collective organization of bone cells in complex curvature fields (2020), in revision, preprint available on bioRxiv.

H. San, M. Paresoglou, M. Minneboo, **I.A.J. van Hengel**, A. Yilmaz, Y. Gonzalez-Garcia, J. Hu, S. Tang, A.C. Fluit, P.L. Hagedoorn, L.E. Fratila-Apachitei, I. Apachitei, A.A. Zadpoor, Additively manufactured porous titanium implants bio-functionalized with reduced graphene oxide and silver nanoparticles, submitted

I.A.J. van Hengel, B. van Dijk, K. Modaresifar, J.F.F. Hooning van Duyvenbode, F. Ruben H.A. Nurmohamed, M.A. Leeflang, A.C. Fluit, L.E. Fratila-Apachitei, I. Apachitei, H. Weinans, A.A. Zadpoor, Porous titanium implants biofunctionalized by plasma electrolytic oxidation to prevent infection by MRSA in a rat tibia infection model, submitted

L. Pontiggia, **I.A.J. van Hengel***, A. Klar, A. Scheidegger, S. Figi, E. Reichmann, U. Moehrlen, T. Biedermann, Bio-printing and plastic compression of large pigmented and vascularized human dermo-epidermal skin substitutes by means of a new robotic platform, Journal of Tissue Engineering 13 (2022).

*Shared first author

Conference presentations

Oral presentations

I.A.J. van Hengel, Strategies to prevent biofilm formation on additive manufactured metal implants, European Orthopaedic Research Society Meeting, September 2017, Munich, Germany

I.A.J. van Hengel, N.E. Putra, M.W.A.M. Tierolf, F.S.A. Gelderman, V.P.M. Valerio, S. Athanasiadis, R.M. Grotenhuis, A.C. Fluit, B.C.J. van der Eerden, L.E. Fratila-Apachitei, I. Apachitei and A.A. Zadpoor, Self-defending implants, Dutch Bio-Medical Engineering Conference, January 2019, Egmond aan Zee, The Netherlands

I.A.J. van Hengel, N.E. Putra, M.W.A.M. Tierolf, M. Minneboo, A.C. Fluit, H. Weinans, S. Amin Yavari, L.E. Fratila-Apachitei, I. Apachitei, A.A. Zadpoor, Rationally Designed Multifunctional Additively Manufactured Bone Implants, Materials Research Society Spring Meeting, April 2019, Phoenix, USA

I.A.J. van Hengel, N.E. Putra, M.W.A.M. Tierolf, M. Minneboo, A.C. Fluit, H. Weinans, S. Amin Yavari, L.E. Fratila-Apachitei, I. Apachitei, A.A. Zadpoor, Additively manufactured bone implants to prevent implant-associated infection, eCM Orthopaedic Infection Conference, June 2019, Davos, Switzerland

I.A.J. van Hengel, M. Minneboo, L.E. Fratila-Apachitei, I. Apachitei, A.A. Zadpoor, Additive manufacturing and surface biofunctionalization of self-defending bone implants, Netherlands society for Biomaterials and Tissue Engineering Meeting, November 2019, Lunteren, The Netherlands

I.A.J. van Hengel, Additively manufactured implants with multifunctional surfaces, M2i Surface, Interfaces & Coatings Workshop, October 2020, virtual

I.A.J. van Hengel, M. Laçin, M. Minneboo, M.A. Leeflang, L.E. Fratila-Apachitei, I. Apachitei, A.A. Zadpoor, Multi-functional additively manufactured bone implants, World Biomaterials Congress, December 2020, virtual

Poster presentations

I.A.J. van Hengel, Antimicrobial additively manufactured implants, Bioday TU Delft, March 2017, Delft, The Netherlands

I.A.J. van Hengel, M. Riool, L.E. Fratila-Apachitei, J. Witte-Bouma, E. Farrell, A.A. Zadpoor, S.A.J. Zaat, I. Apachitei, Antimicrobial surfaces on additively manufactured porous Ti6Al4V implants, Ameland Summer School Smart Materials, May/June 2017, Ameland, The Netherlands

Honors, awards and popular science publications

2018 Op weg naar zelfverdedigende origami implantaten, presentation with Sebastien Callens at Bessensap, NWO congress on science and science communication

2019 Wat hebben Japanse origami en botimplantaten met elkaar gemeen?, lecture at Universiteit van Nederland with Sebastien Callens

Best Oral Presentation Award, Dutch Biomedical Engineering Conference

NBTE Presentation Award, Conference of Netherlands Society of Biomaterials and Tissue Engineering

2020 Journal cover Journal of Materials Chemistry B

Silver lining of hip implants, TU Delta, Tomas van Dijk

New titanium implants could last a lifetime, Materials Today, Cordelia Sealy

2021 Gewaardeerd! Grant awarded for Science Communication, together with Sebastien Callens, Jinne Geelen, Bart van Trigt and Eline van der Kruk, granted by KNAW

Curriculum Vitae

Ingmar Aeneas Jan van Hengel was born in Driebergen-Rijsenburg, The Netherlands. He graduated from high school with a Gymnasium degree. During high school he obtained a Cambridge Certificate of Proficiency in English. His interest lay in human biology and therefore he pursued a Bachelor's degree in Biomedical Sciences at Leiden University. During this period he followed a half year exchange program at Karolinska Institutet in Stockholm, Sweden and an internship at the department of pneumology at the University of Pisa, Italy. He was a student representative, member of the internal body of the Leiden University Medical Center and co-organizer of the national Biomedical Interfaculty Congress. In addition, he participated in the BW Plus program and part of the Honours Class of Leiden University. He obtained his Bachelor's degree in 2012.

Thereafter, he continued with a Master's in Biomedical Sciences at the same university and conducted research internships at the German Cancer Research Center in Heidelberg, Germany and the Tissue Biology Research Unit in Zurich, Switzerland. During his Master's he worked with fellow students on SkinPrint: a start-up that aimed to 3D print skin tissue for burn wound victims. SkinPrint was awarded a Digital Award by the Philips Innovation Award and a Netexplo Award by the Netexplo Observatory in Paris. His thesis received the 2nd price at the Janneke-Fruin Helb Award from the Leiden University Fund and Leiden University Medical Center Research Award. He graduated with distinction (Cum Laude) in 2014.

During his Master's in Biomedical Sciences, Ingmar became interested in the combination of medicine and technology and therefore took part in a bridging program towards Mechanical Engineering at Delft University of Technology in 2013. In 2014 he started with a Master's in Biomedical Engineering at the 3ME faculty. In 2015 he participated in the iPromedai summer school on antibacterial biomaterials and concluded the Master's program with a thesis on self-defending implants in the Biomaterials and Tissue Biomechanics section under supervision of prof.dr. Amir A. Zadpoor and dr.ir Iulian Apachitei. He graduated in 2016 with distinction (Cum Laude).

In 2017 Ingmar started with his PhD on multifunctional implants at the faculty of Mechanical, Maritime and Materials Engineering under the supervision of prof.dr. Amir A. Zadpoor and dr.ir. Iulian Apachitei. During this PhD trajectory he presented his work on numerous national and international conferences and received Best Presentation Awards at the Dutch Biomedical Engineering Conferences and the Netherlands society for Biomaterials and Tissue Engineering meeting in 2019. He participated in the Ameland summer school on Smart Materials, Advanced Leadership Workshop in Lecco, Italy, and the Clinical Development module of Paul Janssen Futurelab. Furthermore, during the ClinMed summer

school in 2019 he co-developed the Continue! platform: an online patient support platform for the Immanuel Klinik in Berlin. With his colleague Sebastien Callens he participated in science communication activities and they gave presentations to a wide audience including lectures at Bessensap and Universiteit van Nederland.